

---

# Investigation on Porous and Magnetic Properties in Stimuli Responsive Dynamic Metal-Organic Frameworks

---

*A Thesis Submitted for the Degree of*

*Doctor of Philosophy*

*by*

**ARPAN HAZRA**



*Chemistry and Physics of Materials Unit (CPMU)*

**Jawaharlal Nehru Centre for Advanced Scientific Research (JNCASR)**

**(A Deemed University)**

**Bangalore 560064**

***July 2015***



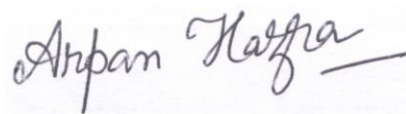
*Dedicated to my family*



# DECLARATION

I hereby declare that the matter embodied in the thesis entitled “*Investigation on Porous and Magnetic Properties in Stimuli Responsive Dynamic Metal-Organic Frameworks*” is the result of investigations carried out by me at the Chemistry and Physics of Materials Unit (CPMU), Jawaharlal Nehru Centre for Advanced Scientific Research (JNCASR), Bangalore, India under the supervision of *Prof. Tapas Kumar Maji* and that it has not been submitted elsewhere for the award of any degree or diploma.

In keeping with the general practice in reporting the scientific observations, due acknowledgements have been made whenever the work described is based on the findings of other investigators. Any omission that might have occurred due to oversight or error in judgment is regretted.



.....  
**Arpan Hazra**

Date: 17/07/15

Place: Bangalore



# CERTIFICATE

I hereby certify that the work described in this thesis "*Investigation on Porous and Magnetic Properties in Stimuli Responsive Dynamic Metal-Organic Frameworks*" has been carried out by Mr. Arpan Hazra under my supervision at the Chemistry and Physics of Materials Unit (CPMU), Jawaharlal Nehru Centre for Advanced Scientific Research (JNCASR), Bangalore, India and that it has not been submitted elsewhere for the award of any degree or diploma.



.....  
**Dr. Tapas Kumar Maji**

(Associate Professor)

(Research Supervisor)

**Dr. Tapas Kumar Maji**  
Associate Professor  
Chemistry & Physics of Materials Unit  
Jawaharlal Nehru Centre for  
Advanced Scientific Research  
Jakkur, Bangalore - 560 064, India.





# ACKNOWLEDGEMENT

Finally it is that time of life for retrospection! A time to say Thank You!

I want to wholeheartedly thank a bunch of people who had a major impact in my life and in the writing of my PhD thesis. It has been seven long years in JNCASR, when I joined as an Integrated PhD student in Chemistry of Physics and Materials Unit (CPMU). Memories after memories keep flashing by as I slowly learnt to deal with various facts of life, of staying miles away from family, of savoring the goodies life offers and most importantly learning the nuances of research life. I have been extremely fortunate to meet quite a few people in this small journey so far, who have influenced my life in more ways than one and I take this opportunity to say a big thank you to all of them!

First and most importantly, I want to thank my parents Mr. Adhir Kumar Hazra and Mrs. Bijoylakshmi Hazra, my sister Mrs. Arpita Bandopadhyay and brother-in-law Mr. Uday Bandopadhyay and all my family members for their never-ending support and instilling in me the lessons of morality and humanity. I am indebted to my parents for their constant encouragement for studies and soar high, keeping my goal fixed. It wouldn't have been possible without them. Thank You!

I want to acknowledge the support and guidance of my supervisor, Prof. Tapas Kumar Maji. The scientific discussions and sharing of ideas have really helped me in developing new thoughts and towards betterment of the work.

Next, I want to thank all my course instructors, Prof. G. U. Kulkarni, Prof. S. Balasubramanian, Prof. N. Chandrabhas, Prof. S. K. Pati, Prof. T. K. Maji, Prof. Eswarmurthy, Prof. N. S. Vidhyadiraja, Dr. Subi George, Dr. T. Govindaraju, Dr. Ranjan Datta, Prof. T. N. Gururao, Prof. S. M. Shivaprasad for giving a clear concept about very new-to-me subjects.

I would like to thank all my excellent collaborators Prof. S. Balasubramanian, Dr. S. K. Reddy, Mr. Satyanarayana Bonakala, Mr. Karthik Bejagam, Mr. Promith, Prof. S. K. Pati and Ms. Arkamita Bandyopadhyay for their cooperation and helpful discussions. I also want to thank Mr. Rana Saha and Mr. Somnath Ghara for helping with the magnetic measurements and Mr. Jiaul Hoque for providing the photoreactor in the initial stage of some experiments.

Of course, how can I forget the immense contribution of my labmates of MOLMAT lab! My present labmates Suresh, Syamantak, Nivedita, Anindita, Papri, Komal, Sohini, SRFs, POCEs ( Salim, Aniket, Aashima) and visiting scientists, and my past labmates Dr. Ritesh Haldar, Dr. K. L. Gurunatha, Dr. Prakash Kanoo, Dr. Sudip Mohapatra always created a vibrant environment inside the lab and outside! I have been fortunate enough for the scientific inputs from them and did learn various things about research work and my field of

study. I would especially like to mention the contributions of Prakash da and Sudip da for helping me since my master's thesis days, and Ritesh for various inputs and exchange of ideas! Discussions, both scientific and unscientific, were always enjoyable with them!

Life outside the lab was equally enjoyable as I have been fortunate enough to make good friends here. They made all these years truly memorable and special mention should be made of Dr. Debabrata Maity, Dr. Arup Chattopadhyay, Dr. Ritesh Haldar, Dr. Sabyasachi Mukhopadhyay, Dr. Pralok Samanta, Dr. Barun Das, Dr. Goutam Chatterjee, Dr. Suman Majumdar, Dr. Partha P. Kundu, Somananda, Moumita, Tarak, Dibyajyoti, Soumyabrata, Ananya, Arkamita, Swastika, Pallabi, Rajkumar, Shubhojit, Jiarul, Amrit, Jiaul, Ashta, Avijit, Abhijit, Rajib, Sisir, Koushik, Dr. Koushik Acharyya, Debasree, Sumanta, Chandradhish, Dheeraj, Anirban, Pawan and Satyanarayan for memories to be cherished forever!

I also want to thank my childhood friends Babul, Debanjan, Arnab, Shawon, Sudeep and Dr. Soumit Sankar Mandal and my Int. PhD batch mates Chidambar, Pandu, Gayatri, Varun, Rana, Sudeshna, Dileep, Sharma, and the seniors and juniors.

Teachers from my schools and college have been my mentors, who instilled in me the love for science and there also goes again the mention of my father, my teacher since childhood. They have been really helpful for shaping me into a better person and I would like to especially mention of Mr. Ashish Choudhury and Sir Harihar Pan. I want to acknowledge Rampur High School, Barchatra Ramkanai Institution (BRKI), Bankura Christian College and JNCASR.

I would also like to thank all the Academic, Administration, Complab, Library, Hostel staff for their everyday efforts for keeping our life smooth in JNCASR, as well as the doctors in our health centre Dhanvantari.

A Big Thank You to Everyone!!!

# PREFACE

The thesis is organized in seven chapters that cover recent developments of dynamic metal-organic frameworks (MOFs) where the physical properties have been tuned by external stimuli. The study demonstrates that how the hexacyanometallate ( $[\text{M}(\text{CN})_6]^{3-/4-}$ ;  $\text{M} = \text{Cr}^{\text{III}}, \text{Fe}^{\text{II/III}}, \text{Mn}^{\text{III}}$ ) can be used as an effecting building block to prepare soft porous crystal to photo-active multifunctional metal-organic frameworks (MOFs).

**Chapter 1** gives a general overview about co-crystals, metal-organic frameworks (MOFs) and their diverse applications in gas storage, separation, magnetism *etc.* This chapter also describes the different strategies to build dynamic porous MOFs and their guest responsive behaviour (particularly magnetism). It also demonstrates the recent development of different stimuli-responsive metal-organic frameworks (MOFs) where the physical property can be modified by employing light.

**Chapter 2** reports the synthesis structural characterization and adsorption properties of five co-crystals obtained from  $[\text{Fe}(\text{CN})_6]^{3-/4-}$  and protonated organic linkers 4,4'-bipyridine (bipy) and 1,2-bis(4-pyridyl)ethylene (bpee). The non-covalent interactions (like H-bonding,  $\pi \cdots \pi$  interaction,  $\text{C}-\text{H} \cdots \pi$  interaction) extends the co-crystals into 3D soft supramolecular porous frameworks. The softness of such co-crystals is realized from the structural change after activating them at two different conditions (mild and extreme) and the soft nature is also reflected from the different solvent vapour adsorption isotherms.

**Chapter 3** comprises of two parts: **Part 3A** demonstrates the synergism of permanent porosity and magnetism based on bimetallic pillared-layer coordination frameworks composed of  $[\text{Cr}(\text{CN})_6]^{3-}/[\text{Mn}(\text{CN})_6]^{3-}$ ,  $\text{Mn}^{\text{II}}$  and 4,4'-bipyridine (bipy) linker. The frameworks show permanent porosity, high heat of hydrogen adsorption and selective uptake of  $\text{C}_2\text{H}_2$  over  $\text{CH}_4$ ,  $\text{C}_2\text{H}_4$  and  $\text{C}_2\text{H}_6$ . Furthermore,  $T_c$  of the frameworks has been modulated with response to guest molecules. In **Part 3B**,  $\text{Zn}^{\text{II}}$  ions has been employed for connecting the hexacyanoferrate ( $[\text{Fe}(\text{CN})_6]^{3-}$ ) and bipy/ 4,4'-azobipyridine (azpy) to construct 3D frameworks where network topology and permanent porosity are controlled by changing the

organic linkers and their stoichiometry. Furthermore, the desolvated frameworks show good CO<sub>2</sub> selectivity over N<sub>2</sub> and CH<sub>4</sub> at ambient conditions. Density functional theory (DFT) based calculations revealed the binding site for the CO<sub>2</sub> molecules in the desolvated frameworks.

**Chapter 4** describes the synthesis and characterization of new 3D photo-responsive pillared layer porous framework composed of [Fe(CN)<sub>6</sub>]<sup>3-</sup>, Mn<sup>II</sup> and 4,4'-azobipyridine. The framework shows selective CO<sub>2</sub> uptake at ambient conditions and most interestingly the adsorbed CO<sub>2</sub> can be released on shining of UV light of wavelength 365 nm. This can be attributed to the deformation of the framework upon UV light irradiation due to the conformation change of the azpy ligand (*trans* to *cis*). The on-demand release of CO<sub>2</sub> using renewable energy such as light is of paramount interest in the current context of environment and energy.

**Chapter 5** demonstrates the synthesis and characterization of a porous magnetic coordination polymer build by [Cr(CN)<sub>6</sub>]<sup>3-</sup>, Co<sup>II</sup> and 1,2-bis(4-pyridyl)ethylene (bpee). We have performed postsynthetic modification (PSM) of the framework by covalent fusion of a guest bpee molecule with a pillared bpee through [2+2] cycloaddition reaction using light. Photo-induced PSM alters the pore size and reveals enhanced CO<sub>2</sub>/N<sub>2</sub> selectivity compare to the un-modified framework. The higher adsorption selectivity of photo-modified framework compared to the assynthesised compound is studied through theoretical free energy calculations, which provide vital insights into the facile adsorption of CO<sub>2</sub> over N<sub>2</sub> in the photo-modified framework. Furthermore, the assynthesized compound shows ferromagnetic ordering with  $T_c = 14.9$  K which changes irreversibly to 8.4 K upon removal of coordinated water and guest molecules. On the contrary, the photo-modified product shows reversible changes of  $T_c$  with response to the water molecule.

**Chapter 6** describes the role of C–H···O interaction on controlling overall adsorption phenomenon in two porous coordination polymers of Cd<sup>II</sup> bridged by bpee and 2,3-pyrazine dicarboxylate. The C–H···O interaction leads to the contraction of pore surface after removing the guest water molecules. But interestingly, in the photo-modified framework, the

absence of C–H···O interaction results structural expansion after dehydration as the 2D layers are moving apart from each other which facilitates the enhanced CO<sub>2</sub> uptake. In another isostructural compound the [2+2] photochemical reaction is subdued by the stronger C–H···O interaction based on the restricted movement of the ethylene carbon atoms. The enhanced gas storage property is also supported by the kinetics measurement based on the methanol adsorption.

**Chapter 7** reports the synthesis of a fluorinated metal-organic framework constructed by using 4,4'-(hexafluoroisopropylidene)bis(benzoic acid), Cd(NO<sub>3</sub>)<sub>2</sub> and 1,2-bis(4-pyridyl)ethene (bpee) as precursors. Due to the presence of –CF<sub>3</sub> functionality, this compound exhibits superhydrophobicity which is established from both water adsorption isotherms and contact angle measurements. After the photo-modification of the framework through [2+2] cycloaddition reaction, it exhibits increased amount of CO<sub>2</sub> uptake at ambient condition. The increased CO<sub>2</sub> uptake in the cyclo-additive MOF is realized due to the enlargement of pore window after photo-modification. The decrease of the diffusion barrier is also supported by the kinetics study based on MeOH adsorption and also correlated by DFT based calculations.



# Contents

<b>Chapter 1</b> .....	1
1.1: A general overview of metal-organic frameworks (MOFs).....	2
1.2: Soft porous crystals .....	6
1.3 Application of metal-organic frameworks .....	8
1.3.1 Small molecules adsorption and separation by MOFs .....	9
1.3.2: Molecular based magnets .....	15
1.3.3: Porous Magnet.....	17
1.4: Postsynthetic Modification of MOFs .....	21
1.5: Photo-induced postsynthetic modification (PSM) by [2+2] cycloaddition reaction....	24
1.6: Scope of this study .....	26
1.7: References .....	27
<b>Chapter 2</b> .....	35
2.1: Introduction .....	39
2.2: Experimental Section .....	41
2.2.1: Materials .....	41
2.2.2: Synthesis .....	41
2.2.3: Physical Measurements .....	48
2.2.4: Single Crystal X-ray Diffraction .....	48
2.2.5: Adsorption Study.....	53
2.3: Results and Discussion.....	53
2.3.1: Crystal Structure Description .....	53
2.3.2: TGA and PXRD analysis.....	65
2.3.3: Adsorption Property .....	68
2.4: Conclusion.....	74
2.5: References .....	75

<b>Chapter 3A</b> .....	83
3.A.1: Introduction .....	87
3A.2: Experimental Section .....	89
3A.2.1: Materials .....	89
3A.2.2: Synthetic procedure .....	89
3A.2.3: Physical Measurements .....	92
3A.2.4: Single Crystal X-ray Diffraction .....	93
3A.2.5: Adsorption Study .....	97
3A.3: Results and Discussion.....	97
3A.3.1: Structural description of 1 ( $\{[\text{Mn}_3(\text{bipy})_3(\text{H}_2\text{O})_4][\text{Cr}(\text{CN})_6]_2 \cdot 2(\text{bipy}) \cdot 3(\text{H}_2\text{O})\}_n$ ): .....	97
3A.3.2: Structural description of $\{[\text{Mn}_3(\text{bipy})_3(\text{H}_2\text{O})_4][\text{Mn}(\text{CN})_6]_2 \cdot 2(\text{bipy}) \cdot 4\text{H}_2\text{O}\}_n$	100
3A.3.3: Structural description of $\{[\text{Mn}_3(\text{bipy})_3(\text{H}_2\text{O})_2][\text{Mn}(\text{CN})_6]_2 \cdot 2(\text{bipy}) \cdot 2\text{H}_2\text{O}\}_n$	101
3A.3.4: Structural description of $\{[\text{Mn}_2(\text{bipy})(\text{CN})][\text{Mn}(\text{CN})_6]\}_n$ .....	102
3A.3.5: Framework stability: Thermogravimetric (TG) and PXRD analysis .....	103
3A.3.6: Adsorption measurement.....	105
3A.3.7: Magnetic Properties .....	116
3A.4: Conclusion.....	122
3A.5: References .....	123

<b>Chapter 3B</b> .....	127
3B.1: Introduction .....	131
3B.2: Experimental Section.....	133
3B.2.2.1 Synthesis of $\{[\text{Zn}_3(\text{bipy})_3(\text{H}_2\text{O})_2][\text{Fe}(\text{CN})_6]_2 \cdot 2(\text{bipy}) \cdot 3\text{H}_2\text{O}\}_n$ .....	133
3B.2.2.2 Preparation of $\{[\text{Zn}_3(\text{bipy})_3][\text{Fe}(\text{CN})_6]_2\}_n$ .....	134
3B.2.2.3 Synthesis of $\{[\text{Zn}_3(\text{bipy})][\text{Fe}(\text{CN})_6]_2 \cdot (\text{C}_2\text{H}_5\text{OH}) \cdot \text{H}_2\text{O}\}_n$ .....	134
3B.2.2.4 Preparation of $\{[\text{Zn}_3(\text{bipy})][\text{Fe}(\text{CN})_6]_2\}_n$ .....	135
3B.2.2.5 Synthesis of $\{[\text{Zn}_3(\text{azpy})_2(\text{H}_2\text{O})_2][\text{Fe}(\text{CN})_6]_2 \cdot 4\text{H}_2\text{O}\}_n$ .....	136
3B.2.2.6 Preparation of $\{[\text{Zn}_3(\text{azpy})_2][\text{Fe}(\text{CN})_6]_2\}_n$ .....	137



3B.2.3: Physical Measurements.....	137
3B.2.4: Single Crystal X-ray Diffraction.....	137
3B.2.5: Adsorption Study .....	142
3B.2.6: Computational Details .....	142
3B.3: Results and Discussion .....	143
3B.3.1 Structural description of $\{[\text{Zn}_3(\text{bipy})_3(\text{H}_2\text{O})_2][\text{Fe}(\text{CN})_6]_2 \cdot 2(\text{bipy}) \cdot 3\text{H}_2\text{O}\}_n$ .....	143
3B.3.2. Structural description of $\{[\text{Zn}_3(\text{bipy})][\text{Fe}(\text{CN})_6]_2 \cdot \text{C}_2\text{H}_5\text{OH} \cdot \text{H}_2\text{O}\}_n$ .....	145
3B.3.3 Structural description of $\{[\text{Zn}_3(\text{azpy})_2(\text{H}_2\text{O})_2][\text{Fe}(\text{CN})_6]_2 \cdot 4\text{H}_2\text{O}\}_n$ .....	147
3B.3.4: Framework stability: Thermogravimetric (TG) and Powder X-ray diffraction (PXRD) analysis .....	149
3B.3.4: Permanent porosity and gas storage property .....	151
3B.3.5: Analysis of Gas Adsorption Isotherms .....	160
3B.4: Conclusion.....	163
3B.5: References .....	164

<b>Chapter 4</b> .....	167
4.1: Introduction .....	171
4.2: Experimental Section .....	173
4.2.1: Materials .....	173
4.2.2: Synthesis.....	173
4.2.2.2: Preparation of $\{[\text{Mn}_3(\text{azpy})_3][\text{Cr}(\text{CN})_6]_2\}_n$ .....	174
4.2.2.3: Synthesis of $\{[\text{Co}_3(\text{azpy})_3(\text{H}_2\text{O})_4][\text{Cr}(\text{CN})_6]_2 \cdot 2(\text{azpy}) \cdot 2\text{EtOH}\}_n$ .....	174
4.2.2.4: Preparation of $\{[\text{Co}_3(\text{azpy})_3][\text{Cr}(\text{CN})_6]_2\}_n$ .....	175
4.2.2.5: Synthesis of $\{[\text{Zn}_3(\text{azpy})_3(\text{H}_2\text{O})_2][\text{Cr}(\text{CN})_6]_2 \cdot 2(\text{azpy}) \cdot 2\text{EtOH}\}_n$ .....	175
4.2.2.6: Preparation of $\{[\text{Zn}_3(\text{azpy})_3][\text{Cr}(\text{CN})_6]_2\}_n$ .....	175
4.2.3: Physical Measurements .....	176
4.2.4: Single Crystal X-ray Diffraction .....	176
4.2.5: Adsorption Study.....	180
4.3: Results and Discussion.....	180
4.3.1: Structural description of $\{[\text{Mn}_3(\text{azpy})_3(\text{H}_2\text{O})_4][\text{Cr}(\text{CN})_6]_2 \cdot 2(\text{azpy}) \cdot 2\text{EtOH}\}_n$ ....	180
4.3.2: Structural description of $\{[\text{Co}_3(\text{azpy})_3(\text{H}_2\text{O})_4][\text{Cr}(\text{CN})_6]_2 \cdot 2(\text{azpy}) \cdot 2\text{EtOH}\}_n$ .....	182

4.3.3: Structural description of $\{[\text{Zn}_3(\text{azpy})_3(\text{H}_2\text{O})_2][\text{Cr}(\text{CN})_6]_2 \cdot 2(\text{azpy}) \cdot 2\text{EtOH}\}_n$ .....	183
4.3.4: Framework stability: Thermogravimetric (TG) and PXRD analysis .....	184
4.3.5 Adsorption Study .....	185
4.4: Conclusion.....	192
4.5: References .....	192
<b>Chapter 5</b> .....	197
5.1: Introduction .....	201
5.2: Experimental Section .....	203
5.2.1: Materials .....	203
5.2.2: Synthesis .....	203
5.2.3: Physical Measurement.....	206
5.2.4: Single Crystal X-ray Diffraction .....	206
5.2.5: Adsorption Study.....	209
5.2.6: Computational details.....	210
5.3: Results and Discussion.....	211
5.3.1: Structural Description.....	211
5.3.2: Framework Stability: Thermogravimetric (TG) and Powder X-ray Diffraction (PXRD) Analysis .....	214
5.3.3: NMR spectra analysis of the bulk powder .....	217
5.3.4: Gas adsorption .....	218
5.3.5: Solvent vapour adsorption study .....	235
5.3.6 Magnetic Property .....	235
5.4 Conclusion.....	239
5.5 References .....	240
<b>Chapter 6</b> .....	247
6.1: Introduction .....	251
6.2: Experimental Section .....	253
6.2.1: Materials .....	253

6.2.2: Synthetic procedure .....	253
6.2.3: Physical Measurements .....	255
6.2.4: Single Crystal X-ray Diffraction .....	255
6.3 Results and Discussion.....	259
6.3.1: Structural Description.....	259
6.3.2 Framework stability: Thermogravimetric (TG) and Powder X-ray diffraction (PXRD) analysis .....	265
6.3.3: Adsorption Study.....	270
6.4: Conclusion.....	279
6.5: References .....	279
<b>Chapter 7</b> .....	283
7.1: Introduction .....	287
7.2: Experimental Section .....	289
7.2.1: Materials .....	289
7.2.2: Synthesis.....	289
7.2.3: Physical Measurements .....	292
7.2.4: Single Crystal X-ray Diffraction .....	293
7.2.5: Adsorption Study.....	295
7.2.6: Computational details .....	296
7.3: Results and Discussion.....	297
7.3.1: Structural description of [ $\{Cd(bpee)(hfbba)\} \cdot EtOH$ ] .....	297
7.3.2: Structural description of $\{Cd_2(rctt-tpcb)(hfbba)_2 \cdot 2H_2O\}$ .....	299
7.3.3: Structural description of [ $\{Co(bpee)(hfbba)\} \cdot EtOH$ ] .....	300
7.3.4: Framework stability: Thermogravimetric (TG) and PXRD analysis .....	300
7.3.5 Gas Adsorption Study.....	302
7.3.6: Computational Study .....	305
7.3.7 Solvent vapor adsorption and superhydrophobicity study of the compounds.....	308
7.3.8 Photo-Physical Study.....	311
7.4: Conclusion.....	312
7.5: References .....	312



# Chapter 1

## *Introduction*



## 1.1: A general overview of metal-organic frameworks (MOFs)

Until the period of mid 1990s, there were mainly two kinds of porous materials, viz. inorganic material and carbon based material. At that time, zeolites and porous carbons were considered as classical porous solids.<sup>1</sup> However, their tedious synthetic conditions and limitations in tuning the porosity forced the scientists to conceive different strategies to discover new materials (Figure 1). The last two decades have witnessed an accomplished development in designing a different type of porous material which is concerned with the linking of metal ions or metal-oxygen clusters (known as secondary building unit (SBU)<sup>2</sup>) with organic bridges by strong chemical bonds to form crystalline, extended structures.<sup>3</sup> This new type of porous materials which are well known as metal-organic frameworks (MOFs) or porous coordination polymers (PCPs) are widely accepted in the scientific community, and creates a colligating bridge between molecular coordination chemistry and materials science. In the history of coordination polymers (CPs), extensive research had been focused only on isolated polyhedral, mononuclear cluster and their different properties. However, very soon it was realized that these isolated structures can be extended to higher dimensionality, giving rise to 1D chain, 2D sheets or 3D framework porous architectures.

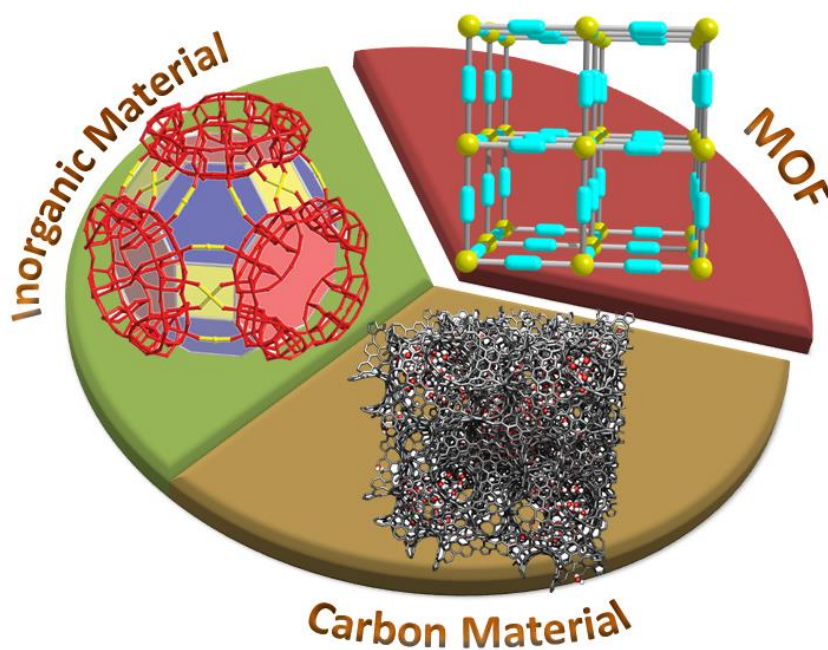


**Figure 1:** Three main classes of porous materials. This figure of the inorganic material has been reproduced with permission from reference 1.

The extension of the MOFs in different direction appears by tethering the metal ions as node and organic linkers as connector. The dimensionality of these materials is solely ascertained by the coordination environment (coordination number) of the metal ions as it depicts the final topology of the system. In this regard, transition metal ions are of popular choice as they can be connected from different directions depending upon their oxidation state and coordination number. A diverse range of architectures can be obtained as these metal centers can easily adopt various geometries like linear, T- or Y-shaped, tetrahedral, square-planar, square pyramidal, trigonal-bipyramidal, octahedral, trigonal-prismatic, pentagonal-bipyramidal and their distorted forms (Figure 2). It is also noteworthy that the coordination environment of such metal centers is dependent on the reaction conditions, solvents organic ligands and the counter anions.<sup>4</sup>

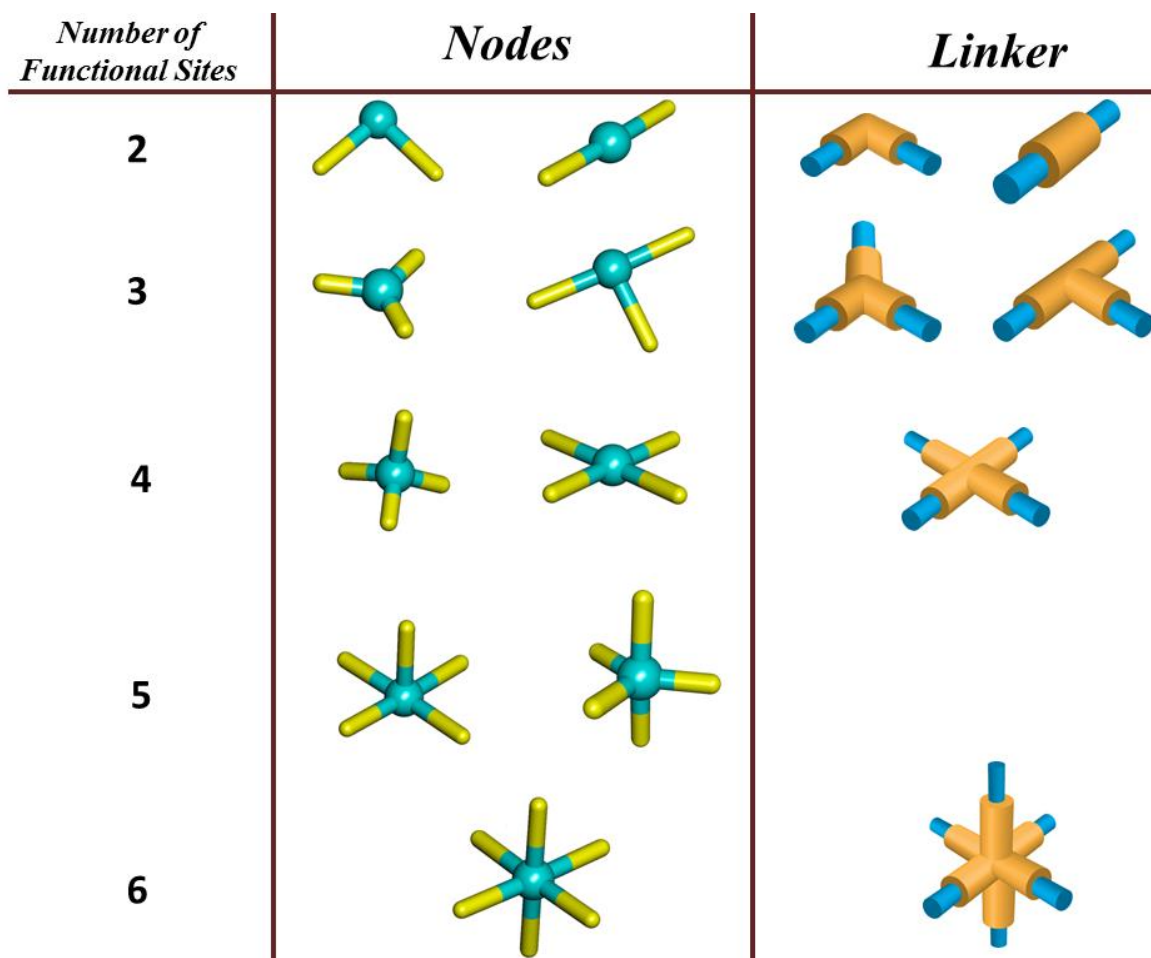


**Figure 2:** Schematic representation of the constituents of metal-organic frameworks (MOFs) with different coordination environment of the metal centers and different geometry of the organic linkers.



Other than the transition metals ions, lanthanide metals have also been employed because of their higher coordination number (varies from 7 to 10) which leads to the formation of metal-organic frameworks (MOFs) with unusual network structure. In this context, use of metalloligand as a node in fabricating metal-organic framework is another popular choice. B. Chen and coworkers has extensively used metallo-porphyrin as a node which is further connected by various organic linkers to obtain higher dimensional porous frameworks.<sup>5</sup> In this thesis, hexacyanometallate has been employed as metalloligand which provides functionality and topological versatility in the structures.

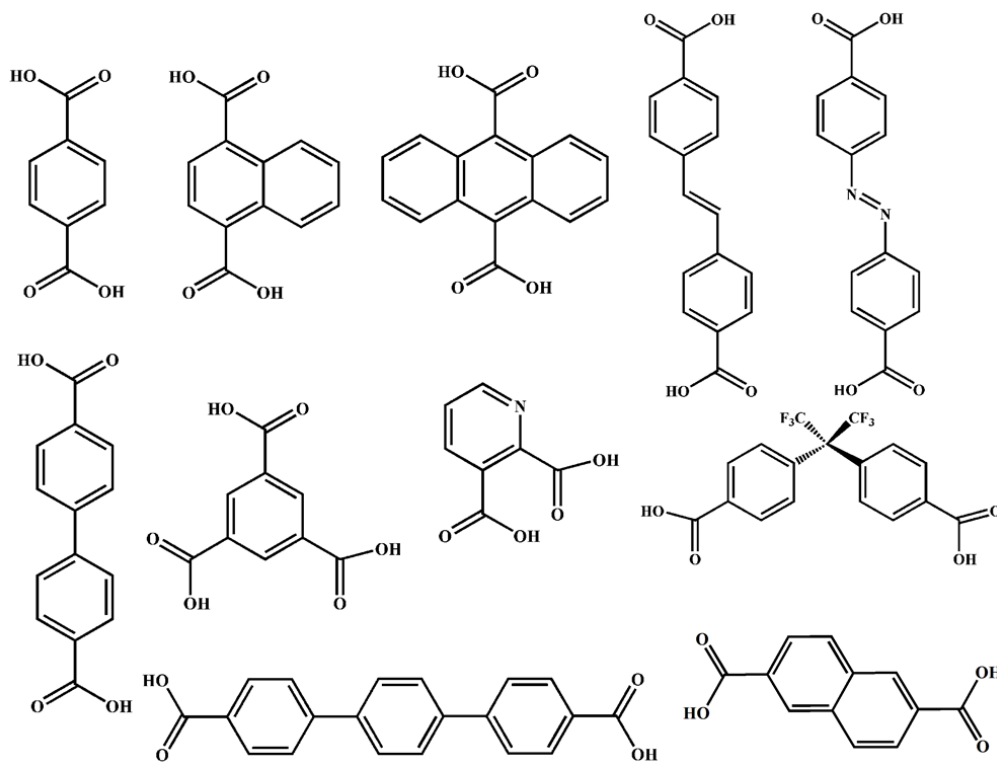


**Figure 3:** Commonly used anionic organic ligands for the construction of higher dimensional MOFs.

Here it is worth mentioning, that the geometry length, charges and the number of binding sites control the pore size (micro as well as the meso) and the surface area of the overall framework material. On the other hand, as presented in Figures 3 and 4, there are enormous choices of the organic linkers and from which one can easily tune the porosity of MOFs from ultramicropore (<0.7 nm) to mesopore (2–50 nm). Furthermore, not only by the pillar lengths but the organic ligands can also be classified according to their charge *viz.* (i) anionic, (ii) cationic and (iii) neutral.<sup>6</sup>

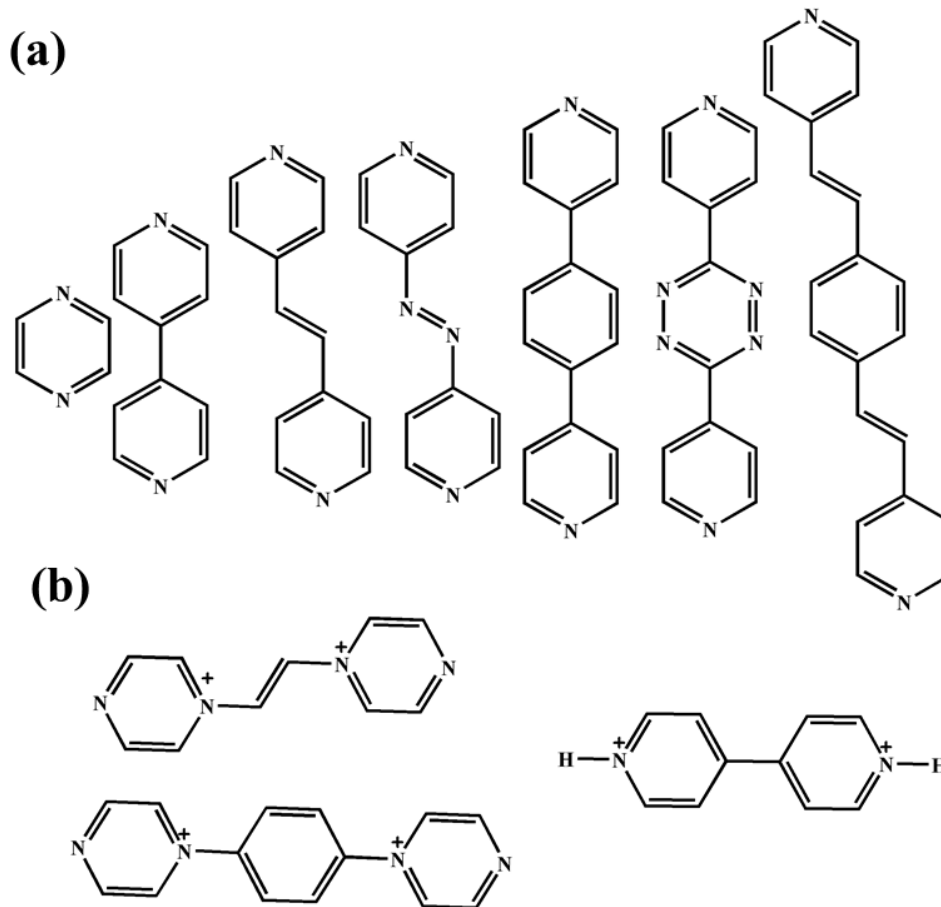


**Figure 4:** Various examples of (a) neutral ligands, and (b) cationic ligands.

Anionic ligands are functionalized with  $-\text{COOH}$ ,  $-\text{OH}$  or  $-\text{SO}_3\text{H}$  groups whereas the neutral linkers contain primarily pyridyl functionality. Cationic ligands are very rare and hence have been used in limited cases. Depending on the pore size, majority of MOFs are in the micropore region, although few mesoporous frameworks have also been reported which are generally unstable upon removal of the solvent molecules.

## ***1.2: Soft porous crystals***

Soft porous crystals are the porous solids which possess both a highly ordered network and structural transformability. They can exhibit themselves as bistable or multistable crystalline materials with long-range structural ordering, reversible transformability between the different states, and permanent porosity. The term permanent porosity refers to the fact that, at least one crystal phase possesses space that can be occupied

by guest molecules, so that the framework exhibits reproducible guest adsorption. It is a well-known fact that strong non-covalent interactions *viz.*, H-bonding and  $\pi$ - $\pi$  interactions are prerequisite for the stability of functional supramolecular networks. For example, Maji *et al.* reported the structural determination of compound  $\text{Co}(\text{bpee})_2(6\text{-me-}2,3\text{-pyrdcH})_2$  where each monomer is engaged in bi-directional H-bonding ( $\text{O}-\text{H}\cdots\text{N}$  and  $\text{C}-\text{H}\cdots\text{O}$ ) interaction to form a 2D supramolecular rectangular grid (Figures 5a and 5b).<sup>7</sup> These rectangular grids further undergo 3-fold interpenetration which results in a 2D interpenetrated supramolecular framework with small hydrophobic pores (Figure 5c).

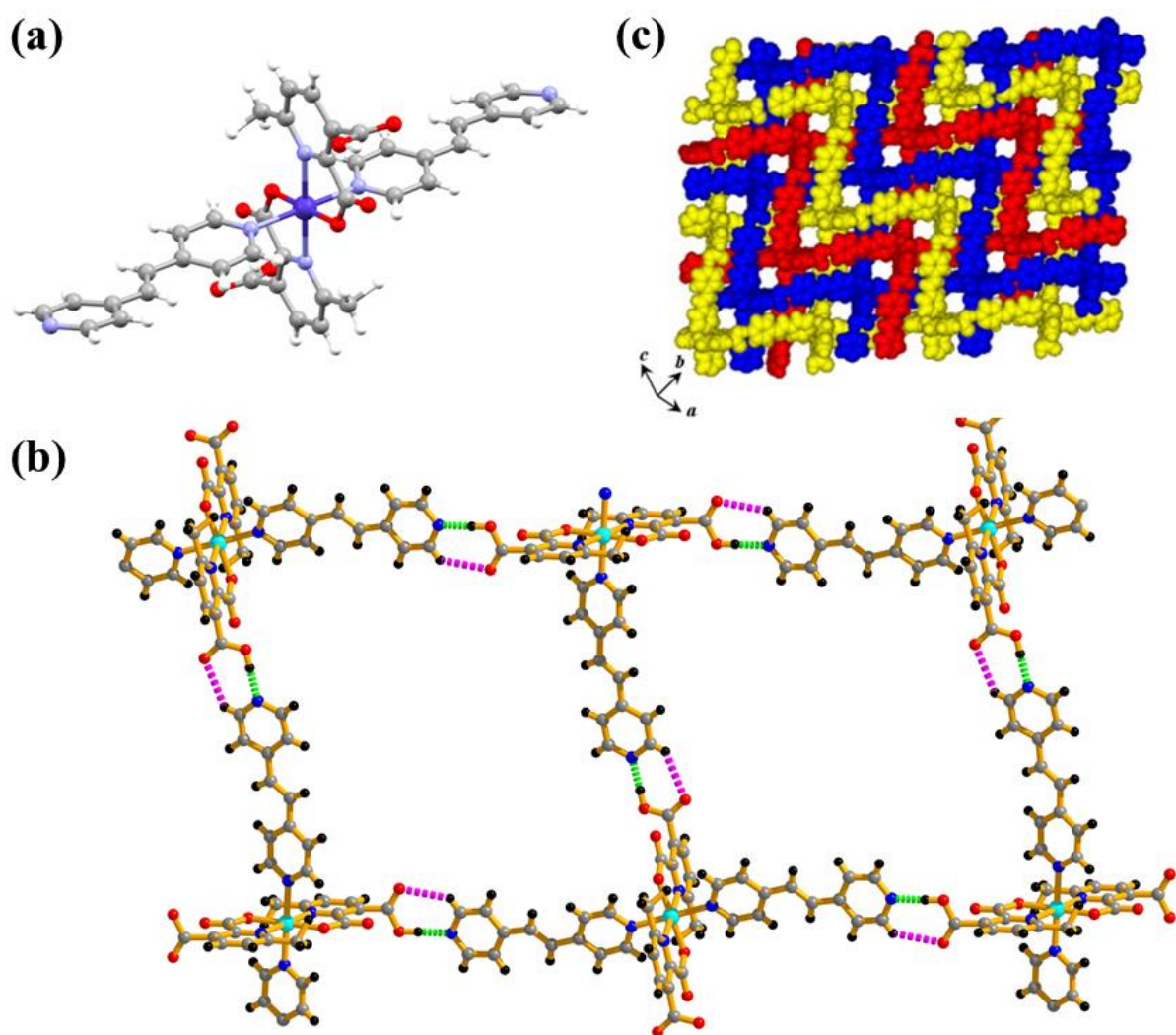


**Figure 5:** (a) monomer complex of  $\text{Co}(\text{bpee})_2(6\text{-me-}2,3\text{-pyrdcH})_2$  (b) formation of rectangular grid by  $\text{O}-\text{H}\cdots\text{N}$  (light green dotted line) and  $\text{C}-\text{H}\cdots\text{O}$  (pink dotted line) H-bonding. (c) 2D 3-fold interpenetrated supramolecular framework. Figure (c) has reproduced from ref 7 with permission.

Therefore, it is very crucial to choose molecular subunits whose structure and functions can be tuned using appropriate strategies with the help of crystal engineering. For this purpose, we have deliberately chosen hexacyanometallate  $[M(CN)_6]^{y-}$  as one of the effective building unit for the design and synthesis of novel supramolecular architecture.

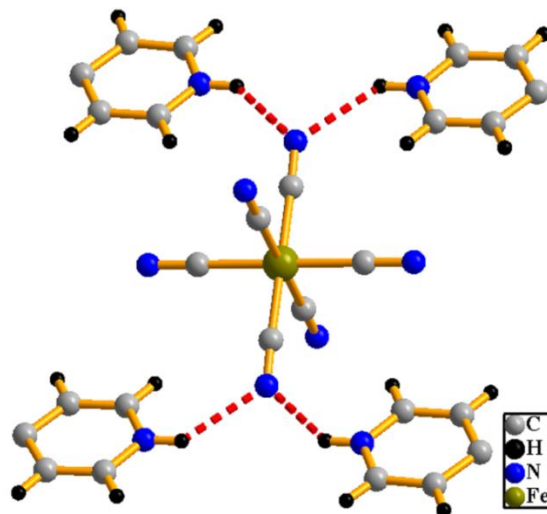


**Figure 6:** Figure shows H-bonding interaction with  $[Fe(CN)_6]^{4-}$  and heterocyclic aromatic molecules.

The nitrogen end of cyanide ligands can play the role of a good acceptor to form H-bonding with other donor atoms. As for example, it can be easily connected with protonated heterocyclic aromatic molecules through H-bonding which leads to 2D or 3D supramolecular structure (Figure 6). Beside this, small molecules like  $H_2O$ ,  $CH_3CN$  can also easily form H-bonding with hexacyanate leading to 1D or 2D array which has an immense importance in forming supramolecular structure based on non-covalent interactions. Such soft supramolecular networks would show interesting guest responsive properties and also can function as novel optical and magnetic material.

### **1.3 Application of metal-organic frameworks**

The last decade has already experienced MOFs as an attractive class of materials on account of their potential application in the arena of magnetism, heterogeneous catalysis, ion exchange, drug delivery, sensing, gas storage and separation.<sup>8</sup> These highly porous ordered materials have established themselves as one of the best storage and separating material due to their high crystallinity, large surface area, tunable pore surface and functionalizable pore

walls.<sup>9</sup> Furthermore, these highly periodic polymeric networks possess tunable pore surface where heterogeneous catalysis or separation of gas and industrially important isomers are also possible. In the interest of this thesis mostly the porous, magnetic properties and postsynthetic modification of MOFs have been discussed in detail.

### **1.3.1 Small molecules adsorption and separation by MOFs**

Contributing to their exceptional structural and chemical tenability, MOFs have recently come under intensive study for use as solid-state adsorbents in gas storage application. Towards the synthesis of some outstanding materials, MOFs have found a large number of applications in the field of separation and storage of small molecules (*e.g.* CO<sub>2</sub>, O<sub>2</sub>, H<sub>2</sub> and C1-C4 hydrocarbons). Judicious choice of metal ions/clusters and organic linkers with various length and directionality has enabled the job easier for us to construct MOFs with different pore structure and properties. Synthesis of these types of materials is quite straightforward allowing effective functional groups into the framework which favors in meliorating interaction of adsorbate molecules with pore surface. Last two decades have seen enormous growth in the design and synthesis of MOF materials with tunable surface area and modifiable pore size for the storage of small molecules. However, it is still far from practical applications, therefore rational approaches need to be undertaken for the synthesis new material, which is quite challenging.

#### **1.3.1.1: MOFs as Hydrogen storage materials**

The use of hydrogen as a clean energy substituting for fossil fuels is still hindered due to the lack of a convenient, safe and cost-effective storage system.<sup>10</sup> In this respect, the porous property of MOFs is gaining increased attention with time and the framework materials have emerged as an excellent storage alternative at high pressure under cryogenic temperature.<sup>8a, 11</sup> Unfortunately, the performance of these materials is greatly decreased at ambient temperature due to weak physisorptive interactions between the internal pore surface and the hydrogen molecules. In fact, the isosteric heat of H<sub>2</sub> adsorption of these materials typically lies in the range of  $-5$  to  $-7$  kJ mol<sup>-1</sup>, which is far below from the optimal value of  $-20$  -  $25$  kJ mol<sup>-1</sup> for a sorbent operating between 1.5-30 bar at 298 K.<sup>12</sup> One of the

promising approaches for achieving stronger framework-H<sub>2</sub> interactions is to study MOF with exposed

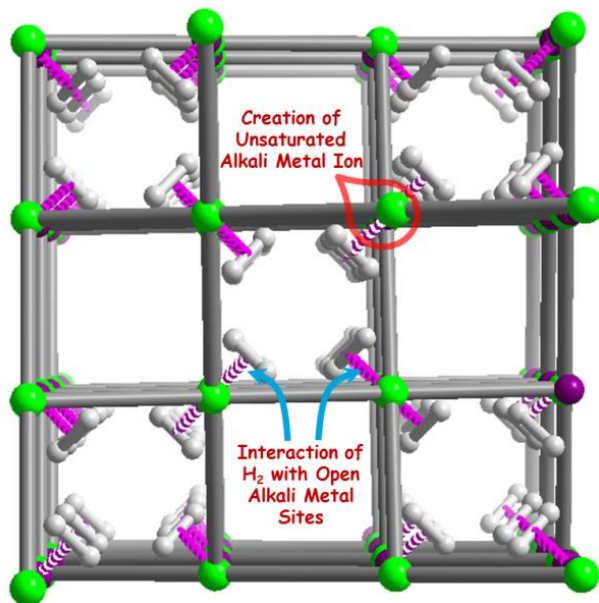


**Figure 7:** Schematic diagram shows the adsorption of hydrogen by unsaturated metal centers.

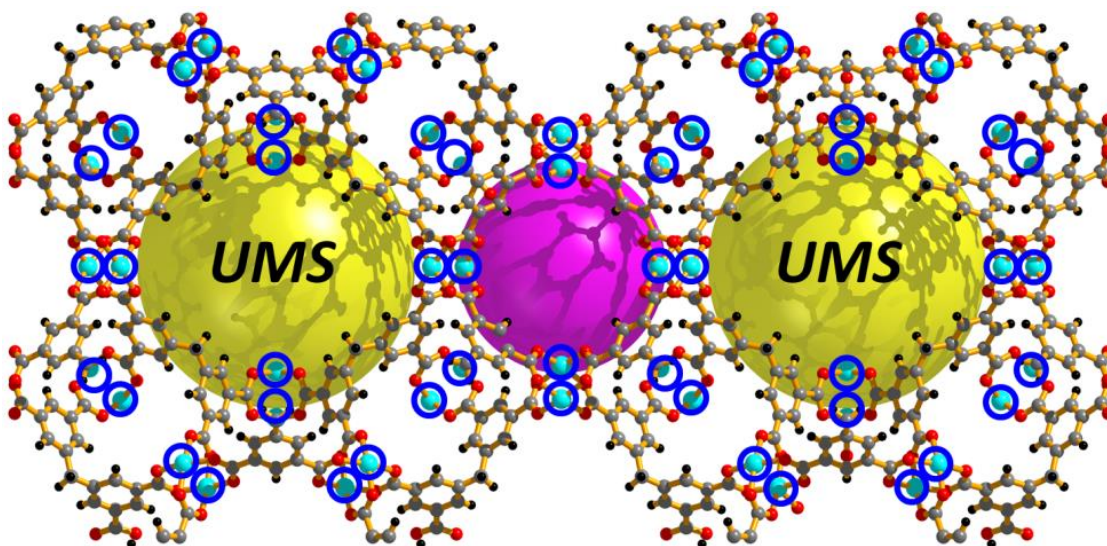


**Figure 8:** Increasing the density of Unsaturated Metal Sites (UMSs) in a cage like porous framework can effectively lead towards the high MOF-H<sub>2</sub> interaction which would be a key strategy to store H<sub>2</sub> at ambient temperature.

metal cation sites, particularly of light cations with a high charge density (Figure 7).<sup>13</sup> This was first demonstrated in  $\text{Mn}_3[(\text{Mn}_4\text{Cl})_3(\text{BTT})_8]_2$ , which contains open  $\text{Mn}^{2+}$  coordination sites and exhibits an isosteric heat of H<sub>2</sub> adsorption of  $10.1 \text{ kJ mol}^{-1}$  at zero coverage of

uptake (Figure 8).<sup>14</sup> Till date, the highest isosteric heat of H<sub>2</sub> adsorption reported for a metal–organic framework is 15.3 kJ mol<sup>-1</sup>, as observed in a compound based on Mn<sup>II</sup> unsaturated sites.<sup>8a, 13a, 15</sup> The direct evidence of H<sub>2</sub> binding to the metal center is very limited, however only very few examples are structurally characterized where hydrogen molecules are interacting with UMSs of MOFs.<sup>15d, 16</sup> The strong interaction of hydrogen is also observed in {Ni<sub>5</sub>O<sub>2</sub>(btb)<sub>2</sub>} ( btb = benzene-1,3,5-tribenzoate), where  $\Delta H$  value for individual H<sub>2</sub> binding site is -13.5 kJ mol<sup>-1</sup>.<sup>16</sup>

### **1.3.1.2: CO<sub>2</sub> capture and separation by MOFs**

CO<sub>2</sub> is the main greenhouse gas emitted from the combustion of fossil fuels in power plants and automobiles and is considered as a major threat in the context of global warming. The relationship between atmospheric CO<sub>2</sub> and increased temperature has been well recognized and the effect of increasing atmospheric CO<sub>2</sub> concentration on global warming is now regarded as one of the most crucial environmental issue. The development of viable carbon capture and sequestration technologies (CCSTs) is a scientific challenge of the highest priority.<sup>5,6,17</sup> Currently, amine scrubbing has widely been used to separate CO<sub>2</sub> from the flue gas (composition: 12.5-12.8% CO<sub>2</sub>, 6.2% H<sub>2</sub>O, ~4.4% O<sub>2</sub>, 50 ppm CO, 420 ppm NO<sub>x</sub>, 420 ppm SO<sub>2</sub>, and 76-77% N<sub>2</sub>)<sup>18</sup> in the power plant. In this technology, at ambient temperature, CO<sub>2</sub> molecules are allowed to adsorb in a low volatile aqueous amine solution.<sup>19</sup> Then the adsorbed CO<sub>2</sub> is regenerated by stripping with water vapor at 100° C to 120°C and hence it reveals the difficulty in breaking the amine–CO<sub>2</sub> carbamate bonds. As a result, this method consumes as much as ~40% of the production costs during the liberation of adsorbed CO<sub>2</sub> from the sorbent materials.<sup>20</sup> To overcome this problem, a diverse range of materials like zeolites, activated carbons and graphene exists for physisorption based capture of CO<sub>2</sub> at different conditions. However, amongst all the available materials, metal-organic frameworks have shown to exhibit exceptional CO<sub>2</sub> storage capacity under equilibrium conditions where pure CO<sub>2</sub> is introduced into the pores.<sup>21</sup> It is worth mentioning that the CO<sub>2</sub> storage capacity of MOFs have outperformed any other porous materials mentioned above in terms of volumetric storage capacity. Recently, Millward and Yaghi reported room temperature adsorption equilibrium data for CO<sub>2</sub> in a large variety of metal-organic

frameworks.<sup>22</sup> MOF-177 was shown to have a volumetric adsorption capacity for CO<sub>2</sub> that was substantially higher than that of commercial materials such as zeolite 13X and activated carbon powder. In a recent breakthrough, led by Yaghi and coworkers have produced two new versions MOF-200 and MOF-210 that can store twice the volume of gases.<sup>23</sup> MIL-100 and MIL-101 represent the two first examples of crystallized hybrid solids with mesoporous cages useful for CO<sub>2</sub> capture. MIL-100<sup>24</sup> is a tri-dimensional trivalent metal-1,3,5- benzenetricarboxylate (BTC) (M = Al<sup>III</sup>, Cr<sup>III</sup>, Fe<sup>III</sup>). Concerning CO<sub>2</sub>, the value of heat of adsorption ( $-62 \text{ kJ mol}^{-1}$ ) is the highest reported so far for the adsorption of this gas on a MOF sample ( $-35 \text{ kJ mol}^{-1}$  for instance in HKUST-1). This shows the relatively strong interaction of this probe molecule with the MOF surface. In a recent elegant example, Long *et al.* suggest the feasibility of high temperature (70 °C) CO<sub>2</sub> uptake in a porous MOF post-synthetically functionalized by a amine linker through the interaction with unsaturated metal sites.<sup>25</sup>

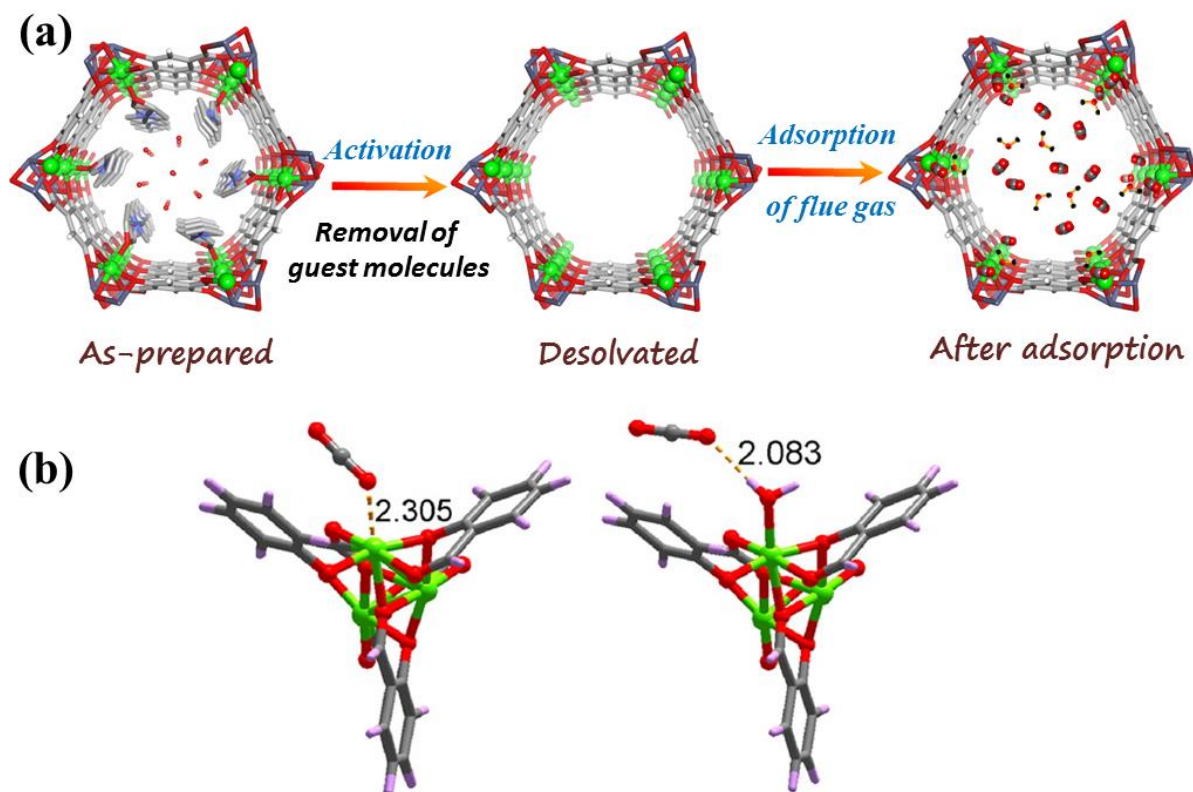


**Figure 9:** (a) The CO<sub>2</sub> adsorption performance of highly porous MOF, MOF-74 reduces drastically in presence water vapour. (b) The water molecules readily coordinate with the unsaturated metal centers (UMSs) and hence reduce the CO<sub>2</sub>-MOF binding energy. The second part of the image has been reproduced with permission of ref. 30.



But to determine the practical CO<sub>2</sub> storage efficiency of such material, the experiment should be executed in the presence of liquid water or moist air condition. Regeneration of the MOF materials with similar uptake capacity and high stability under working condition are also very important. Unfortunately the reported materials in the literature have depicted limited execution on practical gas storage applicability as they have the tendency towards degradation upon exposure to water.<sup>14, 26</sup> An example will illustrate this problem. Mg-MOF-74, reported by Matzger and co-workers<sup>27</sup>, provides an exceptional CO<sub>2</sub> uptake capacity at ambient condition which is turned out to be 23.6 wt % at 0.1 atm and 35.2 wt % at 1 atm.<sup>27-28</sup> But Keskin *et al.* first pointed out about the co-adsorption of H<sub>2</sub>O during the separation of CO<sub>2</sub> from flue gas.<sup>29</sup> It was found that the CO<sub>2</sub> adsorption capacity is decreased by the presence of water molecules as they can easily linked with the unsaturated Mg<sup>II</sup> sites. As a consequence of this, the binding energy between CO<sub>2</sub> and the framework decreases as the new binding energy is related with the CO<sub>2</sub> and water coordinated Mg-MOF74 framework. (Figure 9)<sup>30</sup> To overcome the limitation, new generation MOFs are featured with organic ligands equipped with hydrophobic groups which will create a hydrophobic external surface for restricting the entry of water molecules in to the pores.<sup>31</sup> But the main drawback of this approach is that the long alkyl chains will simultaneously decrease the effective pore volume and thus the storage capacity will be diminished. In an another approach, Kitagawa *et al.* have demonstrated a new strategy to synthesize superhydrophobic MOF by featuring a predominant surface which is decorated with the aromatic hydrocarbons moiety.<sup>31a</sup>

However it shows water vapour adoption behaviour and thus restricts the CO<sub>2</sub> storage capacity under humid conditions. This will be a reduction of CO<sub>2</sub> separation performance from a flue gas mixture where a typical 4% of water vapor is present. To subdue this limitation, fluorinated metal-organic frameworks (FMOFs) would be a new class of advanced porous material whose pore surface is embedded with fluoride functionality that endues hydrophobicity into the system.<sup>32</sup> The fluoride groups not only works as a water resistant but also it can interact strongly with CO<sub>2</sub> molecules by electrostatic interactions.<sup>33</sup> The hydrophobic nature of the fluorine-lined pore surface offers an unprecedented opportunity to enhance the affinity of the material towards CO<sub>2</sub> molecule in presence of liquid water or water vapour.<sup>34</sup> Recently, Maji *et al.* have reported an unusual CO<sub>2</sub> adsorption behavior of a

fluoro-functionalized MOF  $\{[\text{Zn}(\text{SiF}_6)(\text{pyz})_2] \cdot 2\text{MeOH}\}_n$  demonstrating higher  $\text{CO}_2$  uptake at 298 K than 195 K. This result reveals a strong interaction of  $\text{CO}_2$  with F atoms of  $\text{SiF}_6^{2-}$  groups which is also supported by DFT calculation.<sup>34c</sup>

Use of less carbon intensive fuels *e.g.* natural gas<sup>35</sup> will help the environment by emitting lesser amount of  $\text{CO}_2$  where the major component of natural gas is  $\text{CH}_4$ . But  $\text{CO}_2$  is often found as a major impurity in natural gas and its presence can reduce the efficiency. The appropriate solution of this problem is to find separate storage materials for pure  $\text{CO}_2$  and  $\text{CH}_4$  and it is also important to separate them from their mixture. Apart from that, separation between different gas mixtures like  $\text{N}_2/\text{O}_2$ ,  $\text{N}_2/\text{H}_2$ ,  $\text{N}_2/\text{CH}_4$  is also a challenging job for material scientists.

### **1.3.1.3: Separation of hydrocarbons by MOFs**

Separation between alkyl-aromatic compounds BTEX (benzene, toluene, ethyl benzene and xylene isomers) is another challenging issue in petroleum industry because of the similarity of their boiling points (*e.g.* *p*-xylene: 138 °C, *m*-xylene: 138–139 °C, and ethylbenzene: 136 °C) makes it difficult to separate the isomers.<sup>36</sup> Similarly another example of separation where hexane isomers are separated<sup>37</sup> to boost octane ratings in gasoline has been a very important process and predominantly practiced by cryogenic distillation which is found to be costly. Using traditional methods like cryogenic distillation for the separation of small hydrocarbons is very energy consuming and inefficient process. In this regard, adsorption based separation of hydrocarbons might lead to advanced technologies where the implementation of Pressure Swing Adsorption (PSA), Temperature Swing Adsorption (TSA) and adsorbent based membrane devices will reduce the cost of separating hydrocarbons from a natural gas feedstock.

Since the old-hat processes are energy consuming and cost effective, there is an increasing demand to develop novel materials and technologies as an alternative trial. Recently, Zhu and co-workers<sup>38</sup> synthesised a new material which selectively adsorbs *p*-xylene over the other two isomers. By fine tuning the pore size they have smartly included *p*-xylene in a selective manner. Denayer *et al.* has reported the study of vapour adsorption (*p*-xylene, *m*-xylene, *o*-xylene, and ethylbenzene) of MIL-47 where they have shown (Figure

10) the effect of temperature on adsorption coefficient.<sup>39</sup> Long *et al.* has demonstrated MOF ( $\text{Fe}_2(\text{dobdc})$  ( $\text{dobdc}^{4-} = 2,5\text{-dioxido-1,4-benzenedicarboxylate}$ )) with excellent performance for separation of ethylene/ethane and propylene/propane mixtures at 318 K.

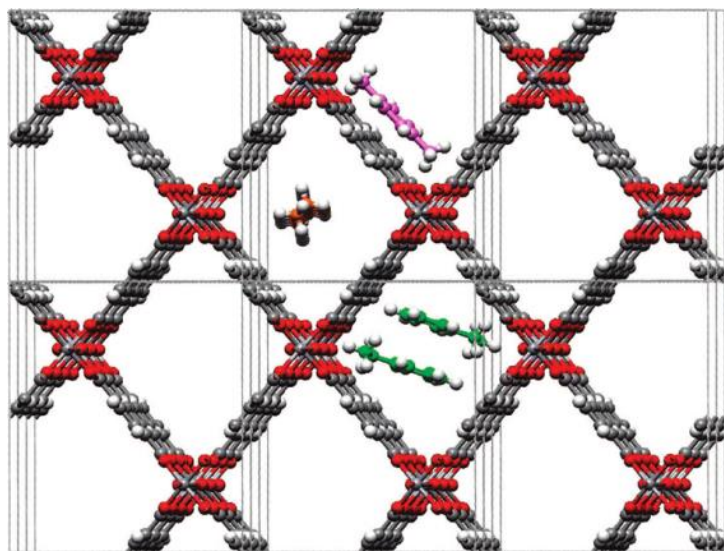


**Figure 10:** The MIL-47 framework with octane (orange), *p*-xylene (purple), and ethylbenzene adsorbed inside its uni-dimensional pores (grey lines indicate the borders of a unit cell). The image has been reproduced with permission of ref. 39.

From the neutron diffraction powder data they have confirmed a side-on coordination between the alkene  $\pi$  clouds and unsaturated  $\text{Fe}^{\text{II}}$  sites. This study reveals that the strong interaction of unsaturated metal sites (UMSs) with the olefinic hydrocarbons is leading towards the selective uptake of alkenes over their corresponding alkane isomers.<sup>40</sup>

### 1.3.2: Molecular based magnets

Magnetism is explained as a phenomenon by which a material exerts attractive or repulsive forces on other materials. Some well-known materials that exhibit easily detectable magnetic property, so called magnets are nickel, iron, cobalt and their alloys. In this regard, the synthesis of molecular based magnets like coordination compounds and metal-radical complexes have obtained considerable amount of interest in the past three decades as they can exhibit spontaneous magnetization. However, the synthesis of molecular based magnets with Curie temperature ( $T_c$ ) close to room temperature remains a challenge as the  $T_c$  of reported compounds are far below of 298 K. To obtain such material, a chemically linked

three-dimensional (3D) network is essential where the distance between the moments carriers (metal centers) should be short for propagating strong exchange interaction. In this aspect, magnetism can be implemented into the MOFs by incorporating magnetic moment carriers such as paramagnetic metals centers connected through small organic linkers.<sup>41</sup> Hence, the capability of cyanide linker to bind two metal centers in linear fashion through two different binding sites has made them more suitable for demonstrating interesting magnetic property.<sup>42</sup> Besides, the binding capability from both ends, soft (nitrogen end) and hard (carbon end) donating sites, giving an opportunity to develop a highly adjustable smart magnetic material only by changing the metal centers (Figure 11). As a result, the linear bridging arrangement originates the possibility to predict the final magnetic exchange coupling<sup>43</sup> between the metal centers where the unpaired spin density from symmetric metal-based orbitals ( $t_{2g}-t_{2g}$  or  $e_g-e_g$ ) will lead towards antiferromagnetic interaction.

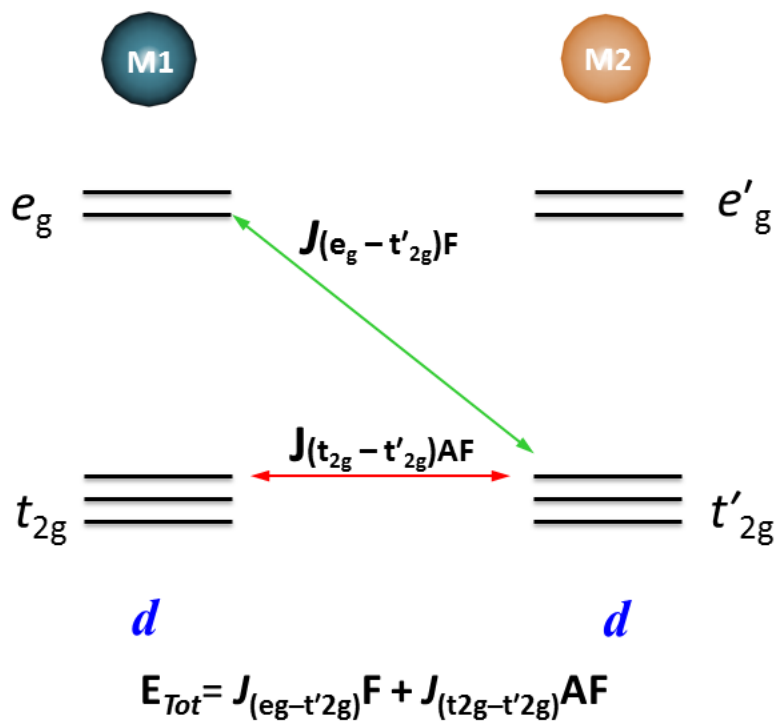


**Figure 11:** Schematic representation of the superexchange interaction between two different transition metal centers separated by cyanide bridges.

On the contrary, spin density from orthogonal orbitals ( $t_{2g}-e_g$ ) will result a net ferromagnetic exchange interaction via Hund's rule.<sup>44</sup> In addition, simultaneous presence of both exchange interactions in a single system will lead towards the ferrimagnetic behaviour and as well as

canted antiferromagnetism. In such synergism, Prussian blue analogues<sup>45</sup> are the most well studied cyano-based frameworks which depicted the combined potential application of magneto-porous,<sup>46</sup> magneto-opto<sup>47</sup> or magneto-electro<sup>48</sup> materials. Thus, hexacyanometallate ( $[M(CN)_6]^{y-}$ ) can be used as metalloligand which can further connect to other metal centers to form a magnetic platform. Now the magnetic layers can be linked through different exobidentate linkers to invoke porosity. The interesting aspects like guest induced magnetic phase transition, tunable  $T_c$  or  $T_n$  of such bimetallic frameworks can be exhibited by rationally designed porous materials based on this inorganic metalloligand.<sup>49</sup>

### 1.3.3: Porous Magnet

Multifunctional materials, *i.e.*, materials which possess a set of well-defined properties (opto-electronic, opto-porous or magneto-porous *etc.*), are of great interest in modern science.<sup>50</sup> The possible synergism between different functionalities furnishes the opportunity to unearth novel physical phenomenon of smart multifunctional materials. However, it is a significant challenge to develop such material that possess programmable structure with chemical functionalities and also offer modulation of their physical properties towards the fabrication of multifunctional materials. In this regard, the combinations of magnetism with other properties like optical property, chirality, conductivity or even porosity has drawn an immense interest to the scientist.<sup>51</sup> Porous magnet is a class of molecular materials where synergism of porosity and magnetic properties has been observed.<sup>32b, 52</sup> Synthesis of microporous solids that behaves as a magnet remains an open challenge as structural demands for high spin density to achieve long range magnetic ordering conflict with those for porosity. But it is interesting to note that, synergism of permanent porosity and magnetism within a framework would open up the prospect of development of magnetic sensors and low-density magnetic materials.<sup>52d, 53</sup> Some fascinating properties like guest dependent modulation of magnetic ordering temperature ( $T_c$ ), spin crossover or guest responsive reversible magnetic phase transition have been realized in magnetic porous frameworks.<sup>49b, 54</sup> So it is expected that, slight change in the coordination environment of the metal center during the dehydration-rehydration procedure will exhibit significant changes in magnetic exchange coupling of such magneto-porous system. Therefore, single crystal structural determination of such materials at various states after guest removal or re-

introduction would be a powerful tool to illuminate the structure-property relationship of such system. But unfortunately, crystal which is able to retain its single crystallinity after guest removal is very rare in the literature. In this context, Kurmoo *et al.* have reported guest dependent magnetic property of a double-walled porous framework,  $[\text{Co}^{\text{II}}_3(\text{lac})_2(\text{pybz})_2] \cdot 3\text{DMF}$  (pybz = 4-pyridyl benzoate, lac = *D*- and *L*-lactate).<sup>52b</sup> Single crystal structure analysis reveals that, the framework structure is not altered during the exchange of guest DMF with water molecules.

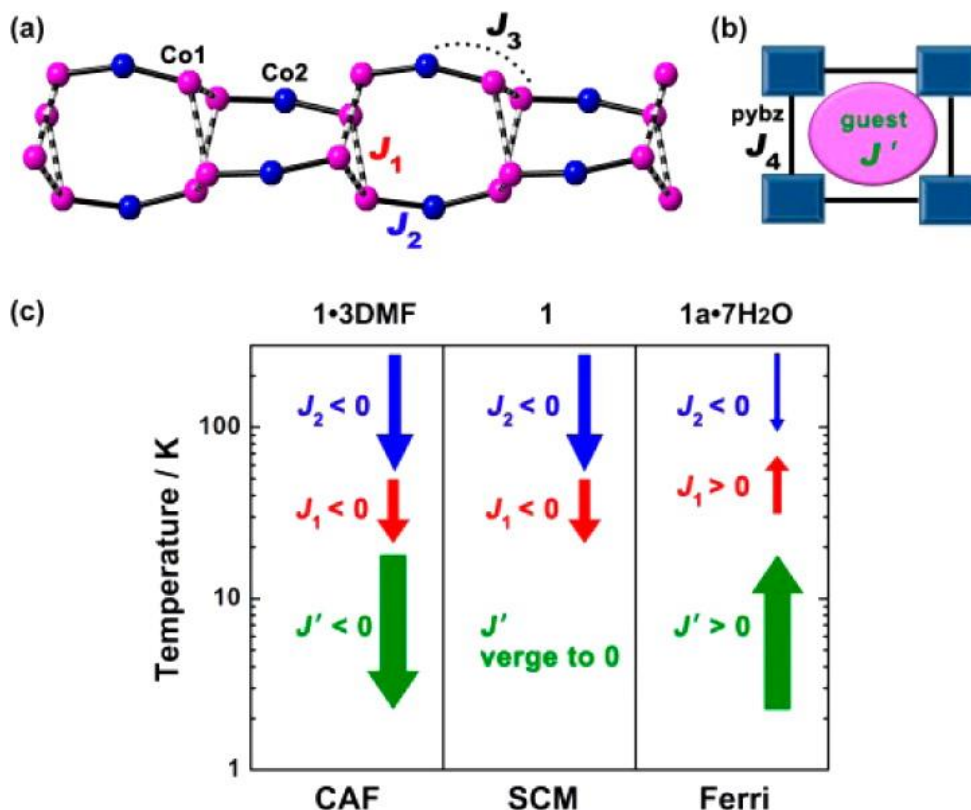


**Figure 12:** Representation of the (a) intrachain exchange interactions of  $J_1$ ,  $J_2$ , and  $J_3$  and (b) interchain exchange interactions of  $J_4$  and  $J'$ . (c) The operative temperature region of relatively strong interaction of  $J_1$ ,  $J_2$ , and  $J'$  to model the magnetic ground states. This figure has been reproduced with permission from ref 52b.

This is a rare example of different magnetic ground state in any material, canted antiferromagnets for  $[\text{Co}^{\text{II}}_3(\text{pybz})_2(\text{lac})_2] \cdot \text{solvent}$ , single-chain magnet for the desolvated  $[\text{Co}^{\text{II}}_3(\text{pybz})_2(\text{lac})_2]$  as  $J'$  approached 0 and ferrimagnet for  $[\text{Co}^{\text{II}}_3(\text{pybz})_2(\text{lac})_2] \cdot 7\text{H}_2\text{O}$  as  $J' > 0$  (Figure 12). In another work, Maji *et al.* have reported the guest induced magnetic modulation of a multifunctional metal-oxalate framework  $\{\text{KDy}(\text{C}_2\text{O}_4)_2(\text{H}_2\text{O})_4\}_n$  composed of two different metal centers.<sup>51a</sup> The dehydrated framework shows permanent porosity

which is revealed from the solvent vapour adsorption study. Interestingly, this compound exhibits guest responsive reversible magnetic phase transition (ferromagnetic to antiferromagnetic and *vice versa*) upon dehydration-rehydration procedure (Figure 13). This compound shows slow magnetic relaxation behavior with energy barrier (417 K) which can be attributed to the single ion anisotropy of  $\text{Dy}^{\text{III}}$  and interestingly slow relaxation as well as energy barrier remains similar in the dehydrated antiferromagnetic state.

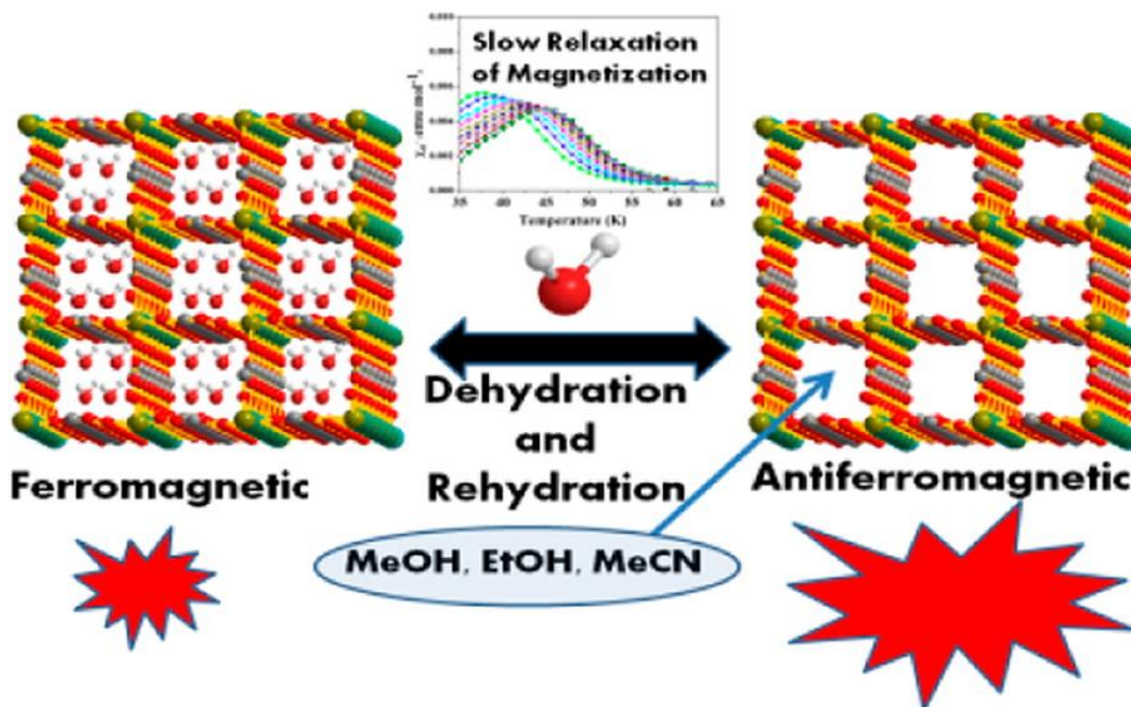


**Figure 13:** Solvent Induced Change in Structure and the corresponding Magnetic Properties in  $\{\text{KDy}(\text{C}_2\text{O}_4)_2(\text{H}_2\text{O})_4\}_n$ . This figure has been reproduced with permission from ref 51a.

Prussian blue analogues are the most known and studied cyanide-based frameworks, and constitute one of the most promising classes of potentially porous magnetic materials. In these compounds, octahedral  $[\text{M}'(\text{CN})_6]^{x-}$  complexes are linked via octahedrally-coordinated, nitrogen-bound  $\text{M}^{y+}$  ions to give a 2D sheet of mixed metals connected via cyanide linker. These 2D layers can be further connected by the pending cyanide linkers to grow along the 3rd direction (Figure 14). With a suitable choice of the transition metal ions M and M', a number of Prussian blue analogues with high magnetic ordering temperatures have been elaborated, reaching up to 376 K for  $\text{KV}[\text{Cr}(\text{CN})_6]_2 \cdot 2\text{H}_2\text{O}$ .<sup>55</sup> Furthermore, based on empirical

and theoretical studies, the nature (ferro- versus antiferro-) and an estimation of the strength of the magnetic coupling through the cyanide bridges can be predicted, facilitating rational design of the magnetic properties of these compounds.

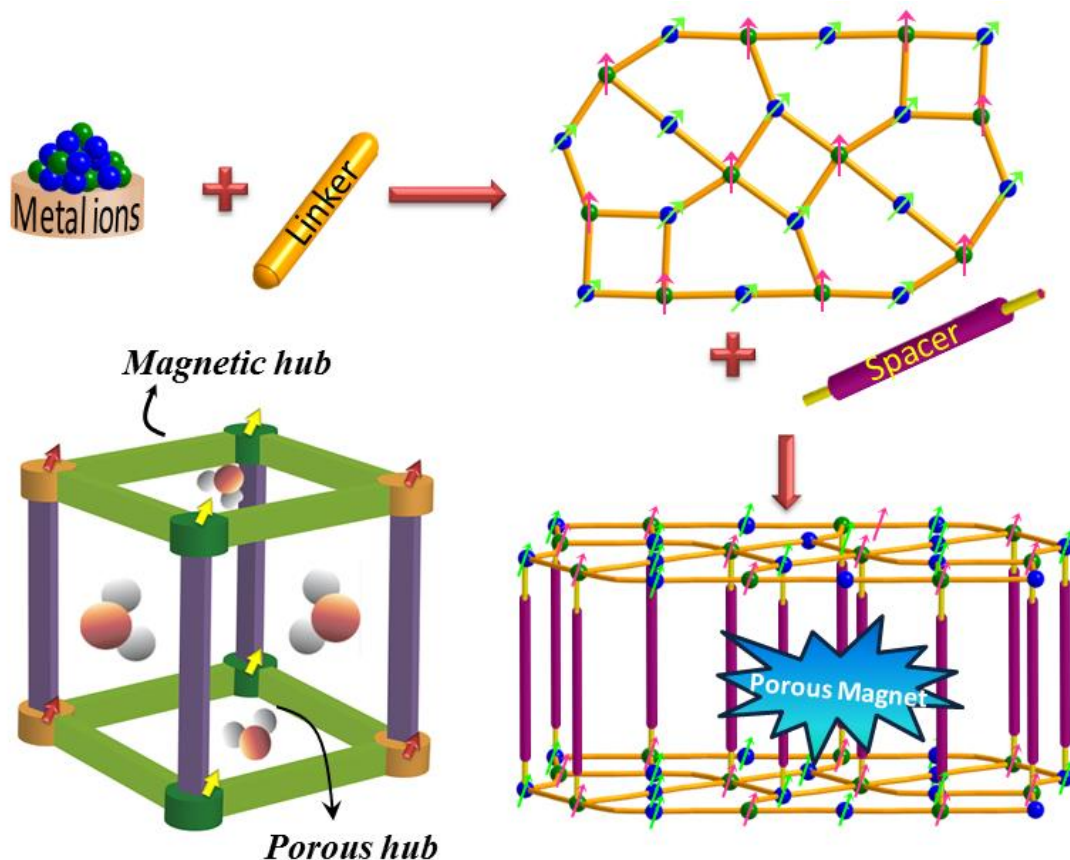


**Figure 14:** Schematic diagram of the preparation of porous magnet by employing hexacyanometallate as a metalloligand.

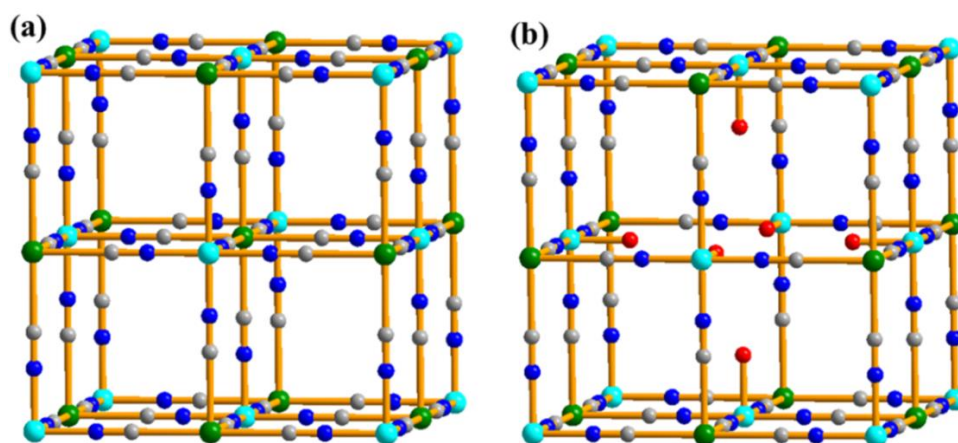


**Figure 15:** (a) Portion of the crystal structure of the Prussian blue analogues  $M^{II}_3[M^{III}(CN)_6]_2$  and (b)  $A^I M^{II}[M^{III}(CN)_6] \cdot nH_2O$ .



Depending on the stoichiometry  $M'/M$  and the respective oxidation states, the structure can also contain monocationic counterions, located in the cavities of the cubic structure. When such vacancies are present, the available coordination sites on  $M$  are occupied by bound water molecules (Figure 15). Other water or small solvent molecules can also be embedded within the pores of the cubic framework. These facts motivate us into thinking that if we can link these 2D layers by any organic linker then magnetic and porosity both can be combined into a single framework. It is worth mentioning that this type of material demands high impact in the field of molecular magnetism and sensor based material.

### 1.4: Postsynthetic Modification of MOFs

It is of substantial interest to augment the physical and chemical properties of MOFs by functionalizing the pore surface. In order to receive better host-guest interaction, incorporation of functionality in MOFs has been performed by modifying the organic ligand with specific functional groups and using them during the desired framework synthesis.

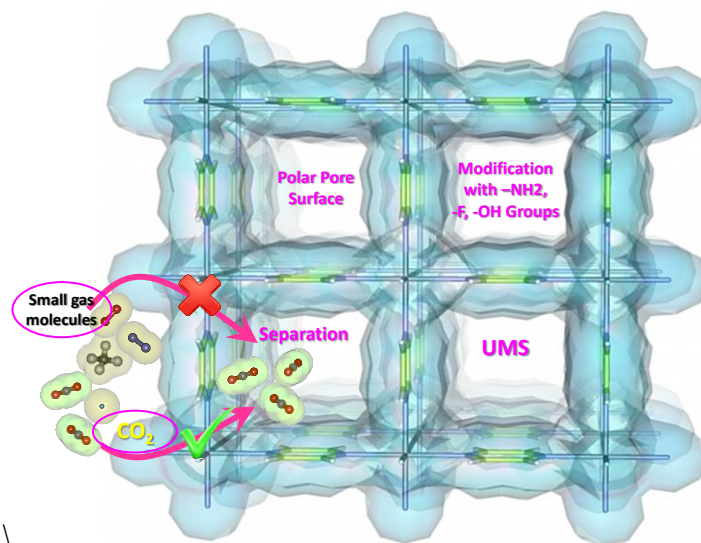


**Figure 16:** Schematic representation of postsynthetic modification of a porous framework by grafting functional groups in the backbone to execute selective CO<sub>2</sub> adsorption.

Following this strategy, MOFs having organic ligands with pendent groups like -NH<sub>2</sub>, -Br, -NO<sub>2</sub> and other substituents have been prepared where the pore surface is

decorated with either electron donating or withdrawing functionalities (Figure 16). As for example, MOF-5, reported by Yaghi *et al.*, constructed from  $Zn^{II}$  and 1,4-benzene dicarboxylic acid (1,4-BDC) is highly porous in nature and contains 55% of void space with respect to the total cell volume.<sup>56</sup> Now, introducing different functionalities such as  $-Br$ ,  $-NH_2$ ,  $-OC_3H_7$ ,  $-OC_5H_{11}$ ,  $-C_2H_4$ , and  $-C_4H_4$  in the BDC linker, a series of new MOF structures has been obtained where the pore volume along with the nature of pore surface has been systematically tuned.<sup>57</sup> Despite having success in obtaining MOFs with different functionalities *via* direct solvothermal synthesis, the scope of further improvement by changing the metal centers or tuning the length of the linker in the structure is limited by this approach. This is mainly because of the fact that, some functional groups are not compatible or stable in the high temperature condition or the obtained framework structure is not the desired one. Sometime, due to the lack of sufficient crystallinity in the final product, the structural characterization process becomes difficult. Hence to devise materials with desired functionalities, postsynthetic modification of MOF is a popular choice in recent times and was first postulated in 1990 by Robson *et al.*<sup>58</sup>

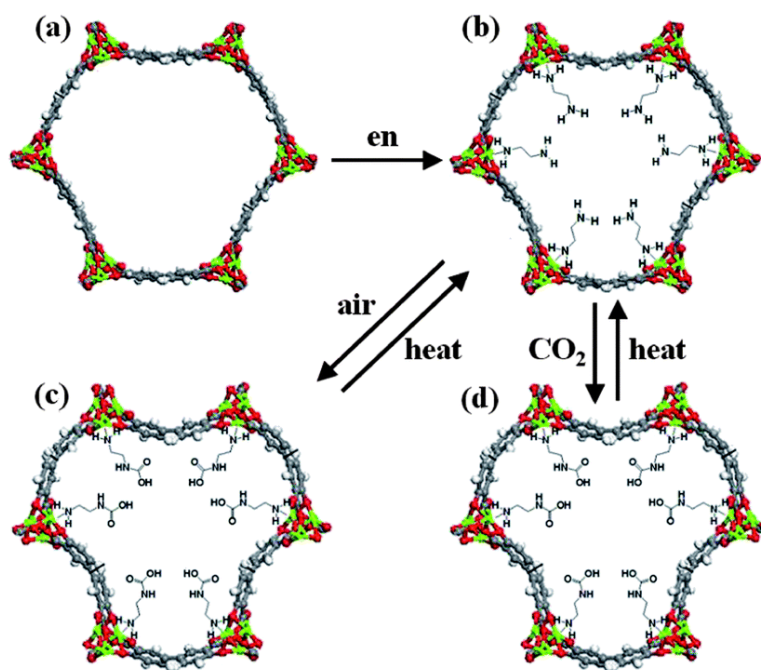


**Figure 17:** (a) and (b) postsynthetic modification of Mg-MOF-74 by engrafting amine group in to the unsaturated  $Mg^{II}$  sites. (c) and (d) PSM improves the  $CO_2$  adsorption capacity of the modified MOF-74 as it can uptake  $CO_2$  in the humid condition. Ref 62 and The Royal Society of Chemistry (RSC) are acknowledged for giving the permission of reproduction.

Since then, several groups, mainly Cohen and his coworkers have extensively worked on the modification of the framework structure by chemical reaction which was executed postsynthetically.<sup>59</sup> Modification of the pore surface has also been performed postsynthetically by engrafting functional groups into backbone of the framework.<sup>31b, 60</sup> As previously mentioned that Mg-MOF74 is one of the several MOF materials with high CO<sub>2</sub> adsorption capacities at the low to moderate CO<sub>2</sub> partial pressures. But it has been observed that, the uptake capacity of this material significantly reduced in presence of moisture due strong Mg<sup>II</sup>-UMS-H<sub>2</sub>O interaction.<sup>61</sup> To overcome this problem, Hong *et al.* functionalized this framework postsynthetically with the primary amine group (en-Mg<sub>2</sub>(dobpdc); en = ethylenediamine) (Figure 17).<sup>62</sup> It is very interesting to note that, this compound adsorbs a significant amount of CO<sub>2</sub> (3.62 mmol g<sup>-1</sup>, 13.7 wt%) at 0.15 bar in the humid condition, whereas the performance of CO<sub>2</sub> adsorption of the mother compound (Mg-MOF74) is very poor in presence of water vapour.

Recently, Farha *et al.* has reported solvent assisted ligand exchange (SALE) of a pillared-paddlewheel metal-organic framework where the porosity of the material has been increased by changing the pillar length from 9 Å to 17 Å (Figure 18).<sup>63</sup> In another example, stepwise exchange strategy has been utilized to prepare a series of IRMOF-100 analogues. In situ ligand exchange with progressively longer dicarboxylate linkers has been performed where the pore volume of the IRMOF100 has been increased from 2.83 cc/g to 4.36 cc/g in IRMOF102 (micropore to mesopore).<sup>64</sup>

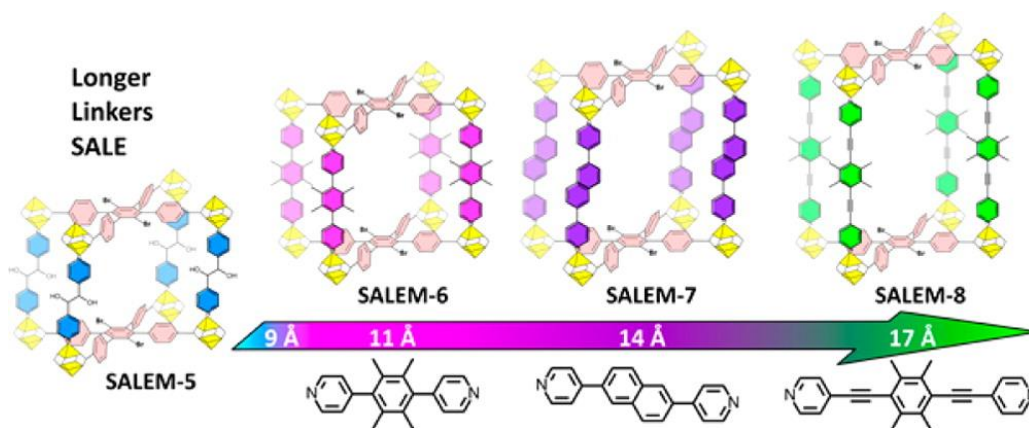


**Figure 18:** Schematic representation of stepwise postsynthetic ligand exchange of non-interpenetrated porous MOF. The figure is reproduced with permission from ref. 63.

But, postsynthetic modification of organic ligand in tedious reaction condition is yet another challenging job as there is a chance of degradation of the framework architecture. In this regard, the implementation of light as an effective low cost, non-destructive external modulator would be an alternative choice for such PSM of the pore surface.<sup>65</sup> The photo-induced PSM of framework have been reported by several groups where the *cis-trans* isomerization of either a coordinated<sup>66</sup> or a guest<sup>67</sup> azo functionalized linkers ( $-N=N-$ ) led to the amendment of the pore surfaces as well as properties. Such photo-induced PSM will open a new horizon in the arena of material science where the desired functionality can be comprehended in a green way.

### **1.5: Photo-induced postsynthetic modification (PSM) by [2+2] cycloaddition reaction**

Photo-induced [2+2] cycloaddition reaction is a popular choice for postsynthetic modification (PSM) toward the modification of size and polarity of pore surface in metal-organic frameworks.<sup>68</sup> The *exo-bidentate* organic spacer 1,2-bis(4-pyridyl)ethylene (bpee), is one of the preferred organic linkers for investigating topochemical cycloaddition reaction and several reports of [2+2] cycloaddition reactions in MOFs have been reported.<sup>69</sup> This solvent-less photochemical reaction is the unique green way to synthesize region- or stere-specific highly strained cyclobutane ring.<sup>68a, 68b, 69f, 69i, 70</sup>

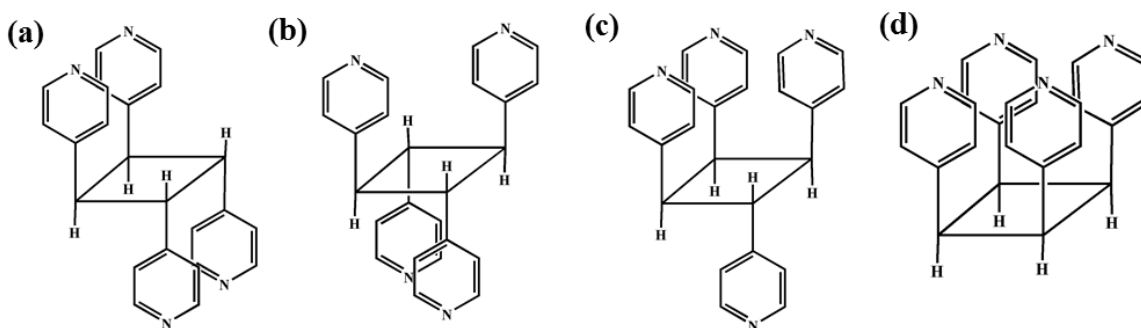


**Figure 19:** Pictorial representations of the possible region-isomers of tetrakis(4-pyridyl)cyclobutane (tpcb). Here *rctt*, for example, means *region, cis, trans, trans* and the geometrical isomers are described with reference to a single pyridyl group, in a clockwise manner.

In the recent days, the reactions followed by the formation and/or breaking of covalent bonds in the MOFs are of particular interest because they extend the possibility of

producing regio- or stereospecific organic ligands (Figure 19).<sup>69g, 70e, 71</sup> This type of structural transformations is generally accompanied with molecular rearrangement (*e.g.* rotation, bending, swinging, sliding, shrinking, or swelling) in the crystal<sup>72</sup> and as a consequence it becomes difficult to study the single-crystal-to-single-crystal (SCSC) transformation through X-ray diffraction. The single crystal has to endure such stresses during the SCSC transformation period as this is the only available tool to perform an unequivocal study over the reaction pathway and the final products in the solid state.<sup>40, 54, 73</sup> So, further advancement in this area is necessary for detailed understanding over the solid state reactions. Single-crystal-to-single-crystal transformations as a result of photo-induced reaction are another important part of this research field. Of these photo-induced structural transformations, [2+2] photodimerization of olefinic C=C bonds in various organic moiety and metal complexes has been widely studied during the past few decades.<sup>69f, 69h, 69i, 70a, 74</sup>

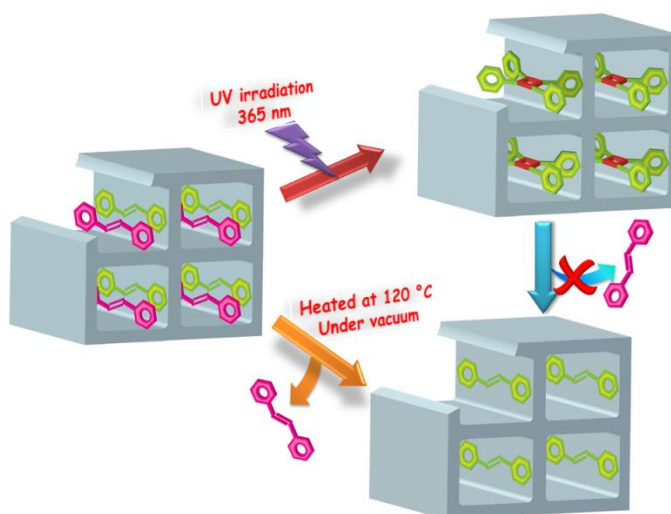


**Figure 20:** Schematic representation of porous MOF where [2+2] photoreaction can be employed for fine tuning the pore size.

In order to facilitate such [2+2] cycloaddition reaction, a pair of olefin groups must satisfy the topochemical criteria of Schmidt<sup>75</sup> which says that the planes of neighboring C=C bonds should be approximately parallel and separated by less than 4.2 Å.<sup>76</sup> [2+2] photocycloaddition reaction in coordination polymer is an emerging topic where the introduction of photo-active organic ligands will give the opportunity of easy post-synthetic modification in the framework along with a subsequent alteration of the physical properties.<sup>5b, 68b, 68c, 70d</sup> However, in higher order coordination polymers, the dimerization reactions occurring in a SCSC fashion has rarely been studied due to the restricted movement

of the C=C bonds in the pillared organic ligands. Recently Vittal and coworkers<sup>70b, 77</sup> have used various organic linkers as a backbone of MOFs where two or multiple double bonds are aligned in parallel fashion for the photodimerization reaction in solid state (Figure 20). Kitagawa *et al.* has employed these solid state [2+2] reactions to fine tune the pore surface of CPs which depicts excellent selective uptake of gas molecules.<sup>68c</sup>

## 1.6: Scope of this study

Structural modulation and tuning the porosity of MOF has been extensively studied during the last two decades. Along these lines designing of new ligands or building new SBUs would be a key to assemble new porous structures. Individual applications of MOFs in the field of adsorption of small molecules, magnetism, drug delivery, sensing catalysis has widely been reported in the literature. But application of MOFs in the practical condition for sequestering of CO<sub>2</sub> or separation of hydrocarbons from a mixture is yet a challenging assignment. Especially, removing CO<sub>2</sub> from the industrial flue gas is restricted due to the water-stability issue of MOFs and hence it should be addressed properly by preparing some water resistant highly porous networks. In this thesis, some MOFs have addressed this problem by selectively capturing CO<sub>2</sub> in presence of water vapour. Not only the adsorption of CO<sub>2</sub> by MOF materials, but the thesis also has described the release of the adsorbed gas molecules in a green and cost effective way. In this purpose, light has been employed as an external stimulus which facilitates the removal of CO<sub>2</sub> molecules by changing the conformation (*trans* to *cis*) of the azo groups. By adopting this strategy, one can apply MOF material as a molecular sponge for on-demand release of gas molecules.

There are handful of examples of multifunctional materials which combine a set of well-defined properties like magneto-porous, magneto-optical or magneto-electronic properties. There are several compounds described in the thesis which are multifunctional in nature. Mainly, I have focused to prepare magneto-porous material which has a wide impact on guest induced magnetic modulation and sensing applications. The second half of the thesis has addressed a new arena MOF by employing [2+2] photochemical reaction on tuning the pore volume and nature of pore surface of various MOFs. For the first time, the effect of [2+2] photochemical reaction has been documented on tuning the pore size of the porous

framework which further depicted an increased CO<sub>2</sub> selectivity in the photo-modified framework. This thesis manifests a better understanding on the strength of C–H···O interaction on controlling the photo-reaction and adsorption processes. The photoreaction also modifies a framework from non-porous to porous one with respect to CO<sub>2</sub> adsorption in the ambient condition.

## 1.7: References

1. N. Withers, *Nature*, 2010, **464**, 366.
2. D. J. Tranchemontagne, J. L. Mendoza-Cortes, M. O'Keeffe and O. M. Yaghi, *Chem. Soc. Rev.*, 2009, **38**, 1257.
3. (a) O. M. Yaghi, H. Li, C. Davis, D. Richardson and T. L. Groy, *Acc. Chem. Res.*, 1998, **31**, 474; (b) L. R. MacGillivray, R. H. Groeneman and J. L. Atwood, *J. Am. Chem. Soc.*, 1998, **120**, 2676; (c) T. P. Vaid, E. B. Lobkovsky and P. T. Wolczanski, *J. Am. Chem. Soc.*, 1997, **119**, 8742; (d) O. M. Yaghi, G. Li and H. Li, *Nature*, 1995, **378**, 703; (e) G. B. Gardner, D. Venkataraman, J. S. Moore and S. Lee, *Nature*, 1995, **374**, 792; (f) T. E. Mallouk, *Nature*, 1997, **387**, 350; (g) B. F. Abrahams, B. F. Hoskins and R. Robson, *J. Am. Chem. Soc.*, 1991, **113**, 3606; (h) M. J. Zaworotko, *Nature*, 1997, **386**, 220; (i) S. L. James, *Chem. Soc. Rev.*, 2003, **32**, 276.
4. (a) T. R. Whitfield, X. Wang, L. Liu and A. J. Jacobson, *Solid State Sci.*, 2005, **7**, 1096; (b) O. M. Yaghi and H. Li, *J. Am. Chem. Soc.*, 1996, **118**, 295.
5. (a) L. X. Chen, X. Zhang, E. C. Wasinger, J. V. Lockard, A. B. Stickrath, M. W. Mara, K. Attenkofer, G. Jennings, G. Smolentsev and A. Soldatov, *Chem. Sci.*, 2010, **1**, 642; (b) M. L. Shelby, M. W. Mara and L. X. Chen, *Coord. Chem. Rev.*, 2014, **277–278**, 291.
6. (a) J.-W. Cheng, S.-T. Zheng and G.-Y. Yang, *Inorg. Chem.*, 2007, **46**, 10261; (b) S. Horike, K. Kishida, Y. Watanabe, Y. Inubushi, D. Umeyama, M. Sugimoto, T. Fukushima, M. Inukai and S. Kitagawa, *J. Am. Chem. Soc.*, 2012, **134**, 9852; (c) M. Higuchi, K. Nakamura, S. Horike, Y. Hijikata, N. Yanai, T. Fukushima, J. Kim, K. Kato, M. Takata, D. Watanabe, S. Oshima and S. Kitagawa, *Angew. Chem. Int. Ed.*, 2012, **51**, 8369.
7. K. L. Gurunatha and T. K. Maji, *Inorg. Chim. Acta*, 2009, **362**, 1541.
8. (a) L. J. Murray, M. Dinca and J. R. Long, *Chem. Soc. Rev.*, 2009, **38**, 1294; (b) P. Horcajada, C. Serre, G. Maurin, N. A. Ramsahye, F. Balas, M. a. Vallet-Regí, M. Sebban, F. Taulelle and G. r. Férey, *J. Am. Chem. Soc.*, 2008, **130**, 6774; (c) J. Lee, O. K. Farha, J. Roberts, K. A. Scheidt, S. T. Nguyen and J. T. Hupp, *Chem. Soc. Rev.*, 2009, **38**, 1450; (d) S. Achmann, G. Hagen, J. Kita, I.

- Malkowsky, C. Kiener and R. Moos, *Sensors*, 2009, **9**, 1574; (e) D. Hermann, H. Emerich, R. Lepski, D. Schaniel and U. Ruschewitz, *Inorg. Chem.*, 2013, **52**, 2744; (f) J. J. Gassensmith, J. Y. Kim, J. M. Holcroft, O. K. Farha, J. F. Stoddart, J. T. Hupp and N. C. Jeong, *J. Am. Chem. Soc.*, 2014, **136**, 8277.
9. B. Li, Y. Zhang, R. Krishna, K. Yao, Y. Han, Z. Wu, D. Ma, Z. Shi, T. Pham, B. Space, J. Liu, P. K. Thallapally, J. Liu, M. Chrzanowski and S. Ma, *J. Am. Chem. Soc.*, 2014, **136**, 8654.
10. (a) L. Schlapbach and A. Züttel, *Nature*, 2001, **414**, 353; (b) P. E. de Jongh, *Nature Mater.*, 2011, **10**, 265.
11. K. M. Thomas, *Dalton Trans.*, 2009, 1487.
12. (a) S. K. Bhatia and A. L. Myers, *Langmuir*, 2006, **22**, 1688; (b) E. Garrone, B. Bonelli and C. Otero Areán, *Chem. Phys. Lett.*, 2008, **456**, 68; (c) C. O. Areán, S. Chavan, C. P. Cabello, E. Garrone and G. T. Palomino, *ChemPhysChem*, 2010, **11**, 3237.
13. (a) M. Dincă, A. Dailly, Y. Liu, C. M. Brown, D. A. Neumann and J. R. Long, *J. Am. Chem. Soc.*, 2006, **128**, 16876; (b) K. Sumida, S. Horike, S. S. Kaye, Z. R. Herm, W. L. Queen, C. M. Brown, F. Grandjean, G. J. Long, A. Dailly and J. R. Long, *Chem. Sci.*, 2010, **1**, 184; (c) H. R. Moon, N. Kobayashi and M. P. Suh, *Inorg. Chem.*, 2006, **45**, 8672; (d) A. Vimont, J.-M. Goupil, J.-C. Lavalley, M. Daturi, S. Surblé, C. Serre, F. Millange, G. Férey and N. Audebrand, *J. Am. Chem. Soc.*, 2006, **128**, 3218; (e) M. Dincă and J. R. Long, *J. Am. Chem. Soc.*, 2005, **127**, 9376; (f) J. Sculley, D. Yuan and H.-C. Zhou, *Energy Environ. Sci.*, 2011, **4**, 2721; (g) S.-L. Li and Q. Xu, *Energy Environ. Sci.*, 2013, **6**, 1656; (h) V. Colombo, S. Galli, H. J. Choi, G. D. Han, A. Maspero, G. Palmisano, N. Masciocchi and J. R. Long, *Chem. Sci.*, 2011, **2**, 1311; (i) K. Sumida, C. M. Brown, Z. R. Herm, S. Chavan, S. Bordiga and J. R. Long, *Chem. Commun.*, 2011, **47**, 1157; (j) G. Xia, Y. Tan, X. Chen, Z. Guo, H. Liu and X. Yu, *J. Mater. Chem. A*, 2013, **1**, 1810; (k) J. L. C. Rowsell and O. M. Yaghi, *Angew. Chem. Int. Ed.*, 2005, **44**, 4670; (l) J. G. Vitillo, L. Regli, S. Chavan, G. Ricchiardi, G. Spoto, P. D. C. Dietzel, S. Bordiga and A. Zecchina, *J. Am. Chem. Soc.*, 2008, **130**, 8386; (m) K. Sumida, D. Stück, L. Mino, J.-D. Chai, E. D. Bloch, O. Zavorotynska, L. J. Murray, M. Dincă, S. Chavan, S. Bordiga, M. Head-Gordon and J. R. Long, *J. Am. Chem. Soc.*, 2013, **135**, 1083.
14. S. S. Kaye, A. Dailly, O. M. Yaghi and J. R. Long, *J. Am. Chem. Soc.*, 2007, **129**, 14176.
15. (a) Z. Guo, G. Li, L. Zhou, S. Su, Y. Lei, S. Dang and H. Zhang, *Inorg. Chem.*, 2009, **48**, 8069; (b) C. Yang, X. Wang and M. A. Omary, *J. Am. Chem. Soc.*, 2007, **129**, 15454; (c) H. J. Choi, M. Dincă and J. R. Long, *J. Am. Chem. Soc.*, 2008, **130**, 7848; (d) M. Dincă and J. R. Long, *Angew. Chem. Int. Ed.*, 2008, **47**, 6766; (e) X. Zhao, B. Xiao, A. J. Fletcher, K. M. Thomas, D. Bradshaw and M. J. Rosseinsky, *Science*, 2004, **306**, 1012; (f) M. Dincă and J. R. Long, *J. Am. Chem. Soc.*, 2007, **129**, 11172.



16. K. Gedrich, I. Senkowska, N. Klein, U. Stoeck, A. Henschel, M. R. Lohe, I. A. Baburin, U. Mueller and S. Kaskel, *Angew. Chem. Int. Ed.*, 2010, **49**, 8489.
17. (a) S. Holloway, *Energy*, 2005, **30**, 2318; (b) A. Arenillas, K. M. Smith, T. C. Drage and C. E. Snape, *Fuel*, 2005, **84**, 2204; (c) C. M. White, D. H. Smith, K. L. Jones, A. L. Goodman, S. A. Jikich, R. B. LaCount, S. B. DuBose, E. Ozdemir, B. I. Morsi and K. T. Schroeder, *Energy & Fuels*, 2005, **19**, 659.
18. , Fluor Daniel, “Engineering and Economic Evaluation of CO<sub>2</sub> Removal from Fossil-Fuel-Fired Power Plants” (IE-7365, Electric Power Research Institute, Palo Alto, CA, 1991).
19. (a) L. M. Romeo, I. Bolea and J. M. Escosa, *Appl. Therm. Eng.*, 2008, **28**, 1039; (b) G. T. Rochelle, *Science*, 2009, **325**, 1652.
20. (a) D. M. D'Alessandro, B. Smit and J. R. Long, *Angew. Chem. Int. Ed.*, 2010, **49**, 6058; (b) K. Sumida, D. L. Rogow, J. A. Mason, T. M. McDonald, E. D. Bloch, Z. R. Herm, T.-H. Bae and J. R. Long, *Chem. Rev.*, 2012, **112**, 724.
21. (a) R. Banerjee, A. Phan, B. Wang, C. Knobler, H. Furukawa, M. O'Keeffe and O. M. Yaghi, *Science*, 2008, **319**, 939; (b) H. Hayashi, A. P. Cote, H. Furukawa, M. O'Keeffe and O. M. Yaghi, *Nature Mater.*, 2007, **6**, 501; (c) B. Wang, A. P. Cote, H. Furukawa, M. O'Keeffe and O. M. Yaghi, *Nature*, 2008, **453**, 207; (d) R. Banerjee, H. Furukawa, D. Britt, C. Knobler, M. O'Keeffe and O. M. Yaghi, *J. Am. Chem. Soc.*, 2009, **131**, 3875.
22. A. R. Millward and O. M. Yaghi, *J. Am. Chem. Soc.*, 2005, **127**, 17998.
23. H. Furukawa, N. Ko, Y. B. Go, N. Aratani, S. B. Choi, E. Choi, A. Ö. Yazaydin, R. Q. Snurr, M. O'Keeffe, J. Kim and O. M. Yaghi, *Science*, 2010, **329**, 424.
24. M. Z. Jacobson, *Energy Environ. Sci.*, 2009, **2**, 148.
25. (a) D. Wu, T. M. McDonald, Z. Quan, S. V. Ushakov, P. Zhang, J. R. Long and A. Navrotsky, *J. Mater. Chem. A*, 2015, **3**, 4248; (b) J. A. Mason, T. M. McDonald, T.-H. Bae, J. E. Bachman, K. Sumida, J. J. Dutton, S. S. Kaye and J. R. Long, *J. Am. Chem. Soc.*, 2015, **137**, 4787; (c) T. M. McDonald, J. A. Mason, X. Kong, E. D. Bloch, D. Gygi, A. Dani, V. Crocella, F. Giordanino, S. O. Odoh, W. S. Drisdell, B. Vlasisavljevich, A. L. Dzubak, R. Poloni, S. K. Schnell, N. Planas, K. Lee, T. Pascal, L. F. Wan, D. Prendergast, J. B. Neaton, B. Smit, J. B. Kortright, L. Gagliardi, S. Bordiga, J. A. Reimer and J. R. Long, *Nature*, 2015, **519**, 303.
26. (a) S. Hausdorf, J. Wagler, R. Moßig and F. O. R. L. Mertens, *J. Phys. Chem. A*, 2008, **112**, 7567; (b) H. K. Chae, D. Y. Siberio-Perez, J. Kim, Y. Go, M. Eddaoudi, A. J. Matzger, M. O'Keeffe and O. M. Yaghi, *Nature*, 2004, **427**, 523.
27. S. R. Caskey, A. G. Wong-Foy and A. J. Matzger, *J. Am. Chem. Soc.*, 2008, **130**, 10870.

28. (a) D.-A. Yang, H.-Y. Cho, J. Kim, S.-T. Yang and W.-S. Ahn, *Energy Environ. Sci.*, 2012, **5**, 6465; (b) J. A. Mason, K. Sumida, Z. R. Herm, R. Krishna and J. R. Long, *Energy Environ. Sci.*, 2011, **4**, 3030.
29. S. Keskin, T. M. van Heest and D. S. Sholl, *ChemSusChem*, 2010, **3**, 879.
30. J. Yu and P. B. Balbuena, *J. Phys. Chem. C*, 2013, **117**, 3383.
31. (a) K. P. Rao, M. Higuchi, K. Sumida, S. Furukawa, J. Duan and S. Kitagawa, *Angew. Chem. Int. Ed.*, 2014, **53**, 8225; (b) J. G. Nguyen and S. M. Cohen, *J. Am. Chem. Soc.*, 2010, **132**, 4560; (c) T. T. Y. Tan, M. R. Reithofer, E. Y. Chen, A. G. Menon, T. S. A. Hor, J. Xu and J. M. Chin, *J. Am. Chem. Soc.*, 2013, **135**, 16272.
32. (a) C. Yang, U. Kaipa, Q. Z. Mather, X. Wang, V. Nesterov, A. F. Venero and M. A. Omary, *J. Am. Chem. Soc.*, 2011, **133**, 18094; (b) B. Xia, Z. Chen, Q. Zheng, H. Zheng, M. Deng, Y. Ling, L. Weng and Y. Zhou, *CrystEngComm*, 2013, **15**, 3484; (c) A. Santra, M. S. Lah and P. K. Bharadwaj, *Z. Anorg. Allg. Chem.*, 2014, **640**, 1134.
33. P. Nugent, Y. Belmabkhout, S. D. Burd, A. J. Cairns, R. Luebke, K. Forrest, T. Pham, S. Ma, B. Space, L. Wojtas, M. Eddaoudi and M. J. Zaworotko, *Nature*, 2013, **495**, 80.
34. (a) N. Yanai, T. Uemura, N. Uchida, S. Bracco, A. Comotti, P. Sozzani, T. Kodani, M. Koh, T. Kanemura and S. Kitagawa, *J. Mater. Chem.*, 2011, **21**, 8021; (b) S.-i. Noro, Y. Hijikata, M. Inukai, T. Fukushima, S. Horike, M. Higuchi, S. Kitagawa, T. Akutagawa and T. Nakamura, *Inorg. Chem.*, 2013, **52**, 280; (c) P. Kanoo, S. K. Reddy, G. Kumari, R. Haldar, C. Narayana, S. Balasubramanian and T. K. Maji, *Chem. Commun.*, 2012, **48**, 8487; (d) P. S. Nugent, V. L. Rhodus, T. Pham, K. Forrest, L. Wojtas, B. Space and M. J. Zaworotko, *J. Am. Chem. Soc.*, 2013, **135**, 10950; (e) P. Deria, J. E. Mondloch, E. Tylianakis, P. Ghosh, W. Bury, R. Q. Snurr, J. T. Hupp and O. K. Farha, *J. Am. Chem. Soc.*, 2013, **135**, 16801.
35. D. Singh, E. Croiset, P. L. Douglas and M. A. Douglas, *Energy Convers. Manage.*, 2003, **44**, 3073.
36. (a) *Ullmann&s Encyclopedia of Industrial Chemistry, 6th ed.*, , 2000 electronic release; ; (b) R. Meyers, *Handbook of Petroleum Refining Processes, 3th ed.*, McGraw-Hill, New York, 2.47.
37. P. S. Bárcia, F. Zapata, J. A. C. Silva, A. E. Rodrigues and B. Chen, *J. Phys. Chem. B*, 2007, **111**, 6101.
38. Z. Jin, H.-Y. Zhao, X.-J. Zhao, Q.-R. Fang, J. R. Long and G.-S. Zhu, *Chem. Commun.*, 2010, **46**, 8612.
39. V. Finsy, H. Verelst, L. Alaerts, D. De Vos, P. A. Jacobs, G. V. Baron and J. F. M. Denayer, *J. Am. Chem. Soc.*, 2008, **130**, 7110.

40. E. D. Bloch, W. L. Queen, R. Krishna, J. M. Zadrozny, C. M. Brown and J. R. Long, *Science*, 2012, **335**, 1606.
41. M. Kurmoo, *Chem. Soc. Rev.*, 2009, **38**, 1353.
42. L. M. C. Beltran and J. R. Long, *Acc. Chem. Res.*, 2005, **38**, 325.
43. (a) A. P. Gingsberg, *Inorg. Chim. Acta Rev.*, 1971, **5**, 45; (b) J. B. Goodenough, *J. Phys. Chem. Solids*, 1958, **6**, 287; (c) M. Nishino, S. Kubo, Y. Yoshioka, A. Nakamura and K. Yamaguchi, *Mol. Cryst. Liq. Cryst.*, 1997, **305**, 109.
44. (a) K. Hashimoto and S. Ohkoshi, *Phil. Trans. R. Soc. Lond. A*, 1999, **357**, 2977; (b) S.-i. Ohkoshi and K. Hashimoto, *J. Photochem. Photobiol., C*, 2001, **2**, 71.
45. H. Tokoro and S.-i. Ohkoshi, *Dalton Trans.*, 2011, **40**, 6825.
46. (a) S. S. Kaye and J. R. Long, *J. Am. Chem. Soc.*, 2005, **127**, 6506; (b) *Catal. Today*, 2007, **120**, 311; (c) J. Jiménez-Gallegos, J. Rodríguez-Hernández, H. Yee-Madeira and E. Reguera, *J. Phys. Chem. C*, 2010, **114**, 5043; (d) F. Karadas, H. El-Faki, E. Deniz, C. T. Yavuz, S. Aparicio and M. Atilhan, *Microporous Mesoporous Mater.*, 2012, **162**, 91.
47. (a) J.-D. Cafun, J. Lejeune, F. Baudalet, P. Dumas, J.-P. Itié and A. Bleuzen, *Angew. Chem. Int. Ed.*, 2012, **51**, 9146; (b) O. Sato, T. Iyoda, A. Fujishima and K. Hashimoto, *Science*, 1996, **272**, 704; (c) S.-i. Ohkoshi and H. Tokoro, *Acc. Chem. Res.*, 2012, **45**, 1749; (d) A. Mondal, Y. Li, M. Seuleiman, M. Julve, L. Toupet, M. Buron-Le Cointe and R. Lescouëzec, *J. Am. Chem. Soc.*, 2013, **135**, 1653.
48. (a) C. D. Wessells, R. A. Huggins and Y. Cui, *Nat Commun*, 2011, **2**, 550; (b) M. Pasta, C. D. Wessells, R. A. Huggins and Y. Cui, *Nat Commun*, 2012, **3**, 1149; (c) M. Okubo and I. Honma, *Dalton Trans.*, 2013, **42**, 15881; (d) Y. Lu, L. Wang, J. Cheng and J. B. Goodenough, *Chem. Commun.*, 2012, **48**, 6544; (e) M. Okubo, D. Asakura, Y. Mizuno, J. D. Kim, T. Mizokawa, T. Kudo and I. Honma, *J. Phys. Chem. Lett.*, 2010, **1**, 2063.
49. (a) M. Kurmoo, H. Kumagai, K. W. Chapman and C. J. Kepert, *Chem. Commun.*, 2005, 3012; (b) W. Kaneko, M. Ohba and S. Kitagawa, *J. Am. Chem. Soc.*, 2007, **129**, 13706; (c) N. Yanai, W. Kaneko, K. Yoneda, M. Ohba and S. Kitagawa, *J. Am. Chem. Soc.*, 2007, **129**, 3496; (d) T. K. Maji, S. Pal, K. L. Gurunatha, A. Govindaraj and C. N. R. Rao, *Dalton Trans.*, 2009, 4426.
50. (a) D. Maspoeh, D. Ruiz-Molina and J. Veciana, *Chem. Soc. Rev.*, 2007, **36**, 770; (b) Y. He, B. Li, M. O'Keeffe and B. Chen, *Chem. Soc. Rev.*, 2014, **43**, 5618; (c) C. J. Kepert, *Chem. Commun.*, 2006, 695; (d) K. Jayaramulu, P. Kanoo, S. J. George and T. K. Maji, *Chem. Commun.*, 2010, **46**, 7906; (e) P. Kanoo, A. C. Ghosh and T. K. Maji, *Inorg. Chem.*, 2011, **50**, 5145; (f) R. Haldar and T. K. Maji, *CrystEngComm*, 2013, **15**, 9276; (g) A. Chakraborty, R. Haldar and T. K. Maji, *Cryst. Growth Des.*, 2013, **13**, 4968.

51. (a) S. Mohapatra, B. Rajeswaran, A. Chakraborty, A. Sundaresan and T. K. Maji, *Chem. Mater.*, 2013, **25**, 1673; (b) Z.-G. Gu, X.-H. Zhou, Y.-B. Jin, R.-G. Xiong, J.-L. Zuo and X.-Z. You, *Inorg. Chem.*, 2007, **46**, 5462; (c) X.-L. Tong, T.-L. Hu, J.-P. Zhao, Y.-K. Wang, H. Zhang and X.-H. Bu, *Chem. Commun.*, 2010, **46**, 8543.
52. (a) P. Dechambenoit and J. R. Long, *Chem. Soc. Rev.*, 2011, **40**, 3249; (b) M.-H. Zeng, Z. Yin, Y.-X. Tan, W.-X. Zhang, Y.-P. He and M. Kurmoo, *J. Am. Chem. Soc.*, 2014, **136**, 4680; (c) M.-H. Zeng, Y.-X. Tan, Y.-P. He, Z. Yin, Q. Chen and M. Kurmoo, *Inorg. Chem.*, 2013, **52**, 2353; (d) Z. M. Wang, Y. J. Zhang, T. Liu, M. Kurmoo and S. Gao, *Adv. Funct. Mater.*, 2007, **17**, 1523.
53. M.-H. Zeng, Z. Yin, Y.-X. Tan, W.-X. Zhang, Y.-P. He and M. Kurmoo, *J. Am. Chem. Soc.*, 2014, **136**, 4680.
54. G. J. Halder, C. J. Kepert, B. Moubaraki, K. S. Murray and J. D. Cashion, *Science*, 2002, **298**, 1762.
55. S. M. Holmes and G. S. Girolami, *J. Am. Chem. Soc.*, 1999, **121**, 5593.
56. H. Li, M. Eddaoudi, M. O'Keeffe and O. M. Yaghi, *Nature*, 1999, **402**, 276.
57. A. Stein, S. W. Keller and T. E. Mallouk, *Science*, 1993, **259**, 1558.
58. B. F. Hoskins and R. Robson, *J. Am. Chem. Soc.*, 1990, **112**, 1546.
59. (a) Z. Wang and S. M. Cohen, *Chem. Soc. Rev.*, 2009, **38**, 1315; (b) K. K. Tanabe and S. M. Cohen, *Chem. Soc. Rev.*, 2011, **40**, 498.
60. (a) S. M. Cohen, *Chem. Rev.*, 2011, **112**, 970; (b) M. Kim, J. F. Cahill, Y. Su, K. A. Prather and S. M. Cohen, *Chem. Sci.*, 2012, **3**, 126.
61. S. Choi, T. Watanabe, T.-H. Bae, D. S. Sholl and C. W. Jones, *J. Phys. Chem. Lett.*, 2012, **3**, 1136.
62. W. R. Lee, S. Y. Hwang, D. W. Ryu, K. S. Lim, S. S. Han, D. Moon, J. Choi and C. S. Hong, *Energy Environ. Sci.*, 2014, **7**, 744.
63. O. Karagiari, W. Bury, E. Tylianakis, A. A. Sarjeant, J. T. Hupp and O. K. Farha, *Chem. Mater.*, 2013, **25**, 3499.
64. T. Li, M. T. Kozlowski, E. A. Doud, M. N. Blakely and N. L. Rosi, *J. Am. Chem. Soc.*, 2013, **135**, 11688.
65. (a) R. Lyndon, K. Konstas, B. P. Ladewig, P. D. Southon, P. C. J. Kepert and M. R. Hill, *Angew. Chem. Int. Ed.*, 2013, **52**, 3695; (b) B. Esser and T. M. Swager, *Angew. Chem. Int. Ed.*, 2010, **49**, 8872.
66. (a) J. Park, L.-B. Sun, Y.-P. Chen, Z. Perry and H.-C. Zhou, *Angew. Chem. Int. Ed.*, 2014, **53**, 5842; (b) J. W. Brown, B. L. Henderson, M. D. Kiesz, A. C. Whalley, W. Morris, S. Grunder, H.

- Deng, H. Furukawa, J. I. Zink, J. F. Stoddart and O. M. Yaghi, *Chem. Sci.*, 2013, **4**, 2858; (c) J. Park, D. Yuan, K. T. Pham, J.-R. Li, A. Yakovenko and H.-C. Zhou, *J. Am. Chem. Soc.*, 2011, **134**, 99.
67. N. Yanai, T. Uemura, M. Inoue, R. Matsuda, T. Fukushima, M. Tsujimoto, S. Isoda and S. Kitagawa, *J. Am. Chem. Soc.*, 2012, **134**, 4501.
68. (a) M. Nagarathinam, A. M. P. Peedikakkal and J. J. Vittal, *Chem. Commun.*, 2008, 5277; (b) K. M. Hutchins, T. P. Rupasinghe, L. R. Ditzler, D. C. Swenson, J. R. G. Sander, J. Baltrusaitis, A. V. Tivanski and L. R. MacGillivray, *J. Am. Chem. Soc.*, 2014, **136**, 6778; (c) H. Sato, R. Matsuda, M. H. Mir and S. Kitagawa, *Chem. Commun.*, 2012, **48**, 7919.
69. (a) M. H. Mir, L. L. Koh, G. K. Tan and J. J. Vittal, *Angew. Chem. Int. Ed.*, 2010, **49**, 390; (b) M. Nagarathinam, A. Chanthapally, S. H. Lapidus, P. W. Stephens and J. J. Vittal, *Chem. Commun.*, 2012, **48**, 2585; (c) J.-K. Sun, W. Li, C. Chen, C.-X. Ren, D.-M. Pan and J. Zhang, *Angew. Chem. Int. Ed.*, 2013, **52**, 6653; (d) L. R. MacGillivray, G. S. Papaefstathiou, T. Frišćić, T. D. Hamilton, D.-K. Bučar, Q. Chu, D. B. Varshney and I. G. Georgiev, *Acc. Chem. Res.*, 2008, **41**, 280; (e) G. S. Papaefstathiou, Z. Zhong, L. Geng and L. R. MacGillivray, *J. Am. Chem. Soc.*, 2004, **126**, 9158; (f) G. K. Kole, T. Kojima, M. Kawano and J. J. Vittal, *Angew. Chem. Int. Ed.*, 2014, **53**, 2143; (g) D. Liu, Z.-G. Ren, H.-X. Li, J.-P. Lang, N.-Y. Li and B. F. Abrahams, *Angew. Chem. Int. Ed.*, 2010, **49**, 4767; (h) S.-Y. Yang, X.-L. Deng, R.-F. Jin, P. Naumov, M. K. Panda, R.-B. Huang, L.-S. Zheng and B. K. Teo, *J. Am. Chem. Soc.*, 2013, **136**, 558; (i) G. S. Papaefstathiou, A. J. E. Duncan and L. R. MacGillivray, *Chem. Commun.*, 2014, **50**, 15960.
70. (a) A. K. Paul, R. Karthik and S. Natarajan, *Cryst. Growth Des.*, 2011, **11**, 5741; (b) I.-H. Park, A. Chanthapally, Z. Zhang, S. S. Lee, M. J. Zaworotko and J. J. Vittal, *Angew. Chem. Int. Ed.*, 2014, **53**, 414; (c) R. Medishetty, T. T. S. Yap, L. L. Koh and J. J. Vittal, *Chem. Commun.*, 2013, **49**, 9567; (d) R. Medishetty, L. L. Koh, G. K. Kole and J. J. Vittal, *Angew. Chem. Int. Ed.*, 2011, **50**, 10949; (e) I. G. Georgiev, D.-K. Bucar and L. R. MacGillivray, *Chem. Commun.*, 2010, **46**, 4956; (f) E. Elacqua, P. Kaushik, R. H. Groeneman, J. C. Sumrak, D.-K. Bučar and L. R. MacGillivray, *Angew. Chem. Int. Ed.*, 2012, **51**, 1037; (g) E. Elacqua, R. H. Groeneman, E. W. Reinheimer, D.-K. Bučar and L. R. MacGillivray, *Supramol. Chem.*, 2013, **26**, 207.
71. (a) A. M. P. Peedikakkal, L. L. Koh and J. J. Vittal, *Chem. Commun.*, 2008, 441; (b) R. Santra, K. Banerjee and K. Biradha, *Chem. Commun.*, 2011, **47**, 10740; (c) R. C. Grove, S. H. Malehorn, M. E. Breen and K. A. Wheeler, *Chem. Commun.*, 2010, **46**, 7322; (d) G. K. Kole, G. K. Tan, L. L. Koh and J. J. Vittal, *CrystEngComm*, 2012, **14**, 6190.
72. (a) R. Medishetty, A. Husain, Z. Bai, T. Runčevski, R. E. Dinnebier, P. Naumov and J. J. Vittal, *Angew. Chem. Int. Ed.*, 2014, **53**, 5907; (b) L. J. Barbour, *Aust. J. Chem.*, 2006, **59**, 595.

73. (a) X.-N. Cheng, W.-X. Zhang and X.-M. Chen, *J. Am. Chem. Soc.*, 2007, **129**, 15738; (b) H. Sato, W. Kosaka, R. Matsuda, A. Hori, Y. Hijikata, R. V. Belosludov, S. Sakaki, M. Takata and S. Kitagawa, *Science*, 2014, **343**, 167.
74. (a) A. Michaelides, S. Skoulika and M. G. Siskos, *Chem. Commun.*, 2011, **47**, 7140; (b) D. Liu, H.-F. Wang, B. F. Abrahams and J.-P. Lang, *Chem. Commun.*, 2014, **50**, 3173; (c) D. Liu, J.-P. Lang and B. F. Abrahams, *Chem. Commun.*, 2013, **49**, 2682; (d) D. Liu and J.-P. Lang, *CrystEngComm*, 2014, **16**, 76; (e) S. Dutta, D.-K. Bucar, E. Elacqua and L. R. MacGillivray, *Chem. Commun.*, 2013, **49**, 1064; (f) S. Bhattacharya, J. Stojaković, B. K. Saha and L. R. MacGillivray, *Org. Lett.*, 2013, **15**, 744.
75. (a) M. D. Cohen, G. M. J. Schmidt and F. I. Sonntag, *J. Chem. Soc.*, 1964, 2000; (b) G. M. J. Schmidt, in *Pure Appl. Chem.*, 1971, p. 647.
76. S. Inagaki and K. Fukui, *J. Am. Chem. Soc.*, 1975, **97**, 7480.
77. (a) A. Chanthapally, W. T. Oh and J. J. Vittal, *CrystEngComm*, 2013, **15**, 9324; (b) I.-H. Park, A. Chanthapally, H.-H. Lee, H. S. Quah, S. S. Lee and J. J. Vittal, *Chem. Commun.*, 2014, **50**, 3665; (c) I.-H. Park, R. Medishetty, S. S. Lee and J. J. Vittal, *Chem. Commun.*, 2014, **50**, 6585.

# Chapter 2

**Charge-Assisted Soft Supramolecular Porous Frameworks:  
Effect of Stimuli on Structural Transformation and Adsorption  
Properties**





## Summary

Five novel supramolecular frameworks  $\{[\text{Fe}(\text{CN})_6] \cdot (\text{H-bipy})_3 \cdot 8\text{H}_2\text{O}\}$  (**1**),  $\{(\text{H}_2\text{-bpee})_4[\text{Fe}(\text{CN})_6]_2 \cdot 9\text{H}_2\text{O}\}$  (**2**),  $\{(\text{H}_2\text{-bpee})(\text{H}_3\text{O})_2[\text{Fe}(\text{CN})_6] \cdot 2\text{H}_2\text{O}\}$  (**3**),  $\{[(\text{H}_2\text{-bpee})(\text{H-bpee})]_2[\text{Fe}(\text{CN})_6]_2 \cdot 5\text{H}_2\text{O}\}$  (**4**) and  $\{[(\text{H}_{1.5}\text{-bpee})_2][\text{Fe}(\text{CN})_6] \cdot 6\text{H}_2\text{O}\}$  (**5**) (bipy = 4,4'-bipyridine and bpee = 1,2-bis(4-pyridyl)ethylene) have been synthesized by the reaction of bipy and  $\text{K}_3[\text{Fe}(\text{CN})_6]$  (for **1**), bpee and  $\text{K}_4[\text{Fe}(\text{CN})_6]$  (for **2** and **3**) or  $\text{K}_3[\text{Fe}(\text{CN})_6]$  (for **4** and **5**) in aqueous medium. The supramolecular structures are constructed by cooperative non-covalent hydrogen bonding and  $\pi \cdots \pi$  interactions between protonated bipy/bpee,  $[\text{Fe}(\text{CN})_6]^{3-/4-}$  and crystalline water molecules. The host, compound **1** houses a discrete octameric water cluster with the conformation of 1,4-substituted cyclohexane molecule where six water molecules are positioned on the vertices of the cyclohexane ring and the seventh and eighth occupy the 1,4-equatorial positions of the ring. DFT calculation suggests, this conformation is more stable (-73.08 kcal/mol) compared to the *a,a* conformation (reported elsewhere). All the supramolecular soft hosts transformed to two different states depending upon the dehydration condition as observed from the PXRD patterns. Upon removal of the water molecules, host network of **1** undergoes structural transformation and the dehydrated phase exhibits stepwise uptake of  $\text{H}_2\text{O}$  molecules and completely excludes  $\text{CO}_2$  gas and other organic solvent molecules ( $\text{CH}_3\text{OH}$ ,  $\text{CH}_3\text{CN}$ ,  $\text{EtOH}$ ). On the other hand, when compounds **2-5** are activated under vacuum at 373 K (**2'-5'**), they exhibit different adsorption behaviour with different adsorbates like  $\text{H}_2\text{O}$ ,  $\text{MeOH}$  and  $\text{EtOH}$  compared to when they were activated under high vacuum at room temperature for 24 hrs (**2''-5''**). Desolvated compounds **1'-5'** show gradual uptake of water while multistep water adsorption profiles were observed with **1''-5''** suggesting difference in hydrophilicity in these two set of compounds. Further, **2'-5'** and **2''-5''** unveil type I and double step  $\text{MeOH}$  (at 293 K) adsorption profiles respectively which have been correlated to guest induced structural transformation in the desolvated soft frameworks obtained at two different activation conditions.

1. A. Hazra, K. L. Gurunatha and T. K. Maji, *Cryst. Growth Des.*, 2013, **13**, 4824.
2. A. Hazra, P. Kanoo, S. Mohapatra, G. Mostafa and T. K. Maji, *CrystEnggComm*, 2010, **12**, 2775.



## 2.1: Introduction

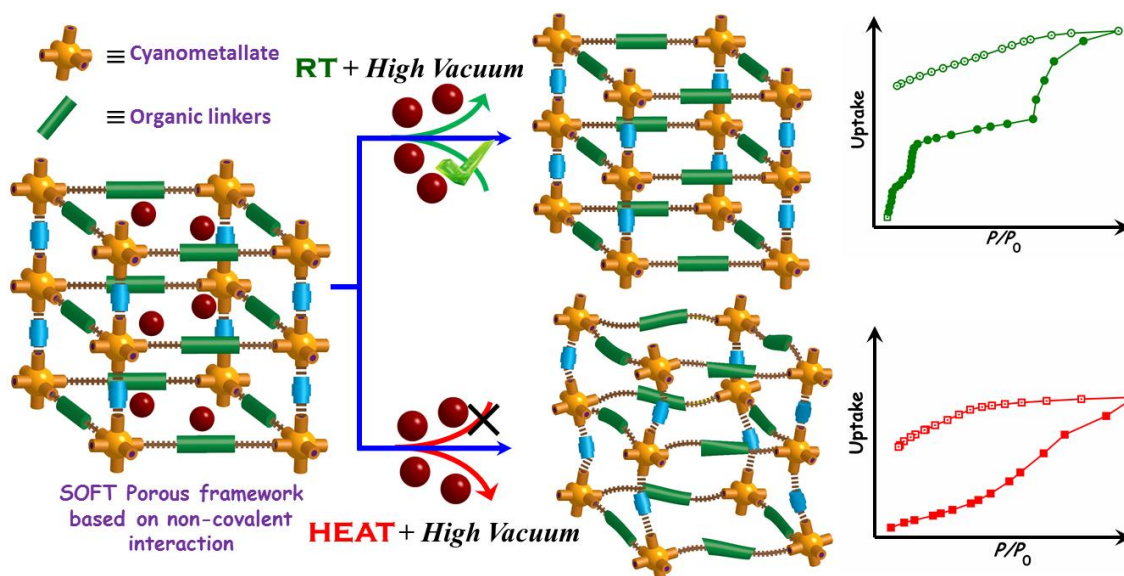
Co-crystals are a class of molecular complexes where two or more components are bonded by non-covalent, non-ionic intermolecular interactions.<sup>1</sup> The process of co-crystallization is governed by molecular recognition and self-assembly, rather than formation and deformation of covalent bonds, which is suitable for meliorating pharmaceutical formulation.<sup>2</sup> The synthesis of co-crystal has immensely interested scientists in recent years<sup>3</sup> because of their application in the field of magnetism,<sup>4</sup> ferroelasticity,<sup>5</sup> nonlinear optical effect,<sup>6</sup> chemical storage,<sup>7</sup> catalysis,<sup>8</sup> semiconductor,<sup>9</sup> adsorption and separation.<sup>10</sup>

Extended structures of co-crystals sustained by non-covalent interactions are rather soft compared to conventional porous framework structures<sup>11</sup> (e.g. metal-organic frameworks and zeolites). This type of structures exhibit some degree of directionality and interesting host-guest property based on non-covalent interactions.<sup>12</sup> The main advantages in the synthesis of such soft materials are very mild reaction conditions and enormous choice of discrete molecular building units which lead to extended networks (host-guest complex) sustained by non-covalent interactions (e.g. H-bonding,  $\pi\cdots\pi$  stacking, C-H $\cdots\pi$  interaction etc).<sup>13</sup> On the other hand, flexible and dynamic MOFs or porous coordination polymers (PCPs), so called 3<sup>rd</sup> generation porous frameworks as classified by Kitagawa *et al.*,<sup>14</sup> exhibit guest induced sliding, framework breathing, and structural asymmetry (expansion or contraction).<sup>15</sup> Furthermore, this type of soft framework materials also demonstrated interesting properties in terms of guest selectivity with gated and stepwise adsorption<sup>10</sup> and drug delivery.<sup>16</sup> Recently, Maji *et al.* reported permanently porous structure based on irreversible sliding of 2D grids and stepwise adsorption in pillared bilayer 2D networks based on two different coordination spaces.<sup>11b,h</sup> In general, the extended networks sustained solely by non-covalent interactions would be more dynamic in nature compared to 3<sup>rd</sup> generation porous coordination polymer.<sup>16b</sup> Such a 'soft' supramolecular network would be suitable for depicting switching properties based on reversible changes from an absorbing state to a close packed inactive polymorph (like enzyme changes their structure according to the substrate) and can be activated by thermal, mechanical, or radioactive stimuli.<sup>17</sup> These soft networks are susceptible to change their structure significantly based on the different activation conditions. Significant changes in the structure may be realized in extreme conditions.

Open framework solids act as a coffer for the templating solvent molecules and they stabilize the overall crystal host and often they formed cluster, particularly water molecules by H-bonding interactions. Exploration of the possible structures and stabilities of water clusters is of immense interest to chemist as well as to physicist because of their unusual properties and of importance to life.<sup>18</sup> The importance in relevance to physical, chemical and biological processes have propelled the scientists to investigate water clusters extensively.<sup>19</sup> Indeed, it is possible to understand the complex nature of bulk water as well as ice by a detailed study of numerous possible structures of water clusters found in supramolecular networks.<sup>20</sup> Although a number of water structures are reported in literature,<sup>21-24</sup> my emphasis in this chapter would be on conformations of octameric water clusters. Octameric clusters observed in organic or inorganic-organic host structures exhibit conformations of cubane,<sup>23a</sup> open cube,<sup>23b</sup> cyclic ring,<sup>23c</sup> book-shaped,<sup>23d</sup> crowned chair<sup>23e,f</sup> due to different environments imposed by the hosts. Of particular interest is the octameric cluster with hexameric core, which has received increased attention in recent years as the hexamer is believed to be the smallest possible unit that can show many properties of bulk water. Nauta *et al.*<sup>25</sup> have reported a less stable cyclic hexamer in liquid helium which is the building block of ice  $I_h$ <sup>26</sup> and is also relevant to liquid water.<sup>27</sup> Recently, Hong *et al.*<sup>23i</sup> reported a new type of octameric water cluster formed by a planar water tetramer and two dangling water dimers.

Therefore, judicious choice of building units (*i.e.* donor and acceptor for H-bonding interaction) is vital where final structures and functions of the co-crystals can be tuned by controlling the synthetic routes and crystallization conditions such as concentration gradients, pH, solvent, temperature *etc.* As the success of co-crystallization is hardly predictable, to get hold of optimum conditions, one needs to perform several reactions with varying conditions.<sup>28</sup> In this chapter, I have exploited the acceptor property of hexacyanometallate  $[\text{Fe}(\text{CN})_6]^{3-}/[\text{Fe}(\text{CN})_6]^{4-}$  (Scheme 1) which is well studied in synthesis of molecular based magnetic materials.<sup>4e-g</sup> This type of metallo-ligand provides acceptor sites in three dimensions and can be linked with a donor like protonated 4,4'-bipyridine (H-bipy) or 1,2-bis(4-pyridyl)ethylene (H/H<sub>2</sub>-bpee) for constructing charge-assisted 3D supramolecular frameworks.<sup>10c-f</sup> This chapter reports the synthesis, structural characterization and interesting vapour adsorption properties of five new co-crystals  $\{[\text{Fe}(\text{CN})_6] \cdot (\text{H-bipy})_3 \cdot 8\text{H}_2\text{O}\}$  **(1)**,  $\{(\text{H}_2\text{-bpee})_4[\text{Fe}(\text{CN})_6]_2 \cdot 9\text{H}_2\text{O}\}$  **(2)**,  $\{(\text{H}_2\text{-bpee})(\text{H}_3\text{O})_2[\text{Fe}(\text{CN})_6] \cdot 2\text{H}_2\text{O}\}$  **(3)**,  $\{[(\text{H}_2\text{-bpee})(\text{H-bpee})]_2[\text{Fe}(\text{CN})_6]_2 \cdot 5\text{H}_2\text{O}\}$  **(4)** and

$\{[(H_{1.5}\text{-bpee})_2][Fe(CN)_6]\cdot 6H_2O\}$  (**5**). The adsorption properties have been studied for each case by activating the samples in two different conditions.



**Scheme 1:** Schematic diagram showing charge assisted construction of 3D supramolecular soft porous frameworks and structural transformation in two different activation conditions and corresponding effect in adsorption properties.

## 2.2: Experimental Section

### 2.2.1: Materials

All the reagents and solvents employed were commercially available and used as supplied without further purification.  $K_4[Fe(CN)_6]$ ,  $K_3[Fe(CN)_6]$ , 4,4'-bipyridine (bipy) and 1,2-bis(4-pyridyl)ethylene (bpee) were obtained from the Aldrich Chemical Co. **Caution!** Cyanide-containing compounds are potentially toxic and should be handled very carefully.

### 2.2.2: Synthesis

**Synthesis of  $\{[Fe(CN)_6]\cdot(H\text{-bipy})_3\cdot 8H_2O\}$  (**1**):** The cocrystal **1** was synthesized according to the following procedure.  $K_3[Fe(CN)_6]$ , 1.0 mmol (0.329 g) was dissolved in 7 mL water in a beaker. In another beaker, 1.5 mmol (0.234 g) of 4,4'-bipyridine was dissolved in 1.5 % (v/v) 7 mL HCl solution. Then both the solutions were mixed together and stirred until some yellow solid separated out. The reaction temperature was

maintained around 10-15 °C. The solution was filtered and light yellow precipitate was discarded and filtrate was kept in open atmosphere for slow evaporation. After one day, yellow block shaped crystals of **1** were separated. The crystals were highly sensitive to open atmosphere and slowly lose single crystallinity. Good quality single crystals were picked up from the mother liquor and immediately covered with paraffin oil and crystal data was collected at 100 K. Yield: 77%, relative to Fe. Anal. calc. for  $C_{36}H_{43}FeN_{12}O_8$ : C, 52.19; H, 5.19; N, 20.29. Found: C, 52.01; H, 5.32; N, 20.09. IR (KBr,  $cm^{-1}$ ):  $\nu(H_2O)$  3440, 3374;  $\nu_{Ar}(C-H)$  3087, 3052;  $\nu(CN)$  2117;  $\nu_{Ar}(C=C)$  1618. IR spectrum of **1** shows two strong and sharp bands around 3375 and 3442  $cm^{-1}$  suggesting the presence of water molecules (Figure 1a). A strong band around 2117  $cm^{-1}$  corroborate to  $\nu(CN)$  stretching frequency and a band around 1618  $cm^{-1}$  indicates the presence bipy molecule.

**Preparation of  $\{[Fe(CN)_6] \cdot (H-bipy)_3\}$  (**1'**):** Compound **1** was placed in a glass sample cell and heated at 80 °C for 5h under reduced pressure of 0.1 Pa that results **1'**. Removal of water molecules was confirmed by IR (Figure 1c) and CHN analysis. Anal. calc. for  $C_{36}H_{27}FeN_{12}$ : C, 63.26; H, 3.98; N, 24.59. Found: C, 62.61; H, 3.21; N, 23.89.

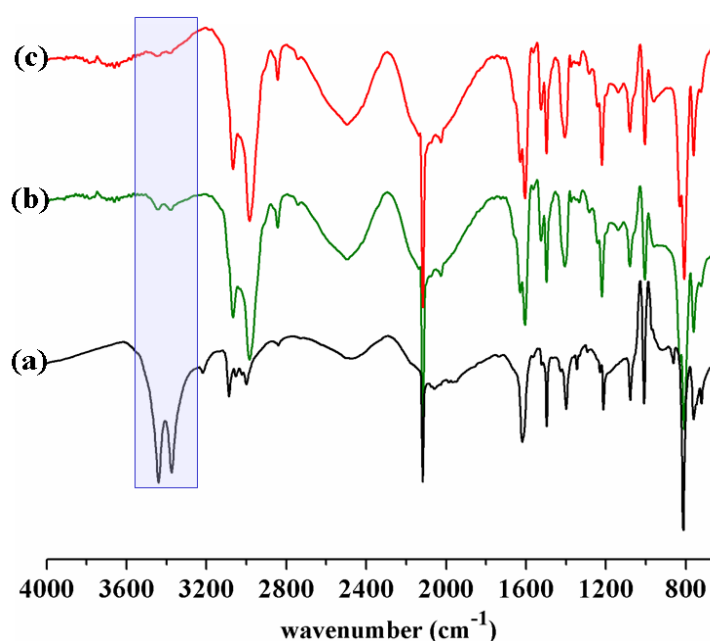


**Figure 1:** IR spectra of compounds **1**(a), **1'** (c) and **1''**(b).

**Preparation of  $\{[Fe(CN)_6] \cdot (H-bipy)_3\}$  (**1''**):** Compound **1** was placed in a glass sample cell and outgassed at room temperature for 20 h under reduced pressure of 0.1 Pa that results **1''**. Removal of water molecules was confirmed by IR (Figure 1b) and CHN

analysis. Anal. calc. for  $C_{36}H_{27}FeN_{12}$ : C, 63.26; H, 3.98; N, 24.59. Found: C, 62.47; H, 3.33; N, 24.01.

**Synthesis of  $\{(H_2-bpee)_4[Fe(CN)_6]_2 \cdot 9H_2O\}$  (2):** Compound **2** was synthesized according to the following procedure. 0.354 g (1 mmol)  $Fe(ClO_4)_3$  was dissolved in 50 mL water and 0.091 g (0.5 mmol) 1,2-bis(4-pyridyl)ethylene (bpee) was dissolved in 50 mL ethanol. These two solutions were mixed together, stirred for 15 min.  $K_4[Fe(CN)_6]$  solution was prepared by dissolving 0.5 mmol (0.211g) in 100 mL water. 2 mL of as prepared first solution was slowly and carefully layered on top of the  $K_4[Fe(CN)_6]$  solution (2 mL) by employing 1 mL buffer ( $H_2O:EtOH = 1:1$ ) in a 15 cm long crystal tube. This crystal tube was left undisturbed for four weeks for crystal growth. Deep blue needle shaped crystals were obtained in the middle of the tubes. Good quality single crystals were picked up from the mother liquor and immediately covered with paraffin oil for single crystal data collection.

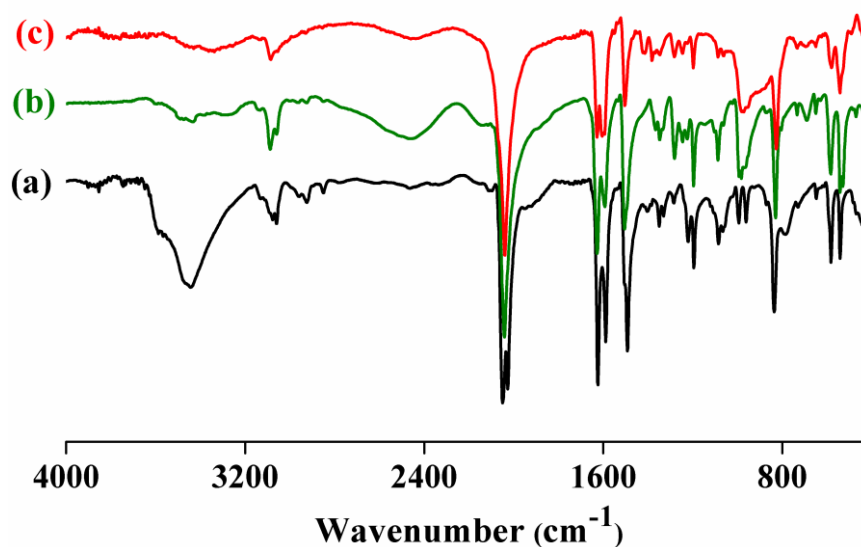


**Figure 2:** IR spectra of compound **2** at different states; (a) as-synthesized, (b) desolvated at room temperature and (c) desolvated at 100 °C.

Different procedure was employed for the preparation of bulk powder sample. 0.5 mmol of bpee was dissolved in 7 mL 1 (N) HCl solution to make the bpee molecules protonated. Above solution was stirred for 15 min and then 15 mL aqueous solution of  $K_4[Fe(CN)_6]$  (0.5 mmol) was added to it. Before mixing the solutions, both of them were cooled in an ice bath and the reaction was carried out in an ice bath. The blue coloured precipitate was then filtered and air dried and phase purity was confirmed by powder X-ray diffraction. Yield: 78%, relative to Fe. Anal. calc. for  $C_{60}H_{66}Fe_2N_{20}O_9$ : C, 54.47; H,

5.03; N, 21.17. Found: C, 53.89; H, 5.19; N, 20.58. IR (KBr,  $\text{cm}^{-1}$ ):  $\nu(\text{H}_2\text{O})$  3580, 3456;  $\nu_{\text{Ar}}(\text{C-H})$  3077, 3058;  $\nu(\text{CN})$  2049, 2026;  $\nu_{\text{Ar}}(\text{C=C})$  1623, 1589. IR spectrum of **2** shows two strong and sharp bands around 3580 and 3456  $\text{cm}^{-1}$  suggesting the presence of water molecules (Figure 2a). A strong band around 2049  $\text{cm}^{-1}$  corroborate to  $\nu(\text{CN})$  stretching frequency and a band around 1623  $\text{cm}^{-1}$  indicates the presence bpee molecule

**Preparation of  $\{(\text{H}_2\text{-bpee})_4[\text{Fe}(\text{CN})_6]_2\}$  (**2'**):** Compound **2** was placed in a glass sample cell and heated at 100 °C for 5h under reduced pressure of 0.1 Pa that results **2'**. Removal of water molecules was confirmed by IR (Figure 2c) and CHN analysis. Anal. calc. for  $\text{C}_{60}\text{H}_{48}\text{Fe}_2\text{N}_{20}$ : C, 62.08; H, 4.17; N, 24.14. Found: C, 61.81; H, 4.58; N, 23.89.

**Preparation of  $\{[\text{Fe}(\text{CN})_6] \cdot (\text{H-bipy})_3\}$  (**2''**):** Compound **2** was placed in a glass sample cell and outgassed at room temperature for 20 h under reduced pressure of 0.1 Pa that results **2''**. Removal of water molecules was confirmed by IR (Figure 2b) and CHN analysis. Anal. calc. for  $\text{C}_{60}\text{H}_{48}\text{Fe}_2\text{N}_{20}$ : C, 62.08; H, 4.17; N, 24.14. Found: C, 61.39; H, 4.51; N, 23.86.

**Synthesis of  $\{(\text{H}_2\text{-bpee})(\text{H}_3\text{O})_2[\text{Fe}(\text{CN})_6] \cdot 2\text{H}_2\text{O}\}$  (**3**):** 0.105 g (0.5 mmol)  $\text{K}_4[\text{Fe}(\text{CN})_6]$  was dissolved in 10 mL water and allowed to cool in an ice bath for 15 min. 0.092 g (0.5 mmol) of bpee was dissolved in 10 mL 1 (N) HCl solution. The two solutions were mixed in a beaker and allowed to stand for slow evaporation. After 10 days, blocked shaped yellowish green crystals were grown in the bottom of the beaker. Good quality single crystals were picked up from the mother liquor and immediately covered with paraffin oil for single crystal data collections. For the bulk synthesis, 0.5 mmol of  $\text{K}_4[\text{Fe}(\text{CN})_6]$  was dissolved in 10 mL water. 0.25 mmol of bpee was also dissolved in 10 mL 1 (N) HCl solution. Then both solutions were mixed under stirring condition. Immediately after mixing, yellowish green coloured precipitate was obtained and the resulting mixture was stirred for overnight. Phase purity was confirmed by powder X-ray diffraction. Yield 71% relative to Fe. Anal. calc. for  $\text{C}_{18}\text{N}_8\text{FeO}_4\text{H}_{22}$ : C, 45.97; H, 4.72; N, 23.83. Found: C, 45.34; H, 4.95; N, 23.19. IR (KBr,  $\text{cm}^{-1}$ ):  $\nu(\text{H}_2\text{O})$  3462, 3423;  $\nu_{\text{Ar}}(\text{C-H})$  3026, 3047;  $\nu(\text{CN})$  2061;  $\nu_{\text{Ar}}(\text{C=C})$  1627, 1606. IR spectrum of **3** shows two strong and sharp bands around 3462 and 3423  $\text{cm}^{-1}$  suggesting the presence of water molecules (Figure 3a). A strong band around 2061  $\text{cm}^{-1}$  corroborate to  $\nu(\text{CN})$  stretching frequency and a band around 1627  $\text{cm}^{-1}$  indicates the presence bpee molecule.



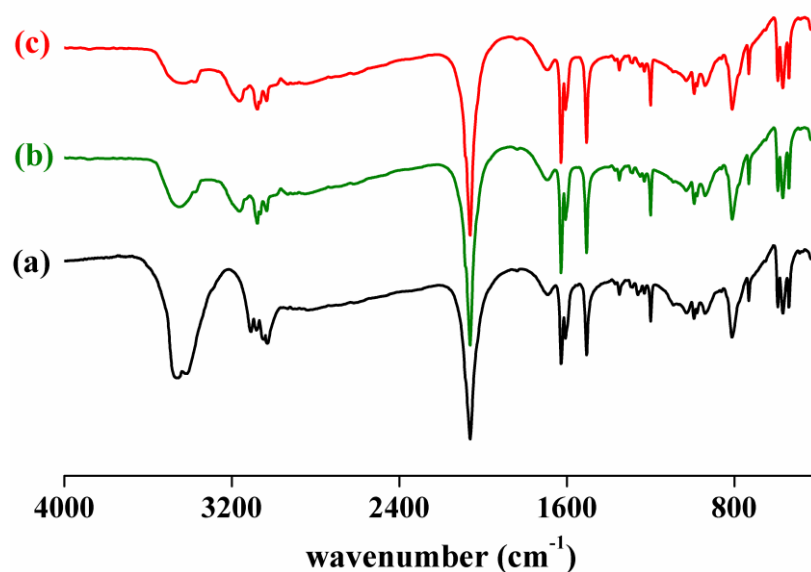


**Figure 3:** IR spectra of compound **3** at different states; (a) as-synthesized, (b) desolvated at room temperature and (c) desolvated at 100 °C.

**Preparation of  $\{(\text{H}_2\text{-bpee})_4[\text{Fe}(\text{CN})_6]_2\}$  (**3'**):** Compound **3** was placed in a glass sample cell and heated at 100 °C for 5h under reduced pressure of 0.1 Pa that results **3'**. Removal of water molecules was confirmed by IR (Figure 3c) and CHN analysis. Anal. calc. for  $\text{C}_{18}\text{N}_8\text{FeO}_2\text{H}_{18}$ : C, 49.78; H, 4.17; N, 25.81. Found: C, 49.31; H, 4.37; N, 25.56.

**Preparation of  $\{[\text{Fe}(\text{CN})_6] \cdot (\text{H-bipy})_3\}$  (**3''**):** Compound **3** was placed in a glass sample cell and outgassed at room temperature for 20 h under reduced pressure of 0.1 Pa that results **3''**. Removal of water molecules was confirmed by IR (Figure 3b) and CHN analysis. Anal. calc. for  $\text{C}_{18}\text{N}_8\text{FeO}_2\text{H}_{18}$ : C, 49.78; H, 4.17; N, 25.81. Found: C, 48.61; H, 4.30; N, 25.19.

**Synthesis of  $\{[(\text{H}_2\text{-bpee})(\text{H-bpee})]_2[\text{Fe}(\text{CN})_6]_2 \cdot 5\text{H}_2\text{O}\}$  (**4**):** Compound **4** was synthesized following the similar method as of compound **2**.  $\text{K}_3[\text{Fe}(\text{CN})_6]$  was taken instead of  $\text{K}_4[\text{Fe}(\text{CN})_6]$ . Greenish yellow block shaped crystals were collected from the crystal tube and subjected for single crystal X-ray diffraction study.

For bulk synthesis of compound **4**, 0.25 mmol of bpee in 5 mL EtOH and 0.25 mmol of  $\text{K}_3[\text{Fe}(\text{CN})_6]$  in 5 mL  $\text{H}_2\text{O}$  were prepared and they were separately allowed to cool in an ice bath. Then both the solutions were mixed under stirring condition. Immediately after mixing, ice cold  $\text{Fe}(\text{ClO}_4)_3$  (0.25 mmol in 5 mL  $\text{H}_2\text{O}$ ) solution was dropwise added with constant stirring. Greenish yellow precipitate was filtered, washed with cold water and ethanol for several time and phase purity was confirmed by powder X-ray diffraction.

Yield: 79%. Anal. calc. for  $C_{60}H_{56}Fe_2N_{20}O_5$ : C, 57.70; H, 4.51; N, 22.43. Found: C, 57.91; H, 4.95; N, 22.01. IR (KBr,  $cm^{-1}$ ):  $\nu(H_2O)$  3426;  $\nu_{Ar}(C-H)$  3089, 3060;  $\nu(CN)$  2113;  $\nu_{Ar}(C=C)$  1619, 1587. IR spectrum of **4** shows two strong and sharp bands around  $3426\text{ cm}^{-1}$  suggesting the presence of water molecules (Figure 4a). A strong band around  $2113\text{ cm}^{-1}$  corroborate to  $\nu(CN)$  stretching frequency and a band around  $1619\text{ cm}^{-1}$  indicates the presence bpee molecule.

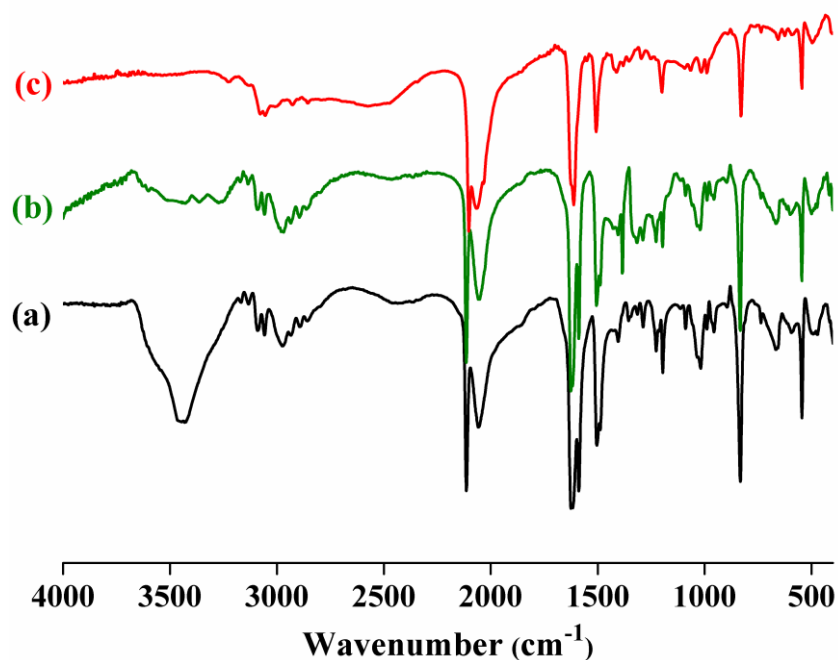


**Figure 4:** IR spectra of compound **4** at different states; (a) as-synthesized, (b) desolvated at room temperature and (c) desolvated at  $100\text{ }^{\circ}\text{C}$ .

**Preparation of  $\{(H_2\text{-bpee})_4[Fe(CN)_6]_2\}$  (**4'**):** Compound **4** was placed in a glass sample cell and heated at  $100\text{ }^{\circ}\text{C}$  for 5h under reduced pressure of  $0.1\text{ Pa}$  that results **4'**. Removal of water molecules was confirmed by IR (Figure 4c) and CHN analysis. Anal. calc. for  $C_{60}H_{46}Fe_2N_{20}$ : C, 62.19; H, 4.00; N, 24.17. Found: C, 61.76; H, 4.12; N, 23.91.

**Preparation of  $\{[Fe(CN)_6]\cdot(H\text{-bipy})_3\}$  (**4''**):** Compound **4** was placed in a glass sample cell and outgassed at room temperature for 20 h under reduced pressure of  $0.1\text{ Pa}$  that results **4''**. Removal of water molecules was confirmed by IR (Figure 4b) and CHN analysis. Anal. calc. for  $C_{60}H_{46}Fe_2N_{20}$ : C, 62.19; H, 4.00; N, 24.17. Found: C, 61.24; H, 4.11; N, 23.81.

**Synthesis of  $\{[(H_{1.5}\text{-bpee})_2][Fe(CN)_6]\cdot 6H_2O\}$  (**5**):** 0.25 mmol (0.165 g) of  $K_3[Fe(CN)_6]$  (dissolved in 25 mL water) was mixed with 0.25 mmol (0.091 g) of 1,2-bis(4-

pyridyl)ethylene (dissolved in 25 mL ethanol) and stirred for 15 min. Then to this solution 0.5 mmol of  $\text{Fe}(\text{ClO}_4)_3$  in 50 mL water was added and stirred for 4 hours. Then reaction mixture was filtered and the filtrate was kept for slow evaporation at room temperature. Orange block shaped crystals were found after two days which were filtered and washed with water and ethanol. Good quality single crystals were picked up and immediately covered with paraffin oil and then subjected for X-ray single crystal structure determination.

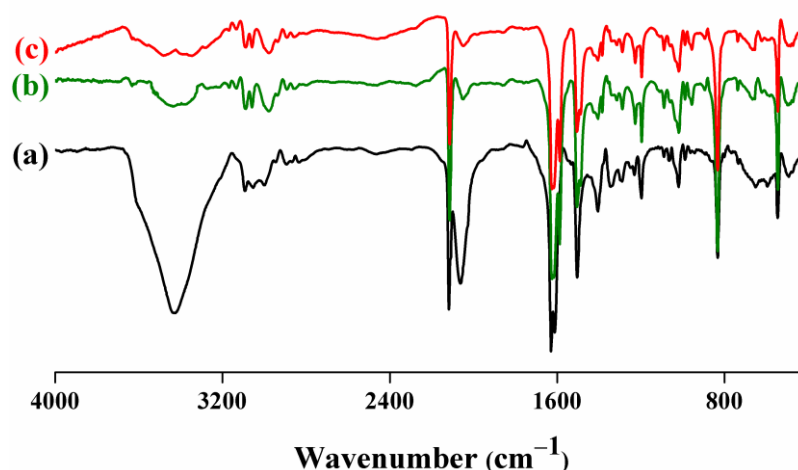


**Figure 5:** IR spectra of compound **5** at different states; (a) as-synthesized, (b) desolvated at room temperature and (c) desolvated at 100 °C.

For the bulk synthesis, an aqueous ice cold solution (10 mL) of  $\text{K}_3[\text{Fe}(\text{CN})_6]$  (0.25 mmol, 0.083 g) was mixed with another ice cold aqueous solution (10 mL) of  $\text{Fe}(\text{ClO}_4)_3$  (0.25 mmol). The above solution was stirred for 5 min and then 0.5 mmol (0.092 g) ice cold bpee solution was added to it. The final solution was stirred for 30 min and then orange precipitate was filtered and air dried and phase purity was confirmed by powder X-ray diffraction. Yield: 65% relative to  $\text{Fe}^{\text{III}}$ . Anal. calc. for  $\text{C}_{30}\text{H}_{35}\text{FeN}_{10}\text{O}_6$ : C, 52.41; H, 5.13; N, 20.37. Found: C, 52.91; H, 5.53; N, 19.89. IR (KBr,  $\text{cm}^{-1}$ ):  $\nu_{\text{H}_2\text{O}}$  3430;  $\nu_{\text{Ar}(\text{C}-\text{H})}$  3093, 3053;  $\nu_{\text{CN}}$  2118, 2063;  $\nu_{\text{Ar}(\text{C}=\text{C})}$  1628, 1612. IR spectrum of **5** shows two strong broad bands around  $3430\text{ cm}^{-1}$  suggesting the presence of water molecules (Figure 5a). A strong band around  $2118\text{ cm}^{-1}$  corroborate to  $\nu(\text{CN})$  stretching frequency and a band around  $1612\text{ cm}^{-1}$  indicates the presence bpee molecule.

**Preparation of  $\{(\text{H}_2\text{-bpee})_4[\text{Fe}(\text{CN})_6]_2\}$  (**5'**):** Compound **5** was placed in a glass sample cell and heated at 100 °C for 5h under reduced pressure of 0.1 Pa that results **5'**. Removal

of water molecules was confirmed by IR (Figure 5c) and CHN analysis. Anal. calc. for  $C_{30}H_{23}FeN_{10}$ : C, 62.19; H, 4.00; N, 24.17. Found: C, 61.61; H, 3.81; N, 23.64.

**Preparation of  $\{[Fe(CN)_6] \cdot (H\text{-bipy})_3 \cdot H_2O\}$  (**5''**):** Compound **5** was placed in a glass sample cell and outgassed at room temperature for 20 h under reduced pressure of 0.1 Pa that results **5''**. Removal of water molecules was confirmed by IR (Figure 5b) and CHN analysis. Anal. calc. for  $C_{30}H_{25}FeN_{10}O$ : C, 60.31; H, 4.22; N, 23.44. Found: C, 59.78; H, 4.02; N, 22.93.

### 2.2.3: Physical Measurements

The elemental analyses of each compounds and their different state were carried out on a Thermo Fisher Flash 2000 Elemental Analyser. Infra-red (IR) spectroscopic studies of all compounds were carried out in the mid-IR region using KBr pellet (Bruker IFS-66v). Thermogravimetric analysis (TGA) was carried out (Mettler Toledo) in nitrogen atmosphere (flow rate = 50 ml min<sup>-1</sup>) in the temperature range 30 – 650 °C (heating rate = 2°C min<sup>-1</sup>). Powder XRD pattern of the products were recorded by using Cu- $K\alpha$  radiation (Bruker D8 Discover; 40 kV, 30 mA).

### 2.2.4: Single Crystal X-ray Diffraction

Suitable single crystals of compound **1-5** were mounted on a thin glass fiber with commercially available super glue. X-ray single crystal data was collected on a Bruker Smart-CCD diffractometer equipped with a normal focus, 2.4 kW sealed tube X-ray source with graphite monochromated Mo- $K\alpha$  radiation ( $\lambda = 0.71073 \text{ \AA}$ ) operating at 50 kV and 30 mA. The program SAINT was used for integration of diffraction profiles and absorption correction was made with SADABS program. The structure was solved by SIR 92<sup>29</sup> and refined by full matrix least square method using SHELXL.<sup>30</sup> All the hydrogen atoms were fixed by HFIX and placed in ideal positions. Potential solvent accessible area or void space was calculated using the PLATON<sup>31</sup> multipurpose crystallographic software. All crystallographic and structure refinement data of **1-5** are summarized in Table 1. Selected bond distances and angles are shown in Table 2-11. All calculations were carried out using SHELXL 97,<sup>30</sup> PLATON,<sup>31</sup> SHELXS 97<sup>32</sup> and WinGX system, Ver 1.80.01.<sup>33</sup>

**Table 1:** Crystallographic data and structure refinement parameters for compounds **1-5**.

Parameters	<b>1</b>	<b>2</b>	<b>3</b>	<b>4</b>	<b>5</b>
Empirical formula	C <sub>36</sub> H <sub>43</sub> FeN <sub>12</sub> O <sub>8</sub>	C <sub>60</sub> H <sub>66</sub> Fe <sub>2</sub> N <sub>20</sub> O <sub>9</sub>	C <sub>18</sub> N <sub>8</sub> FeH <sub>22</sub> O <sub>4</sub>	C <sub>60</sub> H <sub>56</sub> Fe <sub>2</sub> N <sub>20</sub> O <sub>5</sub>	C <sub>30</sub> H <sub>35</sub> FeN <sub>10</sub> O <sub>6</sub>
<i>M</i>	827.67	1322.985	470.264	1248.95	687.53
Crystal system	Triclinic	Monoclinic	Monoclinic	Triclinic	Triclinic
Space group	<i>P1</i> (No. 1)	<i>C2/m</i> (No. 12)	<i>C2/m</i> (No. 12)	<i>P1̄</i> (No. 2)	<i>P1̄</i> (No. 2)
<i>a</i> (Å)	9.7496(10)	13.3574(5)	10.7437(5)	8.9644(2)	9.1823(8)
<i>b</i> (Å)	10.3079(5)	16.1239(5)	12.6595(6)	10.3952(3)	9.2949(8)
<i>c</i> (Å)	11.9451(6)	10.8192(4)	17.0436(7)	18.1383(5)	9.9680(9)
$\alpha$ (°)	114.920(2)	90	90	79.091(2)	86.070(5)
$\beta$ (°)	110.933(4)	137.015(1)	103.230(2)	82.964(2)	71.890(4)
$\gamma$ (°)	91.374(3)	90	90	75.009(2)	76.950(4)
<i>V</i> (Å <sup>3</sup> )	995.02(13)	1588.72(10)	2256.57(18)	1598.39(8)	787.72(12)
<i>Z</i>	1	1	4	1	1
<i>T</i> (K)	100	295	295	295	295
$\lambda$ (Mo-K $\alpha$ )	0.71073	0.71073	0.71073	0.71073	0.71073
<i>D<sub>c</sub></i> (g cm <sup>-3</sup> )	1.381	1.381	1.384	1.298	1.449
$\mu$ (mm <sup>-1</sup> )	0.445	0.528	0.709	0.517	0.539
$\theta_{\max}$ (°)	25.1	23.2	25.0	24.1	23.9
Total data	14096	5349	15232	15552	10538
Data [ <i>I</i> > 2 $\sigma$ ( <i>I</i> )]	5346	900	1380	3099	1896
<i>R</i> <sup><i>a</i></sup>	0.0493	0.0260	0.0650	0.0584	0.0775
<i>R<sub>w</sub></i> <sup><i>b</i></sup>	0.1028	0.0673	0.2002	0.1786	0.2110
<i>GOF</i>	1.01	1.10	1.06	1.02	1.06
<i>Flack</i> ( <i>x</i> )	0.26(2)	–	–	–	–

$${}^a R = \sum ||F_o| - |F_c|| / \sum |F_o| ; \quad {}^b R_w = [\sum \{w(F_o^2 - F_c^2)^2\} / \sum \{w(F_o^2)\}]^{1/2}$$

The [Fe(CN)<sub>6</sub>]<sup>3-</sup> part of compound **1** was easily solved with direct methods and Patterson method in both space groups *P1* and *P1̄*. Initial attempts to model the structure in the space group *P1̄* with Fe atom on the origin gave moderately good agreement with the diffraction data but attempts to use the resulting phases to generate a Fourier map gave a non-interpretable result and the refinement was not at all satisfactory. The structure was then modeled in the space group *P1* and the phase extension agreed well with the diffraction data with the appearance chemically feasible structure. During refinement, we observed that ADDSYM detects a pseudo center of symmetry. A closer look into the refinement of data for compound **1** revealed a Flack parameter of ~0.26. We assigned the additional apparent pseudo-symmetry to be due to the presence of highly symmetrical [Fe(CN)<sub>6</sub>]<sup>3-</sup> moiety coupled with the existence of twinning. Further a transformation of coordinates of *P1* to *P1̄* gives chemically unfeasible structure. All the reasons unequivocally establish the space group as *P1*. Therefore, the ADDSYM message can be regarded as harmless.

**Table 2:** Selected bond distances (Å) and angles (°) for **1**.

Bond Distance			
Fe1-C5	1.945(7)	Fe1-C1	1.921(9)
Fe1-C6	1.938(7)	Fe1-C2	1.955(7)
Fe1-C3	1.943(7)	Fe1-C4	1.937(8)
Bond Angle			
C2-Fe1-C5	178.8(3)	C2-Fe1-C6	89.5(3)
C3-Fe1-C4	88.0(3)	C3-Fe1-C5	91.3(3)
C3-Fe1-C6	179.1(3)	C4-Fe1-C5	87.5(3)
C4-Fe1-C6	91.3(3)	C5-Fe1-C6	89.3(3)
C1-Fe1-C2	87.9(3)	C1-Fe1-C3	91.2(3)
C1-Fe1-C4	179.3(3)	C1-Fe1-C5	92.3(3)
C1-Fe1-C6	89.4(3)	C2-Fe1-C3	89.9(3)
C2-Fe1-C4	92.3(3)	Fe1-C1-N1	179.3(7)
Fe1-C2-N2	179.8(8)	Fe1-C3-N3	179.8(8)
Fe1-C4-N4	178.4(6)	Fe1-C5-N5	178.6(7)
Fe1-C6-N6	179.0(5)		

**Table 3:** Geometrical parameters (Å, °) of hydrogen bonds for the water octamer<sup>a</sup>

O1W...O5W#1	2.692(8)	O1W--H2W...O5W	167.00
O2W...O6W#2	2.737(8)	O2W--H4W...O6W	172.00
O4W...O1W#3	2.750(8)	O4W--H7W...O1W	174.00
O4W...O3W#3	2.750(9)	O4W--H8W...O3W	174.00
O5W...O8W	2.738(8)	O5W--H10W...O8W	180.00
O6W...O4W	2.732(9)	O6W--H12W...O4W	179.00
O8W...O7W#4	2.750(8)	O8W--H15W...O7W	160.00
O8W...O2W#4	2.713(9)	O8W--H16W...O2W	158.00

<sup>a</sup> Symmetry: (#1) x, 1 + y, z; (#2) x, -1 + y, z; (#3) -1 + x, y, z; (#4) 1 + x, y, z.

**Table 4.** Selected bond distances (Å) for compound **2**.

Bonds	Distance (Å)	Bonds	Distance (Å)
Fe1-C2	1.906(3)	N2-C2	1.166(4)
Fe1-C3	1.901(3)	N3-C3	1.166(4)
Fe1-C1_b	1.911(6)	C4-C5	1.372(5)
Fe1-C2_b	1.906(3)	C5-C8	1.387(4)
Fe1-C3_c	1.901(3)	C6-C7	1.375(5)
Fe1-C1	1.911(6)	C7-C8	1.400(4)
C8-C9	1.472(5)	N4-C4	1.337(3)
N4-C6	1.336(3)	N1-C1	1.169(8)

**Table 5.** Selected bond angles (°) for compound 2.

Angles	Degree (°)	Angles	Degree (°)
C2_b-Fe1-C3	90.00(1)	C3-Fe1-C3_c	180.00
C1_b-Fe1-C2_b	91.47(18)	C1_b-Fe1-C3_c	90.00(1)
C2_b-Fe1-C3_c	90.00(1)	C1_b-Fe1-C2	88.54(18)
C1-Fe1-C2	91.47(18)	C1-Fe1-C3	90.00(1)
C1-Fe1-C1_b	180.00	C1-Fe1-C2_b	88.54(18)
C1-Fe1-C3_c	90.00(1)	C2-Fe1-C3	90.00(1)
C1_b-Fe1-C3	90.00(1)	C2-Fe1-C2_b	180.00
C2-Fe1-C3_c	90.00(1)	Fe1-C1-N1	177.7(3)
Fe1-C2-N2	179.5(5)	Fe1-C3-N3	179.98(3)

Symmetry code: a =-x,y,-1-z; b = 1-x,y,1-z; c = 1-x,-y,1-z; d =x,-y,z; e =1/2-x,1/2-y,-z; f =1+x,y,1+z

**Table 6.** Selected bond distances (Å) for compound 3.

Bonds	Distance (Å)	Bonds	Distance (Å)
Fe1-C2	1.936(4)	N1-C1	1.138(5)
Fe1-C3	1.945(3)	N2-C2	1.145(5)
Fe1-C1_a	1.944(3)	N3-C3	1.141(5)
Fe1-C2_a	1.936(4)	C4-C5	1.366(7)
Fe1-C3_a	1.945(3)	C5-C6	1.402(6)
Fe1-C1	1.944(3)	C6-C9	1.491(6)
C6-C7	1.383(7)	C7-C8	1.348(7)
C9-C9_b	1.268(5)	N4-C4	1.325(6)
N4-C8	1.332(6)		

**Table 7.** Selected bond angles (°) for compound 3.

Angles	Degree (°)	Angles	Degree (°)
C2_a-Fe1-C3	93.35(15)	C3-Fe1-C3_a	180.00
C1_a-Fe1-C2_a	89.06(15)	C1_a-Fe1-C3_a	89.74(14)
C2_a-Fe1-C3_a	86.65(15)	C1_a-Fe1-C2	90.94(15)
C1-Fe1-C2	89.06(15)	C1-Fe1-C3	89.74(14)
C1-Fe1-C1_a	180.00	C1-Fe1-C2_a	90.94(15)
C1-Fe1-C3_a	90.26(14)	C2-Fe1-C3	86.65(15)
C1_a-Fe1-C3	90.26(14)	C2-Fe1-C2_a	180.00
C2-Fe1-C3_a	93.35(15)	Fe1-C1-N1	177.0(3)
C4-N4-C8	122.1(4)	Fe1-C2-N2	176.7(3)
C4-N4-H4	119.00	Fe1-C3-N3	176.1(3)

Symmetry code: a =3/2-x,-1/2-y,1-z; b = 2-x,y,3/2-z; c =1-x,-y,1-z; d =1/2+x,1/2+y,z; e =2-x,-y,1-z

**Table 8.** Selected bond distances (Å) for compound 4.

Bonds	Distance (Å)	Bonds	Distance (Å)
Fe1-C1	1.944(7)	Fe1-C2	1.943(7)
Fe1-C3	1.914(5)	Fe1-C1_a	1.944(7)
Fe1-C2_a	1.943(7)	Fe1-C3_a	1.914(5)
Fe2-C4_b	1.926(10)	Fe2-C5	1.937(8)
Fe2-C6	1.939(7)	Fe2-C5_b	1.937(8)
Fe2-C6_b	1.939(7)	Fe2-C4	1.926(10)

**Table 9.** Selected bond angles (°) for compound 4.

Angles	Degree (°)	Angles	Degree (°)
C1_a-Fe1-C2_a	89.6(3)	C1_a-Fe1-C3_a	90.6(2)
C5_b-Fe2-C6_b	89.4(3)	C2_a-Fe1-C3_a	90.3(2)
C1_a-Fe1-C2	90.4(3)	C1-Fe1-C2	89.6(3)
C1-Fe1-C3	90.6(2)	C1-Fe1-C1_a	180.00
C1-Fe1-C2_a	90.4(3)	C1-Fe1-C3_a	89.5(2)
C2-Fe1-C3	90.3(2)	C1_a-Fe1 -C3	89.5(2)
C2-Fe1-C2_a	180.00	C2-Fe1 -C3_a	89.7(2)
C2_a-Fe1-C3	89.7(2)	C3-Fe1-C3_a	180.00
C4_b-Fe2-C5_b	90.8(4)	C5_b-Fe2-C6	90.6(3)
C6-Fe2-C6_b	180.00	C4-Fe2-C6_b	86.9(3)
C5-Fe2-C6	89.4(3)	C4_b-Fe2-C6_b	93.1(3)
C4-Fe2-C5	90.8(4)	C4-Fe2-C6	93.1(3)
C4-Fe2-C4_b	180.00	C4-Fe2-C5_b	89.2(4)
C5-Fe2-C5_b	180.00	C5-Fe2-C6_b	90.6(3)
C4_b-Fe2 -C5	89.2(4)		

Symmetry code: a =-x,-y,1-z; b =-x,-y,-z; c =-1+x,y,z; d =-1+x,y,z; e =1+x,y,z.

**Table 10.** Selected bond distances (Å) for compound 5.

Bonds	Distance (Å)	Bonds	Distance (Å)
Fe1-C3_a	1.932(6)	C4-C6	1.371(7)
Fe1-C2_a	1.933(7)	C5-C7	1.378(8)
Fe1-C2	1.933(7)	C6-C8	1.396(7)
Fe1-C3	1.932(6)	C7-C8	1.391(7)
Fe1-C1_a	1.934(5)	C9-C10	1.346(7)
C10-C11	1.459(8)	C11-C12	1.396(7)
C11-C13	1.391(7)	C12-C14	1.381(8)
C13-C15	1.375(8)	N4-C4	1.340(7)
N4-C5	1.341(7)	N5-C15	1.345(7)
N5-C14	1.337(7)	N1-C1	1.152(6)
N2-C2	1.142(10)	N3-C3	1.161(9)

**Table 11.** Selected bond angles (°) for compound 5.

Angles	Degree (°)	Angles	Degree (°)
C1_a-Fe1-C2	92.2(2)	C2-Fe1-C2_a	180.00
C2-Fe1-C3_a	87.4(3)	C1_a-Fe1-C3	89.8(2)
C2_a-Fe1-C3	87.4(3)	C3-Fe1-C3_a	180.00
C1_a-Fe1-C2_a	87.8(2)	C1_a-Fe1-C3_a	90.2(2)
C2_a-Fe1-C3_a	92.6(3)	C1-Fe1-C2	87.8(2)
C1-Fe1-C3	90.2(2)	C1-Fe1-C1_a	180.00
C1-Fe1-C2_a	92.2(2)	C1-Fe1-C3_a	89.8(2)
C2 -Fe1-C3	92.6(3)		

Symmetry code: a = 2-x,2-y,-z; b = -1+x,y,1+z; c =-1-x,1-y,1-z; d =1+x,y,z



### 2.2.5: Adsorption Study

We have activated all the samples in two different ways. The first procedure is by heating the samples at 80 °C (**1**) and 100 °C (**2-5**) under vacuum ( $10^{-1}$  Pa) whereas the second one by evacuating the samples (**1-5**) in high vacuum ( $10^{-1}$ Pa) at room temperature for longer time. For all the measurements, in the sample tube adsorbent samples (~ 100–150 mg) were placed which were prepared at 80 °C (to obtain **1'**) and 100 °C for about 8 hours (to obtain **2'-5'**) or at RT for about 24 hours (to obtain **1''-5''**) under vacuum prior to measurement of the isotherms. N<sub>2</sub> (77 K), and CO<sub>2</sub> (195 K), adsorption studies were carried out with the desolvated samples i.e. **1'-5'** by using QUANTACHROME QUADRASORB SI analyzer. The adsorption of different solvents like MeOH at 293 K and H<sub>2</sub>O, EtOH at 298 K were measured in the vapour state by using BELSORP-aqua-3 analyzer. The different solvent molecules used to generate the vapour were degassed fully by repeated evacuation. Dead volume was measured with helium gas. The adsorbates were placed into the sample tubes, then the change of the pressure was monitored and the degree of adsorption was determined by the decrease in pressure at the equilibrium state. All operations were computer controlled and automatic.

## 2.3: Results and Discussion

### 2.3.1: Crystal Structure Description

**2.3.1.1: Structural description of  $\{[\text{Fe}(\text{CN})_6] \cdot (\text{H-bipy})_3 \cdot 8\text{H}_2\text{O}\}$  (**1**):** Compound **1** crystallizes in triclinic system with *P1* space group. The asymmetric unit consists of one molecule of  $[\text{Fe}(\text{CN})_6]^{3-}$ , three protonated 4,4'-bipyridyl (H-bipy) linkers and eight lattice water molecules (Figure 6a). Fe<sup>III</sup> in **1** locates itself in a distorted octahedral geometry with six coordination furnished by six cyanide ligands. Distortion from perfect octahedral geometry is reflected in *cisoid* (87.5(3)-92.3(3)°) and *transoid* (178.4(6)-179.8(8)°) angles. Fe–C bond lengths are fairly uniform and it ranges from 1.921(9)–1.955(7) Å. C–N bond length in cyanide ligand ranges from 1.132(9)–1.180(9) Å. Each singly protonated bipy molecules form a linear chain through N⋯H–N hydrogen bonding interaction (2.692(10) – 2.707(8) Å) in *a* direction. Three independent chains are associated through  $\pi \cdots \pi$  interactions (cg⋯cg distances are in the range of 3.795(4) – 5.425(4) Å) to form a 2D corrugated sheet lying in the crystallographic *ab* plane (Figure 6b).

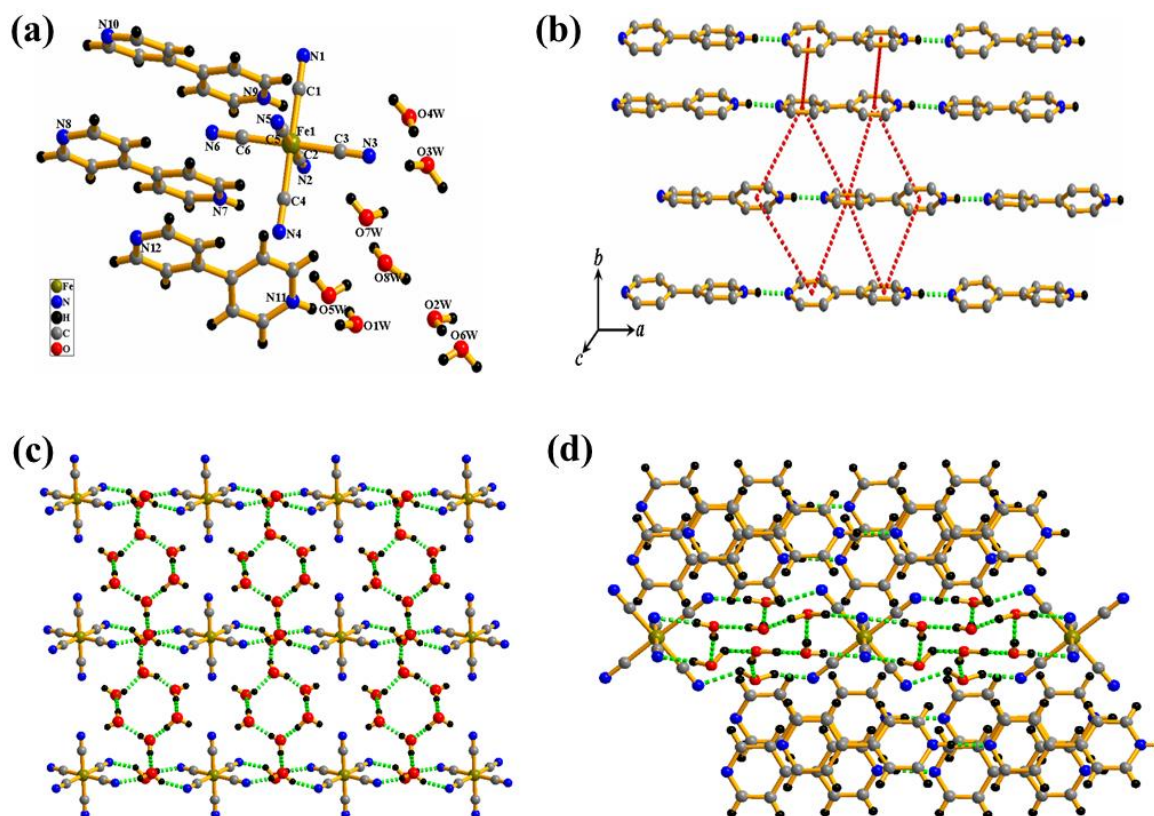


**Figure 6:** (a) View of the asymmetric unit of supramolecular host **1** shows one molecule of  $[\text{Fe}(\text{CN})_6]^{3-}$ , three protonated bipy molecule and eight lattice water molecules. (b) View of the 2D sheet formed by N–H $\cdots$ N H-bonding (green dashed lines) and  $\pi\cdots\pi$  interactions (red dashed lines) between the ring centroids of H-bipy cations. (c) Figure shows each water cluster is in close contact with four neighboring  $[\text{Fe}(\text{CN})_6]^{3-}$  anions by hetero-molecular O–H $\cdots$ N H-bonding to form a extended sheet like structure. (d) 3D supramolecular host **1** generated by H-bonding and  $\pi\cdots\pi$  interactions with the channels occupied by lattice water molecules. H-bonding specification (dashed lines): brown, O–H $\cdots$ O; pink, O–H $\cdots$ N; green, N–H $\cdots$ N; blue, C–H $\cdots$ O; C–H $\cdots$ N, grey.

The most interesting structural aspect of **1** is the presence of an octameric water cluster where the eight lattice water molecules assembled through hydrogen bonding interactions (2.692(8) – 2.750(9) Å) (Figure 7a). The structure of the water cluster is very fascinating and is similar to a *e,e*-1,4- substituted cyclohexane molecule where six water molecules are positioned on the vertices of the cyclohexane ring and the seventh and eighth occupy the 1,4-equatorial positions of the ring. Each octameric water cluster is connected to four nearest  $[\text{Fe}(\text{CN})_6]^{3-}$  moiety through O–H $\cdots$ N hydrogen bonding (2.802(8) – 2.977(8) Å) between O-atom of water molecules and N-atom of cyanide ligands to form a sheet like structure. Further hydrogen bonding between water clusters and cyanide ligands in *a* and *b* directions extend the 2D sheet in the *ab* plane (Figure 6c).

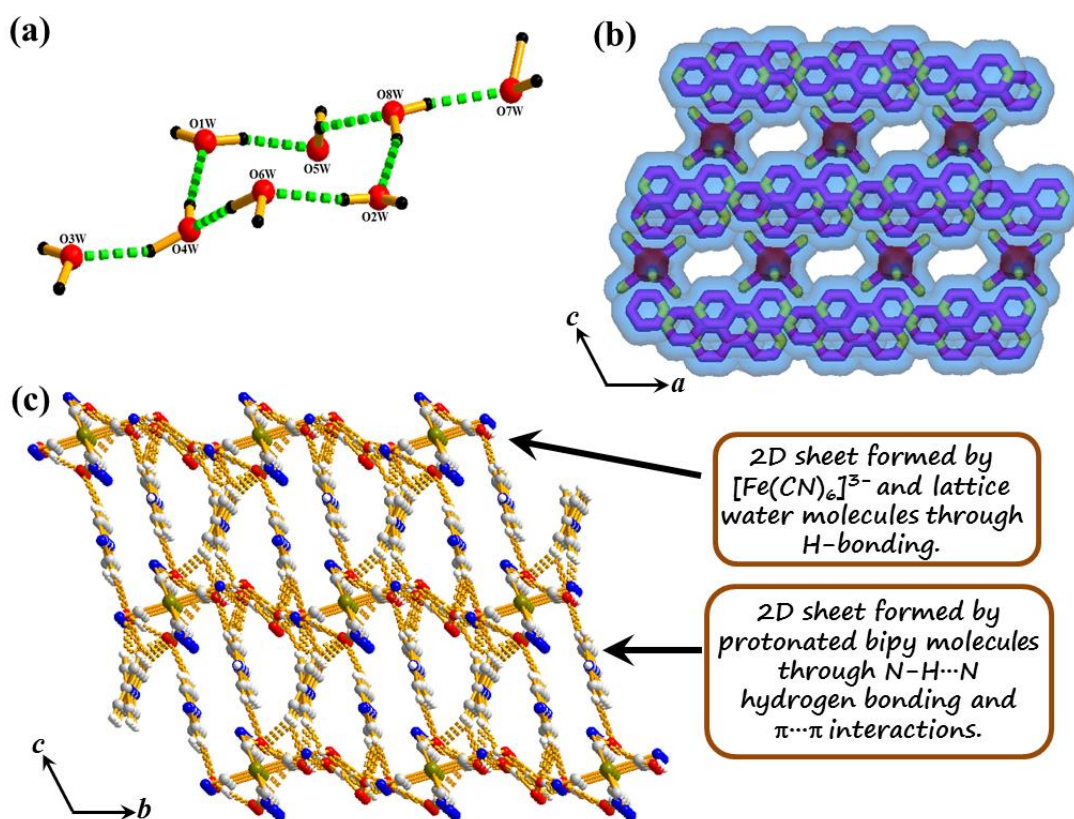


**Figure 7:** (a) View of the 1,4-substituted chair conformer of octameric water cluster in **1**. (b) Surface stick view of supramolecular host **1** after removal of water molecules showing 1D channels of  $4.6 \times 2 \text{ \AA}$  along crystallographic  $b$  direction. (c) Figure shows the ABAB type stacking of 2D sheets in host network **1**.

The H-bipy corrugated sheets and the 2D sheets formed by  $[\text{Fe}(\text{CN})_6]^{3-}$  and water clusters stack in AB fashion along  $c$  direction (Figure 7c). C-H...N and C-H...O hydrogen bonding between these 2D sheets results a 3D supramolecular host with six-sided voids along  $b$  direction occupied by lattice water molecules (Figure 6d). The dimension of the channels is about  $4.6 \times 2 \text{ \AA}^2$ , calculated considering the van der Waals radii of the atoms (Figure 7b). The void volume of the host calculated by PLATON<sup>20</sup> after removal of the lattice water molecules is about 22.2% to the total unit cell volume.

**Water cluster conformation of Compound 1:** Six lattice water molecules O1W, O2W, O4W, O5W, O6W and O8W attain chair conformation of cyclohexane by cooperative H-bonding to form a hexameric core. The remaining two molecules O3W and O7W are crowned at 1,4-equatorial positions of the cyclohexane ring to form a discrete octameric water cluster with  $S_2$  symmetry. A schematic diagram showing the conformations of different water octamers with their corresponding energies is given in Figure 8.

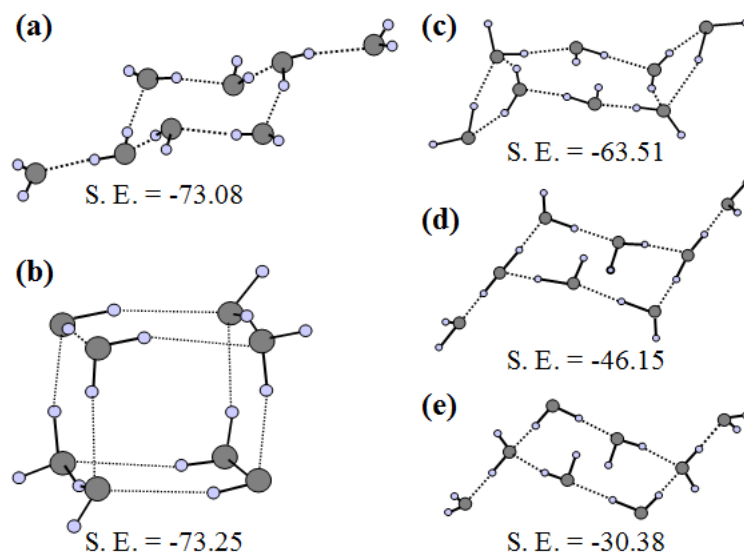


**Figure 8:** Comparison of the stabilization energies of various octamers (S. E. is stabilization energy in kcal/mol). Conformer ‘a’ is presented in this report and its energy calculation is mentioned in the text. Energy calculations for the conformers ‘b-e’ can be found in reference 13f.

The host lattice plays a crucial role in determining the conformation of the water cluster. A good comparison can be made with the octameric water cluster found in host **1** to that reported by Rajsekharan *et al.*<sup>13f</sup> Both the clusters have hexameric core, however, 1,4-substitution in the water cluster reported by Rajsekharan *et al.* is axial type instead of equatorial as found in **1**, and for good reasons. They showed that the 1,4-axially substituted water molecules are involved in hydrogen bonding with carboxylate oxygens of the dipicolinate ligand. The 1,4-equatorial positioning of the water molecules will miss these hydrogen bonding interactions and hence, favours the axial conformation. In case of host **1**, the 1,4-equatorially substituted water molecules are involved in hydrogen bonding with the cyanide groups of  $[\text{Fe}(\text{CN})_6]^{3-}$  moiety. On the other hand, 1,4-axial positioning of these water molecules would be lacking such hydrogen bonding interactions and hence favours the more stable equatorial conformation. The average O–O distance in the cluster is 2.733 Å at 100 K as determined from X-ray crystallography. The corresponding value in Ice- $I_h$  at 183 K is 2.759 Å. On the basis of the accuracy of the water structure as well as the proper hydrogen-bond donor-acceptor matching, the indicated positions of the hydrogen atoms are believed to be correct. The H-bonding saturation inside the hexameric core is not reached, and therefore further stabilization of the cluster results from the O–H $\cdots$ N H-bonding assisted by the presence of CN groups in  $[\text{Fe}(\text{CN})_6]^{3-}$  anions.

**Stability of the water cluster:** Studies based on isomeric water clusters isolated in different host led us to compute the effect of spatial confinement on the properties of the water cluster, its stabilization due to the confinement by ranking in energy and the complementarity relationship. Hence, for a quantitative understanding about the stability of the water cluster, we performed ab initio geometry optimization of the H-atom positions with 6-31++G(d,p) basis set by freezing the positions of the heavy oxygen atoms. The corrected stabilization energy of the water cluster was found to be  $-73.08$  kcal/mol and the value is almost equal to the cubic conformer ( $-73.25$  kcal/mol, higher than the axial conformer) which is reported as the most stable one (Figure 8).<sup>13f</sup> Corrected stabilization energy includes the basis set superposition error (BSSE) and has been defined as  $E_{\text{int}} = \{ (E_{\text{water-n-mer}} + \text{BSSE}_{\text{water-n-mer}}) - (n \cdot E_{\text{water}}) \}$ . The optimized configuration of  $(\text{H}_2\text{O})_8$  cluster with the conformation of *e,e*-1,4-substituted cyclohexane is found to be similar as observed in compound **1**, suggesting *e,e*-1,4-substituted cyclohexane chair conformation is the most stable with the resemblance of organic molecules.

**2.3.1.2: Structural description of  $\{(\text{H}_2\text{-bpee})_4[\text{Fe}(\text{CN})_6]_2 \cdot 9\text{H}_2\text{O}\}$  (**2**):** Compound **2** crystallizes in monoclinic system with  $C2/m$  space group. The asymmetric unit consists of 0.5 of  $[\text{Fe}(\text{CN})_6]^{4-}$ , one doubly protonated 1,2-bis(4-pyridyl)ethylene ( $\text{H}_2\text{-bpee}$ ) and 2.25 lattice water molecules (Figure 9a). In compound **2**,  $\text{Fe}^{\text{II}}$  center is in a slightly distorted octahedral geometry which is reflected from the cisoid ( $88.54(18) - 91.47(18)^\circ$ ) angles. Fe–C bond lengths vary from 1.906(3) to 1.911(6) Å. The crystalline water molecules (O2 and O3) are assembled through hydrogen bonding interaction (2.770(2) Å) resulting in the formation of a  $R_4$  cyclic quasi-planar water tetramers with  $D_{2h}$  configuration<sup>34</sup> (Figure 9b).  $[\text{Fe}(\text{CN})_6]^{4-}$  moiety forms a 1D chain through another crystalline water molecule (O1) and each chains are linked by the water cluster (with O3) resulting in a 2D layer lying in the *ac* plane (Figure 9c).  $\text{H}_2\text{-bpee}$  molecules form a 1D chain through H-bonding with water (O2) molecule and such chains are aligned parallel through  $\pi \cdots \pi$  interaction leading to a 2D sheet (Figure 9d) (*cg*···*cg* distance are in the range of 3.7003(13) to 3.9111(12) Å) in the crystallographic *bc* plane. The dihedral angle between the pyridyl rings varies from  $0^\circ$  to  $10.87^\circ$  whereas the slip angle between these two is varying from  $61.88^\circ$  to  $77.74^\circ$ .

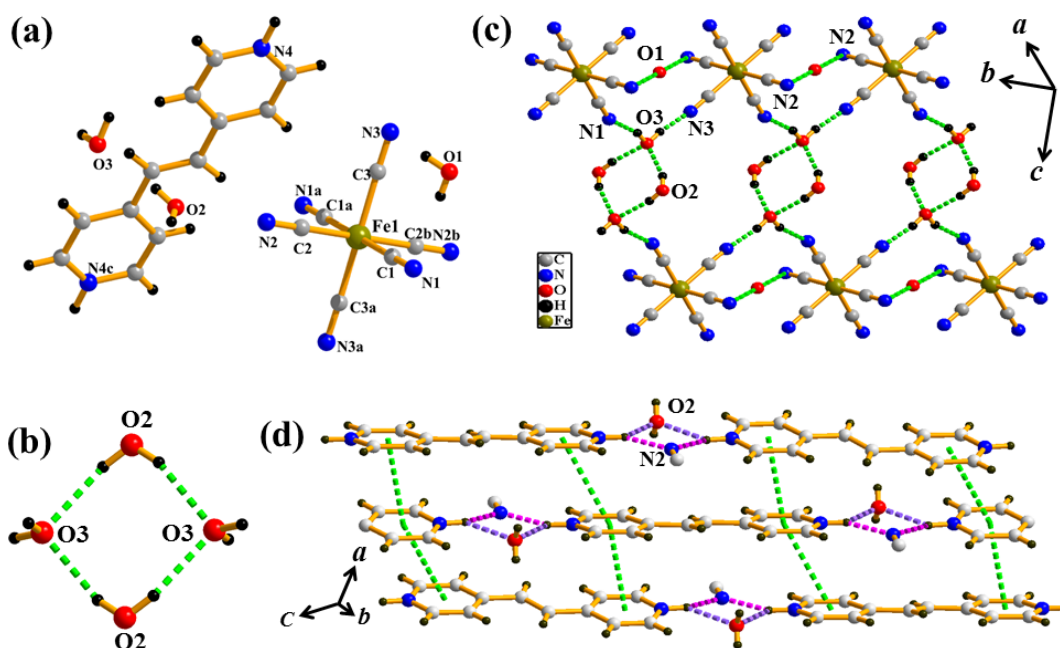


**Figure 9:** (a) Asymmetric unit of **2**. Symmetry codes:  $a = 1-x, y, 1-z$ ;  $b = 1-x, -y, 1-z$ ;  $c = 0.5-x, 0.5-y, -z$ . (b) Tetranuclear water cluster formed by the guest water molecules in **2**. (c) 2D corrugated sheet formed by the H-bonding interaction between tetrameric water cluster and  $[\text{Fe}(\text{CN})_6]^{4-}$ . (d) ABAB stacking supported by  $\pi$ -stacking between the 1D hydrogen bonded  $\text{H}_2$ -bpee molecules.

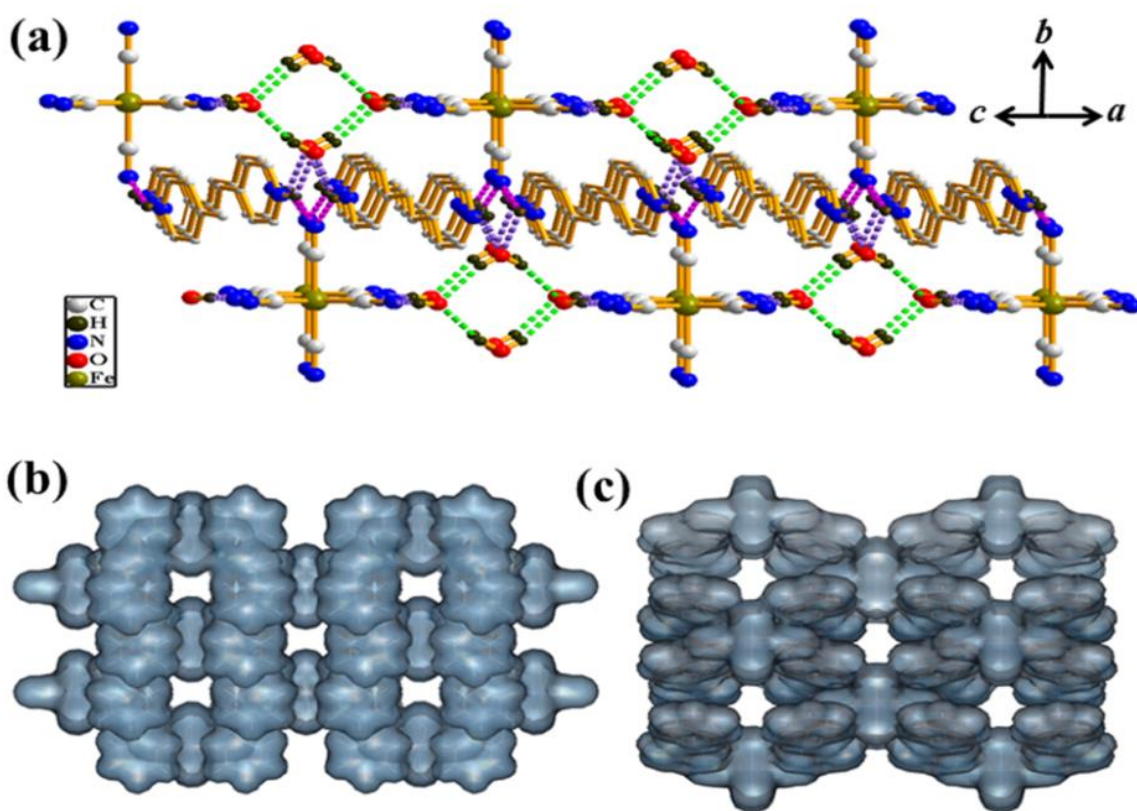


**Figure 10:** (a) 3D supramolecular architecture of **2** formed by the cooperative H-bonding between  $[\text{Fe}(\text{CN})_6]^{4-}$ , protonated bpee and water molecules. View of different pores in the supramolecular framework: (b) along crystallographic  $c$ -direction and (c) along  $[101]$  direction.

Therefore each oxygen atom in the cluster is in a tetrahedral environment where it is involved in the formation of four hydrogen bonds, two with water molecules in the cluster itself and the another two with H<sub>2</sub>-bpee molecules (N4–H···O2 = 3.045(4) Å) for O2 (Figure 10a) and [Fe(CN)<sub>6</sub>]<sup>4-</sup> moiety for O3 (O3–H···N = 2.732(5) – 2.771(8) Å). The 2D layer generated by H<sub>2</sub>O and [Fe(CN)<sub>6</sub>]<sup>4-</sup> is connected to H<sub>2</sub>-bpee molecules through N–H···O and N–H···N H-bonding leading to the formation of a 3D supramolecular architecture (Figure 10a) with two type of voids along [101] and *c* direction. The dimension of the voids are 2.6 × 1.7 Å<sup>2</sup> (along *c* direction) and 3.23 × 3.23 Å<sup>2</sup> (along [101] direction) calculated considering van der Waals radii of the atom (Figures 10b &c). After removal of the lattice water molecules, calculation using PLATON suggests 20.7% void volume per unit cell volume in **2**.

**2.3.1.3: Structural description of {(H<sub>2</sub>-bpee)(H<sub>3</sub>O)<sub>2</sub>[Fe(CN)<sub>6</sub>]·2H<sub>2</sub>O} (**3**):** Compound **3** crystallizes in monoclinic system with *C2/c* space group. The asymmetric unit consist of one molecule of [Fe(CN)<sub>6</sub>]<sup>4-</sup>, one doubly protonated bpee (H<sub>2</sub>-bpee) molecule, two protonated water molecules and two lattice water molecules (Figure 11a).

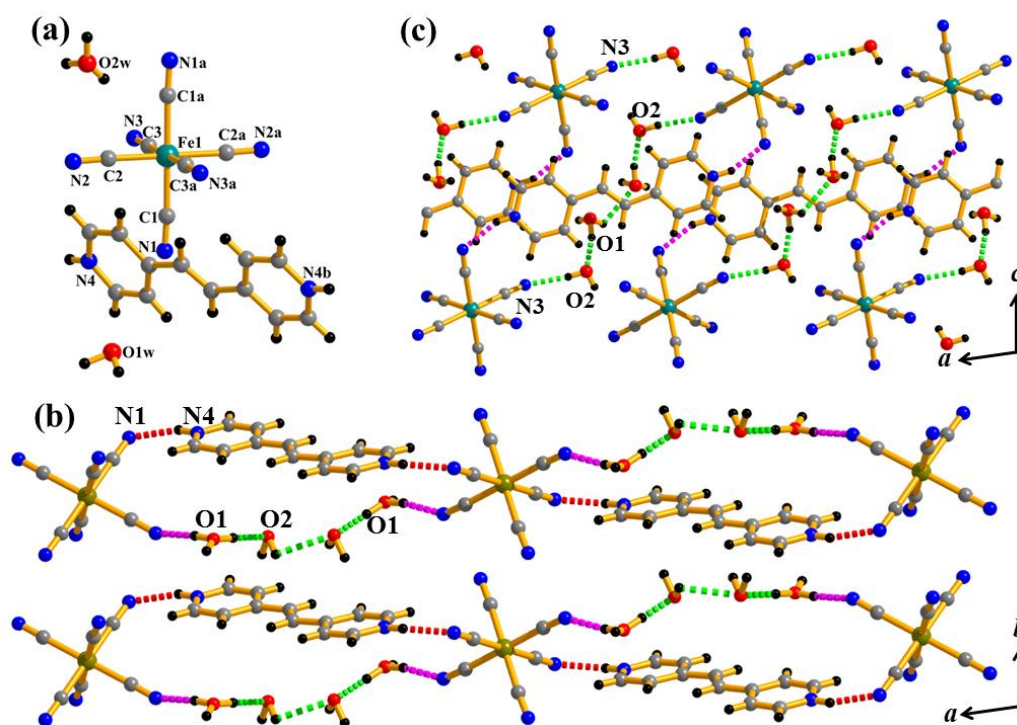


**Figure 11:** (a) Asymmetric unit of **3**. Symmetry codes:  $a = 1.5-x, 0.5-y, 1-z$ ;  $b = 2-x, y, 1.5-z$ . (b) H-bonded 1D chains of [Fe(CN)<sub>6</sub>]<sup>4-</sup> and water molecules are interconnected by the H<sub>2</sub>bpee molecules leading towards the formation of 2D sheet in *ac* plane. (c) 1D chains along *a* direction formed by N–H···N H-bonding between [Fe(CN)<sub>6</sub>]<sup>4-</sup> and water molecules where H<sub>2</sub>-bpee molecules are alternatively linked.

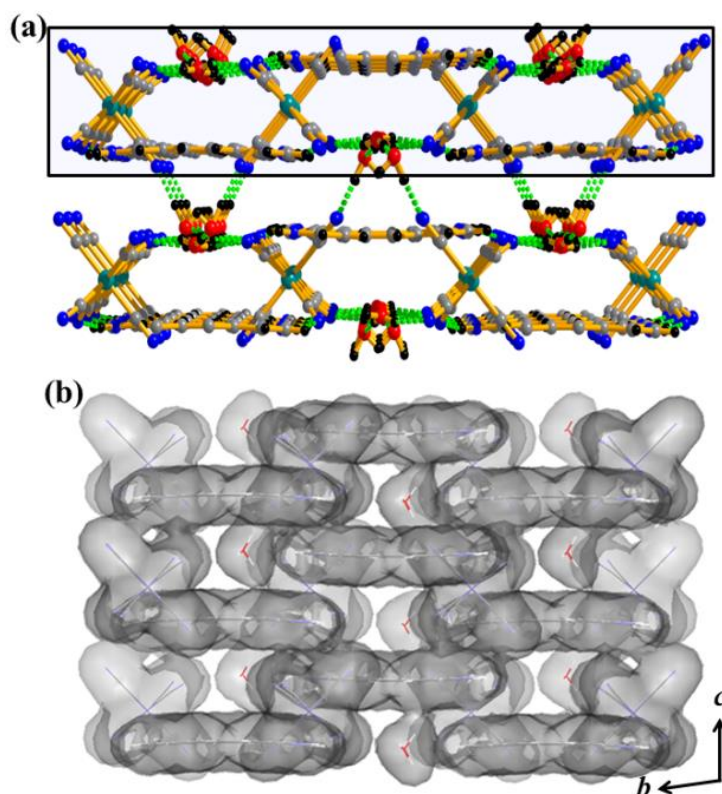


**Figure 12:** (a) View of 3D supramolecular architecture of **3** along crystallographic *a* direction formed by  $[\text{Fe}(\text{CN})_6]^{4-}$ , protonated bpee and water molecules. (b) View of the dumbbell shaped pore in **3** along crystallographic *a* direction.

Similar to **2**, in compound **3**  $\text{Fe}^{\text{II}}$  center in  $[\text{Fe}(\text{CN})_6]^{4-}$  places itself in a slightly distorted octahedral geometry. All the four water molecules (including protonated) are connected with each other by  $\text{O}-\text{H}\cdots\text{O}$  hydrogen bonding ( $\sim 2.585-2.617$  Å) interactions. The  $[\text{Fe}(\text{CN})_6]^{4-}$  moieties interact with  $\text{H}_2\text{-bpee}$  cations and water molecule (O2w) through  $\text{N4}-\text{H4}\cdots\text{N1}$  and  $\text{O1}-\text{H2c}\cdots\text{N3}$  hydrogen bonding ( $2.810(8)$  to  $2.843(7)$  Å), resulting in a 1D supramolecular chain along *a* direction (Figure 11b). The  $\text{H}_2\text{bpee}$  cations are oriented in zigzag fashion along the chain as shown in Figure 11b. The 1D chains are connected with each other via H-bonding interaction between  $[\text{Fe}(\text{CN})_6]^{4-}$  and the water molecules (O2w) ( $\text{O2w}-\text{H}(2\text{b}/2\text{c})\cdots\text{N3} = 2.843 - 3.054$  Å and  $\text{O1w}\cdots\text{O1w} = 2.617$  Å) to generate a 2D sheet in the crystallographic *ac* plane (Figure 11c). The 2D sheets (highlighted in Figure 12a) further interact with each other by  $\text{O1W}-\text{H1a}\cdots\text{N2}$  ( $2.672(7)$  Å) hydrogen bonding and construct a 3D supramolecular architecture (Figure 12a). The framework contains 1D supramolecular dumbbell shaped water filled channel along *a*-axis and calculation using PLATON suggest 5.5% void volume per unit cell volume (Figure 12b).

**2.3.1.4: Structural description of  $\{[(\text{H}_2\text{-bpee})(\text{H-bpee})]_2[\text{Fe}(\text{CN})_6]_2 \cdot 5\text{H}_2\text{O}\}$  (**4**):** Compound **4** crystallizes in triclinic system with  $P\bar{1}$  space group. The asymmetric unit



consist of two molecules of  $[\text{Fe}(\text{CN})_6]^{3-}$  unit, two doubly protonated bpee ( $\text{H}_2\text{-bpee}$ ) molecules, two singly protonated bpee ( $\text{H-bpee}$ ) and five lattice water molecules (Figure 13a).  $\text{Fe}^{\text{III}}$  centers are slightly distorted from the perfect octahedral geometry which is reflected from the *cisoid* ( $86.9(3) - 93.1(3)^\circ$ ) angles. The  $[\text{Fe}(\text{CN})_6]^{3-}$  (Fe1) moiety is connected to water molecules (O1 and its symmetry related compounds O1\*) through O-H $\cdots$ N H-bonding (bond distance varies from  $2.874(8) - 2.897(9)$  Å) and thus forming a 1D square chain along *a* direction (Figure 13b). Other three crystalline water molecules (O2, O3, O4) and their symmetry related components are linking themselves by O-H $\cdots$ O hydrogen bonding ( $2.701(3) - 3.027(18)$  Å) and thus leads to a hexameric water cluster with chair conformation (Figure 13c). O2 and O4 atoms are further connected with N5 and N4 atoms from second  $[\text{Fe}(\text{CN})_6]^{3-}$  (Fe2)) moieties through O-H $\cdots$ N hydrogen bonding and generate a 2D corrugated layer along  $[110]$  plane (Figure 13d).

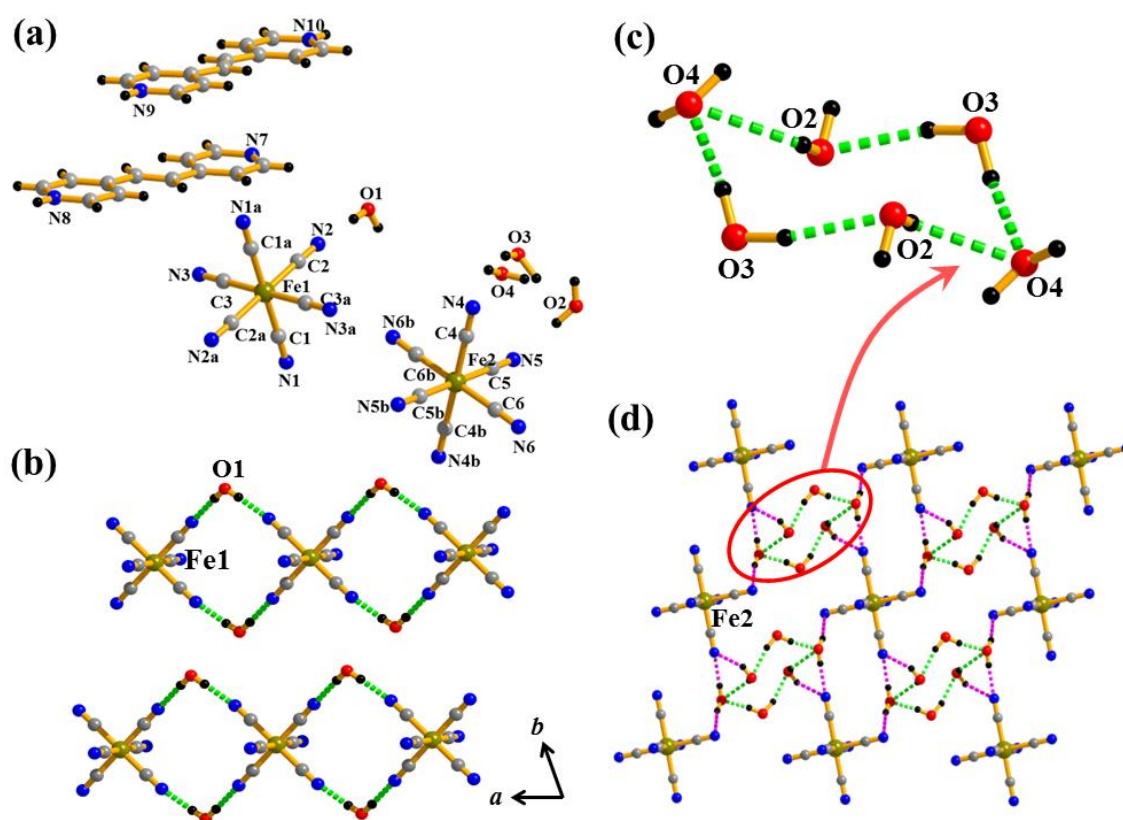


**Figure 13:** (a) Asymmetric unit of **4**. Symmetry codes:  $a = -x, -y, 1-z$ ;  $b = -x, -y, -z$ . (b) H-bonding interaction between  $[\text{Fe}(\text{CN})_6]^{3-}$  (Fe1 center) unit and with  $\text{H}_2\text{O}$  (O1) resulting in a 1D square chains along crystallographic *a* direction (c) Hexameric water cluster formed in **4**. (d) 2D layer along the *ab* plane formed by the H-bonding between  $[\text{Fe}(\text{CN})_6]^{3-}$  and hexameric water cluster.

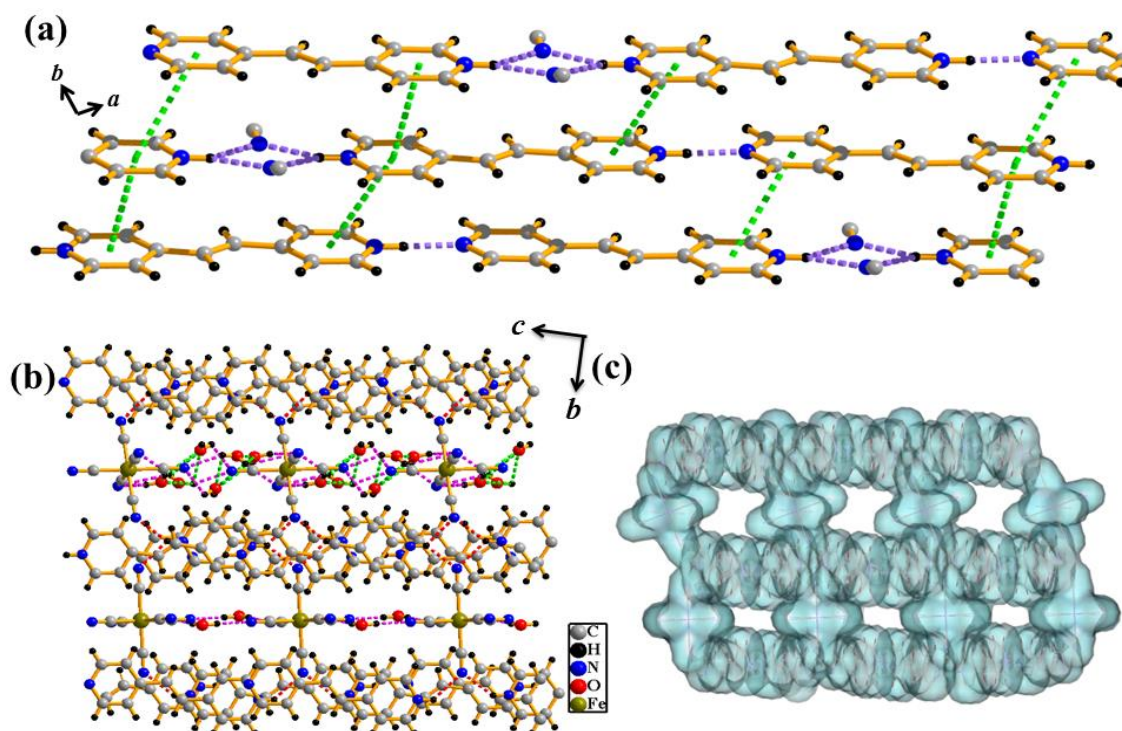


**Figure 14:** (a) Protonated bpee molecules are forming 1D chain through N–H...N hydrogen bonding which stacks in ABC manner in the  $ab$  plane through  $\pi$ ... $\pi$  interactions. (b) Two different 2D layers of protonated bpee and  $\{[\text{Fe}(\text{CN})_6]^{3-}\}(\text{H}_2\text{O})_6$  stack alternatively through H-bonding interactions along crystallographic  $a$  axis forming a 3D supramolecular architecture. (c) View of two different types of pore in **4** along crystallographic  $a$  direction.

The two types of bpee molecules *i.e.* H<sub>2</sub>-bpee and H-bpee are connected with each other by N–H...N H-bonding (Figure 14a) forming a dimer which leads to a 1D chain by further interacting with cyanide nitrogen atoms (N3 and N6) along  $a$  direction.  $\pi$ ... $\pi$  interaction ( $cg$ ... $cg$  distance are in the range of 3.590 to 4.487 Å) between these chains generates a 2D sheet along the crystallographic  $ab$  plane. In compound **4**, dihedral angle between the adjacent pyridyl rings is 1.29° whereas the slip angles between these two are varying from 63.92° to 80.53°. These two sheets are aligned in parallel fashion where two different layers of  $\{[\text{Fe}(\text{CN})_6]^{3-}\}(\text{H}_2\text{O})_6$  and  $\{[\text{Fe}(\text{CN})_6]^{3-}\}(\text{H}_2\text{O})$  are intercalated with each other through N–H...N H-bonding (2.855(7) to 2.953(7) Å) resulting a 3D supramolecular structure (Figure 14b). The host houses two types of void along crystallographic  $a$  direction occupied by the lattice water molecules (Figure 14c). After removal of the lattice water molecules, calculation using PLATON suggest 16.2% void volume per unit cell volume in **4**. The dimension of the voids are  $3.60 \times 2.66 \text{ \AA}^2$  and  $2.66 \times 1.60 \text{ \AA}^2$  calculated considering van der Waals radii of the atom (Figure 14c).

**2.3.1.5: Structural description of  $\{[(H_{1.5}\text{-bpee})_2][Fe(CN)_6]\cdot 6H_2O\}$  (5):** Compound **5** crystallizes in triclinic space group  $P\bar{1}$ . The formula unit of compound **5** contains one molecule  $[Fe(CN)__6]^{3-}$ , two protonated 1,2-bis(4-pyridyl)ethylene ( $H_{1.5}\text{-bpee}$ ) molecules, and six lattice water molecules (Figure 15a). The coordination environment of  $Fe^{III}$  center in compound **5** is similar to that of compound **4**, and here similar  $Fe-C$  bond length and angles were observed. Six water molecules are connected with each other by  $O-H\cdots O$  (2.579(16) – 2.766(13) Å) H-bonding interactions. Nitrogen ends (N1 and N3) of each  $[Fe(CN)_6]^{3-}$  moiety engage themselves into  $O-H\cdots N$  (2.792(9) – 3.020(17) Å) H-bonding with water molecules to generate a 2D sheet along crystallographic  $ac$  plane (Figure 15b).

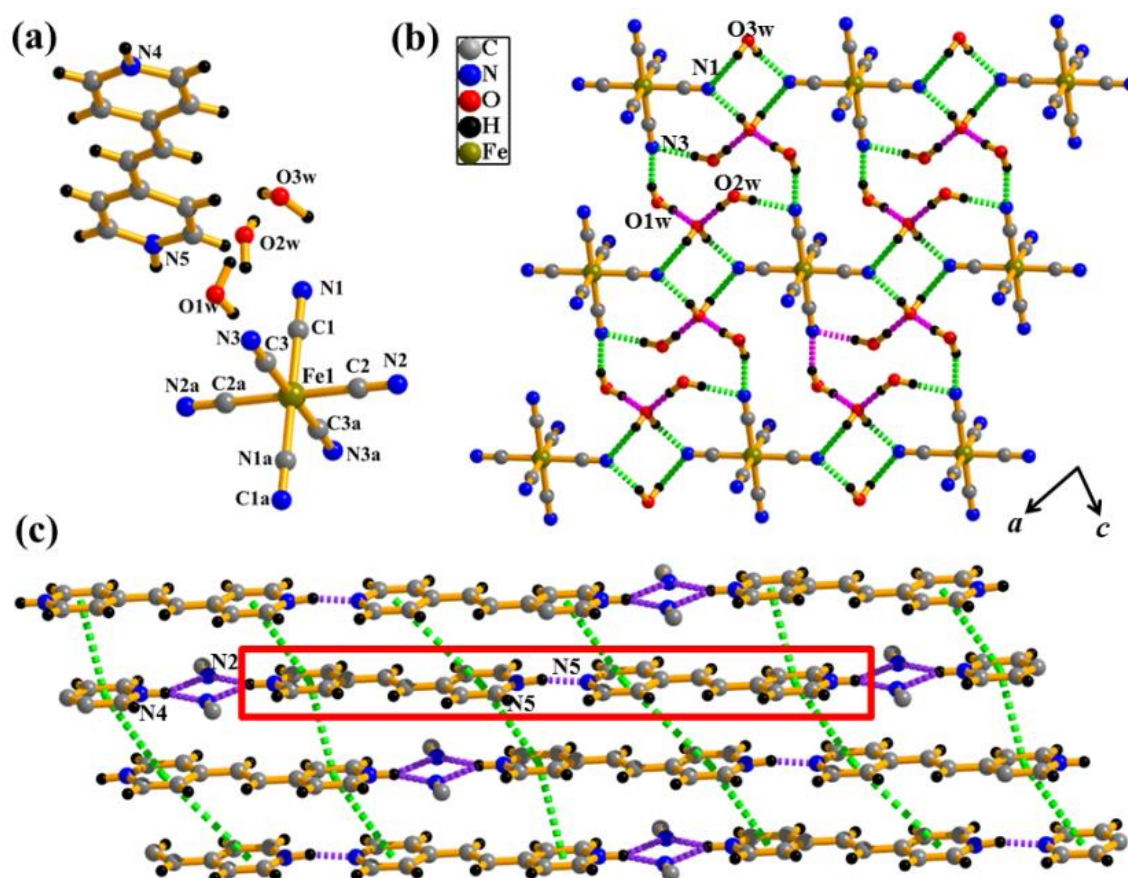


**Figure 15:** (a) Asymmetric unit of **5**. Symmetry code:  $a = 2-x, 2-y, z$ . (b) 2D extended sheet like structure form by the  $O-H\cdots N$  H-bonding interaction between tetrameric water cluster and  $[Fe(CN)_6]^{3-}$ . (c) 1D chains formed by the H-bonding interaction between dimeric bpee molecules are stacked in ABC fashion through  $\pi\cdots\pi$  interactions resulting to the formation of 2D corrugated sheet.

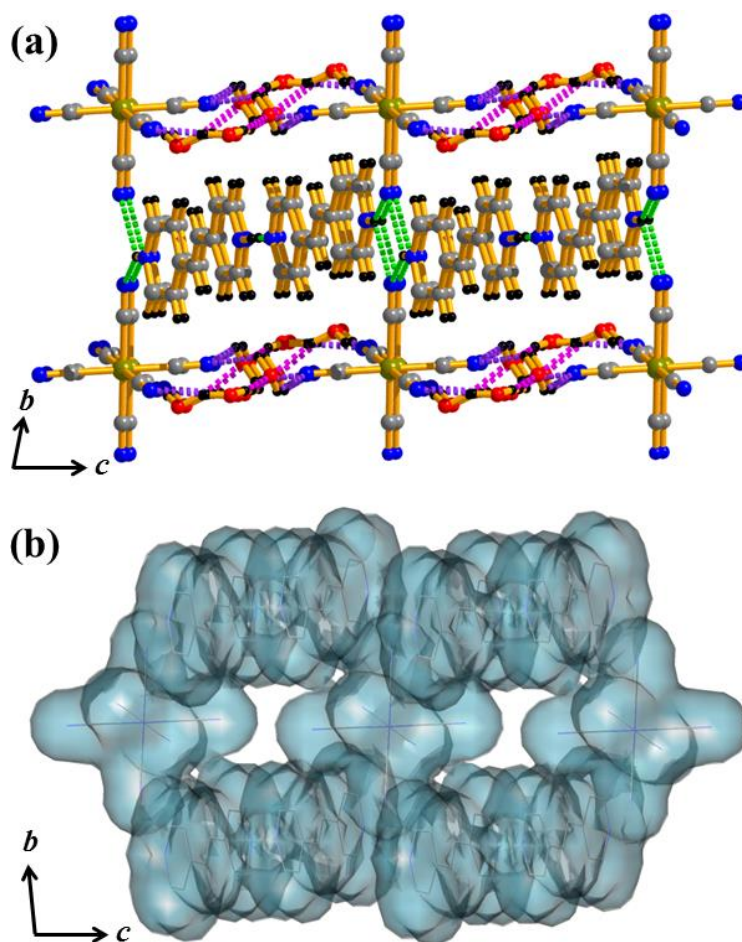


**Figure 16:** (a) Different types of hydrogen bonding interaction between protonated bpee,  $[\text{Fe}(\text{CN})_6]^{3-}$  and  $\text{H}_2\text{O}$  molecules host the 3D supramolecular architecture to form compound **5**. (b) Figure shows the pore in **5** along crystallographic *a* direction.

Along *a* direction, two  $\text{H}_{1.5}$ -bpee molecules form a dimer (Figure 15c, red marked box) through H-bonding. Further  $\text{N}-\text{H}\cdots\text{N}$  hydrogen bonding between these dimers and the N2 (from pendant cyanide ligand of  $[\text{Fe}(\text{CN})_6]^{3-}$ ) atoms leads to the formation of 1D chain along *a* direction. These 1D chains are stacked through  $\pi\cdots\pi$  interaction ( $cg\cdots cg$  distance are in the range of 3.778(3) to 3.893(3) Å) in ABC fashion along the crystallographic *ac* plane resulting in a 2D corrugated sheet (Figure 15c). In this corrugated sheet, the dihedral angle between the benzene rings is  $4.97^\circ$  whereas the slip angle between these two is varying from  $59.61^\circ$  to  $78.74^\circ$ . These sheets are intercalated between the 2D sheets formed by  $[\text{Fe}(\text{CN})_6]^{3-}$  and water clusters through  $\text{N}-\text{H}\cdots\text{N}$  hydrogen bonding resulting in a 3D supramolecular host with channels along *a* direction which are filled by lattice water molecules (Figure 16a). After removal of the lattice water molecules, the framework suggests 16.4% void volume per unit cell

volume as calculated by PLATON. The dimension of the channels is about  $4.23 \times 3.85 \text{ \AA}^2$  calculated considering van der Waals radii of the atom (Figure 16b).

### 2.3.2: TGA and PXRD analysis

Thermogravimetric analysis (TGA) and powder X-ray diffraction (PXRD) measurement were carried out to study the stability of the supramolecular frameworks. TGA measurement of compound **1** suggests (Figure 17a) weight loss of 9.96 wt% in the temperature range of 40-80 °C which is less than eight lattice water molecules (20 wt%) occupied in the channels. The inconsistency of TGA can be correlated with the release of some lattice water molecules at room temperature. We observed that **1** loses single crystallinity slowly after taking out the crystals from mother liquor. The dehydrated compound is stable up to 200 °C without further weight loss; after that framework decomposes to unidentified product.

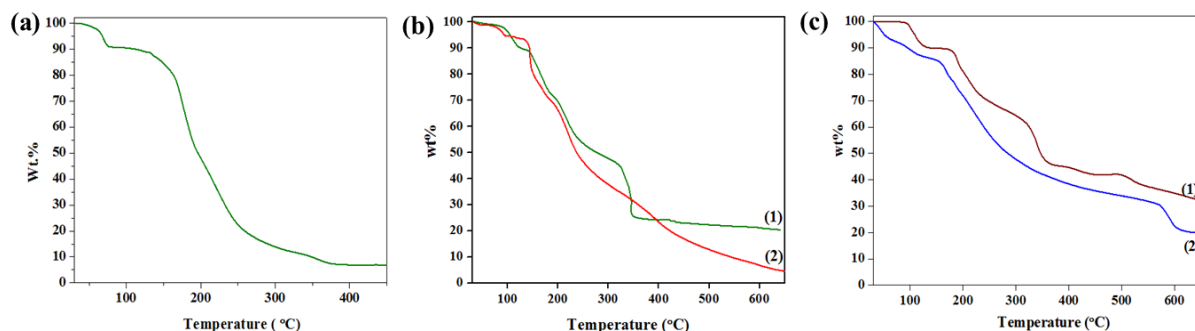


**Figure 17:** (a) TGA curve of **1** in the temperature range 30 – 450 °C (Heating rate 5 °C/min under nitrogen). (b) TGA plots of compounds **2** (1) and **3** (2) over the temperature range 30 to 650 °C under nitrogen atmosphere. (c) TGA plots of compounds **4** (1) and **5** (2) over the temperature range 30 to 650 °C under nitrogen atmosphere.

Compound **2** (Figure 17b1) shows a wt. loss of about 11.25% in temperature range 120-130°C which corresponds of about  $\approx 8$  water molecules (calc. wt. loss 11.50%). After that it gradually decomposes into unidentified products. In case of **3** (Figure 17b2), it releases  $\approx 2$  molecules of water at 120 °C (calc. wt. loss 7.29%; exp. wt. loss 7.56%) and then desolvated framework is stable up to 180 °C without further weight loss. TGA plot of compound **4** (Figure 17c1) shows a release of four lattice water molecules at 125 °C (calc. wt. loss 8.53%; exp. wt. loss 8.71%). The dehydrated compound of **4** is stable up to 170 °C without any further weight loss. Compound **5** (Figure 17c2) reveals stepwise release of water molecules. The first step indicates the

release of three water molecules (calc. wt. loss 7.86%; exp. wt. loss 7.5%) at 75 °C, and the second one corresponds the release of other three water molecules at 155 °C (total calc. wt loss for 6 molecules = 15.72%, total exp. wt. loss = 15.99%).

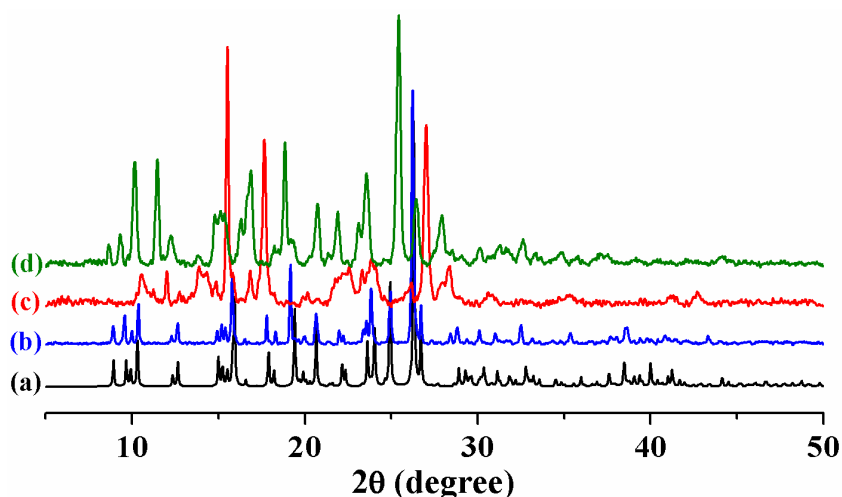


**Figure 18:** PXRD patterns of **1** in different state: (a) simulation based on single crystal X-ray analysis, (b) as-synthesized, (c) dehydrated at 80 °C, and (d) exposed to the water vapor for three days.

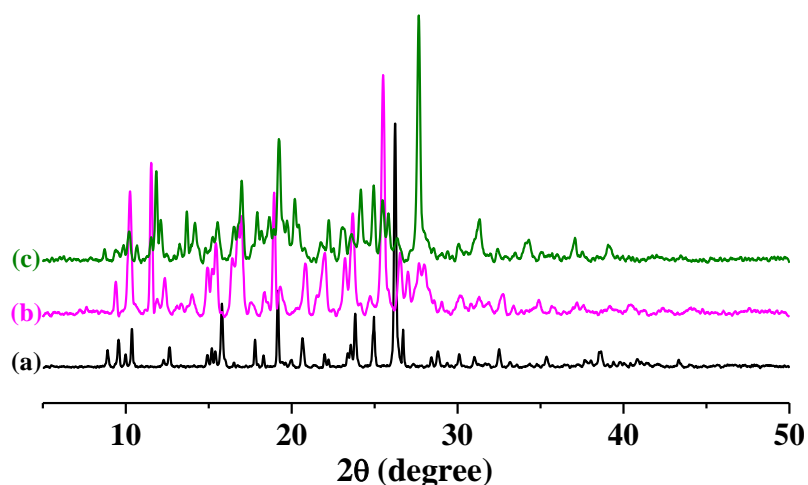


**Figure 19:** PXRD patterns of **1** in different state: (a) as-synthesized **1**, (b) outgassed at RT for 20h, **1**' and (c) exposed to the water vapor for three days.

The PXRD pattern of **1**' shows (Figure 18) drastic change with shifting of peaks and also appearance of some new peaks after removal of water molecules. However, we were able to index the pattern using the programme TREOR that suggest a monoclinic crystal system with unit cell parameters,  $a = 18.5208 \text{ \AA}$ ,  $b = 7.3948 \text{ \AA}$ ,  $c = 16.8450 \text{ \AA}$  and  $\beta = 110.622^\circ$ . A change in crystal system from triclinic to monoclinic together

with noticeable changes in cell parameter suggest significant structural transformation upon removal of water molecules from **1**. The PXRD pattern of **1''** (Figure 19b) also shows difference in peak positions suggesting structural transformation upon removal of water molecules. The PXRD patterns of water vapor exposed samples of **1'** (Figure 18d) and **1''** (Figure 19c) do not match well with **1**, suggesting that the structure is not completely reversible upon rehydration. Elemental analyses suggest that water vapour exposed samples of **1'** and **1''** can hold ~6 and ~7 number of water molecules, respectively. The host **1**, **1'** and **1''** dissolves when directly poured in water at RT. PXRD patterns of compounds **2-5** are shown in Figures 20. The PXRD patterns of all as-synthesized compounds matches well with the simulated patterns obtained from X-ray single crystal data, suggesting phase purity of as-synthesized compounds. All the compounds have been activated (or desolvated) in two different ways.

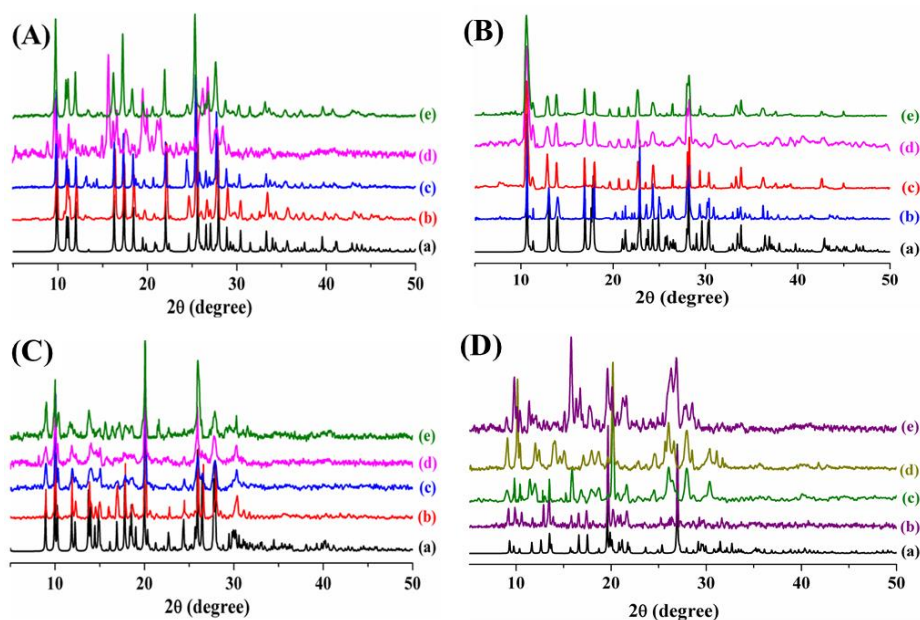


**Figure 20:** PXRD patterns of compound **2** (A), **3** (B), **4** (C) and **5** (D) in different states. (a) simulated (b) as-synthesized, (c) desolvated at room temperature under vacuum, (d) desolvated at 100 °C under vacuum and (e) rehydrated.

The PXRD pattern of the degassed compounds (**2'-5'**) at 100 °C under vacuum show some new peaks and changes of some peak positions compared to the as-synthesized compounds suggesting structural reorganization. However the degassed samples (**2''-5''**) obtained at room temperature evacuation show almost similar powder pattern as of as-synthesized compounds revealing that there is no significant structural change. The removal of all the water molecules in both cases has been confirmed by IR spectroscopy and elemental analyses.

### 2.3.3: Adsorption Property

These frameworks have been activated in two different methods; under a high vacuum and applying temperature with vacuum. The desolvated frameworks (**1'**-**5'**) are found to be nonporous with respect to  $N_2$  (kinetic diameter  $3.6 \text{ \AA}$ )<sup>35</sup> and  $CO_2$  (kinetic diameter  $3.3 \text{ \AA}$ )<sup>36</sup> as revealed by the type-II adsorption profiles (Figure 21 and 22), suggesting only surface adsorption. This is probably due to the structural transformation of the supramolecular frameworks after dehydration, or smaller pore size compared to the kinetic diameter of the gases and hence resulting diffusion barrier for  $N_2 / CO_2$  to pass through the pores. However, interesting results were obtained with solvent vapor adsorption study.

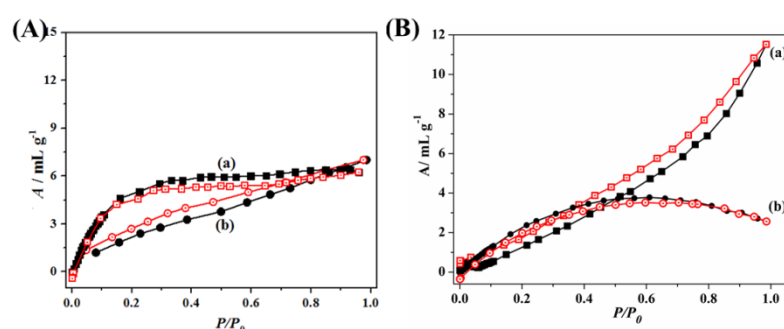


**Figure 21:** (a)  $N_2$  adsorption isotherm and (b)  $CO_2$  adsorption isotherm of compound **1'** (A) and compound **2'** (B) measured at 77 and 195 K respectively.  $P_0$  is the atmospheric pressure. The closed and open circles/cube symbols used to indicate adsorption and desorption isotherms respectively.

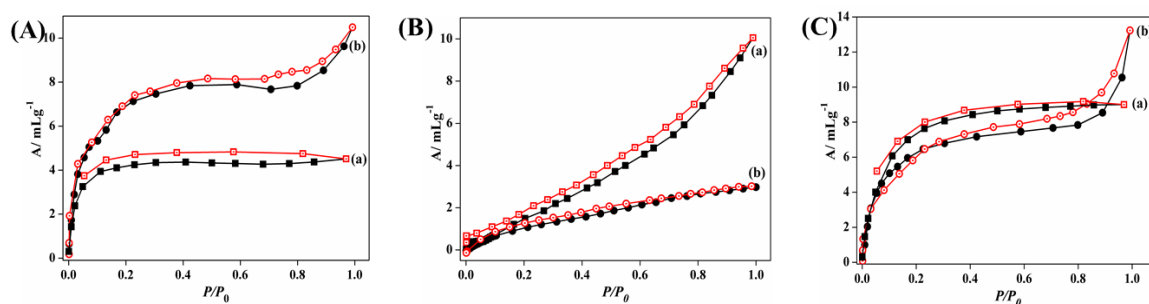


**Figure 22:** (a)  $N_2$  adsorption isotherm and (b)  $CO_2$  adsorption isotherm of compound **3'** (A), compound **4'** (B) and compound **5'** (C) measured at 77 and 195 K respectively. The closed and open circles/cube symbols used to indicate adsorption and desorption isotherms respectively.

#### 2.3.3.1: Solvent vapour Adsorption study of Compound 1

Multistep isotherm was obtained with  $H_2O$  adsorption experiment at 298 K as shown in Figure 23. The adsorption isotherm of **1'** reveals, initially at low  $P/P_0$  it is difficult for the  $H_2O$  molecules to get adsorbed and hence up to  $P/P_0 \sim 0.55$  the uptake



is only about  $32 \text{ mLg}^{-1}$ . Then there is a sudden adsorption jump at  $P/P_0 \sim 0.62$  and the uptake volume reaches to about  $120 \text{ mLg}^{-1}$ . This steep uptake suggests a kind of gate opening at  $P/P_0 \sim 0.55$  because of structural transformation upon dehydration which blocks the  $\text{H}_2\text{O}$  molecules at low pressure. Once the gate opens, adsorption gradually increases with pressure and ends without saturation with net adsorption amount of  $189 \text{ mLg}^{-1}$  at  $P/P_0 \sim 1$ .

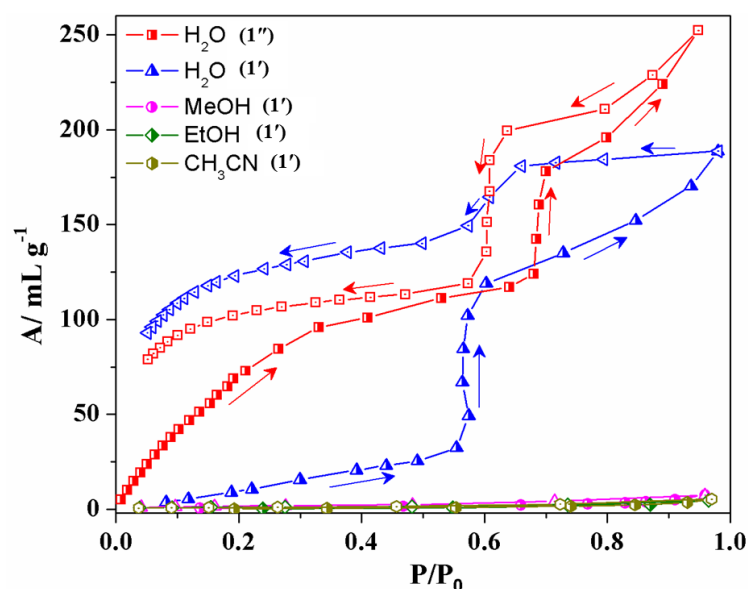


**Figure 23:** Solvent vapor adsorption isotherms of **1'** and **1''**;  $\text{H}_2\text{O}$  (blue, **1'** and red, **1''**), EtOH,  $\text{CH}_3\text{CN}$  at 298 K and MeOH at 293 K, shows selective adsorption of  $\text{H}_2\text{O}$  vapor over organic solvents.  $P_0$  saturated vapour pressure of the respective solvents at the measuring temperature. The closed and open circles/triangle symbols used to indicate adsorption and desorption isotherms respectively.

Interestingly, desorption also occurs in a stepwise fashion and exhibits large hysteresis. The desorption isotherm does not retrace the adsorption one; instead it shows abrupt decrease at  $P/P_0 \sim 0.66$  to reach  $P/P_0 \sim 0.57$  and then decreases gradually. Therefore certain adsorption jump with gate opening phenomenon and desorption drops suggest structural transformation with pore opening at some threshold pressure. This type of phenomena is well documented for flexible metal-organic coordination frameworks.<sup>37</sup> However, to the best of our knowledge, such stepwise adsorption in supramolecular host composing of two discrete molecular entities is yet to be reported. Calculation using the final adsorption amount suggests that only 5.6 molecules of  $\text{H}_2\text{O}$  are occluded into the host **1'**, less than the as-synthesized compound **1**, which is also reflected from unsaturated adsorption profile at  $P/P_0 \sim 1$ . Realising significant structural transformation upon dehydration at  $80^\circ\text{C}$  from PXRD

and closed structure of **1'** from adsorption studies, we decided to outgas the sample of **1** at room temperature under vacuum and then check the H<sub>2</sub>O adsorption property. The removal of H<sub>2</sub>O molecules at RT under vacuum in the outgassed sample (**1''**) has been confirmed by IR and elemental analysis. Surprisingly, the H<sub>2</sub>O adsorption of **1''** also shows stepwise profile but different than **1'** (Figure 23). Unlike **1'**, **1''** allows the H<sub>2</sub>O molecules to diffuse through it even at low  $P/P_0$ . The profile of **1''** shows gradual uptake of H<sub>2</sub>O molecules up to  $P/P_0 \sim 0.7$  and then there is a sudden adsorption jump and finally reaches to maximum uptake volume of 252 mL/g at  $P/P_0 \sim 1$ . This indicates that even at room temperature the removal of H<sub>2</sub>O molecules led to the shrinkage in the host structure that completely opens up at  $P/P_0 \sim 0.7$ . It is worth mentioning that, H<sub>2</sub>O uptake at  $P/P_0 \sim 0.55$  for **1'** and **1''** differs significantly and corresponding values are 32 mL/g for **1'** and 113 mL/g for **1''**. Higher H<sub>2</sub>O uptake of **1''** at low pressures indicate that structure of **1''** is more open than **1'**. Calculation using the final adsorption amount suggests that total 7.7 molecules of H<sub>2</sub>O invade into the host **1''**. Similar to **1'**, desorption occurs in a stepwise fashion and at the end of the adsorption process **1''** holds  $\sim 2.4$  number of water molecules. The value of  $\beta E_0$ , which reflects adsorbate-adsorbent affinity, is about 4.29 kJ/mol for **1'** and 5.43 kJ/mol for **1''**, suggests that the later has stronger hydrophilicity than **1'**. The number of H<sub>2</sub>O molecules adsorbed per formula unit, by **1'** and **1''**, are in good agreement with elemental analysis of H<sub>2</sub>O vapour exposed samples and adsorption experiments. MeOH (293 K), CH<sub>3</sub>CN (298 K), and EtOH (298 K) adsorption studies of **1'** suggest only surface adsorption as revealed by their type-II adsorption properties (Figure 23). The size of these adsorbates is larger than the pore size, correlating the non-inclusion of such organic vapours in **1'**.

### 2.3.3.2: Solvent vapour adsorption study of compound 2-5

H<sub>2</sub>O (2.68 Å)<sup>29</sup> adsorption profiles for **2'-5'** (Figure 25) show a gradual uptake with increasing pressure and reach a final amount of 104, 103, 115 and 112 mLg<sup>-1</sup> for **2'-5'** respectively at  $P/P_0 \sim 0.98$ . In all the cases desorption curves do not follow the adsorption one revealing prominent hysteric sorption profiles. Interestingly, stepwise H<sub>2</sub>O adsorption profiles were observed with compound **2''-5''**. In each case there is an initial steep uptake at low pressure regions suggesting strong interactions with the pore surfaces. Desorption curves do not follow the adsorption one and

accompanied with large hysteresis. The details of the water adsorption data are summarized in Table 12.

**Table 12.** Summarized data of water adsorption experiments for compounds **2'-5'** and **2''-5''**.

Comp	$P_{th}$ ( $P/P_0$ )	Uptake at $P_{th}$ (mL $g^{-1}$ )	Final uptake (mL $g^{-1}$ )	$\beta E_0$ ( $kJmol^{-1}$ )	Molecules adsorbed at saturation
<b>2'</b>	N/A	N/A	104	2.13	5.40
<b>2''</b>	0.62	85	157	8.82	8.14
<b>3'</b>	N/A	N/A	103	3.03	1.99
<b>3''</b>	0.13	120	162	6.1	3.8
<b>4'</b>	N/A	N/A	115	2.09	5.94
<b>4''</b>	0.25	64	155	6.87	8.02
<b>5'</b>	N/A	N/A	112	4.5	2.9
<b>5''</b>	0.41	59	166	6.9	5.89

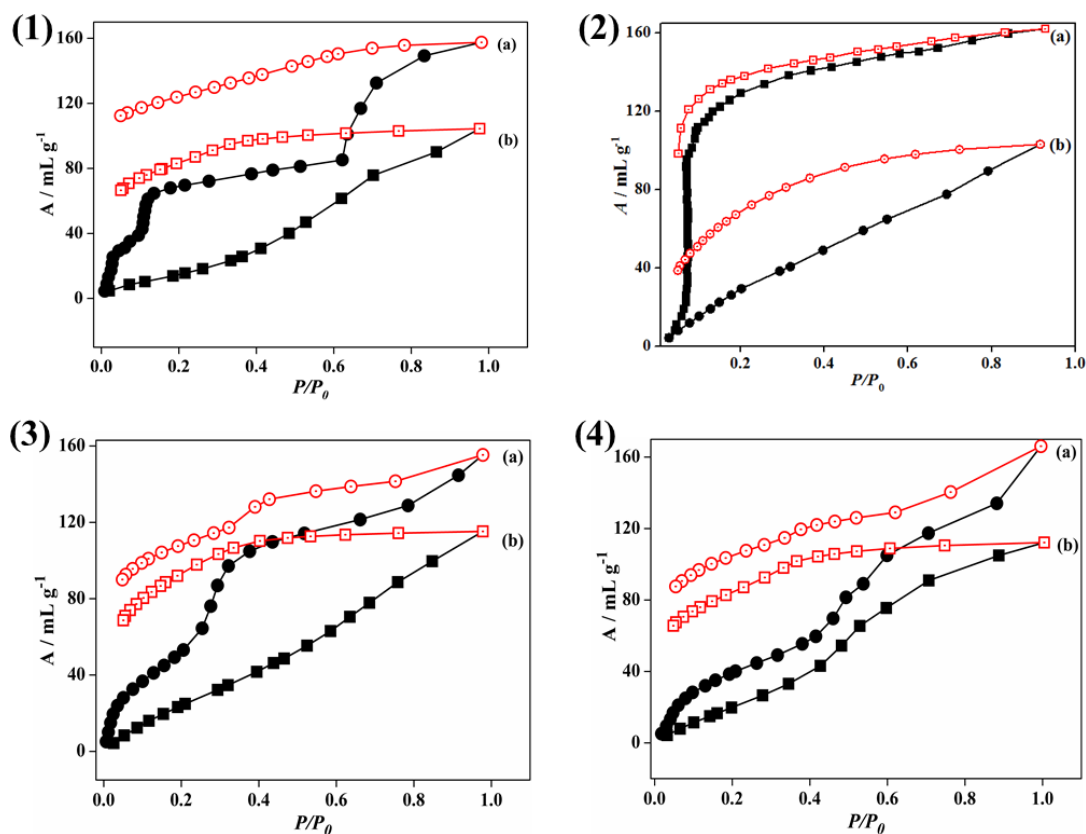


**Figure 24:** Water vapour adsorption (298 K) profile of **2'-5'** (1(b)-4(b)) and **2''-5''** (1(a)-4(a)).  $P_0$  is the saturated vapour pressure of the corresponding solvent at the respective temperature. The closed and open circles/cube symbols used to indicate adsorption and desorption isotherms respectively.

The initial low pressure uptake of water molecules for **2''-5''** is suggesting hydrophilic nature of the pore surfaces compared to **2'-5'**, which is also supported by  $\beta E_0$  values

(Table 12) calculated using DR (Dubinin-Radushkevich) equation (considering the low pressure data).<sup>42</sup>

Methanol ( $3.6 \text{ \AA}$ )<sup>29</sup> adsorption studies of compound **2'** and **3'** reveal a type-I (Figure 25 (1) and (2)) profiles with final uptake values of  $30 \text{ mL g}^{-1}$ ,  $63 \text{ mL g}^{-1}$ , respectively. But a gate opening type sorption profiles were obtained with threshold pressure of 0.06 and 0.1 for **4'** and **5'** respectively (Figure 25 (3) and (4)). After the gate opening, adsorption amount ended at  $74 \text{ mL g}^{-1}$  and  $60 \text{ mL g}^{-1}$  for **4'** and **5'** respectively. But when the same experiments were performed for **2''-5''**, double step adsorption profiles were achieved (Figure 25 (1) and (2)) with final uptake of  $78 \text{ mL g}^{-1}$ ,  $97 \text{ mL g}^{-1}$ ,  $93 \text{ mL g}^{-1}$  and  $80 \text{ mL g}^{-1}$  for **2''-5''** respectively. The uptake amount for first step (type -I) is same for both set of compounds, indicating that a similar channel structure exists for MeOH molecules. The second step in compound **2''-5''** suggests the presence of other adsorption sites which allows further uptake based on structural transformation in the framework.

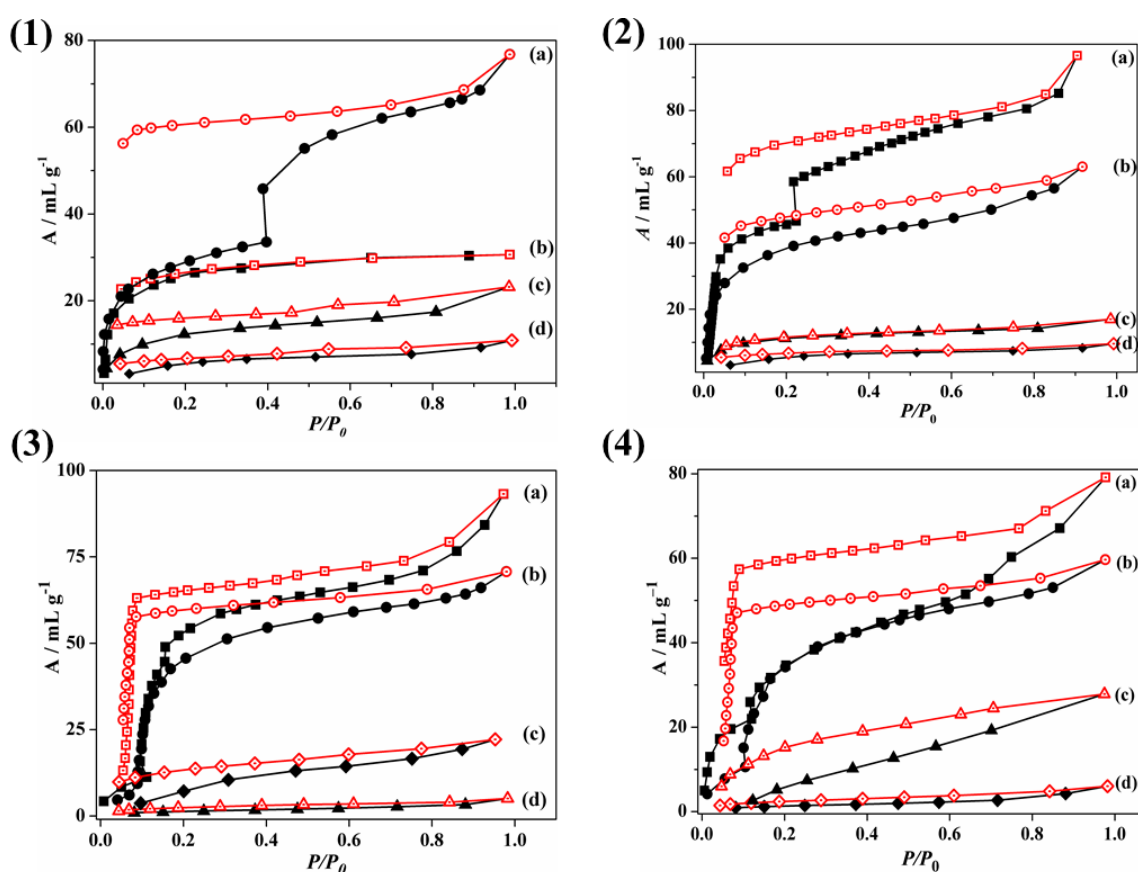


**Figure 25:** Methanol adsorption (293 K) profile of **2'-5'** (1(b)-4(b)) and **2''-5''** (1(a)-4(a)) and ethanol adsorption (298 K) profile **2'-5'** (1(c)-4(c)) and **2''-5''** (1(d)-4(d)).  $P_0$  is the saturated vapour pressure of the corresponding solvent at the respective temperature. The closed and open circles/cube symbols used to indicate adsorption and desorption isotherms respectively.

A detailed analysis of the adsorption studies has been given in Table 13. EtOH (4.5 Å)<sup>38</sup> adsorption studies for **2'-5'** suggest only surface adsorption as revealed by their type-II adsorption properties. However, small amount of uptakes were observed in case of **2''-5''** (23, 17, 22 and 28 mL g<sup>-1</sup> for **2''-5''** respectively).

The adsorption profiles in two different set of adsorbates obtained in two different activated conditions are quite interesting and not previously explored in such supramolecular systems. H<sub>2</sub>O adsorption profiles for **2''-5''** reveal multistep (Figure 24) typical type-VI profile according to the IUPAC classification.<sup>36, 39</sup> Similar type of adsorption behavior was previously reported in flexible porous coordination polymers and such type of compounds classified as soft porous crystals by Kitagawa *et al.*<sup>40</sup> Multistep adsorption profile in a soft porous material is accomplished due to the structural flexibility where framework undergoes several metastable states during the adsorption and such structural change occurs from the response of specific host guest interactions. It is worth mentioning that multistep adsorption profile in a robust framework appears from the distribution of different pore volumes. Here the presence of different adsorption sites such as free cyanide (-CN) from [Fe(CN)<sub>6</sub>]<sup>4-/3-</sup>, protonated bpee and adsorbate-adsorbate interactions at high pressure regions resulting in the stepwise adsorption.<sup>41</sup>

**Table 13.** Summarized data of methanol adsorption experiment of compound **2'-5'** and **2''-5''**.

Comp	$P_{th}$ ( $P/P_0$ )	Uptake at $P_{th}$ (mL g <sup>-1</sup> )	Final uptake (mL g <sup>-1</sup> )	$\beta E_0$ (kJmol <sup>-1</sup> )	Molecules adsorbed at saturation
<b>2'</b>	N/A	N/A	30	10.58	1.55
<b>2''</b>	0.40	34	78	13.92	4.04
<b>3'</b>	N/A	N/A	103	10.78	1.99
<b>3''</b>	0.22	47	97	13.52	1.88
<b>4'</b>	0.08	10	70	6.86	1.87
<b>4''</b>	0.11	11	93	8.23	2.48
<b>5'</b>	0.10	10	60	6.29	1.6
<b>5''</b>	0.12	22	80	9.02	2.2

**Table 14.** Summarized data of ethanol adsorption experiment of compound **2'-5'** and **2''-5''**.

Comp.	( $P/P_0$ )	Final uptake (mL g <sup>-1</sup> )	Molecules adsorbed at saturation
<b>2'</b>	0.99	10.88	0.56
<b>2''</b>	0.985	23.17	1.2

<b>3'</b>	0.99	9.60	0.18
<b>3''</b>	0.98	17.02	0.33
<b>4'</b>	0.98	5.04	0.13
<b>4''</b>	0.95	22.19	0.57
<b>5'</b>	0.98	6.04	0.16
<b>5''</b>	0.975	27.84	0.77

Our results show that the number of H<sub>2</sub>O molecules adsorbed per formula unit of **2''-5''** are greater than that of the numbers present in their corresponding as-synthesized compound further indicating the presence of adsorbate-adsorbate interaction (through hydrogen bonding) at higher  $P/P_0$ . Comparison of  $\beta E_0$  values (Table 12 and 13) between the water and methanol uptake profiles reveal a stronger interaction for methanol molecules with the dehydrated compounds of **2'-5'**. We reasoned that, upon dehydration there is a structural rearrangement in the framework, where pore environment in the activated compounds has been changed in such a way that both the hydrophobic pyridine part (from bpee moiety) and also the hydrophilic -CN groups are surrounded the pore surface. As the MeOH molecule contains both hydrophobic -CH<sub>3</sub> part and hydrophilic -OH part, they feel ideal space for accommodation in the framework. The above results and discussion clearly divulge the fact that this type of soft porous materials can transform to the different phases based on the activation procedure and different interesting adsorption profiles can be obtained.

## **2.4: Conclusion**

In conclusion, we have successfully synthesized five new charge assisted supramolecular frameworks by employing simple molecular building units  $[\text{Fe}(\text{CN})_6]^{4-}$  or  $[\text{Fe}(\text{CN})_6]^{3-}$  and protonated 4,4'-bipyridine and 1,2-bis(4-pyridyl)ethylene molecules as hydrogen bonding acceptor and donor respectively. We have elegantly demonstrated a synthetic strategy to obtain different co-crystals by simply changing the reaction conditions. Two different dehydrated phases have been achieved by changing the activation conditions and this has been realized by exploiting the softness of the compounds which are solely extended by the supramolecular interactions. Our work unveils that material properties based on porosity can be significantly tuned by simple activation process in soft porous materials which can open up the new possibility of such novel hybrid system for selective guest uptake for separation and as a sensor material.

## 2.5: References

1. (a) M. J. Zaworotko, *Cryst. Growth Des.* 2007, **7**, 4. (b) A. D. Bond, *CrystEngComm* 2007, **9**, 833. (c) C. B. Aakeroy and D. J. Salmon, *CrystEngComm* 2005, **7**, 439. (d) G. P. Stahly, *Cryst. Growth Des.* 2007, **7**, 1007. (e) D. Braga and F. Grepioni, *Chem. Commun.* 2005, 3635. (f) T. Friščić and W. Jones, *Cryst. Growth Des.* 2009, **9**, 1621. (g) S. Horiuchi, T. Hasegawa and Y. Tokura, *J. Phys. Soc. Jpn.* 2006, **75**, 1865. (h) S. Marivel, E. Suresh and V. R. Pedireddi, *Tetrahedron Lett.* 2008, **49**, 3666. (i) Y. Manjare and V. R. Pedireddi, *Cryst. Growth Des.* 2011, **11**, 5079. (j) C. B. Aakeroy, M. E. Fasulo and J. Desper, *Mol. Pharm.* 2007, **4**, 317. (k) S. Mohamed, D. A. Tocher, M. Vickers, P. G. Karamertzanis and S. L. Price, *Cryst. Growth Des.* 2009, **9**, 2881. (l) S. K. Ghosh, J. Ribas, El Fallah, M. Salah and P. K. Bharadwaj, *Inor. Chem.* 2005, **44**, 3856. (m) F. Lara-Ochoa and G. Espinosa-Petrez, *Supramol. Chem.* 2007, **19**, 553. (n) A. Mukherjee, P. Grobelny, T. S. Thakur and G. R. Desiraju, *Cryst. Growth Des.* 2011, **11**, 2637. (o) S. K. Ghosh and P. K. Bharadwaj, *Angew. Chem. Int. Ed.* 2004, **43**, 3577. (p) Y. J. Jeon, P. K. Bharadwaj, S. W. Choi, J. W. Lee and K. Kim, *Angew. Chem. Int. Ed.* 2002, **41**, 4474. (q) T. Chatterjee, M. Sarma and S. K. Das, *Tetrahedron Lett.* 2010, **51**, 1985. (r) R. Mondal and J. A. K. Howard, *Cryst. Growth & Des.*, 2008, **8**, 4359. (s) S. Aitipamula, R. Banerjee, A. K. Bansal, K. Biradha, M. L. Cheney, A. R. Choudhury, G. R. Desiraju, A. G. Dikundwar, R. Dubey, N. Duggirala, P. P. Ghogale, S. Ghosh, P. K. Goswami, N. R. Goud, R. R. K. R. Jetti, P. Karpinski, P. Kaushik, D. Kumar, V. Kumar, B. Moulton, A. Mukherjee, G. Mukherjee, A. S. Myerson, V. Puri, A. Ramanan, T. Rajamannar, C. M. Reddy, N. Rodriguez-Hornedo, R. D. Rogers, T. N. G. Row, P. Sanphui, N. Shan, G. Shete, A. Singh, C. C. Sun, J. A. Swift, R. Thaimattam, T. S. Thakur, R. Kumar Thaper, S. P. Thomas, S. Tothadi, V. R. Vangala, N. Variankaval, P. Vishweshwar, D. R. Weyna and M. J. Zaworotko, *Cryst. Growth Des.* 2012, **12**, 2147.
2. (a) J. C. MacDonald and G. M. Whitesides, *Chem. Rev.* 1994, **94**, 2383. (b) J. F. Remenar, S. L. Morissette, M. L. Peterson, B. Moulton, J. M. MacPhee, H. R. Guzmán and Ö. Almarsson, *J. Am. Chem. Soc.* 2003, **125**, 8456. (c) S. L. Childs, L. J. Chyall, J. T. Dunlap, V. N. Smolenskaya, B. C. Stahly, G. P. Stahly, *J. Am. Chem. Soc.* 2004, **126**, 13335. (d) G. Bettinetti, M. R. Caira, A. Callegari, M. Merli, M. Sorrenti and C. Tadini, *J. Pharm. Sci.* 2000, **89**, 478. (e) N. Schultheiss and A. Newman, *Cryst. Growth Des.* 2009, **9**, 2950. (f) B. R. D. Walsh, M. W. Bradner, S. Fleischman, L. A. Morales, B. Moulton, N. Rodríguez-Hornedo and M. J. Zaworotko, *Chem. Commun.* 2003, 186. (g) I. D. H. Oswald, D. R. Allan, P. A. McGregor, W. D. S. Motherwell, S. Parson and C. R. Pulham, *Acta Cryst. B: Struct. Crystallogr. Cryst. Chem.* 2002, **B58**, 1057. (h) P. Vishweshwar, J. A. McMahon, J. A. Bis and M. J. Zaworotko, *J. Pharm. Sci.* 2006, **95**, 499. (i) G.

- Springuel, B. Norberg, K. Robeyns, J. Wouters and T. Leyssens, *Cryst. Growth Des.* 2012, **12**, 475. (j) A. V. Trask, *Mol. Pharm.* 2007, **4**, 301
3. (a) N. Blagden, D. J. Berry, A. Parkin, H. Javed, A. Ibrahim, P. T. Gavan, L. L. De Matos and C. C. Seaton, *New J. Chem.*, 2008, **32**, 1659. (b) G. P. Stahly, *Cryst. Growth Des.* 2009, **9**, 4212. (c) D. R. Weyna, M. L. Cheney, N. Shan, M. Hanna, L. Wojtas and M. J. Zaworotko, *CrystEngComm* 2012, **14**, 2377. (d) A. J. Smith, P. Kavuru, L. Wojtas, M. J. Zaworotko and R. D. Shytle, *Mol. Pharm.*, 2011, **8**, 1867 (e) B. R. Bhogala, S. Basavoju and A. Nangia, *CrystEngComm* 2005, **7**, 551. (f) D. Cincic, T. Friscic, W. Jones, *Chem. Eur. J.* 2008, **14**, 747.
4. (a) P. J. Langley, J. M. Rawson, J. N. B. Smith, M. Schuler, R. Bachmann, A. Schweiger, F. Palacio, G. Antorrena, G. Gescheidt, A. Quintel, P. Rechsteiner and J. Hulliger, *J. Mater. Chem.* 1999, **9**, 1431. (b) C. Y. Liao, M. Nayak, H. H. Wei and S. Mohanta, *Polyhedron* 2008, **27**, 2693. (c) C. C. Chou, C. C. Su, H. L. Tsai and K. H. Lii, *Inorg. Chem.* 2005, **44**, 628. (d) S. Horiuchi, F. Ishii, R. Kumai, Y. Okimoto, H. Tachibana, N. Nagaosa and Y. Tokura, *Nat. Mater.* 2005, **4**, 163. (e) H. Miyasaka, N. Matsumoto, N. Re, E. Gallo and C. Floriani, *Inorg. Chem.* 1997, **36**, 670. (f) H. Miyasaka, N. Matsumoto, H. Ōkawa, N. Re, E. Gallo and C. Floriani, *J. Am. Chem. Soc.* 1996, **118**, 981. (g) H. Miyasaka, N. Matsumoto, H. Ōkawa, N. Re, E. Gallo and C. Floriani, *Angew. Chem. Int. Ed.* 1995, **34**, 1446. (h) M. Ohba, N. Maruono, H. Okawa, T. Enoki and J. M. Latour, *J. Am. Chem. Soc.* 1994, **116**, 11566. (i) P. Mukherjee, M. G. B. Drew, C. J. Gómez-García and A. Ghosh, *Inorg. Chem.* 2009, **48**, 4817. (j) P. T. Manoharan, B. Sambandam, R. Amsarani, B. Varghese, C. S. Gopinath and K. Nomura, *Inorg. Chim. Acta* 2011, **374**, 586.
5. M. E. Brown and M. D. Hollingsworth, *Nature* 1995, **376**, 323.
6. (a) V. Ramamurthy and D. F. Eaton, *Chem. Mater.* 1994, **6**, 1128. (b) H. G. Brittain, *Cryst. Growth Des.* 2010, **10**, 1990
7. F. Toda, S. Hyoda, K. Okada and K. Hirotsu, *J. Chem. Soc., Chem. Commun.* **1995**, 1531.
8. (a) K. Endo, T. Koike, T. Sawaki, O. Hayashida, H. Masuda and Y. Aoyama, *J. Am. Chem. Soc.* 1997, **119**, 4117. (b) S. K. Yoo, J. Y. Ryu, J. Y. Lee, C. Kim, S. J. Kim and Y. Kim, *Dalton Trans.* 2003, 1454.
9. S. Roy, S. P. Mondal, S. K. Ray and K. Biradha, *Angew. Chem. Int. Ed.* 2012, **51**, 12012
10. (a) A. Hazra, P. Kanoo, S. Mohapatra, G. Mostafa and T. K. Maji, *CrystEngComm* 2010, **12**, 2775 (b) S. Das and P. K. Bharadwaj, *Inor. Chem.* 2006, **45**, 5257. (c) J. A. Schlueter, R. J. Funk and U. Geiser, *Acta Cryst. C* 2005, **61**, m304. (d) C. Biswas, M. G. B. Drew, D. Escudero, A.



Frontera and A. Ghosh, *Eur. J. Inorg. Chem.* 2009, **2009**, 2238. (e) N. W. Alcock, A. Samotus and J. Szklarzewicz, *J. Chem. Soc., Dalton Trans.* **1993**, 885. (f) Y. Sun, J. Zhang, Z. Ju and G. Yang, *Aust. J. Chem.* **2005**, *58*, 572.

11. (a) P. Kanoo, A. C. Ghosh, A. T. Cyriac and T. K. Maji, *Chem. Eur. J.*, 2012, **18**, 237. (b) P. Kanoo, G. Mostafa, R. Matusuda, S. Kitagawa and T. K. Maji, *Chem. Commun.* 2011, **47**, 8106. (c) N. Yanai, K. Kitayama, Y. Hijikata, H. Sato, R. Matsuda, Y. Kubota, M. Takata, M. Mizuno, T. Uemura and S. Kitagawa, *Nat. Mater.* 2011, **10**, 787. (d) P. Kanoo and T. K. Maji, *Eur. J. Inorg. Chem.* 2010, **2010**, 3762. (e) Y. Takashima, S. Furukawa and S. Kitagawa, *CrystEngComm* 2011, **13**, 3360. (f) X. Zhao, B. Xiao, A. J. Fletcher, K. M. Thomas, D. Bradshaw and M. J. Rosseinsky, *Science* 2004, **306**, 1012. (g) P. Kar, R. Biswas, M. G. B. Drew, A. Frontera and A. Ghosh, *Inorg. Chem.* 2012, **51**, 1837 (h) P. Kanoo, R. Sambhu and T. K. Maji, *Inorg. Chem.* 2010, **50**, 400; (i) M. F. Manfrin, N. Sabbatini, L. Moggi, V. Balzani, M. W. Hosseini and J. M. Lehn, *J. Chem. Soc., Chem. Commun.* **1984**, 0, 555; (j) A. Hazra, S. Bonakala, S. K. Reddy, S. Balasubramanian and T. K. Maji, *Inorg. Chem.* 2013, **52**, 11385.

12. (a) D. A. Fowler, S. J. Teat, G. A. Baker and J. L. Atwood, *Chem. Commun.* 2012, **48**, 5262. (b) S. Bhattacharya and B. K. Saha, *Cryst. Growth Des.* 2011, **11**, 2194. (c) P. Rashidi-Ranjbar, B. Vafakish, A. Abbasi and A. Fischer, *Z. Kristall.* 2009, **224**, 499. (d) A. R. Albulnia, L. Annunziata and G. Guerra, *Macromolecules* 2008, **41**, 2683. (e) F. Pina, L. Moggi, M. F. Manfrin, V. Balzani, M. E. Hosseini and J. M. Lehn, *Gazz. Chim. Ital.* 1989, **119**, 65. (f) M. F. Manfrin, L. Moggi, V. Castelvetro, V. Balzani, M. W. Hosseini and J. M. Lehn, *J. Am. Chem. Soc.* 1985, **107**, 6888.

13. (a) M. L. Cheney, G. J. McManus, J. A. Perman, Z. Wang and M. J. Zaworotko, *Cryst. Growth Des.* 2007, **7**, 616. (b) G. R. Desiraju, *CrystEngComm* 2003, **5**, 466. (c) G. R. Desiraju, *Cryst. Growth Des.* 2011, **11**, 896. (d) V. R. Hathwar, T. S. Thakur, R. Dubey, M. S. Pavan, T. N. G. Row and G. R. Desiraju, *J. Phys. Chem. A* 2011, **115**, 12852. (e) M. C. Etter and S. M. Reutzel, *J. Am. Chem. Soc.* 1991, **113**, 2586. (f) S. Joseph, R. Sathishkumar, S. Mahapatra and G. R. Desiraju, *Acta Cryst. B* 2011, **67**, 525. (g) A. S. Rao, B. K. Tripuramallu, K. Ravada and S. K. Das, *Acta Cryst. E* 2010, **66**, o1945. (h) P. Raghavaiah, S. Supriya and S. K. Das, *CrystEngComm* **2005**, *7*, 167. (i) R. Haldar, K. V. Rao, S. J. George and T. K. Maji, *Chem. Eur. J.*, 2012, **18**, 5848. (j) M. W. Hosseini, Molecular tectonics: In Applications of supramolecular chemistry, Ed. H. J. Schneider, Taylor&Francis /CRC, 2011, Soumis presse. (k) M. Sarma, T. Chatterjee and S. K. Das. *RSC Adv.*, 2012, **2**, 3920. (l) R. Mondal, J. A. K. Howard, R. Banerjee and G. R. Desiraju, *Cryst. Growth Des.*, 2006, **6**, 2507. (m) T. Basu, H. A. Sparkes and R. Mondal. *Cryst. Growth*

*Des.*, 2009, **9**, 5164. (n) P. Kar, M. G. B. Drew, C. J. Gómez-García and A. Ghosh, *Polyhedron* 2013, **50**, 229.

14. S. Horike, S. Shimomura and S. Kitagawa, *Nat. Chem.* 2009, **1**, 695.

15. (a) N. R. Goud, S. Gangavaram, K. Suresh, S. Pal, S. G. Manjunatha, S. Nambiar and A. Nangia, *J. Pharm. Sci.* 2012, **101**, 664. (b) N. A. Meanwell, In Annual Reports in *Medicinal Chemistry*, Macor, J. E., Ed. Elsevier Academic Press Inc: San Diego, 2008, **43**, 373. (c) I. Miroshnyk, S. Mirza and N. Sandlert, *Expert Opinion on Drug Delivery* 2009, **6**, 333.

16. (a) C. L. Chen and A. M. Beatty, *J. Am. Chem. Soc.* 2008, **130**, 17222. (b) M. B. Dewal, M. W. Lufaso, A. D. Hughes, S. A. Samuel, P. Pellechia and L. S. Shimizu, *Chem. Mater.* 2006, **18**, 4855. (c) S. A. Dalrymple and G. K. H. Shimizu, *Chem. Commun.* 2006, **956**.

17. (a) T. Friščić, A. V. Trask, W. D. S. Motherwell and W. Jones, *Cryst. Growth Des.* 2008, **8**, 1605. (b) G. J. Halder, C. J. Kepert, B. Moubaraki, K. S. Murray and J. D. Cashion, *Science* 2002, **298**, 1762.

18. (a) R. Ludwig, *Angew. Chem. Int. Ed.*, 2001, **40**, 1808; (b) D. Eisenberg and W. Kauzmann, *The Structure and Properties of Water*, Oxford University Press, Oxford, 1969.

19. (a) K. Mitsuoka, K. Murata, T. Walz, T. Hirai, P. Agre, J. B. Heymann, A. Engel and Y. J. Fujiyoshi, *Struct. Biol.*, 1999, **128**, 34; (b) E. Tajkhorshid, P. Nollert, M. Ø. Jensen, L. J. W. Miercke, J. O'Connell, R. M. Stroud and K. Schulten, *Nature*, 2002, **296**, 525.

20. (a) M. Yoshizawa, T. Kusukawa, M. Kawano, T. Ohhara, I. Tanaka, K. Kurihara, N. Nimura and M. Fujita, *J. Am. Chem. Soc.*, 2005, **127**, 2798; (b) B. Sreenivasulu and J. Vittal, *Angew. Chem. Int. Ed.*, 2004, **43**, 5769; (c) B. Q. Ma, H. L. Sun and S. Gao, *Angew. Chem., Int. Ed.*, 2004, **43**, 1374; (d) C. Biswas, M. G. B. Drew and A. Ghosh, *Inorg. Chem.*, 2008, **47**, 4513; (e) M. T. Ng, T. C. Deivaraj, W. T. Klooster, G. J. McIntyre and J. J. Vittal, *Chem. Eur. J.*, 2004, **10**, 5853; (f) K. V. Katti, P. K. Bharadwaj, J. J. Vittal and R. Kannan, *Synthesis and Reactivity in Inorganic, Metal-Organic and Nano-Metal Chemistry* 2008, **38**, 1.

21. Dodecameric Cluster: (a) S. K. Ghosh and P. K. Bharadwaj, *Angew. Chem., Int. Ed.*, 2004, **43**, 3577; (b) S. Neogi, G. Savitha and P. K. Bharadwaj, *Inorg. Chem.*, 2004, **43**, 3771; (c) S. Nishikiori and T. Iwamoto, *Chem. Commun.*, 1993, 1555.

22. Decamer: (a) L. J. Barbour, G. W. Orr and J. L. Atwood, *Nature*, 1998, **393**, 671; (b) A. Michaelides, S. Skoulika, E. G. Bakalbassis and J. Mrozinski, *Cryst. Growth Des.*, 2003, **3**, 487; (c) R. D. Bergognant, A. Y. Robin and K. M. Fromm, *Cryst. Growth Des.*, 2005, **5**, 1691.

23. Octamer: (a) W. B. Blanton, S. W. Gordon-Wylie, G. R. Clark, K. D. Jordan, J. T. Wood, U. Geiser and T. J. Collins, *J. Am. Chem. Soc.*, 1999, **121**, 3551; (b) R. J. Doedens, E. Yohannes and M. I. Khan, *Chem. Commun.*, 2002, 62; (c) J. L. Atwood, L. J. Barbour, T. J. Ness, C. L. Raston and P. L. Raston, *J. Am. Chem. Soc.*, 2001, **123**, 7192; (d) B. -Q. Ma, H. -L. Sun and S. Gao, *Chem. Commun.*, 2005, 2336; (e) S. K. Ghosh and P. K. Bharadwaj, *Inorg. Chim. Acta*, 2006, **359**, 1685; (f) T. K. Prasad and M. V. Rajasekharan, *Cryst. Growth Des.*, 2006 **6**, 488; (g) D. Li, Y. Wang, X. Luan, P. Liu, C. Zhou, H. Ma, and Q. Shi, *Eur. J. Inorg. Chem.*, 2005, 2678; (h) S. Das and P. K. Bharadwaj, *Cryst. Growth Des.*, 2006, **6**, 187; (i) W. Wei, F. Jiang, M. Wua, Q. Gao, Q. Zhang, C. Yan, L. Ning and M. Hong, *Inorg. Chem. Commun.*, 2009, **12**, 290. (j) J. Y. Wua, J. F. Yin, T. W. Tseng and L. L. Kuang, *Inorg. Chem. Commun.*, 2008, **11**, 314; (k) S. K. Ghosh and P. K. Bharadwaj, *Eur. J. Inorg. Chem.*, 2005, 4886.

24. Hexamer: (a) R. Custecean, C. Afloroaei, M. Vlassa and M. Polverejan, *Angew. Chem., Int. Ed.*, 2000, **39**, 3094; (b) B. Q. Ma, H. -L. Sun and S. Gao, *Chem. Commun.*, 2005, 2336; (c) B. H. Ye, B. -B. Ding, Y. Q. Weng and X. -M. Chen, *Inorg. Chem.*, 2004, **43**, 6866; (d) K. M. Park, R. Kuroda and T. Iwamoto, *Angew. Chem., Int. Ed.*, 1993, **32**, 884; (e) J. N. Moorthy, R. Natarajan and P. Venugopalan, *Angew. Chem., Int. Ed.*, 2002, **41**, 3417; (f) K. -M. Park, R. Kuroda and T. Iwamoto, *Angew. Chem., Int. Ed. Engl.*, 1993, **32**, 884; (g) U. Mukhopadhyay and I. Bernal, *Cryst. Growth Des.*, 2005, **5**, 1687; (h) Y. -C. Liao, Y. -C. Jiang and S. -L. Wang, *J. Am. Chem. Soc.*, 2005, **127**, 12794; (i) Y. -P. Ren, L. -S. Long, B. -W. Mao, Y. -Z. Yuan, R. -B. Huang and L. -S. Zheng, *Angew. Chem., Int. Ed.*, 2003, **42**, 532; (j) S. K. Ghosh and P. K. Bharadwaj, *Inorg. Chem.*, 2003, **42**, 8250; (k) X. -M. Zhang, R. -Q.; Fang and H. -S. Wu, *Cryst. Growth Des.*, 2005, **5**, 1335.

25. K. Nauta and R. E. Miller, *Science*, 2000, **287**, 293.

26. D. Eisenberg and W. Kauzmann, *The Structure and Properties of Water*, Oxford university Press, Oxford, **1969**.

27. (a) R. J. Speedy, J. D. Madura and W. L. Jorgensen, *J. Chem. Phys.*, 1987, **91**, 909; (b) A. C. Belch and S. A. Rice, *J. Chem. Phys.*, 1987, **86**, 5676.

28. (a) H. B. Burgi, J. Hulliger and P. J. Langley, *Curr. Opin. Solid State Mat. Sci.* 1998, **3**, 425. (b) N. Issa, P. G. Karamertzanis, G. W. A. Welch and S. L. Price, *Cryst. Growth Des.* 2008, **9**, 442. (c) T. Rager and R. Hilfiker, *Cryst. Growth Des.* 2010, **10**, 3237. (d) S. Ebenezer, P.T. Muthiah and R. J. Butcher, *Cryst. Growth Des.* 2011, **11**, 3579. (e) S. Tothadi, A. Mukherjee and G. R. Desiraju, *Chem. Commun.* 2011, **47**, 12080. (f) S. M. Curtis, N. Le, F. W. Fowler and J. W.

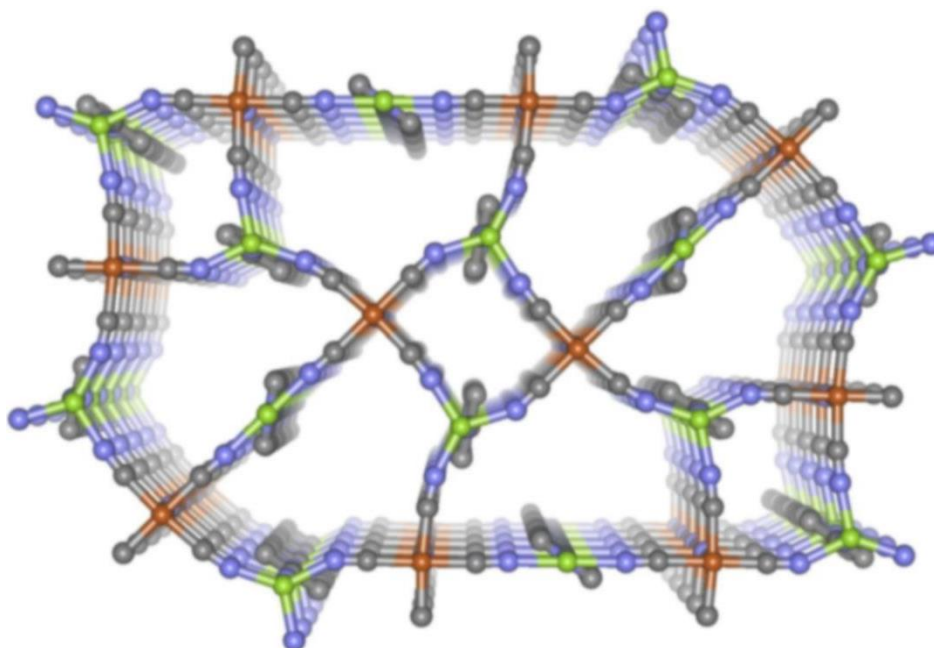
- Lauher, *Cryst. Growth Des.* 2005, **5**, 2313. (g) V. K. Srirambhatla, A. Kraft, S. Watt and A. V. Powell, *Cryst. Growth Des.* 2012, **12**, 4870
29. A. Altomare, G. Cascarano, C. Giacovazzo and A. Gualaradi, *J. Appl. Cryst.* 1993, **26**, 343.
30. G. M. Sheldrick, SHELXL 97 Program for the Solution of Crystal Structure, University of Göttingen, Germany, 1997.
31. A. L. Spek, *J. Appl. Cryst.* 2003, **36**, 7.
32. G. M. Sheldrick, SHELXS 97, Program for the Solution of Crystal Structure, University of Göttingen, Germany, 1997.
33. L. J. Farrugia, WinGX - A Windows Program for Crystal Structure Analysis. *J. Appl. Crystallogr.* 1999, **32**, 837.
34. O. Fabelo, J. Pasan, L. Canadillas-Delgado, F. S. Delgado, A. Labrador, F. Lloret, M. Julve and C. Ruiz-Perez, *CrystEngComm* 2008, **10**, 1743.
35. (a) Molecular area is calculated from liquid density, assuming spherical symmetry and a hexagonal close packing. The equation and values are in ref. 22 (b). (b) C. E. Webster, R. S. Drago and M. C. Zerner, *J. Am. Chem. Soc.* 1998, **120**, 5509.
36. R. S. Pillai, S. A. Peter and R. V. Jasra, *Microporous Mesoporous Mater.* 2008, **113**, 268.
37. (a) T. K. Maji, G. Mostafa, R. Matsuda and S. Kitagawa, *J. Am. Chem. Soc.*, 2005, **127**, 17152; (b) T. K. Maji, K. Uemura, H. C. Chang, R. Matsuda and S. Kitagawa, *Angew. Chem. Int. Ed.*, 2004, **43**, 3269.
38. Metal-Organic Frameworks, Design and Application, Edited by Macgillivray, L. R.; Published by *John Wiley & Sons, Inc., Hoboken, New Jersey*. (b) T. Borjigin, F. Sun, J. Zhang, K. Cai, H. Rena and G. Zhu, *Chem. Commun.*, 2012, **48**, 7613.
39. K. S. W. Sing, D. H. Everett, R. A. W. Haul, L. Moscou, R. A. Pierotti, J. Rouquerol and T. Siemieniowska, *Pure Appl. Chem.* 1985, **57**, 603. 33.
40. (a) G. Akiyama, R. Matsuda and S. Kitagawa, *Chem. Lett.* 2010, **39**, 360. (b) J. Seo, R. Matsuda, H. Sakamoto, C. Bonneau and S. Kitagawa, *J. Am. Chem. Soc.* 2009, **131**, 12792.
41. G. Akiyama, R. Matsuda, H. Sato, A. Hori, M. Takata and S. Kitagawa, *Microporous Mesoporous Mater.* 2012, **157**, 89.

42. M. M. Dubinin, *Chem. Rev.* 1960, **60**, 235.



# Chapter 3A

*High Heat of Hydrogen Adsorption, Selective Hydrocarbon  
Storage and Guest-responsive Magnetic Modulation in 3D  
Porous Pillared-layer Metal-organic Frameworks*







## Summary

This chapter describes the synthesis, structural characterization, adsorption and magnetic properties of three new 3D metal-organic frameworks (MOFs)  $\{[\text{Mn}_3(\text{bipy})_3(\text{H}_2\text{O})_4][\text{Cr}(\text{CN})_6]_2 \cdot 2(\text{bipy}) \cdot 4\text{H}_2\text{O}\}_n$  (**1**),  $\{[\text{Mn}_3(\text{bipy})_3(\text{H}_2\text{O})_4][\text{Mn}(\text{CN})_6]_2 \cdot 2(\text{bipy}) \cdot 4\text{H}_2\text{O}\}_n$  (**2**) and  $\{[\text{Mn}_2(\text{bipy})][\text{Mn}(\text{CN})_6](\text{CN})\}_n$  (**3**) obtained by the self-assembly of  $\text{Mn}^{\text{II}}$  and  $[\text{Cr}/\text{Mn}(\text{CN})_6]^{3-}$  and 4,4'-bipyridine ligands. Compound **1** and **2** feature a three dimensional (3D) pillared-layer framework with two types of 1D channel along the *c* axis. The activated structure of compound **1** shows a moderate  $\text{H}_2$  uptake with a  $\Delta H_{\text{H}_2}$  value of 11.4 kJ/mol, which depicts the presence of strong  $\text{H}_2$ -framework interaction. Compound **1** exhibits ferrimagnetic behaviour where magnetic ordering temperature ( $T_c$ ) changes with response to the guest molecules. The  $\text{C}_2$ -hydrocarbon storage capacity of compound **2** has also been studied, where it unveils excellent selectivity for  $\text{C}_2\text{H}_2$  over  $\text{C}_2\text{H}_4$  and  $\text{C}_2\text{H}_6$  gas molecules. In compounds **2** and **3**, the alternate arrangement of high spin  $\text{Mn}^{\text{II}}$  and low spin  $\text{Mn}^{\text{III}}$  centers separated by cyanide bridges results ferrimagnetic and spin canting behaviour, respectively. Furthermore, compound **2** shows interesting single-crystal-to-single-crystal structural transformation where selectively one coordinated and one guest water molecules were removed to obtain **2a** ( $\{[\text{Mn}_3(\text{bipy})_3(\text{H}_2\text{O})_2][\text{Mn}(\text{CN})_6]_2 \cdot 2(\text{bipy}) \cdot 2\text{H}_2\text{O}\}_n$ ).

A. Hazra, P. Kanoo and T. K. Maji, *Chem. Commun.*, 2011, **47**, 538

A. Hazra and T. K. Maji, *Manuscript under preparation*

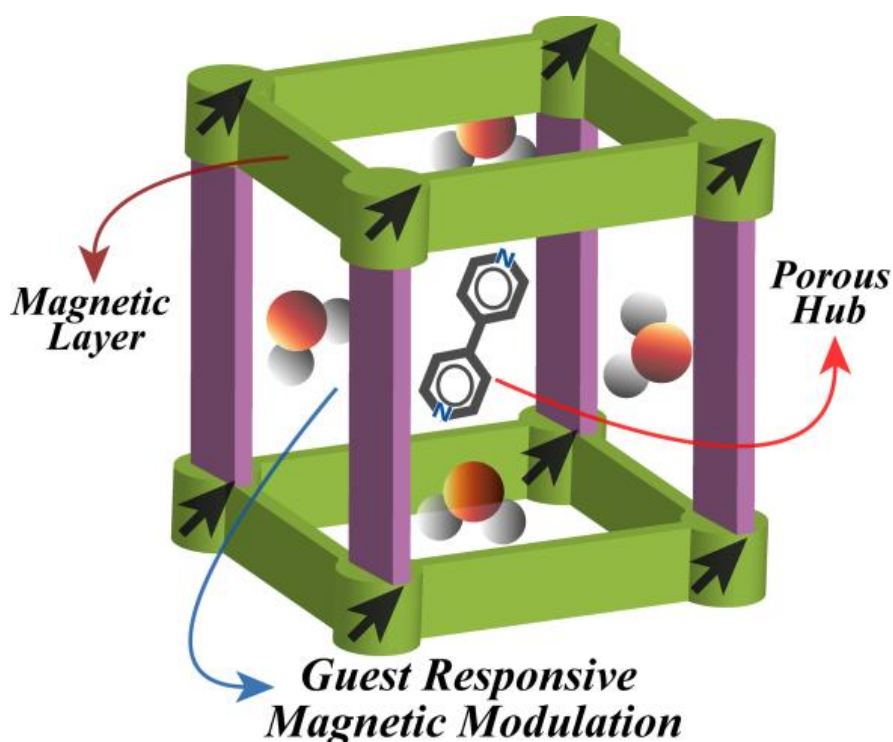


### 3.A.1: Introduction

Metal-organic frameworks (MOFs) or porous coordination polymers (PCPs) are promising materials for applications in gas storage, separation, sensing, catalysis, magnetism, drug delivery *etc.*<sup>1</sup> Multifunctional materials, *i.e.* materials which combine a set of well-defined properties (*e.g.* porosity and magnetism, porosity and optical) for specific applications are gaining importance recently.<sup>1a,e,2</sup> Such synergism, where two different functionalities are combined, would open up the possibility and prospect of finding novel physical phenomena for designing smart materials.<sup>3</sup> Magnetism has generic dependence on distance while the porosity is enhanced with long linkers and hence combination of these two is not always easy or straightforward. Presence of porosity provides the opportunity to study gas storage property, selectivity as well as guest-dependent magnetism<sup>4</sup> and magnetic sensing which are of particular interest for applications such as magnetic devices and sensors (Scheme 1).<sup>2b,5</sup> Several fascinating properties like guest-dependent spin crossover,<sup>4d,6</sup> magnetic ordering sensitive to guest removal/exchange,<sup>7</sup> and different magnetic behaviour corresponding to reversible solvent-induced structural changes<sup>8</sup> have been reported in porous magnets. On the other hand, the porous property of MOFs are gaining increased attention with time and the framework materials have emerged as an excellent storage alternative to high pressure and liquefied hydrogen tanks.<sup>1a,9</sup> In this respect, recent reports indicate that presence of unsaturated metal site (UMS) is crucial for strong interaction of H<sub>2</sub> molecule and also largely enhances the value of enthalpy of adsorption.<sup>10,11</sup> So it will be a great interest for hydrogen storage material if we invoke UMS in the framework along with the permanent porosity.

On the other hand, separation of small hydrocarbons such as methane, acetylene, ethylene and ethane is a very important industrial process as they are the very basic raw materials for various industrial and consumer products such as acetic acid and polymers.<sup>12</sup> Steam cracking is one of widely used procedure where hydrocarbon feedstocks like naphtha is being converted to a mixture of light olefins such as ethylene, acetylene and other small hydrocarbons.<sup>13</sup> Use of traditional methods like cryogenic distillation for separating such small hydrocarbons is very energy consuming and inefficient process. It has been envisioned that the adsorption based separation of small hydrocarbons might lead to advanced technologies where the implementation of pressure swing adsorption

(PSA), temperature swing adsorption (TSA) and adsorbent based membrane devices will reduce the cost of separating C2 hydrocarbons from a natural gas feedstock. Owing to modular nature, microporous MOF materials showed the promises for kinetic based separation of small hydrocarbons from their mixture and thus receiving much attention in terms of adsorption applications.<sup>14</sup> Compared to conventional porous material (such as zeolites and porous carbons), the surface area and pore size of MOFs can be systematically tuned by altering the lengths and geometry of organic ligands while their pore surface can also be functionalized by the immobilization of different functional groups (*e.g.*  $-\text{NH}_2$ ,  $-\text{OH}$ ,  $-\text{F}$ ). Moreover, by creating open metal sites, isosteric heat of adsorption for olefin molecules can be further enhanced and thus thermodynamic based separation can be implicated. Those microporous MOFs, where the dimension of the channel windows are comparable and/or slightly larger than the kinetic diameter of such small hydrocarbons (3.3–4.4 Å) will be of special interest for kinetic based separation.



**Scheme 1:** Bimodal functionality in a framework material.

This chapter reports a rational design for the synthesis of 3D porous magnetic pillared-layer systems based on hexacyanometallate and organic exo-bidentate linkers connected with different transition metal centers. To the best of our knowledge, such porous magnets based on hexacyanometallate as a building unit is yet to be accounted. Different hexacyanometallate ( $[\text{Cr}(\text{CN})_6]^{3-}$ / $[\text{Mn}(\text{CN})_6]^{3-}$ ) have been used as

metalloligand to connects  $\text{Mn}^{\text{II}}$  ions to form a 2D sheet which is extended to form 3D architectures,  $\{[\text{Mn}_3(\text{bipy})_3(\text{H}_2\text{O})_4][\text{Cr}(\text{CN})_6]_2 \cdot 2(\text{bipy}) \cdot 4\text{H}_2\text{O}\}_n$  (**1**),  $\{[\text{Mn}_3(\text{bipy})_3(\text{H}_2\text{O})_4][\text{Mn}(\text{CN})_6]_2 \cdot 2(\text{bipy}) \cdot 4\text{H}_2\text{O}\}_n$  (**2**) and  $\{[\text{Mn}_2(\text{bipy})][\text{Mn}(\text{CN})_6](\text{CN})\}_n$  (**3**) by pillaring with 4,4'-bipyridine (bipy) linker. Compound **1** and **2** manifest ferrimagnetic behaviour whereas compound **3** exhibits canted antiferromagnetism. Furthermore, guest responsive magnetic modulation with change in  $T_C$  was also demonstrated by compound **1**. Compound **1** shows selective sorption of  $\text{CO}_2/\text{H}_2$  over  $\text{N}_2$  and exhibits very high value of enthalpy of adsorption for  $\text{H}_2$  ( $-11.5 \text{ kJ mol}^{-1}$ ). The dehydrated compound of **2** shows high adsorption enthalpy and excellent selectivity of  $\text{C}_2\text{H}_2$  over  $\text{C}_2\text{H}_4$  and  $\text{C}_2\text{H}_6$  molecules. The alternate arrangement of high spin  $\text{Mn}^{\text{II}}$  and low spin  $\text{Mn}^{\text{III}}$  centers separated by cyanide bridges introduces antiferromagnetic exchange coupling between the metal ions in compounds **2** and **3**.

### 3A.2: Experimental Section

#### 3A.2.1: Materials

All the reagents and solvents employed were commercially available and used as supplied without further purification.  $\text{K}_3[\text{Cr}(\text{CN})_6]$ ,  $\text{K}_3[\text{Mn}(\text{CN})_6]$ , 4,4'-bipyridine (bipy) and  $\text{MnCl}_2 \cdot 4\text{H}_2\text{O}$  were obtained from the Aldrich Chemical Co.

#### 3A.2.2: Synthetic procedure

**3A.2.2.1 Synthesis of  $\{[\text{Mn}_3(\text{bipy})_3(\text{H}_2\text{O})_4][\text{Cr}(\text{CN})_6]_2 \cdot 2(\text{bipy}) \cdot 4(\text{H}_2\text{O})\}_n$  (**1**):** An aqueous solution (12.5 mL) of  $\text{K}_3[\text{Cr}(\text{CN})_6]$  (0.25 mmol, 0.0426 g) was added to an ethanolic solution (12.5 mL) of 4,4'-bipyridine (0.25 mmol, 0.039 g) and stirred for 30 min.  $\text{MnCl}_2 \cdot 4\text{H}_2\text{O}$  (0.25 mmol, 0.0494 g) was dissolved in 12.5 ml distilled water and 2.5 mL of this metal solution was carefully layered with the 2.5 mL of mixed bipy and  $\text{K}_3[\text{Cr}(\text{CN})_6]$  solution using an ethanol : water buffer solution (1 mL, 1:1) in a crystal tube. After 15 days, transparent block shaped crystals were appeared in the middle of the tube and separated and washed with ethanol. Yield: 72%, relative to  $\text{Mn}^{\text{II}}$ . The bulk amount of the sample was prepared by the direct mixing of the reagents in ethanol/water mixed solution with stirring for 24 h and the phase purity was checked with the PXRD and elemental analysis. This powdered sample was used for studying different physical properties. IR (KBr,  $\text{cm}^{-1}$ ):  $\nu(\text{C}\equiv\text{N})$  2125, 2154 and 2170  $\text{cm}^{-1}$ ;  $\nu(\text{C}=\text{C})$ : 1608  $\text{cm}^{-1}$ , 1536

$\text{cm}^{-1}$ ;  $\nu(\text{O-H})$ :  $3477 \text{ cm}^{-1}$  and  $3592 \text{ cm}^{-1}$  (Figure 1). Anal. calc. for  $\text{C}_{62}\text{H}_{56}\text{Cr}_2\text{Mn}_3\text{N}_{22}\text{O}_8$ : C, 49.44; H, 3.75; N, 20.46. Found: C, 48.98; H, 3.31; N, 20.66%.

**3A.2.2.2 Preparation of  $\{[\text{Mn}_3(\text{bipy})_3][\text{Cr}(\text{CN})_6]_2\}$  (1a):** Compound **1a** was prepared by heating **1** at  $165 \text{ }^\circ\text{C}$  under vacuum ( $< 10^{-1} \text{ Pa}$ ) for 72 hours. During the heating period, the removed guest bipy molecules were deposited in the inner cell of the adsorption cell. The heating procedure was continued following with the change of the sample cells unless there was no tress of sublimated guest bipy molecule. This powdered sample was used for characterization of different physical properties. IR:  $\nu(\text{C}\equiv\text{N})$   $2162 \text{ cm}^{-1}$ ;  $\nu(\text{C}=\text{C})$ :  $1603 \text{ cm}^{-1}$ ,  $1531 \text{ cm}^{-1}$  (Figure 1). Anal. calc. for  $\text{C}_{42}\text{H}_{22}\text{Cr}_2\text{Mn}_3\text{N}_{18}$ : C, 48.16; H, 2.12; N, 24.07. Found: C, 47.52; H, 1.92; N, 23.66%.

**3A.2.2.3 Preparation of  $\{[\text{Mn}_3(\text{bipy})_3][\text{Cr}(\text{CN})_6]_2 \cdot 8\text{H}_2\text{O}\}$  (1b):** Compound **1b** was prepared by exposing water vapour into **1a** for 6 days. Anal. calc. for  $\text{C}_{42}\text{H}_{38}\text{Cr}_2\text{Mn}_3\text{N}_{18}\text{O}_8$ : C, 42.33; H, 3.21; N, 21.16. Found: C, 41.92; H, 3.34; N, 20.96%.

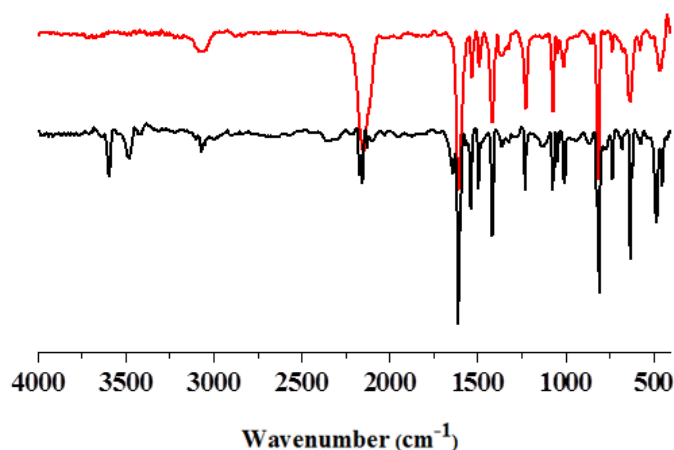


**Figure 1:** IR spectra of **1** (black) and **1a** (red).

**3A.2.2.4 Synthesis of  $\{[\text{Mn}_3(\text{bipy})_3(\text{H}_2\text{O})_4][\text{Mn}(\text{CN})_6]_2 \cdot 2(\text{bipy}) \cdot 4\text{H}_2\text{O}\}_n$  (2):** A aqueous solution (12.5 mL) of  $\text{K}_3[\text{Mn}(\text{CN})_6]$  (0.25 mmol) was added to an ethanolic solution (12.5 mL) of bipy (0.5 mmol) and stirred for 30 min.  $\text{MnCl}_2 \cdot 4\text{H}_2\text{O}$  (0.25 mmol) was dissolved in 12.5 mL water and 2.5 mL of this metal solution was carefully layered with the 2.5 mL of mixed bipy and  $\text{K}_3[\text{Mn}(\text{CN})_6]$  solution using an ethanol : water buffer solution (1 mL, 1:1) in a test tube. The reaction was performed under completely dark condition and the test tube was kept in a fridge ( $\sim 4^\circ\text{C}$ ) after wrapping with aluminium foil. After 15 days, dark brown block crystals were appeared in the middle of the tube and separated and

washed with ethanol. The bulk amount of the sample was prepared in similar reaction condition by the direct mixing of the respective reagents in ethanol–water solution under stirring for 24 h and the phase purity was checked with the PXRD and elemental analysis. Yield: 79%, relative to Mn<sup>II</sup>. Anal. calc. for C<sub>62</sub>H<sub>56</sub>Mn<sub>5</sub>N<sub>22</sub>O<sub>8</sub>: C, 49.25; H, 3.73; N, 20.38. Found: C, 49.81; H, 3.58; N, 20.18. IR (KBr, cm<sup>-1</sup>) :  $\nu(\text{H}_2\text{O})$  3679, 3585, 3488;  $\nu(\text{ArC-H})$  3066, 3051;  $\nu(\text{C}\equiv\text{N})$  2154, 2131;  $\nu(\text{ArC=C})$  1604, 1560, 1534. IR spectrum of **2** (Figure 2) shows strong and broad bands around 3490 cm<sup>-1</sup> suggesting the presence of water molecules. A strong band around 2131 cm<sup>-1</sup> corroborate to  $\nu(\text{C}\equiv\text{N})$  stretching frequency and a band around 1604 cm<sup>-1</sup> indicates the presence bipy molecule.

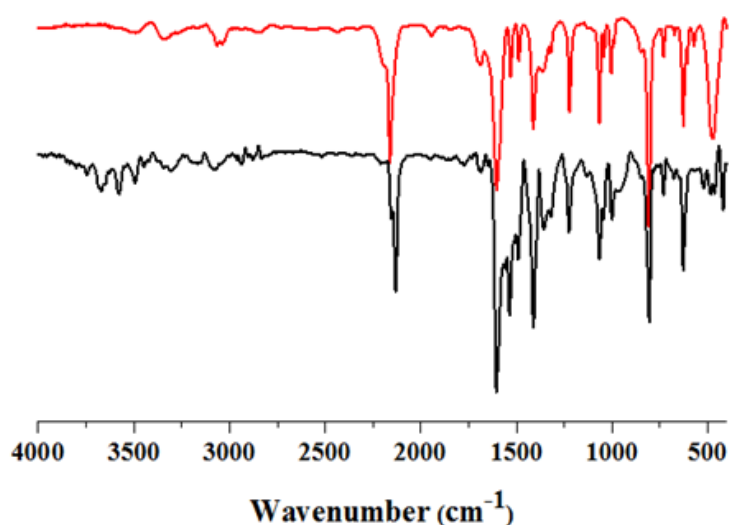


**Figure 2:** IR spectra of **2** (black) and **2b** (red).

**3A.2.2.5 Preparation of {[Mn<sub>3</sub>(bipy)<sub>3</sub>][Mn(CN)<sub>6</sub>]<sub>2</sub>]<sub>n</sub> (**2b**):** Compound **2b** was prepared by adopting the similar procedure of as of **1a**. The removal of the water molecules (coordinated and guest) was confirmed by the elemental analysis. This powdered sample was used for characterization of different physical properties. Anal. calc. for C<sub>42</sub>H<sub>24</sub>Mn<sub>5</sub>N<sub>18</sub>: C, 47.80; H, 2.29; N, 23.89. Found: C, 47.29; H, 2.41; N, 23.45.

**3A.2.2.6 Synthesis of {[Mn<sub>2</sub>(bipy)(CN)][Mn(CN)<sub>6</sub>]<sub>n</sub> (**3**):** Synthesis of the single crystals of **3** was very similar to that of **2** except the presence of light. After preparing the tri-layered test tubes, they were kept at room temperature under the presence of normal light. After 15 days, dark brown block shaped crystals were appeared in the middle of the tube and separated and washed with ethanol. For the bulk synthesis of compound **3**, a different procedure was adopted. 0.1 mmol of K<sub>3</sub>[(Mn(CN)<sub>6</sub>] was dissolved in 7 mL of

distilled water and kept under air for 5 hrs. Black precipitation was observed in the bottom of the beaker which was separated upon filtration. The colorless filtrate, enriched with cyanide ions was further degassed for 8 hrs under the Ar flow. This cyanide containing water was used for dissolving  $K_3[Mn(CN)_6]$  in the bulk preparation of compound **3**. Though the single crystals were obtained in presence of light, the bulk synthesis was performed under dark to avoid further decomposition of  $K_3[Mn(CN)_6]$ . During synthesis, the molar ratio of the reagents was determined from the formula obtained from single crystal structure. Yield: 71%, relative to  $Mn^{II}$ . Anal. calc. for  $C_{17}H_8Mn_3N_9$ : C, 40.58; H, 1.60; N, 25.06. Found: C, 40.41; H, 1.82; N, 25.18. IR (KBr,  $cm^{-1}$ ):  $\nu(H_2O)$  3599, 3469;  $\nu(ArC-H)$  3072, 3052;  $\nu(C\equiv N)$  2174, 2157, 2129;  $\nu(ArC=C)$  1608, 1596, 1536. IR spectrum of **3** (Figure 3) shows strong and broad bands around 3599  $cm^{-1}$  suggesting the presence of water molecules. A strong band around 2157  $cm^{-1}$  corroborate to  $\nu(C\equiv N)$  stretching frequency and a band around 1608  $cm^{-1}$  indicates the presence bipy molecule.

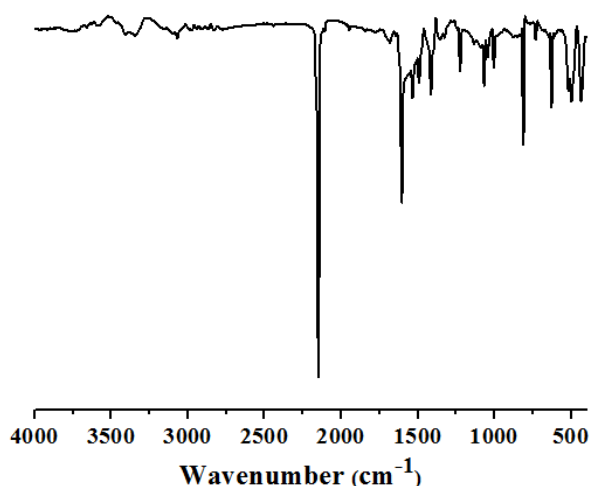


**Figure 3:** IR spectra of **3**.

### **3A.2.3: Physical Measurements**

The elemental analyses were carried out on a Thermo Fisher Flash 2000 Elemental Analyzer. Thermogravimetric analyses (TGA) were carried out with a Mettler Toledo TGA850 instrument under nitrogen atmosphere. IR spectra were recorded in the region 4000–400  $cm^{-1}$  on a Bruker IFS 66v/S spectrophotometer with samples prepared in KBr pellets. Powder X-ray diffraction (PXRD) data were collected on a Bruker D8 Discover instrument using  $Cu-K\alpha$  radiation. Magnetic measurements were carried out



with a superconducting quantum interference device (SQUID) magnetometer (Quantum Design) in *dc* scan mode.

### 3A.2.4: Single Crystal X-ray Diffraction

Suitable single crystals of compounds **1**, **2**, **2a**, **3** were mounted on a thin glass fibre with commercially available super glue. X-Ray single crystal structural data were collected on a Bruker Smart- CCD diffractometer equipped with a normal focus, 2.4 kW sealed tube X-ray source with graphite monochromated Mo- $K\alpha$  radiation ( $\lambda = 0.71073$  Å) operating at 50 kV and 30 mA. The program SAINT<sup>15</sup> was used for integration of diffraction profile and absorption corrections were made with SADABS<sup>16</sup> program. The structures were solved by SIR 92<sup>17</sup> and refined by full matrix least squares method using SHELXL-97.<sup>18</sup> The non-hydrogen atoms were refined anisotropically. The hydrogen atoms were fixed by HFIX command and placed in ideal positions (except for H<sub>2</sub>O molecules which were located from Fourier map). Potential solvent accessible area or void space was calculated using the PLATON 99<sup>19</sup> multipurpose crystallographic software. All crystallographic and structure refinement data of the compounds **1**, **2**, **2a**, **3** are summarized in Table 1. Selected bond distances and angles are shown in Table 2-9. All calculations were carried out using SHELXL-97,<sup>18</sup> PLATON 99,<sup>19</sup> SHELXS-97<sup>20</sup> and WinGX system, Ver 1.80.01.<sup>21</sup>

**Table 1:** Crystallographic data and structure refinement parameters for compounds **1**, **2**, **2a** and **3**.

	<b>1</b>	<b>2</b>	<b>2a</b>	<b>3</b>
Empirical formula	C <sub>62</sub> H <sub>56</sub> Cr <sub>2</sub> Mn <sub>3</sub> N <sub>22</sub> O <sub>8</sub>	C <sub>62</sub> H <sub>56</sub> Mn <sub>5</sub> N <sub>22</sub> O <sub>8</sub>	C <sub>62</sub> H <sub>48</sub> Mn <sub>5</sub> N <sub>22</sub> O <sub>4</sub>	C <sub>17</sub> H <sub>8</sub> Mn <sub>3</sub> N <sub>9</sub>
M	1488.09	1511.99	1439.92	503.14
Crystal system	Orthorhombic	Orthorhombic	Orthorhombic	Monoclinic
space group	<i>Pbam</i> (No. 55)	<i>Pbam</i> (No. 55)	<i>Pbam</i> (No. 55)	<i>C2/m</i> (No.12)
<i>a</i> (Å)	16.7961(4)	16.2079(18)	16.039(5)	12.9719(9)
<i>b</i> (Å)	18.1575(4)	17.833(2)	17.851(4)	7.7902(5)
<i>c</i> (Å)	11.6335(2)	11.6508(12)	11.558(3)	12.2890(13)
$\alpha$ (deg)	90	90	90	90
$\beta$ (deg)	90	90	90	120.699(2)
$\gamma$ (deg)	90	90	90	90
<i>V</i> (Å <sup>3</sup> )	3547.93(13)	3367.5(6)	3309.2(15)	1067.82(15)
Z	2	2	2	2
<i>T</i> (K)	293	296	408	110
$\lambda$ (Mo $K\alpha$ )	0.71073	0.71073	0.71073	0.71073
<i>D<sub>c</sub></i> (g cm <sup>-3</sup> )	1.393	1.491	1.445	1.565
$\mu$ (mm <sup>-1</sup> )	0.881	0.982	0.991	1.768

$\theta_{\max}/\theta_{\min}$ (deg)	26.4/1.6	28.4/3.1	25.0/2.3	27.0/3.1
total data	33673	55943	18701	6073
unique reflection	3815	4388	3018	1244
$R_{\text{int}}$	0.053	0.060	0.110	0.082
data [ $I > 2\sigma(I)$ ]	3380	3325	2669	890
$R^a$	0.0943	0.0428	0.1307	0.0459
$R_w^b$	0.2300	0.1328	0.3735	0.1162
GOF	1.13	1.04	1.61	1.02
$\Delta\rho$ min/max [ $e \text{ \AA}^{-3}$ ]	-1.17, 0.86	-0.57, 0.79	-0.89, 1.04	-0.79, 0.94

$$^a R = \sum ||F_o| - |F_c|| / \sum |F_o| ; \quad ^b R_w = [\sum \{w(F_o^2 - F_c^2)^2\} / \sum \{w(F_o^2)\}]^{1/2}$$

**Table 2:** Selected bond distance ( $\text{\AA}$ ) for **1**.

Bonds	Bond length ( $\text{\AA}$ )	Bonds	Bond length ( $\text{\AA}$ )
Mn1-O1	2.222(8)	Mn1-N5	2.192(9)
Mn1-N6	2.270(6)	Mn1-N2_a	2.168(9)
Mn1-N4_c	2.203(8)	Mn1-N6_j	2.270(6)
Mn2-O2	2.263(8)	Mn2-N3	2.192(9)
Mn2-N7	2.271(10)	Mn2-O2_b	2.263(8)
Mn2-N3_b	2.192(9)	Mn2-N7_h	2.271(10)
Cr1-C1	2.082(8)	Cr1-C2	2.073(11)
Cr1-C3	2.063(10)	Cr1-C4	2.056(9)
Cr1-C5	2.048(10)	Cr1-C1_j	2.082(8)

$$a = -x, -y, z; \quad b = 1-x, -y, z; \quad c = -1/2+x, 1/2-y, 1-z; \quad h = 1-x, -y, 1-z; \quad j = x, y, 1-z$$

**Table 3:** Selected bond angles ( $^\circ$ ) for **1**.

	Angles ( $^\circ$ )		Angles ( $^\circ$ )
O1-Mn1-N5	82.7(3)	O2_b-Mn2-N7_h	90.00
O1-Mn1-N6	88.57(15)	N3_b-Mn2-N7_h	90.00
O1-Mn1-N2_a	175.7(3)	C1-Cr1-C2	89.6(2)
O1-Mn1-N4_c	83.8(3)	C1-Cr1-C3	89.1(2)
O1-Mn1-N6_j	88.57(15)	C1-Cr1-C4	90.4(2)
N5-Mn1-N6	89.74(17)	C1-Cr1-C5	90.9(2)
N2_a-Mn1-N5	93.0(3)	C1-Cr1-C1_j	178.0(3)
N4_c-Mn1-N5	166.5(3)	C2-Cr1-C3	88.1(4)
N5-Mn1-N6_j	89.74(17)	C2-Cr1-C4	175.9(4)
N2_a-Mn1-N6	91.42(14)	C2-Cr1-C5	92.3(4)
N4_c-Mn1-N6	89.92(17)	C1_j-Cr1-C2	89.6(2)
N6-Mn1-N6_j	177.1(2)	C3-Cr1-C4	87.8(4)
N2_a-Mn1-N4_c	100.5(3)	C3-Cr1-C5	179.6(4)
N2_a-Mn1-N6_j	91.42(14)	C1_j-Cr1-C3	89.1(2)
N4_c-Mn1-N6_j	89.92(17)	C4-Cr1-C5	91.8(4)
O2-Mn2-N3	94.7(3)	C1_j-Cr1-C4	90.4(2)
O2-Mn2-N7	90.00	C1_j-Cr1-C5	90.9(2)
O2-Mn2-O2_b	180.00	Mn1-O1-H1A	119(7)
O2-Mn2-N3_b	85.3(3)	O2-Mn2-N7_h	90.00
Mn2-O2-H2A_j	126(6)	N3-Mn2-N7	90.00
Mn2-O2-H2A	126(7)	O2_b-Mn2-N3	85.3(3)
N3-Mn2-N3_b	180.00	Mn1_a-N2-C2	177.8(8)
N3-Mn2-N7_h	90.00	Mn2-N3-C3	170.8(9)

O2_b-Mn2-N7	90.00	Mn1_d-N4-C4	145.5(7)
N3_b-Mn2-N7	90.00	Mn1-N5-C5	173.0(8)
N7-Mn2-N7_h	180.00	Mn1-N6-C6	122.4(5)
O2_b-Mn2-N3_b	94.7(3)	C6-N6-C10	117.7(6)
Mn1-N6-C10	119.9(5)	Mn2-N7-C11	122.6(6)
Mn2-N7-C11_b	122.6(6)	C10-C9-H9	120.00
Cr1-C1-N1	178.7(7)	N7-C11-H11	118.00
Cr1-C2-N2	177.3(9)	C12-C11-H11	118.00
Cr1-C3-N3	175.6(9)	Cr1-C4-N4	171.8(8)
Cr1-C5-N5	178.8(9)		

a = -x,-y,z; b = 1-x,-y,z; c = -1/2+x,1/2-y,1-z; h = 1-x,-y,1-z; j = x,y,1-z

**Table 4:** Selected bond lengths (Å) in compound 2.

Bonds	Bond length (Å)	Bonds	Bond length (Å)
Mn1-C1	1.882(3)	Mn1-C2	1.887(3)
Mn1-C3	1.917(2)	Mn1-C4	1.892(3)
Mn1-C5	1.877(3)	Mn1-C3_h	1.917(2)
Mn2-O2W	2.259(2)	Mn2-N5	2.185(3)
Mn2-N6	2.270(2)	Mn2-O2W_a	2.259(2)
Mn2-N5_a	2.185(3)	Mn2-N6_f	2.270(2)
Mn3-O1W	2.204(3)	Mn3-N4	2.229(3)
Mn3-N7	2.274(2)	Mn3-N1_c	2.193(3)
Mn3-N2_d	2.148(3)	Mn3-N7_h	2.274(2)

**Table 5:** Selected bond angles (°) in compound 2.

	Angles (°)		Angles (°)
C1-Mn1-C2	90.48(14)	O2W_a-Mn2-N6_f	90.00
C1-Mn1-C3	89.80(7)	N5_a-Mn2-N6_f	90.00
C1-Mn1-C4	92.64(14)	O1W-Mn3-N4	80.93(11)
C1-Mn1-C5	179.31(14)	O1W-Mn3-N7	88.10(6)
C1-Mn1-C3_h	89.80(7)	O1W-Mn3-N1_c	82.02(11)
C2-Mn1-C3	89.84(7)	O1W-Mn3-N2_d	175.52(12)
C2-Mn1-C4	176.88(13)	O1W-Mn3-N7_h	88.10(6)
C2-Mn1-C5	88.83(14)	N4-Mn3-N7	90.48(6)
C2-Mn1-C3_h	89.84(7)	N1_c-Mn3-N4	162.95(11)
C3-Mn1-C4	90.17(7)	N2_d-Mn3-N4	103.56(11)
C3-Mn1-C5	90.20(7)	N4-Mn3-N7_h	90.48(6)
C3-Mn1-C3_h	179.49(11)	N1_c-Mn3-N7	88.96(6)
C4-Mn1-C5	88.05(14)	N2_d-Mn3-N7	91.83(6)
C3_h-Mn1-C4	90.17(7)	N7-Mn3-N7_h	175.89(9)
C3_h-Mn1-C5	90.20(7)	N1_c-Mn3-N2_d	93.50(12)
O2W-Mn2-N5	85.12(10)	N1_c-Mn3-N7_h	88.96(6)
O2W-Mn2-N6	90.00	N2_d-Mn3-N7_h	91.83(6)
O2W-Mn2-O2W_a	180.00	O2W-Mn2-N5_a	94.88(10)
O2W-Mn2-N6_f	90.00	O2W_a-Mn2-N5_a	85.12(10)
N5-Mn2-N6	90.00	Mn2-N6-C6_a	122.26(14)
O2W_a-Mn2-N5	94.88(10)	Mn2-N5-C5	170.2(3)
N5-Mn2-N5_a	180.00	Mn3-N4-C4	148.4(3)
N5-Mn2-N6_f	90.00	O2W_a-Mn2-N6	90.00
N5_a-Mn2-N6	90.00	Mn3_b-N1-C1	177.6(3)
N6-Mn2-N6_f	180.00	Mn3_e-N2-C2	175.9(3)

a = 1-x,1-y,z; c = 1/2+x,1/2-y,2-z; d = 1/2-x,-1/2+y,2-z; f = 1-x,1-y,2-z; h = x,y,2-z

**Table 6:** Selected bond lengths (Å) in compound **2a**.

Bonds	Bond length (Å)	Bonds	Bond length (Å)
Mn1–C1	2.005(11)	Mn1–C2	2.037(10)
Mn1–C3	2.041(8)	Mn1–C4	2.029(12)
Mn1–C5	2.002(12)	Mn1–C3_h	2.041(8)
Mn2–O2W	2.222(11)	Mn2–N5	2.121(12)
Mn2–N6	2.270(9)	Mn2–O2W_a	2.222(11)
Mn2–N5_a	2.121(12)	Mn2–N6_f	2.270(9)
Mn3–N4	2.024(12)	Mn3–N7	2.269(7)
Mn3–N1_c	2.049(11)	Mn3–N2_d	2.037(11)
Mn3–N7_h	2.269(7)		

**Table 7:** Selected bond angles (°) in compound **2a**.

	Angles (°)		Angles (°)
C1–Mn1–C2	93.1(5)	O2W_a–Mn2–N6_f	90.00
C1–Mn1–C3	89.9(3)	N5_a–Mn2–N6_f	90.00
C1–Mn1–C4	91.7(4)	N4–Mn3–N7	89.6(2)
C1–Mn1–C5	177.7(5)	N1_c–Mn3–N4	139.6(5)
C1–Mn1–C3_h	89.9(3)	N2_d–Mn3–N4	115.8(5)
C2–Mn1–C3	89.5(3)	N4–Mn3–N7_h	89.6(2)
C2–Mn1–C4	175.3(5)	N1_c–Mn3–N7	87.2(2)
C2–Mn1–C5	89.2(5)	N2_d–Mn3–N7	94.43(18)
C2–Mn1–C3_h	89.5(3)	N7–Mn3–N7_h	170.5(3)
C3–Mn1–C4	90.6(3)	N1_c–Mn3–N2_d	104.6(5)
C3–Mn1–C5	90.1(3)	N1_c–Mn3–N7_h	87.2(2)
C3–Mn1–C3_h	178.9(4)	N2_d–Mn3–N7_h	94.43(18)
C4–Mn1–C5	86.1(5)	Mn3_b–N1–C1	152.0(10)
C3_h–Mn1–C4	90.6(3)	Mn3_e–N2–C2	168.1(13)
C3_h–Mn1–C5	90.1(3)	Mn1–C2–N2	177.4(12)
O2W–Mn2–N5	86.3(5)	Mn1–C3–N3	174.8(10)
O2W–Mn2–N6	90.00	O2W_a–Mn2–N5_a	86.3(5)
O2W–Mn2–O2W_a	180.00	Mn3–N4–C4	160.3(11)
O2W–Mn2–N5_a	93.7(5)	Mn2–N5–C5	169.9(14)
O2W–Mn2–N6_f	90.00	Mn2–N6–C6	121.7(5)
N5–Mn2–N6	90.00	Mn2–N6–C6_a	121.7(5)
O2W_a–Mn2–N5	93.7(5)	Mn1–C4–N4	170.2(10)
N5–Mn2–N5_a	180.00	Mn3–N7–C13	124.1(6)
N5–Mn2–N6_f	90.00	Mn3–N7–C9	121.4(8)
O2W_a–Mn2–N6	90.00	N5_a–Mn2–N6	90.00
Mn1–C1–N1	179.0(10)	Mn1–C5–N5	175.7(14)
N6–Mn2–N6_f	180.00		

$$a = 1-x, 1-y, z; c = 1/2+x, 1/2-y, 2-z; d = 1/2-x, -1/2+y, 2-z; f = 1-x, 1-y, 2-z; h = x, y, 2-z$$

**Table 8:** Selected bond lengths (Å) in compound **3**.

Bonds	Bond length (Å)	Bonds	Bond length (Å)
Mn1–C1	1.975(4)	Mn1–C2	1.994(7)
Mn1–C1_a	1.975(4)	Mn1–C2_a	1.994(7)
Mn1–C1_c	1.975(4)	Mn1–C1_e	1.975(4)
Mn2–N1	2.108(3)	Mn2–N3	2.317(6)
Mn2–N4	2.139(5)	Mn2–C9	2.139(5)
Mn2–N1_f	2.108(3)	Mn2–N2_g	2.185(6)

**Table 9:** Selected bond angles (°) in compound **3**.

	Angles (°)		Angles (°)
C1-Mn1-C2	90.45(18)	N1_f-Mn2-C9	125.06(9)
C1-Mn1-C1_a	91.04(15)	N2_g-Mn2-C9	91.36(19)
C1-Mn1-C2_a	89.55(18)	N1_f-Mn2-N2_g	92.84(13)
C1-Mn1-C1_c	180.00	Mn2-N1-C1	168.5(3)
C1-Mn1-C1_e	88.97(15)	Mn2_h-N2-C2	171.5(5)
C1_a-Mn1-C2	89.55(18)	Mn2-N3-C4	124.7(5)
C2-Mn1-C2_a	180.00	Mn2-N3-C8	119.7(4)
C1_c-Mn1-C2	89.55(18)	C1_e-Mn1-C2	90.45(18)
Mn1-C1-N1	178.7(3)	C1_a-Mn1-C2_a	90.45(18)
Mn1-C2-N2	178.3(6)	C1_a-Mn1-C1_c	88.97(15)
C1_a-Mn1-C1_e	180.00	C1_c-Mn1-C2_a	90.45(18)
C1_e-Mn1-C2_a	89.55(18)	C1_c-Mn1-C1_e	91.04(15)
N1-Mn2-N3	87.14(13)	N1-Mn2-N4	125.06(9)
N1-Mn2-C9	125.06(9)	N1-Mn2-N1_f	109.40(14)
N1-Mn2-N2_g	92.84(13)	N3-Mn2-N4	88.68(19)
N3-Mn2-C9	88.68(19)	N1_f-Mn2-N3	87.14(13)
N1_f-Mn2-N4	125.06(9)	N2_g-Mn2-N4	91.36(19)

a = -x,y,-z; b = 1-x,y,1-z; c = -x,-y,-z; d = 1-x,1-y,1-z; e = x,-y,z; f = x,1-y,z; g = -1/2+x,1/2+y,z; h = 1/2+x,-1/2+y,z

### 3A.2.5: Adsorption Study

N<sub>2</sub> (77 K), H<sub>2</sub> (77 K), CO<sub>2</sub> (195 K, 273 and 283 K), C<sub>2</sub>H<sub>2</sub> (273 and 283 K), C<sub>2</sub>H<sub>4</sub> (273 and 283 K) and C<sub>2</sub>H<sub>6</sub> (273 and 283 K) adsorption studies were carried out with the deguest samples of **1** and **2** by using an AUTOSORB IQ2 instrument. High-pressure hydrogen adsorption isotherm measurements at 77 and 87 K were carried out on a fully computer controlled volumetric BELSORP-HP, BEL JAPAN high pressure instrument. Dead volume of the samples cell were measured using helium gas of 99.999% purity. The gases used for the high pressure measurements were of scientific/research grade with 99.999% purity. For the high pressure measurements, approximately 200 mg of sample was taken in a stainless-steel sample holder and degassed at 438 K for about 72 hours. Non-ideal correction for hydrogen gas was made by applying virial coefficients at the measurement temperature. Due to the very less uptake capacity of C<sub>2</sub>H<sub>4</sub> and C<sub>2</sub>H<sub>6</sub> at 273 and 283 K, around 350 mg of sample was used for the adsorption measurement which gives good virial and Langmuir-Freundlich fitting over the uptake isotherms.

### 3A.3: Results and Discussion

#### 3A.3.1 Structural description of ([Mn<sub>3</sub>(bipy)<sub>3</sub>(H<sub>2</sub>O)<sub>4</sub>][Cr(CN)<sub>6</sub>]<sub>2</sub>·2(bipy)·4H<sub>2</sub>O)<sub>n</sub>(**1**):

Single crystal structure determination study reveals that **1** is a neutral 3D coordination

architecture of  $\text{Mn}^{\text{II}}$  built by  $[\text{Cr}(\text{CN})_6]^{3-}$  and bipy with the formulation  $\{[\text{Mn}_3(\text{bipy})_3(\text{H}_2\text{O})_4][\text{Cr}(\text{CN})_6]_2 \cdot 2(\text{bipy}) \cdot 3(\text{H}_2\text{O})\}_n$ . There are two crystallographically independent Mn (Mn1 and Mn2) atoms in the asymmetric unit and each octahedral Mn1 is coordinated to three CN groups from three different  $[\text{Cr}(\text{CN})_6]^{3-}$ , one water molecule (O1) and two bipy, whereas each octahedral Mn2 is coordinated two CN groups, two bipy and two water molecules (O2, O2\*) (Figure 4a).

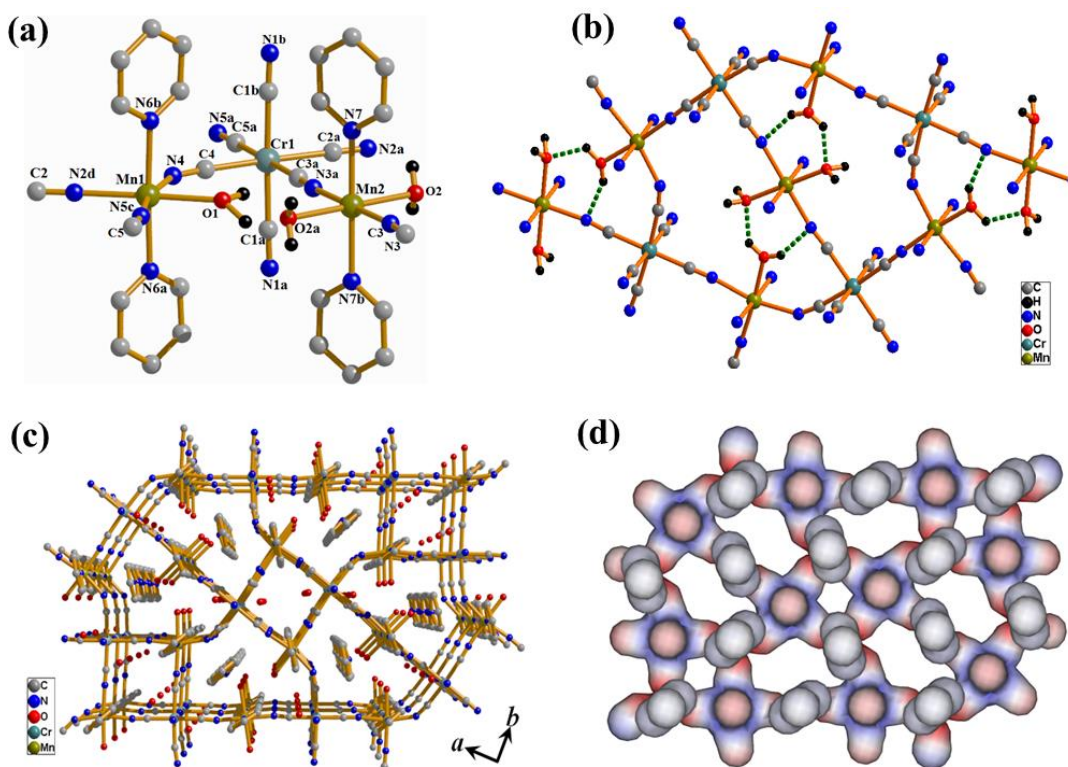


**Figure 4:** (a) View of coordination environment around Mn1, Mn2 and Cr1 in **1**. Symmetry codes: a = 2-x, 1-y, z; b = 2-x, 1-y, 1-z; c = 2.5-x, 0.5-y, 1-z; d = -0.5+x, 1.5-y, 1-z. (b) In the 2D layer, coordinated water molecules are involved in H-bonding with each other and also with the CN groups. (c) 3D view of compound **1** along *c* direction shows two different type of channels; one square occupied by water molecules and the other distorted triangular occupied by coordinated water and guest bipy molecules. (d) View of two different kind of channels in **1** along *c* direction.

Both Mn1 and Mn2 are slightly distorted from the perfect octahedron as reflected in the *cisoid* angles (83.52–89.97) $^\circ$  for Mn1 and (90.00–94.58) $^\circ$  for Mn2. The Mn–N and Mn–O bond distances are in the range of 2.1854–2.2755 Å and 2.2125–2.2694 Å, respectively. In the 2D layers (Figure 4b), the twelve-membered  $\text{Mn}_2\text{Cr}_2(\text{CN})_4$  ring surrounded by six eighteen-membered  $\text{Mn}_3\text{Mn}_2\text{Cr}_3(\text{CN})_{12}$  rings and each 2D layer connected by the bipy linker through the  $\text{Mn}^{\text{II}}$  centres forms a 3D pillared-layer network with two kind of

channels along the  $c$ -axis (Figure 4c). Examination with TOPOS<sup>23</sup> reveals that **1** is a tri-nodal (4- $c$ )3(5- $c$ )2-periodic 3D net formed by 5-connected (5- $c$ ) Mn- nodes, 4- $c$  Cr-nodes and 2- $c$  bipy and CN linkers. In a layer, the vertex symbol for Mn1, Mn2 and Cr1 points are represented by Schläfli symbols,  $\{4.6^8.8\}$ ,  $\{6^5.8\}$  and  $\{4.6^5\}$ , respectively. Further examination shows that **1** adopts an unprecedented network topology with the Schläfli symbol  $\{4.6^5\}_2\{4.6^8.8\}_2\{6^5.8\}$ . The square-shaped smaller channel ( $2.8 \times 2.2 \text{ \AA}^2$ ) contains

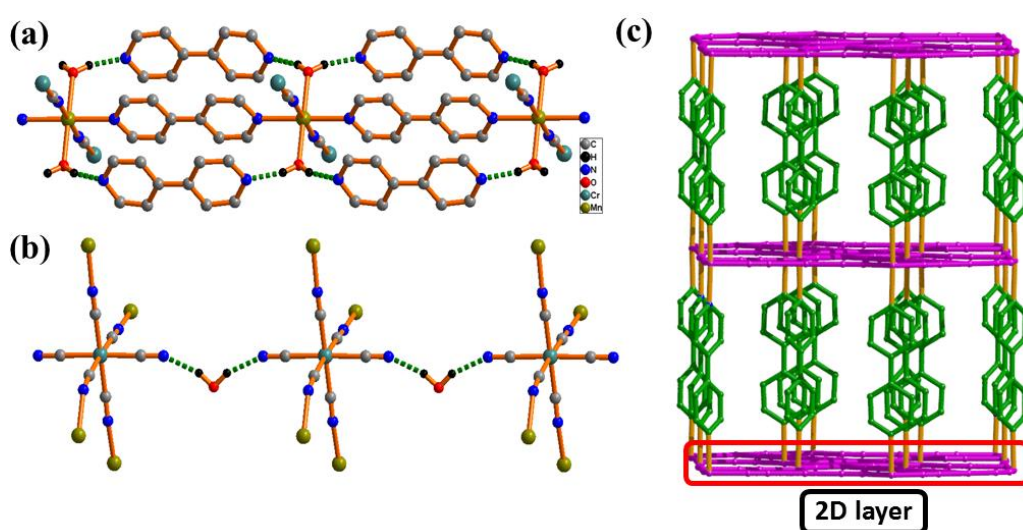


**Figure 5:** The supramolecular interaction in **1**; (a) Two Mn2 centres interact via hydrogen bonding of coordinated H<sub>2</sub>O and guest bipy molecule, (b) Two neighbouring Cr1 centres interact via N-H...O hydrogen bonding of coordinated CN and guest H<sub>2</sub>O molecule, (c) Pillared-layer structure of **1**. The layers formed by  $[\text{Cr}(\text{CN})_6]^{3-}$  and Mn<sup>II</sup> are shown in pink colour and the pillars (bipy) are shown in green colour.

two water molecules and the large channel ( $7.7 \times 5.5 \text{ \AA}^2$ ) contains one water and bipy molecule as guests, both of which providing about 34% void spaces to the total crystal volume (Figures 4c and d). Thus, **1** acts as a biporous host. Upon removal of the coordinated water molecules, framework shows 40.3% void space to the total volume with coordinatively unsaturated Mn<sup>II</sup> centers on the pore surface. The guest bipy undergoes strong face to face and edge to face  $\pi \cdots \pi$  interactions with two different coordinated bipy (cg...cg distances are in the range of 3.689–5.210 Å) linkers connected to Mn1 and Mn2 centres (Figure 5a). The guest water molecule O3 is making a bridge between the two layers through N1 of the pendant CN group (N1...O3, 2.944 Å) (Figure 5b). In the 3D network, separation between the layers through Mn<sup>II</sup>–bipy–Mn<sup>II</sup> is 11.628 Å while in the 2D layer, the Mn1–Cr1 and Mn2–Cr1 distances are 5.230 Å and 5.240 Å, respectively (Figure 5c).

**3A.3.2: Structural description of  $\{[\text{Mn}_3(\text{bipy})_3(\text{H}_2\text{O})_4][\text{Mn}(\text{CN})_6]_2 \cdot 2(\text{bipy}) \cdot 4\text{H}_2\text{O}\}_n$  (2):** Single crystal structure determination reveals that compound **2** is isostructural with compound **1** (Figures 6). Here  $[\text{Cr}(\text{CN})_6]^{3-}$  has been replaced with  $[\text{Mn}(\text{CN})_6]^{3-}$ . Briefly, the Mn–N and Mn–O bond distances are in the range of 2.220–2.983 Å and 2.079–2.186 Å respectively. The nitrogen ends of four equatorial cyanide ligands connects  $\text{Mn}^{\text{II}}$  centers to form a 2D layer in the  $bc$  plane and each 2D layer is connected by the bipy linker through the  $\text{Mn}^{\text{II}}$  centers forming a 3D pillared-layer framework with two kind of channels along the  $c$ -axis (Figures 6b and c).

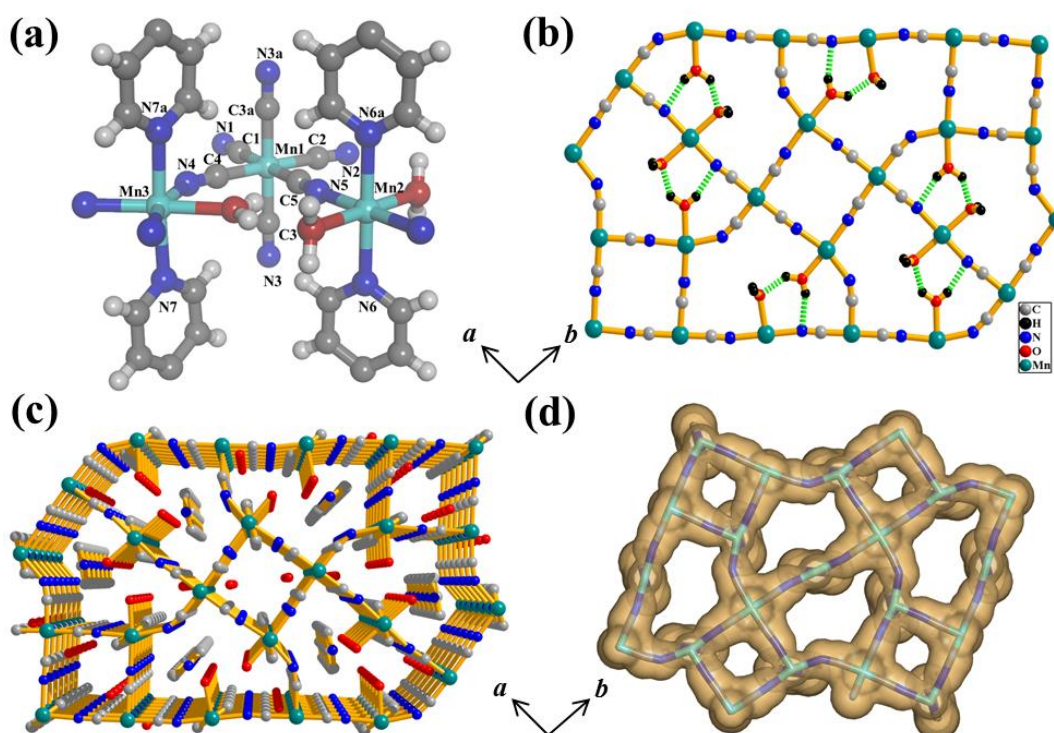


**Figure 6:** (a) Asymmetric unit of compound **2**; (b) 2D magnetic layer formed by connection between  $\text{Mn}^{\text{II}}$  and  $\text{Mn}^{\text{III}}$  centers through the equatorial cyanide ligands of  $[\text{Mn}(\text{CN})_6]^{3-}$  moiety; (c) View of the 3D supramolecular framework of compound **2** along  $c$  direction. (d) After the removal of guest *bpee*, water and coordinated water molecules, two types of 1D channel present in compound **2**.

After the removal of the guest bipy molecules, rectangular-shaped voids (diameter  $5.5 \times 4.0 \text{ \AA}^2$ ) are observed along  $c$  direction (Figure 6d). Upon removal of the coordinated water and guest (water, bipy) molecules framework shows 37.9% void space to the total volume with coordinatively unsaturated  $\text{Mn}^{\text{II}}$  centers on the pore surface. In the 3D network, separation between the layers through  $\text{Mn}^{\text{II}}\text{-bipy-Mn}^{\text{II}}$  is 11.628 Å while in the 2D layer, the Mn1–Mn1 and Mn2–Mn1 distances are 5.044 Å and 5.143 Å, respectively.



**3A.3.3: Structural description of  $\{[\text{Mn}_3(\text{bipy})_3(\text{H}_2\text{O})_2][\text{Mn}(\text{CN})_6]_2 \cdot 2(\text{bipy}) \cdot 2\text{H}_2\text{O}\}_n$  (2a) (Single-crystal-to-single-crystal-transformation):** The single crystal of Compound **2** was heated at 150 °C at the goniometer of the single crystal X-ray diffractometer to yields compound **2a** where it loses four out of eight water molecules. The transparency of compound **2** was lost after heating. Compound **2a** retains the orthorhombic system and *Pbam* space group after the partial dehydration procedure. The structure determination of compound **2a** reveals that after dehydration, the same framework structure was intact as that of compound **2** with a slight change in the cell

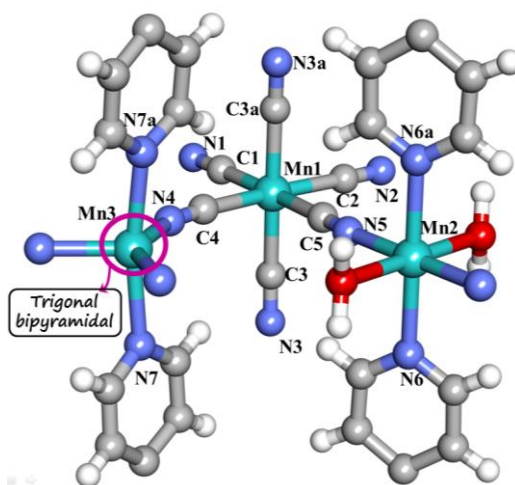


**Figure 7:** Asymmetric unit of compound **2a**. After removing the coordinated water molecule, the geometry of the Mn3 center has converted from octahedral to trigonal bipyramidal.

parameter (Table 1). It is worth noticing that, in compound **2a**, one coordinated water molecule (from Mn3) and one guest water molecule have been removed whereas another guest water (O3w) remains intact in the structure (Figures 7 and 8). This can be attributed to the strong hydrogen bonding operating between O3w and two pendent cyanide from the  $[\text{Mn}(\text{CN})_6]^{3-}$  moiety. Now the geometry of the Mn3 center in **2a** has been changed to trigonal bipyramidal from octahedral geometry in compound **2** (Figure 7). The average Mn–C bond distance in  $[\text{Mn}(\text{CN})_6]^{3-}$  moiety (2.002(12) – 2.041(8) Å) are shorter than those in compound **2** (1.882(3) – 1.917(2) Å) whereas the Mn–N bond lengths lies in the range of 2.222(11) to 2.270(9) Å. Further structural analysis reveals that, after dehydration, the Mn–N bond length of Mn3 center has been decreased from (2.148(5)-2.193(3) Å to 2.024(11)-2.049(11) Å) due to the geometry change of the metal center.

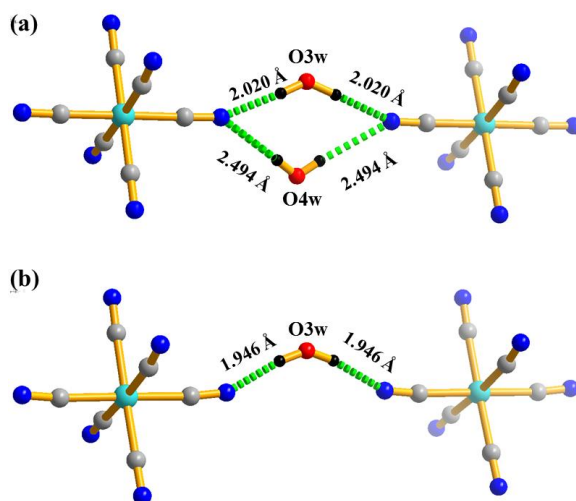


**Figure 8:** (a) View of the H- bonding interaction between pendent cyanide and guest water molecules in compound **2**. (b) View of the H- bonding interaction between pendent cyanide and guest water molecule in compound **2a**. During single-crystal-to-single-crystal transformation (*i.e.* **2**→**2a**) the loosely bounded water molecule (O4w) has been removed while the strongly bounded water molecule (O3w) is still present in the structure.

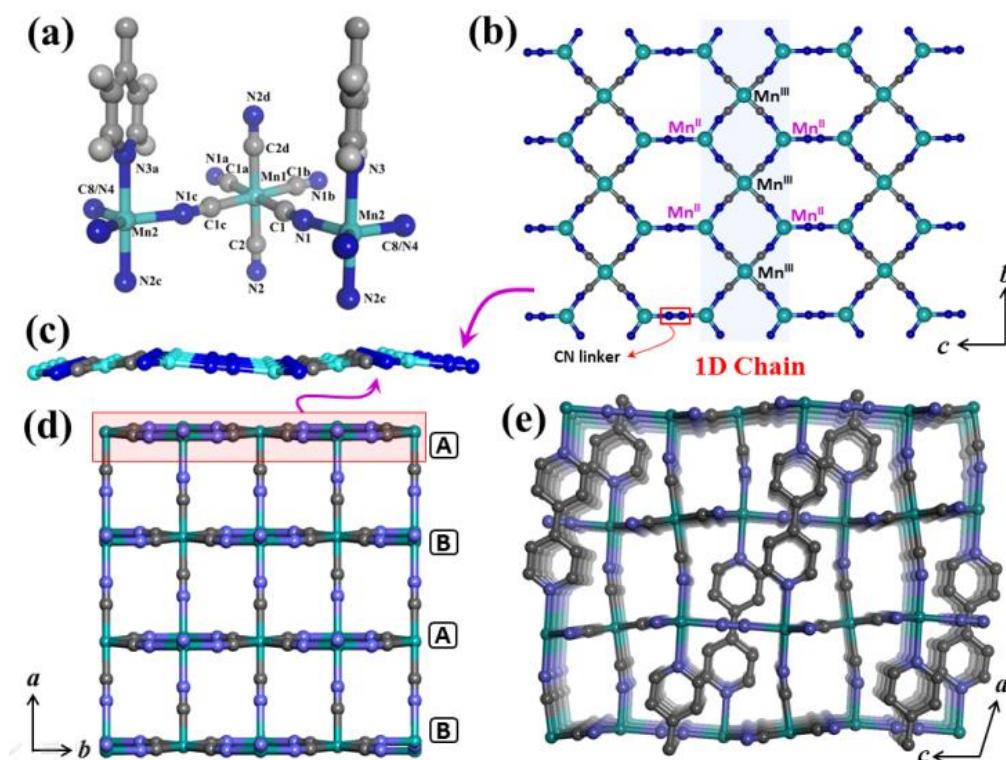


**Figure 9:** (a) Asymmetric unit of compound **3**; (b) connection between the Mn<sup>III</sup> and Mn<sup>II</sup> centers through cyanide bridges generates the 2D sheet along the *bc* plane. (c) View of the 2D sheet long the *c* direction (d) Arrangement of the 2D sheet in AB-AB fashion along the *a* direction. (e) View of the 3D architecture of compound **3**.

**3A.3.4: Structural description of  $\{[\text{Mn}_2(\text{bipy})(\text{CN})][\text{Mn}(\text{CN})_6]\}_n$  (**3**):** Compound **3** crystallizes in monoclinic *C2/m* space group and single-crystal structure determination

reveals a neutral 3D coordination framework of  $\text{Mn}^{\text{II}}$  bridged by  $[\text{Mn}(\text{CN})_6]^{3-}$  and bipy with the formulation of  $\{[\text{Mn}_2(\text{bipy})(\text{CN})][\text{Mn}(\text{CN})_6]\}_n$  (Figure 9a). Each  $\text{Mn}^{\text{III}}$  atoms in the  $[\text{Mn}(\text{CN})_6]^{3-}$  unit locates itself in a slightly distorted octahedral geometry and connected with six crystallographically identical  $\text{Mn}^{\text{II}}$  centers through cyanide linker. Connection between the  $\text{Mn}^{\text{III}}$  and  $\text{Mn}^{\text{II}}$  centers through four equatorial cyanide bridges ( $\text{Mn}^{\text{III}}\text{-Mn}^{\text{II}}$  distance is 5.205 Å) generates a 1D chain along the  $b$  axis (Figure 9b). These 1D chains further connect with each other by free cyanide ligand through the  $\text{Mn}^{\text{II}}$  centers and thus generate a 2D sheet along the crystallographic  $bc$  plane (Figures 9b and c). The actual position of the carbon and nitrogen atoms of the above maintained free cyanide ligand was not determined separately and hence they were assigned by providing equal contribution at both side. The arrangement of 2D sheets along  $a$  direction is in ABAB fashion where one sheet (A) is connected with its next neighbour (B) through the  $\text{Mn}^{\text{III}}\text{-CN(axial)}\text{-Mn}^{\text{II}}$  linkage (average distance  $\sim 5.326$  Å) and thus form a 3D architecture of compound **3** (Figure 9d). The 3D structure is also supported by the bipy linkers which connects two consecutive AA (or BB) layer by satisfying the fifth coordination of each  $\text{Mn}^{\text{II}}$  centers ( $\text{Mn}^{\text{II}}\text{-Mn}^{\text{II}} = 11.724$  Å) (Figure 9e). Such binding of  $[\text{Mn}(\text{CN})_6]^{3-}$  and bipy with  $\text{Mn}^{\text{II}}$  results in a highly condensed nonporous structure. Examination with TOPOS<sup>27</sup> reveals that **3** is a two-nodal (5-c)2(6-c)-periodic 3D net formed by 5-connected (5-c)  $\text{Mn}^{\text{II}}$ -nodes, (6-c)  $\text{Mn}^{\text{III}}$ -nodes. In a layer, the vertex symbol for Mn1 and Mn2 points are represented by Schläfli symbols,  $\{4^6.6^7.8^2\}$  and  $\{4^3.6^7\}$  respectively. Further examination shows that **2** adopts a topology with a Schläfli symbol  $\{4^3.6^7\}_2\{4^6.6^7.8^2\}$ .

### 3A.3.5: Framework stability: Thermogravimetric (TG) and PXRD analysis

Thermal studies were carried out to analyse the stability and integrity of the frameworks. TG analysis of compound **1** (Figure 10(1)) under nitrogen flow suggests two-step release of guest and coordinated water molecules (obs. 9.1 %; calc. 9.55 %) in the temperature range 40 – 180 °C. However, when **1** is heated at 165 °C under high vacuum (to prepare **1a**) we observed loss of guest bipy together with guest and coordinated water molecules. This was confirmed by IR spectroscopy and elemental analysis. The TGA profile of compound **2** (Figure 10(2)) indicates a weight loss of 4.1% at 150 °C, which corroborates the removal of four guest water molecules (cal. 5.3%).

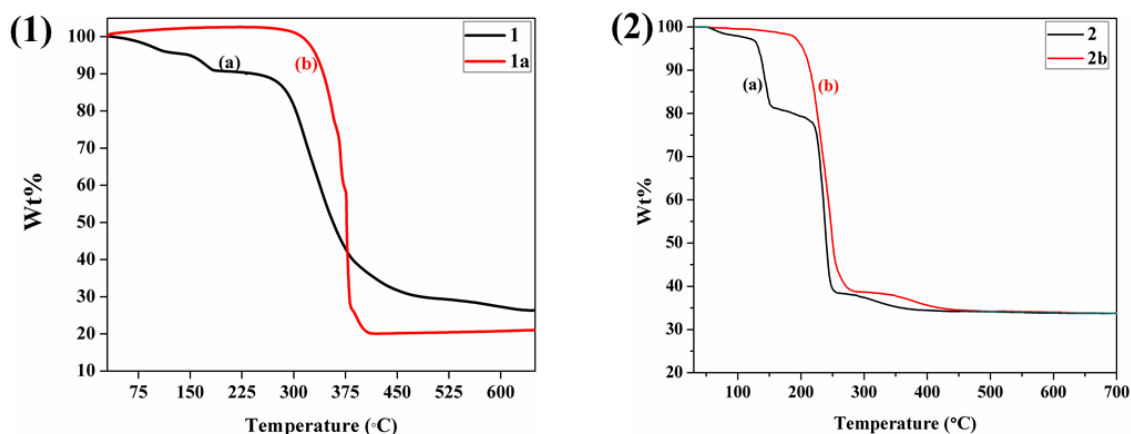


**Figure 10:** (1) TGA of **1** (black) and **1a** (red) recorded under  $N_2$  atmosphere in the temperature range 30 – 650 °C. (2) TGA plots of compounds **2** (black) and **2b** (red) over the temperature range 30 – 700 °C under nitrogen atmosphere.

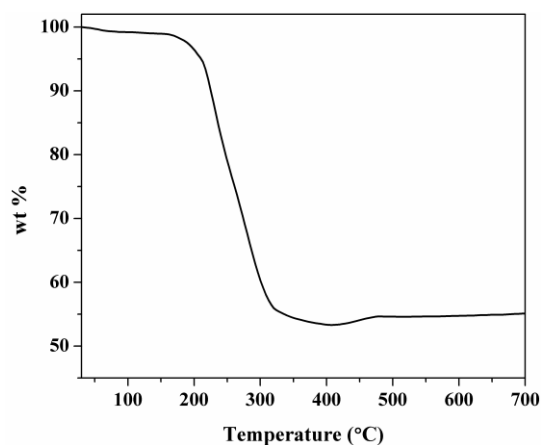


**Figure 11:** TGA plots of compound **3** over the temperature range 30 to 700 °C under nitrogen atmosphere.

The second step was observed at 215 °C with a weight loss of 24.8%, indicating the removal of all guest bipy and coordinated water molecules (cal. 28.3%). The desolvated framework is stable up to 260 °C. Compound **3** does not show any step in the TGA profile (Figure 11) and gradually loses weight with increasing temperature.

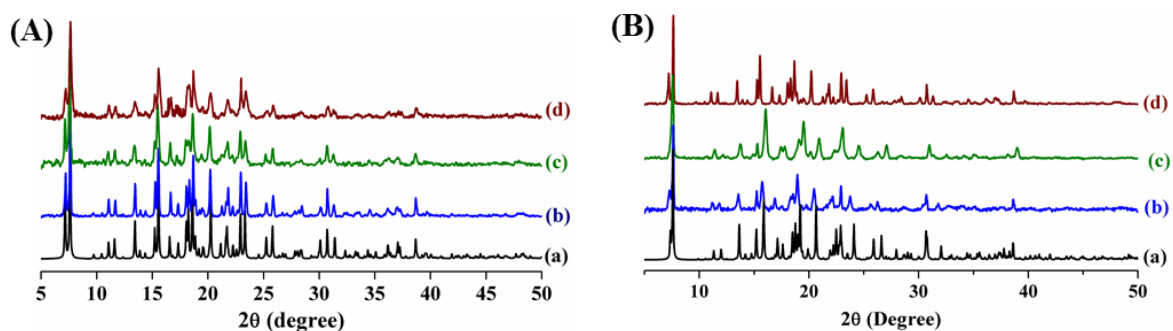


**Figure 12:** PXRD plot of **1** (A) and **2** (B) at different states: (a) simulated; (b) as-synthesized; (c) heated at 165 °C under vacuum for 72 hrs and (d) rehydrated.

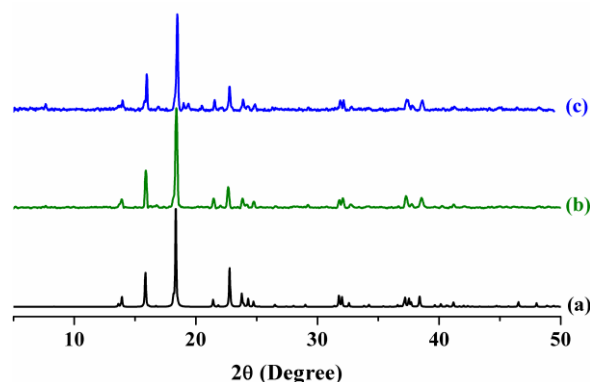


**Figure 13:** PXRD patterns of compound **3** in different states: (a) simulated, (b) as-synthesized, (c) compound **3** treated with the boiling water for 24 h.

The PXRD patterns of compounds **1–3** are shown in Figures 12–13. Good correspondence of the different peak positions in the simulated and as-synthesized patterns suggests the phase purity of the as-synthesized compounds. Powder X-ray diffraction (PXRD) patterns of **1a** and **2b** were recorded after heating the sample under vacuum at 165 °C and 150 °C respectively. The patterns suggest that the 3D framework structures remain intact even after the removal of water (guest and coordinated) and guest bipy molecules (Figure 12).

### 3A.3.6: Adsorption measurement

**3A.3.6.1 Gas adsorption study:** Removal of guest bipy and water (guest and coordinated) molecules offers two types of 1D channels which encouraged us to study the permanent porosity and storage capacity of compound **1a** and **2b**. N<sub>2</sub> adsorption at 77 K reveals a type II profile indicating only surface adsorption (Figure 14a).

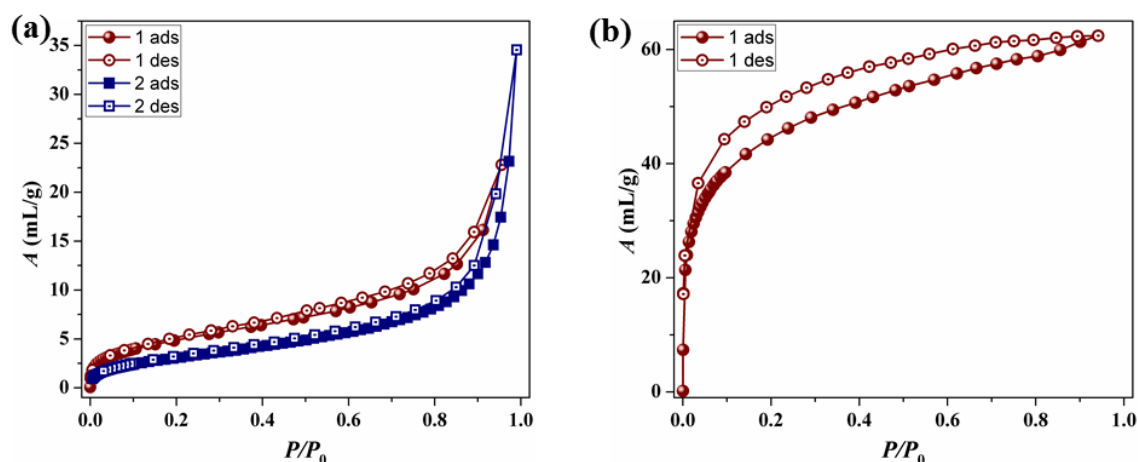


**Figure 14:** (a) N<sub>2</sub> adsorption isotherm of **1a** and **2b** at 77 K. (b) CO<sub>2</sub> adsorption isotherm of **1a** at 195 K. ( $P_0=760$  mm of Hg).

The final uptake amounts were turned out to be 23 mL/g and 35 mL/g for **1a** and **2b** respectively.

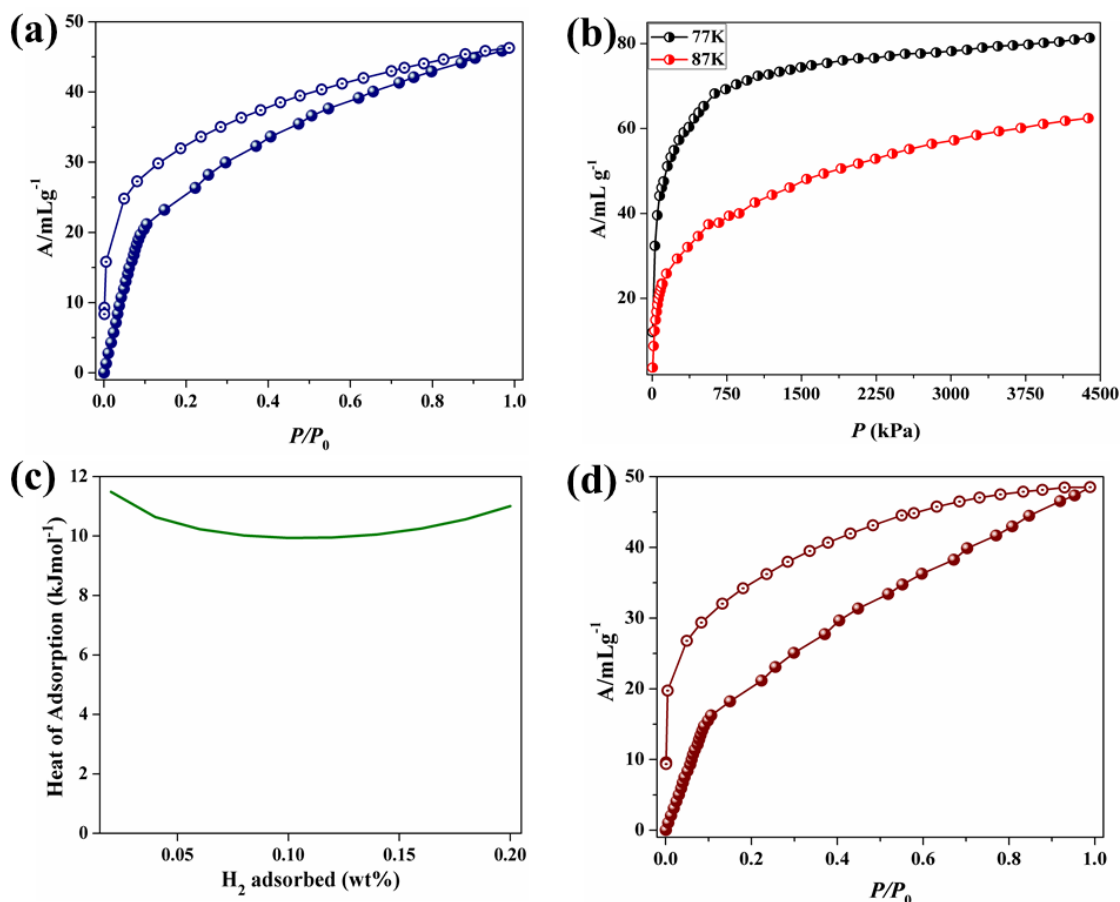


**Figure 15:** (a) H<sub>2</sub> adsorption isotherm of **1a** at 77 K (b) High pressure H<sub>2</sub> isotherm (only adsorption) of **1a** measured at 77 K (black) and 87 K (Red). (c) Enthalpy of H<sub>2</sub> adsorption for **1a** calculated using Clausius-Clapeyron equation. (d) H<sub>2</sub> adsorption isotherm of **2b** at 77 K ( $P_0 = 760$  mm of Hg).

Compound **1a** was tested for its H<sub>2</sub>-storage capacity at cryogenic temperature. High pressure adsorption measurement at 77 K reveals a type I profile with steep uptake at low pressure and the final uptake volume is  $\sim 81 \text{ mLg}^{-1}$  at  $\sim 45$  bar. Interestingly, a careful measurement at 77 K and low pressure ( $P \sim 1$  atm) (Figure 15a) shows a prominent hysteresis in the adsorption profile suggesting strong interaction of H<sub>2</sub> molecules with the pore surface. The high pressure profiles measured at 77 and 87 K (Figure 15b) were used for the calculation of enthalpy of adsorption ( $\Delta H_{ads}$ ) applying Clausius-Clapeyron equation which provides a value of  $\sim 11.5 \text{ kJmol}^{-1}$  (Figure 15c).<sup>10a</sup> The high value of  $\Delta H_{ads}$  can be linked to the highly polar nature of **1a** decorated with cyanide groups (free as well as coordinated) and unsaturated Mn<sup>II</sup> sites (Mn1 and Mn2) which bind H<sub>2</sub> molecules strongly in the pore. This is also in line with

the hysteresis obtained from the low pressure measurement. It is noteworthy that the value of  $\Delta H_{ads}$  obtained for **1a** is one of the highest among the reported values.<sup>10</sup> We have also tested the hydrogen storage capacity at 77 K (up to 1 bar) of compound **2b** which shows an uptake amount of 49 mL/g at saturation (Figure 15d).

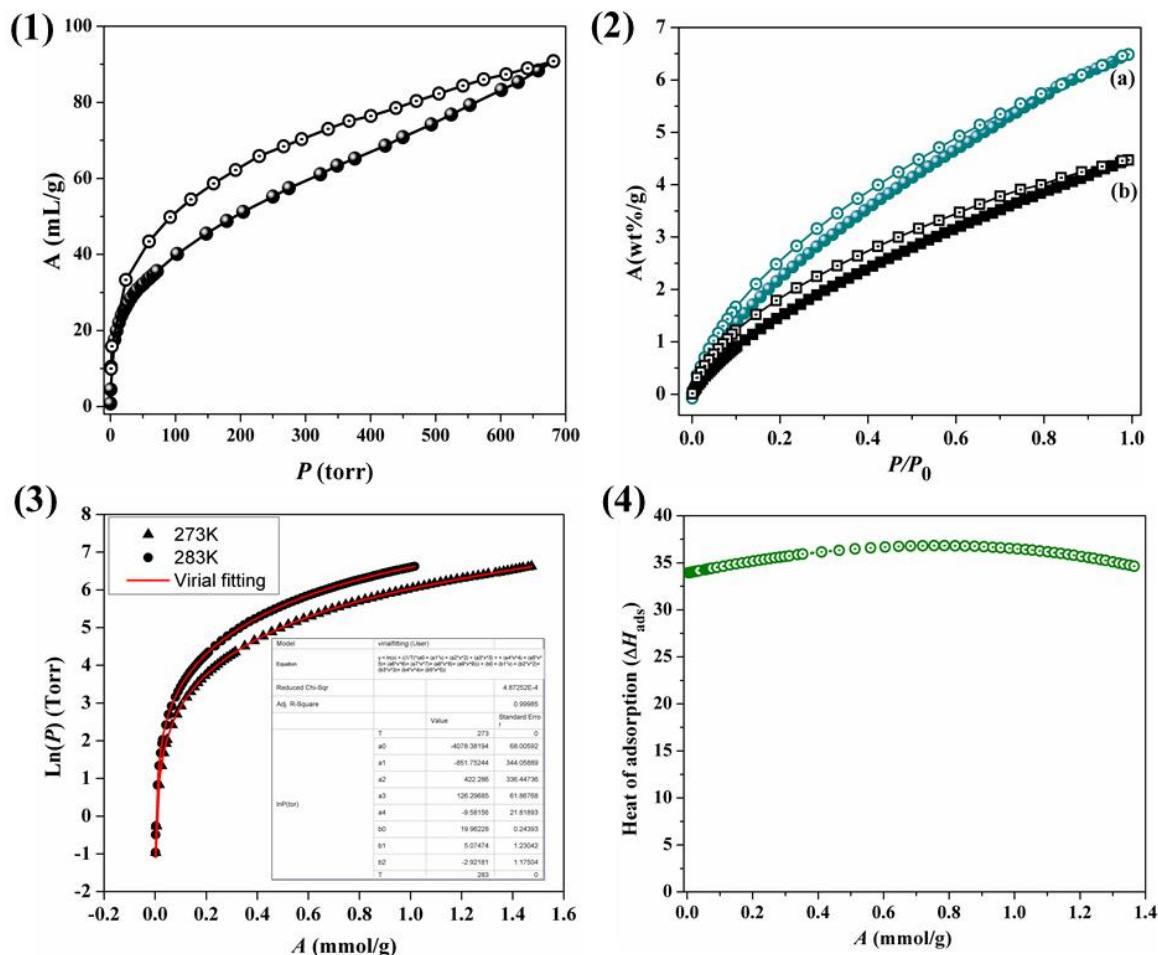


**Figure 16:** (1) CO<sub>2</sub> adsorption isotherm of compound **2b** (black circle) at 195K. (2) CO<sub>2</sub> adsorption isotherm of **2b** measured at 273 K (a) and 283 K (b). (3) CO<sub>2</sub> isotherms for activated compound **2b** measured at 273 K (triangle) and 283 K (circle). Fitted curves (red solid lines), obtained from the virial-type expansion, were used for the  $Q_{st}$  estimation. (4) Change of enthalpy of adsorption for CO<sub>2</sub> with the increase of loading for **2b** calculated based on adsorption at 273 and 283 K by using the virial equation. ( $P_0=760$  mm of Hg)

CO<sub>2</sub> adsorption measurements of compounds **1a** and **2b** at 195 K show a typical type I profile with steep uptake at low pressure regions (Figure 14b and 16(1)). The final uptake amounts were assessed to be 63 mLg<sup>-1</sup> and 82 mLg<sup>-1</sup> at saturation. The Langmuir surface area calculated from CO<sub>2</sub> profiles, turns out to be 353 m<sup>2</sup>g<sup>-1</sup> and 362 m<sup>2</sup>g<sup>-1</sup> for compound **1a** and **2b** respectively. The hysteretic sorption and large isosteric heat of adsorption, ( $q_{st}$  value of ~34.3 and ~36.1 kJ/mol for **1a** and **2b** respectively; calculated using Dubinin-Radushkevich equation<sup>12</sup>) suggest strong

interaction of CO<sub>2</sub> molecules with deguest frameworks of **1** and **2**. This could be correlated with the well established fact where the electric field generated in the framework by UMSs and aromatic  $\pi$ -cloud interacts firmly with the quadrupole moment of CO<sub>2</sub> ( $-1.4 \times 10^{-39}$  Cm<sup>2</sup>) causing rapid uptake at low pressure. We have also tested the CO<sub>2</sub> storage capacity of compound **2b** at 273 and 283 K. The CO<sub>2</sub> adsorption uptake of **2b** was assessed to be 33 mL/g (7 wt%) and 23 mL/g (4 wt%) at 760 torr respectively at 273 and 283 K (Figure 16b). We have performed a further study over the CO<sub>2</sub>-MOF interaction through estimating the zero coverage isotheric heat of adsorption ( $Q_{st}$ ). We have calculated the zero coverage isotheric heat of adsorption by employing a virial type equation on adsorption data collected at 273 and 283K (Figure 16c). As shown in the Figure 16d, the zero coverage isotheric heat of adsorption of compound **2b** was turned out to be 34 kJmol<sup>-1</sup> which is comparable with other reported compounds having unsaturated metal sites (UMSs).<sup>13</sup> Interestingly, the observed  $Q_{st}$  value is increasing with increase in loading which may be attributed to the filling of different adsorption sites at higher pressure or the CO<sub>2</sub>-CO<sub>2</sub> cooperative interactions.

The window size ( $5.5 \times 4.0$  Å<sup>2</sup>) of the 1D channel present in compound **2b** further encouraged us to probe the adsorption property of C<sub>2</sub> hydrocarbons having the similar kinetic diameter to the pore size (C<sub>2</sub>H<sub>2</sub> = 3.3 Å, C<sub>2</sub>H<sub>4</sub> = 4.2 Å and C<sub>2</sub>H<sub>6</sub> = 4.5 Å).<sup>22</sup> The low pressure single component C<sub>2</sub>H<sub>2</sub>, C<sub>2</sub>H<sub>4</sub> and C<sub>2</sub>H<sub>6</sub> isotherms were examined accordingly at two different temperatures of 273 and 283K. As shown in figure 17a, at 273 K, compound **2b** adsorbs 26 mL/g of C<sub>2</sub>H<sub>2</sub> whereas a very less amount of uptake of C<sub>2</sub>H<sub>4</sub> (5.5 mL/g) and C<sub>2</sub>H<sub>6</sub> (4.5 mL/g) were recorded at the saturation. The higher acetylene adsorption capacity in comparison with the other C<sub>2</sub> hydrocarbons indicates that compound **2b** is a very attractive material for the selective adsorptive based separation of acetylene from the three gas mixture.

Based on the IAST (Ideal Adsorbed Solution Theory), we have determined the selectivity of the binary gas mixture of C<sub>2</sub>H<sub>2</sub>/C<sub>2</sub>H<sub>4</sub> and C<sub>2</sub>H<sub>2</sub>/C<sub>2</sub>H<sub>6</sub>. We have used Langmuir-Freundlich equation to obtain a perfect fit over the single component isotherms and the obtained precise fitting parameters were employed to accurately perform the necessary integrations. The IAST predicted binary gas mixture selectivity of C<sub>2</sub>H<sub>2</sub> over C<sub>2</sub>H<sub>4</sub> and C<sub>2</sub>H<sub>6</sub> are 10 and 64 respectively at zero coverage regions (Figures 17c and d) which are comparable with other reported literature.<sup>23</sup> The values suggest that



compound **2** may have potential application in the separation of C<sub>2</sub>H<sub>2</sub> from a binary C<sub>2</sub>H<sub>2</sub>/C<sub>2</sub>H<sub>4</sub> and C<sub>2</sub>H<sub>2</sub>/C<sub>2</sub>H<sub>6</sub> mixture.

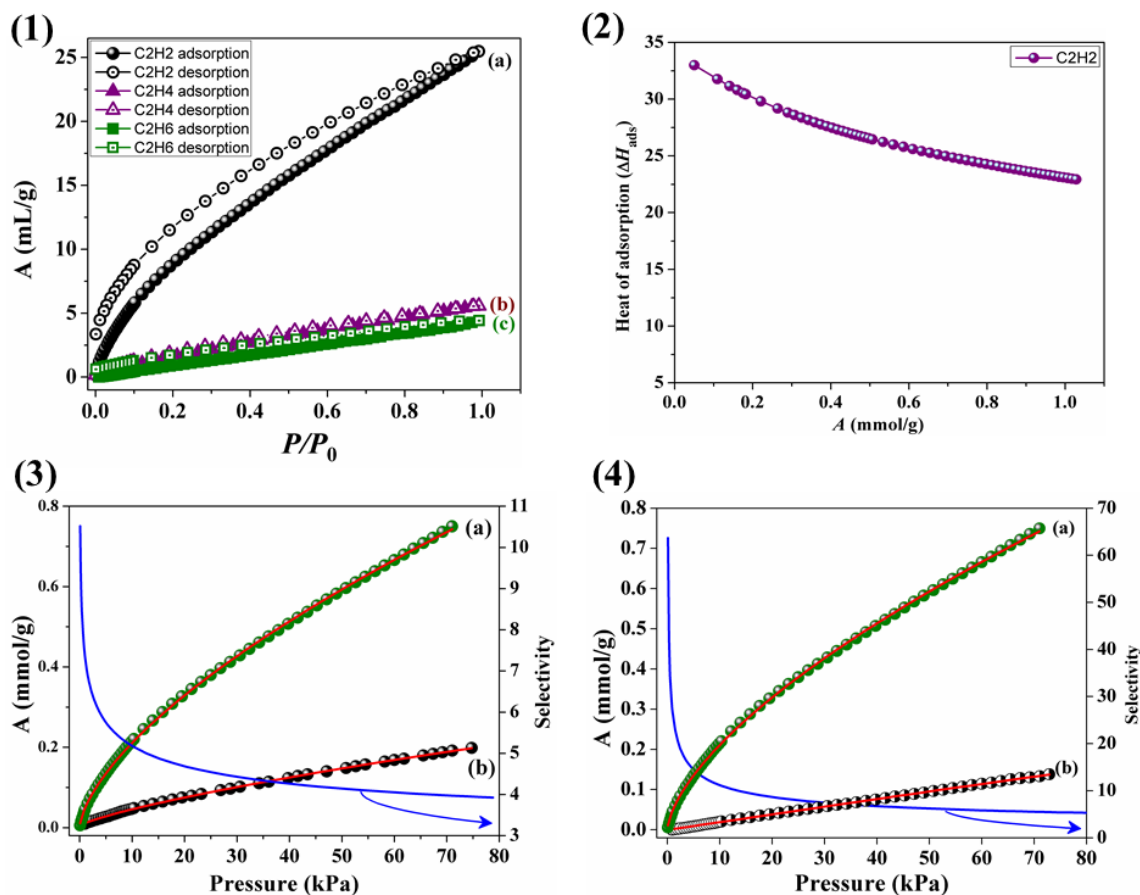


**Figure 17:** (1) C<sub>2</sub>H<sub>2</sub>, C<sub>2</sub>H<sub>4</sub> and C<sub>2</sub>H<sub>6</sub> adsorption isotherms of compound **2b** measured at 273 K. Closed symbols represents adsorption and open symbols represents desorption curves. (2) Change of enthalpy of adsorption for C<sub>2</sub>H<sub>2</sub> with the increase of loading for **2b** (calculation based on adsorption at 273 and 283 K by using the virial equation (1<sup>st</sup> type)). C<sub>2</sub>H<sub>2</sub> (a) vs. C<sub>2</sub>H<sub>4</sub> (b) in plot (3) and C<sub>2</sub>H<sub>2</sub> (a) vs. C<sub>2</sub>H<sub>6</sub> (b) in plot (4) adsorption selectivity of compound **2b** measured at 273 K. Red curves represent the Langmuir–Freundlich fitting over the adsorption isotherms whereas the blue curves represent the predicted selectivity obtained by the calculation from IAST theory.

To understand the separation selectivity of C<sub>2</sub>H<sub>2</sub> over C<sub>2</sub>H<sub>4</sub> and C<sub>2</sub>H<sub>6</sub>, the zero coverage isosteric enthalpies of adsorption was calculated by obtaining a virial fit of following form to the individual pure-component isotherm (Figures 17 (3) and (4)) measured at 273 and 283 K.

$$\ln(n/p) = A_0 + A_1 n + A_2 n^2 + A_3 n^3 \dots$$

where  $p$  is pressure,  $n$  is amount adsorbed and  $A_0$ ,  $A_1$  etc. are virial coefficients.  $A_0$  is related to adsorbate-adsorbent interactions, while  $A_1$  describes adsorbate-adsorbate interactions.<sup>24</sup> For further details please see section 3A.3.6.2. At low surface coverage,  $A_2$

and higher terms can be ignored. The isosteric enthalpy of adsorption at zero coverage ( $Q_{st}$ ) is a fundamental measure of adsorbate–adsorbent interactions ( $A_0$ ) which were calculated to be 31.8, 18.7 and 28.2 respectively for  $C_2H_2$ ,  $C_2H_4$  and  $C_2H_6$ . It was a very challenging job to determine the  $Q_{st}$  value for  $C_2H_4$  and  $C_2H_6$  as the uptake amounts were very less for the following gases. Interestingly, the high isosteric enthalpies of  $C_2H_2$  (31.8 kJ/mol) attributes a stronger  $C_2H_2$ –framework interaction compare to the other two  $C_2$  hydrocarbons.

**Table 10:** Virial graph analysis data for Compound **2b**; zero coverage enthalpy of  $C_2H_2$ ,  $C_2H_4$  and  $C_2H_6$  and predicted separation selectivity of  $C_2H_2$  over  $C_2H_4$  and  $C_2H_6$  at 273 and 283 K. For further details please see section 3A.3.6.2.

Adsorbate	T (K)	$K_H$ [ $\text{molg}^{-1}\text{Pa}^{-1}$ ]	$A_0$ [ $\ln(\text{molg}^{-1}\text{Pa}^{-1})$ ]	$A_1$ [ $\text{gmol}^{-1}$ ]	$R^2$	$S_{ij}^{[a]}$	$Q_{st}$ [ $\text{kJmol}^{-1}$ ]
$C_2H_2$	273	$4.8032 \times 10^{-8}$	$-16.8514 \pm 0.03280$	-4139.842	0.99611		31.75
	283	$7.8741 \times 10^{-8}$	$-16.3571 \pm 0.05886$	-8645.476	0.98404		
$C_2H_4$	273	$3.6127 \times 10^{-9}$	$-19.4388 \pm 0.00272$	-13531.003	0.99947	13.3	18.74
	283	$6.6824 \times 10^{-8}$	$-16.5212 \pm 0.03507$	-7499.263	0.99435	1.18	
$C_2H_6$	273	$2.7362 \times 10^{-9}$	$-19.7167 \pm 0.00513$	-15011.416	0.99931	17.55	28.29
	283	$1.7613 \times 10^{-9}$	$-20.1572 \pm 0.00859$	-14133.047	0.99248	44.70	

<sup>[a]</sup>  $S_{ij} = K_H(C_2H_2)/K_H(i)$ ;  $i = C_2H_4/C_2H_6$

The isosteric heat of adsorption for  $C_2H_2$  was also calculated by employing the 1st type of virial equation which results a similar value of  $33.0 \text{ kJmol}^{-1}$  at the zero coverage region (Figure 17(2)).

The high value of  $Q_{st}$  is presumably a result of the efficient packing of the  $C_2H_2$  molecules at the pore surface of the material which is originated from the strong interaction of the gas molecule with the exposed  $Mn^{II}$  sites and aromatic  $\pi$  clouds. The fewer uptake and lower  $Q_{st}$  value of  $C_2H_4$  and  $C_2H_6$  can be correlated with the fact that, the channel window size ( $5.5 \times 4.0 \text{ \AA}^2$ ) of compound **2b** is not sufficient enough for the inclusion of those gas molecules ( $C_2H_4 = 4.2 \text{ \AA}$  and  $C_2H_6 = 4.5 \text{ \AA}$ ) of comparable size. On the other hand acetylene molecules having a lesser kinetic diameter ( $3.2 \text{ \AA}$ ) than the window size of **2b** can easily enrol itself into the 1D channel and interacts with exposed metal sites, aromatic  $\pi$  cloud and hanging cyanide ligands.

### 3A.3.6.2: Analysis of Gas Adsorption Isotherms

#### 3A.3.6.2.1: Heat of Adsorption (kJ mol<sup>-1</sup>)

**3A.3.6.2.1.1 Clausius-Clapeyron equation:** Hydrogen (77 and 87 K) adsorption isotherms were fitted to the Langmuir-Freundlich<sup>25</sup> equation instead of the more commonly used Langmuir equation.<sup>26</sup> An accurate fit was obtained by using this equation which results a precise prediction over the quantity of hydrogen adsorbed at saturation. A variant of the Clausius-Clapeyron equation was used to calculate enthalpy of adsorption.

$$\ln \left( \frac{P_1}{P_2} \right) = \Delta H_{ads} \times \left( \frac{T_2 - T_1}{R \times T_2 T_1} \right) \dots \dots \dots (1)$$

Where,  $P_n$  is = Pressure for isotherm  $n$

$T_n$  = Temperature for isotherm  $n$

$R$  = Universal Gas constant = 8.314 J mol<sup>-1</sup> K<sup>-1</sup>

Pressure as a function of amount of adsorption was determined by using the Langmuir-Freundlich fit for each isotherm.

$$\frac{Q}{Q_m} = \frac{B \times P^{\left(\frac{1}{t}\right)}}{1 + (B \times P^{\left(\frac{1}{t}\right)})} \dots \dots \dots (2)$$

Where,  $Q$  = moles adsorbed

$Q_m$  = moles adsorbed at saturation

$P$  = Pressure

$B$  and  $t$  = constant

By rearranging this equation we get

$$P = \left( \frac{\frac{Q}{Q_m}}{B - \left( B \times \frac{Q}{Q_m} \right)} \right)^t \dots \dots \dots (3)$$

Substituting this into Clausius-Clapeyron equation we get

$$\Delta H_{ads} = \frac{R \times T_1 \times T_2}{T_2 - T_1} \ln \frac{\left(\frac{Q}{Q_{m1}}\right)^{t_1}}{\left(\frac{Q}{Q_{m2}}\right)^{t_2}} \dots\dots\dots(4)$$

Where, the subscript 1 and 2 are representing the data corresponding to 77 and 87 K respectively.

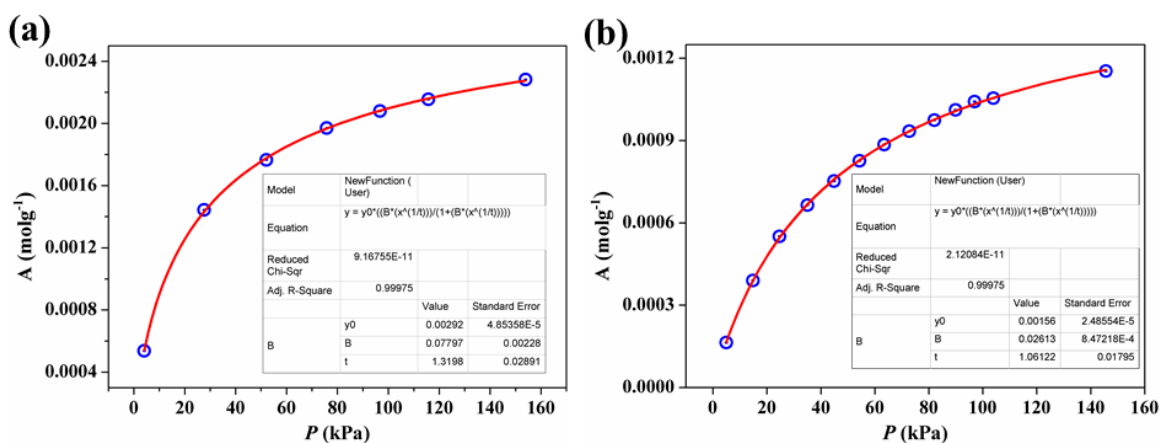


**Figure 18:** (a) H<sub>2</sub> adsorption isotherm for **1** at 77 K (a) and 87 K (b). The solid line represents the best fit to the data using the Langmuir-Freundlich equation, as described above.

**3A.3.6.2.1.2 Virial Equation (1<sup>st</sup> type):** We have used a virial type expression of the following type to fit the combined C<sub>2</sub>H<sub>2</sub> adsorption isotherm data of collected 273 and 283 K.

$$\ln(P) = \ln(A) + \frac{1}{T} \sum_{i=0}^m a_i A^i + \sum_{i=0}^n b_i A^i \dots\dots\dots(5)$$

Here, *P* is the pressure expressed in torr, *A* is the amount adsorbed in mmol/g, *T* is the temperature in K, *a<sub>i</sub>* and *b<sub>i</sub>* are virial coefficients, and *m*, *n* represent the number of coefficients required to adequately describe the isotherms. The value of *m* and *n* was gradually increased until the contribution of extra added *a* and *b* coefficients were negligible towards the overall final fit. The values of the virial coefficient *a<sub>i</sub>* were taken to calculate the isosteric heat of adsorption using the following expression.

$$Q_{st} = -R \sum_{i=0}^m a_i A^i \dots\dots\dots(6)$$

$Q_{st}$  is the coverage dependent isosteric heat of adsorption and  $R$  is the universal gas constant.

**3A.3.6.2.1.3 Virial Equation, Henry's Law (2<sup>nd</sup> type):** Henry's law says that, in the low pressure region, amount of adsorption ( $n$ ) is proportional to the equilibrium pressure ( $P$ ).

$$n = K_H P \dots\dots\dots(7)$$

Where  $K_H$  is known as the Henry's constant. To calculate Henry's law constants, adsorption in the low-pressure region can be accurately modelled by a virial-type equation where the higher terms ( $A_2, A_3..etc$ ) can be ignored.

$$\ln(n/p) = A_0 + A_1 n + A_2 n^2 + A_3 n^3 \dots \dots\dots(8)$$

By carefully measuring adsorption isotherms in the low-pressure region using a high resolution pressure transducer (0.1 torr from QUANTACHROM), we can therefore obtain accurate Henry's law constants at 273 K, and 283 K (Table 10). The virial method based on eq.-8 is perfect at low pressure region because the obtained linearity with satisfactory  $R^2$  value (Table 10). The intercept of the graphs gives  $A_0$  values which determines the Henry's Law constant  $K_H = \exp(A_0)$ . The zero coverage isosteric enthalpies of adsorption were calculated from the van't Hoff equation.

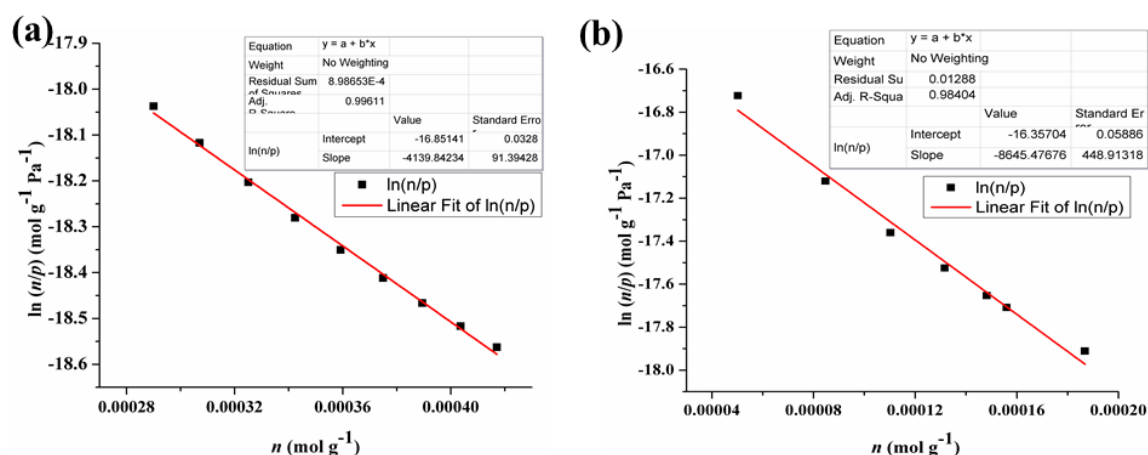


**Figure 19:** Virial plot for the low pressure adsorption data (zero coverage) of  $C_2H_2$  on compound **2b** measured at 273 K (a) and 283 K (b).

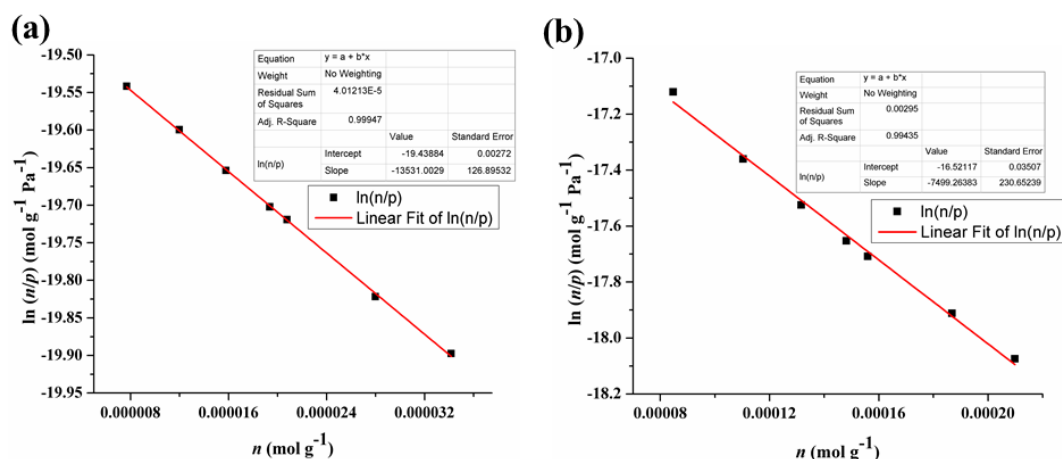


**Figure 20:** Virial plot for the low pressure adsorption data (zero coverage) of C<sub>2</sub>H<sub>4</sub> on compound **2b** measured at 273 K (a) and 283 K (b).

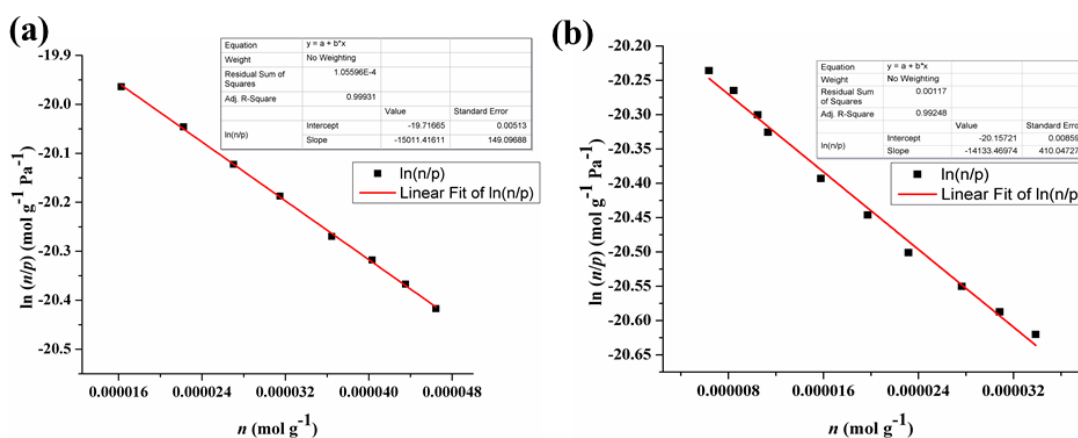


**Figure 21:** Virial plot for the low pressure adsorption data (zero coverage) of C<sub>2</sub>H<sub>6</sub> on compound **2b** measured at 273 K(a) and 283 K (b).

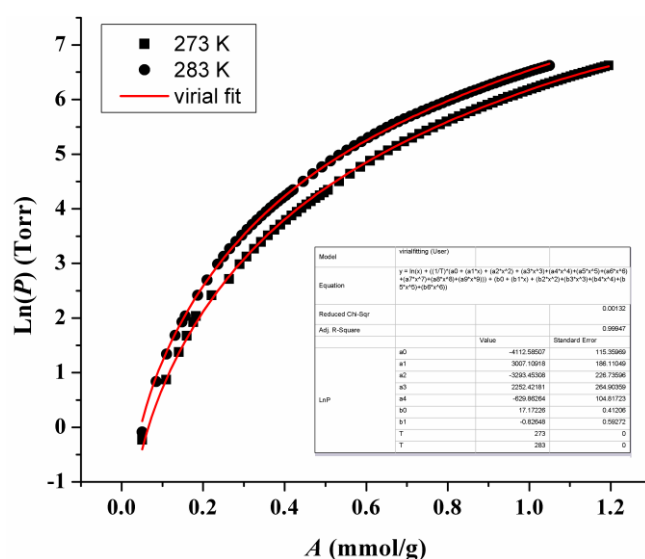


**Figure 22:** C<sub>2</sub>H<sub>2</sub> isotherms for activated compound **2b** measured at 273 K (rectangle) and 283 K (circle). Fitted curves (red solid lines), obtained from the virial-type expansion, were used for the  $Q_{st}$  estimation.

**3A.3.6.2.2 IAST Selectivity:** The ideal adsorbed solution theory (IAST) was used to predict the binary mixture adsorption of C<sub>2</sub>H<sub>2</sub>/C<sub>2</sub>H<sub>4</sub> and C<sub>2</sub>H<sub>2</sub>/C<sub>2</sub>H<sub>6</sub> from the experimental pure-gas isotherms. Previous reports have depicted that this method can predict the adsorption selectivity for mixture of isotherms in nanoporous materials, including metal-organic frameworks. The single-component isotherms were fit to a single-site Langmuir-Freundlich equation (equation 11). The IAST assumes that the adsorbed phase is a two-dimensional solution in equilibrium with the bulk phase. For binary adsorption of A and B, the IAST requires these two equations to be followed:

$$yP_t = xP_a \dots\dots\dots(9)$$

$$(1 - y)P_t = (1 - x)P_b \dots\dots\dots(10)$$

Where *x* and *y* denote the molar fraction of A in the adsorbed phase and the molar fraction of A in the bulk phase, respectively. *P<sub>t</sub>* is the total gas pressure; *P<sub>a</sub>* and *P<sub>b</sub>* are the pressure of component A and B at the same spreading pressure as that of the mixture, respectively. The equation used for the fitting the single component gas mixture is as follows.

$$Y = Y_0 \left( \ln \frac{BP^n}{(1+BP^n)} \right) \dots\dots\dots(11)$$

Furthermore, the molar fraction of A in the adsorbed phase can be obtained from the following equation:

$$Y_{0,a} \ln \left( 1 + \frac{B_a P_t^{n1} y}{x} \right) - Y_{0,b} \ln \left( 1 + \frac{B_b P_t^{n2} (1-y)}{(1-x)} \right) = 0 \dots\dots\dots(12)$$

where *Y<sub>0,a</sub>*, *B<sub>a</sub>* and *n1* are the Langmuir-Freundlich fitting parameters of adsorption equilibrium of pure A, *Y<sub>0,b</sub>*, *B<sub>b</sub>* and *n2* are Langmuir-Freundlich parameters of adsorption equilibrium of pure B. The unknown *x* in Eq. (12) has been solved by Matlab (Version 7.8 (R2009a), The MathWorks, Inc.) for fixed *P<sub>t</sub>* and *y* values.

Then calculated the predicted adsorption selectivity, which is defined as

$$S = \left( \frac{\frac{x_1}{y_1}}{\frac{x_2}{y_2}} \right) \dots \dots \dots (13)$$

where  $x_i$  and  $y_i$  are the mole fractions of component  $i$  ( $i = 1, 2; A, B$ ) in the adsorbed and bulk phases, respectively. The IAST calculations were carried out for equimolar gas-phase mixtures.

### 3A.3.7: Magnetic Properties

**3A.3.7.1 Magnetic Property of compound ( $\{[\text{Mn}_3(\text{bipy})_3(\text{H}_2\text{O})_4][\text{Cr}(\text{CN})_6\text{]}_2 \cdot 2(\text{bipy}) \cdot 4\text{H}_2\text{O}\}_n$ ) (**1**) at different states:** We have successively measured magnetic data of as-synthesized **1**, **1a** and **1b** (rehydrated). The *dc* magnetic susceptibilities are shown in the form  $\chi_M T$  vs  $T$  (**1** and **1a**) in Figure 23. The  $\chi_M$  value for **1** at 300 K is  $0.0531 \text{ cm}^3 \text{ mol}^{-1}$  ( $\chi_M T = 16.17 \text{ cm}^3 \text{ mol}^{-1} \text{ K}$ ) which agrees well with the spin only value ( $0.0558 \text{ cm}^3 \text{ mol}^{-1}$ ;  $16.74 \text{ cm}^3 \text{ mol}^{-1} \text{ K}$ ) expected for magnetically isolated three  $\text{Mn}^{\text{II}}$  ( $S = 5/2$ ) and two  $\text{Cr}^{\text{III}}$  ( $S = 3/2$ ) ions.

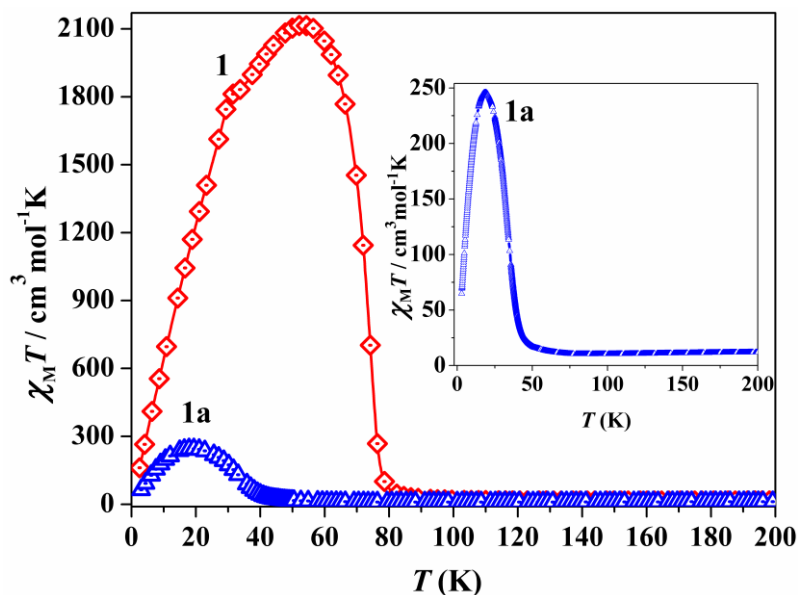


**Figure 23:** Temperature dependence of the magnetic susceptibility of **1** and **1a** in an applied field of 500 Oe under zero field cooled condition. Inset shows the same for **1a** to give a clear understanding of ordering at low  $T$ .

The  $\chi_M T$  value gradually decreases with decreasing temperature to reach a minimum value of  $14.96 \text{ cm}^3 \text{ mol}^{-1} \text{ K}$  at 85 K, and then rapidly increases to a maximum value of  $2114.96 \text{ cm}^3 \text{ mol}^{-1} \text{ K}$  at 53 K and then again decreases to  $161.65 \text{ cm}^3 \text{ mol}^{-1} \text{ K}$  at 2.5 K.



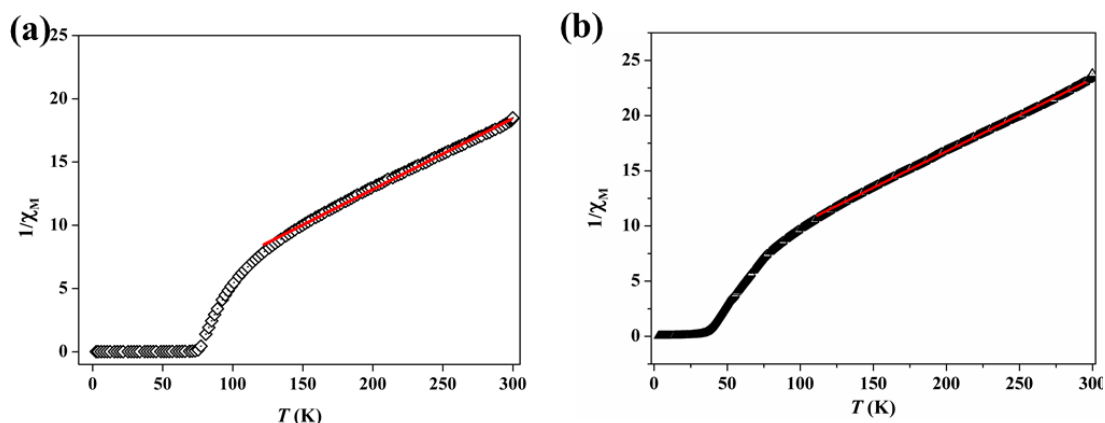


**Figure 24:** (a) Curie–Weiss fitting of **1** above 150 K with  $C = 18.50 \text{ cm}^3\text{K mol}^{-1}$ , and  $\theta = -39.3 \text{ K}$ . (b) Curie–Weiss fitting of **1a** above 150 K with  $C = 15.46 \text{ cm}^3\text{K mol}^{-1}$ , and  $\theta = -59.8 \text{ K}$ .

The  $1/\chi_M$  vs  $T$  plot in the temperature range of 300 – 150 K obeys the Curie-Weiss law (Figure 24a) with a Weiss constant  $\theta = -39.3 \text{ K}$ , which suggest the antiferromagnetic interaction between the adjacent  $\text{Mn}^{\text{II}}$  and  $\text{Cr}^{\text{III}}$  ions through cyanide bridges as has already been observed.<sup>11</sup> The rapid increase in  $\chi_M T$  value indicates a magnetic ordering, which was determined accurately as 80 K ( $T_c$ ) by  $dM/dT$  differential plot (Figure 25a). Thus compound **1** is a ferrimagnet. The decrease in  $\chi_M T$  value after 53 K suggests further interaction between the layers through the bipy linker. The magnetic data of **1a** also shows a typical magnetic ordering below 50 K and  $dM/dT$  plot suggest the  $T_c$  is about 45.3 K (Figure 25b). The Weiss constant  $\theta$  was calculated as -59.8 K (300 -150 K, Figure 24b)) suggesting stronger antiferromagnetic interaction in **1a** compared to **1**.

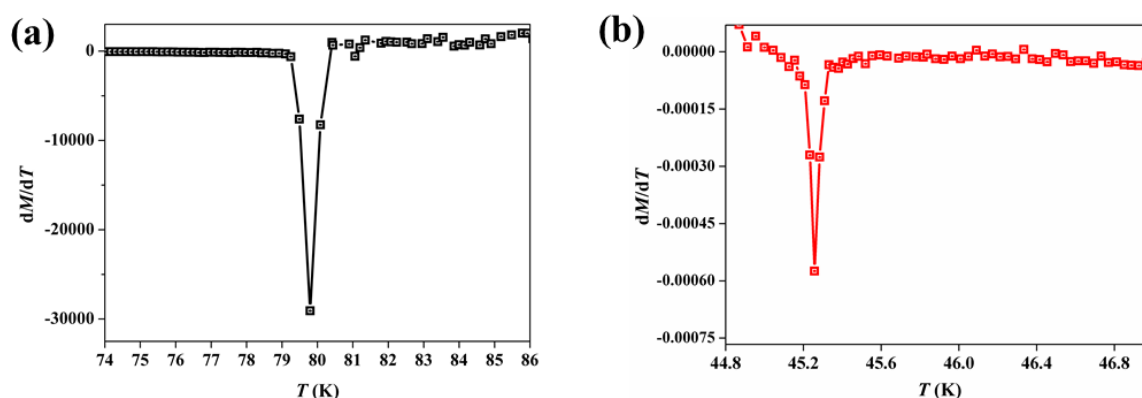


**Figure 25:**  $dM/dT$  plot for compound **1** and **1a**.

The change in Weiss constant,  $T_c$  and maxima in the  $\chi_M T$  value suggest there are

changes in the magnetic pathways in **1a**. The value of  $T_c$  depends on the overall magnetic interaction via covalent (cyanide or as well as bipy bridges) and noncovalent interactions (like H-bond,  $\pi \cdots \pi$  interactions).

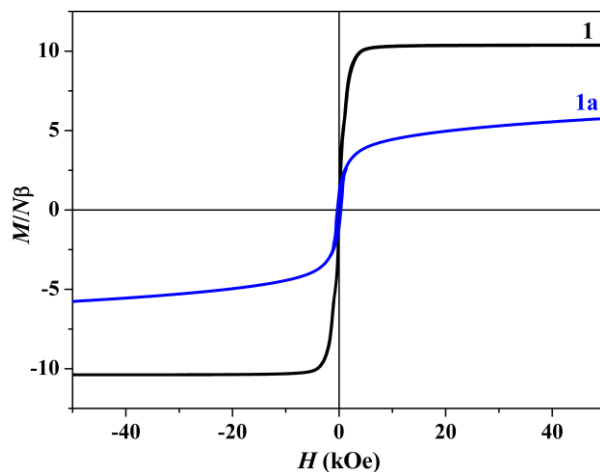


**Figure 26:** Magnetization plot for **1** and **1a** measured at 2.5 K.

In **1a** upon removal of the guest water, bipy and coordinated water molecules all the H-bonding interactions (Figures 5a and b) between the magnetic centres are destroyed. These noncovalent interactions provide ferromagnetic interactions in **1** and their absence in **1a** might be responsible for lowering the Curie temperature. Moreover, the structural strain in deguest phase (like bent Cr-CN-Mn pathway) also provides the negative contribution of  $T_c$ .<sup>3c</sup>

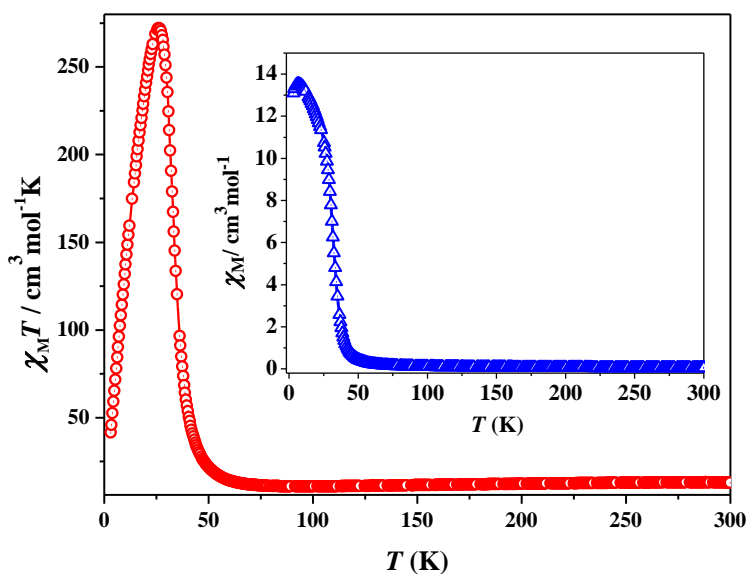


**Figure 27:** Temperature dependence of the magnetic susceptibility ( $\chi_M T$ ) of **1b** in an applied field of 500 Oe under zero field cooled condition. Inset shows the  $\chi_M$  vs  $T$  plot for **1b** measured at 500 Oe under zero field cooled condition.

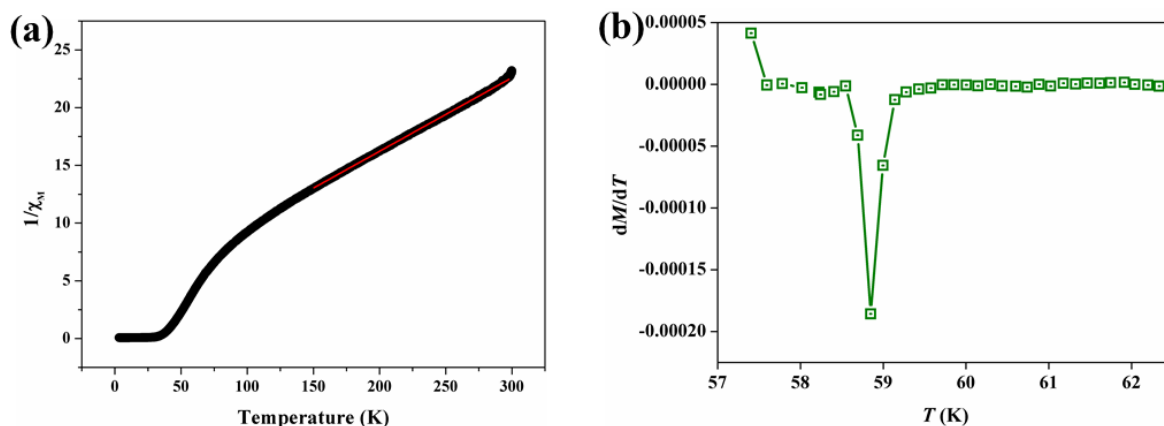


**Figure 28:** (a) Curie–Weiss fitting of **1b** above 150 K with  $C = 15.68 \text{ cm}^3\text{K mol}^{-1}$ , and  $\theta = -54.5 \text{ K}$ . (b)  $dM/dT$  plot for **1b**.

The increase in  $T_c$  (59 K) in **1b** (Figures 27 and 28b) also unequivocally suggests the role of water molecules in ferromagnetic interactions as they are involved in several H-bonding interactions. The field dependence magnetization curve of **1** shows rapid increase to saturate at 8 kOe which is also the signature of magnetic ordering within the compound (Figure 26). The saturation magnetization value in **1** is  $10 N_\beta$  which is in good agreement with the theoretical value ( $9 N_\beta$ ) expected for a ferrimagnet where antiferromagnetic coupling between  $\text{Cr}^{\text{III}}$  and  $\text{Mn}^{\text{II}}$  exists. The decrease in magnetization value ( $6 N_\beta$ ) in **1a** (Figure 26) at high field suggests strong antiferromagnetic interaction operating between  $\text{Cr}^{\text{III}}$  and  $\text{Mn}^{\text{II}}$  which is also in line with observed high weiss constant and low  $T_c$ .

**3A.3.7.2 Magnetic Property of compound  $\{[\text{Mn}_3(\text{bipy})_3(\text{H}_2\text{O})_4][\text{Mn}(\text{CN})_6]_2 \cdot 2(\text{bipy}) \cdot 4\text{H}_2\text{O}\}_n$  (**2**):** The *dc* magnetic susceptibilities of **2** is discussed in the form of  $\chi_M T$  vs  $T$  plots. The  $\chi_M T$  value for **2** at 300 K is  $14.92 \text{ cm}^3\text{mol}^{-1}\text{K}$  which agrees well with the spin only value ( $15.00 \text{ cm}^3\text{mol}^{-1}\text{K}$ ) expected for magnetically isolated three  $\text{Mn}^{\text{II}}$  ( $S = 5/2$ ) and two  $\text{Mn}^{\text{III}}$  ( $S = 2/2$ ) ions. The  $\chi_M T$  value gradually decreases with decreasing temperature to reach a minimum value of  $14.50 \text{ cm}^3\text{mol}^{-1}\text{K}$  at 84 K, and then rapidly increases to a maximum value of  $59.29 \text{ cm}^3\text{mol}^{-1}\text{K}$  at 14 K and then again decreases to a minimum value of  $4.2 \text{ cm}^3\text{mol}^{-1}\text{K}$  at 2 K (Figure 29a). A Curie–Weiss plot fitted in the temperature range of 100–300 K (Figure 30) shows a negative Weiss constant of  $\theta = -6.8 \text{ K}$ . The first decrease of  $\chi_M T$  and the negative  $\theta$  value suggest the operation of an antiferromagnetic interaction between the adjacent  $\text{Mn}^{\text{II}}$  and  $\text{Mn}^{\text{III}}$  ions through cyanide bridges and a small contribution of spin-orbit coupling of low-spin  $\text{Mn}^{\text{III}}$  (ground state

$^3T_1$ ). The magnetic phase transition temperatures ( $T_c$ ) was determined to be 14.6 K by  $dM/dT$  plots (inset of Figure 29a) and this suggest compound **2** is a ferrimagnet. The decrease in  $\chi_M T$  value after 14 K, can be attributed to the spin-orbit coupling of low spin  $Mn^{III}$  or antiferromagnetic interactions between the layers through the bipy linker at low temperatures.

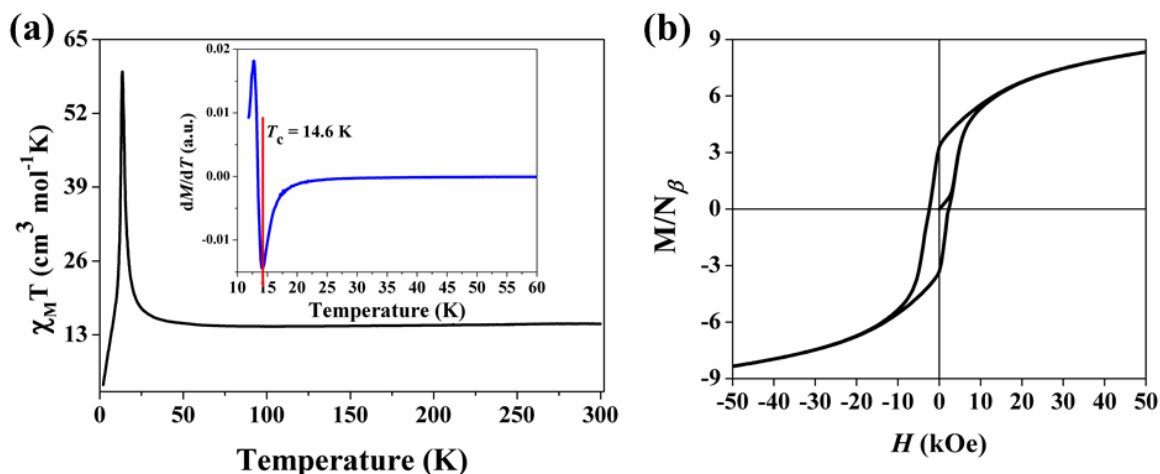


**Figure 29:** (a) Temperature dependence of the magnetic susceptibility of compound **2** at an external field of 500 Oe under field cooled condition. Inset:  $dM/dT$  vs  $T$  plot of compound **2** revealed the  $T_c$  value to be 14.6 K. (b) The field dependent magnetization curve of **2** measured at 2K.

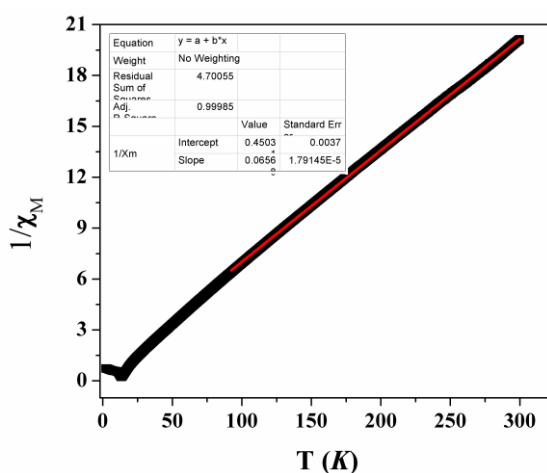


**Figure 30:** Curie–Weiss fitting of **2b** above 100 K with  $C = 15.24 \text{ cm}^3\text{K mol}^{-1}$ , and  $\theta = -6.8 \text{ K}$ .

The isothermal field dependent magnetization curve of **2** has been shown in Figure 29b. At 2 K, a typical magnetic hysteresis loop was observed with remnant magnetization and coercive field of  $3.32 N_\beta$  and 2.3 kOe respectively (Figure 29b). The magnetization value increases rapidly below 0.5 kOe, and then gradually increases to attain its maximum at 50 kOe indicating the signature of magnetic ordering within the compound. The saturation

magnetization value per  $\text{Mn}^{\text{II}}_3\text{Mn}^{\text{III}}_2$  unit at 50 kOe is  $8.5 N_{\beta}$ , which is lesser compared to the theoretical value of  $11 N_{\beta}$  ( $g_{\text{Mn}} = 2$ ) and this can be corroborated to antiferromagnetic coupling between two  $\text{Mn}^{\text{III}}$  and three  $\text{Mn}^{\text{II}}$  ions. The larger coercive field must be associated with the magnetic anisotropy of  $\text{Mn}^{\text{III}}$  ion.

**3A.3.7.3 Magnetic Property of compound 3**  $\{[\text{Mn}_2(\text{bipy})(\text{CN})][\text{Mn}(\text{CN})_6]\}_n$ : The  $\chi_{\text{M}}T$  value for **3** at 300 K is  $6.26 \text{ cm}^3\text{mol}^{-1}\text{K}$  which also agrees well with the spin only value ( $6.32 \text{ cm}^3\text{mol}^{-1}\text{K}$ ) expected for magnetically isolated one  $\text{Mn}^{\text{II}}$  ( $S = 5/2$ ) and two  $\text{Mn}^{\text{III}}$  ( $S = 2/2$ ) ions (Figure 31a).

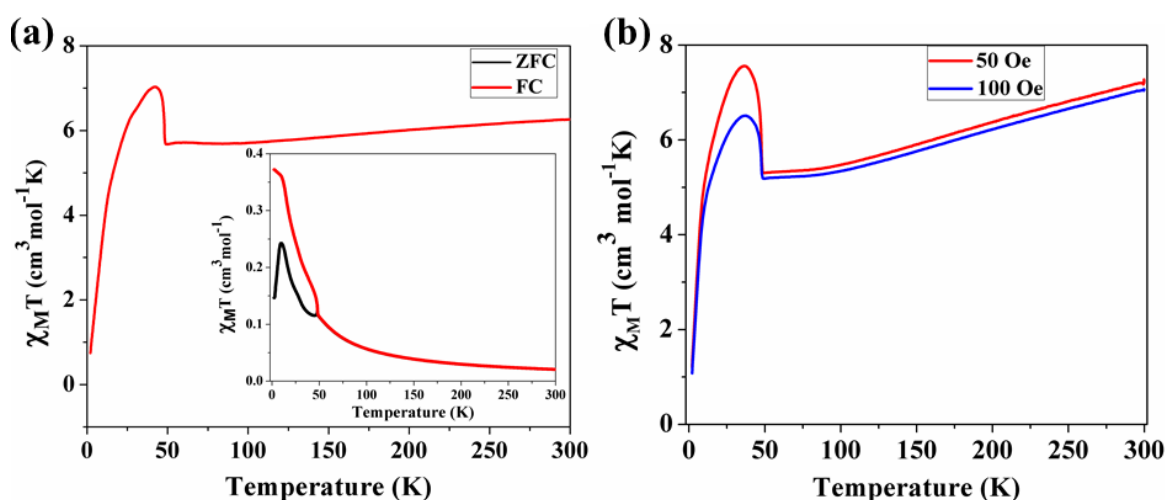


**Figure 31:** (a) Temperature dependence of the magnetic susceptibility of compound **3** at an external field of 500 Oe under the field cooled condition. Inset  $\chi_{\text{M}}T$  vs  $T$  plot of compound **3** at field-cooled (FC) and zero-field cooled (ZFC) condition. (b) Temperature dependence of the magnetic susceptibility of **3** at 50 and 100 Oe under field-cooled (FC) condition.

The temperature dependence of the reciprocal susceptibility above 150 K (Figure 32a) follows the Curie–Weiss law with a Weiss constant ( $\theta$ ) of  $-6.59 \text{ K}$ , which can be a result of antiferromagnetic interaction operating between the  $\text{Mn}^{\text{II}}$  and  $\text{Mn}^{\text{III}}$  ions through the cyanide bridges and a spin-orbit coupling of the low-spin  $\text{Mn}^{\text{III}}$  ions. The product  $\chi_{\text{M}}T$  first decreases up to 48 K and then increases steadily and reaches to  $7.06 \text{ cm}^3\text{mol}^{-1}\text{K}$  at 50 K. Then further decreasing of temperature the  $\chi_{\text{M}}T$  decreases to  $0.76 \text{ cm}^3\text{mol}^{-1}\text{K}$  at 2 K (Figure 31a). The spontaneous increase in  $\chi_{\text{M}}T$  at low temperature indicates a possibility of long-range ordering. The field-cooled (FC) and zero-field-cooled (ZFC) magnetization measured at 500 Oe show a bifurcation at 48 K, suggesting a phase transition (Figure 31a *inset*). A plot of FC susceptibility vs  $T$  at different  $dc$  field strengths shows a field-dependent behavior below 48 K (Figure 31b) and the spontaneous increase

of the  $\chi_M T$  product is more pronounced at lower field strength, suggesting spin-canting behaviour in this system.

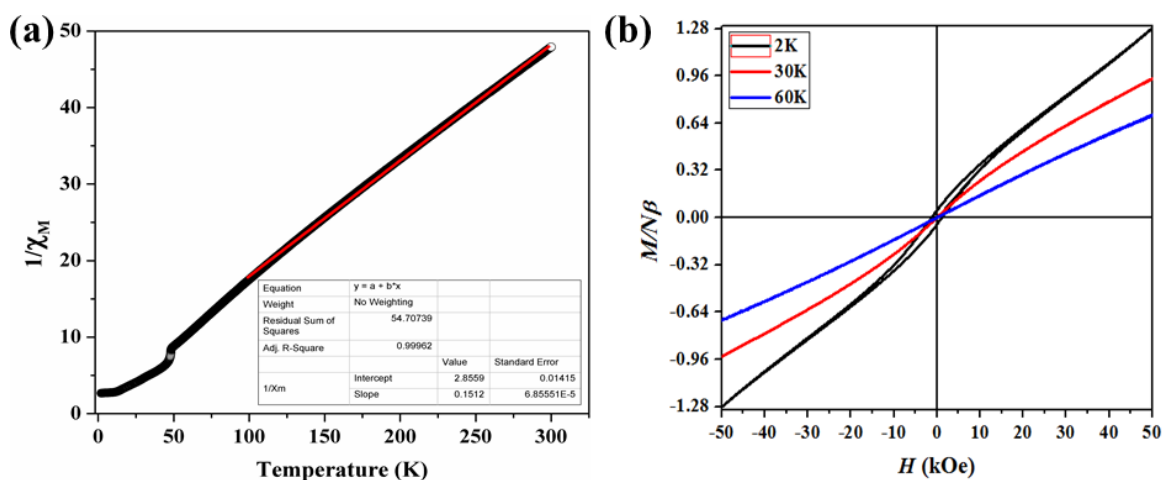


**Figure 32:** (a) Curie–Weiss fitting of compound **3** above 150 K with  $C = 6.59 \text{ cm}^3 \text{ K mol}^{-1}$ , and  $\theta = -18.63 \text{ K}$ . (b) The field dependent magnetization curve of **3** at different temperatures.

The magnetization curve measured at 2 K shows a small hysteresis loop, with values of the coercive field ( $H_c$ ) and remnant magnetization ( $M_r$ ) of 1.17 kOe and  $0.05 N_\beta$  respectively, revealing that complex **3** is a soft ferromagnet (Figure 32b). With increasing the field, the magnetization value gradually increases and ends with a value of  $1.13 N_\beta$  at 50 kOe without any saturation. The highest value of magnetization is quite low compare to the theoretical value of  $3 N_\beta$  which suggests the presence of antiferromagnetic coupling between  $\text{Mn}^{\text{III}}$  and two  $\text{Mn}^{\text{II}}$  ions in the compound. Assuming the saturation magnetization value of  $3 N_\beta$ , the estimated canting angle for **3** ( $\sin^{-1}(0.05/3)$ ) is  $0.96^\circ$ . Furthermore, saturation magnetization value decreases with temperature also support the spin canting behaviour in the system (Figure 32b). The lower value of magnetization may be ascribed to non-compensated canting between the Mn centers which is leading to weak ferromagnetic or canted antiferromagnetic behaviour.

### 3A.4: Conclusion

Summarizing the chapter, we have thus conceived a rational strategy to assemble 2D magnetic layers into a 3D rigid porous framework that exhibits permanent porosity and ferrimagnetic behaviour between  $\text{Mn}^{\text{II}}$  and  $[\text{Cr}(\text{CN})_6]^{3-} / [\text{Mn}(\text{CN})_6]^{3-}$ . The highly polar nature of **1a** was found to be exceedingly promising for high heat of  $\text{H}_2$  adsorption and establishes itself to be the first member of cyanometallate systems having heat of  $\text{H}_2$

adsorption value of  $\sim 11.5 \text{ kJmol}^{-1}$ . The framework demonstrates interesting guest responsive magnetic modulation with change in  $T_c$  as observed from *dc* susceptibility measurements. Compound **2** is a ferrimagnet based on the alternative arrangement of high spin  $\text{Mn}^{\text{II}}$  and low spin  $\text{Mn}^{\text{III}}$  centers in 2D layers. Compound **2** is a novel microporous material that showed highly selective adsorption for acetylene ( $\text{C}_2\text{H}_2$ ) over the other two  $\text{C}_2$  hydrocarbons like ethylene ( $\text{C}_2\text{H}_4$ ) and ethane ( $\text{C}_2\text{H}_6$ ). Such high selectivity and separation capacity can be attributed to the perfect window size of the 1D pore in compound **2** where  $\text{C}_2\text{H}_2$  molecules can easily enter and strongly interact with the exposed  $\text{Mn}^{\text{II}}$  sites; whereas the other two  $\text{C}_2$  hydrocarbons with relatively higher kinetic diameter than  $\text{C}_2\text{H}_2$  cannot enter into the 1D channel.

### 3A.5: References

1. (a) L. J. Murray, M. Dincă and J. R. Long, *Chem. Soc. Rev.*, 2009, **38**, 1294; (b) S. Kitagawa, R. Kitaura and S. Noro, *Angew. Chem. Int. Ed.*, 2004, **43**, 2334; (c) J. R. Li, R. J. Kuppler and H.-C. Zhou, *Chem. Soc. Rev.*, 2009, **38**, 1477; (d) J. Lee, O. K. Farha, J. Roberts, K. A. Scheidt, S. T. Nguyen and J. T. Hupp, *Chem. Soc. Rev.*, 2009, **38**, 1450; (e) D. Maspoch, D. Ruiz-Molina and J. Veciana, *Chem. Soc. Rev.*, 2007, **36**, 770; (f) S. Achmann, G. Hagen, J. Kita, I. M. Malkowsky, C. Kiener and R. Moos, *Sensors*, 2009, **9**, 1574; (g) P. Horcajada, C. Serre, G. Maurin, N. A. Ramsahye, F. Balas, M. Vallet-Regi, M. Sebban, F. Taulelle and G. Férey, *J. Am. Chem. Soc.*, 2008, **130**, 6774; (h) P. Kanoo, R. Matsuda, M. Higuchi, S. Kitagawa and T. K. Maji, *Chem. Mater.*, 2009, **21**, 5860.
2. (a) N. R. Champness, *Dalton Trans.*, 2006, 877; (b) C. J. Kepert, *Chem. Commun.*, 2006, 695; (c) Z. M. Wang, B. Zhang, Y. J. Zhang, M. Kurmoo, T. Liu, S. Gao and H. Kobayashi, *Polyhedron*, 2007, **26**, 2207; (d) P. Kanoo, K. L. Gurunatha and T. K. Maji, *J. Mater. Chem.* 2010, **20**, 1322.
3. (a) M. Ohba, K. Yoneda and S. Kitagawa, *CrystEngComm*, 2010, **12**, 159; (b) T. Mallah, S. Thiebaut, M. Verdaguer and P. Veillet, *Science*, 1993, **262**, 1554; (c) W. Kaneko, M. Ohba and S. Kitagawa, *J. Am. Chem. Soc.*, 2007, **129**, 13706.
4. (a) X. N. Cheng, W. X. Zhang, Y. Y. Lin, Y. Z. Zheng and X. M. Chen, *Adv. Mater.*, 2007, **19**, 1494; (b) M. Kurmoo, H. Kumagai, K. W. Chapman and C. J. Kepert, *Chem. Commun.*, 2005, 3012; (c) D. Maspoch, D. Ruiz-Molina, K. Wurst, N. Domingo, M. Cavallini, F. Biscarini, J. Tejada, C. Rovira and J. Veciana, *Nat. Mater.*, 2003, **2**, 190; (d) G. J. Halder, C. J. Kepert, B. Moubaraki, K. S. Murray and J. D. Cashion, *Science*, 2002, **298**, 1762.
5. (a) D. Maspoch, D. Ruiz-Molina and J. Veciana, *J. Mater. Chem.*, 2004, **14**, 2713; (b) E. Coronado, F. Palacio and J. Veciana, *Angew. Chem. Int. Ed.*, 2003, **42**, 2570.

5. (a) V. Niel, A. L. Thompson, M. C. Munoz, A. Galet, A. S. E. Goeta and J. A. Real, *Angew. Chem. Int. Ed.*, 2003, **42**, 3760; (b) Z. M. Wang, B. Zhang, H. Fujiwara, H. Kobayashi and M. Kurmoo, *Chem. Commun.*, 2004, 416; (c) M. Kurmoo, H. Kumagai, M. Akita-Tanaka, K. Inoue and S. Takagi, *Inorg. Chem.*, 2006, **45**, 1627.
6. (a) M. H. Zeng, X. L. Feng, W. X. Zhang and X. M. Chen, *Dalton Trans.*, 2006, 5294; (b) L. G. Beauvais and J. R. Long, *J. Am. Chem. Soc.*, 2002, **124**, 12096.
7. (a) K. Barthelet, J. Marrot, D. Riou and G. Férey, *Angew. Chem. Int. Ed.*, 2002, **41**, 281; (b) C. Livage, N. Guillou, J. Chaigneau, P. Rabu, M. Drillon and G. Férey, *Angew. Chem. Int. Ed.*, 2005, **44**, 6488; (c) C. Serre, F. Millange, C. Thouvenot, M. Nogues, G. Marsolier, D. Louer and G. Férey, *J. Am. Chem. Soc.*, 2002, **124**, 13519.
- K. M. Thomas, *Dalton Trans.*, 2009, 1487.
8. (a) S. S. Kaye and J. R. Long, *J. Am. Chem. Soc.*, 2005, **127**, 6506; (b) J. G. Vitillo, L. Regli, S. Chavan, G. Ricchiardi, G. Spoto, P. D. C. Dietzel, S. Bordiga and A. Zecchina *J. Am. Chem. Soc.*, 2008, **130**, 8386; (c) B. Chen, X. Zhao, A. Putkham, K. Hong, E. B. Lobkovsky, E. J. Hurtado, A. J. Fletcher and K. M. Thomas, *J. Am. Chem. Soc.*, 2008, **130**, 6411; (d) S. Mohapatra, K. Hembram, U. Waghmare and T. K. Maji, *Chem. Mater.* 2009, **21**, 5406.
9. T. K. Maji, S. Pal, K. L. Gurunatha, A. Govindaraj and C. N. R. Rao, *Dalton Trans.*, 2009, 4426.
10. M. M. Dubinin, *Chem. Rev.*, 1960, **60**, 235.
11. Y. Yoshida, K. Inoue, and M. Kurmoo, *Chem. Lett.*, 2008, **37**, 586; (b) T. Glaser, M. Heidemeier, T. Weyhermüller, R. D. Hoffmann, H. Rupp and P. Müller, *Angew. Chem. Int. Ed.*, 2006, **45**, 6033; (c) A. Marvilliers, S. Parsons, E. Rivière, J. P. Audière and T. Mallah, *Chem. Commun.*, 1999, 2217.
12. (a) Y. He, Z. Zhang, S. Xiang, F. R. Fronczek, R. Krishna and B. Chen, *Chem. Eur. J.*, 2012, **18**, 613; (b) M. C. Das, H. Xu, S. Xiang, Z. Zhang, H. D. Arman, G. Qian and B. Chen, *Chem. Eur. J.*, 2011, **17**, 7817.
13. T. Ren, M. K. Patel and K. Blok, *Energy*, 2008, **33**, 817.
14. (a) K. Liu, D. Ma, B. Li, Y. Li, K. Yao, Z. Zhang, Y. Han and Z. Shi, *J. Mater. Chem. A*, 2014, **2**, 15823; (b) X. Duan, Q. Zhang, J. Cai, Y. Yang, Y. Cui, Y. He, C. Wu, R. Krishna, B. Chen and G. Qian, *J. Mater. Chem. A*, 2014, **2**, 2628; (c) H.-R. Fu, Y. Kang and J. Zhang, *Inorg. Chem.*, 2014, **53**, 4209; (d) J. A. Mason, M. Veenstra and J. R. Long, *Chem. Sci.*, 2014, **5**, 32; (e) Z. R. Herm, E. D. Bloch and J. R. Long, *Chem. Mater.*, 2013, **26**, 323.
15. SAINT+, 6.02 ed.; Bruker AXS: Madison, WI, **1999**.
16. G. M. Sheldrick, *SADABS, Empirical Absorption Correction Program*; University of Göttingen, Göttingen, Germany, **1997**.



17. Altomare, G. Cascarano, C. Giacovazzo and A. Gualaradi, *J. Appl. Crystallogr.*, 1993, **26**, 343.
18. G. M. Sheldrick, SHELXL 97, *Program for the Solution of Crystal Structure*, University of Göttingen, Germany, 1997.
19. A. L. Spek, *J. Appl. Crystallogr.*, 2003, **36**, 7.
20. G. M. Sheldrick, SHELXS 97, *Program for the Solution of Crystal Structure*, University of Göttingen, Germany, 1997.
21. L. J. Farrugia, WinGX - A Windows Program for Crystal Structure Analysis, *J. Appl. Crystallogr.*, 1999, **32**, 837.
22. S. J. Geier, J. A. Mason, E. D. Bloch, W. L. Queen, M. R. Hudson, C. M. Brown and J. R. Long, *Chem. Sci.*, 2013, **4**, 2054.
23. J. H. Cole, D. H. Everett, C. T. Marshall, A. R. Paniego, J. C. Powl and F. Rodriguez-Reinoso, *J. Chem. Soc., Faraday Trans.*, 1974, **70**, 2154.
24. R. T. Yang, *Gas Separation by Adsorption Processes*; Butterworth:Boston, 1997.
25. F. Roquerol, J. Rouquerol, K. Sing, *Adsorption by Powders and Solids:Principles, Methodology, and Applications*; Academic Press: London,1999.
26. (a) V. A. Blatov, A. P. Shevchenko and V. N. Serezhkin, *J. Appl. Crystallogr.*, 2000, **33**, 1193; (b) V. A. Blatov, L. Carlucci, G. Ciani and D. M. Proserpio, *CrystEngComm*, 2004, **6**, 377.
27. V. A. Blatov, A. P. Shevchenko and V. J. Serezhkin, *J. Appl. Crystallogr.* 2000, **33**, 1193.
28. (a) E.-Q. Gao, Y.-F. Yue, S.-Q. Bai, Z. He and C.-H. Yan, *J. Am. Chem. Soc.* 2004, **126**, 1419; (b) L.-M. Zheng, S. Gao, H.-H. Song, S. Decurtins, A. J. Jacobson and X.-Q. Xin, *Chem. Mater.* 2002, **14**, 3143; (c) P. S. Mukherjee, S. Dalai, E. Zangrando, F. Lloret, N. R. Chaudhuri, *Chem. Commun.* 2001, 1444; (d) X. Hao, Y.-G. Wei, S.-W. Zhang, *Chem. Commun.* 2000, 2271; (e) M. Monfort, I. Resino, J. Ribas, H. Stoeckli-Evans, *Angew. Chem. Int. Ed.* 2000, **39**, 191.



# Chapter 4

**Metal-organic frameworks with Azo Functionalized Pillar Modules:**

**Photo-induced On-demand Release of CO<sub>2</sub> molecules**



## Summary

This chapter deals with the synthesis, single crystal structural characterization and photo-controlled tunable gas adsorption properties of three new 3D metal-organic frameworks  $\{[\text{Mn}_3(\text{azpy})_3(\text{H}_2\text{O})_4][\text{Cr}(\text{CN})_6]_2 \cdot 2(\text{azpy}) \cdot 2\text{EtOH}\}_n$  (**1**),  $\{[\text{Co}_3(\text{azpy})_3(\text{H}_2\text{O})_4][\text{Cr}(\text{CN})_6]_2 \cdot 2(\text{azpy}) \cdot 2\text{EtOH}\}_n$  (**2**) and  $\{[\text{Zn}_3(\text{azpy})_3(\text{H}_2\text{O})_2][\text{Cr}(\text{CN})_6]_2 \cdot 2(\text{azpy}) \cdot 2\text{EtOH}\}_n$  (**3**) constructed with the self-assembly of  $\text{Mn}^{\text{II}}/\text{Co}^{\text{II}}/\text{Zn}^{\text{II}}$ ,  $[\text{Cr}(\text{CN})_6]^{3-}$  and 4,4'-azobipyridine (azpy) as a exo-bidentate organic linker. The phenomenon of conformation change in the azo group upon photo-irradiation has been employed to release the gas molecules from the pores of the deguest frameworks. At room temperature, *in situ*  $\text{CO}_2$  adsorption study with light demonstrates an immediate release of gas molecules on shining the adsorbent material with 365 nm UV light. However, on switching off the UV light, distortion around the structure vanishes, which comprehends the reversible on-demand release of the  $\text{CO}_2$  molecules. The isosteric heats of  $\text{CO}_2$  adsorption values at zero coverage regions are 34.5, 53.9 and 40.6  $\text{kJ mol}^{-1}$  for **1**, **2** and **3**, respectively as calculated using a virial type equation. Despite of having high interaction between the  $\text{CO}_2$  and the pore surface, the release of the gas molecules has easily been triggered by using light as a low cost and non-destructive source. *In situ* PXRD measurement of the photo-irradiated product depicts structural integrity which proves the behavior to be dynamic and localized.

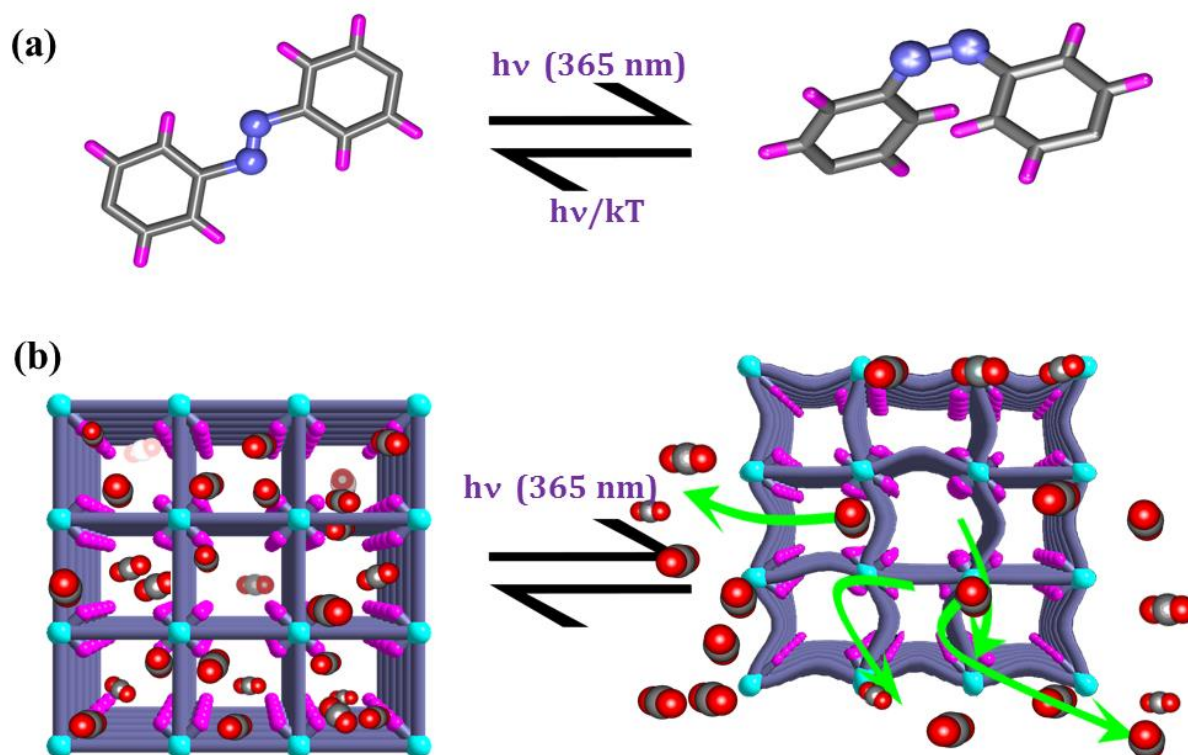


## 4.1: Introduction

With the rapid growth of industrialization, the consumption of fossil fuels is exponentially increasing, which results in releasing of large amount of CO<sub>2</sub> into the atmosphere.<sup>1</sup> Since 1991, amine scrubbing has been employed to separate CO<sub>2</sub> from the flue gas which expels out from the power plants.<sup>2</sup> In this widely used technology, at ambient temperature, CO<sub>2</sub> molecules are allowed to adsorb in a low volatile aqueous amine solution (20% monoethanolamine, commonly known as MEA).<sup>3</sup> Then the adsorbed CO<sub>2</sub> is regenerated by stripping with water vapor at 100° C to 120°C and hence it reveals the difficulty in breaking the amine–CO<sub>2</sub> generated carbamate bond. As a result, this method consumes as much as ~40% of the production costs during the liberation of adsorbed CO<sub>2</sub> from the sorbent materials.<sup>4</sup> In this regard, use of porous material as solid-state sorbents in CO<sub>2</sub> capture is an alternative cost effective novel approach.<sup>5</sup> Processes involved in releasing the captured CO<sub>2</sub>, such as vacuum or heating, are very expensive as it also requires extra energy.<sup>6</sup> So the goal is to develop new material where the releasing procedure is triggered by a cost-effective external stimulus (like natural light) that does not require extra energy from the industry.

In this context, solid porous materials like metal-organic frameworks (MOFs) or porous coordination polymers (PCPs) would be an attractive candidate for CO<sub>2</sub> capture which has already shown potential in several applications like drug delivery, catalysis, magnetism *etc.*<sup>7</sup> Furthermore, MOFs also showed great promises in CO<sub>2</sub> capture at ambient conditions as well as at high pressure and temperature. Several MOFs, with immobilized CO<sub>2</sub>-philic functional groups on the pore surface, have been reported which also showed potential in separating CO<sub>2</sub> from other gases like N<sub>2</sub>, CH<sub>4</sub> and H<sub>2</sub>. Moreover, high surface area, feasibility of tunable pore size, modifiable pore surfaces of MOF frameworks can easily be achieved by modifying the frameworks postsynthetically.<sup>8</sup> Cohen *et al.* have significantly contributed to the postsynthetic chemical modification of different types of MOF for the alteration of physical properties by introducing several functional groups to the organic linkers.<sup>9</sup> However, the implementation of light as an effective low cost, non-destructive external modulator for such modification of the physical properties is underexplored.<sup>10</sup> It is a significant challenge to develop such MOFs that possess programmable structure with

complex chemical functionalities and that also expected to offer the modulation of their physical properties in response to light as an external stimulus.<sup>11</sup> Such specific photo-responsive MOFs would show properties like molecular recognition, guest selectivity and controlled uptake and release of guest molecules over the original host framework.<sup>12</sup> However, despite of having a large library of reported MOFs, very few have demonstrated on-demand release of stored guest molecules in response to light as a controllable external stimulus.<sup>13</sup> In this regard, MOFs constructed by organic linker with azo ( $-N=N-$ ) functionalization<sup>14</sup> has depicted promise for the photo-induced controlled release of guest molecules from the pore surface. The photo-induced reversible conformational change of azobenzene (*cis-trans* isomerization)<sup>15</sup> offers photo-switchable porosity which facilitates on-demand release of the gas molecules from the porous materials (Scheme 1).<sup>13, 15c, 16</sup> Recently, Hill *et al.* reported photo-responsive dynamic framework for CO<sub>2</sub> release based on azo-functionalized linkers where the both ends are connected with the metal centers.<sup>10a</sup>



**Scheme 1:** (a) *cis-trans* isomerism of azobenzene. (b) Dynamic photo-switching in the light-responsive Metal-organic Framework (MOF) leads to instant release of CO<sub>2</sub> molecules.



This chapter demonstrates the synthesis of three new isostructural metal-organic frameworks,  $\{[\text{Mn}_3(\text{azpy})_3(\text{H}_2\text{O})_4][\text{Cr}(\text{CN})_6]_2 \cdot 2(\text{azpy}) \cdot 2\text{EtOH}\}_n$  (**1**),  $\{[\text{Co}_3(\text{azpy})_3(\text{H}_2\text{O})_4][\text{Cr}(\text{CN})_6]_2 \cdot 2(\text{azpy}) \cdot 2\text{EtOH}\}_n$  (**2**) and  $\{[\text{Zn}_3(\text{azpy})_3(\text{H}_2\text{O})_2][\text{Cr}(\text{CN})_6]_2 \cdot 2(\text{azpy}) \cdot 2\text{EtOH}\}_n$  (**3**) constructed by hexacyanochromate as a metallo-ligand and 4,4'-azobipyridine (azpy) as exobidentate pillar. As the *cis-trans* conformational change mediated by light is restricted due to the bidental coordination mode of azpy, a bending about the azo group is occurring on a local scale in a dynamic fashion which leads to the on-demand release of  $\text{CO}_2$  molecules at the ambient conditions. The *in situ* PXRD in presence of UV light measurement was performed to probe structural change which exhibits structural integrity during photo-irradiation procedure.

## 4.2: Experimental Section

### 4.2.1: Materials

All the reagents and solvents employed were commercially available and used as supplied without further purification.  $\text{MnCl}_2 \cdot 4\text{H}_2\text{O}$ ,  $\text{CoCl}_2 \cdot 4\text{H}_2\text{O}$ ,  $\text{Zn}(\text{NO}_3)_2 \cdot 6\text{H}_2\text{O}$  and  $\text{K}_3[\text{Cr}(\text{CN})_6]$  were obtained from the Aldrich Chemical Co. 4,4'-azobipyridine (azpy) had been synthesized according to the literature procedure.<sup>17</sup>

### 4.2.2: Synthesis

**4.2.2.1: Synthesis of  $\{[\text{Mn}_3(\text{azpy})_3(\text{H}_2\text{O})_4][\text{Cr}(\text{CN})_6]_2 \cdot 2(\text{azpy}) \cdot 2\text{EtOH}\}_n$  (**1**):** An aqueous solution (12.5 mL) of  $\text{K}_3[\text{Cr}(\text{CN})_6]$  (0.25 mmol, 0.0426 g) was added to an ethanolic solution (12.5 mL) of azpy (0.25 mmol, 0.0461 g) and stirred for 30 min.  $\text{MnCl}_2 \cdot 4\text{H}_2\text{O}$  (0.25 mmol, 0.0494 g) was dissolved in 12.5 ml distilled water and 2.5 mL of this metal solution was carefully layered with the 2.5 mL of mixed azpy and  $\text{K}_3[\text{Cr}(\text{CN})_6]$  solution using an ethanol : water buffer solution (1 mL, 1:1) in a crystal tube. After 15 days, reddish-orange block shaped crystals were appeared in the middle of the tube and separated and washed with ethanol. The bulk amount of the sample was prepared by direct mixing of the reagents in ethanol/water mixed solution with stirring for 24 hrs and the phase purity was checked with the PXRD and elemental analysis. This powdered sample was used for studying the different physical properties. Yield: 77%, relative to  $\text{Mn}^{\text{II}}$ . Anal. calc. for  $\text{C}_{66}\text{H}_{60}\text{N}_{32}\text{O}_6\text{Mn}_3\text{Cr}_2$ : C,

47.58; H, 3.63; N, 26.90. Found: C, 47.04; H, 3.18; N, 26.08. IR (KBr,  $\text{cm}^{-1}$ ):  $\nu(\text{H}_2\text{O})$  3510, 3426;  $\nu(\text{ArC-H})$  3044, 3015;  $\nu(\text{C}\equiv\text{N})$  2192, 2091;  $\nu(\text{ArC=C})$  1621, 1547 (Figure 1a).

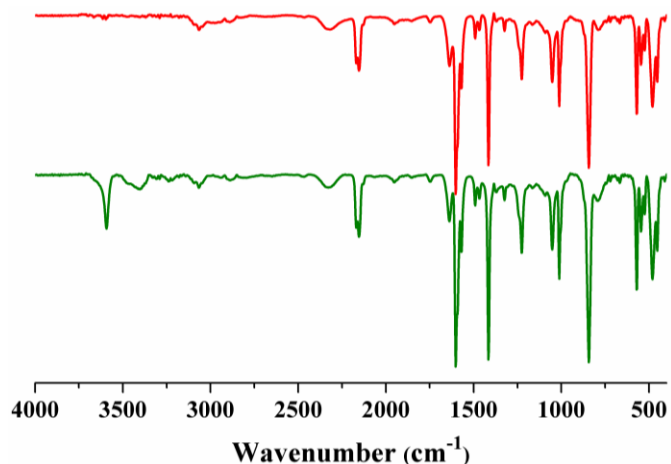


**Figure 1:** IR spectra of compound **1** (green) and **1a** (red).

**4.2.2.2: Preparation of  $\{[\text{Mn}_3(\text{azpy})_3][\text{Cr}(\text{CN})_6]_2\}_n$  (**1a**):** Compound **1a** was prepared by heating **1** at 120 °C under vacuum ( $< 10^{-1}$  Pa) for long time. During the heating period, the removed guest azpy molecules were deposited in the inner cell of the adsorption cell. The heating procedure was continued following with the change of the sample cells unless there was no trace of sublimated guest azpy molecule. The removal of the coordinated water and guest azpy and ethanol molecules was confirmed by elemental analysis, TGA and IR spectroscopy. IR (KBr,  $\text{cm}^{-1}$ ):  $\nu(\text{ArC-H})$  3041, 3034;  $\nu(\text{C}\equiv\text{N})$  2102, 2087;  $\nu(\text{ArC=C})$  1615, 1556 (Figure 1b). This powdered sample was used for different characterizations. Anal. calc. for  $\text{C}_{42}\text{H}_{24}\text{Mn}_3\text{Cr}_2\text{N}_{24}$ : C, 43.80; H, 2.28; N, 29.19. Found: C, 43.63; H, 2.29; N, 28.96.

**4.2.2.3: Synthesis of  $\{[\text{Co}_3(\text{azpy})_3(\text{H}_2\text{O})_4][\text{Cr}(\text{CN})_6]_2 \cdot 2(\text{azpy}) \cdot 2\text{EtOH}\}_n$  (**2**):** The single crystals of compound **2** were prepared by adopting similar procedure that of compound **1** where  $\text{CoCl}_2 \cdot 4\text{H}_2\text{O}$  was taken instead of  $\text{MnCl}_2 \cdot 4\text{H}_2\text{O}$ . The bulk amount of sample was prepared by direct mixing of the reagents in ethanol/water mixed solution with stirring for 24 h and the phase purity was checked with the PXRD and elemental analysis. This powdered sample was used for studying of different physical properties. Yield: 74%, relative to  $\text{Co}^{\text{II}}$ . Anal. calc. for  $\text{C}_{66}\text{H}_{60}\text{N}_{32}\text{O}_6\text{Co}_3\text{Cr}_2$ : C, 47.24; H, 3.61; N, 26.71. Found: C, 46.98; H, 3.01; N, 26.72. IR (KBr,  $\text{cm}^{-1}$ ):  $\nu(\text{H}_2\text{O})$  3545, 3486;  $\nu(\text{ArC-H})$  3051, 3034;  $\nu(\text{C}\equiv\text{N})$  2254, 2053;  $\nu(\text{ArC=C})$  1619, 1598, 1557 (Figure 2a).

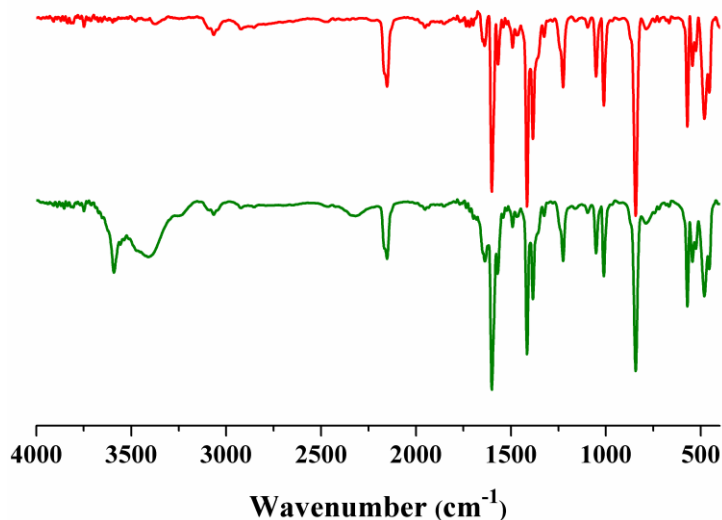


Figure 2: IR spectra of compound **2** (green) and **2a** (red).

**4.2.2.4: Preparation of  $\{[\text{Co}_3(\text{azpy})_3][\text{Cr}(\text{CN})_6]_2\}_n$  (**2a**):** Compound **2a** was prepared by following the similar procedure of preparing compound **1a**. The removal of the coordinated water and guest azpy and ethanol molecules was confirmed by elemental analysis, TGA and IR spectroscopy. This powdered sample was used for different characterizations. IR (KBr,  $\text{cm}^{-1}$ ):  $\nu(\text{ArC-H})$  3038;  $\nu(\text{C}\equiv\text{N})$  2102, 2098;  $\nu(\text{ArC}=\text{C})$  1620, 1575 (Figure 1b). Anal. calc. for  $\text{C}_{42}\text{H}_{24}\text{Co}_3\text{Cr}_2\text{N}_{24}$ : C, 44.03; H, 2.11; N, 29.34. Found: C, 43.50; H, 2.25; N, 28.89.

**4.2.2.5: Synthesis of  $\{[\text{Zn}_3(\text{azpy})_3(\text{H}_2\text{O})_2][\text{Cr}(\text{CN})_6]_2 \cdot 2(\text{azpy}) \cdot 2\text{EtOH}\}_n$  (**3**):** The single crystals of compound **3** were grown by adopting similar procedure that of compound **1** where  $\text{Zn}(\text{NO}_3)_2 \cdot 6\text{H}_2\text{O}$  was taken in place of  $\text{MnCl}_2 \cdot 4\text{H}_2\text{O}$ . The bulk amount of the sample was prepared by direct mixing of the reagents in ethanol/water mixed solution with stirring for 24 h and the phase purity was checked with the PXRD and elemental analysis. This powdered sample was used for studying of different physical properties. Yield: 78%, relative to  $\text{Zn}^{\text{II}}$ . Anal. calc. for  $\text{C}_{66}\text{H}_{56}\text{N}_{32}\text{O}_4\text{Zn}_3\text{Cr}_2$ : C, 47.71; H, 3.40; N, 26.98. Found: C, 47.18; H, 3.01; N, 26.72. IR (KBr,  $\text{cm}^{-1}$ ):  $\nu(\text{H}_2\text{O})$  3510, 3426;  $\nu(\text{ArC-H})$  3044, 3015;  $\nu(\text{C}\equiv\text{N})$  2075;  $\nu(\text{ArC}=\text{C})$  1612, 1536 (Figure 3a).

**4.2.2.6: Preparation of  $\{[\text{Zn}_3(\text{azpy})_3][\text{Cr}(\text{CN})_6]_2\}_n$  (**3a**):** Compound **3a** was prepared by following the similar procedure of preparing compound **1a**. The removal of the coordinated water and guest azpy and ethanol molecules was confirmed by elemental analysis, TGA and

IR spectroscopy. IR (KBr,  $\text{cm}^{-1}$ ):  $\nu(\text{ArC-H})$  3102, 3074;  $\nu(\text{C}\equiv\text{N})$  2075;  $\nu(\text{ArC}=\text{C})$  1611, 1537 (Figure 1b). This powdered sample was used for different characterizations. Anal. calc. for  $\text{C}_{42}\text{H}_{24}\text{Zn}_3\text{Cr}_2\text{N}_{24}$ : C, 42.64; H, 2.22; N, 28.42. Found: C, 42.03; H, 2.25; N, 28.67.

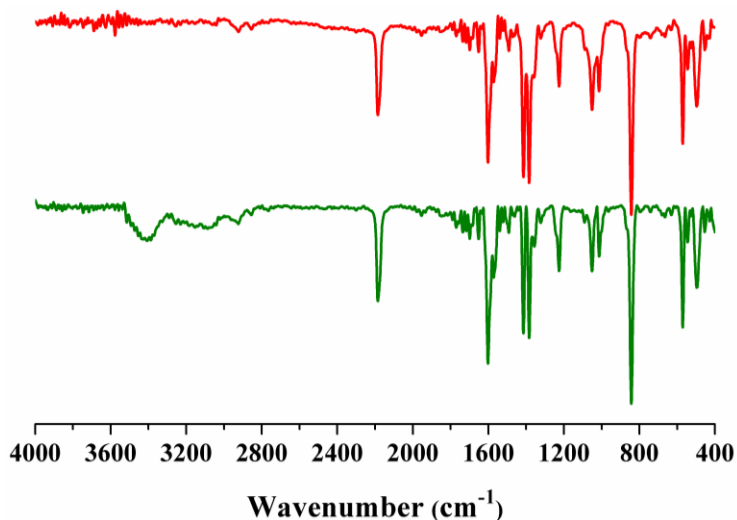


**Figure 3:** IR spectra of compound **3** (green) and **3a** (red).

#### **4.2.3: Physical Measurements**

The elemental analyses of each compounds and their different state were carried out on a Thermo Fisher Flash 2000 Elemental Analyser. Infra-red (IR) spectroscopic studies were carried out in the mid-IR region by making samples with KBr pellet (Bruker IFS-66v). Thermogravimetric analysis (TGA) was carried out (Mettler Toledo) in nitrogen atmosphere (flow rate =  $50 \text{ ml min}^{-1}$ ) in the temperature range  $30 - 700 \text{ }^\circ\text{C}$  (heating rate =  $5^\circ\text{C min}^{-1}$ ). Powder XRD pattern of the products were recorded by using  $\text{Cu-K}\alpha$  radiation (Bruker D8 Discover; 40 kV, 30 mA).

#### **4.2.4: Single Crystal X-ray Diffraction**

Suitable single crystals of compound **1**, **2** and **3** were mounted on a thin glass fiber with commercially available super glue. X-ray single crystal data were collected on a Bruker Smart-CCD diffractometer equipped with a normal focus, 2.4 kW sealed tube X-ray source with graphite monochromated  $\text{Mo-K}\alpha$  radiation ( $\lambda = 0.71073 \text{ \AA}$ ) operating at 50 kV and 30 mA. The program SAINT<sup>18</sup> was used for integration of diffraction profiles and absorption correction was made with SADABS<sup>19</sup> program. All the structure were solved by SIR 92<sup>20</sup>

and refined by full matrix least square method using SHELXL.<sup>21</sup> All the hydrogen atoms for **1-3** were fixed by HFIX and placed in ideal positions. Potential solvent accessible area or void space was calculated using the PLATON<sup>22</sup> multipurpose crystallographic software. All crystallographic and structure refinement data of **1**, **2** and **3** are summarized in Table 1. Selected bond distances and angles are shown in Table 2-7. All calculations were carried out using SHELXL 97,<sup>21</sup> PLATON,<sup>22</sup> SHELXS 97<sup>21</sup> and WinGX system, Ver 1.80.01.<sup>23</sup>

**Table 1:** Crystal data and structure refinement parameters for **1**, **2** and **3**.

Parameters	<b>1</b>	<b>2</b>	<b>3</b>
Empirical formula	C <sub>66</sub> H <sub>60</sub> N <sub>32</sub> O <sub>6</sub> Mn <sub>3</sub> Cr <sub>2</sub>	C <sub>66</sub> H <sub>60</sub> N <sub>32</sub> O <sub>6</sub> Co <sub>3</sub> Cr <sub>2</sub>	C <sub>66</sub> H <sub>56</sub> N <sub>32</sub> O <sub>4</sub> Zn <sub>3</sub> Cr <sub>2</sub>
<i>M</i>	1666.28	1678.19	1697.53
Crystal system	Monoclinic	Monoclinic	Monoclinic
Space group	<i>P2<sub>1</sub>/c</i> (No. 14)	<i>P2<sub>1</sub>/c</i> (No. 14)	<i>P2<sub>1</sub>/c</i> (No. 14)
<i>a</i> (Å)	13.5794(6)	13.2123(3)	13.2946(2)
<i>b</i> (Å)	18.3313(9)	18.0828(4)	17.9937(3)
<i>c</i> (Å)	16.5853(8)	16.1174(4)	15.8326(2)
<i>α</i> (°)	90	90	90
<i>β</i> (°)	101.195(2)	100.824(1)	90.159(1)
<i>γ</i> (°)	90	90	90
<i>V</i> (Å <sup>3</sup> )	4050.0(3)	3782.19(15)	3787.45(10)
<i>Z</i>	2	2	2
<i>T</i> (K)	295	293	293
<i>λ</i> (Mo-K <sub>α</sub> )	0.71073	0.71073	0.71073
<i>D<sub>c</sub></i> (g cm <sup>-3</sup> )	1.366	1.449	1.448
<i>μ</i> (mm <sup>-1</sup> )	0.782	0.995	1.282
<i>θ</i> <sub>max</sub> (°)	28.3	31.5	29.5
Total data	78786	80013	56274
Data [ <i>I</i> > 2σ( <i>I</i> )]	6892	4974	5677
Uniq. Data	10049	12060	10393
<i>R</i> <sub>int</sub>	0.075	0.140	0.079
<i>R</i> <sup><i>a</i></sup>	0.0513	0.0654	0.0540
<i>R</i> <sub>w</sub> <sup><i>b</i></sup>	0.1686	0.2228	0.1575
<i>GOF</i>	1.06	1.21	1.02
Min./Max. Resd.	-1.03, 1.19	-0.63, 1.21	-0.57, 1.17
Dens. [e/Å <sup>3</sup> ]			

$$^a R = \sum ||F_o| - |F_c|| / \sum |F_o| ; \quad ^b R_w = [\sum \{w(F_o^2 - F_c^2)^2\} / \sum \{w(F_o^2)^2\}]^{1/2}$$

**Table 2:** Selected bond distances (Å) for compound 1.

Bonds	Distance (Å)	Bonds	Distance (Å)
Mn2–O2W	2.269(2)	Mn2–N6	2.187(3)
Mn2–N11	2.297(3)	Mn2–O2W_e	2.269(2)
Mn2–N6_e	2.187(3)	Mn2–N11_e	2.297(3)
Mn3–O1W	2.236(2)	Mn3–N5	2.201(3)
Mn3–N7	2.301(3)	Mn3–N8_a	2.284(3)
Mn3–N3_c	2.148(3)	Mn3–N4_g	2.184(3)
Cr1–C1	2.074(4)	Cr1–C2	2.070(4)
Cr1–C3	2.062(3)	Cr1–C4	2.057(3)
Cr1–C5	2.074(3)	Cr1–C6	2.073(3)

**Table 3:** Selected bond angles (°) for compound 1.

Angles	Degree (°)	Angles	Degree (°)
N4_g–Mn3–N8_a	90.43(10)	N3_c–Mn3–N4_g	92.24(11)
C1–Cr1–C2	177.93(13)	C1–Cr1–C3	89.70(12)
C1–Cr1–C4	90.74(12)	N6–Mn2–N11	89.35(9)
C1–Cr1–C5	90.85(12)	C1–Cr1–C6	89.90(12)
N6–Mn2–N6_e	180.00	C2–Cr1–C3	90.12(12)
N6–Mn2–N11_e	90.66(9)	C2–Cr1–C4	91.32(12)
C2–Cr1–C5	89.18(12)	N6_e–Mn2–N11	90.66(9)
C2–Cr1–C6	88.04(12)	N11–Mn2–N11_e	180.00
C3–Cr1–C4	92.01(12)	C3–Cr1–C5	175.86(12)
C3–Cr1–C6	87.87(12)	N6_e–Mn2–N11_e	89.35(9)
C4–Cr1–C5	92.10(11)	C4–Cr1–C6	179.35(11)
C5–Cr1–C6	88.03(11)	N5–Mn3–N7	89.75(10)
N5–Mn3–N8_a	89.56(10)	N3_c–Mn3–N5	103.02(10)
N4_g–Mn3–N5	164.74(10)	N7–Mn3–N8_a	178.33(10)
Mn3_b–N8–C16	121.7(2)	Mn2–N11–C17	119.9(2)

**Table 4:** Selected bond distances (Å) for compound 2.

Bonds	Distance (Å)	Bonds	Distance (Å)
Co1–N6	2.151(3)	Co1–N7	2.225(4)
Co1–N8	2.245(4)	Co1–N2_c	2.117(4)
Co1–N4_g	2.122(3)	Co2–O2W	2.223(3)
Co2–N1	2.130(3)	Co2–N11	2.234(4)
Co2–O2W_f	2.223(3)	Co2–N1_f	2.130(3)
Co2–N11_f	2.234(4)	Cr1–C1	2.025(5)
Cr1–C2	2.033(5)	Cr1–C3	2.037(5)
Cr1–C4	2.008(5)	Cr1–C5	2.040(7)
Cr1–C6	2.040(4)		

**Table 5:** Selected bond angles (°) for compound 2.

Angles	Degree (°)	Angles	Degree (°)
N1_f-Co2-N11_f	91.12(14)	C1-Cr1-C2	86.88(17)
C1-Cr1-C3	87.79(18)	C1-Cr1-C4	179.11(19)
N6-Co1-N7	89.99(16)	C1-Cr1-C5	90.5(2)
N6-Co1-N8	89.57(16)	C1-Cr1-C6	88.69(17)
N2_c-Co1-N6	103.06(16)	C2-Cr1-C3	90.3(2)
N4_g-Co1-N6	164.82(14)	C2-Cr1-C4	92.91(18)
N7-Co1-N8	178.37(14)	C2-Cr1-C5	89.5(2)
N2_c-Co1-N7	91.18(15)	C2-Cr1-C6	175.50(19)
N4_g-Co1-N7	89.79(16)	C3-Cr1-C4	91.3(2)
N2_c-Co1-N8	90.44(15)	C3-Cr1-C5	178.3(2)
N4_g-Co1-N8	90.23(16)	C3-Cr1-C6	88.73(19)
N2_c-Co1-N4_g	92.13(16)	C4-Cr1-C5	90.4(2)
C4-Cr1-C6	91.51(17)	C5-Cr1-C6	91.3(2)
N1-Co2-N11	91.12(14)	N1-Co2-N1_f	180.00
N1-Co2-N11_f	88.88(14)	Co2-N1-C1	166.3(4)
Co1_d-N2-C2	171.9(4)	N1_f-Co2-N11	88.88(14)
Co1_h-N4-C4	168.5(4)	N11-Co2-N11_f	180.00
Co1-N6-C6	146.8(3)	Co1-N7-C7	121.3(4)

**Table 6:** Selected Bond Distances (Å) for compound 3.

Bonds	Distance (Å)	Bonds	Distance (Å)
Zn1-N1	2.036(3)	Zn1-N9	2.208(4)
Zn1-N10_a	2.212(4)	Zn1-N5_e	2.045(4)
Zn1-N6_h	2.022(3)	Zn2-O1W	2.202(3)
Zn2-N4	2.079(3)	Zn2-N7	2.188(4)
Zn2-O1W_d	2.202(3)	Zn2-N4_d	2.079(3)
Zn2-N7_d	2.188(4)	Cr1-C1	1.910(5)
Cr1-C2	1.865(5)	Cr1-C3	1.872(5)
Cr1-C4	1.899(5)	Cr1-C5	1.929(4)
Cr1-C6	1.923(4)		

**Table 7:** Selected bond angles (°) for compound 3.

Angles	Degree (°)	Angles	Degree (°)
N1-Zn1-N9	87.45(14)	N1-Zn1-N10_a	87.43(14)
N1-Zn1-N5_e	105.57(14)	N1-Zn1-N6_h	134.65(14)
N9-Zn1-N10_a	171.69(13)	N5_e-Zn1-N9	93.87(15)
N6_h-Zn1-N9	89.64(14)	N5_e-Zn1-N10_a	93.80(15)
C3-Cr1-C5	88.9(2)	N6_h-Zn1-N10_a	89.31(14)
C3-Cr1-C6	90.9(2)	N5_e-Zn1-N6_h	119.78(13)
C4-Cr1-C5	87.32(15)	C4-Cr1-C6	86.39(18)
C5-Cr1-C6	173.70(17)	N4-Zn2-N7	90.03(14)
N4-Zn2-N4_d	180.00	N4-Zn2-N7_d	89.97(14)

Zn1-N1-C1	156.1(3)	N4_d-Zn2-N7	89.97(14)
Zn2-N4-C4	178.7(3)	N7-Zn2-N7_d	180.00 Z
n1_e-N5-C5	176.8(3)	Zn1_g-N6-C6	166.9(3)
N4_d-Zn2-N7_d	90.03(14)	C1-Cr1-C2	90.74(19)
C1-Cr1-C3	90.88(19)	C1-Cr1-C4	179.83(14)

Symmetry code: a = -1+x,y,z; b = 1+x,y,z; c = -x,-1/2+y,3/2-z; d = -x,1/2+y,3/2-z; e = -x,1-y,1-z; f = -1-x,1-y,1-z; g = x,1/2-y,-1/2+z; h = x,1/2-y,1/2+z; i = -x,1-y,1-z; j = 1-x,1-y,1-z.

#### 4.2.5: Adsorption Study

N<sub>2</sub> (77 K), CO<sub>2</sub> (195 K, 273 K and 283 K) adsorption studies were carried out with the deguest samples (*i.e.* **1a**, **2a** and **3a**; prepared at 418 K under high vacuum (<10<sup>-1</sup> Pa) for long time) by using AUTOSORB IQ2 instrument. Dead volume was measured with helium gas. The adsorbents were placed into the sample tubes, then the change of the pressure was monitored and the degree of adsorption was determined by the decrease in pressure at the equilibrium state. All operations were computer controlled and automatic.

### 4.3: Results and Discussion

#### 4.3.1: Structural description of {[Mn<sub>3</sub>(azpy)<sub>3</sub>(H<sub>2</sub>O)<sub>4</sub>][Cr(CN)<sub>6</sub>]<sub>2</sub>·2(azpy)·2EtOH}<sub>n</sub> (**1**):

Compound **1** crystallizes in a monoclinic crystal system with *P*2<sub>1</sub>/*c* space group. There are two crystallographically independent Mn<sup>II</sup> centers (Mn1 and Mn2) connected by [Cr(CN)<sub>6</sub>]<sup>3-</sup> metalloligand (Figure 4a) in two directions to form a 2D sheet in the crystallographic *bc* plane (Figures 4b). Each octahedral Mn1 is connected to three different [Cr(CN)<sub>6</sub>]<sup>3-</sup> moieties (N2, N4 and N6), two azpy (N7, N8) and one water molecule (O1w).

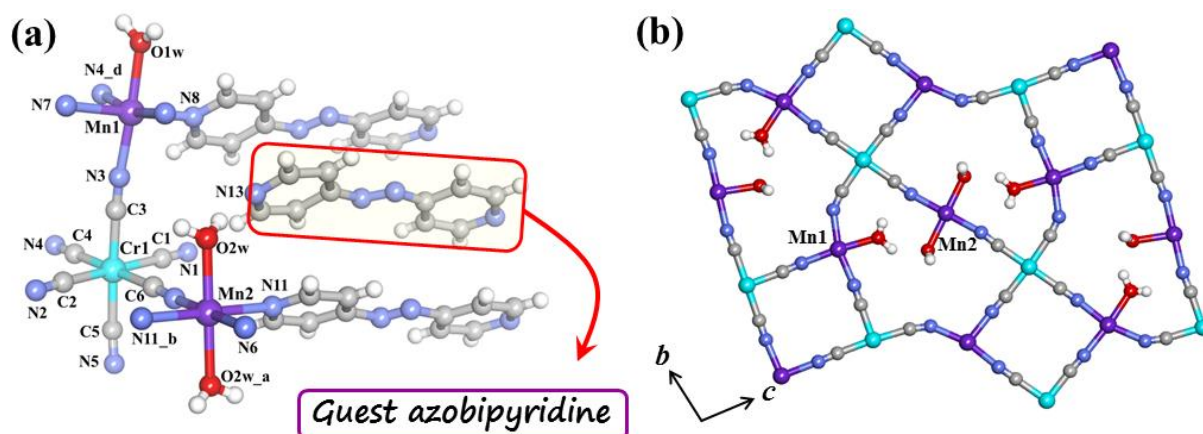


**Figure 4:** (a) Asymmetric unit of compound **1**, (b) 2D layers formed by the connection between Mn<sup>II</sup> and Cr<sup>III</sup> centers through the equatorial cyanide ligands of hexacyanochromate.



The other octahedral Mn2 is located in a special position and is connected to two  $[\text{Cr}(\text{CN})_6]^{3-}$  (N6, N6\*), two water molecules (O2w and O2w\*; \* represents the symmetry related counterpart) in equatorial position, whereas the axial sites are occupied by N11 and N11\* from two azpy pillars (Figure 5a). The Cr–C bond distance varies from 2.057(3) to 2.074(4) Å, whereas the Mn–N bond lengths are in the range of 2.187(3) to 2.297(3) Å. In the 2D layer, a 12 membered  $\text{Mn}_2\text{Cr}_2(\text{CN})_4$  ring is surrounded by a 18 membered  $\text{Mn}_1\text{Co}_2\text{Cr}_3(\text{CN})_6$  and such 2D sheets are connected by azpy pillars (along *a* axis) through the Mn1 and Mn2 centers to form a 3D pillared-layer framework. The framework has two different channels along *a* direction (Figures 5b, c and 6); the larger one with dimension  $5.9 \times 4.3 \text{ \AA}^2$  is occupied by the guest azpy molecule, whereas the smaller one ( $2.0 \times 2.0 \text{ \AA}^2$ ) is occupied by guest ethanol molecules. Compound **1** also possesses a channel along *b* direction with a dimension of  $4.1 \times 3.2 \text{ \AA}^2$  (Figure 6b). Calculation using PLATON<sup>22</sup> shows 43% void space present in the guest-removed framework (*i.e.* compound **1a**).

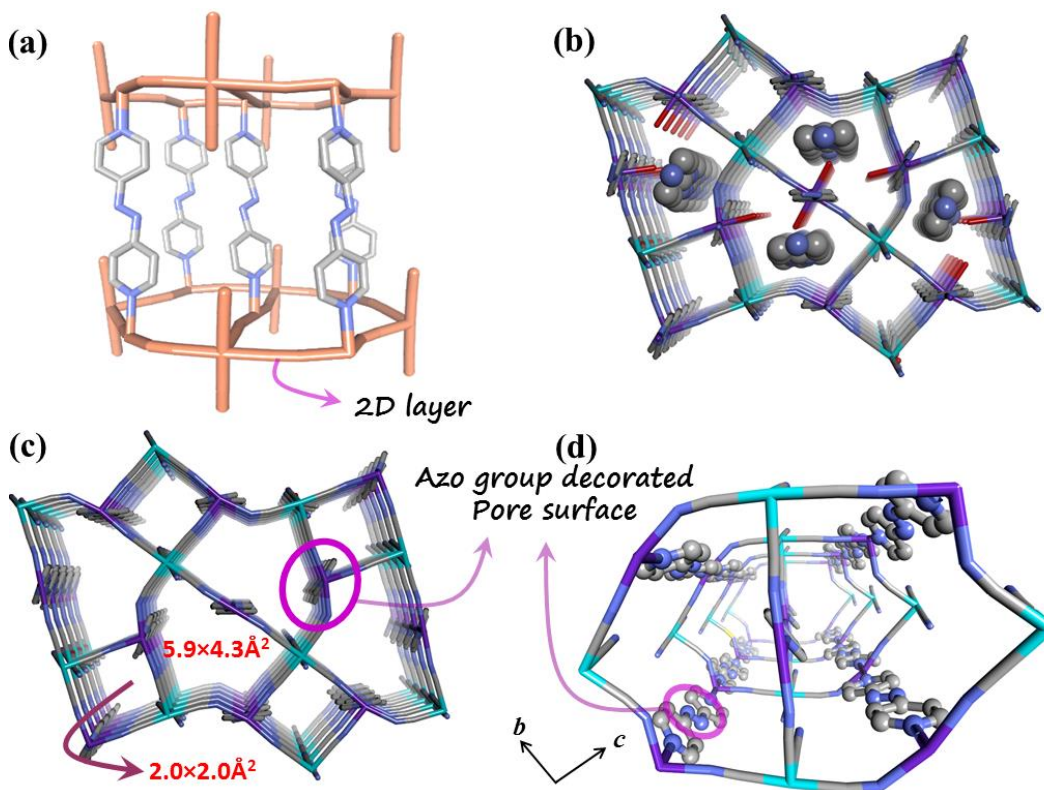


**Figure 5:** (a) View of the pillared-layer structure by connecting the 2D layers through azpy linker. (b) View of the 3D framework along *a* direction. Guest azpy ligands (CPK model) are aligned in the bigger 1D channel, (c) After removing the coordinated water and guest molecules compound **1** offers two kind of 1D channel along *a* direction. (d) The pore surface of compound **1** which is decorated with azo-functionalization.

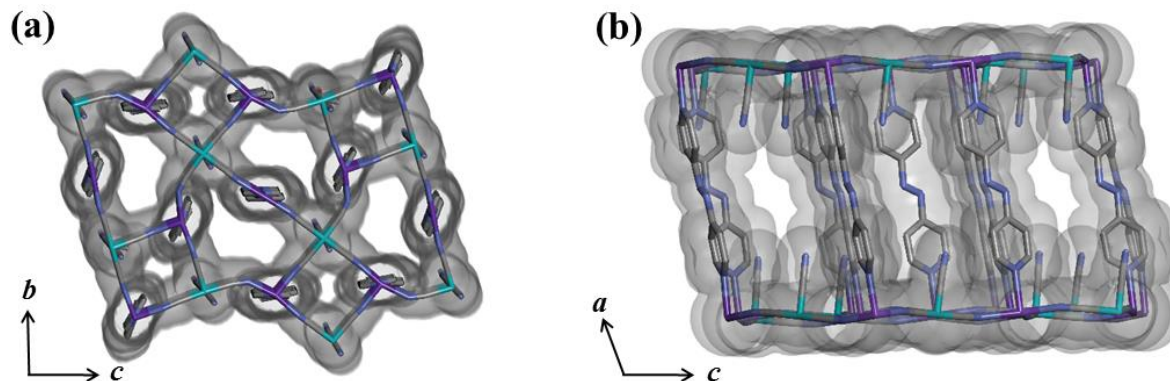


**Figure 6:** View of the pore surface of compound **1a** along *a* (a) and *b* (b) directions after adding the van der Waals radius.

The guest azpy molecules are present in a face-to-face arrangement with the pillared azpy molecules ( $c_g \cdots c_g$  distances are in the range of 3.83–3.96 Å) mediated by  $\pi \cdots \pi$  interaction. Such an arrangement is also supported by H-bonding between the coordinated water molecules (O1w) and nitrogen atom of the guest azpy. It is worth mentioning that, the 1D channel created after removing the guest azpy molecules is decorated with the azo groups (Figure 5d) of pillar azpy linkers which increase the polarity of the pore surface.

#### 4.3.2: Structural description of $\{[\text{Co}_3(\text{azpy})_3(\text{H}_2\text{O})_4][\text{Cr}(\text{CN})_6]_2 \cdot 2(\text{azpy}) \cdot 2\text{EtOH}\}_n$ (**2**):

Compound **2** is isostructural with compound **1** and it also crystallizes in a monoclinic crystal system with  $P2_1/c$  space group (Figure 7a).

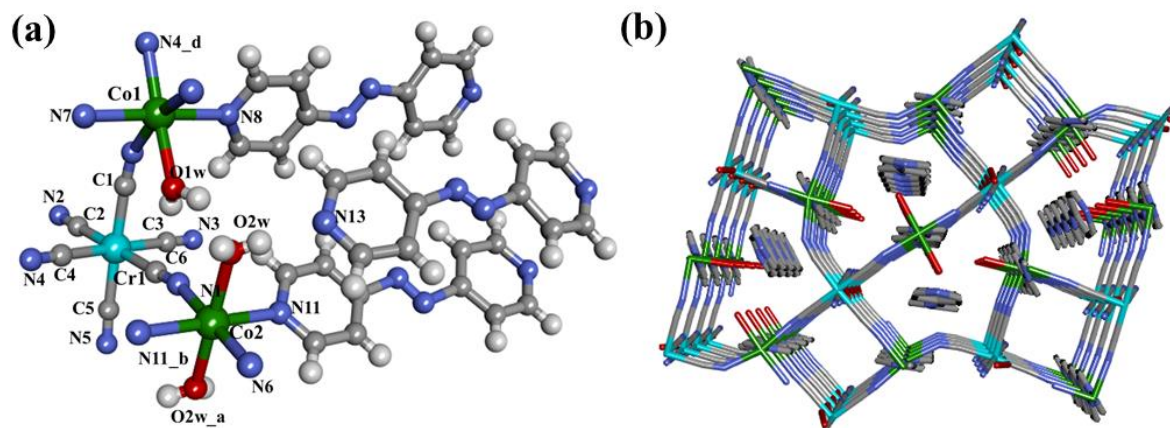


**Figure 7:** (a) Asymmetric unit of compound **2**, (b) View of the 3D framework along *a* direction.

Briefly, the Cr–C and Co–N bond lengths varies from 2.008(5) to 2.037(5) and 2.117(4) to 2.245(4) respectively whereas the distance between the 2D layer along azpy linker is 13.212

(4) Å. Similar to compound **1**, compound **2** offers 44.3 % void space after removing the coordinated water and guest ethanol and azpy molecules, as calculated from PLATON. The guest removed framework possess two different channels along *a* direction; the larger one with dimension  $5.8 \times 4.4 \text{ \AA}^2$  is occupied by the guest azpy molecule, whereas the smaller one ( $2.0 \times 2.0 \text{ \AA}^2$ ) is occupied by guest ethanol molecules (Figure 7b). Compound **2** also possesses a channel along *b* direction with a dimension of  $4.0 \times 3.3 \text{ \AA}^2$ .

#### 4.3.3: Structural description of $\{[\text{Zn}_3(\text{azpy})_3(\text{H}_2\text{O})_2][\text{Cr}(\text{CN})_6]_2 \cdot 2(\text{azpy}) \cdot 2\text{EtOH}\}_n$ (**3**):

Compound **3** is also isostructural with compound **1** and it also crystallizes in a monoclinic crystal system with  $P2_1/c$  space group (Figure 8a). Briefly, the Cr–C and Zn–N bond lengths varies from

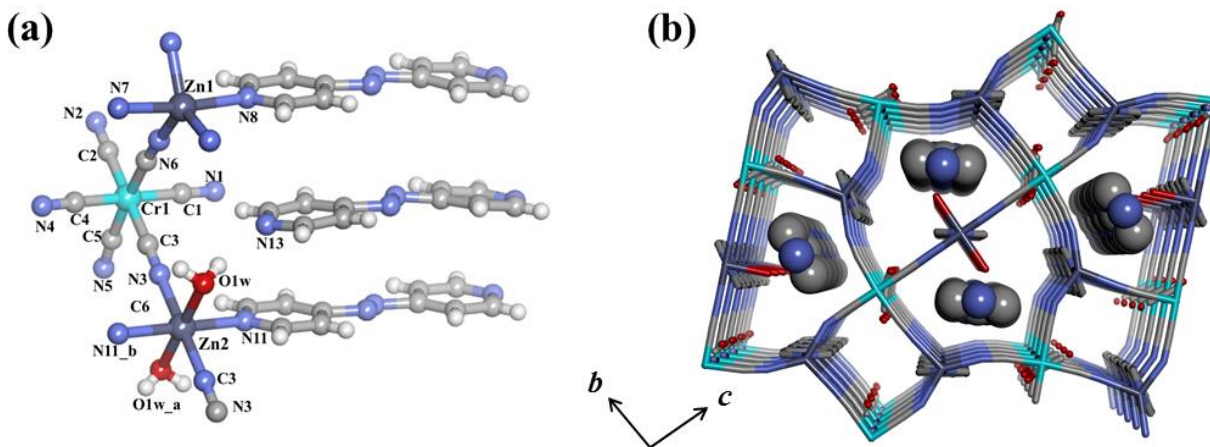


**Figure 8:** (a) Asymmetric unit of compound **3**, (b) 3D pillared-layer porous structure of compound **3** where the 1D channels are filled with guest azpy and ethanol molecules.

1.865(5) to 1.929(4) and 2.022(3) to 2.208(4), respectively, whereas the distance between the 2D layer along azpy linker is 13.295(6) Å. However, it is worth to mention that, unlike compound **1** or **2**, in compound **3** Zn(1) center is penta-coordinated without coordinated water molecules and shows trigonal bipyramidal geometry. Compound **3** also have two kinds of 1D channel along *a* direction ( $5.6 \times 4.4 \text{ \AA}^2$  and  $2.0 \times 2.0 \text{ \AA}^2$ ; Figure 8b) along with the presence of another 1D channel along *b* direction ( $3.9 \times 3.3 \text{ \AA}^2$ ). After removing the coordinated water molecules and guest ethanol and azpy molecules compound **3** offers 39.1 % void space to the total cell volume.

#### 4.3.4: Framework stability: Thermogravimetric (TG) and PXRD analysis

Thermal studies were carried out to analyse the stability and integrity of the frameworks. TGA analysis for **1**, **2**, and **3** showed step-wise release of guest EtOH, azpy and coordinated water molecules in the temperature range 40-280 °C. The weight loss in the first step (cal. 5.9%, obs. 6.0% for **1**; cal. 5.7%, obs. 5.6% for **2**; and cal. 5.5%, obs. 5.1% for **3**) can be attributed to the release of guest ethanol molecules. The framework releases coordinated water and guest azpy molecules in temperature range of 180 to 250 °C. The deguest is stable upto 350 °C. The TGA profile of compound **1** has been shown in Figure 9.

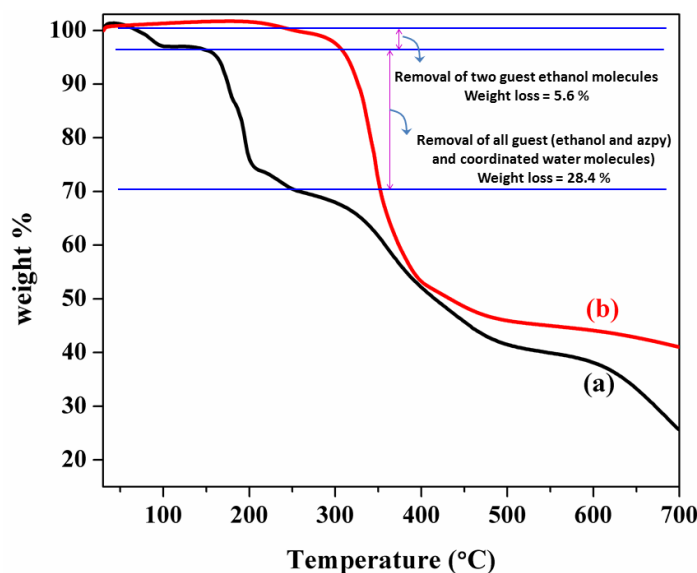


**Figure 9:** TGA profile of **1** (black) and **1a** (red) recorded under N<sub>2</sub> atmosphere in the temperature range 30 – 700 °C. Similar type of TGA profiles were also obtained for compound **2** and **3**.

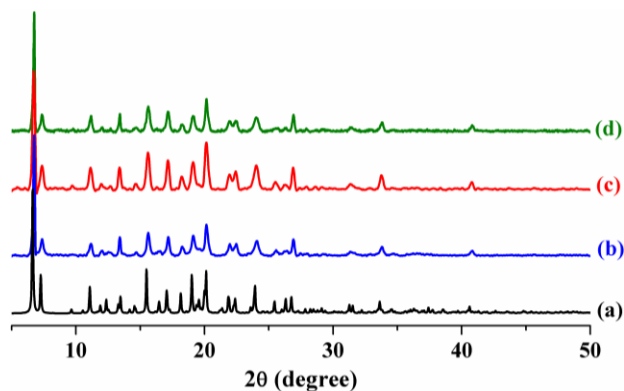


**Figure 10:** PXRD patterns of compounds **1** in different conditions; (a) simulated, (b) As-prepared (c) activated at 120 °C under vacuum, and (d) exposed to water vapour for 2 days.

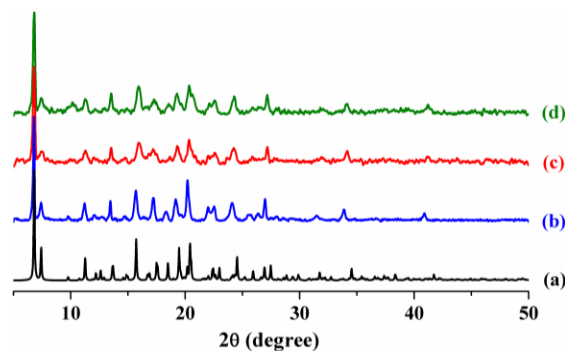


**Figure 11:** PXRD patterns of compounds **2** in different conditions; (a) simulated, (b) As-prepared (c) activated at 120 °C under vacuum, and (d) exposed to water vapour for 2 days.

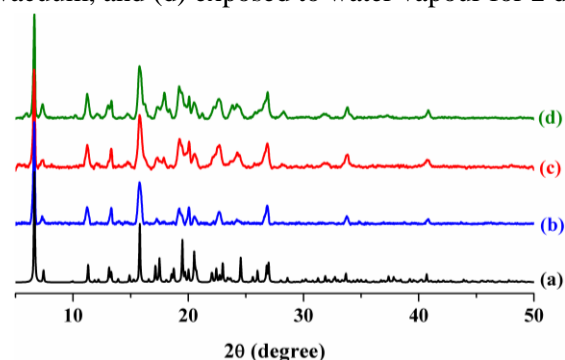


**Figure 12:** PXRD patterns of compounds **3** in different conditions; (a) simulated, (b) As-prepared (c) activated at 120 °C under vacuum, and (d) exposed to water vapour for 2 days.

The PXRD patterns of compounds **1**, **2**, and **3** are shown in Figures 10 and 12. Good correspondence of the different peak positions in the simulated and as-synthesized patterns suggests the phase purity of the as-prepared compounds. Powder X-ray diffraction (PXRD) patterns of **1a**, **2a**, and **3a** were recorded after heating the as-synthesized sample at 120 °C under vacuum. The patterns suggest that the 3D framework structures remain intact even after the removing of coordinated water and guest molecules. We have also exposed the deguest samples to water vapour for two days and these samples show almost similar patterns to the as-synthesized compounds suggesting structural stability in presence of water molecules.

#### 4.3.5 Adsorption Study

Removal of coordinated water, guest azpy and ethanol molecules offers 1D channel along two directions which encouraged us to study the permanent porosity and storage capacity of compound **1a**, **2a** and **3a**.

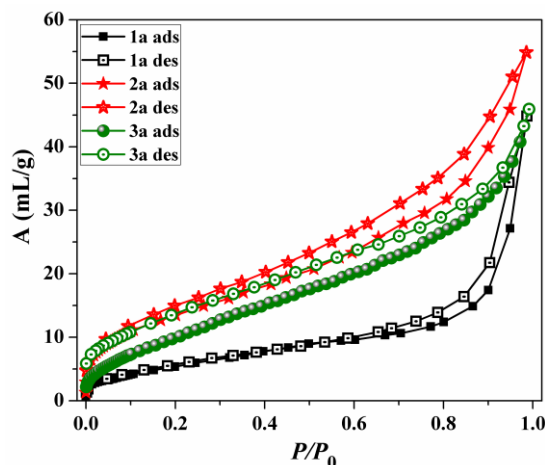


**Figure 13:**  $N_2$  adsorption isotherm of compound **1a** (black square), **2a** (red star) and **3a** (green circle) measured at 77K.  $P_0$  is the atmospheric pressure.

$N_2$  adsorption measurement at 77 K shows a typical type-II profile which ends with a final uptake of 44 mL/g (**1a**), 55 mL/g (**2a**) and 48 mL/g (**3a**) (Figure 13). Hysteresis in the sorption profiles is suggesting the presence of high diffusion barrier for  $N_2$  in the deguest framework. The sudden increased uptake at around  $P/P_0 = 0.88$  is due to the pore filling of  $N_2$  molecules at higher pressure.

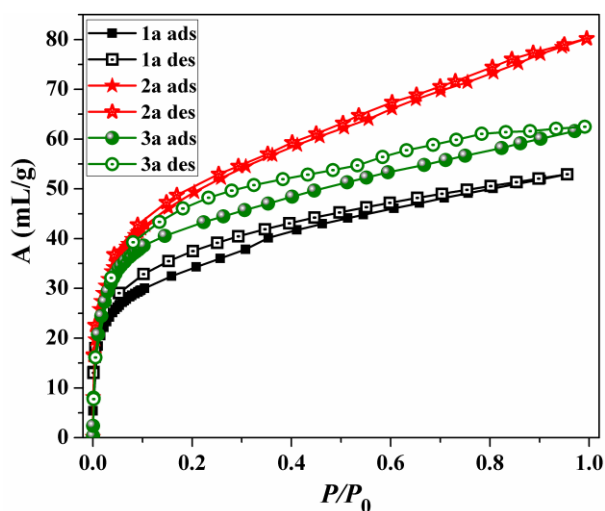


**Figure 14:**  $CO_2$  adsorption isotherm of compound **1a** (black square), **2a** (red star) and **3a** (green circle) measured at 195 K.  $P_0$  is the atmospheric pressure.

On the contrary,  $CO_2$  adsorption measurement at 195 K shows a typical type-I profile with a reasonable amount of uptake at low pressure regions (Figure 14). Compound **1a**, **2a** and **3a** adsorbs 27, 40 and 35 mL/g respectively at  $P/P_0 = 0.1$  ( $\approx 80$  torr). After steep uptake

at low pressure, a gradual increase in the uptake profiles were observed with increase in pressure which ends to final amount of 51, 82 and 63 mL/g respectively for **1a**, **2a** and **3a**. The BET surface area from the CO<sub>2</sub> adsorption isotherms were calculated to 234, 285 and 242 m<sup>2</sup>/g respectively. The realization of permanent porosity of all the frameworks from CO<sub>2</sub> study at 195 K prompted us to analyze the CO<sub>2</sub> storage capacity at 273 and 283 K upto 1 bar. The CO<sub>2</sub> adsorption studies at 273 K showed the final uptake of 4.9 wt% (25 mL/g), 6.3 wt% (32 mL/g) and 5.5 wt% (28 mL/g) at 760 torr respectively for **1a**, **2a** and **3a**. Further, we have also investigated CO<sub>2</sub> adsorption properties at 283 K which show final uptake of 4.2 wt% (22 mL/g), 5.5 wt% (27 mL/g) and 5.4 wt% (25 mL/g) for **1a**, **2a** and **3a** (Figure 15a-c) respectively. To estimate the CO<sub>2</sub>-framework interaction, we have used a virial type expression<sup>7m, 24</sup> of the following type to fit the combined isotherm data collected at 273 and 283 K for CO<sub>2</sub> (Figure 16-18).

$$\ln(P) = \ln(A) + \frac{1}{T} \sum_{i=0}^m a_i A^i + \sum_{i=0}^n b_i A^i \dots\dots\dots(1)$$

Here,  $P$  is the pressure expressed in torr,  $A$  is the amount adsorbed in mmol/g,  $T$  is the temperature in K,  $a_i$  and  $b_i$  are virial coefficients, and  $m$ ,  $n$  represent the number of coefficients required to adequately describe the isotherms. The value of  $m$  and  $n$  was gradually increased until the contribution of extra added  $a$  and  $b$  coefficients were negligible towards the overall final fit. The values of the virial coefficient  $a_i$  were taken to calculate the isosteric heat of adsorption using the following expression.

$$Q_{st} = -R \sum_{i=0}^m a_i A^i \dots\dots\dots(2)$$

$Q_{st}$  is the coverage dependent isosteric heat of adsorption and  $R$  is the universal gas constant.

The isosteric heat of adsorption ( $Q_{st}$ ) for CO<sub>2</sub> is estimated to be 34.5, 53.9 and 40.6 kJ mol<sup>-1</sup> for **1a**, **2a** and **3a**, respectively at zero coverage (Figure 15d). Comparatively higher heat of adsorption values refer to the strong interaction operating between the pore surface and CO<sub>2</sub> molecules which further reflects the difficulties related to the release of gas molecules.

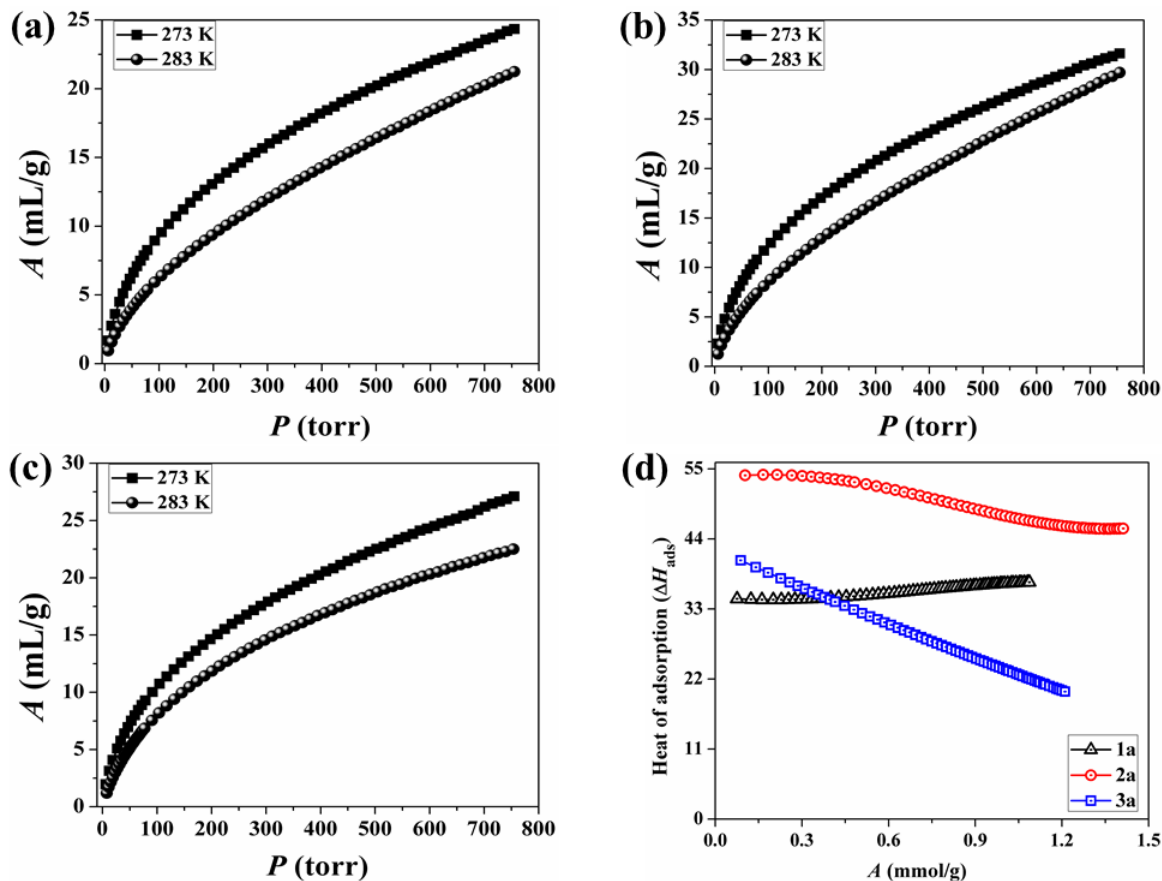


**Figure 15:** CO<sub>2</sub> adsorption isotherms of compound **1a** (a), **2a** (b) and **3a** (c) measured at 273 K (black square) and 283 K (black circle), (d) Change of enthalpy of CO<sub>2</sub> adsorption based on loading calculated from the data measured at 273 and 283 K.  $P_0 = 760$  mm of Hg.

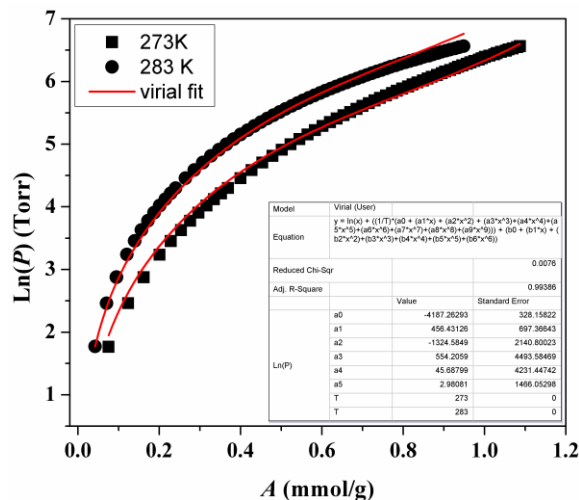


**Figure 16:** CO<sub>2</sub> isotherms for activated compound **1** (**1a**) measured at 273 K (circle) and 283 K (triangle). Fitted curves (red solid lines) obtained from the virial-type expansion, were used for the  $Q_{st}$  estimation.



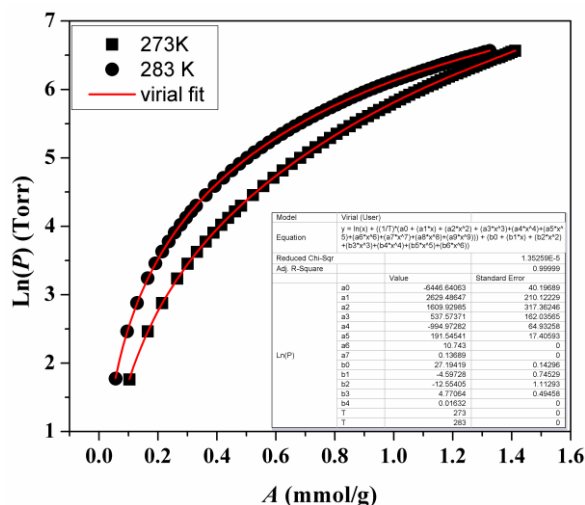


**Figure 17:** CO<sub>2</sub> isotherms for activated compound **2** (**2a**) measured at 273 K (circle) and 283 K (triangle). Fitted curves (red solid lines) obtained from the virial-type expansion, were used for the  $Q_{st}$  estimation.

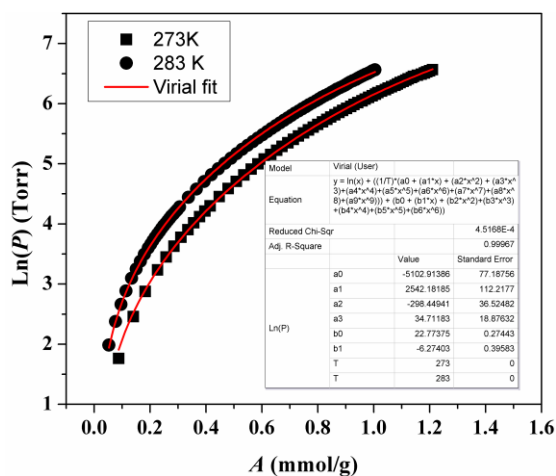


**Figure 18:** CO<sub>2</sub> isotherms for activated compound **3** (**3a**) measured at 273 K (circle) and 283 K (triangle). Fitted curves (red solid lines) obtained from the virial-type expansion, were used for the  $Q_{st}$  estimation.

As described in the introduction part, we anticipated that upon UV irradiation, there will be a dynamic structural change and corresponding distortion in the channel aperture would affect the CO<sub>2</sub> adsorption properties. We have used our lab-made set up to investigate the effect on porosity of the compounds upon UV irradiation (Figure 23a). Figures 19-21 showed that the absolute CO<sub>2</sub> uptake at 283 K has decreased after shining the adsorbent material with 365 nm UV light. It is very interesting to observe that, as soon as we irradiate with light, there is an immediate decrease in the absolute gas uptake and *vice versa*.

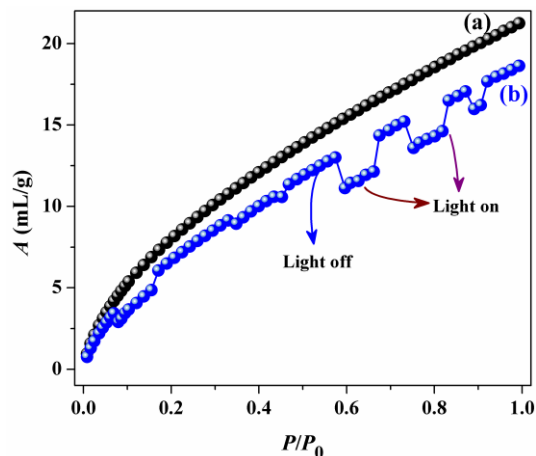


**Figure 19:** (a) CO<sub>2</sub> adsorption isotherm of compound **1a** measured at 283 K (b) The same isotherm measured in the presence and absence of light (light switching environment) which shows release of CO<sub>2</sub> in presence of UV light.  $P_0 = 760$  mm of Hg.

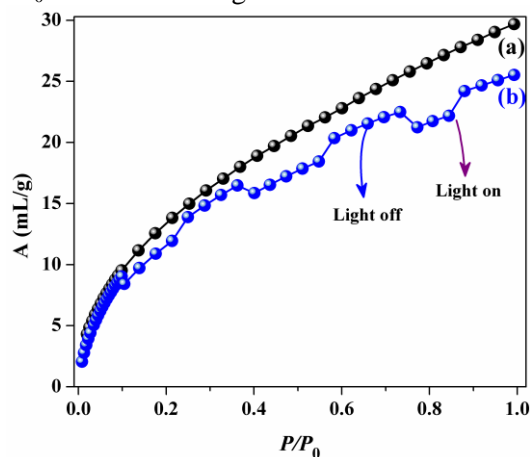


**Figure 20:** (a) CO<sub>2</sub> adsorption isotherm of compound **2a** measured at 283 K (b) The same isotherm measured in the presence and absence of light (light switching environment).  $P_0 = 760$  mm of Hg.

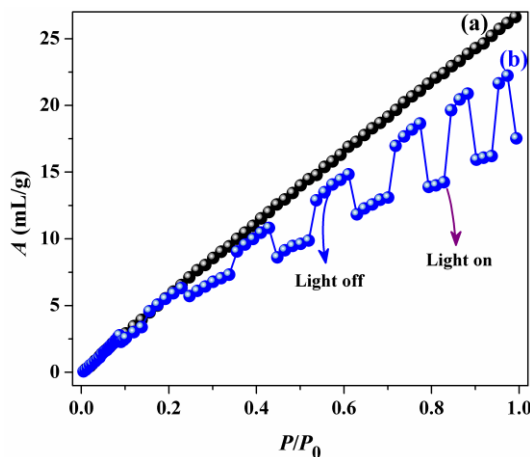


**Figure 21:** (a) CO<sub>2</sub> adsorption isotherm of compound **3a** measured at 283 K (b) The same isotherm measured in the presence and absence of light (light switching environment).  $P_0 = 760$  mm of Hg.

In all the cases the final uptake amount in the UV irradiated measurements are lower compared to the normal measurements which suggest the fact that the reversal in uptake was not entirely complete under the employed measurement conditions. It is noteworthy that, the effect of UV on releasing CO<sub>2</sub> molecules is most pronounced at higher partial pressure which is of paramount important for releasing large amount of CO<sub>2</sub> from the material having high CO<sub>2</sub> concentration. During the adsorption measurement, we have also monitored the local temperature of the sample using a thermocouple which indicates minor localized heating with a temperature fluctuation of  $\pm 1$  K. This change in temperature is not a significant factor to show an uptake variation in presence of light and thus, the assumption of releasing gas molecule due to local heating can be rejected. Interestingly, here we have noticed that, despite having high interaction between the CO<sub>2</sub> and the pore surface, the release of the gas molecules has easily been triggered by using UV light.

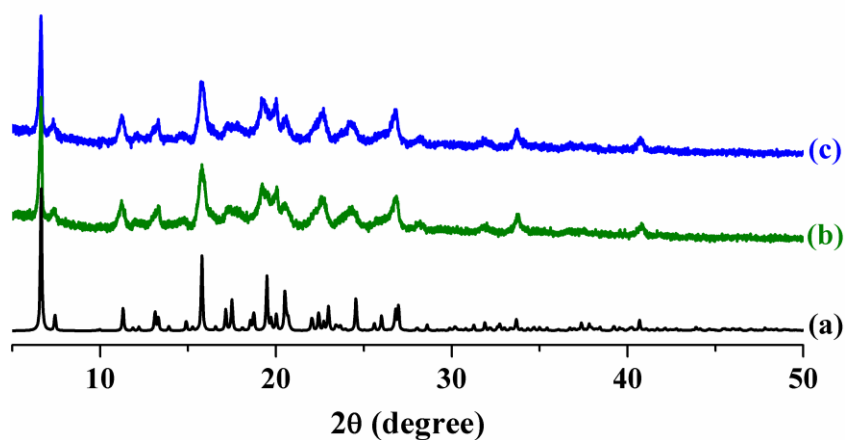


**Figure 22:** PXRD patterns of compound **3a** in different conditions; (a) simulated (b) deguest (**3a**) and the same sample measured in presence of 365 nm UV light. The similarity in the PXRD patterns depicts no structural change during photo-irradiation procedure.

*In situ* PXRD measurements in presence of UV light have been performed (Figure 23b) to examine any presumed structural change during the photo irradiation process. We have measured the PXRD pattern of compound **3a** in two different conditions, namely in presence and absence of UV light (Figure 22). There is no significant change in the PXRD upon UV exposure and therefore such on-demand release of gas molecules under light can be attributed to local structure change in the framework which is cooperative throughout the bulk crystal.

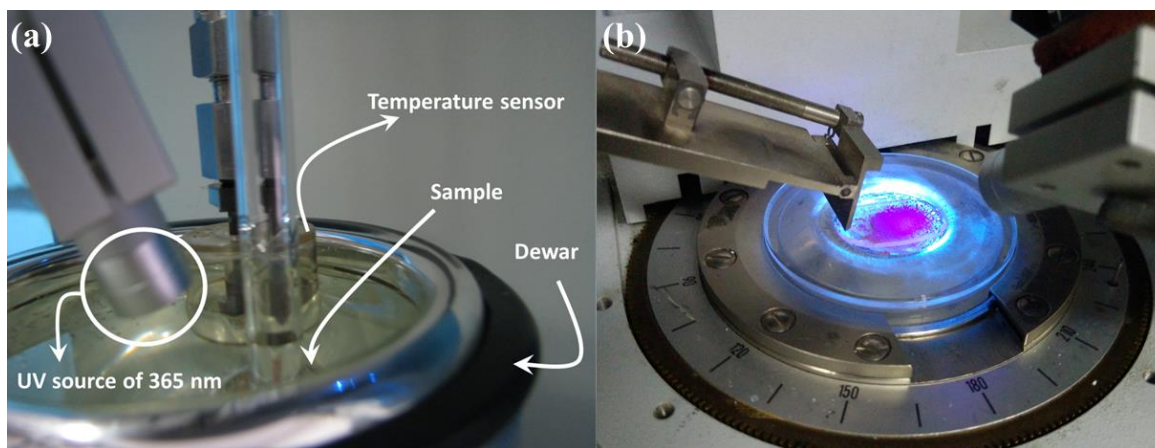


**Figure 23:** Photograph of *in situ* (a) CO<sub>2</sub> measurement and (b) PXRD measurement in presence of UV light.

#### 4.4: Conclusion

In summary, three new isostructural metal-organic frameworks have been synthesized based on self-assembly of Mn<sup>II</sup>/Co<sup>II</sup>/Zn<sup>II</sup>, [Cr(CN)<sub>6</sub>]<sup>3-</sup> and 4,4'-azobipyridine (azpy) and structurally characterized. The deguest frameworks showed permanent porosity reflected from the CO<sub>2</sub> adsorption isotherms measured at 195 K. At 283 K, the *in situ* UV coupled CO<sub>2</sub> adsorption measurements revealed the release of adsorbed CO<sub>2</sub> from the frameworks on shining of 365 nm light. This result demonstrates that the 3D framework can undergo dynamic light-induced structural distortion which results in on-demand release and uptake of gas molecules can be triggered in a cost efficient and ecofriendly manner. *In situ* PXRD measurement depicts no structural change which proves the behavior to be dynamic and localized. This approach will pave a potential pathway to prepare photo-active porous material where the adsorbing and releasing of gas molecules can be triggered in cost efficient and ecofriendly manner. Further investigation in this area will lead to discovery of new photo-active porous materials which can respond to sunlight.

#### 4.5: References

1. (a) J. D. Figueroa, T. Fout, S. Plasynski, H. McIlvried and R. D. Srivastava, *Int. J. Greenhouse Gas Control*, 2008, **2**, 9; (b) J.-R. Li, Y. Ma, M. C. McCarthy, J. Sculley, J. Yu, H.-K. Jeong, P. B. Balbuena and H.-C. Zhou, *Coord. Chem. Rev.*, 2011, **255**, 1791; (c) A. Sayari, Y. Belmabkhout and

- R. Serna-Guerrero, *Chem. Eng. J.*, 2011, **171**, 760; (d) S. A. Rackley, *Carbon Capture and Storage*, Elsevier, 2010.
2. , Fluor Daniel, "Engineering and Economic Evaluation of CO<sub>2</sub> Removal from Fossil-Fuel-Fired Power Plants" (IE-7365, Electric Power Research Institute, Palo Alto, CA, 1991).
3. (a) L. M. Romeo, I. Bolea and J. M. Escosa, *Appl. Therm. Eng.*, 2008, **28**, 1039; (b) G. T. Rochelle, *Science*, 2009, **325**, 1652.
4. (a) D. M. D'Alessandro, B. Smit and J. R. Long, *Angew. Chem. Int. Ed.*, 2010, **49**, 6058; (b) K. Sumida, D. L. Rogow, J. A. Mason, T. M. McDonald, E. D. Bloch, Z. R. Herm, T.-H. Bae and J. R. Long, *Chem. Rev.*, 2012, **112**, 724.
5. J. Rolker and M. Seiler, *ACES*, 2011, **1**, 280.
6. (a) A. S. Bhowan and B. C. Freeman, *Environ. Sci. Technol.*, 2011, **45**, 8624; (b) P. H. M. Feron, *Int. J. Greenhouse Gas Control*, 2010, **4**, 152.
7. (a) P. K. Thallapally, C. A. Fernandez, R. K. Motkuri, S. K. Nune, J. Liu and C. H. F. Peden, *Dalton Trans.*, 2010, **39**, 1692; (b) P. K. Thallapally, R. K. Motkuri, C. A. Fernandez, B. P. McGrail and G. S. Behrooz, *Inorg. Chem.*, 2010, **49**, 4909; (c) D. Maspoch, D. Ruiz-Molina and J. Veciana, *Chem. Soc. Rev.*, 2007, **36**, 770; (d) J. R. Long and O. M. Yaghi, *Chem. Soc. Rev.*, 2009, **38**, 1213; (e) Z. Guo, G. Li, L. Zhou, S. Su, Y. Lei, S. Dang and H. Zhang, *Inorg. Chem.*, 2009, **48**, 8069; (f) P. Horcajada, C. Serre, G. Maurin, N. A. Ramsahye, F. Balas, M. a. Vallet-Regí, M. Sebban, F. Taulelle and G. r. Férey, *J. Am. Chem. Soc.*, 2008, **130**, 6774; (g) S. Achmann, G. Hagen, J. Kita, I. Malkowsky, C. Kiener and R. Moos, *Sensors*, 2009, **9**, 1574; (h) L. J. Murray, M. Dinca and J. R. Long, *Chem. Soc. Rev.*, 2009, **38**, 1294; (i) R. A. Agarwal, A. Aijaz, M. Ahmad, E. C. Sañudo, Q. Xu and P. K. Bharadwaj, *Cryst. Growth Des.*, 2012, **12**, 2999; (j) R. A. Agarwal, A. Aijaz, C. Sañudo, Q. Xu and P. K. Bharadwaj, *Cryst. Growth Des.*, 2013, **13**, 1238; (k) B. L. Chen, N. W. Ockwig, A. R. Millward, D. S. Contreras and O. M. Yaghi, *Angew. Chem. Int. Ed.*, 2005, **44**, 4745; (l) B. L. Chen, S. C. Xiang and G. D. Qian, *Acc. Chem. Res.*, 2010, **43**, 1115; (m) M. Dinca and J. R. Long, *J. Am. Chem. Soc.*, 2005, **127**, 9376; (n) G. Férey, C. Mellot-Draznieks, C. Serre, F. Millange, J. Dutour, S. Surble and I. Margiolaki, *Science*, 2005, **309**, 2040; (o) X.-C. Huang, Y.-Y. Lin, J.-P. Zhang and X.-M. Chen, *Angew. Chem. Int. Ed.*, 2006, **45**, 1557; (p) K. S. Park, Z. Ni, A. P. Cote, J. Y. Choi, R. D. Huang, F. J. Uribe-Romo, H. K. Chae, M. O'Keeffe and O. M. Yaghi, *Proc. Natl. Acad. Sci. U.S.A.*, 2006, **103**, 10186; (q) Y.-Q. Tian, Y.-M. Zhao, Z.-X. Chen, G.-N. Zhang, L.-H. Weng and D.-Y. Zhao, *Chem. Eur. J.*, 2007, **13**, 4146.
8. (a) J. Seo, R. Matsuda, H. Sakamoto, C. Bonneau and S. Kitagawa, *J. Am. Chem. Soc.*, 2009, **131**, 12792; (b) J. J. Vittal, *Coord. Chem. Rev.*, 2007, **251**, 1781; (c) P. Kanoo, R. Sambhu and T. K. Maji, *Inorg. Chem.*, 2010, **50**, 400; (d) A. Hazra, P. Kanoo, S. Mohapatra, G. Mostafa and T. K. Maji,

- CrystEngComm*, 2010, **12**, 2775; (e) H. Sato, R. Matsuda, M. H. Mir and S. Kitagawa, *Chem. Commun.*, 2012, **48**, 7919.
9. (a) K. K. Tanabe and S. M. Cohen, *Chem. Soc. Rev.*, 2011, **40**, 498; (b) S. M. Cohen, *Chem. Rev.*, 2011, **112**, 970; (c) C. A. Allen and S. M. Cohen, *J. Mater. Chem.*, 2012, **22**, 10188; (d) P. V. Dau, K. K. Tanabe and S. M. Cohen, *Chem. Commun.*, 2012, **48**, 9370; (e) M. Kim, J. F. Cahill, H. Fei, K. A. Prather and S. M. Cohen, *J. Am. Chem. Soc.*, 2012, **134**, 18082.
10. (a) R. Lyndon, K. Konstas, B. P. Ladewig, P. D. Southon, P. C. J. Kepernt and M. R. Hill, *Angew. Chem. Int. Ed.*, 2013, **52**, 3695; (b) B. Esser and T. M. Swager, *Angew. Chem. Int. Ed.*, 2010, **49**, 8872.
11. (a) M. Kondo, S. Furukawa, K. Hirai, T. Tsuruoka, J. Reboul, H. Uehara, S. Diring, Y. Sakata, O. Sakata and S. Kitagawa, *J. Am. Chem. Soc.*, 2014, **136**, 4938; (b) J. S. Costa, S. Rodríguez-Jiménez, G. A. Craig, B. Barth, C. M. Beavers, S. J. Teat and G. Aromí, *J. Am. Chem. Soc.*, 2014, **136**, 3869; (c) E. Coronado, M. Giménez-Marqués, G. M. Espallargas and L. Brammer, *Nat. Commun.*, 2012, **3**, 828.
12. (a) E. C. Spencer, M. S. R. N. Kiran, W. Li, U. Ramamurty, N. L. Ross and A. K. Cheetham, *Angew. Chem. Int. Ed.*, 2014, **53**, 5583; (b) S. Thies, H. Sell, C. Schütt, C. Bornholdt, C. Näther, F. Tuczek and R. Herges, *J. Am. Chem. Soc.*, 2011, **133**, 16243; (c) E. S. Koumoussi, I.-R. Jeon, Q. Gao, P. Dechambenoit, D. N. Woodruff, P. Merzeau, L. Buisson, X. Jia, D. Li, F. Volatron, C. Mathonière and R. Clérac, *J. Am. Chem. Soc.*, 2014, **136**, 15461; (d) R. Haldar, R. Matsuda, S. Kitagawa, S. J. George and T. K. Maji, *Angew. Chem. Int. Ed.*, 2014, **53**, 11772; (e) N. Yanai, K. Kitayama, Y. Hijikata, H. Sato, R. Matsuda, Y. Kubota, M. Takata, M. Mizuno, T. Uemura and S. Kitagawa, *Nature Mater.*, 2011, **10**, 787.
13. J. W. Brown, B. L. Henderson, M. D. Kiesz, A. C. Whalley, W. Morris, S. Grunder, H. Deng, H. Furukawa, J. I. Zink, J. F. Stoddart and O. M. Yaghi, *Chem. Sci.*, 2013, **4**, 2858.
14. (a) G. Abellán, E. Coronado, C. Martí-Gastaldo, A. Ribera, J. L. Jordá and H. García, *Adv. Mater.*, 2014, **26**, 4156; (b) Z.-F. Chen, R.-G. Xiong, B. F. Abrahams, X.-Z. You and C.-M. Che, *J. Chem. Soc., Dalton Trans.*, 2001, 2453; (c) S. Bernt, M. Feyand, A. Modrow, J. Wack, J. Senker and N. Stock, *Eur. J. Inorg. Chem.*, 2011, **2011**, 5378.
15. (a) H. M. D. Bandara and S. C. Burdette, *Chem. Soc. Rev.*, 2012, **41**, 1809; (b) S. K. Surampudi, H. R. Patel, G. Nagarjuna and D. Venkataraman, *Chem. Commun.*, 2013, **49**, 7519; (c) O. S. Bushuyev, T. C. Corkery, C. J. Barrett and T. Friscic, *Chem. Sci.*, 2014, **5**, 3158; (d) M. Muller, A. Devaux, C.-H. Yang, L. De Cola and R. A. Fischer, *Photochem. Photobiol. Sci.*, 2010, **9**, 846.

- 
16. (a) J. Park, L.-B. Sun, Y.-P. Chen, Z. Perry and H.-C. Zhou, *Angew. Chem. Int. Ed.*, 2014, **53**, 5842; (b) J. Park, D. Yuan, K. T. Pham, J.-R. Li, A. Yakovenko and H.-C. Zhou, *J. Am. Chem. Soc.*, 2011, **134**, 99.
17. E. V. Brown and G. R. Granneman, *J. Am. Chem. Soc.*, 1975, **97**, 621.
18. S. V. a. SMART (V 5.628), XPREP, SHELXTL; Bruker AXS Inc. Madison, Wisconsin, USA, 2004.
19. G. M. Sheldrick, *SADABS, Empirical Absorption Correction Program, University of Göttingen, Göttingen*, 1997.
20. A. Altomare, G. Cascarano, C. Giacovazzo and A. Guagliardi, *J. Appl. Crystallogr.*, 1993, **26**, 343.
21. G. M. Sheldrick, *SHELXL 97, Program for the Solution of Crystal Structure, University of Göttingen, Germany*, 1997.
22. A. Spek, *J. Appl. Crystallogr.*, 2003, **36**, 7.
23. L. Farrugia, *J. Appl. Crystallogr.*, 1999, **32**, 837.
24. J. L. C. Rowsell and O. M. Yaghi, *Angew. Chem. Int. Ed.*, 2005, **44**, 4670.





# Chapter 5

**Photo-Induced Postsynthetic Modulation of Porous and Magnetic Properties in a Bimodal Metal-organic frameworks**



## Summary

Simultaneous tuning of permanent porosity and modulation of magnetic properties by postsynthetic modification (PSM) using light in a metal-organic framework is yet to be realized. Aiming at such a photo-responsive porous magnetic material, a 3D biporous framework  $\{[\text{Co}_3(\text{bpee})_3(\text{H}_2\text{O})_4][\text{Cr}(\text{CN})_6]_2 \cdot 2(\text{bpee}) \cdot 2(\text{C}_2\text{H}_5\text{OH}) \cdot 2(\text{H}_2\text{O})\}_n$  (**MOF1**) (bpee = 1,2-bis(4-pyridyl)ethylene) has been synthesized and systematically characterized. **MOF1** has a 2D channels occupied by the guest bpee, H<sub>2</sub>O and EtOH molecules and the guest bpee in **MOF1** is aligned parallel to the pillared bpee with a distance of 3.9 Å between the ethylenic groups which allows photo-induced PSM of the pore surface via [2+2] cycloaddition reaction to yield **MOF2** ( $\{[\text{Co}_3(\text{rctt-tpcb})_2(\text{bpee})(\text{H}_2\text{O})_4][\text{Cr}(\text{CN})_6]_2 \cdot 2(\text{C}_2\text{H}_5\text{OH}) \cdot 2(\text{H}_2\text{O})\}_n$ ). Such photo-induced PSM of the framework structure introduces enhanced selectivity of CO<sub>2</sub> over N<sub>2</sub> at ambient condition. The higher adsorption selectivity of **MOF2** compared to **MOF1** is studied through theoretical free energy calculations, which provide vital insights into the facile adsorption of CO<sub>2</sub> over N<sub>2</sub> in the activated framework of **MOF2**. Furthermore, **MOF1** shows ferromagnetic ordering with  $T_c = 14.9$  K which changes irreversibly to 8.4 K upon removal of coordinated water and guest molecules. On the contrary, **MOF2** shows reversible changes of  $T_c$  (14.1 K for **MOF2**) in response to the water molecule. This result suggests photo-induced PSM is a powerful tool for fabricating novel functional materials.

A. Hazra, S. Bonakala, K. Bejagam, S. Balasubramanian and T. K. Maji, *Manuscript Communicated*.



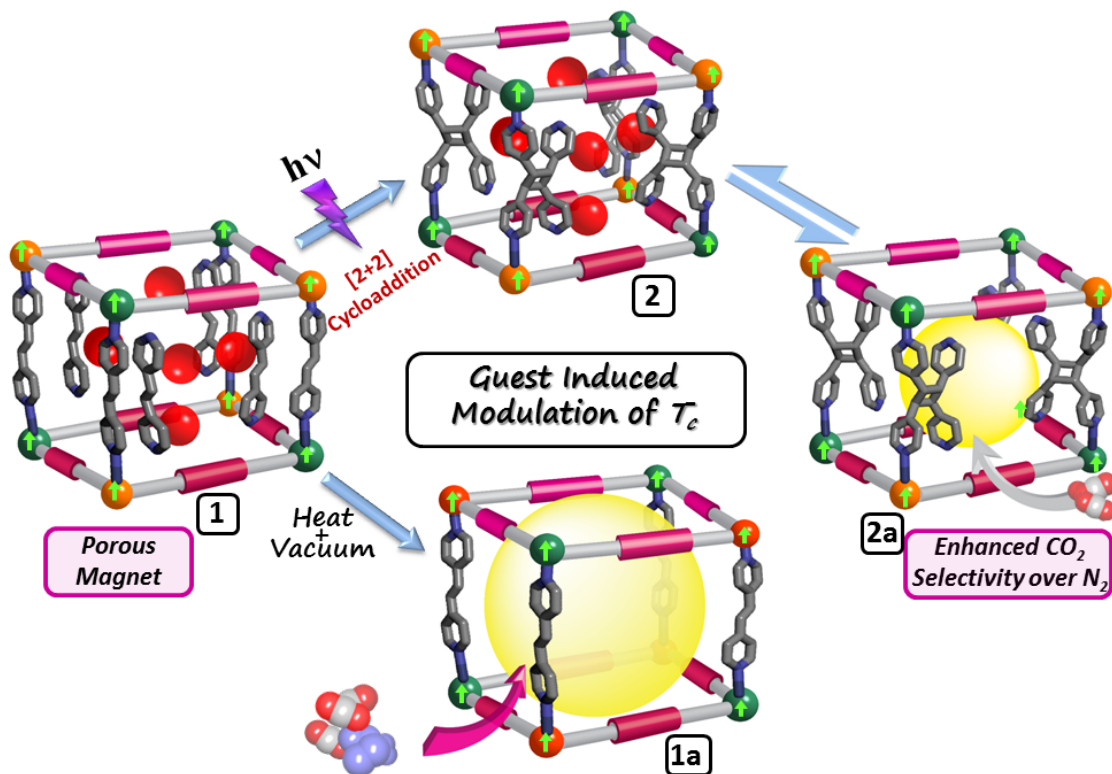
## 5.1: Introduction

Recently, there is an upsurge in research to design and synthesize porous coordination polymers (PCPs) or metal-organic frameworks (MOFs) that combine a set of well-defined properties like optical response and porosity, magnetism and porosity, electrical conductivity and magnetism and synergistic guest responsive behavior.<sup>1</sup> However, it is a significant challenge to develop such MOFs that possess programmable structure with chemical functionalities and also offer modulation of their physical properties in response to external stimuli. Structurally bistable or multistable MOFs with modifiable pore surface by postsynthetic modification (PSM) using external stimuli such as heat, light, pH, redox potential, and pressure are a novel class of stimuli responsive materials.<sup>2</sup> Such specific stimuli modified MOFs would show advantages in several functionalities like molecular recognition, mechanical strength, magnetism, optical and guest selectivity over the original host framework.<sup>3</sup> In this context, Cohen *et al.* have significantly contributed to the postsynthetic chemical modification of different type of MOFs for a variety of applications, by introducing several functional groups to the organic linkers.<sup>4</sup> However, the implementation of light as an effective low cost, non-destructive external modulator for such covalent modification of the pore surface to manipulate the structure-property relationship is underexplored.<sup>5</sup>

Recently, several groups have reported photo-induced PSM of framework where the *cis-trans* isomerization of either a coordinated<sup>6</sup> or a guest<sup>7</sup> azo functionalized linkers ( $-N=N-$ ) led to the amendment of the pore surfaces as well as properties. In this regard, photo-induced [2+2] cycloaddition reaction is another popular choice for PSM toward the modification of size and polarity of pore surface in metal-organic frameworks.<sup>8</sup> The exo-bidentate organic spacer 1,2-bis(4-pyridyl)ethylene (bpee), is one of the preferred organic linkers for investigating topochemical cycloaddition reaction and several reports of [2+2] cycloaddition reactions in coordination polymers have been reported.<sup>9</sup> However, guest responsive PSM of pore surfaces using such photochemical reactions is yet to be accounted, as the encapsulation and alignment of a photo-responsive guest in a host lattice which satisfies Schmidt's [2+2] topochemical reaction criteria<sup>10</sup> is a highly challenging assignment.

Synergism of permanent porosity and magnetism within a framework would open up the prospect of development of magnetic sensors and low-density magnetic materials.<sup>11</sup>

Some fascinating properties like guest dependent modulation of magnetic ordering temperature ( $T_c$ ) and spin crossover or guest responsive reversible magnetic phase transition have been realized in magnetic porous frameworks.<sup>12</sup> By maintaining the framework structure intact, the development of stimuli responsive MOF to tune the pore size/surface as well as magnetic property is of paramount importance for introducing novel functions.<sup>13</sup> Recently, Maji *et al.* have espoused a scheme to build porous magnetic materials using hexacyanometallate  $[M(CN)_6]^{3-}$  as a metalloligand, where the equatorial  $CN^-$  groups could connect with transition metal ions to build a 2D layer and further pillaring of such 2D network by organic exo-bidentate linkers ensues the formation of a 3D pillared layer porous framework.<sup>14</sup> Such 3D ferromagnetic porous framework based on  $Co^{II}$  and  $[Cr(CN)_6]^{3-}$  is yet to be explored. This chapter reports the design and synthesis of a 3D pillared-layer framework ( $\{[Co_3(bpee)_3(H_2O)_4][Cr(CN)_6]_2 \cdot 2(bpee) \cdot 2(C_2H_5OH) \cdot 2(H_2O)\}_n$  (**MOF1**), (bpee = 1,2-bis(4-pyridyl)ethene) and photo-induced postsynthetic modification of the framework structure by light as an external stimulus (Scheme 1). In **MOF1**, guest and pillared bpee molecules undergo [2+2] cycloaddition reaction by UV irradiation to yield  $\{[Co_3(rctt-tpcb)_2(bpee)(H_2O)_4][Cr(CN)_6]_2 \cdot 2(C_2H_5OH) \cdot 2(H_2O)\}_n$  (**MOF2**) (*rctt-tpcb* = regio *cis,trans,trans*-tetrakis(4-pyridyl)cyclobutane). **MOF2** shows negligible surface area; however, it demonstrates a superior performance of  $CO_2$  selectivity over  $N_2$  compared to **MOF1**. Furthermore, theoretical examination of the free energy surfaces sampled by  $CO_2$  and  $N_2$  in **MOF1** and **MOF2** provides a direct visualization of energy barriers for  $N_2$  in the photo-modified framework resulting in a high selectivity between  $CO_2$  and  $N_2$  at 283 K. Furthermore, **MOF1** and **MOF2** show ferromagnetic ordering where in **MOF2**,  $T_c$  reversibly changes in response to water molecules.



**Scheme 1:** Postsynthetic cycloaddition reaction between host and guest shows high selectivity and reversible guest responsive magnetic properties compared to the un-modified framework.

## 5.2: Experimental Section

### 5.2.1: Materials

All the reagents and solvents employed were commercially available and used as supplied without further purification.  $\text{K}_3[\text{Cr}(\text{CN})_6]$ , 1,2-bis(4-pyridyl)ethene (bpee) and  $\text{CoCl}_2 \cdot 4\text{H}_2\text{O}$  were obtained from the Aldrich Chemical Co. *Caution! Cyanide-containing compounds are potentially toxic and should be handled very carefully.*

### 5.2.2: Synthesis

**5.2.2.1 Synthesis of  $\{[\text{Co}_3(\text{bpee})_3(\text{H}_2\text{O})_4][\text{Cr}(\text{CN})_6]_2 \cdot 2(\text{bpee}) \cdot 2(\text{C}_2\text{H}_5\text{OH}) \cdot 2(\text{H}_2\text{O})\}_n$  (MOF1):** An aqueous solution (12.5 mL) of  $\text{K}_3[\text{Cr}(\text{CN})_6]$  (0.25 mmol) was added to an ethanolic solution (12.5 mL) of bpee (0.5 mmol) and stirred for 30 min.  $\text{CoCl}_2 \cdot 4\text{H}_2\text{O}$  (0.25 mmol) was dissolved in 12.5 mL distilled water and 2.5 mL of this metal solution was carefully layered with 2.5 mL of mixed bpee and  $\text{K}_3[\text{Cr}(\text{CN})_6]$  solution using an ethanol :

water buffer solution (1 mL, 1:1) in a test tube. The whole reaction setup was covered with aluminum foil and kept under dark for one month. After one month, light pink coloured block shaped crystals appeared in the middle of the tube and separated and washed with ethanol. The bulk amount of the sample was prepared by the direct mixing of the respective reagents in ethanol–water solution under stirring for 24 h in the dark. The phase purity was checked with the PXRD and elemental analysis. Yield: 64%, relative to  $\text{Co}^{\text{II}}$ . Anal. calc. for  $\text{C}_{76}\text{H}_{74}\text{Cr}_2\text{Co}_3\text{N}_{22}\text{O}_8$ : C, 53.56; H, 4.38; N, 18.08. Found: C, 54.09; H, 4.21; N, 17.48. IR (KBr,  $\text{cm}^{-1}$ , Figure 1a):  $\nu(\text{H}_2\text{O})$  3595, 3427;  $\nu(\text{ArC-H})$  3101, 2972;  $\nu(\text{C}\equiv\text{N})$  2164, 2127;  $\nu(\text{ArC=C})$  1611, 1560. A strong band around  $2164\text{ cm}^{-1}$  corroborates to  $\nu(\text{C}\equiv\text{N})$  stretching frequency and a band around  $1611\text{ cm}^{-1}$  indicates the presence bpee molecule.

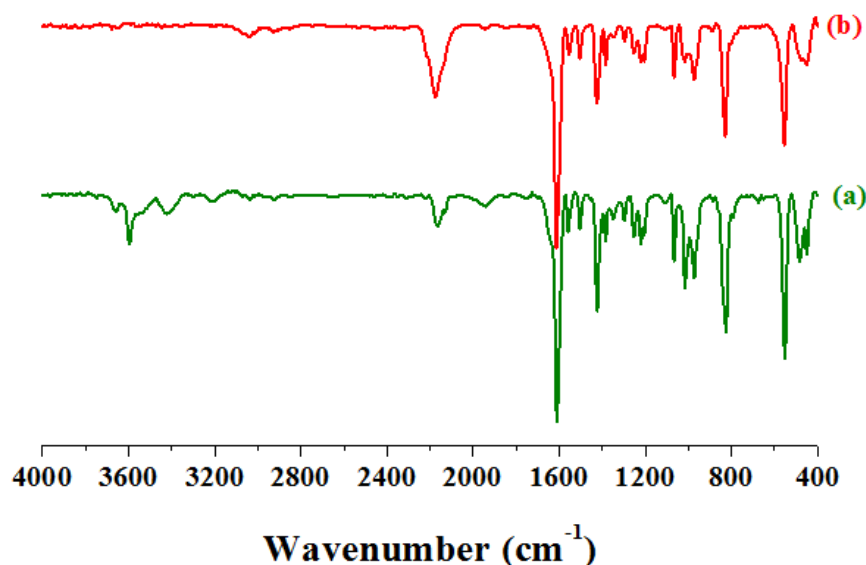


**Figure 1:** IR spectra of **MOF1** (a) and **MOF1a** (b).

**5.2.2.2: Preparation of  $\{[\text{Co}_3(\text{bpee})_3][\text{Cr}(\text{CN})_6]_2\}_n$  (MOF1a):** **MOF1a** was prepared by heating **MOF1** at consecutive two temperatures under high vacuum ( $< 10^{-1}$  Pa). At first **MOF1** was activated at  $75\text{ }^\circ\text{C}$  for 12 hrs and then the temperature was increased to  $120\text{ }^\circ\text{C}$  at the rate of  $1\text{ }^\circ\text{C}/\text{min}$ . At that temperature the sample was evacuated until the outgas rate was less than 10 mtorr/min. This powdered sample was used for different characterizations. Anal. calc. for  $\text{C}_{48}\text{H}_{30}\text{Cr}_2\text{Co}_3\text{N}_{18}$ : C, 50.59; H, 2.65; N, 22.12. Found: C, 51.21; H, 2.62; N, 21.93. IR (KBr,  $\text{cm}^{-1}$  Figure 1b):  $\nu(\text{ArC-H})$  2981, 2942;  $\nu(\text{C}\equiv\text{N})$  2179;  $\nu(\text{ArC=C})$  1625, 1537.



**5.2.2.3: Preparation of  $\{[\text{Co}_3(\text{bpee})_3][\text{Cr}(\text{CN})_6]_2 \cdot 8\text{H}_2\text{O}\}_n$  (MOF1b):** MOF1b was prepared by exposing MOF1a to water vapour for 7 days. The number of water molecules was confirmed from TGA (Figure 7) and elemental analysis. Anal. calc. for  $\text{C}_{48}\text{H}_{46}\text{Cr}_2\text{Co}_3\text{N}_{18}\text{O}_8$ : C, 44.91; H, 3.61; N, 19.64. Found: C, 44.13; H, 3.24; N, 18.94. The amount uptake at saturation in the water vapour adsorption profile (Figure 26a) of MOF1a also supports that MOF1a can adsorb  $\sim 8$   $\text{H}_2\text{O}$  molecules per formula unit.

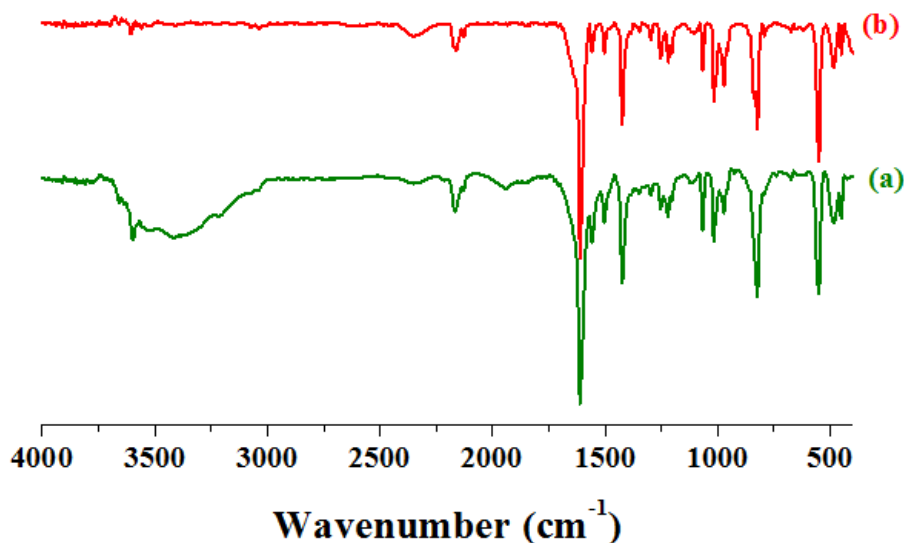


**Figure 2:** IR spectra of MOF2 (a) and MOF2a (b).

**5.2.2.4: Preparation of  $\{[\text{Co}_3(\text{rctt-tpcb})_2(\text{bpee})(\text{H}_2\text{O})_4][\text{Cr}(\text{CN})_6]_2 \cdot 2(\text{C}_2\text{H}_5\text{OH}) \cdot 2(\text{H}_2\text{O})\}_n$  (MOF2):** MOF2 was synthesized using a UV photochemical reactor with 365 nm LASER light made by Hamamatsu, Japan. Before photoreaction, MOF1 was continuously ground for 30 min. Then the powder of 1 sandwiched between a pair of quartz glass plates and irradiated for 10 h. During the photo reaction, the sample was mixed properly in every 30 min to make sure about the homogeneous irradiation. Anal. calc. for  $\text{C}_{76}\text{H}_{74}\text{Cr}_2\text{Co}_3\text{N}_{22}\text{O}_8$ : C, 53.56; H, 4.38; N, 18.08. Found: C, 54.26; H, 4.07; N, 18.31. IR (KBr,  $\text{cm}^{-1}$  Figure 2a):  $\nu(\text{H}_2\text{O})$  3591, 3417;  $\nu(\text{ArC-H})$  3074, 2961;  $\nu(\text{C}\equiv\text{N})$  2167, 2130;  $\nu(\text{ArC=C})$  1609, 1557. A strong band around  $2167 \text{ cm}^{-1}$  corroborate to  $\nu(\text{C}\equiv\text{N})$  stretching frequency and a band around  $1609 \text{ cm}^{-1}$  indicates the presence bpee molecule. The phase purity was checked with the PXRD and elemental analysis and NMR spectroscopy (Figures 11 and 12).

**5.2.2.5: Preparation of  $\{[\text{Co}_3(\text{rctt}\text{-tpcb})_2(\text{bpee})][\text{Cr}(\text{CN})_6]_2\}_n$  (MOF2a):** MOF2a was prepared from MOF2 following the same procedure as of MOF1a. This powdered sample was used for further characterizations. Anal. calc. for  $\text{C}_{72}\text{H}_{50}\text{Cr}_2\text{Co}_3\text{N}_{22}$ : C, 57.49; H, 3.35; N, 20.49. Found: C, 57.91; H, 3.03; N, 19.89. IR (KBr,  $\text{cm}^{-1}$  Figure 2b):  $\nu(\text{ArC-H})$  2942, 2912;  $\nu(\text{C}\equiv\text{N})$  2098;  $\nu(\text{ArC=C})$  1633, 1560.

**5.2.2.6: Preparation of  $\{[\text{Co}_3(\text{rctt}\text{-tpcb})_2(\text{bpee})][\text{Cr}(\text{CN})_6]_2\cdot 8\text{H}_2\text{O}\}_n$  (MOF2b):** MOF2b was prepared by exposing MOF2a to water vapour for 7 days. The number of water molecules was confirmed from TGA (Figure 8) and elemental analysis. Anal. calc. for  $\text{C}_{72}\text{H}_{66}\text{Cr}_2\text{Co}_3\text{N}_{22}\text{O}_8$ : C, 52.46; H, 4.04; N, 18.70. Found: C, 52.11; H, 3.03; N, 19.01. IR (KBr,  $\text{cm}^{-1}$ ):  $\nu(\text{H}_2\text{O})$  3495, 3414;  $\nu(\text{ArC-H})$  2981, 2953;  $\nu(\text{C}\equiv\text{N})$  2081;  $\nu(\text{ArC=C})$  1622, 1557. The amount uptake at saturation in the water vapour adsorption profile (Figure 26b) of MOF2a also supports that MOF2a can adsorb  $\sim 8$   $\text{H}_2\text{O}$  molecules per formula unit.

### 5.2.3: Physical Measurements

The elemental analyses of all the compounds were carried out on a Thermo Fisher Flash 2000 Elemental Analyser. Fourier transformed IR spectroscopic studies were carried out using a KBr pellet (Bruker IFS-66v). Thermogravimetric analysis (TGA) was carried out (Mettler Toledo) in nitrogen atmosphere (flow rate =  $50 \text{ ml min}^{-1}$ ) in the temperature range  $30 - 650 \text{ }^\circ\text{C}$  (heating rate =  $2^\circ\text{C min}^{-1}$ ). Powder XRD pattern of MOF1-MOF1b and MOF2-MOF2b were recorded by using Bruker D8 Discover; 40 kV, 30 mA and PANalytical Empyrean alpha-1 diffractometer using monochromatized  $\text{Cu } K_{\alpha 1}$  radiation.  $^1\text{H-NMR}$  spectra were measured on a Bruker AV-400 spectrometer with chemical shifts reported as ppm (in  $\text{DCI}/d_6\text{-DMSO}$ , TMS as internal standard). Magnetic measurements were carried out with a Superconducting Quantum Interference Device (SQUID) magnetometer (Quantum Design) in *dc* scan mode.

### 5.2.4: Single Crystal X-ray Diffraction

Suitable single crystals of MOF1 and MOF2 were mounted on a thin glass fiber with commercially available super glue. X-ray single crystal structural data were collected on a

Bruker Smart-CCD diffractometer equipped with a normal focus, 2.4 kW sealed tube X-ray source with graphite monochromated Mo- $K\alpha$  radiation ( $\lambda = 0.71073 \text{ \AA}$ ) operating at 50 kV and 30 mA. The program SAINT<sup>15</sup> was used for the integration of diffraction profiles and absorption correction was made with SADABS<sup>16</sup> program. All the structures were solved by SIR 92<sup>17</sup> and refined by full matrix least square method using SHELXL.<sup>18</sup> All the hydrogen atoms were fixed by HFIX and placed in ideal positions with isotropic displacement parameters set to  $1.2 \times U_{eq}$  of the attached atom. Potential solvent accessible area or void space was calculated using the PLATON<sup>19</sup> multipurpose crystallographic software. All crystallographic and structure refinement data of **MOF1** and **MOF2** are summarized in Table 1. The metal related bond distances and angles are summarized in Tables 2–5. All calculations were carried out using SHELXL 97,<sup>18</sup> PLATON,<sup>19</sup> SHELXS 97<sup>18</sup> and WinGX system, Ver 1.80.05.<sup>20</sup>

In **MOF1**, the carbon atoms of ethylenic double bond of the guest bpee molecule were found to be disordered over two different positions. The disorder was resolved by changing the occupancy of each carbon atom to 0.5.

**Table 1:** Crystallographic data and structure refinement parameters for compounds **MOF1** and **MOF2**.

	<b>MOF1</b>	<b>MOF2</b>
Empirical formula	C <sub>76</sub> H <sub>74</sub> Cr <sub>2</sub> Co <sub>3</sub> N <sub>22</sub> O <sub>8</sub>	C <sub>76</sub> H <sub>74</sub> Cr <sub>2</sub> Co <sub>3</sub> N <sub>22</sub> O <sub>8</sub>
M	1692.27	1692.27
Crystal system	Monoclinic	Monoclinic
space group	<i>P21/c</i> (No. 14)	<i>P21/c</i> (No. 14)
<i>a</i> (Å)	13.9190(4)	13.7644(8)
<i>b</i> (Å)	17.8965(5)	17.7645 (9)
<i>c</i> (Å)	16.1361(5)	16.3912 (6)
$\alpha$ (°)	90	90
$\beta$ (°)	98.619(1)	91.261(3)
$\gamma$ (°)	90	90
<i>V</i> (Å <sup>3</sup> )	3974.1(2)	4007.0(3)
Z	2	2
<i>T</i> (K)	295	295

$\lambda(\text{Mo K}\alpha)$	0.71073	0.71073
$D_c (\text{g cm}^{-3})$	1.414	1.366
$\mu (\text{mm}^{-1})$	0.946	0.935
$\theta_{\text{max}}/\theta_{\text{min}} (^\circ)$	25.0/1.9	25.3/1.9
total data	54038	41314
unique reflection	6980	7212
$R_{\text{int}}$	0.116	0.134
data [ $I > 2\sigma(I)$ ]	4365	3493
$R^a$	0.0671	0.0914
$R_w^b$	0.2025	0.2881
GOF	1.04	1.00
$\Delta\rho \text{ min/max [e \AA}^{-3}]$	-0.85, 1.19	-0.90, 0.98

$$^a R = \sum |F_o| - |F_c| / \sum |F_o| ; \quad ^b R_w = [\sum \{w(F_o^2 - F_c^2)^2\} / \sum \{w(F_o^2)^2\}]^{1/2}$$

**Table 2:** Selected bond distances (Å) for MOF1.

Bonds	Distance (Å)	Bonds	Distance (Å)
Co1-N1	2.227(5)	Co1-N7	2.279(6)
Co1-N8_b	2.270(6)	Co1-N2_c	2.158(6)
Co1-N4_h	2.182(5)	Co2-N3	2.185(6)
Co2-N9	2.270(6)	Co2-O1W_f	2.254(4)
Co2-N3_f	2.185(6)	Co2-N9_f	2.270(6)
Cr1-C1	1.881(6)	Cr1-C2	1.887(7)
Cr1-C3	1.879(6)	Cr1-C4	1.881(6)
Cr1-C5	1.928(7)	Cr1-C6	1.918(7)

**Table 3:** Selected bond angles (°) for MOF1.

Angles	Degree (°)	Angles	Degree (°)
C1-Cr1-C3	88.8(3)	C1-Cr1-C4	92.1(3)
N1-Co1-N7	90.5(2)	C1-Cr1-C5	89.9(3)
N1-Co1-N8_b	90.0(2)	C1-Cr1-C6	89.9(3)
N1-Co1-N2_c	104.7(2)	C2-Cr1-C3	88.2(3)
N1-Co1-N4_h	162.7(2)	C2-Cr1-C4	90.9(3)
N7-Co1-N8_b	176.3(2)	C2-Cr1-C5	90.1(3)
N2_c-Co1-N7	92.4(2)	C2-Cr1-C6	90.1(3)
N4_h-Co1-N7	88.7(2)	C3-Cr1-C4	179.1(2)
N2_c-Co1-N8_b	91.0(2)	C3-Cr1-C5	90.0(3)
N4_h-Co1-N8_b	89.7(2)	C3-Cr1-C6	89.4(3)
N2_c-Co1-N4_h	92.6(2)	C4-Cr1-C5	90.2(3)
C4-Cr1-C6	90.4(3)	C5-Cr1-C6	179.4(3)
N3-Co2-N9	89.69(19)	N3-Co2-N3_f	180.00

N3-Co2-N9_f	90.31(19)	Co1-N1-C1	147.2(5)
N3_f-Co2-N9	90.31(19)	Co1_d-N2-C2	174.4(6)
N9-Co2-N9_f	180.00	Co2-N3-C3	170.2(5)
Co1_g-N4-C4	174.4(5)	Co1-N7-C7	123.4(5)
C13-C16-C15	123.7(8)	Co1-N7-C11	120.4(5)
C13-C16-C17	120.7(8)		

**Table 4:** Selected bond distances (Å) for MOF2.

Bonds	Distance (Å)	Bonds	Distance (Å)
Co1-N1	2.260(7)	Co1-N7	2.270(7)
Co1-N10_b	2.269(8)	Co1-N2_c	2.131(9)
Co1-N4_g	2.169(7)	Co2-O1W	2.280(6)
Co2-N3	2.180(8)	Co2-N8	2.257(7)
Co2-O1W_e	2.280(6)	Co2-N3_e	2.180(8)
Co2-N8_e	2.257(7)	Cr1-C1	1.900(9)
Cr1-C2	1.934(10)	Cr1-C3	1.886(8)
Cr1-C4	1.883(10)	Cr1-C5	1.915(10)
Cr1-C6	1.903(10)		

**Table 5:** Selected bond angles (°) for MOF2.

Angles	Degree (°)	Angles	Degree (°)
N3_e-Co2-N8_e	90.3(3)	C1-Cr1-C2	177.3(4)
C1-Cr1-C3	88.9(4)	C1-Cr1-C4	93.1(4)
N1-Co1-N7	89.6(3)	C1-Cr1-C5	89.3(4)
N1-Co1-N10_b	89.6(3)	C1-Cr1-C6	91.0(4)
N1-Co1-N2_c	101.5(3)	C2-Cr1-C3	88.5(4)
N1-Co1-N4_g	161.9(3)	C2-Cr1-C4	89.6(4)
N7-Co1-N10_b	175.8(4)	C2-Cr1-C5	90.1(4)
N2_c-Co1-N7	92.0(3)	C2-Cr1-C6	89.6(4)
N4_g-Co1-N7	89.3(3)	C3-Cr1-C4	178.0(4)
N2_c-Co1-N10_b	92.3(3)	C3-Cr1-C5	89.3(4)
N4_g-Co1-N10_b	90.2(3)	C3-Cr1-C6	89.8(4)
N2_c-Co1-N4_g	96.6(3)	C4-Cr1-C5	91.1(4)
C4-Cr1-C6	89.9(4)	C5-Cr1-C6	179.0(4)
N3-Co2-N8_e	89.7(3)	Co1-N1-C1	148.6(6)
Co1_d-N2-C2	176.0(7)	N3_e-Co2-N8	89.7(3)
Co2-N3-C3	170.5(7)	N8-Co2-N8_e	180.00
Co1_f-N4-C4	176.3(7)	Co1-N7-C14	123.6(8)

### 5.2.5: Adsorption Study

N<sub>2</sub> (77 K, and 283 K), CO<sub>2</sub> (195 K, 273 K and 283 K), adsorption studies were carried out with the activated samples *i.e.* MOF1a and MOF2a by using

QUANTACHROME QUADRASORB *SI* analyser and AUTOSORB *IQ2* instrument. All the gases used for adsorption measurement are of scientific/research grade with 99.999% purity. Dead volume was measured with helium gas. Adsorbent samples weighing around 100–150 mg were placed in the sample tube. All operations were computer controlled and automatic. Prior to the measurement of the isotherms, the samples were activated for about 72 h under high vacuum conditions ( $< 0.1$  Pa) following different activation procedure. The water adsorption isotherm at 298 K was measured in the vapour state by using BELSORP–aqua–3 analyzer. Dead volume was measured with helium gas. The adsorbates were placed into the sample tubes, then the change of the pressure was monitored and the degree of adsorption was determined by the decrease in pressure at the equilibrium state. All operations were computer controlled and automatic.

### 5.2.6: Computational details

#### 5.2.6.1: Quantum Calculations

Periodic density functional theory calculations were performed using the QUICKSTEP module in CP2K software to identify locations of a gas molecule inside the metal-organic framework (MOF)<sup>21</sup>. All valence electrons were treated in a mixed basis set with an energy cutoff of 280 Ry. The short-range version of the double- $\zeta$  single polarization basis set was used. The effect of core electrons and nuclei was considered by using pseudopotentials of Goedecker–Teter–Hutter (GTH)<sup>22</sup>. The exchange and correlation interactions between electrons was treated with the Perdew–Burke–Ernzerhof (PBE)<sup>23</sup> functional. van der Waals interactions between the gas and the framework are very important, and their contributions were accounted for by employing empirical corrections developed by Grimme<sup>24</sup>. Such an approach has been successfully employed by us in MOFs earlier<sup>25</sup>. The simulation cell consisted of  $1 \times 1 \times 1$  unit cell each for the as-synthesized MOF (before irradiation) (**MOF1a**) and the irradiated MOF (**MOF2a**). Optimized cell parameters of **MOF1a** and **MOF2a** are shown in Table 6 and 7. The binding energy was calculated as follows:

$$\Delta E = E_{(\text{MOF-gas})} - E_{(\text{MOF})} - n \times E_{(\text{gas})} \quad (1)$$

where  $\Delta E$ ,  $E_{(\text{MOF-gas})}$ ,  $E_{(\text{MOF})}$ , and  $E_{(\text{gas})}$  are the binding energy of gas ( $\text{CO}_2$  or  $\text{N}_2$ ), total energies of MOF with gas molecule, of MOF, and of the molecule alone.  $n$  is the number of gas molecules considered to be adsorbed in the MOF. The energies were corrected for the basis set superposition error (BSSE) using the counterpoise method. All structures were visualized using VMD<sup>26</sup>, Mercury<sup>27</sup> and GaussView<sup>28</sup>.

### 5.3: Results and Discussion

#### 5.3.1: Structural Description

**5.3.1.1: Structural description of  $\{[\text{Co}_3(\text{bpee})_3(\text{H}_2\text{O})_4][\text{Cr}(\text{CN})_6]_2 \cdot 2(\text{bpee}) \cdot 2(\text{C}_2\text{H}_5\text{OH}) 2(\text{H}_2\text{O})\}_n$  (MOF1):** MOF1 crystallizes in a monoclinic crystal system with  $P2_1/c$  space group. There are two crystallographically independent  $\text{Co}^{\text{II}}$  centers (Co1 and Co2) connected by  $[\text{Cr}(\text{CN})_6]^{3-}$  metalloligand in two directions to form a 2D sheet in the crystallographic  $bc$  plane (Figures 3a and b). Each octahedral Co1 is connected to three different  $[\text{Cr}(\text{CN})_6]^{3-}$  moiety (N1, N2 and N4), two bpee (N7, N8) and one water molecule (O2w). The other octahedral Co2 is located in a special position and is connected to N3, N3\* (from  $[\text{Cr}(\text{CN})_6]^{3-}$ ), O1w and O1w\* (\* represents the symmetry related counterpart;  $2-x, 1-x, 1-z$ ), whereas the axial sites are occupied by N9 and N9\* from two bpee pillars. In the 2D layer, a 12 membered  $\text{Co}_1\text{Co}_2\text{Cr}_2(\text{CN})_4$  ring is surrounded by a 18 membered  $\text{Co}_1\text{Co}_2\text{Cr}_3(\text{CN})_6$  and such 2D sheets are connected by bpee pillars (along  $a$  axis) through the Co (1 and 2) centers to form a 3D pillared-layer framework (Figure 3c). The Cr–CN–Co is quite linear through cyanide bridges ( $171.3^\circ$ – $175.5^\circ$ ), except in the case of Cr1–C1N1–Co1 where it decreases to  $148.3^\circ$ . The framework has a 1D channel along  $a$  direction (Figures 5a–b) ( $5.9 \times 4.1 \text{ \AA}^2$ ) which is occupied by the guest bpee and water molecules. MOF1 also possesses a channel along  $b$  direction with a dimension of  $6.1 \times 3.2 \text{ \AA}^2$  (Figures 5c–d). Calculation using PLATON shows 46% void space present in the guest-removed framework (*i.e.* MOF1a). It is worth mentioning that guest bpee molecules are present in a face-to-face arrangement with the pillared bpee molecule ( $c_g \cdots c_g$  distance is in the range of  $3.83$ – $3.96 \text{ \AA}$ ) mediated by  $\pi \cdots \pi$  interaction (Figures 3d).

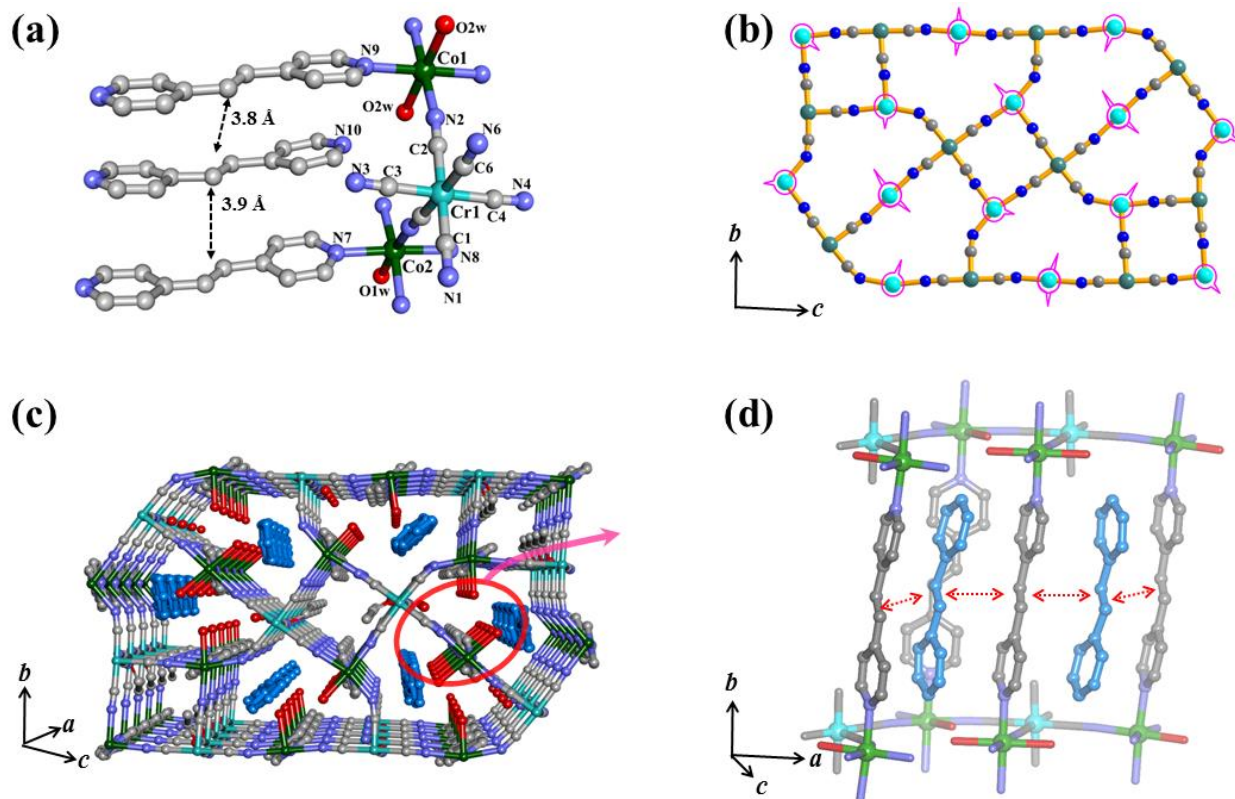


**Figure 3:** (a) View of the coordination environment of Co1 and Co2 in **MOF1**, (b) 2D layer along the *bc* plane formed by the connection between  $\text{Co}^{\text{II}}$  and  $[\text{Cr}(\text{CN})_6]^{3-}$ , Pink circles indicate unsaturated metal sites (UMSs), (c) 3D view of **MOF1** along *a* direction showing 1D channel occupied by guest bpee (sky blue coloured) molecules. (d) Expanded view of the parallel arrangement of coordinated and guest bpee molecules.

Such an arrangement is also supported by H-bonding between the coordinated water molecules (O1w) and nitrogen atom of the guest bpee. Remarkably, the distances between the carbon atoms of two adjacent olefinic double bonds in **MOF1** (guest and bridged bpee molecules) are in the range of 3.83–3.96 Å which satisfies the Schmidt's criteria for a photochemical cycloaddition reaction.<sup>10</sup> To study the feasibility of such topo-chemical solid state [2+2] cycloaddition reaction between host and guest, we have irradiated a single crystal of **MOF1** under UV light (365 nm) for about 1 minute following which crystal data were collected (Figure 4f).



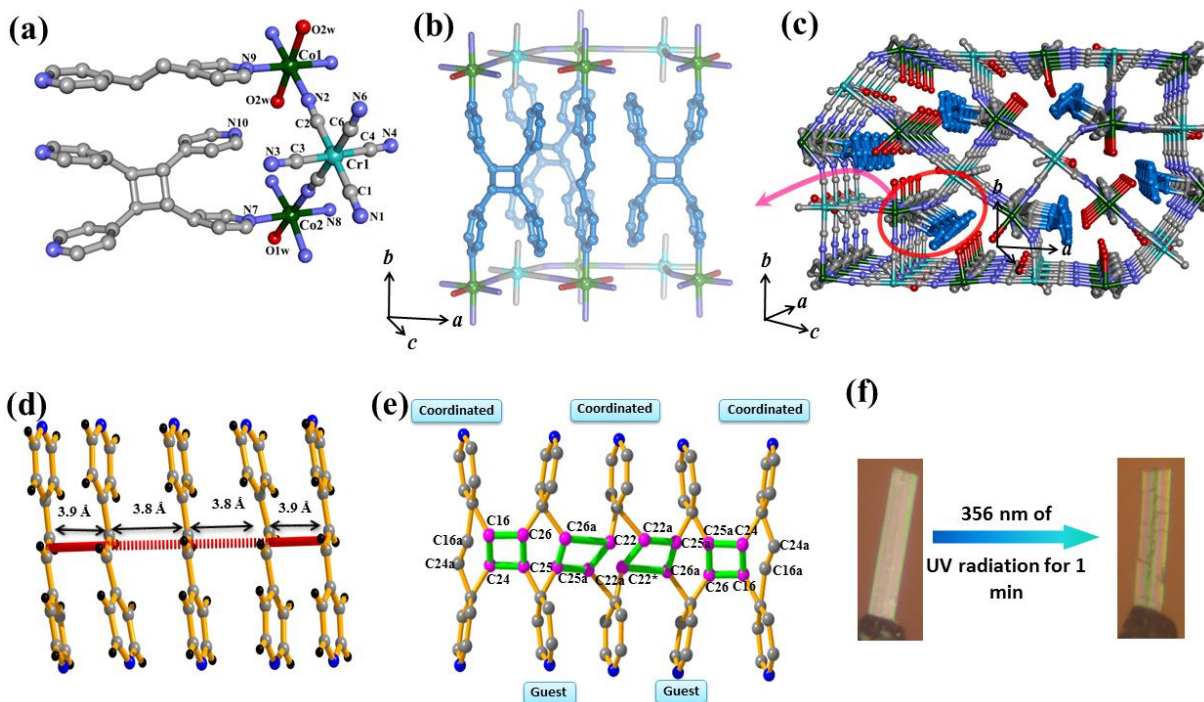


**Figure 4:** (a) Asymmetric unit of **MOF2**, (b) Detailed view of the formation of the *rctt*-*tpcb* ligand after the [2+2] cycloaddition reaction, (c) 3D view of **MOF2** along *a* direction; (d) Parallel arrangement of the five consecutive *bpee* molecules (three pillars and two guests) in **MOF1**, (e) Possibility of all the *bpee* molecules are involved in [2+2] cycloaddition reaction which is observed in single crystal X-ray structure determination, (f) Single crystals of **MOF1** and **MOF2**; after photo irradiation, a drastic loss in single crystallinity was observed. Linear dimension of the crystal is 1.2mm×0.3mm.

**5.3.1.2: Structural description of  $\{[\text{Co}_3(\textit{rctt}\text{-}\textit{tpcb})_2(\textit{bpee})(\text{H}_2\text{O})_4][\text{Cr}(\text{CN})_6]_2 \cdot 2(\text{C}_2\text{H}_5\text{OH}) \cdot 2(\text{H}_2\text{O})\}_n$  (**MOF2**):** Structure determination of the photo-irradiated crystal reveals that the guest and bridged *bpee* linkers undergo [2+2] cycloaddition reaction with the formation of a new pillar *rctt*-tetrakis(4-pyridyl)cyclobutane (*rctt*-*tpcb*), thus resulting in a new MOF  $\{[\text{Co}_3(\textit{rctt}\text{-}\textit{tpcb})_2(\textit{bpee})(\text{H}_2\text{O})_4][\text{Cr}(\text{CN})_6]_2 \cdot 2(\text{C}_2\text{H}_5\text{OH}) \cdot 2(\text{H}_2\text{O})\}_n$  (**MOF2**) (Figures 4a). Now the guest *bpee* became part of the main framework that significantly changes the overall structure (Figure 4b and c). In **MOF2**, sliding of two successive 2D layers was observed as the  $\beta$  angle changes from  $98.6^\circ$  to  $91.2^\circ$  and corresponding lattice parameter *a* decreased from 13.92 to 13.76 Å. Furthermore, the continuous 1D bigger channel of **MOF1** along *a* direction is blocked in **MOF2** due to the formation of *rctt*-*tpcb* pillar which is clearly observed in CPK and Connolly surface figures (Figures 5e–h).

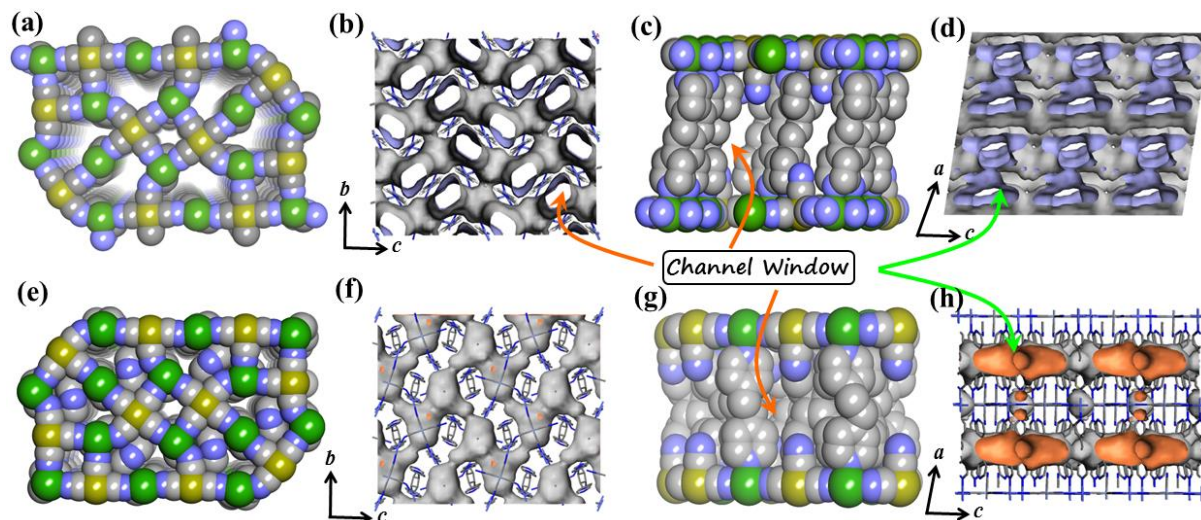


**Figure 5:** (a) and (c): Pore view of **MOF1** along the crystallographic  $a$  and  $b$  direction respectively in CPK diagram. (b) and (d): Connolly surface of the 1D channel of **MOF1a** along  $a$  and  $b$  direction respectively. (e) and (g): Pore view of **MOF2** along the crystallographic  $a$  and  $b$  direction respectively in CPK diagram. (f) Connolly surface of **MOF2a** along  $a$  direction (continuous 1D channels along  $a$  direction in **MOF1** has been blocked in **MOF2** after photo irradiation). (h) Connolly surface of **MOF2a** along  $b$  direction is showing the window of the interconnected cages.

Therefore, **MOF2** has modified to interconnected cage like pore structure which is only accessible along the  $b$  direction (Figures 5h). Such a PSM of the pore structure using light in a MOF system involving a guest is unprecedented. The  $\text{Co}^{\text{II}}\text{-N}$  and  $\text{Co}^{\text{II}}\text{-O}$  bond distances and bond angles related to  $\text{Co}^{\text{II}}$  centers in **MOF1** and **MOF2** remain similar; however the void volume is reduced by 29.7 % in **MOF2** compared to **MOF1**. Another remarkable feature of the **MOF1** framework is the parallel arrangement of five consecutive bpee linkers in a higher dimensional network and the corresponding photochemical transformation of such an arrangement in a single-crystal-to-single-crystal transformation fashion is yet to be realized (Figure 4d and e).

### **5.3.2: Framework Stability: Thermogravimetric (TG) and Powder X-ray Diffraction (PXRD) Analysis**

TGA profile of **MOF1** (Figure 6(a)) indicates a weight loss of 8.7% at 65 °C which corroborates the removal of two guest molecules each of water and ethanol (cal. 7.6 %). The second step observed at 216 °C with a wt. loss of 31.8 %, indicates the removal of guest bpee

and coordinated water molecules (cal. 33.1 %). The phase with complete removal of guest molecules and also coordinated water molecules, which we consider as **MOF1a**, is stable up to 245 °C. **MOF2** shows stepwise release of the guest (water and EtOH) and metal-bound coordinated water molecules at 115 and 240 °C respectively (Figure 6(b)). The deguest framework *i.e.*, **MOF2a** is stable up to 265 °C. This suggests that PSM provides thermal stability to **MOF2**.

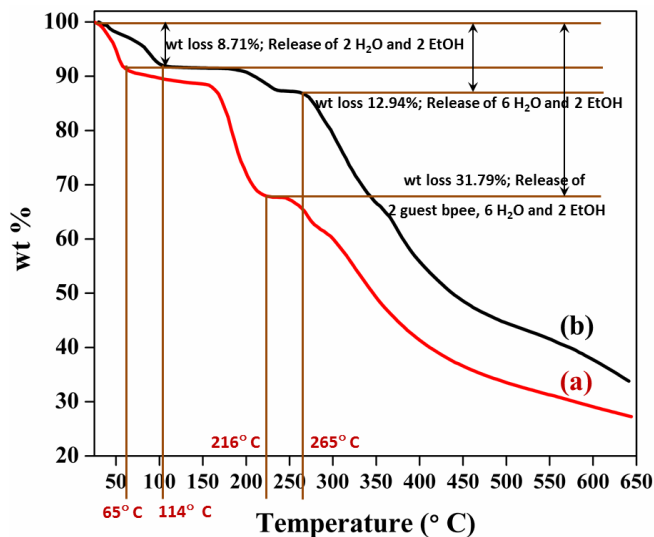


**Figure 6:** TGA profiles (heating rate = 2 °C/min) of compounds **MOF1** (a) and **MOF2** (b) in the temperature range of 30 to 650 °C.

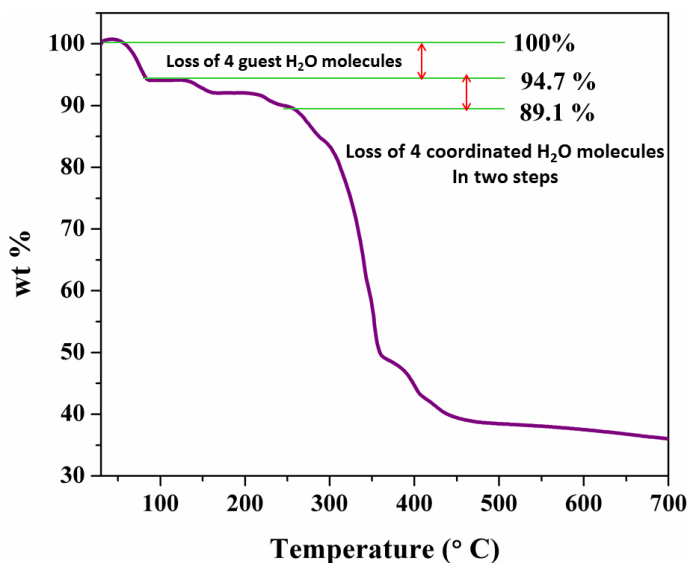


**Figure 7:** TGA profile of **MOF1b** confirms the presence of total eight water molecules.

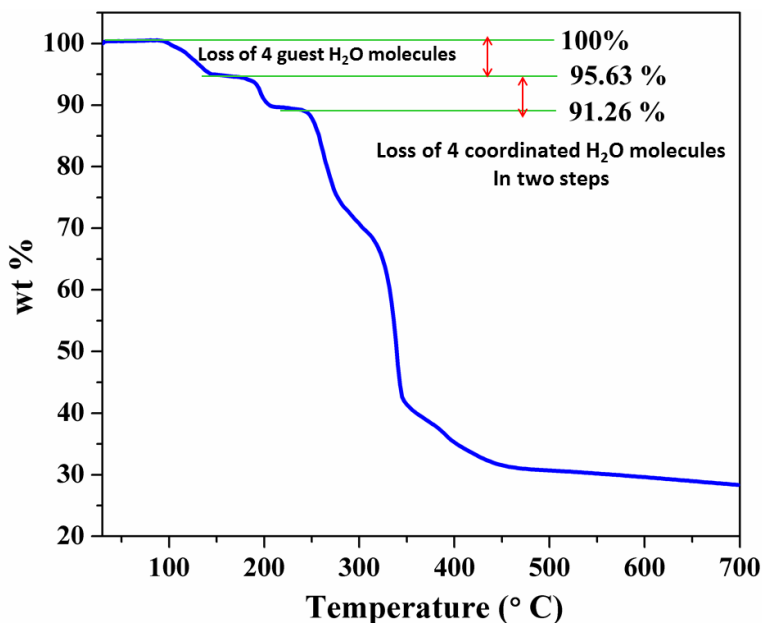


**Figure 8:** TGA profile of **MOF2b** confirms the presence of total eight water molecules.

The TGA profiles (Figure 7 and 8) of the rehydrated frameworks (**MOF1b** and **MOF2b**) show stepwise release of total eight water molecules. The experimental PXRD patterns (Figure 9 and 10) of **MOF1** and **MOF2** show good agreement with their corresponding simulated ones which demonstrate their phase purity. A detailed analysis of the patterns of **MOF1** and **MOF1a** reveals that the peak at  $2\theta = 6.42^\circ$  ( $d = 14.06 \text{ \AA}$ ; (100) plane) of the as-synthesized compound is shifted to  $6.50^\circ$  ( $d = 13.57 \text{ \AA}$ ) in the guest-removed compound, suggesting structural shrinkage upon activation. The removal of guest bpee molecules is a likely reason for the decrease of the distance between two successive 2D layers, which results in a shift of the PXRD peak towards higher angle. We do not observe a similar change in the PXRD pattern of **MOF2a** which suggests enhanced structural rigidity after the fusion of the guest bpee molecules with the main part of the framework. We have exposed **MOF1a** and **MOF2a** to water vapor for 7 days and the PXRD patterns of water exposed samples remain unchanged with respect to the **MOF1** and **MOF2** respectively, indicating water stability of these metal-organic frameworks.

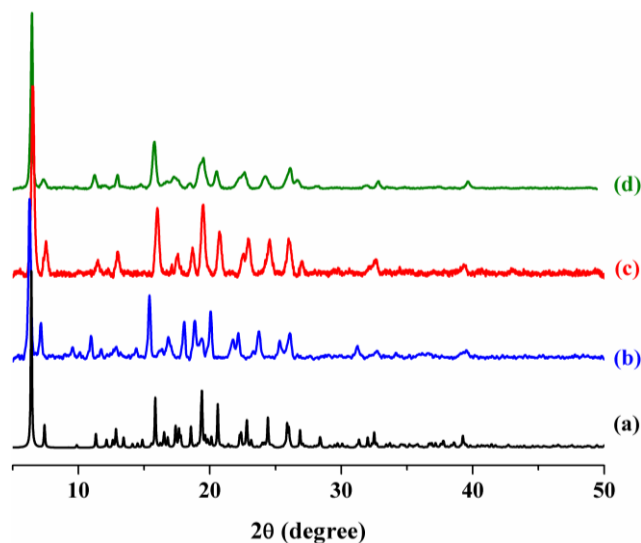


**Figure 9:** PXRD patterns of **MOF1** at different states. (a) simulated, (b) as-synthesized, (c) heated at 120 °C and (d) exposed to water vapor for 7 days.

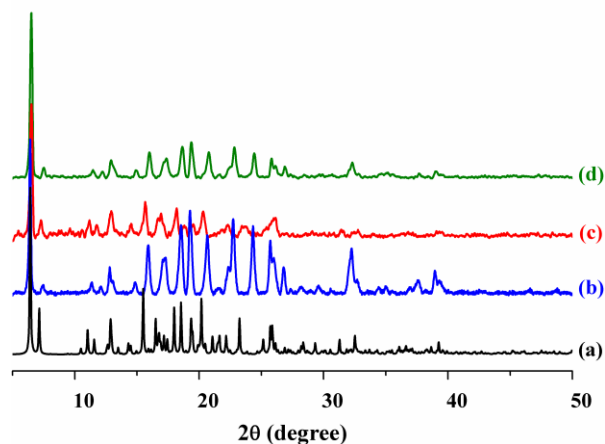


**Figure 10:** PXRD patterns of **MOF2** at different states. (a) simulated, (b) as-synthesized, (c) heated at 120 °C and (d) exposed to water vapor for 7 days.

### **5.3.3: NMR spectra analysis of the bulk powder of MOF1 and MOF2**

The quantitative yield of *rctt*-*tpcb* has been calculated from NMR spectra (Figure 11 and 12) and is found to be ~75 %. This is expected in a five layered arrangement of *bpee* where only 4 out of 5 molecules (*i.e.* maximum 80%) can undergo photodimerization. The  $^1\text{H}$  NMR spectrum of **MOF2** shows features arising from the cyclobutane protons of *rctt*-*tpcb* ( $d = 5.62$  ppm) as well as a shift in the signals of pyridine protons (from  $d = 8.96$  and  $8.38$  ppm to  $8.75$  and  $8.1$  ppm).

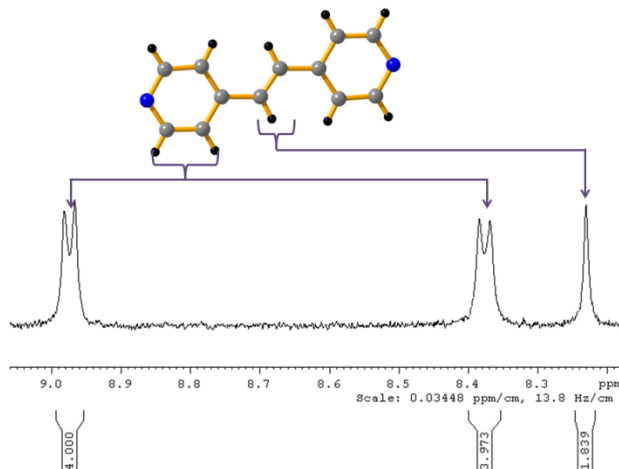


**Figure 11:**  $^1\text{H}$ -NMR spectra of **MOF1** digested in  $\text{DMSO}-d_6/\text{aq.HCl}$  at 293 K. Two doublet signals at  $\delta = 8.96$  and  $8.38$  ppm are due to the hydrogen atoms of pyridine ring and a singlet at  $\delta = 7.92$  is due to the hydrogen atoms of olefinic double bond.

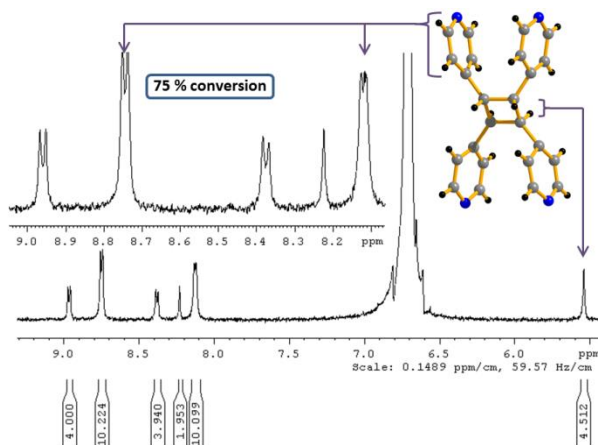


**Figure 12:**  $^1\text{H}$ -NMR spectra of **MOF2** digested in  $\text{DMSO}-d_6/\text{aq.HCl}$  at 293 K. Two doublet signals at  $\delta = 8.75$  and  $8.1$  ppm are due to the hydrogen atoms of pyridine ring and a singlet at  $\delta = 5.62$  is due to the hydrogen atoms of cyclobutane ring. The presence of unreacted bpee molecules is reflected from the signals at  $\delta = 8.97$ ,  $8.39$  and  $8.23$ .

### 5.3.4: Gas adsorption

#### 5.3.4.1: Experimental

The porosity of **MOF1a** and **MOF2a** were studied using  $\text{N}_2$  (kinetic diameter  $3.64 \text{ \AA}$ )<sup>29</sup> adsorption experiment (Figure 13(a)).  $\text{N}_2$  adsorption isotherm of **MOF1a** at 77 K shows an initial uptake of  $19 \text{ mL/g}$  at very low pressure region (up to  $P/P_0 = 0.01$ ). With increasing pressure, the uptake amount gradually increases and reaches to an amount of  $60 \text{ mL/g}$  at  $P/P_0$

= 0.56. (inset Figure 13a(1)), suggesting microporous nature of the framework. Beyond this pressure, the gradient of uptake profile increases which ends to a final amount of 157 mL/g at  $P/P_0 = 0.98$ . The surface area of **MOF1a** is 151  $\text{m}^2/\text{g}$  calculated using BET method. However, **MOF2a** shows very little initial uptake of  $\text{N}_2$  at low pressure (Figure 13a (2); BET surface area 32  $\text{m}^2/\text{g}$ ). The reduced uptake of  $\text{N}_2$  by **MOF2a** may be due to the presence of discrete cages which are interconnected through the narrow channel that prevents further diffusion of  $\text{N}_2$  to other cages. Such drastic change of  $\text{N}_2$  uptake after PSM has been corroborated by theoretical studies.

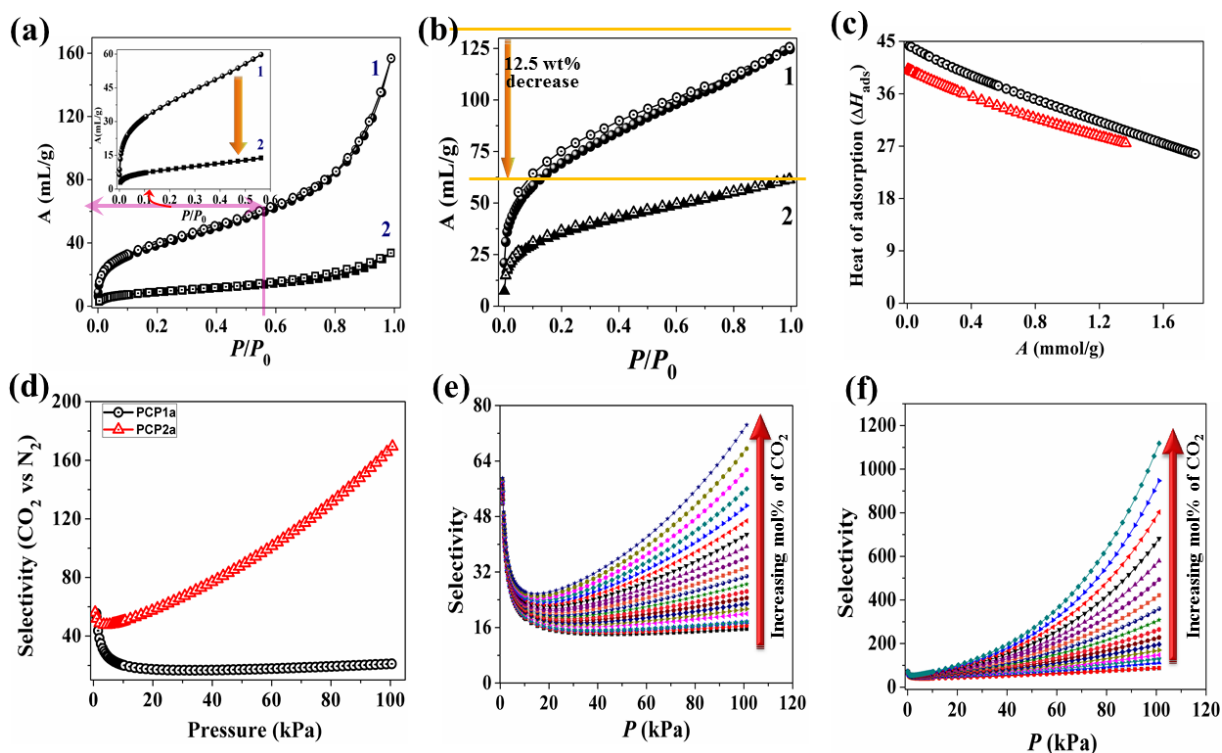


**Figure 13:** (a)  $\text{N}_2$  adsorption isotherms of **MOF1a** (1) and **MOF2a** (2) at 77 K. Inset:  $\text{N}_2$  uptake profile at low pressure region shows effective decrease in adsorption amount after photo irradiation. (b)  $\text{CO}_2$  adsorption isotherms of **MOF1a** (1) and **MOF2a** (2) at 195 K. Closed and open symbols correspond to adsorption and desorption, respectively. (c) Heat of adsorption of  $\text{CO}_2$  vs. loading for compound **MOF1a** (black circle) and **MOF2a** (red triangle). (d) Predicted adsorption selectivity of  $\text{CO}_2/\text{N}_2$  for **MOF1a** (black circle) and **MOF2a** (red triangle) at 283K. (e) & (f) Change of the predicted adsorption selectivity in **MOF1a** and **MOF2a** with increasing mol% of  $\text{CO}_2$  (from 10% to 30% in the interval of 1% increase) in the binary mixture of  $\text{CO}_2\text{-N}_2$ .

On the other hand,  $\text{CO}_2$  (kinetic diameter 3.30 Å)<sup>30</sup> adsorption (at 195 K, Figure 13b) in **MOF1a** and **MOF2a** show typical type-I adsorption profiles with final uptake amounts of

24.7 wt% (126 mL/g; ~6 molecules/formula unit) and 12.2 wt% (62 mL/g; ~4 molecules/formula unit) respectively. Such a selective uptake of CO<sub>2</sub> after PSM is remarkable although the amount of CO<sub>2</sub> uptake decreases. This suggests that discrete cages are accessible for CO<sub>2</sub> molecules through narrow channels. In order to evaluate the CO<sub>2</sub> storage performance of the compounds, we have performed an initial CO<sub>2</sub> adsorption study at 283 K. The CO<sub>2</sub> adsorption uptake is assessed to be 6.29 and 4.52 wt% (32 and 23 mL/g) at 760 torr for **MOF1a** and **MOF2a** respectively. Further, we have also investigated CO<sub>2</sub> adsorption property at 273 K which shows the final uptake of 7.86 wt% (40 mL/g) and 5.51 wt% (28 mL/g) at 760 torr. The isosteric heat of adsorption ( $Q_{st}$ ) for CO<sub>2</sub> is estimated to be 44.2 and 40.3 kJ mol<sup>-1</sup> at zero coverage (Figure 13c) for **MOF1a** and **MOF2a**, respectively obtained by using virial type equation (Figures 21 and 22). It is interesting to note that almost similar binding energy and decreasing trend in  $Q_{st}$  value with increase in gas loading are observed for both **MOF1a** and **MOF2a** that suggest the presence of same adsorption sites in both, at initial loading of CO<sub>2</sub>.

These  $Q_{st}$  vs loading study reveals a strong affinity of **MOF1a** and **MOF2a** towards the CO<sub>2</sub> gas molecule which encouraged us to examine the performance of CO<sub>2</sub> separation from a CO<sub>2</sub>/N<sub>2</sub> mixture (15:85 molar ratio) at ambient temperature and pressure. Employing the IAST (Ideal Adsorbed Solution Theory)<sup>31</sup> on the pure component isotherm fittings (measured at 283 K), adsorption selectivity for both the compounds were calculated (Figures 23–25). The predicted adsorption selectivity of **MOF1a** and **MOF2a** at zero coverage loading is 55 and 70 respectively (Figure 13d). The selectivity value for **MOF1a** decreases drastically with increase of loading, whereas that for **MOF2a** increases in an exponential manner, demonstrating that **MOF2a** would be a better material in the separation of CO<sub>2</sub> from its mixture with N<sub>2</sub>. We have also tested the selectivity by increasing the molar ratio of CO<sub>2</sub> from 10% to 30% with increment of 1 mol% in CO<sub>2</sub>:N<sub>2</sub> mixture which shows that the predicted selectivity for **MOF1a** is in the range of 55 to 80 at higher loading. However, at higher molar concentration of CO<sub>2</sub> in gas mixture, the selectivity value for **MOF2a** is increased very rapidly with increase in pressure (Figures 13e and f) which reaches to a final value around 1170. Such enhanced selectivity after PSM is quite remarkable. To understand this differential selectivity behavior between **MOF1a** and **MOF2a**, we have performed a detailed theoretical study which has been discussed in the following section.



**5.3.4.2: Theoretical insight on the high CO<sub>2</sub> selectivity of the photo-modified framework**

To obtain a microscopic understanding of the distinction in the adsorption of CO<sub>2</sub> and N<sub>2</sub> in these compounds, we employed periodic density functional theory (DFT) based calculations. The geometry and cell parameters of **MOF1a** and **MOF2a** were optimized at PBE–D3 level of theory. The same are provided in Table 6 and Table 7. Binding energies of CO<sub>2</sub> and N<sub>2</sub> molecules in one unit cell each of **MOF1a** and **MOF2a** were also calculated.

**Table 6:** Comparison of cell parameters of **MOF1a** calculated using PBE–D3 based DFT method against experimental data.

Method	<i>a</i> (Å)	<i>b</i> (Å)	<i>c</i> (Å)	$\beta$ (°)	<i>V</i> (Å <sup>3</sup> )	$\left(\frac{\Delta V}{V}\right)$
Experiment <b>MOF1</b>	13.919	17.897	16.136	98.619	3974.13	
DFT <b>MOF1a</b>	13.519	17.887	16.096	97.719	3856.89	–3.0%

**Table 7:** Comparison of cell parameters of **MOF2a** calculated using PBE–D3 based DFT method against experimental data.

Method	<i>a</i> (Å)	<i>b</i> (Å)	<i>c</i> (Å)	$\beta$ (°)	<i>V</i> (Å <sup>3</sup> )	$\left(\frac{\Delta V}{V}\right)$
Experiment <b>MOF2</b>	13.764	17.765	16.391	91.261	4006.97	
DFT <b>MOF2</b>	13.514	17.135	16.101	91.561	3727.0	–7.0%
DFT <b>MOF2a</b>	13.514	16.664	16.101	91.361	3624.88	–9.5%

The calculated cell parameters of **MOF2** and **MOF2a** exhibit non-negligible differences with the experimental value (Table 7). Given that the comparison between theory and experiment was good for **MOF1** and **MOF1a**, the methods adopted for the calculations can be assumed to be appropriate. Thus, the differences seen for the photodimerized compound, is likely due to the model for **MOF2a** used in computation.

There are three adsorption sites (four and five-coordinated Co<sup>II</sup> unsaturated sites and pendent CN group (four pairs)) for CO<sub>2</sub> molecules in **MOF1a**. It is important to note that in

**MOF1**, the solvent molecules too are located near these sites. Thus,  $\text{CO}_2$  molecules are found to substitute for the solvent molecules, upon desolvation.  $\text{CO}_2$  molecules interact electrostatically with the unsaturated  $\text{Co}^{\text{II}}$  sites (two molecules with four coordinated and one with five coordinated metal), whereas the free cyanide groups exhibit Lewis acid–base type interaction (one  $\text{CO}_2$  molecule per pair of free CN) between the C atoms of  $\text{CO}_2$  and N atom of the CN groups.

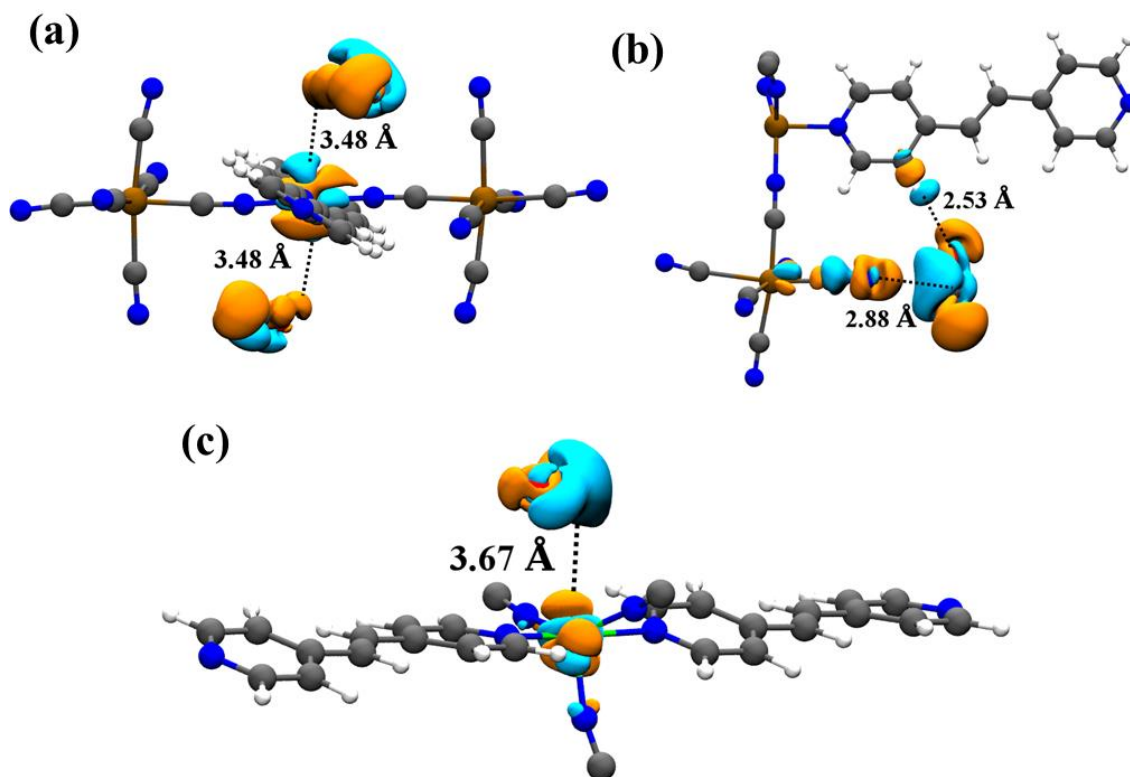


**Figure 14:** Interaction sites of  $\text{CO}_2$  in **MOF1a**. At a) four-coordinated  $\text{Co}^{\text{II}}$ , b) pendent  $-\text{CN}$  site and c) five-coordinated  $\text{Co}$ . Cyan and orange regions indicate decreased and increased electron densities with respect to isolated MOF and isolated  $\text{CO}_2$  molecule respectively. Iso-surface value is  $4 \times 10^{-4}$  a. u. The electron density differences were calculated for the entire MOF crystal, although only a part (fragment) of the MOF is shown here for clarity. Color scheme: MOF atoms are in C– gray, H– white, N– blue and Co–green;  $\text{CO}_2$  atoms: C– grey and O–red.

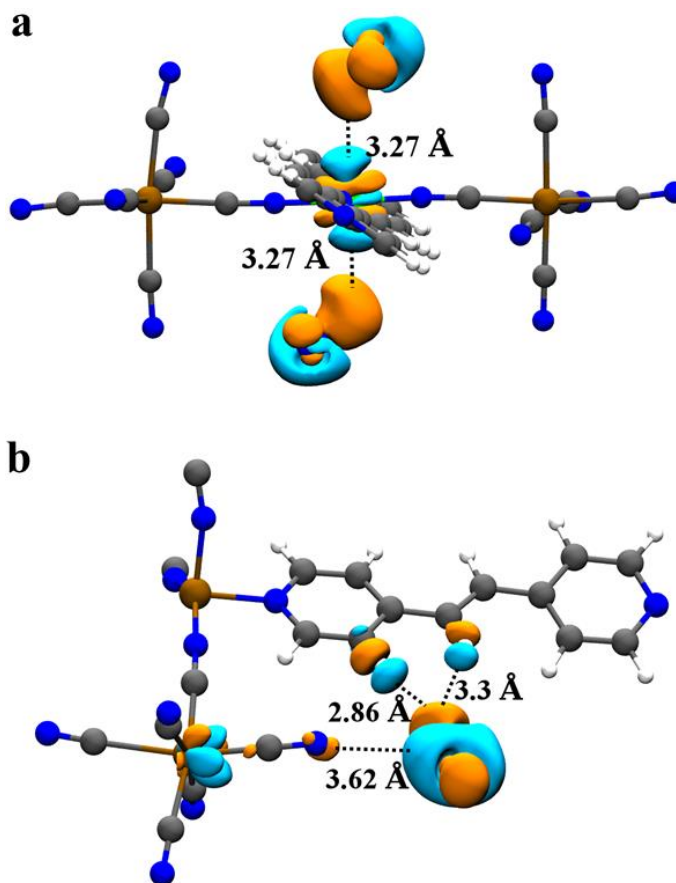


**Figure 15:** Interaction sites of N<sub>2</sub> in **MOF1a**. At (a) four-coordinated Co<sup>II</sup>, and (b) CN site. Cyan and orange regions indicate decreased and increased electron densities with respect to isolated MOF and isolated N<sub>2</sub> molecule respectively. Iso-surface value is  $4 \times 10^{-4}$  a.u. The electron density differences were calculated for the entire MOF crystal, although only a part (fragment) of the MOF is shown here for clarity. Color scheme: MOF atoms: C– grey, H– white, N– blue and Co–green.

The specific nature of interactions can be understood through Figure 14, which shows the region of the MOFs that are proximal to the gas molecules. The experimental isosteric heat of adsorption for CO<sub>2</sub> in **MOF1a** is 44.3 kJ/mol which is comparable to the binding energy of CO<sub>2</sub> (43.0 kJ/mol) at the –CN site obtained from the PBE–D3 approach (Table 8). This result suggests that CO<sub>2</sub> prefers to bind at the –CN site at low coverage. Binding energy values of CO<sub>2</sub> are also comparable to enthalpies of adsorption in other systems functionalized with hydroxyl or amino groups (39–46 kJ/mol)<sup>32</sup>. The calculations suggest that, a maximum of twelve CO<sub>2</sub> molecules can be adsorbed per unit cell of **MOF1a** which matches with the experimental observation of a maximum of six CO<sub>2</sub> molecules adsorbed per formula unit of **MOF1a** (a unit cell of **MOF1a** contains two formula units).

**Table 8:** Binding energies of CO<sub>2</sub> and N<sub>2</sub> at the three binding sites in **MOF1a** obtained at PBE–D3 level of theory.

Binding site in <b>MOF1a</b>	Molecule	Binding energy (kJ/mol)
4-coordinated Co	CO <sub>2</sub>	–32.1
5-coordinated Co	CO <sub>2</sub>	–32.7
–CN	CO <sub>2</sub>	–43.0
5-coordinated Co	N <sub>2</sub>	–22.3
4-coordinated Co	N <sub>2</sub>	–22.2
–CN	N <sub>2</sub>	–22.1

N<sub>2</sub> binds near the same binding sites as CO<sub>2</sub> except near the five-coordinated Co sites, thus, there can be a maximum of eight N<sub>2</sub> molecules per unit cell. The number of gas molecules per unit cell calculated thus matches the experimental uptake of CO<sub>2</sub> and N<sub>2</sub>. Optimized geometries of CO<sub>2</sub> and N<sub>2</sub> in **MOF1a** are shown in Figures 14 and 15, respectively. The binding energies of N<sub>2</sub> at all possible interaction sites are tabulated in Table 8, and are higher than those reported in literature for Co(1,4-benzenedipyrzolate) MOF (14.7 kJ/mol)<sup>33</sup> but are comparable to the value observed in alkali metal ion exchange zeolites (19–26 kJ/mol)<sup>34</sup>.

Similar to **MOF1a**, three binding sites also exist in **MOF2a**. However, after PSM, the guest bpee molecules are bonded with the framework, and thus both the unsaturated Co<sup>II</sup> metal (UMS) sites are inaccessible for CO<sub>2</sub> binding. Thus CO<sub>2</sub> can effectively interact only with pendent CN groups. Eight CO<sub>2</sub> molecules are present near four pairs of CN groups, which interact via Lewis acid–base interactions between the –CN group and the C atom of CO<sub>2</sub>, thus, totaling to a maximum of eight CO<sub>2</sub> molecules per unit cell of **MOF2a**. The maximum number of CO<sub>2</sub> molecules predicted to bind per unit cell of **MOF2a** thus matches the experimentally determined uptake. Binding energies of CO<sub>2</sub> calculated from the PBE–D3 approach compare well with the experimentally determined low coverage isosteric heat of adsorption of 40 kJ/mol.

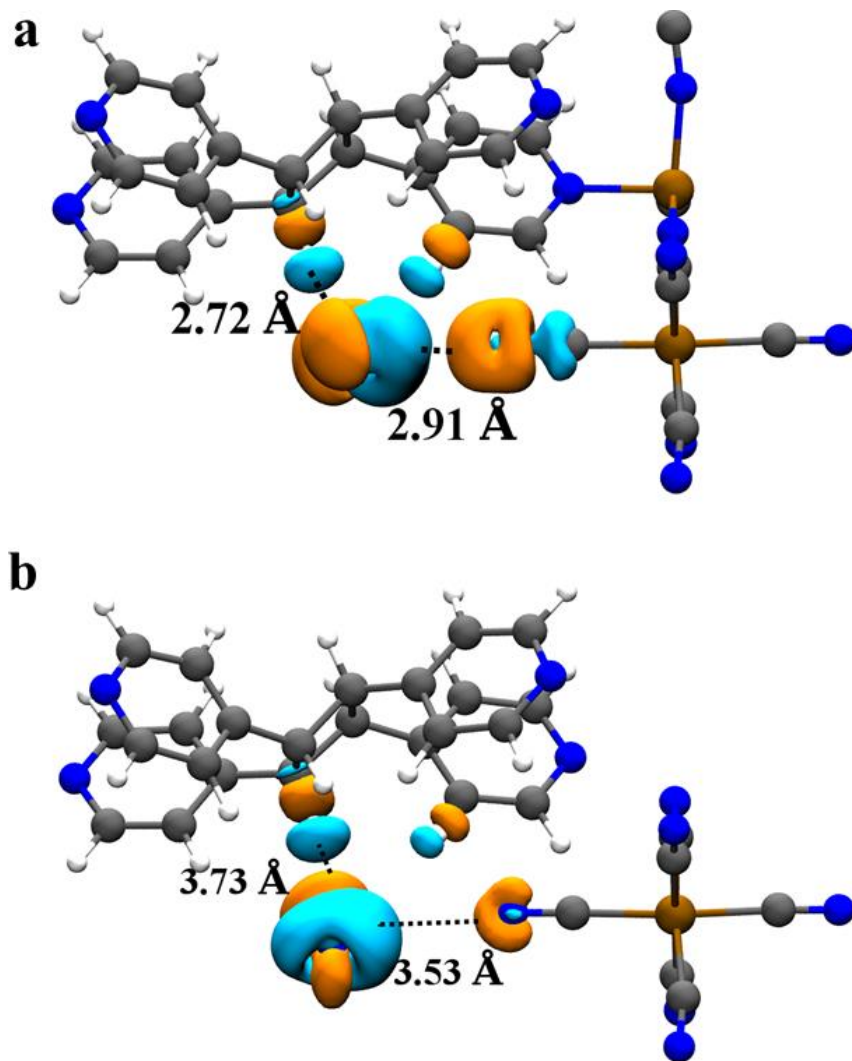


**Figure 16:** (a) CO<sub>2</sub> and b) N<sub>2</sub> binding sites near the –CN group of MOF2a. Cyan and orange regions indicate the decreased and increased electron densities respectively, with respect to isolated MOF and isolated gas molecules. Iso-surface value is  $4 \times 10^{-4}$  a. u. The electron density differences were calculated for the entire MOF crystal, although only a part (fragment) of the MOF is shown for clarity. Color scheme: MOF atoms are in C– gray, H– white, N– blue, Cr– ochre and Co–green; CO<sub>2</sub> atoms: C– gray and O–red.

**Table 9:** Binding energies of CO<sub>2</sub> and N<sub>2</sub> at the pendent CN molecular group of MOF2a obtained at PBE–D3 level of theory.

Binding sites in MOF2a	Molecule	Binding energy (kJ/mol)
CN site	N <sub>2</sub>	–23.5
CN site	CO <sub>2</sub>	–43.0

However, in the case of N<sub>2</sub>, eight molecules are expected to bind **MOF2a** theoretically whereas only two are observed experimentally. This issue will be discussed later. The optimized geometries of CO<sub>2</sub> and N<sub>2</sub> in **MOF2a** are shown in Figure 16, and the binding energies are tabulated in Table 9. Experimental adsorption measurements demonstrate facile adsorption of both CO<sub>2</sub> and N<sub>2</sub> in **MOF1a**. However, **MOF2a** is seen to adsorb only CO<sub>2</sub> and not N<sub>2</sub>. The binding energies shown in Table 9 support the favorable interaction of N<sub>2</sub> with the CN group. However, a given N<sub>2</sub> molecule adsorbed at a CN group experiences a large kinetic barrier to explore another CN site. This aspect is explored further in the next section which presents free energy data for CO<sub>2</sub> and N<sub>2</sub> in **MOF1a** and **MOF2a** obtained through the Adaptive Biasing Force (ABF) method.

### **Free energy (FE) calculations:**

Experimentally determined 2×2×2 super cells of both MOFs were considered as simulation cells. Free energy calculations were carried out at 298 K using LAMMPS package. Temperature was maintained through the use of a N ose–Hoover chain thermostat<sup>35</sup>. The equations of motion were integrated with a time step of 2.0 fs employing the velocity Verlet algorithm. UFF<sup>36</sup> and TraPPE<sup>37</sup> force field parameters were considered for the MOF and CO<sub>2</sub> respectively. The atom site chargeless model was considered for N<sub>2</sub> molecule<sup>38</sup>. For van der Waals interaction, the cut-off radius is considered to be 12.8   and the potential parameters are tabulated in Tables 10, 11. Cross interactions were handled via Lorentz–Berthelot mixing rules. During free energy calculations, MOF, CO<sub>2</sub> and N<sub>2</sub> were considered as rigid entities.

**Table 10:** Force field parameters employed to model **MOF1a** and **MOF2a**.

Atom	$\sigma$ (�)	$\epsilon$ (kcal/mol)
C	3.431	0.105
Cr	2.872	0.014
Co	3.023	0.015
H	2.571	0.044
N	3.261	0.069

**Table 11:** Force field parameters for CO<sub>2</sub> and N<sub>2</sub>.

Atom	Bond length (Å)	$\sigma$ (Å)	$\epsilon$ (kcal/mol)
C	1.16	2.8	0.054
O		3.05	0.157
N	1.09	3.31	0.074

**Adaptive Biasing Force (ABF):**

‘Colvars’ (collective variable) module embedded in LAMMPS package is used to determine the FE profiles. ABF is a force based FE technique which applies an external force ( $F_{ABF}$ ) on the system to sample the entire phase space. If the average force exerted on the reaction coordinate (RC) over a given number of steps ( $N_{\text{samples}}$ ) is  $\langle F_{\text{avg}} \rangle$ , then ABF applies a force equal in magnitude but opposite in direction to nullify it. For the application of this force, the entire range of RC is divided into bins. We considered 500 for  $N_{\text{samples}}$  and 0.1 Å as the bin-width.

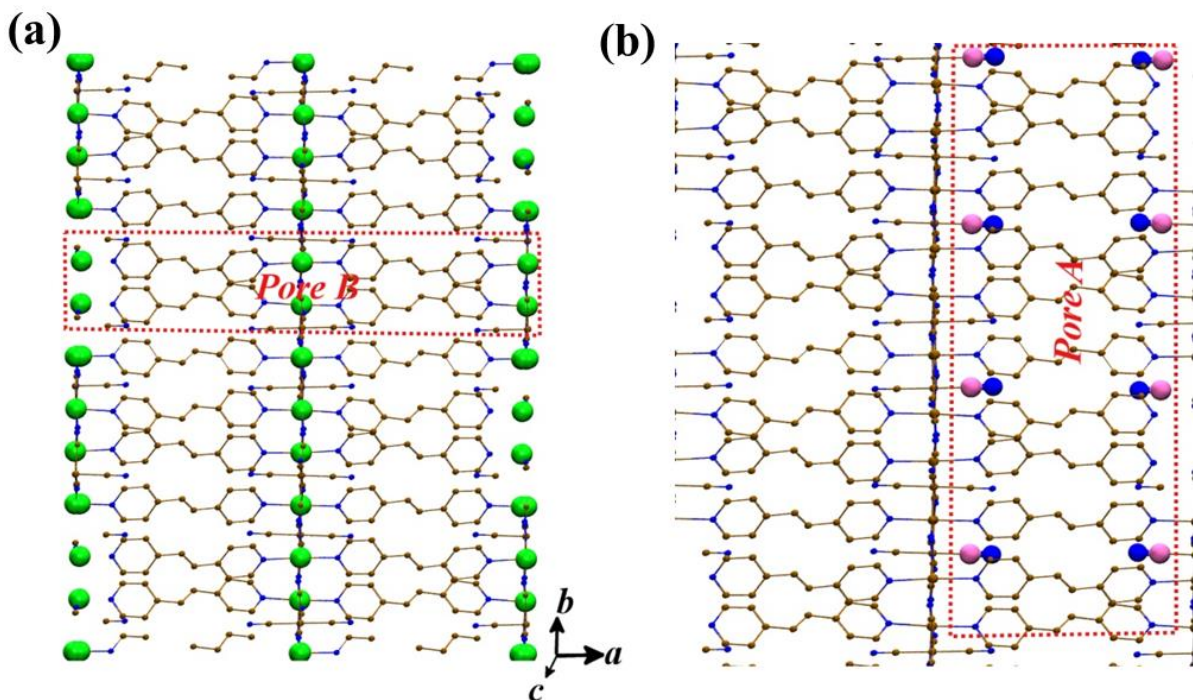


**Figure 17:** Architecture of (a) *Pore A* (aligned along Co atoms) and (b) *pore B* (aligned along the CN groups) in **MOF1a**. Red box indicates the schematic of *pore A* and *pore B* in *a*, *b* respectively. Color scheme: Co–green, C– brown, N–blue; CN groups: C–pink, N–blue. All H atoms are hidden for the sake of clarity.

Binding energy calculations provide an idea of adsorption sites at 0 K. However, what matters in an experimental adsorption isotherm is the free energy (FE) of binding at a finite temperature as well as the barriers the adsorbent experiences. Such FE calculations are robust enough to determine not only the binding sites of a gas molecule, but also can be used to delineate the pathways in which it can traverse through the framework. We have employed the Adaptive Biasing Force (ABF) method<sup>39</sup> to determine the FE of a gas molecule on a two dimensional surface in **MOF1a** and **MOF2a** at 298 K. These were obtained for CO<sub>2</sub> and N<sub>2</sub> by considering 2×2×2 unit cells. In the following, we denote the pore lined by Co<sup>II</sup> atoms as *pore A* (along *a*-axis) and one lined by CN groups as *pore B* (along *b*-axis) in both **MOF1a** and **MOF2a**.

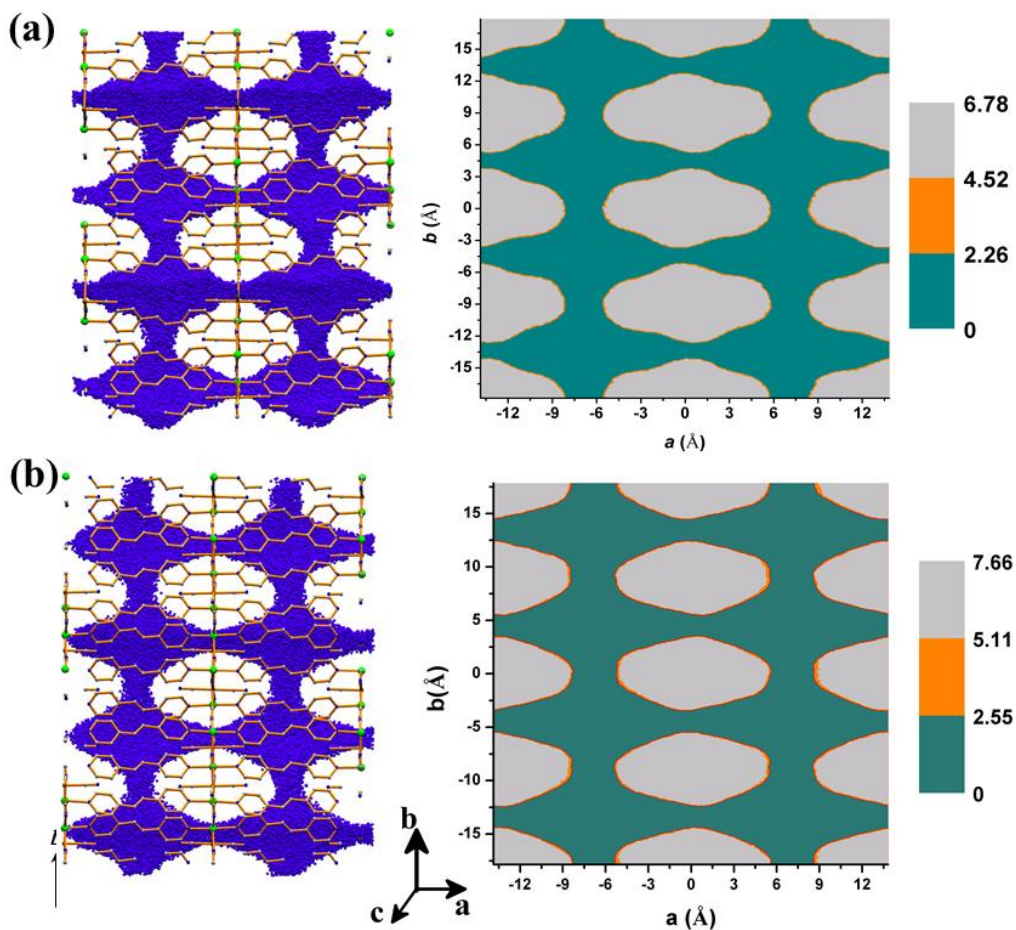


**Figure 18: Theoretical insight on the dynamic pathway of gas adsorption in MOF1a:** Dynamical pathways (left) and computed free energy surfaces (right) for (a) CO<sub>2</sub> and (b) N<sub>2</sub> molecules in **MOF1a**. Vertical bars are free energies in kcal/mol at 298 K. The framework is represented as sticks and the center of mass of CO<sub>2</sub>, and N<sub>2</sub> as spheres. H atoms of MOF are hidden for the sake of clarity. (Color scheme for left panel: C– Silver, Co– green, CO<sub>2</sub>/N<sub>2</sub> – violet).



Gas molecules can adsorb in both *pore A* and *pore B* of **MOF1a** (see Figure 17). An appropriate reaction coordinate (RC) needs to be defined which will enable the molecule to sample the pores efficiently. Consider the distance between one of the Cr atoms of **MOF1a** and the center of mass of the gas molecule. The projection of this distance along the *a* and *b* crystallographic axes are defined as the two RCs. Using the colvars<sup>40</sup> module in LAMMPS<sup>21a</sup>, ‘distance Z’ style was employed to determine such FE profiles. The trajectory of CO<sub>2</sub> and N<sub>2</sub> and the FE profiles in **MOF1a** are shown in Figure 18. Figures on the left side show the MOF framework as sticks and instantaneous locations of the gas molecule in violet color. Two dimensional FE surface for the same framework is depicted on the right side. Both CO<sub>2</sub> and N<sub>2</sub> are found to pass easily from one pendent CN group to another and also from one metal site to another. In **MOF1a**, both *pores A* and *B* are interconnected with each other. The movement of the gas molecule through the pores is accompanied with a small energy barrier of around 0.5 kcal/mol, which is easily accessed at room temperature as well as at experimental conditions. The symmetry in the crystal structure of **MOF1a** is reflected in the FE surface, as expected. In the right panels of Figure 19, gray color indicates the location of **MOF1a** atoms and green indicates the pathway of the gas molecule. The FE well for CO<sub>2</sub> is deeper as compared to that for N<sub>2</sub>, suggesting the stronger binding of the former.

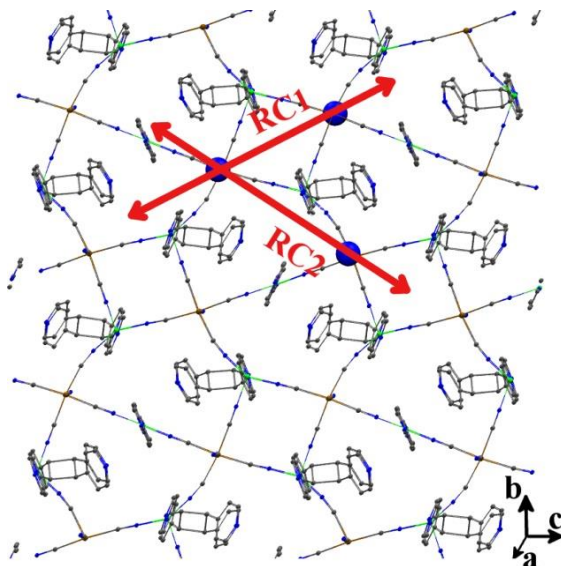


**Figure 19:** Definition of reaction coordinated in **MOF2a**. Red arrows indicate the RC1 and RC2 which are defined by combining the N atoms of CN groups along the pores. Color scheme: C–gray, N–blue and Co–green. H atoms are hidden for the sake of clarity.

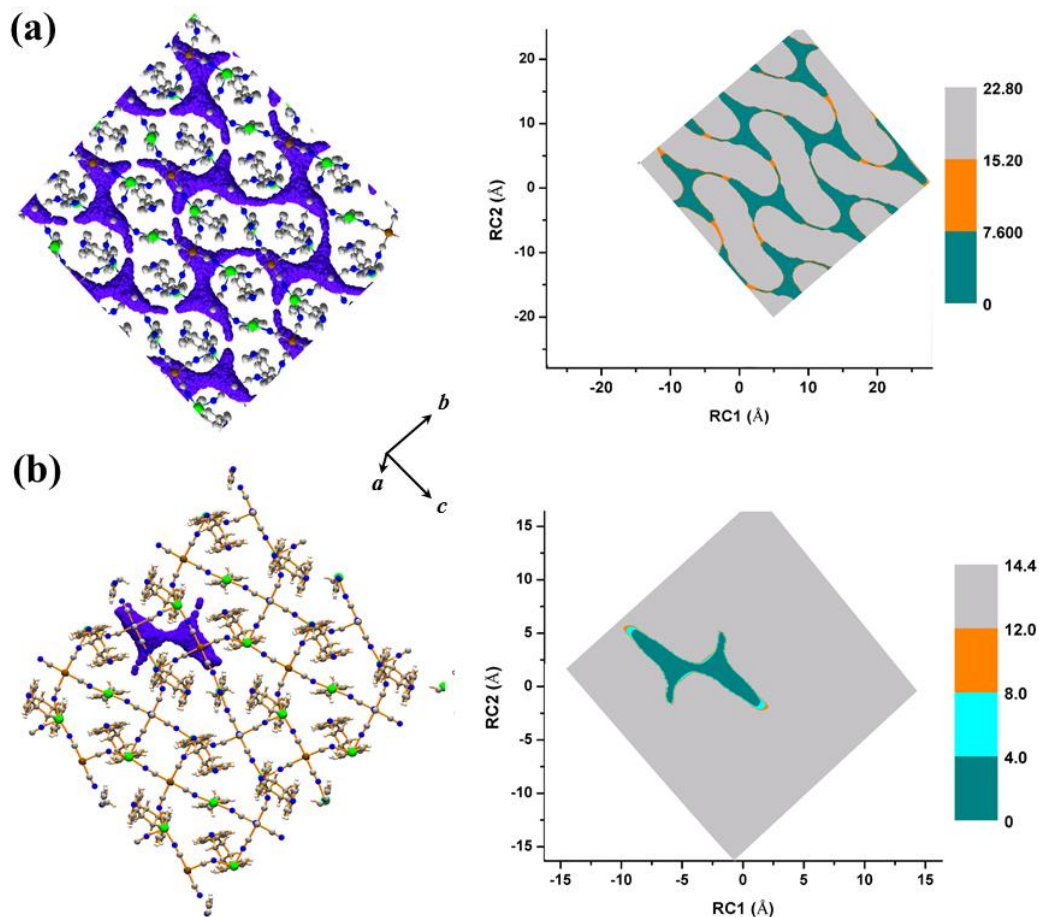


**Figure 20: Theoretical insight on the dynamic pathway of gas adsorption in MOF2a:** Dynamical pathways (left) and computed free energy surfaces (right) for (a)  $\text{N}_2$  and (b)  $\text{CO}_2$  molecules in **MOF2a**. Vertical bars are free energies in kcal/mol at 298 K and RC1 and RC2 are reaction coordinates defined in Figure 19. The framework is represented as sticks and center of mass of  $\text{CO}_2$ , and  $\text{N}_2$  as spheres. H atoms of MOF are hidden for the sake of clarity. (Color scheme for left panel: C– Silver, Co– green,  $\text{CO}_2/\text{N}_2$  – violet).

The porosity of **MOF2a** is much different from that of **MOF1a**. *Pore A* is inaccessible to the gas molecule after PSM as mentioned earlier. Thus, the gas molecule can adsorb only in *Pore B*. All pores of type B are interconnected through narrow channels. Consider the distance between the N atom of one of the CN group of **MOF2a** and the center of mass of the gas molecule. Projection of this distance along the narrow channels is considered as RC1 and RC2 (Figure 19). Note that the two projections are not along any of the crystallographic axes (Figure 20 for the orientation). Unlike the case in **MOF1a**, only the  $\text{CO}_2$  molecule can hop from one freely hanging CN site to another, whereas  $\text{N}_2$  cannot pass through the pores

due to its larger kinetic diameter. We have carried out FE simulations by placing N<sub>2</sub> molecule in one of the sites of *pore B* for a duration of 1.2 μs, which was found to be insufficient for its escape into another site. On the other hand, CO<sub>2</sub> was observed to sample the entire MOF through the interconnected pore. During the movement from one pore to another, CO<sub>2</sub> was found to adopt many orientations which facilitate it to traverse through the narrow channel between interconnected pore. Figure 20 shows the dynamical pathways and FE profiles of CO<sub>2</sub> and N<sub>2</sub> in **MOF2a**. For each pore, there are two CN groups hanging from top and bottom. It is thus clear that the process of cycloaddition narrows down the pores. The same is captured through enhanced barriers in free energy for CO<sub>2</sub> and N<sub>2</sub> in **MOF2a**, relative to the values in **MOF1a**. Thus, CO<sub>2</sub> and N<sub>2</sub> can adsorb easily in **MOF1a**, whereas only CO<sub>2</sub> can adsorb in **MOF2a** and N<sub>2</sub> cannot. These results are well correlated with the experimental adsorption isotherms.

### 5.3.5.3 Analysis of Gas Adsorption Isotherms

**Heat of Adsorption (kJ mol<sup>-1</sup>):** We have used a virial type expression<sup>41</sup> of the following type to fit the combined isotherm data collected 273 and 283 K for CO<sub>2</sub>.

$$\ln(P) = \ln(A) + \frac{1}{T} \sum_{i=0}^m a_i A^i + \sum_{i=0}^n b_i A^i \dots\dots\dots(2)$$

Here,  $P$  is the pressure expressed in torr,  $A$  is the amount adsorbed in mmol/g,  $T$  is the temperature in K,  $a_i$  and  $b_i$  are virial coefficients, and  $m$ ,  $n$  represent the number of coefficients required to adequately describe the isotherms. The values of  $m$  and  $n$  were gradually increased until the contribution of  $a$  and  $b$  coefficients added further were negligible towards the overall final fit. The values of the virial coefficient  $a_i$  were taken to calculate the isosteric heat of adsorption using the following expression.

$$Q_{st} = -R \sum_{i=0}^m a_i A^i \dots\dots\dots(3)$$

$Q_{st}$  is the coverage dependent isosteric heat of adsorption and  $R$  is the universal gas constant.

**IAST Selectivity:** The ideal adsorbed solution theory (IAST)<sup>2</sup> was used to predict the binary mixture adsorption of CO<sub>2</sub> and N<sub>2</sub> from the experimental pure-gas isotherms. Previous

reports have depicted that this method can predict the adsorption selectivity for mixture of isotherms in nanoporous materials, including metal-organic frameworks.<sup>3</sup> The single-component isotherms were fit to a single-site Langmuir-Freundlich equation<sup>4</sup>. The IAST assumes that the adsorbed phase is a two-dimensional solution in equilibrium with the bulk phase.<sup>2a</sup> For binary adsorption of A and B, the IAST requires these two equations to be followed:

$$yP_t = xP_a \dots\dots\dots(4)$$

$$(1 - y)P_t = (1 - x)P_b \dots\dots\dots(5)$$

Where  $x$  and  $y$  denote the molar fraction of A in the adsorbed phase and the molar fraction of A in the bulk phase, respectively.  $P_t$  is the total gas pressure;  $P_a$  and  $P_b$  are the pressure of component A and B at the same spreading pressure as that of the mixture, respectively. The equation used for the fitting the single component gas mixture is as follows.

$$Y = Y_0 \left( \ln \frac{BP^n}{(1+BP^n)} \right) \dots\dots\dots(6)$$

Furthermore, the molar fraction of A in the adsorbed phase can be obtained from the following equation:

$$Y_{0,a} \ln \left( 1 + \frac{B_a P_t^{n_1} y}{x} \right) - Y_{0,b} \ln \left( 1 + \frac{B_b P_t^{n_2} (1-y)}{(1-x)} \right) = 0 \dots\dots\dots(7)$$

where  $Y_{0,a}$ ,  $B_a$  and  $n_1$  are the Langmuir-Freundlich fitting parameters of adsorption equilibrium of pure A,  $Y_{0,b}$ ,  $B_b$  and  $n_2$  are Langmuir-Freundlich parameters of adsorption equilibrium of pure B. The unknown  $x$  in Eq. (7) has been solved by Matlab (Version 7.8 (R2009a), The MathWorks, Inc.) for fixed  $P_t$  and  $y$  values.

Then calculated the predicted adsorption selectivity, which is defined as

$$S = \frac{\frac{x_1}{y_1}}{\frac{x_2}{y_2}} \dots\dots\dots(8)$$

where  $x_i$  and  $y_i$  are the mole fractions of component  $i$  ( $i = 1, 2$ ; A, B) in the adsorbed and bulk phases, respectively. The IAST calculations were carried out for a binary mixture containing 15% CO<sub>2</sub> ( $y_1$ ) and 85% N<sub>2</sub> ( $y_2$ ), which is typical of flue gases. We have also tested the predicted selectivity of the compounds by changing the mol% of CO<sub>2</sub> from 10% to 30% in the gas mixture.

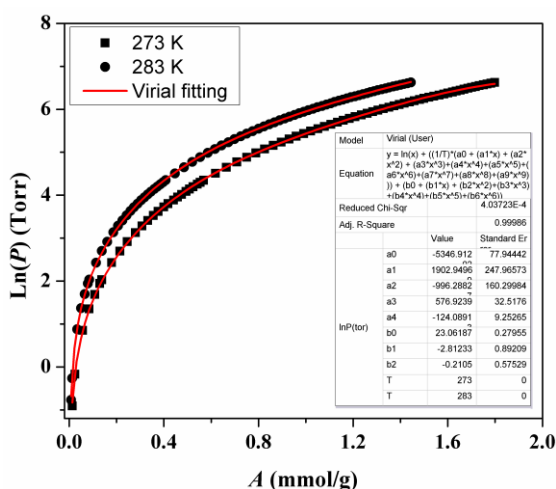


**Figure 21:** CO<sub>2</sub> isotherms for activated MOF1 (MOF1a) measured at 273 K (black square) and 283 K (black circle). Fitted curves (red solid lines), obtained from the virial-type expansion, were used for the  $Q_{st}$  estimation.

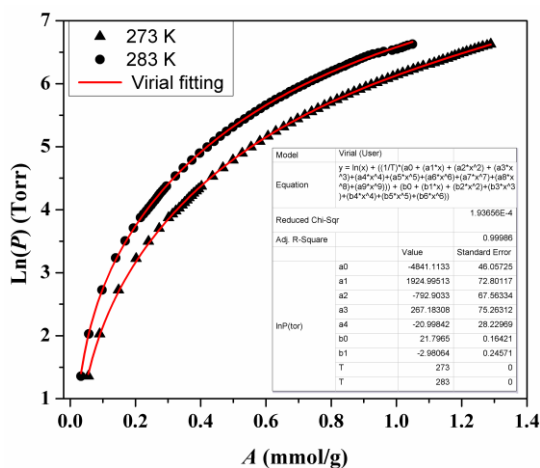


**Figure 22:** CO<sub>2</sub> isotherms for activated MOF2 (MOF2a) measured at 273 K (black triangle) and 283 K (black circle). Fitted curves (red solid lines), obtained from the virial-type expansion, were used for the  $Q_{st}$  estimation.

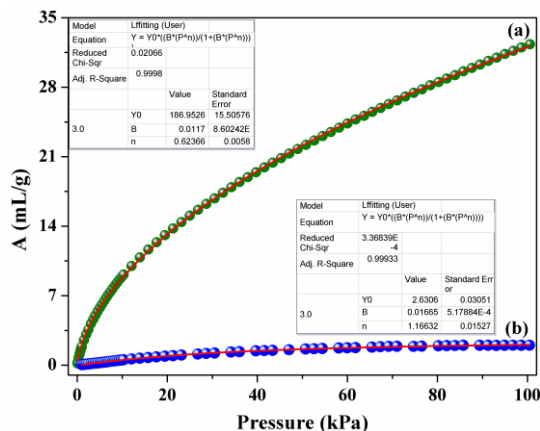


**Figure 23:** Langmuir–Freundlich fittings (red lines) for (a) CO<sub>2</sub> (green circle) and (b) N<sub>2</sub> (blue circle) isotherms measured at 283 K for **MOF1a**.

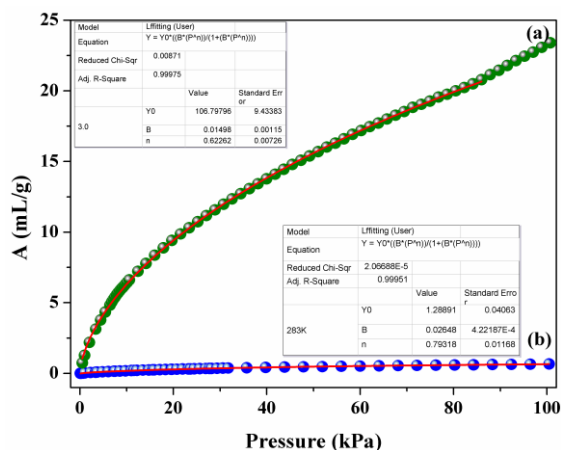


**Figure 24:** Langmuir–Freundlich fittings (red lines) for (a) CO<sub>2</sub> (green circle) and (b) N<sub>2</sub> (blue circle) isotherms measured at 283 K for **MOF2a**.

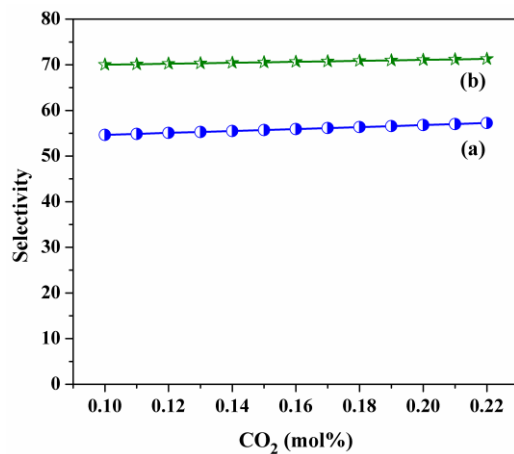


**Figure 25:** Predicted selectivity value of (a) **MOF1a** and (b) **MOF2a** at zero coverage regions with increasing the mol% of CO<sub>2</sub> (0.1 to 0.22 mol%) in a CO<sub>2</sub>–N<sub>2</sub> gas mixture.

### 5.3.5: Solvent vapour adsorption study

For calculating the number of water molecules present in the rehydrated frameworks (**MOF1b** and **MOF2b**) we have carried out water vapour adsorption experiment on the desolvated structures (**MOF1a** and **MOF2a**).

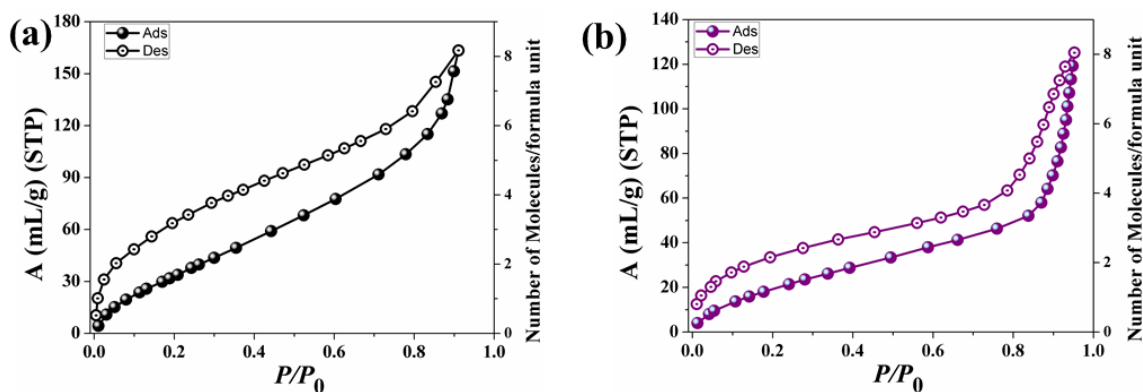


**Figure 26:** Water vapour adsorption isotherm for **MOF1a** (a) and **MOF2a** (b) measured at 298K. They adsorb  $\sim 8$   $\text{H}_2\text{O}$  molecules/formula unit at saturation.  $P_0$  is the saturated vapour pressure of water at 298 K. Closed symbols and open symbols are corresponding to adsorption and desorption respectively.

$\text{H}_2\text{O}$  (2.68 Å) adsorption profiles (Figure 26) show a gradual uptake with increasing pressure and reach a final amount of 172 and  $134 \text{ mLg}^{-1}$  for **MOF1a** and **MOF2a** respectively at  $P/P_0 \sim 0.98$ . In all the cases desorption curves do not follow the adsorption one revealing prominent hysteric sorption profiles. The hysteric uptake of water molecules for **MOF1a** and **MOF2a** is suggesting hydrophilic nature of the pore surfaces of the compounds, which is also supported by  $\beta E_0$  values (6.13 and 7.09 kcal/mol). It is worth to notice that, at saturation both compounds adsorbs 8  $\text{H}_2\text{O}$  molecules/formula unit which is in line with the number water molecules present in the rehydrated structures. To examine the water stability of the compounds we have checked the PXRD patterns of the samples after adsorption measurements which show good agreement with their corresponding mother compounds.

### 5.3.6 Magnetic Property of MOF1 and MOF2

The zero field-cooled *dc* magnetic susceptibilities of **MOF1** is shown in the form of  $\chi_M T$  vs.  $T$  in Figure 28a. The room temperature  $\chi_M T$  value for **MOF1** is  $11.9 \text{ cm}^3 \text{ mol}^{-1} \text{ K}$  which is higher compared to the spin only value ( $9.3 \text{ cm}^3 \text{ mol}^{-1} \text{ K}$ ) for magnetically isolated three  $\text{Co}^{\text{II}}$  (high spin,  $S = 3/2$ ) and two  $\text{Cr}^{\text{III}}$  ( $S = 3/2$ ) centers.

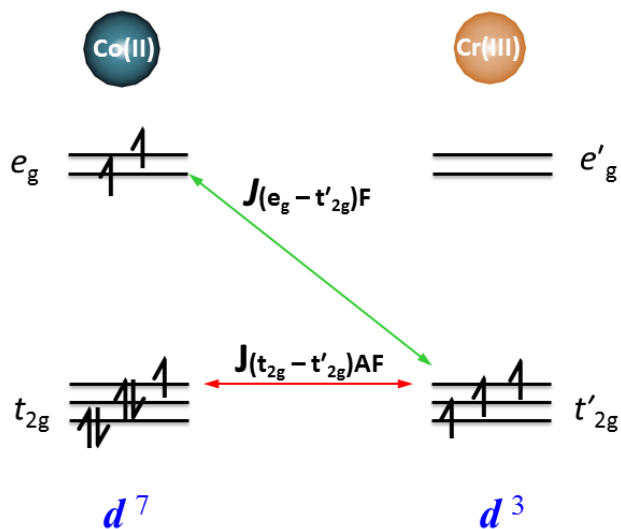


**Figure 27:** Schematic representation of the superexchange interaction between  $\text{Co}^{\text{II}}$  ( $t_{2g}^5 e_g^2$ , high spin) and  $\text{Cr}^{\text{III}}$  ( $t_{2g}^3$ ) ions in the reported MOF. The superexchange interaction ( $J_{\text{Co-Cr}}$ ) between  $\text{Co}^{\text{II}}$  and  $\text{Cr}^{\text{III}}$  can be expressed by the summation of the  $J(e_g-t'_{2g})F$  and  $J(t_{2g}-t'_{2g})AF$  orbital contribution.

This indicates the presence of significant orbital contribution from the octahedral  $\text{Co}^{\text{II}}$  centers. The  $\chi_{\text{M}}T$  value gradually increases with decrease in temperature to reach a value of  $21.3 \text{ cm}^3 \text{ mol}^{-1} \text{ K}$  at 36 K. Below 36 K, a rapid increase in the  $\chi_{\text{M}}T$  value was observed which suggests the presence of ferromagnetic ordering in **MOF1**. The sudden decrease in  $\chi_{\text{M}}T$  value below the 11 K may be attributed to the presence of zero-field splitting and/or field saturation effect. The  $1/\chi_{\text{M}}$  vs.  $T$  (Figure 29a) plot in the temperature range of 300–100 K obeys the Curie–Weiss law with a Weiss constant ( $\theta$ ) of 22.9 K which also supports the existence of ferromagnetic interaction between the adjacent  $\text{Co}^{\text{II}}$  and  $\text{Cr}^{\text{III}}$  ions through cyanide bridges (Figure 27).<sup>42</sup> The ferromagnetic ordering temperature ( $T_{\text{c}}$ ) was determined accurately as 14.9 K from the  $dM/dT$  plot (Figure of 28(b)). The field dependent magnetization plot of **MOF1** shows a pronounced magnetic hysteresis loop at 2 K with a remnant magnetization ( $M_{\text{r}}$ ) of  $5.8 N_{\beta}$  and a coercive field ( $H_{\text{c}}$ ) of  $3.3 \text{ kOe}$ , indicating that **MOF1** is a ferromagnet (inset of Figure 28a and b). The saturation magnetization value ( $10.4 N_{\beta}$  at  $50 \text{ kOe}$ ) is lower compared to the theoretical value ( $15.6 N_{\beta}$ ;  $g_{\text{Cr}} = 2.00$  and  $g_{\text{Co}} = 2.14$ ) which is expected in a  $\text{Cr}^{\text{III}}\text{-CN-Co}^{\text{II}}$  system where appreciable magnetic anisotropy is present due to  $\text{Co}^{\text{II}}$  ions. We envisioned that the guest removed state of **MOF1** may show subtle change in the magnetic property based on the change in geometry of the  $\text{Co}^{\text{II}}$  centers and



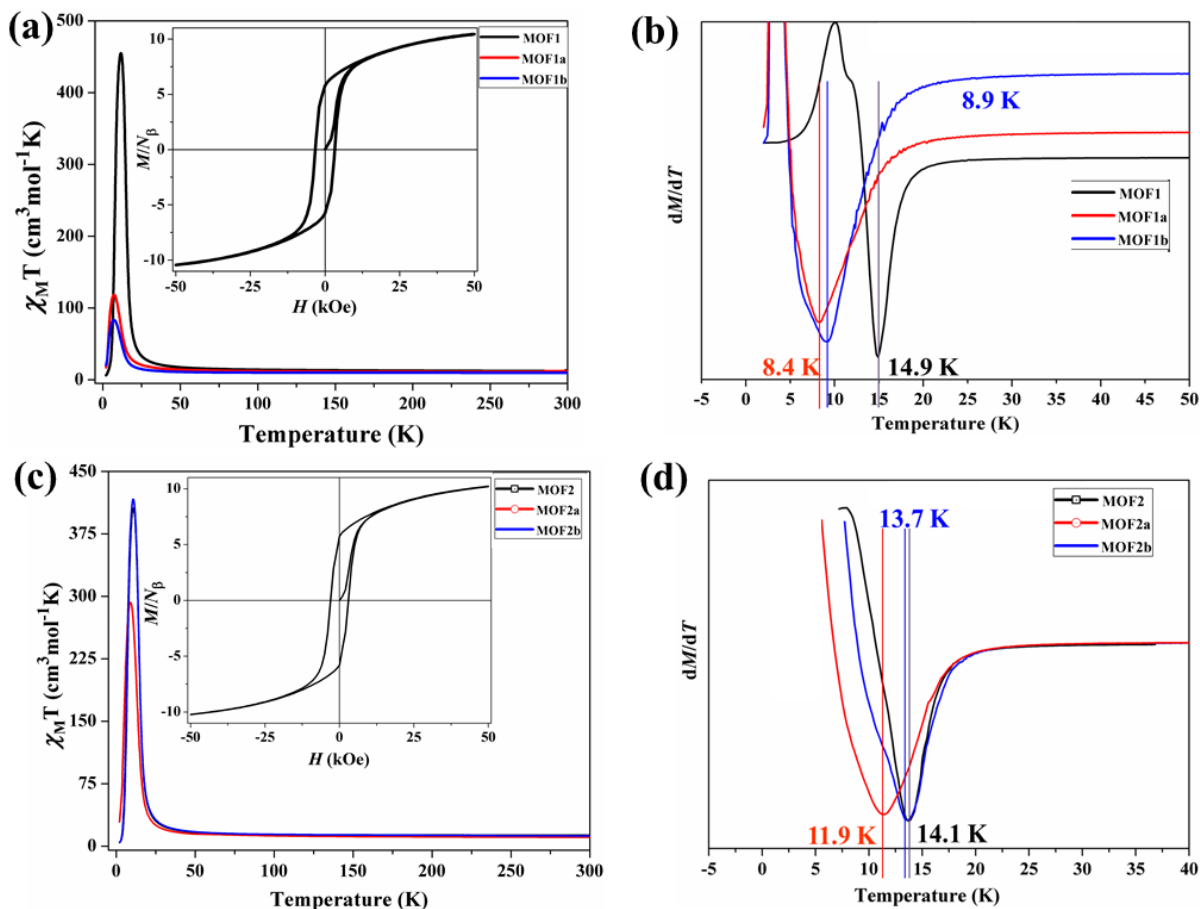


**Figure 28: Guest induced magnetic modulation in MOF1a and MOF2a:** (a) and (c) Temperature dependence of the magnetic susceptibility of **MOF1**, **MOF2** and their different states in an applied field of 500 Oe under zero field cooled condition. *Inset* shows  $M$  vs.  $H$  plot of **MOF1** and **MOF2** measured at 2K. (b) and (d)  $dM/dT$  vs.  $T$  plot showing accurate  $T_c$  values for **MOF1**, **MOF2** and their different states. **MOF2** clearly exhibits reversible magnetic property upon dehydration–rehydration cycle.

corresponding angles between the magnetic centers through cyanide linker. The *dc* magnetic susceptibility data of **MOF1a** demonstrates similar (Figure 28a) ferromagnetic ordering with a  $T_c$  value of 8.4 K which is lower than **MOF1**. The  $1/\chi_M$  vs.  $T$  (Figure 29b) plot obeys the Curie–Weiss law in the temperature range of 300–100 K with a Weiss constant of  $\theta = 11.70$  K suggesting that the ferromagnetic interaction is weaker in **MOF1a** than **MOF1**. The change in the value of  $\theta$ ,  $T_c$  and maxima in  $\chi_M T$  value in **MOF1a** suggest a certain alteration in the magnetic exchange pathways which is due to the change in the geometry of the Co<sup>II</sup> centers after removing the coordinated water molecules. The rehydrated sample of **MOF1a** (*i.e.*, **MOF1b**) shows a  $T_c$  value of 8.9 K which reflects that magnetic state is irreversible with respect dehydration–rehydration procedure (Figure 28b).

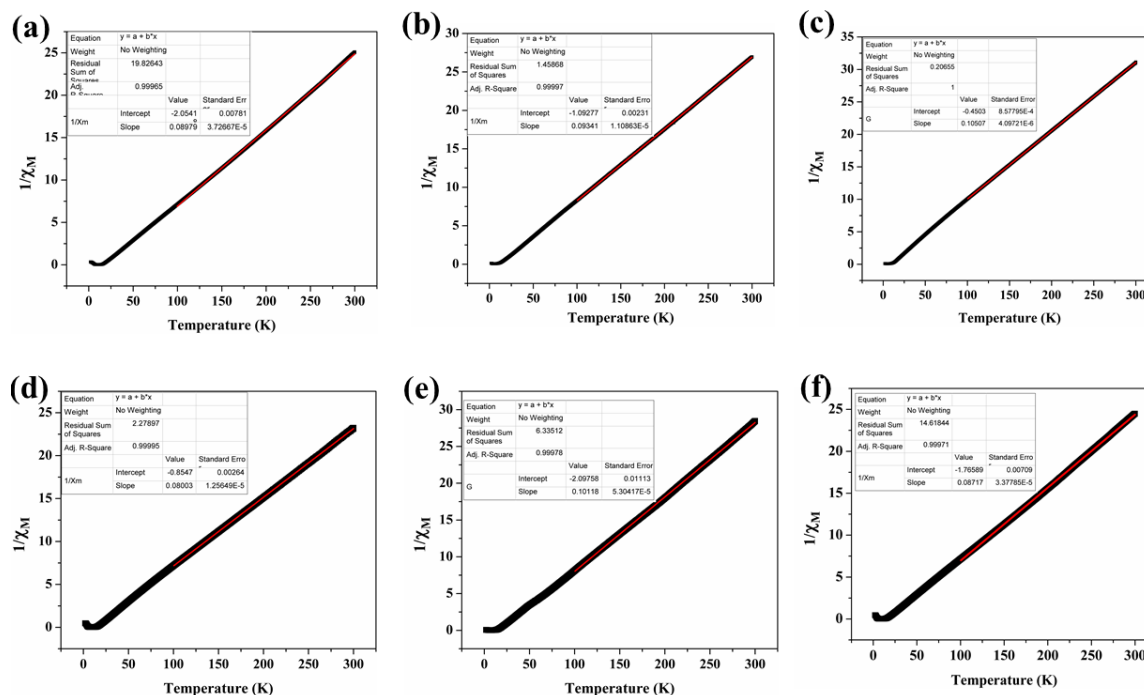


**Figure 29:** Curie–Weiss fitting of **MOF1** (a) ( $C = 11.15 \text{ cm}^3\text{K mol}^{-1}$ , and  $\theta = 22.90 \text{ K}$ ); **MOF1a** (b) ( $C = 10.71 \text{ cm}^3\text{K mol}^{-1}$ , and  $\theta = 11.70 \text{ K}$ ); **MOF1b** (c) ( $C = 9.52 \text{ cm}^3\text{K mol}^{-1}$ , and  $\theta = 12.29 \text{ K}$ ); **MOF2** (d) ( $C = 12.50 \text{ cm}^3\text{K mol}^{-1}$ , and  $\theta = 21.50 \text{ K}$ ); **MOF2a** (e) ( $C = 10.03 \text{ cm}^3\text{K mol}^{-1}$ , and  $\theta = 17.73 \text{ K}$ ); **MOF2b** (f) ( $C = 12.50 \text{ cm}^3\text{K mol}^{-1}$ , and  $\theta = 20.56 \text{ K}$ ).

This can be attributed to the structural irreversibility as once we remove the guest bpee molecules from the 1D channel, the regeneration of same structure of **MOF1** is unlikely.

Moreover, the photo-modified framework **MOF2** too exhibits a similar trend as **MOF1** as observed in the  $\chi_M T$  vs.  $T$  plot and it shows  $T_c = 14.1 \text{ K}$  (Figures 28c and 28d). The slight decrease in  $T_c$  compare to **MOF1** can be corroborated to the distortion in the 2D magnetic layer due to bending in pillar *rect*–*tpcb* after cycloaddition reaction. It is notable that the desolvation of **MOF2** is only concerned with the removal of guest and coordinated solvent molecules as the guest bpee molecules are now connected to the main framework. This introduces extra thermal stability and rigidity in the photo-modified framework which are reflected from the TGA profile and PXRD pattern of the **MOF2a** (*vide infra*). Such characteristics encouraged us to probe the solvent dependent magnetic properties of **MOF2**. The  $\chi_M T$  vs.  $T$  plot for **MOF2a** is shown in Figure 28c and  $dM/dT$  plot suggests the  $T_c$  is 11.9 K, that is higher compared to that of **MOF1a** (Figure 28d). In addition, the rehydrated compound, *i.e.*, **MOF2b** shows a  $T_c$  value of 13.9 K which suggests the **MOF2** is magnetically reversible upon desolvation and resolvation. Reversible magnetic property of

**MOF2** (saturation magnetization =  $10.2 N_{\beta}$ ;  $H_c = 2.4 kOe$  and  $M_r = 6.2 N_{\beta}$ ) is also reflected in the magnetization data (Figure inset of 28a) where the rehydrated compound of **MOF2a** (*i.e.* **MOF2b**) shows a value of  $10.8 N_{\beta}$  which is similar to that of the as-synthesized **MOF2**.

In hexacyanometallate based magnetic coordination polymers, the value of  $T_c$  always depends on the overall magnetic interactions between the metal centers via covalent (cyanide) and non-covalent interactions (like H-bond). The guest induced magnetic modulation can be roughly explained by considering the molecular field theory

$$T_c = \frac{2(n_{Cr}n_{Co})^{0.5}|J_{CoCr}| \times \{S_{Cr}(S_{Cr}+1)S_{Co}(S_{Co}+1)\}^{0.5}}{3k_B} \dots\dots\dots(9)$$

It is evident from the equation that,  $T_c$  depends on the number of nearest neighbour magnetic centers around the metal ( $n_M$ ) and exchange interaction ( $J$ ) between them. But in these compounds,  $T_c$  is directly proportional to the exchange interaction ( $J$ ) as the the number of nearest neighbour ( $n_M$ ) around the metal is constant in all the cases (**MOF1–MOF1b** and **MOF2–MOF2b**). So, upon dehydration, the removal of guest solvents, bpee and coordinated water molecules introduces changes in angle between the interacting magnetic orbitals of the adjacent Co and Cr centers which leads to the alteration of the exchange coupling ( $J_{CoCr}$ ) operating between them. Thus, in **MOF1a**, the change in the overall structure as well as in geometry of the Co centers (hexacoordinated to tetra and penta coordinated) after removing the coordinating  $H_2O$  molecules culminates in lowering of  $T_c$  by altering overlap between the magnetic orbitals of Co and Cr centers which is not reversible upon rehydration. But in **MOF2**, due to the additional structural rigidity and stability after PSM, the reversible change in geometry is more facile compare to **MOF1** upon removing and reinserting the guest molecules. In case of the rehydrated sample of **MOF2a**, it is easy to get back to its original structure and demonstrates the magnetic property similar to original compound (**MOF2**).

## 5.4 Conclusion

In conclusion, for the first time we have shown PSM of metal-organic frameworks by covalent fusion of a guest molecule with a host framework through [2+2] cycloaddition

reaction using light as an external stimulus. Such a topochemical reaction using a low cost, non-destructive external modulator in a confined nanospace, results in a new linker yielding a novel porous host with enhanced thermal stability and structural rigidity. Photo-induced PSM alters the pore size and offers improved CO<sub>2</sub>/N<sub>2</sub> selectivity and bistability in magnetic transition with response to dehydration and rehydration. This straight-forward strategy of PSM by light based on simple host-guest strategy can open up a new horizon in the material science, where physical properties like luminescence, conductivity and catalytic activities can be tuned by altering the host framework. Our work would pave the way to design more photo-responsive porous materials that can lead to a photo-trigger release of the gas molecule which is of paramount interest in energy and environmental domains of current age.

## 5.5 References

1. (a) S. Kitagawa, R. Kitaura and S.-i. Noro, *Angew. Chem. Int. Ed.*, 2004, **43**, 2334; (b) D. Maspoch, D. Ruiz-Molina and J. Veciana, *Chem. Soc. Rev.*, 2007, **36**, 770; (c) C. J. Kepert, *Chem. Commun.*, 2006, 695; (d) M. Ohba, K. Yoneda and S. Kitagawa, *CrystEngComm*, 2010, **12**, 159; (e) K. Jayaramulu, P. Kanoo, S. J. George and T. K. Maji, *Chem. Commun.*, 2010, **46**, 7906; (f) E. Coronado and G. Minguez Espallargas, *Chem. Soc. Rev.*, 2013, **42**, 1525; (g) Y. Cui, Y. Yue, G. Qian and B. Chen, *Chem. Rev.*, 2012, **112**, 1126.
2. (a) X. Lin, I. Telepeni, A. J. Blake, A. Dailly, C. M. Brown, J. M. Simmons, M. Zoppi, G. S. Walker, K. M. Thomas, T. J. Mays, P. Hubberstey, N. R. Champness and M. Schröder, *J. Am. Chem. Soc.*, 2009, **131**, 2159; (b) S. Xiang, W. Zhou, Z. Zhang, M. A. Green, Y. Liu and B. Chen, *Angew. Chem. Int. Ed.*, 2010, **49**, 4615; (c) S. Horike, S. Shimomura and S. Kitagawa, *Nature Chem.*, 2009, **1**, 695; (d) M. Ohba, W. Kaneko, S. Kitagawa, T. Maeda and M. Mito, *J. Am. Chem. Soc.*, 2008, **130**, 4475.
3. (a) E. C. Spencer, M. S. R. N. Kiran, W. Li, U. Ramamurty, N. L. Ross and A. K. Cheetham, *Angew. Chem. Int. Ed.*, 2014, **53**, 5583; (b) S. Thies, H. Sell, C. Schütt, C. Bornholdt, C. Näther, F. Tucek and R. Herges, *J. Am. Chem. Soc.*, 2011, **133**, 16243; (c) N. Yanai, K. Kitayama, Y. Hijikata, H. Sato, R. Matsuda, Y. Kubota, M. Takata, M. Mizuno, T. Uemura and S. Kitagawa, *Nat Mater*, 2011, **10**, 787; (d) E. S. Koumoussi, I.-R. Jeon, Q. Gao, P. Dechambenoit, D. N. Woodruff, P. Merzeau, L. Buisson, X. Jia, D. Li, F. Volatron, C. Mathonière and R. Clérac, *J. Am. Chem. Soc.*, 2014, **136**, 15461; (e) R. Haldar, R. Matsuda, S. Kitagawa, S. J. George and T. K. Maji, *Angew. Chem. Int. Ed.*, 2014, **53**, 11772.

4. (a) K. K. Tanabe and S. M. Cohen, *Chem. Soc. Rev.*, 2011, **40**, 498; (b) S. M. Cohen, *Chem. Rev.*, 2011, **112**, 970.
5. (a) R. Lyndon, K. Konstas, B. P. Ladewig, P. D. Southon, P. C. J. Kepert and M. R. Hill, *Angew. Chem. Int. Ed.*, 2013, **52**, 3695; (b) B. Esser and T. M. Swager, *Angew. Chem. Int. Ed.*, 2010, **49**, 8872.
6. (a) J. Park, L.-B. Sun, Y.-P. Chen, Z. Perry and H.-C. Zhou, *Angew. Chem. Int. Ed.*, 2014, **53**, 5842; (b) J. W. Brown, B. L. Henderson, M. D. Kiesz, A. C. Whalley, W. Morris, S. Grunder, H. Deng, H. Furukawa, J. I. Zink, J. F. Stoddart and O. M. Yaghi, *Chem. Sci.*, 2013, **4**, 2858; (c) J. Park, D. Yuan, K. T. Pham, J.-R. Li, A. Yakovenko and H.-C. Zhou, *J. Am. Chem. Soc.*, 2011, **134**, 99.
7. N. Yanai, T. Uemura, M. Inoue, R. Matsuda, T. Fukushima, M. Tsujimoto, S. Isoda and S. Kitagawa, *J. Am. Chem. Soc.*, 2012, **134**, 4501.
8. (a) M. Nagarathinam, A. M. P. Peedikakkal and J. J. Vittal, *Chem. Commun.*, 2008, 5277; (b) K. M. Hutchins, T. P. Rupasinghe, L. R. Ditzler, D. C. Swenson, J. R. G. Sander, J. Baltrusaitis, A. V. Tivanski and L. R. MacGillivray, *J. Am. Chem. Soc.*, 2014, **136**, 6778; (c) H. Sato, R. Matsuda, M. H. Mir and S. Kitagawa, *Chem. Commun.*, 2012, **48**, 7919.
9. (a) M. H. Mir, L. L. Koh, G. K. Tan and J. J. Vittal, *Angew. Chem. Int. Ed.*, 2010, **49**, 390; (b) M. Nagarathinam, A. Chanthapally, S. H. Lapidus, P. W. Stephens and J. J. Vittal, *Chem. Commun.*, 2012, **48**, 2585; (c) J.-K. Sun, W. Li, C. Chen, C.-X. Ren, D.-M. Pan and J. Zhang, *Angew. Chem. Int. Ed.*, 2013, **52**, 6653; (d) L. R. MacGillivray, G. S. Papaefstathiou, T. Friščić, T. D. Hamilton, D.-K. Bučar, Q. Chu, D. B. Varshney and I. G. Georgiev, *Acc. Chem. Res.*, 2008, **41**, 280; (e) G. S. Papaefstathiou, Z. Zhong, L. Geng and L. R. MacGillivray, *J. Am. Chem. Soc.*, 2004, **126**, 9158; (f) G. K. Kole, T. Kojima, M. Kawano and J. J. Vittal, *Angew. Chem. Int. Ed.*, 2014, **53**, 2143; (g) D. Liu, Z.-G. Ren, H.-X. Li, J.-P. Lang, N.-Y. Li and B. F. Abrahams, *Angew. Chem. Int. Ed.*, 2010, **49**, 4767; (h) S.-Y. Yang, X.-L. Deng, R.-F. Jin, P. Naumov, M. K. Panda, R.-B. Huang, L.-S. Zheng and B. K. Teo, *J. Am. Chem. Soc.*, 2013, **136**, 558; (i) G. S. Papaefstathiou, A. J. E. Duncan and L. R. MacGillivray, *Chem. Commun.*, 2014, **50**, 15960.
10. M. D. Cohen, G. M. J. Schmidt and F. I. Sonntag, *J. Chem. Soc.*, 1964, 2000.
11. (a) Z. M. Wang, Y. J. Zhang, T. Liu, M. Kurmoo and S. Gao, *Adv. Funct. Mater.*, 2007, **17**, 1523; (b) M.-H. Zeng, Z. Yin, Y.-X. Tan, W.-X. Zhang, Y.-P. He and M. Kurmoo, *J. Am. Chem. Soc.*, 2014, **136**, 4680.
12. (a) Y. Yoshida, K. Inoue and M. Kurmoo, *Inorg. Chem.*, 2008, **48**, 267; (b) E. Coronado, M. Giménez-Marqués, G. Mínguez Espallargas, F. Rey and I. J. Vitórica-Yrezábal, *J. Am. Chem. Soc.*, 2013, **135**, 15986; (c) G. J. Halder, C. J. Kepert, B. Moubaraki, K. S. Murray and J. D. Cashion, *Science*, 2002, **298**, 1762; (d) M. Ohba, K. Yoneda, G. Agustí, M. C. Muñoz, A. B. Gaspar, J. A.

- Real, M. Yamasaki, H. Ando, Y. Nakao, S. Sakaki and S. Kitagawa, *Angew. Chem. Int. Ed.*, 2009, **48**, 4767.
13. (a) P. Dechambenoit and J. R. Long, *Chem. Soc. Rev.*, 2011, **40**, 3249; (b) S. Mohapatra, B. Rajeswaran, A. Chakraborty, A. Sundaresan and T. K. Maji, *Chem. Mater.*, 2013, **25**, 1673.
14. A. Hazra, P. Kanoo and T. K. Maji, *Chem. Commun.*, 2011, **47**, 538.
15. S. V. a. SMART (V 5.628), XPREP, SHELXTL; Bruker AXS Inc. Madison, Wisconsin, USA, 2004.
16. G. M. Sheldrick, *SADABS, Empirical Absorption Correction Program, University of Göttingen, Göttingen*, 1997.
17. A. Altomare, G. Casciarano, C. Giacovazzo and A. Guagliardi, *J. Appl. Crystallogr.*, 1993, **26**, 343.
18. G. M. Sheldrick, *SHELXL 97, Program for the Solution of Crystal Structure, University of Göttingen, Germany*, 1997.
19. A. Spek, *J. Appl. Crystallogr.*, 2003, **36**, 7.
20. L. Farrugia, *J. Appl. Crystallogr.*, 1999, **32**, 837.
21. (a) H. R. Lewis and C. W. Nielson, *J. Comput. Phys.*, 1975, **17**, 1; (b) J. Hutter, M. Iannuzzi, F. Schiffmann and J. VandeVondele, *Wiley Interdisciplinary Reviews: Computational Molecular Science*, 2014, **4**, 15.
22. M. Elstner, D. Porezag, G. Jungnickel, J. Elsner, M. Haugk, T. Frauenheim, S. Suhai and G. Seifert, *Physical Review B*, 1998, **58**, 7260.
23. J. P. Perdew, K. Burke and M. Ernzerhof, *Phys. Rev. Lett.*, 1996, **77**, 3865.
24. S. Grimme, J. Antony, S. Ehrlich and H. Krieg, *J. Chem. Phys.*, 2010, **132**.
25. (a) A. Hazra, S. Bonakala, S. K. Reddy, S. Balasubramanian and T. K. Maji, *Inorg. Chem.*, 2013, **52**, 11385; (b) R. Haldar, S. Bonakala, P. Kanoo, S. Balasubramanian and T. K. Maji, *CrystEngComm*, 2014, **16**, 4877.
26. W. Humphrey, A. Dalke and K. Schulten, *J. Mol. Graphics*, 1996, **14**, 33.
27. (a) C. F. Macrae, P. R. Edgington, P. McCabe, E. Pidcock, G. P. Shields, R. Taylor, M. Towler and J. van de Streek, *J. Appl. Crystallogr.*, 2006, **39**, 453; (b) <http://www.ccdc.cam.ac.uk/Solutions/CSDSystem/Pages/Mercury.aspx>.
28. R. Dennington, T. Keith and J. Millam, *GaussView {V}ersion {5} Semichem Inc. Shawnee Mission KS*, 2009.
29. C. E. Webster, R. S. Drago and M. C. Zerner, *J. Am. Chem. Soc.*, 1998, **120**, 5509.
30. R. S. Pillai, S. A. Peter and R. V. Jasra, *Microporous Mesoporous Mater.*, 2008, **113**, 268.
31. A. L. Myers and J. M. Prausnitz, *AlChE J.*, 1965, **11**, 121.

32. (a) D. Britt, H. Furukawa, B. Wang, T. G. Glover and O. M. Yaghi, *Proc. Natl. Acad. Sci.*, 2009, **106**, 20637; (b) J. An, S. J. Geib and N. L. Rosi, *J. Am. Chem. Soc.*, 2009, **132**, 38.
33. F. Salles, G. Maurin, C. Serre, P. L. Llewellyn, C. Knöfel, H. J. Choi, Y. Filinchuk, L. Oliviero, A. Vimont, J. R. Long and G. Férey, *J. Am. Chem. Soc.*, 2010, **132**, 13782.
34. R. V. Jasra, N. V. Choudary and S. G. T. Bhat, *Ind. Eng. Chem. Res.*, 1996, **35**, 4221.
35. R. W. Hockney and J. W. Eastwood, *Computer Simulation Using Particles*; Adam Hilger, 1988.
36. A. K. Rappe, C. J. Casewit, K. S. Colwell, W. A. Goddard and W. M. Skiff, *J. Am. Chem. Soc.*, 1992, **114**, 10024.
37. M. G. Martin and J. I. Siepmann, *J. Phys. Chem. B*, 1998, **102**, 2569.
38. G. Galassi and D. J. Tildesley, *Molecular Simulation*, 1994, **13**, 11.
39. E. Darve, D. Rodríguez-Gómez and A. Pohorille, *J. Chem. Phys.*, 2008, **128**.
40. G. Fiorin, M. L. Klein and J. Hénin, *Mol. Phys.*, 2013, **111**, 3345.
41. M. Dincă, A. Dailly, Y. Liu, C. M. Brown, D. A. Neumann and J. R. Long, *J. Am. Chem. Soc.*, 2006, **128**, 16876.
42. (a) Y.-Z. Zhang and O. Sato, *Inorg. Chem.*, 2009, **49**, 1271; (b) L. J. Batchelor, M. Sangalli, R. Guillot, N. Guihéry, R. Maurice, F. Tuna and T. Mallah, *Inorg. Chem.*, 2011, **50**, 12045; (c) S.-i. Ohkoshi and K. Hashimoto, *Chem. Phys. Lett.*, 1999, **314**, 210; (d) M. Ohba and H. Ōkawa, *Coord. Chem. Rev.*, 2000, **198**, 313.





# Chapter 6

**“Pore Contraction” to “Pore Expansion” triggered by Light in  
Photo-responsive Metal-organic Frameworks: Unraveling the Role  
of C-H···O Interaction**



## Summary

This chapter describes the synthesis, structural characterization and tunable adsorption properties of two metal-organic frameworks (MOFs)  $[\{\text{Cd}(\text{pzdc})(\text{bpee})\}_2 \cdot 3\text{H}_2\text{O}]_n$  (**MOF1**) and  $[\{\text{Cd}(\text{pzdc})(\text{bpee})\}_2 \cdot (\text{bpee})_{0.5} \cdot \text{H}_2\text{O}]_n$  (**MOF2**) constructed by  $\text{Cd}^{\text{II}}$ , 1,2-bis(4-pyridyl)ethylene (bpee) and 2,3-pyrazinedicarboxylate (pzdc). In the first compound, the C-H...O interaction leads to the contraction of pore surface after removing the guest water molecules. But interestingly, in the photo-modified framework of **MOF1** (*i.e.*  $[\{\text{Cd}_2(\text{pzdc})_2(\text{rctt}-\text{tpcb})\} \cdot 3\text{H}_2\text{O}]_n$ , **MOF1IR**), the absence of C-H...O interaction results in structural expansion after dehydration as the 2D layers are moving apart from each other which facilitates the enhanced  $\text{CO}_2$  uptake. The lesser diffusion barrier for  $\text{CO}_2$  in the irradiated framework is also supported by the kinetic measurements based on the MeOH adsorption. In the second compound (**MOF2**), the [2+2] photochemical reaction is subdued by the stronger C-H...O interaction based on the restricted movement of the ethylene carbon atoms.



## 6.1: Introduction

Metal–organic frameworks (MOFs) or porous coordination polymers (PCPs) are a novel class of modular crystalline hybrid porous materials and have shown potential applications in different areas including storage and separation of small molecules, catalysis, drug delivery, and sensing.<sup>1</sup> The key to such tailorable properties and versatile applications by MOFs is the modulation of pore surface and structure with different organic linkers.<sup>2</sup> The functional groups of such organic linkers determine the polarity or philicity of pore surface and have a great influence on the selective inclusion of a particular molecule.<sup>3</sup> Furthermore, to correlate the structure property relationship of such porous materials, molecular level understanding of the pore structure before and after the guest removal is of paramount importance.<sup>4</sup> Recently, postsynthetic modification of pore surface is gaining interest to introduce advance functionalities in porous materials.<sup>5</sup> In this regard, postsynthetic chemical modifications *via* tedious organic reactions in different MOFs have been significantly studied.<sup>6</sup> The highlight of such postsynthetic modifications is to enhance or introduce superior properties in the framework system compared to the as-synthesized framework.<sup>7</sup>

One of the great advantages in MOFs is structural flexibility which is not generally observed in other contemporary porous materials like zeolites, porous silica or porous carbons. Those flexible frameworks show guest induced dynamic behavior (related to structural contraction and expansion in the framework) that modulate overall functionalities.<sup>8</sup> Such structural changes induced by sliding or shearing of the nets or breaking of metal–linker bonds or change in packing, and can also be tuned through non–bonding supramolecular interactions (H–bonding,  $\pi\cdots\pi$  interaction, C–H $\cdots\pi$  interaction *etc.*).<sup>9</sup> These non–covalent interactions introduce local change in the structure which induces an overall reorientation in the global structure and corresponding properties.<sup>10</sup> Among such short contact interactions, the importance of hydrogen bonds in chemical, physical and biological processes are widespread and the properties of hydrogen bonding have been studied intensively. Among the various strengths of hydrogen bonding, the O–H $\cdots$ O, O–H $\cdots$ N or N–H $\cdots$ N hydrogen bridges are considered as strong (5 to 40 kcal mol<sup>-1</sup>) whereas the energy of C–H $\cdots$ O hydrogen bonds is significantly lower (less than 5 kcal mol<sup>-1</sup>).<sup>11</sup> Recently, a trend has emerged among crystal engineers to make an understanding over the role of weak

interactions in designing MOFs with desired properties.<sup>10b, 12</sup> In this aspect, Kepart *et al.* has depicted the influence of O-H...S hydrogen bonding interaction in fine-tuning the ligand field splitting which further affects the spin crossover behavior of the Fe<sup>II</sup> based MOFs.<sup>13</sup>

There are several reports with variety of frameworks built up from metal complexes by strong hydrogen bonds; very few examples are documented about the weak C-H...O interaction. In this chapter, the role of C-H...O bonding has been described on tuning the porosity of a framework by controlling over the contraction and expansion of pore surface. Kitagawa *et al.* reported guest induced framework contractions and expansion in two isostructural frameworks  $[\{\text{Cd}(\text{pzdc})(\text{bpee})\}_2 \cdot 3\text{H}_2\text{O}]_n$  and  $[\{\text{Cd}(\text{pzdc})(\text{azpy})\} \cdot 2\text{H}_2\text{O}]_n$  (bpee = 1,2-bis(4-pyridyl)ethylene, pzdc = 2,3-pyrazinedicarboxylate and azpy = 4,4'-azobipyridine) respectively by changing the pillar functionalities.<sup>14</sup> The structural contraction in first compound is induced by C-H...O interactions whereas expansion in later case was prompted by the lone pair-lone pair repulsion between the azo groups. The parallel arrangement of bpee linkers in  $[\{\text{Cd}(\text{pzdc})(\text{bpee})\}_2 \cdot 3\text{H}_2\text{O}]_n$  (**MOF1**) helps the ethylenic part to obey Schmidt's photochemical criteria<sup>15</sup>. This encouraged us to postsynthetically modify the framework using light which resulted in a new MOF ( $[\{\text{Cd}_2(\text{pzdc})_2(\text{rctt-tpcb})\} \cdot 3\text{H}_2\text{O}]_n$ ; **MOF1IR**). Such modification of the pore surface inhibits the C-H...O interaction which results in an expansion of the framework after the removal of guest water molecules. The higher uptake of CO<sub>2</sub> is attributed to the lesser diffusion barrier for CO<sub>2</sub> in the photo-irradiated framework, which is supported by the kinetic measurements based on the MeOH adsorption. The strength of the C-H...O interaction is also revealed from another isostructural compound  $[\{\text{Cd}(\text{pzdc})(\text{bpee})\}_2 \cdot (\text{bpee})_{0.5} \cdot \text{H}_2\text{O}]_n$  (**MOF2**) where the photocycloaddition reaction is manipulated by the C-H...O H-bonding.

## 6.2: Experimental Section

### 6.2.1: Materials

All the reagents and solvents employed were commercially available and used as supplied without further purification. Cd(NO<sub>3</sub>)·6H<sub>2</sub>O, 1,2-bis(4-pyridyl)ethylene (bpee) and 2,3-pyrazinedicarboxylate (pzdc) were obtained from the Aldrich Chemical Co.

### 6.2.2: Synthetic procedure

**6.2.2.1 Synthesis of MOF1 and MOF2:** MOF1 was synthesized following the reported procedure.<sup>14</sup> Yield: 82%, relative to Cd<sup>II</sup>. Anal. calc. for C<sub>36</sub>H<sub>30</sub>Cd<sub>2</sub>N<sub>8</sub>O<sub>11</sub>: C, 44.32; H, 3.10; N, 11.49. Found: C, 44.54; H, 3.17; N, 10.88. IR (KBr, cm<sup>-1</sup>): ν(H<sub>2</sub>O) 3425; ν<sub>as</sub>(COO) 1642, ν<sub>s</sub>(COO) 1362; ν(ArC-H) 3042, 3014; ν(ArC=C) 1624, 1567 (Figure 1). To prepare single crystal of MOF2, a mixture of cadmium nitrate (0.031 g, 0.1 mmol), 2,3-pyrazinedicarboxylic acid (0.017 g, 0.1 mmol), 1,2-bis(4-pyridyl)ethylene (0.018 g, 0.1 mmol) and NaOH (0.004 g, 0.1 mmol) was taken in a teflon autoclave. Then 6 mL of H<sub>2</sub>O was added in that mixture and kept at 105°C in oven maintained at constant temperature for 24 hrs. Very small sized transparent block shaped single crystals were obtained and subjected to single crystal X-ray diffraction after washing with H<sub>2</sub>O-EtOH mixture. Different procedure was employed to prepare MOF2 in bulk amount. To prepare MOF2 in bulk, a mixture of cadmium nitrate (0.031 g, 0.1 mmol), 2,3-pyrazinedicarboxylic acid (0.017 g, 0.1 mmol), 1,2-bis(4-pyridyl)ethylene (0.025 g, 0.135 mmol), NaOH (0.004 g, 0.1 mmol) and 6 mL of H<sub>2</sub>O was taken in a teflon autoclave. Then reaction mixture was kept at 105°C in oven maintained at constant temperature for 36 hours. After cooling the autoclave for 24 hours, the obtained product was filtered and washed with H<sub>2</sub>O-EtOH mixture and kept for drying. Yield: 76%, relative to Cd<sup>II</sup>. Anal. calc. for C<sub>42</sub>H<sub>29</sub>Cd<sub>2</sub>N<sub>9</sub>O<sub>9</sub>: C, 49.04; H, 2.84; N, 12.26. Found: C, 49.56; H, 2.96; N, 11.89. IR (KBr, cm<sup>-1</sup>): ν(H<sub>2</sub>O) 3425; ν(ArC-H) 3042, 3014; ν<sub>as</sub>(COO) 1613, ν<sub>s</sub>(COO) 1332; ν(ArC=C) 1624, 1567 (Figure 2).

**6.2.2.2 Preparation of MOF1IR and MOF2IR:** Irradiated compound of MOF1 and MOF2 were prepared using a UV photochemical reactor with 365 nm LASER light made by Hamamatsu, Japan. Before photoreaction, MOF1 and MOF2 were continuously grinded for

30 min. Then the powder samples were sandwiched between a pair of quartz glass plates and irradiated for 10 h. During the photo reaction, the sample was mixed properly every 30 mins to ensure about the homogeneous irradiation. The phase purity was checked with the PXRD (Figure 10 and 11) and elemental analysis (Table 1).

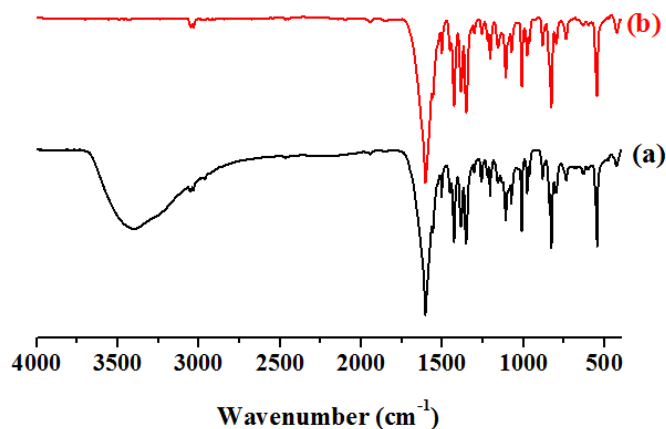


**Figure 1:** IR spectra of MOF1 (a) and MOF1a (b).

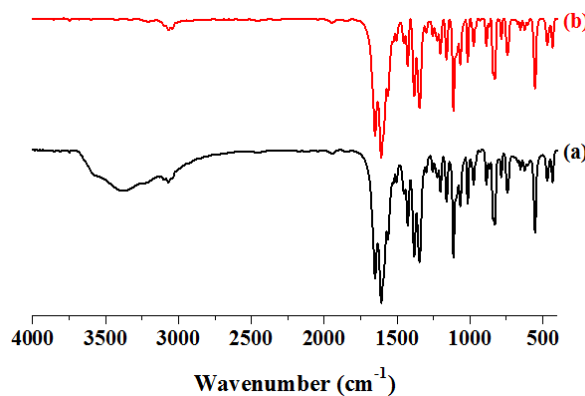


**Figure 2:** IR spectra of MOF2 (a) and MOF2a (b).

**6.2.2.3 Preparation of MOF1a, MOF2a, MOF1IRa and MOF2IRa:** Dehydrated frameworks were prepared by heating their corresponding mother compounds at 140 °C under high vacuum ( $10^{-1}$  Pa). The structural integrity and removal of guest molecules were confirmed by PXRD (Figure 10 and 11), elemental analysis (Table 1) and TGA analysis (Figure 8 and 9).

**6.2.2.4 Preparation of MOF1b, MOF2b MOF1IRb and MOF2IRb:** The dehydrated frameworks were exposed to water vapour under closed atmosphere for 7 days. Structural integrity was checked through PXRD analysis (Figure 10 and 11).



**6.2.2.5 Preparation of  $[\{\text{Cd}(\text{pzdc})(\text{bpee})\}_2 \cdot 0.3\text{H}_2\text{O}]_n$  (MOF1c):** Suitable single crystal of MOF1 was mounted on a thin glass fiber with commercially available super glue. In the goniometer the crystal was heated at 135 °C for 12 hrs.

**Table 1:** Elemental analyses data.

MOF	Molecular Formula	Elemental Formula	Elemental Analysis					
			Predicted			Experimental		
			C	H	N	C	H	N
<b>1a</b>	$[\{\text{Cd}(\text{pzdc})(\text{bpee})\}_2]_n$	$\text{C}_{36}\text{H}_{24}\text{Cd}_2\text{N}_8\text{O}_8$	46.92	2.62	12.16	46.57	2.28	12.85
<b>2a</b>	$[\{\text{Cd}(\text{pzdc})(\text{bpee})\}_2]_n$	$\text{C}_{36}\text{H}_{24}\text{Cd}_2\text{N}_8\text{O}_8$	46.92	2.62	12.16	46.23	2.01	11.75
<b>1IR</b>	$[\{\text{Cd}_2(\text{pzdc})_2(\text{rctt}-\text{tpcb})\} \cdot 3\text{H}_2\text{O}]_n$	$\text{C}_{36}\text{H}_{30}\text{Cd}_2\text{N}_8\text{O}_{11}$	44.33	3.10	11.49	44.01	2.91	11.01
<b>2IR</b>	$[\{\text{Cd}_2(\text{pzdc})_2(\text{rctt}-\text{tpcb})\} \cdot (\text{bpee})_{0.5} \cdot \text{H}_2\text{O}]_n$	$\text{C}_{42}\text{H}_{29}\text{Cd}_2\text{N}_9\text{O}_9$	49.04	2.85	12.26	48.85	2.74	11.88
<b>1IRa</b>	$[\{\text{Cd}_2(\text{pzdc})_2(\text{rctt}-\text{tpcb})\}]_n$	$\text{C}_{36}\text{H}_{24}\text{Cd}_2\text{N}_8\text{O}_8$	46.92	2.62	12.16	46.31	2.98	12.72
<b>2IRa</b>	$[\{\text{Cd}_2(\text{pzdc})_2(\text{rctt}-\text{tpcb})\}]_n$	$\text{C}_{36}\text{H}_{24}\text{Cd}_2\text{N}_8\text{O}_8$	46.92	2.62	12.16	46.24	2.43	12.02

### 6.2.3: Physical Measurements

The elemental analyses of each compounds and their different state were carried out on a Thermo Fisher Flash 2000 Elemental Analyser. Infrared (IR) spectroscopic studies were carried out in the mid-IR region by preparing the sample in KBr pellet (Bruker IFS-66v). Thermogravimetric analysis (TGA) was carried out (Mettler Toledo) in nitrogen atmosphere (flow rate = 50 mL min<sup>-1</sup>) in the temperature range 30 – 700 °C (heating rate = 5°C min<sup>-1</sup>). Powder XRD pattern of the products were recorded by using Cu- $K_\alpha$  radiation (Bruker D8 Discover; 40 kV, 30 mA).

### 6.2.4: Single Crystal X-ray Diffraction

Suitable single crystals of compound MOF1c, MOF1IR, MOF2 and MOF2IR were mounted on a thin glass fiber with commercially available super glue. X-ray single crystal data was collected on a Bruker Smart-CCD diffractometer equipped with a normal focus, 2.4 kW sealed tube X-ray source with graphite monochromated Mo- $K_\alpha$  radiation ( $\lambda = 0.71073 \text{ \AA}$ ) operating at 50 kV and 30 mA. The program SAINT<sup>16</sup> was used for integration of diffraction profiles and absorption correction was made with SADABS<sup>17</sup> program. The

structure was solved by SIR 92<sup>18</sup> and refined by full matrix least square method using SHELXL.<sup>19</sup> All the hydrogen atoms were fixed by HFIX and placed in ideal positions. Potential solvent accessible area or void space was calculated using the PLATON<sup>20</sup> multipurpose crystallographic software. All crystallographic and structure refinement data of the crystals are summarized in Table 2. Selected bond distances and angles are shown in Table 3–10. All calculations were carried out using SHELXL 97,<sup>19</sup> PLATON,<sup>20</sup> SHELXS 97<sup>19</sup> and WinGX system, Ver 1.80.01.<sup>21</sup>

**Table 2:** Crystallographic data and structure refinement parameters for **MOF1c**, **MOF1IR**, **MOF2** and **MOF2IR**.

Parameters	MOF1c	MOF1IR	MOF2	MOF2IR
Empirical formula	C <sub>36</sub> H <sub>24</sub> Cd <sub>2</sub> N <sub>8</sub> O <sub>8.3</sub>	C <sub>36</sub> H <sub>30</sub> Cd <sub>2</sub> N <sub>8</sub> O <sub>11</sub>	C <sub>42</sub> H <sub>29</sub> Cd <sub>2</sub> N <sub>9</sub> O <sub>9</sub>	C <sub>42</sub> H <sub>29</sub> Cd <sub>2</sub> N <sub>9</sub> O <sub>9</sub>
<i>M</i>	466.40	492.73	1030.58	1030.58
Crystal system	Monoclinic	Monoclinic	Triclinic	Triclinic
Space group	C2/c (No. 15)	C2/c (No. 15)	P $\bar{1}$ (No. 2)	P $\bar{1}$ (No. 2)
<i>a</i> (Å)	24.617(3)	25.408(5)	11.488(5)	11.3875(8)
<i>b</i> (Å)	10.6422(11)	11.090(5)	14.070(5)	13.8664(9)
<i>c</i> (Å)	14.3033(12)	13.873(5)	14.094(4)	13.9337(9)
$\alpha$ (°)	90	90	103.272(5)	101.854(3)
$\beta$ (°)	104.492(3)	105.152(5)	90.497(6)	93.080(3)
$\gamma$ (°)	90	90	113.280(5)	113.107(3)
<i>V</i> (Å <sup>3</sup> )	3627.9(7)	3773(2)	2024.1(13)	1958.3(2)
<i>Z</i>	8	8	2	2
<i>T</i> (K)	408	100	100	100
$\lambda$ (Mo–K $\alpha$ )	0.71073	0.71073	0.71073	0.71073
<i>D<sub>c</sub></i> (g cm <sup>-3</sup> )	1.708	1.735	1.691	1.744
$\mu$ (mm <sup>-1</sup> )	1.237	1.202	1.120	1.157
$\theta_{\max}$ (°)	25.0	25.0	25.0	25.1
Total data	12542	11449	32386	29365
Data [ <i>I</i> > 2 $\sigma$ ( <i>I</i> )]	2153	1537	5478	5323
Uniq. Data	3108	3341	7058	6927
<i>R<sub>int</sub></i>	0.124	0.249	0.059	0.070
<i>R<sup>a</sup></i>	0.1014	0.1284	0.0932	0.0757
<i>R<sub>w</sub><sup>b</sup></i>	0.2153	0.3167	0.2307	0.2049
<i>GOF</i>	1.17	1.05	1.15	1.10
Min./Max. Resd.	-3.13, 1.3	-1.42, 1.39	-3.17, 1.51	-1.52, 2.04
Dens. [e/Å <sup>3</sup> ]				

$$^a R = \sum ||F_o| - |F_c|| / \sum |F_o| ; \quad ^b R_w = [\sum \{w(F_o^2 - F_c^2)^2\} / \sum \{w(F_o^2)^2\}]^{1/2}$$

**Table 3.** Selected bond distances (Å) for compound **MOF1c**.

Bonds	Distance (Å)	Bonds	Distance (Å)
Cd1–O1	2.269(12)	Cd1–N1	2.242(15)
Cd1–O3_d	2.459(10)	Cd1–N3_d	2.305(11)
Cd1–N2_f	2.252(13)	Cd1–O3_g	2.201(10)

**Table 4.** Selected bond angles (°) for compound **MOF1c**.

Angles	Degree (°)	Angles	Degree (°)
O1–Cd1–N1	98.2(5)	O1–Cd1–O3_d	177.3(5)
O1–Cd1–N3_d	116.7(5)	O1–Cd1–N2_f	82.9(5)
O1–Cd1–O3_g	111.5(5)	O3_d–Cd1–N1	83.6(4)
N1–Cd1–N3_d	91.0(5)	N1–Cd1–N2_f	178.8(4)
O3_g–Cd1–N1	89.6(5)	O3_d–Cd1–N3_d	65.2(3)
O3_d–Cd1–N2_f	95.4(4)	O3_d–Cd1–O3_g	66.4(3)
N2_f–Cd1–N3_d	89.1(4)	O3_g–Cd1–N3_d	131.1(4)
O3_g–Cd1–N2_f	89.4(4)		

Symmetry code a = 1-x,1+y,3/2-z; b = 1-x,2-y,1-z; c = x,2-y,-1/2+z; d = x,2-y,1/2+z; e = -1/2+x,-1/2+y,z; f = 1/2+x,1/2+y,z; g = 3/2-x,-1/2+y,3/2-z

**Table 5.** Selected bond distances (Å) for compound **MOF1IR**.

Bonds	Distance (Å)	Bonds	Distance (Å)
Cd1–O3	2.74(3)	Cd1–O4	2.217(16)
Cd1–N1	2.377(19)	Cd1–O1_c	2.404(14)
Cd1–N3_c	2.44(2)	Cd1–N2_e	2.339(16)
Cd1–O1_h	2.332(16)		

**Table 6.** Selected bond angles (°) for compound **MOF1IR**.

Angles	Degree (°)	Angles	Degree (°)
O3–Cd1–O4	47.2(9)	O3–Cd1–N1	79.1(9)
O1_c–Cd1–O3	140.1(8)	Cd1_f–N2–C6	117.5(16)
O3–Cd1–N3_c	76.9(8)	Cd1_f–N2–C10	124.5(14)
O3–Cd1–N2_e	103.0(9)	O1_h–Cd1–O3	149.1(8)
Cd1_d–N3–C14	117.9(15)	O4–Cd1–N1	93.8(7)
Cd1_d–N3–C15	125.0(19)	O1_c–Cd1–O4	172.3(6)
O4–Cd1–N3_c	119.9(6)	O4–Cd1–N2_e	83.3(7)
O1_h–Cd1–O4	106.7(6)	O1_c–Cd1–N1	90.8(5)
N1–Cd1–N3_c	95.5(6)	N1–Cd1–N2_e	173.3(7)
O1_h–Cd1–N1	88.2(6)	O1_c–Cd1–N3_c	65.7(6)
O1_c–Cd1–N2_e	91.5(5)	O1_c–Cd1–O1_h	67.2(5)
N2_e–Cd1–N3_c	91.2(6)	O1_h–Cd1–N3_c	132.7(6)
O1_h–Cd1–N2_e			

Symmetry code: a = -1+x,-1+y,z; b = 1+x,1+y,z; c = -1-x,-y,-1-z; d = -1-x,-y,-z; e = -x,1-y,-z; f = -2-x,-y,-1-z; g = -1+x,y,z; h = -2-x,1-y,-1-z; i = -1+x,y,z

**Table 7.** Selected bond distances (Å) for compound **MOF2**.

Bonds	Distance (Å)	Bonds	Distance (Å)
Cd1–O1	2.331(10)	Cd1–O5	2.230(10)
Cd1–N1	2.338(10)	Cd1–N2_d	2.397(12)
Cd1–O1_h	2.390(8)	Cd1–N5_h	2.485(12)
Cd2–O4	2.254(10)	Cd2–N3	2.390(11)
Cd2–N4_a	2.332(12)	Cd2–O8_e	2.325(11)
Cd2–O8_g	2.404(10)	Cd2–N7_g	2.459(12)

**Table 8.** Selected bond angles (°) for compound **MOF2**.

Angles	Degree (°)	Angles	Degree (°)
O1–Cd1–O5	111.8(4)	O8_e–Cd2–N7_g	135.6(3)
O1–Cd1–N1	88.1(4)	O8_g–Cd2–N7_g	67.5(3)
O1–Cd1–N2_d	88.2(4)	O1–Cd1–O1_h	68.0(3)
Cd1–O1–Cd1_h	112.0(4)	O1–Cd1–N5_h	135.2(3)
O5–Cd1–N1	96.8(4)	O5–Cd1–N2_d	82.7(4)
O1_h–Cd1–O5	177.7(4)	O5–Cd1–N5_h	112.3(4)
N1–Cd1–N2_d	175.8(5)	O1_h–Cd1–N1	85.5(4)
N1–Cd1–N5_h	94.3(4)	O1_h–Cd1–N2_d	95.0(3)
N2_d–Cd1–N5_h	89.7(4)	O1_h–Cd1–N5_h	67.6(3)
O4–Cd2–N3	94.8(4)	O4–Cd2–N4_a	83.9(4)
O4–Cd2–O8_e	106.4(4)	O4–Cd2–O8_g	174.2(4)
O4–Cd2–N7_g	117.9(4)	N3–Cd2–N4_a	176.3(4)
O8_e–Cd2–N3	84.0(4)	O8_g–Cd2–N3	82.5(4)
N3–Cd2–N7_g	94.0(4)	O8_e–Cd2–N4_a	93.1(4)
O8_g–Cd2–N4_a	98.6(3)	N4_a–Cd2–N7_g	89.7(4)
O8_e–Cd2–O8_g	68.4(4)		

Symmetry code a = -1+x,-1+y,z; b = -1+x,y,z; c = x,-1+y,z; d = x,1+y,z; e = 1+x,y,z; f = 1+x,1+y,z; g = 1-x,1-y,1-z; h = 1-x,1-y,2-z

**Table 9.** Selected bond distances (Å) for compound **MOF2IR**.

Bonds	Distance (Å)	Bonds	Distance (Å)
Cd1–O1	2.306(9)	Cd1–O5	2.291(8)
Cd1–N1	2.378(10)	Cd1–N2_f	2.355(12)
Cd1–O1_g	2.421(8)	Cd1–N6_g	2.449(11)
Cd2–O4	2.214(7)	Cd2–N3	2.345(8)
Cd2–N4_c	2.348(8)	Cd2–O8_e	2.343(7)
Cd2–O8_h	2.385(7)	Cd2–N7_h	2.443(10)

**Table 10.** Selected bond angles (Å) for compound **MOF2IR**.

Angles	Degree (°)	Angles	Degree (°)
O1–Cd1–O5	107.0(3)	O1–Cd1–N1	90.6(3)
O1–Cd1–N2_f	86.5(4)	O1–Cd1–O1_g	68.7(3)
O1–Cd1–N6_g	134.9(3)	O5–Cd1–N1	82.9(3)
O5–Cd1–N2_f	95.2(4)	O1_g–Cd1–O5	175.4(3)
O5–Cd1–N6_g	117.7(3)	N1–Cd1–N2_f	175.9(4)
O1_g–Cd1–N1	98.6(3)	N1–Cd1–N6_g	88.9(4)
O1_g–Cd1–N2_f	83.1(3)	N2_f–Cd1–N6_g	95.2(4)
O1_g–Cd1–N6_g	66.8(3)	O4–Cd2–N3	82.8(3)
O4–Cd2–N4_c	95.7(3)	O4–Cd2–O8_e	105.2(3)
O4–Cd2–O8_h	171.2(3)	O4–Cd2–N7_h	118.6(3)
N3–Cd2–N4_c	178.5(3)	O8_e–Cd2–N3	89.2(3)
O8_h–Cd2–N3	92.2(3)	N3–Cd2–N7_h	87.4(3)
O8_e–Cd2–N4_c	91.5(3)	O8_h–Cd2–N4_c	89.3(3)
N4_c–Cd2–N7_h	93.0(3)	O8_e–Cd2–O8_h	67.4(3)

Symmetry code a = -1+x,-1+y,z; b = -1+x,y,z; c = x,-1+y,z; d = x,1+y,z; e = 1+x,y,z; f = 1+x,1+y,z; g = 1-x,1-y,-z; h = 1-x,1-y,1-z

## 6.3 Results and Discussion

### 6.3.1: Structural Description

**6.3.1.1 Structural description of  $[\{\text{Cd}(\text{pzdc})(\text{bpee})\}_2 \cdot 3\text{H}_2\text{O}]_n$  (MOF1) and  $[\{\text{Cd}_2(\text{pzdc})_2(\text{rctt}-\text{tpcb})\} \cdot 3\text{H}_2\text{O}]_n$  (MOF1IR):** MOF1 crystallizes in monoclinic system in  $C2/c$  space group. Each distorted octahedral  $\text{Cd}^{\text{II}}$  center is surrounded by three oxygen atoms (O1, O4 and O4\*) and one nitrogen atom (N2) from three different pzdc ligands whereas the axial position are ligated by two nitrogen atoms (N3 and N4) from two different bpee linkers (Figure 3a). Each pzdc linker is chelated to one  $\text{Cd}^{\text{II}}$ , forms  $\mu$ -oxo bridges to another  $\text{Cd}^{\text{II}}$  and further connects to a third  $\text{Cd}^{\text{II}}$  through monodentate carboxylate oxygen atoms. Such binding resulted a 2D  $[\text{Cd}(\text{pzdc})]_n$  corrugated sheet along the  $bc$  plane (Figure 3b). The Cd–O bond distances for bridging oxygen atom varies from 2.319(8) to 2.414(8) Å and for the monodentate binding, the distance is 2.258(10) Å. The equatorial Cd–N bond distance is around 2.467(11) Å whereas the axial Cd–N bonds vary is 2.322(11) Å. To generate the 3D structure of MOF1,  $\text{Cd}^{\text{II}}$  centers of two consecutive 2D sheets are connected along  $a$  direction by bpee linkers in a criss-cross fashion. This 3D architecture contains a 1D channel along the  $c$  direction which is filled with the guest  $\text{H}_2\text{O}$  molecules (Figure 3c). After removing the guest water molecules, MOF1 offers 19.3% voids space with the channel window size of  $3.1 \times 4.4 \text{ \AA}^2$  (Figure 4a).

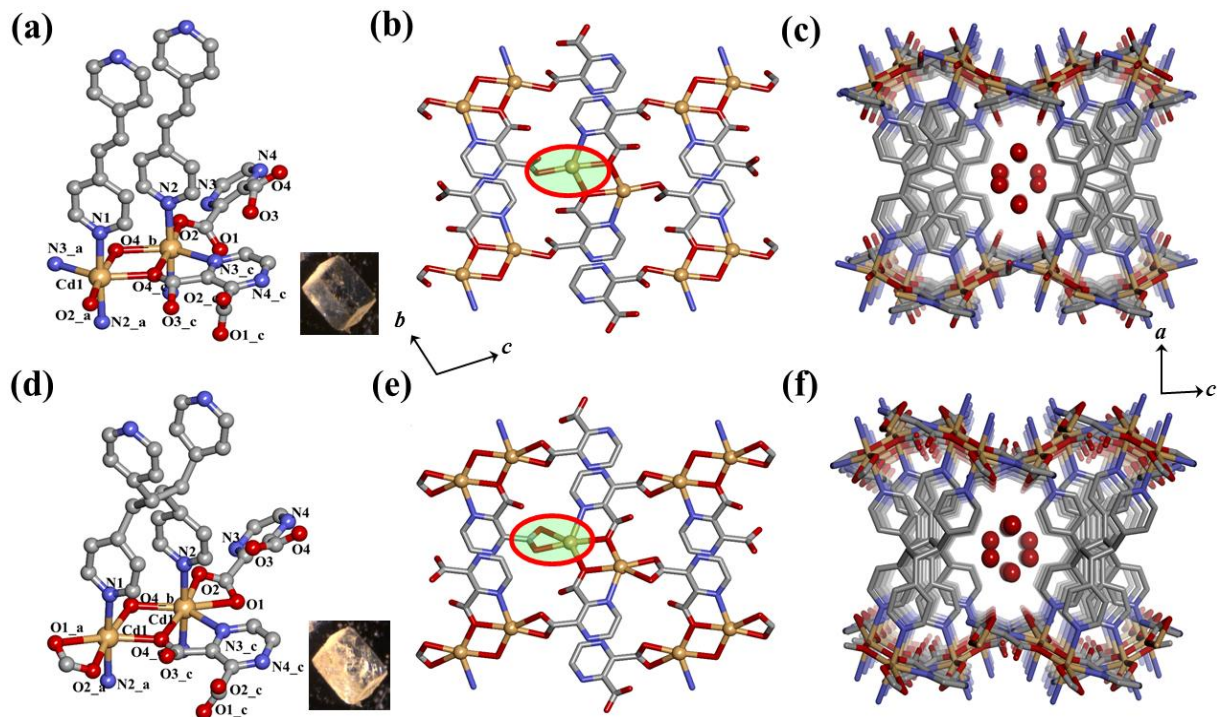


**Figure 3:** (a) and (d) Asymmetric unit of **MOF1** and **MOF1IR**; (b) and (e) 2D layer of **MOF1** and **MOF1IR** formed by connecting the Cd<sup>II</sup> dimers through pzdc ligand; (c) and (f) 3D framework of **MOF1** and **MOF1IR** with 1D channel along the *b* direction which is occupied with guest water molecules.

The guest water molecules have engaged themselves in a H-bonding ( $O6 \cdots O2 = 2.68 \text{ \AA}$ ) with the non-coordinated oxygen atom (O2) of the carboxylate moiety. Most interestingly, the structure contains basic centrosymmetric dimeric units  $[Cd_2(COO)_2(\mu-O)_2]$  which are extended by the pillar bpee linkers to form 3D pillared layer framework. The dimeric unit guides the parallel orientation of bpee pillar in such a way that they are in a face to face having  $\pi \cdots \pi$  interaction (sidewise and lengthwise slip angle is  $6.62^\circ$  and  $3.99^\circ$  respectively) with each other and the distance between the centers of two successive olefinic double bonds is  $3.54 \text{ \AA}$ . Photo irradiation of **MOF1** yields **MOF1IR**, which retains the same crystal system with a slight alteration in the numeric values in cell parameters (Table 2). In **MOF1IR** Cd<sup>II</sup> center has now changed from hexa coordinated to hepta coordinated by the chelation of carboxylate during the course of photo-irradiation (Figure 3d). The newly form bond between the oxygen atom (O2) and Cd<sup>II</sup> ion ( $Cd-O = 2.69 \text{ \AA}$ ) introduces more distortion in the hepta coordinated Cd<sup>II</sup> center (Figure 3e). This also results in a total increase in angle between the two planes containing  $Cd_2(O_4)_2$  and pyrazine ring ( $7.97^\circ$  to  $10.07^\circ$ ).

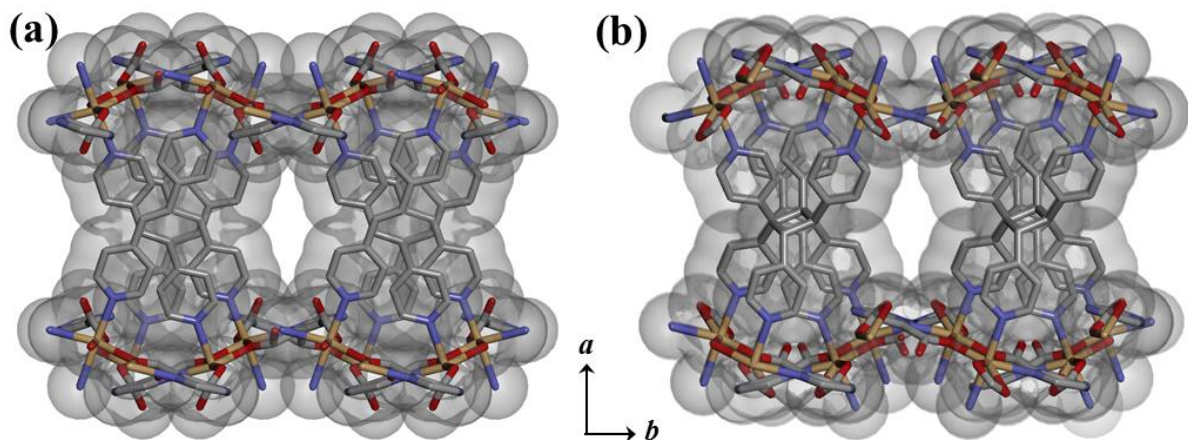


**Figure 4:** View of the pore surface of (a) **MOF1** and (b) **MOF1IR** along the *c* direction after adding the van der Waals radius.

Similar to **MOF1**, the 1D channel is also present in **MOF1IR** with the presence of same number of guest water molecules (Figure 3f). Even after the photo-irradiation, the guest water molecules also interact through hydrogen bonding interaction with the coordinated carboxylate oxygen atoms. The strength of the H-bonding between O2...O(1w) has been decreased as the distance between donor and acceptor atom has increased from 2.68 Å to 2.95 Å. Calculation with PLATON reveals that **MOF1IR** possess 17.5% void space (window size 3.2 × 4.6 Å<sup>2</sup>) after removing the guest water molecules (Figure 4b).

**6.3.1.2 Structural Description of  $[\{\text{Cd}(\text{pzdc})(\text{bpee})\}_2 \cdot 0.3\text{H}_2\text{O}]_n$  (**MOF1c**):** After heating at 135 °C for 12 hrs, **MOF1** retains only 0.3 water molecules. As of its mother compound **MOF1**, the original crystal system and symmetry has been maintained by **MOF1c**. However, significant changes were observed in the following unit cell parameters along with the volume; for **MOF1**;  $a = 25.65(1)$  Å,  $b = 11.215(5)$  Å,  $c = 13.983(9)$  Å,  $V = 3874(4)$  Å<sup>3</sup> and for **MOF1c**;  $a = 24.617(3)$  Å,  $b = 10.6422(11)$  Å,  $c = 14.3033(12)$  Å,  $V = 3627.9(7)$  Å<sup>3</sup>. The Cd–N and Cd–O bond distances are also decreased in the dehydrated framework. The distance between the 2D layers through bpee ligand has also reduced by 0.58 Å which reveals the structural contraction upon desolvation. Most interestingly the C(12)–H(12)...O2 hydrogen bonding distance decreased from 3.46 Å to 3.27 Å which also established the fact that after dehydration, the stronger C–H...O bonding leads to the overall the structural contraction. This is also evident from the desolvated PXRD pattern which is discussed in later part of this chapter.

**6.3.1.3 Structural Description of  $[\{\text{Cd}(\text{pzdc})(\text{bpee})\}_2 \cdot (\text{bpee})_{0.5} \cdot \text{H}_2\text{O}]$  (MOF2) and  $[\{\text{Cd}_2(\text{pzdc})_2(\text{rctt}-\text{tpcb})\} \cdot (\text{bpee})_{0.5} \cdot \text{H}_2\text{O}]$  (MOF2IR):** MOF2 crystallizes in triclinic system in  $P\bar{1}$  space group. There are two crystallographically independent  $\text{Cd}^{\text{II}}$  centers (Cd1 and Cd2) which are highly distorted from the perfect octahedral geometry. The four equatorial position of each metal centers are occupied by three carboxylate oxygen atoms from three different pzdc moieties (O1, O1\*, O5 for Cd1; O4, O8 O8\* for Cd2) and one nitrogen atom (N5 for Cd1 and N7 for Cd2) of pzdc linker (Figure 5a).

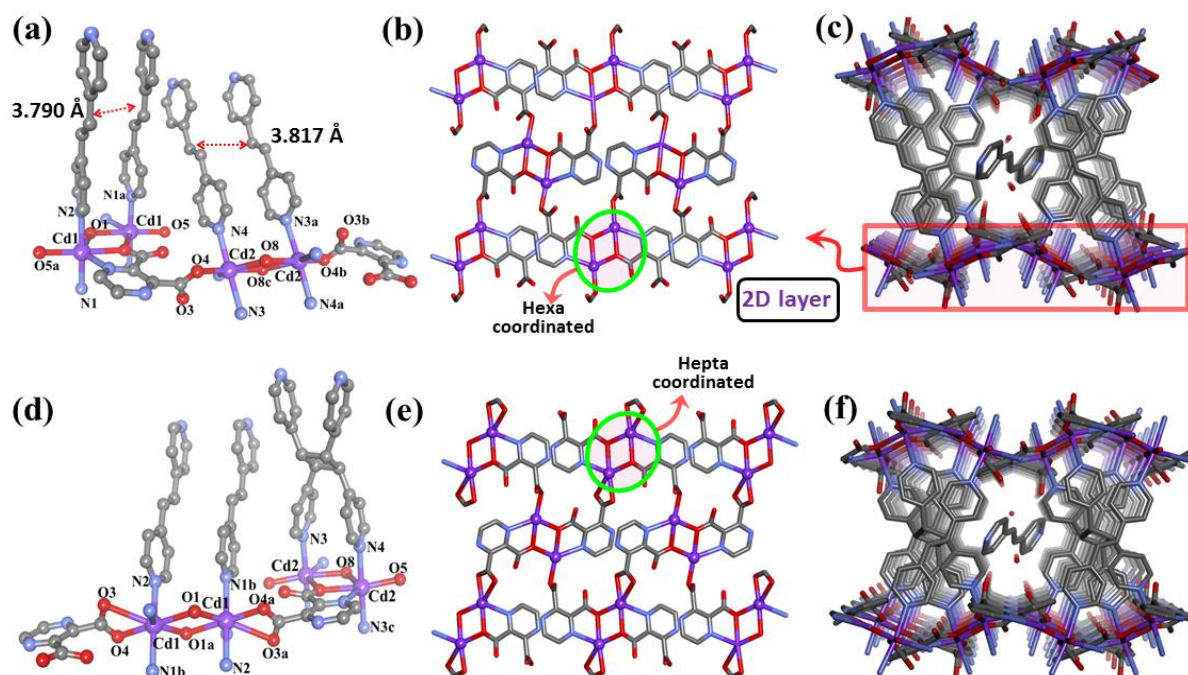


**Figure 5:** (a) Presence of two types of dimeric unit has been observed in the asymmetric unit of **MOF2**. (b) & (e) 2D layer formed by the connection between Cd dimers and pzdc molecules. The coordination environment of  $\text{Cd}^{\text{II}}$  center has changed from hexa to hepta-coordination after photo-irradiation. (d) Photo-irradiated product (**MOF2IR**) shows the formation of cyclobutane ring in one out of two bpee pairs. (c) & (f) View of the 3D architecture of **MOF2** and **MOF2IR** along  $c$  direction. The 1D channel is occupied by the guest bpee and  $\text{H}_2\text{O}$  molecules.

The distorted octahedral coordination sphere is completed by the two nitrogen atoms (N1, N2 for Cd1 and N3, N4 for Cd2) from two different bpee molecules. The Cd–O and Cd–N bonds are in the range of 2.228(9)–2.404(11) Å and 2.340 to 2.398 Å respectively. Each pzdc linker is coordinated to three  $\text{Cd}^{\text{II}}$  centers through three carboxylate oxygen and one nitrogen atom to generate a 2D corrugated sheet along the  $ac$  plane (Figure 5b).



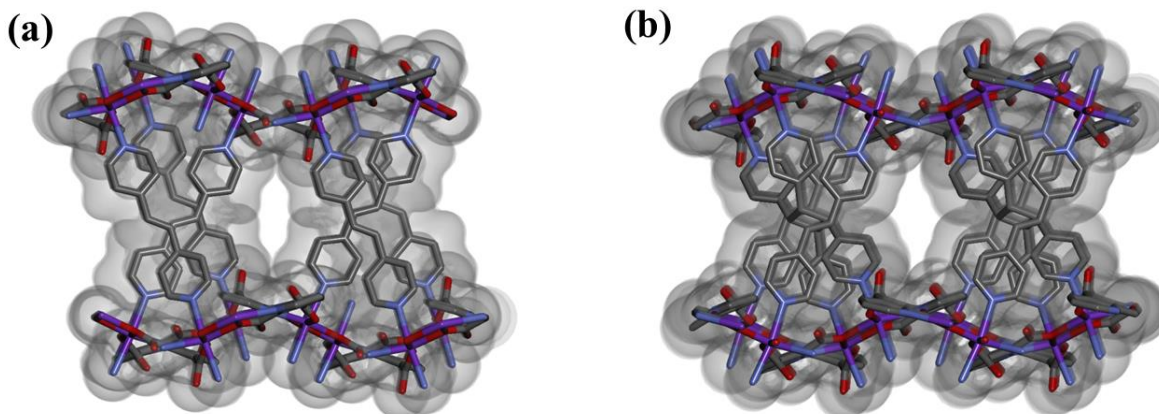


**Figure 6:** View of the pore surface of **MOF2** (a) and **MOF2IR** (b) along the *c* direction after adding the van der Waals radius.

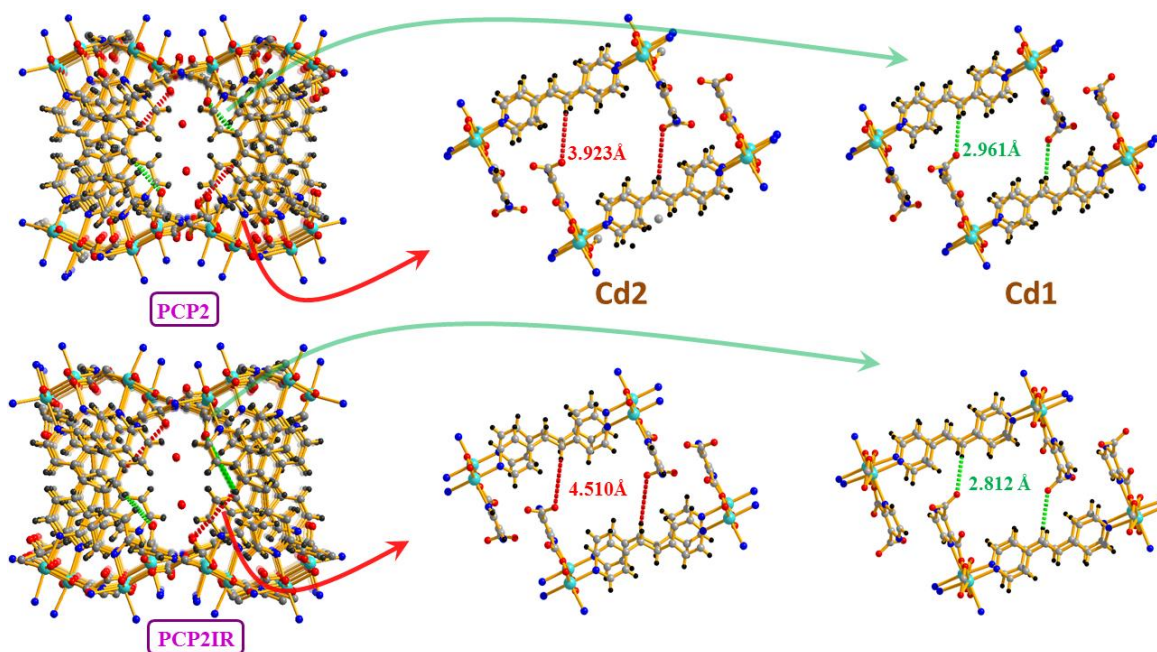


**Figure 7:** Detailed view of the different types of C-H...O interaction in two different Cd dimers in **MOF2**. The first one is showing no interaction while in case of Cd2 a strong interaction is present. After photo-irradiation, the distance between ethylenic hydrogen and free carboxylate in first dimer (Cd1) has been increased to 4.42 Å whereas the same has been decreased to 2.95 Å in second dimer.

To generate the 3D structure of **MOF2**, Cd<sup>II</sup> centers of two consecutive 2D sheets are linked by bpee linker in a criss-cross fashion along *b* direction. This 3D architecture contains a 1D channel along the *c* direction which is filled with the guest bpee and H<sub>2</sub>O molecules (Figure 5c). After removing the guest molecules, calculation using PLATON shows a void space of 422 Å<sup>3</sup> (window size 3.4 × 4.9 Å<sup>2</sup>) which is 20.6% with respect to total cell volume (Figure

6a). This structure also contains two basic centrosymmetric dimeric units of formula  $[\text{Cd}_2(\text{COO})_2(\mu\text{-O})_2]$  which are extended by the coordination of bpee pillars. Similar to **MOF1**, they are interacting with each other through  $\pi\cdots\pi$  interaction ( $Cg\cdots Cg$  distance 3.778 Å (Cd1 unit) and 3.807 (Cd2 unit) Å respectively). Detailed analyses revealed that one ethylenic hydrogen (H24) of the second pair (Cd2 dimer) is forming a C-H...O hydrogen bonding ( $C24\text{-H}24\cdots\text{O}6$ , 2.961 Å) with the hanging carboxylate oxygen atom (O6) whereas the same is missing as the distance is quite high ( $C12\text{-H}12\cdots\text{O}3 = 3.923$  Å) (Figure 7). The  $Cg\cdots Cg$  distances between the centroids of two adjacent pyridine rings of bpee molecules are 3.831 and 3.867 Å, respectively for dimer 1 (containing Cd1) and dimer 2 (containing Cd2).

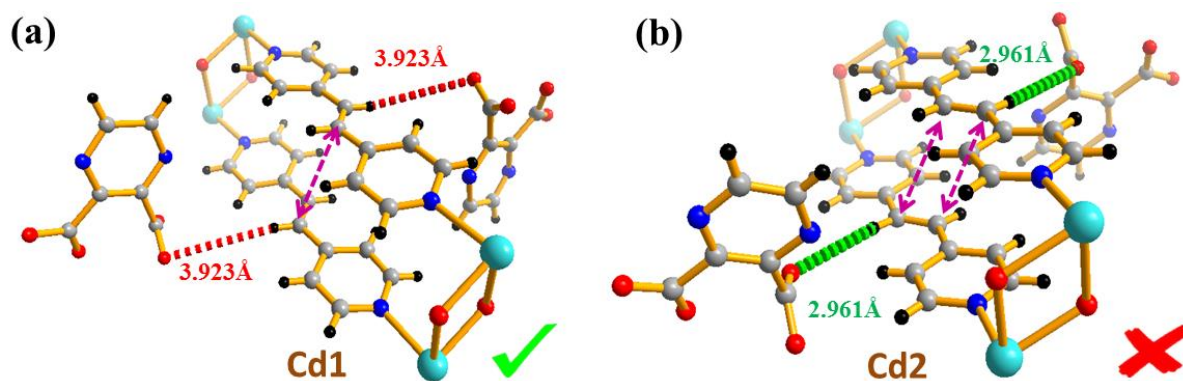


**Figure 8:** Closer view of the C-H...O interaction between the olefinic hydrogen atom and carboxylic oxygen atoms in Cd1 (a) and Cd2 (b) centers. Due to very weak C-H...O interaction, [2+2] photoreaction is taking place in Cd1 dimers whereas in latter case strong interaction is restricting the movement of the ethylenic carbon atoms.

It is also observed that, the arrangement of bpee molecules in both the dimers is not exactly in eclipsed configuration while they are parallelly displaced along the sidewise and as well as the lengthwise direction. The sidewise and lengthwise slip angle for 1<sup>st</sup> dimer is 0.11° and 18.51° whereas the same for the 2<sup>nd</sup> dimer are 4.64° and 17.74° respectively. Such orientation of bpee molecules encouraged us to study the photo-induced cycloaddition reaction and after irradiation with UV light for 30 sec **MOF2IR** is formed with the effective formation of *rctt*-tpcb molecule. **MOF2IR** crystallizes in same triclinic system in *P1* space group. Surprisingly we observed that only one pair of bpee out of two, undergoes [2+2] cycloaddition reaction in **MOF2IR** (Figures 5d–5f). Coordination environment of the metal centers are remaining same as of **MOF1** with slight alteration in  $\text{Cd}^{\text{II}}\text{-O}$  and  $\text{Cd}^{\text{II}}\text{-N}$  bond

lengths. In **MOF2IR**, the Cd–O bond distances are in the range of 2.318(10) Å to 2.377(12) Å whereas the Cd–N varies in the range of 2.248(18) to 2.318 Å(16). The equatorial bond distance is around 2.327(13) Å whereas the axial Cd–N bond varies in the range of 2.445 (9) to 2.425(12) Å. The following fact may explain the formation of cyclobutane ring through [2+2] cycloaddition reaction in first pair though there was equal probability in the second pair to undergo photo-dimerization. Absence of C–H...O hydrogen bonding in first dimer is not restricting the carbon atoms of ethylenic double bond for further movement to form the cycloaddition (Figure 8a) product whereas the strong interaction in the second pair is hindering the cycloaddition reaction (Figure 8b). The above structural observation in **MOF1** and **MOF2** is clearly demonstrating the role of weak C–H...O supramolecular interactions. This effect has also made a significant effect in the adsorption study of the dehydrated compounds which has been described later part in this chapter. After the removal of guest molecules, calculation using PLATON shows a void space of 374 Å<sup>3</sup> (window size 4.1 × 4.9 Å<sup>2</sup>) which is 19.3% with respect to total cell volume (Figure 6b).

### 6.3.2 Framework stability: Thermogravimetric (TG) and Powder X-ray diffraction (PXRD) analysis

Thermogravimetric analysis (TGA) and powder X-ray diffraction (PXRD) measurements at different temperatures were carried out to study the stability of the framework compounds. TGA of compounds **MOF1–2** and **MOF1IR–2IR** were performed in the temperature range of 30 – 700 °C under nitrogen atmosphere.

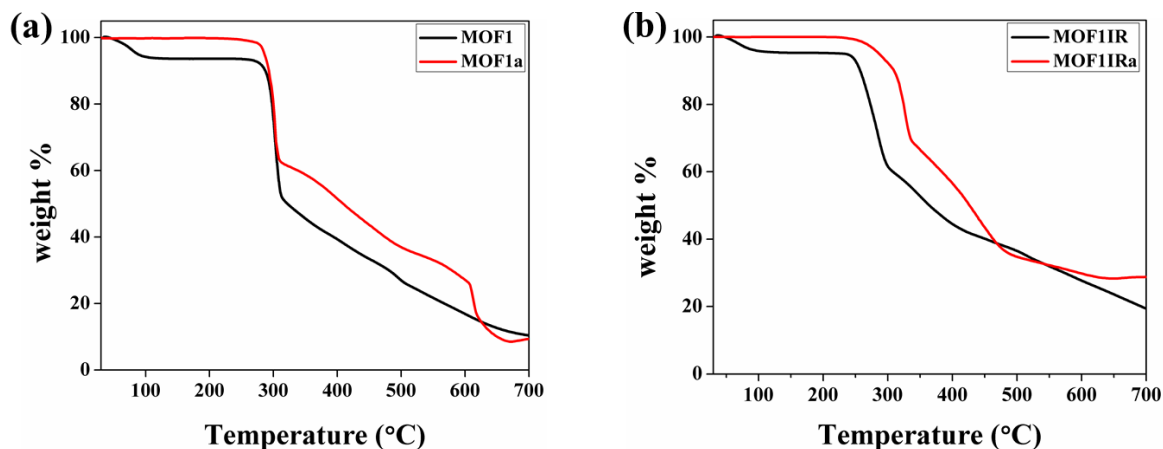


**Figure 9:** TGA profiles of **MOF1** (a) and **MOF1IR** (b) at their different states; As-synthesized (black) and dehydrated (red). (Heating rate 5 °C/min under nitrogen).

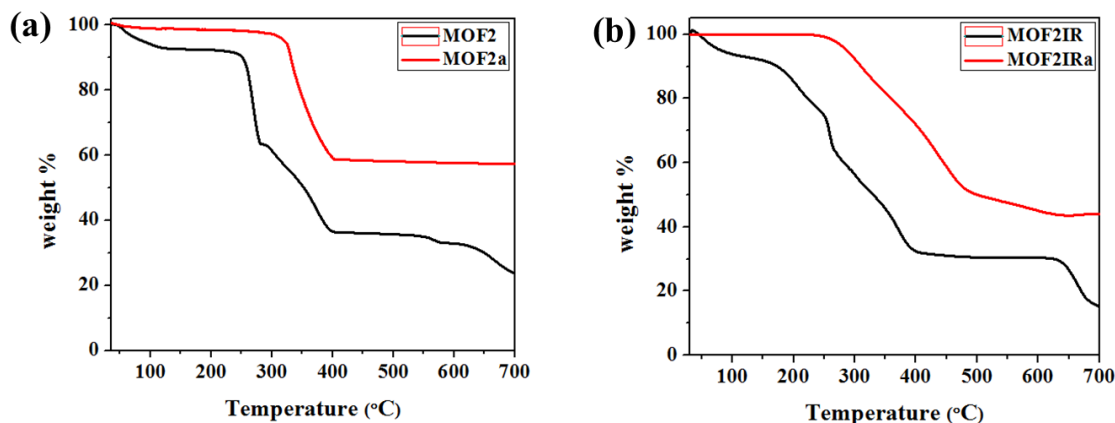


**Figure 10:** TGA profiles of **MOF2** (a) and **MOF2IR** (b) at their different states; As-synthesized (black) and dehydrated (red). (Heating rate 5 °C/min under nitrogen atmosphere).

TGA profile of **MOF1** (Figure 9a) indicates a weight loss of 6.1 % at 120 °C which corroborates the removal of three guest water molecules (Cal. 5.6 %). The desolvated framework is stable up to 270 °C without showing any further weight loss. Similar kind of stability was also reflecting from the TGA curve of **MOF1IR** (Figure 9b). **MOF2** and **MOF2IR** also shows a weight loss of 9.3 % in the temperature range 40-120 °C which is equal to the removal of guest bpee and water molecule (calc. 10.1%) and the deguest sample is stable up to 250 °C (Figure 10a–b). Beyond this temperature, the compound decomposes to unidentified products. PXRD patterns of all the MOFs show well correspondence of the different peak positions in the simulated and as-synthesized patterns which suggest the phase purity of the compounds (Figures 11 and 12).

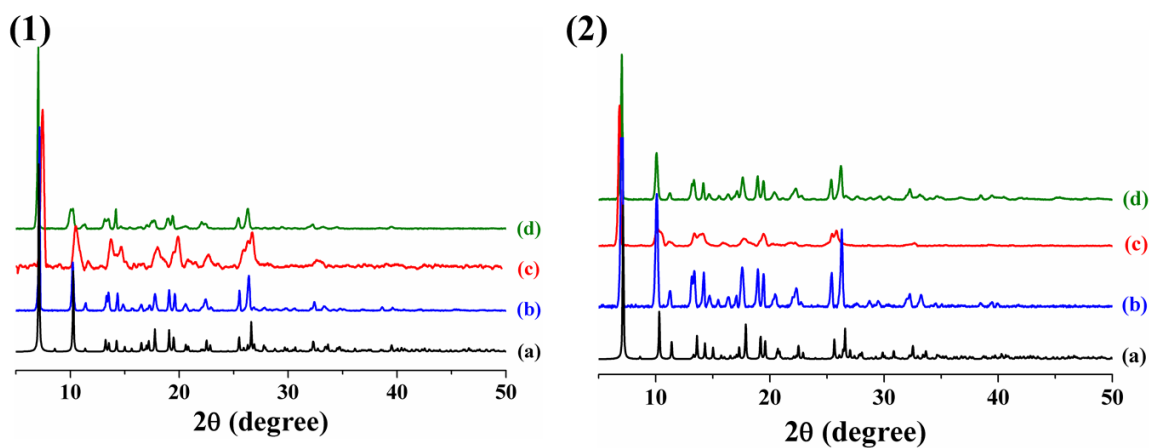


**Figure 11:** PXRD patterns of **MOF1** (1), **MOF1IR** (2) at different states. (a) simulated (b) as-synthesized, (c) desolvated at 140 °C under vacuum, (d) rehydrated.

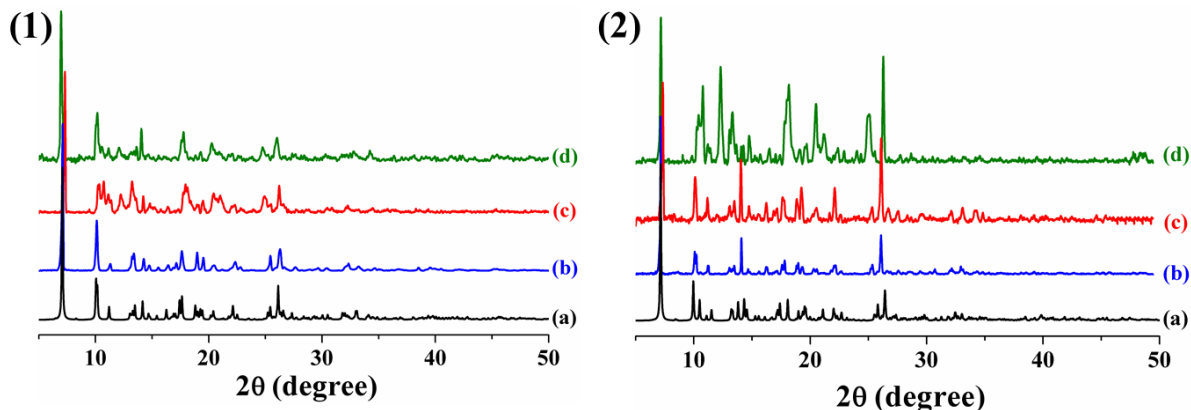


**Figure 12:** PXRD patterns of **MOF2** (1), **MOF2IR** (2) at different states. (a) simulated (b) as-synthesized, (c) desolvated at 140 °C under vacuum, (d) rehydrated.

PXRD patterns of all dehydrated compounds (**MOF1a**, **MOF1IRa**, **MOF2a** and **MOF2IRa**) show similar diffraction pattern as of their corresponding as-synthesized forms which reflect structural integrity even after the desolvation procedure.

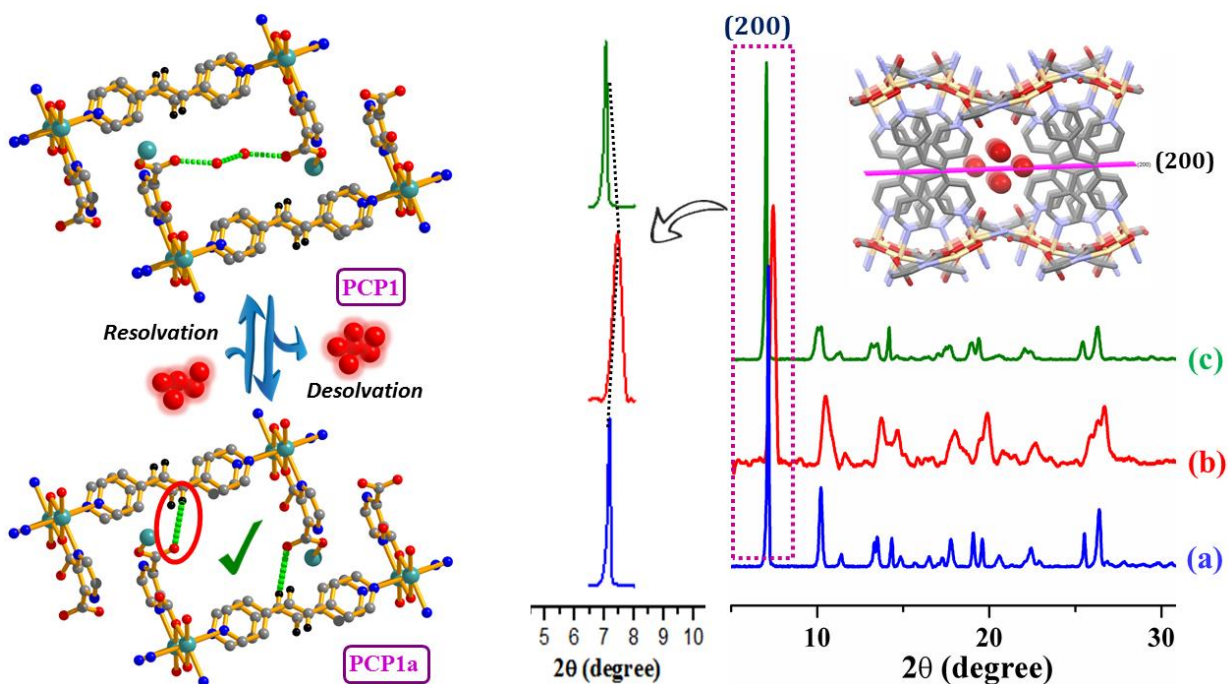


**Figure 13:** Detailed view of the H-bonding interaction between guest water and carboxylate oxygen atoms. After the removal of guest H<sub>2</sub>O molecules, formation of C-H...O hydrogen bonding in the non-irradiated framework results in shrinkage between the 2D layers. The contraction of the structure is also reflecting from the PXRD patterns of **MOF1** (blue), **MOF1a** (red), and **MOF1b** (olive green). The shift of the highlighted peak at 7.02° has moved to 7.13° after dehydration which reflects the structural contraction during this procedure. The peak position has been restored to its earlier position after exposing with H<sub>2</sub>O for 7 days.

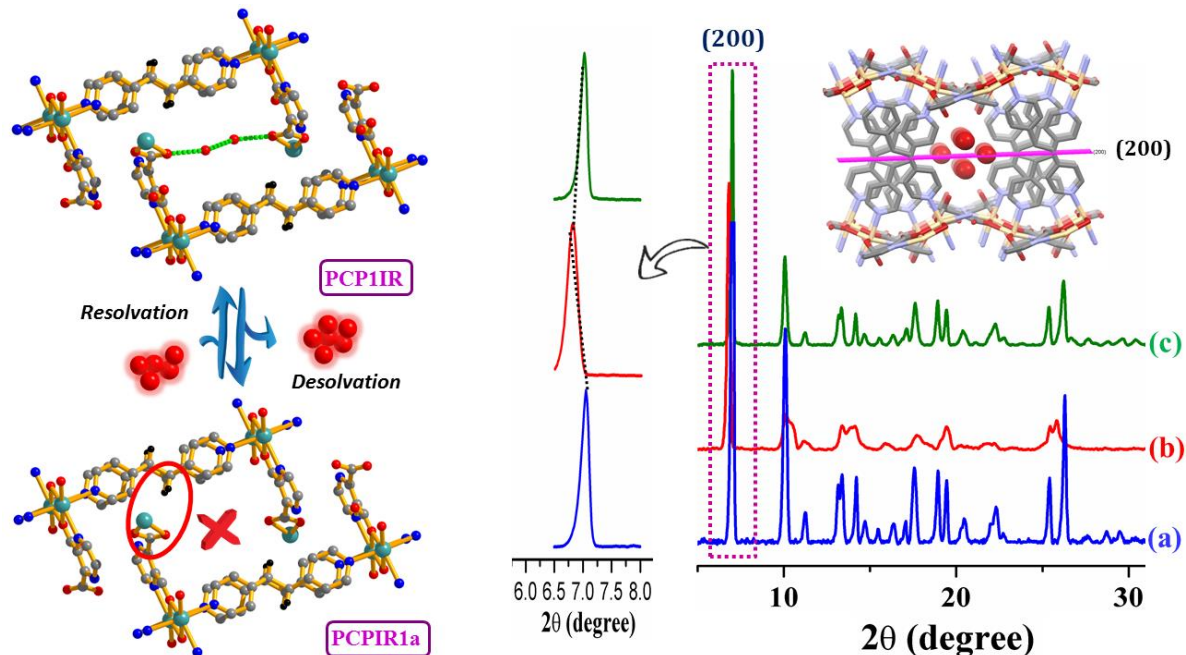


**Figure 14:** Detailed view of the H-bonding interaction between guest water and carboxylate oxygen atoms. Unlike the earlier case, after the removal of guest H<sub>2</sub>O molecules there is no C-H...O hydrogen bonding as the *sp*<sup>2</sup> hydrogen is converted to *sp*<sup>3</sup> one which facilitates the structural elongation. The elongation of the structure is also reflecting from the PXRD patterns of **MOF1IR** (blue), **MOF1IRa** (red), and **MOF1IRb** (olive green). The shift of the highlighted peak at 7.02° has moved to 7.13° after dehydration which reflects the structural contraction during this procedure. The peak position has been restored to its earlier position after exposing with H<sub>2</sub>O for 7 days.

But detailed investigation over the dehydrated diffraction patterns shows a shift in the (200) Bragg's reflection in **MOF1** which is passing through the guest molecules (inset of Figure 13). After dehydration, lower angle peak in the PXRD pattern of the dehydrated framework of the non-irradiated compound moves towards the right side (**MOF1** to **MOF1a** 7.02° to 7.13°) which exhibits a contraction of the structure by decreasing the interlayers distance. On the contrary, the same Bragg's reflection in the dehydrated frameworks of the irradiated sample have shifted towards left side (**MOF1IR** to **MOF1IRa** 7.05° to 6.96°) corroborating the slight increase in the interlayer distance upon the dehydration process (Figure 14). This observation may be explained by the following discussion. After dehydration of **MOF1**, the bpee pillar and pzdc from the 2D layer come closer, probably reinforced by the C-H...O interactions between the ethylenic hydrogen and the pendent carboxylate oxygen atom (O<sub>2</sub>), thus an overall contraction in the framework is realized. But, in case of **MOF1IRa**, such interactions are not feasible due to the following reasons; (a) after [2+2] cycloaddition

reaction  $sp^2$  hybridized ethylenic carbons transform to  $sp^3$ , which changes the H atom position and also reduces the acidic character of the hydrogen atoms, (b) secondly the pendent oxygen atom (O2) is now connected to  $Cd^{II}$ , thus position of O2 atom is also changed. Therefore, the possibility of C-H...O interactions in **MOF1IRa** is almost nil (Figure 13), rather PXRD pattern suggests slight expansion in the framework after dehydration.

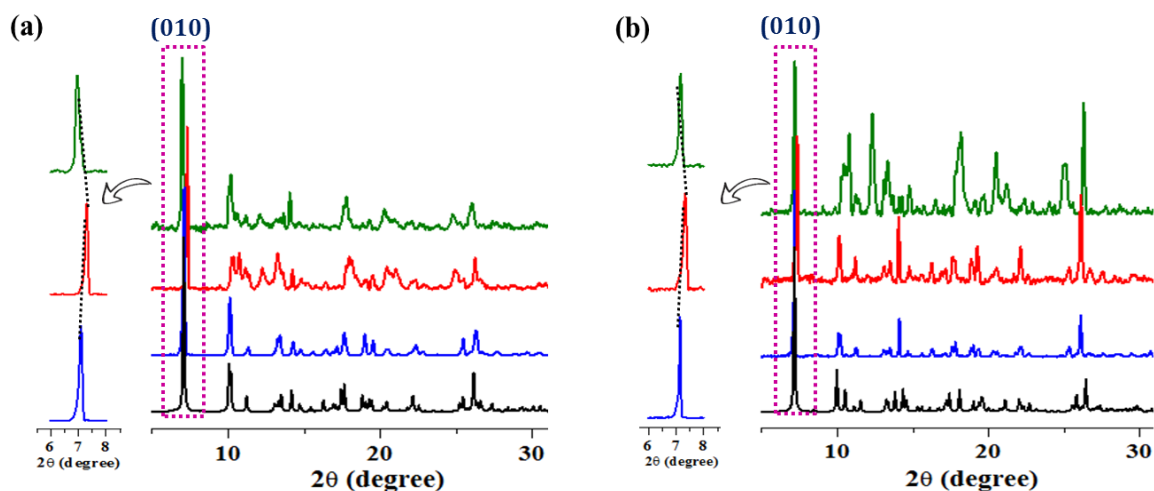


**Figure 15:** PXRD patterns of **MOF2** (a) and **MOF2IR** (b) at different states. After Dehydration, in both cases, the peak at  $7.02^\circ$  shifted to higher angle ( $7.13^\circ$  (**MOF2**) and  $7.10^\circ$  (**MOF2IR**)) which reflects the structural contraction.

But in case of **MOF2a**, C-H...O hydrogen bonding between the ethylenic hydrogen and coordinated oxygen molecule is contracting the structure (Figures 7, 8 and 15a). After photoirradiation of **MOF2**, one pair of C-H...O hydrogen bonding acting in second dimer is sufficient enough to restrict the total elongation procedure along the  $b$  direction (Figure 15b). All the dehydrated frameworks were exposed to water vapor for one week and all the samples return to its earlier peak position. Inclusion of water molecules is reconstructing the hydrogen bonding with free (**MOF1**) or coordinated (**MOF2**) oxygen atoms and this is helping the 2D layers to return to its original position. In the water exposed compounds, restoring of the PXRD peaks to its original position is also supporting the role C-H...O interaction during the structural transformation by dehydration–rehydration procedure.

### 6.3.3: Adsorption Study

To investigate the permanent porosity of **MOF1**, **MOF1IR**, **MOF2** and **MOF2IR**,  $N_2$  adsorption measurement was carried out at 77 K. Despite having sufficient pore windows in all the MOFs, typical type-II adsorption profiles were observed (Figures 16 (1) and 16 (2)). The final  $N_2$  uptake amount has been recorded to be 3 mL/g, 20 mL/g, 27 mL/g and 36 mL/g at  $P/P_0 \sim 0.99$  respectively for **MOF1a**, **MOF1IRa**, **MOF2a** and **MOF2IRa**. Two probable reasons might be considered regarding the surface adsorption of  $N_2$ . Firstly, the pore walls of both the compounds are  $N_2$  phobic due to the presence of hanging carboxylic oxygen atoms and aromatic  $\pi$  cloud and secondly, the window size is not sufficiently big enough for the diffusion of comparatively larger  $N_2$  molecules.

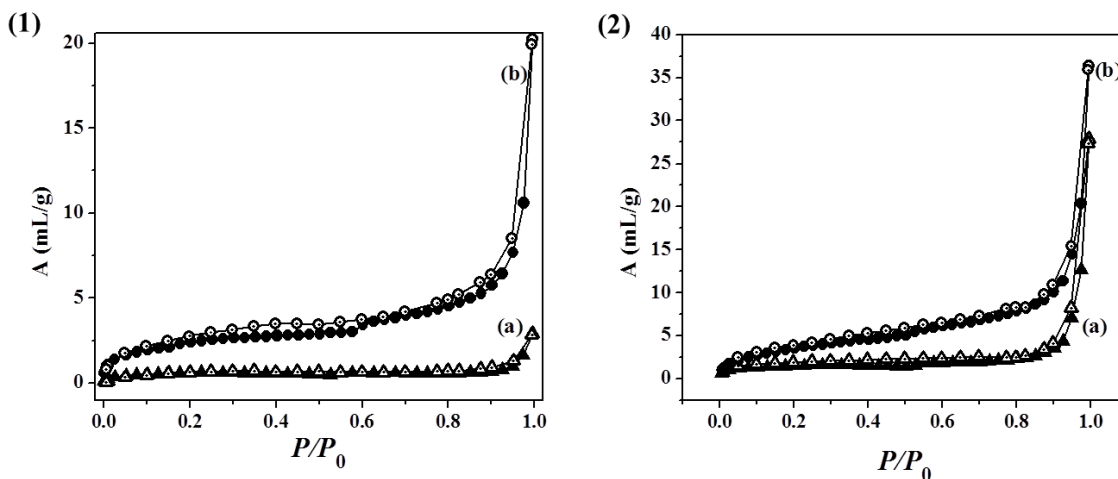


**Figure 16:**  $N_2$  adsorption isotherms of **MOF1a** (1a) and **MOF1IRa** (1b) and **MOF2a** (2a) and **MOF2IRa** (2b) measured at 77K.  $P_0$  is the atmospheric pressure.

Presence of pore surface decorated with hanging polar groups and aromatic- $\pi$  cloud inspired us to examine the  $CO_2$  storage capacity of these MOFs. Both the as-synthesized and irradiated compounds were subjected to  $CO_2$  adsorption at 195 K (Figure 17c). **MOF1a** shows a gradual uptake of gas molecules with increase in pressure and reach to a final amount of 39 mL/g. But in case of **MOF1IR**, a steep uptake at low pressure was observed (12 mL/g at  $P/P_0 = 0.01$ ) suggesting a lesser kinetic barrier was experienced by the  $CO_2$  gas molecules while entering in the dehydrated framework of the irradiated compound (Figures 17a and b). After the step uptake at lower pressure, a gradual adsorption profile with increasing pressure was monitored for **MOF1IR** which ends with a final amount of 52 mL/g



at  $P/P_0 \sim 0.99$ . Comparison of  $\text{CO}_2$  adsorption profiles between the as-synthesized and irradiated compounds at low pressure region reveals that the rate of incorporation of  $\text{CO}_2$  molecules is much higher in the irradiated framework compared to the as-synthesized framework.

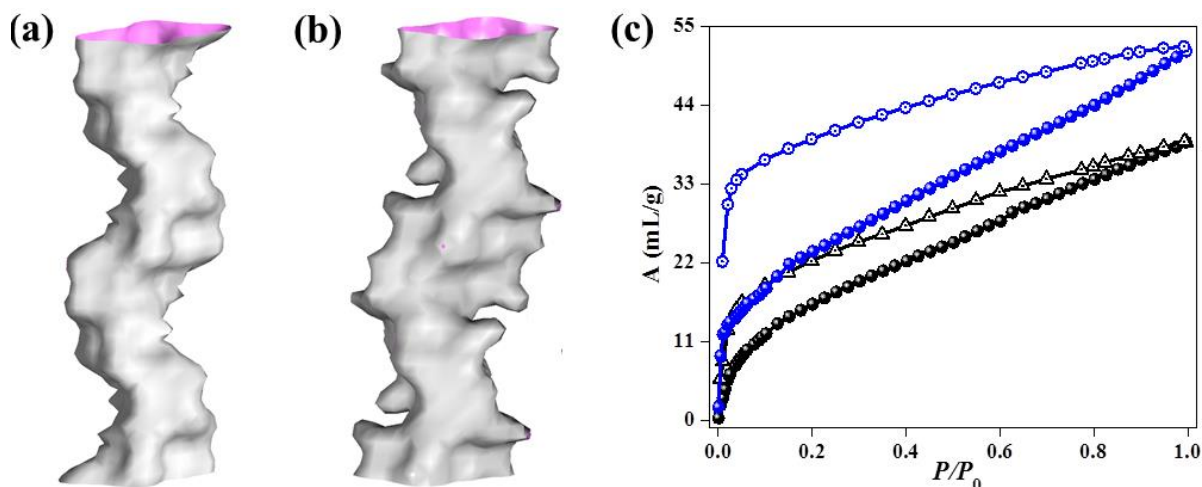


**Figure 17:** (a) & (b) Connolly surface of **MOF1** and **MOF1IRa** with probe radius of  $0.75 \text{ \AA}$ . The channel diameter and accessibility has been increased after the photo-modification. (c)  $\text{CO}_2$  adsorption profiles of **MOF1** (black circle) and **MOF1IRa** (blue circle) measured at 195 K. Higher  $\text{CO}_2$  uptake capacity has been monitored in irradiated compound (**MOF1IRa**) (filled and empty symbols are representing adsorption and desorption curves respectively).

Interesting observation was recorded when we examine the  $\text{CO}_2$  capture capacity of **MOF1a** and **MOF1IRa** at ice temperature (Figure 18a). At 273 K, the uptake amount of **MOF1a** is found to be  $\sim 5 \text{ mL/g}$  which is quite less comparative to the amount  $22 \text{ mL/g}$  adsorbed by **MOF1IRa**. At low pressure region, steep uptake of  $\text{CO}_2$  was observed by **MOF1IRa** which is further followed by a gradual uptake up to  $P/P_0 = 0.87$ . To estimate the interaction between  $\text{CO}_2$  and pore wall of **MOF1IRa**, we have measured the  $\text{CO}_2$  adsorption profiles at 263 K and fitting of two curves (263 K and 273 K) by employing virial equation (Figure 22) results in a heat of adsorption value of  $\sim 22 \text{ kJ/mol}$  (Figure 18b) which is comparable with other reported literatures.<sup>22</sup> We have also tested the  $\text{N}_2$  and  $\text{CH}_4$  sorption capacity at 273 K and both the MOFs shows complete exclusion of such small molecules. In case of **MOF1IRa**, by using the ideal adsorbed solution theory (IAST) model, the selectivity of  $\text{CO}_2$  over the  $\text{N}_2$  and  $\text{CO}_2$  over  $\text{CH}_4$  are also predicted to be 22 and 32 respectively (Figures 18c and d) and the value increases sharply with further loading of gas molecules at higher pressure. But in case

of **MOF1a**, the amount of CO<sub>2</sub> uptake was so less that we were unable to predict any IAST selectivity.

Surprisingly at 195K the CO<sub>2</sub> adsorption profiles of **MOF2** and **MOF2IR** shows completely reverse trend (Figure 19). Dehydrated framework of **MOF2** shows a gradual uptake of CO<sub>2</sub> upon increase in pressure, which finally ends with a volume uptake of 36 mL/g. In case of **MOF2IRa**, the uptake amount was 27 mL/g which is lesser than that of **MOF2a**.

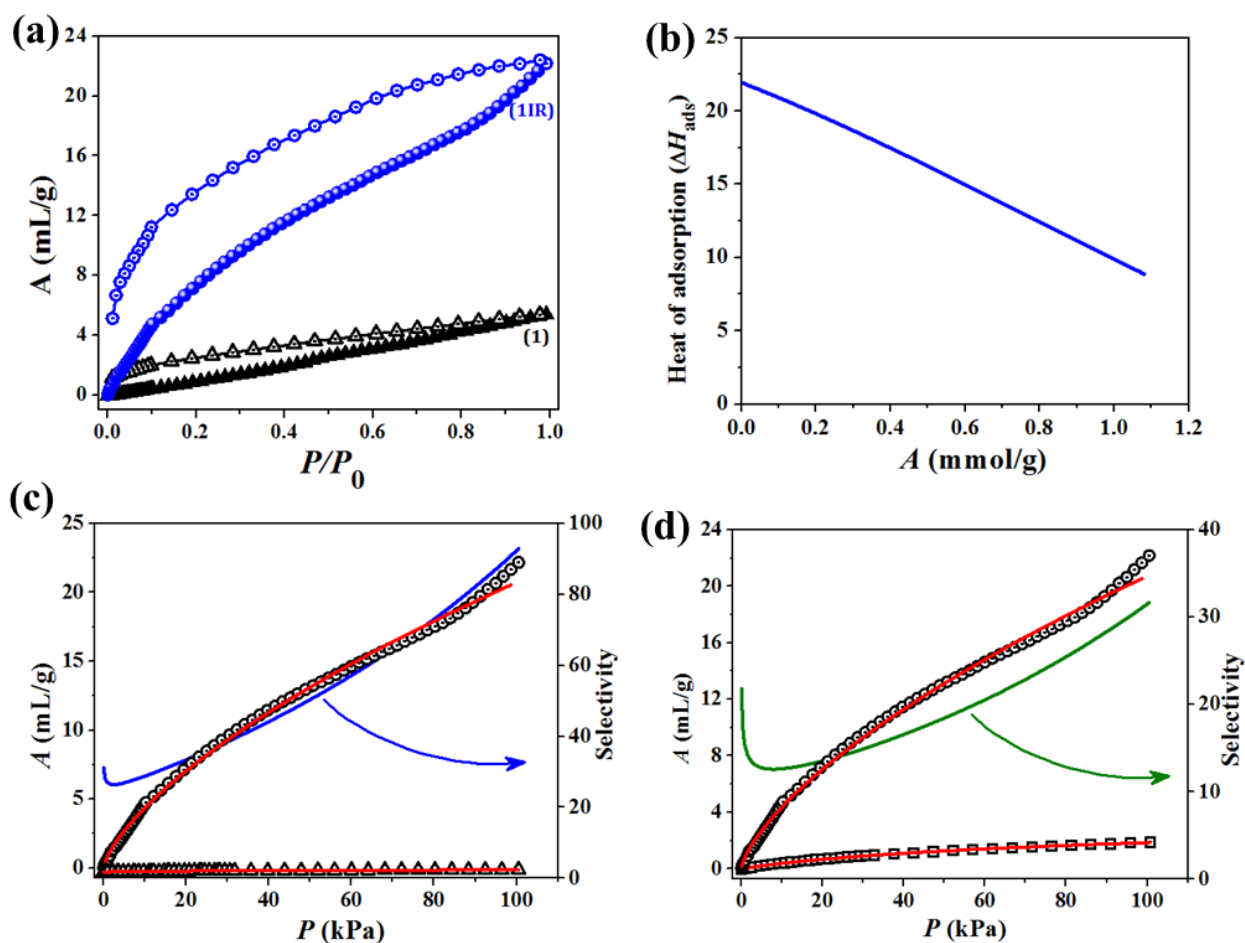


**Figure 18:** (a) CO<sub>2</sub> adsorption isotherms of **MOF1IRa** (blue circle) shows much higher uptake compare to **MOF1a** (black triangle) reflecting higher kinetic barrier present in the non-irradiated compound where CO<sub>2</sub> is unable to diffuse at ambient temperature (filled and empty symbols are representing adsorption and desorption curves respectively). (b) Heat of CO<sub>2</sub> adsorption of **MOF1IRa** vs. CO<sub>2</sub> loading show a continuous fall with increasing uptake. (c) & (d) Selective CO<sub>2</sub> capture by **MOF1IRa** over N<sub>2</sub> and CH<sub>4</sub> respectively. Blue lines are showing CO<sub>2</sub> selectivity with increasing loading of bi-component gas mixture.

The dramatic tuning of CO<sub>2</sub> capture at 273 K in **MOF1** by postsynthetic modification regulated by light as an external stimulus is unprecedented in the literature of metal-organic frameworks. Detailed analyses of the structure of **MOF1** and **MOF1IR** would explain this further. Interestingly after postsynthetic modification in **MOF1IR**, the void space slightly reduced compared to parent **MOF1**, however window size is enhanced as mentioned earlier. Furthermore, in **MOF1** bpee pillars are parallel and decorated along the pore surface and after cycloaddition reaction two such pillars are fused together and their thermal vibration along the pores are restricted.

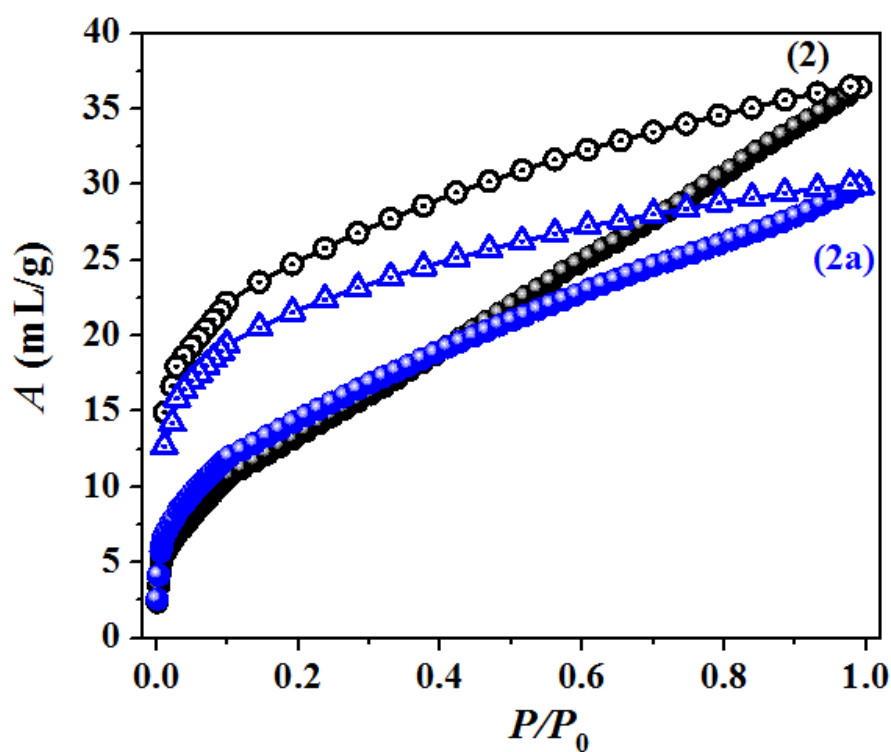


**Figure 19:** CO<sub>2</sub> adsorption isotherms of **MOF2IRa** (blue triangle) and **MOF2a** (black circle) measured at 195 K.  $P_0$  is atmospheric pressure.

On the other hand, dehydration of **MOF1IRa** suggests structural expansion as realized in PXRD pattern. All these cumulative effects after postsynthetic modification decrease the diffusion barrier, thus enhanced CO<sub>2</sub> uptake was observed. But in the second case, after photoirradiation in **MOF2**, the C-H...O hydrogen bonding interaction becomes stronger in **MOF2IR** and the dehydrated structure contracted rendering lesser CO<sub>2</sub> uptake in the dehydrated framework.

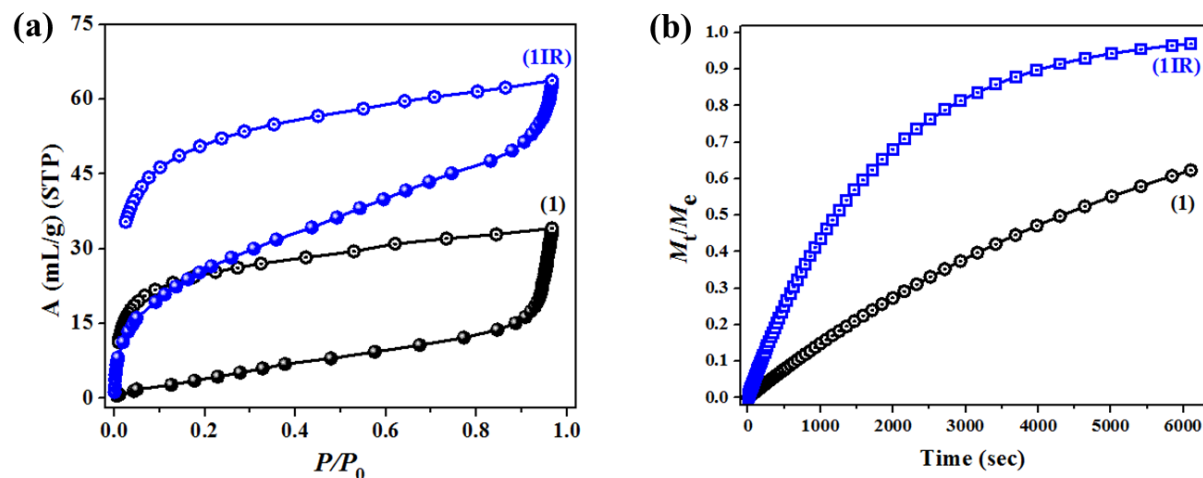


**Figure 20:** (a) Methanol adsorption isotherms of **MOF1a** (black) and **MOF1IRa** framework (blue). Steep uptake in the latter case reflects a lesser kinetic barrier experienced by adsorbent molecules. (b) Kinetics of methanol adsorption vs time shows higher rate of mass diffusion in the irradiated frameworks compare to the non-irradiated compounds. Details have been discussed in the main text.

For further understanding of the different adsorption dynamics in the as-synthesized and photo-modified framework, we have carried out methanol vapor adsorption studies. Interesting results were observed when both the compounds were subjected to MeOH (kinetic diameter 3.6 Å) adsorption isotherm at 293 K. In case of **MOF1a**, a gradual uptake was perceived up to  $P/P_0 = 0.91$  and after that a sudden jump in the adsorption profile was observed which ends to a final volume of 47 mL/g (Figure 20a). A double step adsorption profile with a steep uptake in the low pressure regions (up to  $P/P_0 = 0.04$ ) was observed for **MOF1IRa** which is followed by a gradual uptake that ended at 67 mL/g at  $P/P_0 = 0.9$ . After that, a sudden jump in the adsorption profile was noticed with a final uptake amount of 63 mL/g and this sudden jump is quite similar to that of the as-synthesized one. Comparison of these two uptake profiles at lower pressure region clearly indicates that the occlusion of methanol molecules is quite easier in **MOF1IRa** rather than in **MOF1a**, which is also supported by the difference between the final uptake volumes of these two compounds (Figure 20a). In order to compare the different rate of diffusion of the adsorbates in **MOF1a** and **MOF1IRa**, detailed sorption kinetics study with methanol vapor has been carried out with an equilibrium time of 6000 sec/adsorption point. Obtained kinetic data have been fitted onto the linear driving force mass transfer (LDF) model which gives satisfactory agreement between the experimental points and the fitted plot. The model is quite acceptable to describe

the most vapor/gas adsorption kinetics on carbon based molecular sieves, active carbon and even metal–organic frameworks (MOFs). The  $M_t/M_e$  vs.  $t$  plots are clearly demonstrating the difference in the rate of mass diffusion in **MOF1a** and **MOF1IRa** for methanol vapor adsorption for a particular constant time (Figure 20b). It is observed that **MOF1IRa** compounds demonstrate much faster rate of adsorption compared to the non–irradiated compounds by reaching the  $M_t/M_e$  value to 1 *i.e.* towards equilibrium. The same is also apparent from the kinetic rate constant values which are listed in table 11.

**Table 11:** Rate constant values of the methanol adsorption measurements at low pressure region.

MOFs	$P/P_0$	$k$ ( $s^{-1}$ )
<b>MOF1a</b>	0.0497	$1.60 \times 10^{-4}$
<b>MOF1IRa</b>	0.0013	$5.73 \times 10^{-4}$
<b>MOF2a</b>	0.0294	$3.92 \times 10^{-3}$
<b>MOF2IRa</b>	0.0065	$2.79 \times 10^{-3}$

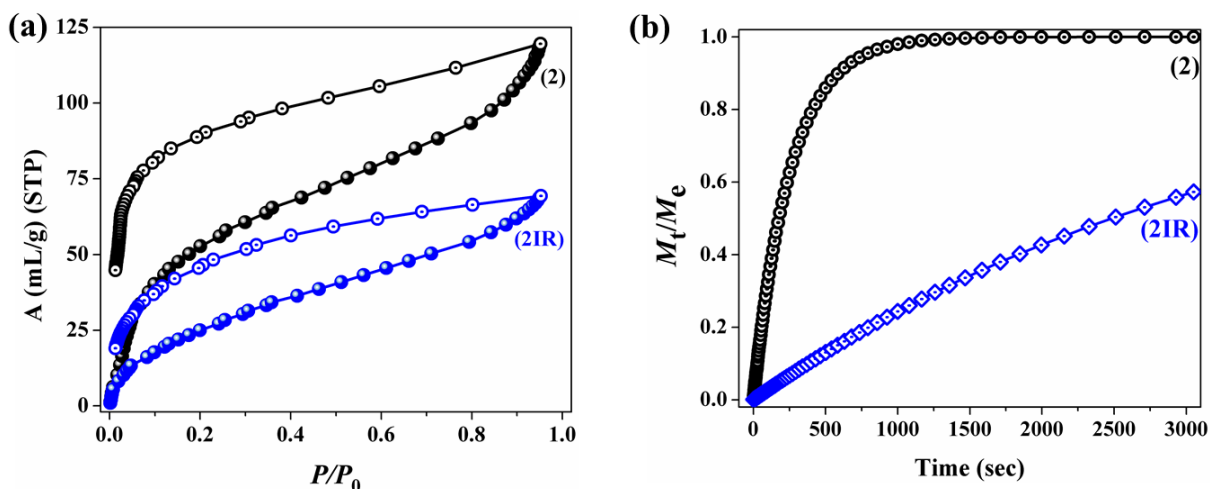


**Figure 21:** (a) Methanol adsorption isotherms of **MOF2a** (black) and **MOF2IRa** framework (blue). Steep uptake in the first case reflects a lesser kinetic barrier experienced by adsorbent molecules. (b) Kinetics of methanol adsorption vs. time shows higher rate of mass diffusion in the non-irradiated frameworks compare to the irradiated compounds. Details have been discussed in the main text.

Methanol adsorption behavior was also recorded in case of **MOF2a** and **MOF2IRa** (Figure 21a). The photo-irradiated compound *i.e.* **MOF2IRa** adsorbs methanol vapor in a gradual manner which ends with a final amount of 61 mL/g whereas **MOF2a** adsorbs about 115 mL/g methanol with a steep uptake at lower pressure regions. In order to compare the different CO<sub>2</sub> and methanol adsorption capacities, detail sorption kinetic studies based on methanol vapor were carried out with an equilibrium time of 3000 sec/per adsorption point. It is observed that **MOF2a** demonstrates much faster rate of adsorption compared to the photo-modified **MOF2IRa** by reaching the  $M_t/M_e$  value to 1 *i.e.* towards equilibrium in smaller time. This result is also in line with the reduced CO<sub>2</sub> uptake (195 K) in **MOF2IRa**.

This result univocally suggests that the diffusion barrier is significantly higher for **MOF1a** compared to **MOF1IRa** and this causes higher uptake of methanol in the photo-modified framework. The less diffusion barriers in **MOF1IRa** is due to the absence of C-H...O hydrogen bonding which facilitates the expansion in the postsynthetically modified framework by [2+2] cycloaddition reaction. In the second case the stronger C-H...O hydrogen bonding after cycloaddition reaction is playing a reverse role by reducing the final uptake amount in the irradiated framework (**MOF2IRa**).

#### 6.3.4: Analysis of Gas Adsorption Isotherms

**Heat of Adsorption (kJ/mol):** We have used a virial type expression of the following type to fit the combined isotherm data collected at 263 and 273 K.

$$\ln(P) = \ln(A) + \frac{1}{T} \sum_{i=0}^m a_i A^i + \sum_{i=0}^n b_i A^i \quad \dots\dots\dots(1)$$

Here,  $P$  is the pressure expressed in torr,  $A$  is the amount adsorbed in mmol/g,  $T$  is the temperature in K,  $a_i$  and  $b_i$  are virial coefficients, and  $m$ ,  $n$  represent the number of coefficients required to adequately describe the isotherms. The value of  $m$  and  $n$  was gradually increased until the contribution of extra added  $a$  and  $b$  coefficients were negligible towards the overall final fit. The values of the virial coefficient  $a_i$  were taken to calculate the isosteric heat of adsorption using the following expression.

$$Q_{st} = -R \sum_{i=0}^m a_i A^i \dots\dots\dots(2)$$

$Q_{st}$  is the coverage dependent isosteric heat of adsorption and R is the universal gas constant.

**IAST Selectivity:** The ideal adsorbed solution theory (IAST) was used to predict the binary mixture adsorption of CO<sub>2</sub> and N<sub>2</sub> from the experimental pure-gas isotherms. Previous reports have depicted that this method can predict the adsorption selectivity for mixture of isotherms in nanoporous materials, including metal-organic frameworks. The single-component isotherms were fit to a single-site Langmuir-Freundlich equation (equation 5). The IAST assumes that the adsorbed phase is a two-dimensional solution in equilibrium with the bulk phase. For binary adsorption of A and B, the IAST requires these two equations to be followed:

$$yP_t = xP_a \dots\dots\dots(3)$$

$$(1 - y)P_t = (1 - x)P_a \dots\dots\dots(4)$$

Where  $x$  and  $y$  denote the molar fraction of A in the adsorbed phase and the molar fraction of A in the bulk phase, respectively.  $P_t$  is the total gas pressure;  $P_a$  and  $P_b$  are the pressure of component A and B at the same spreading pressure as that of the mixture, respectively. The equation used for the fitting the single component gas mixture is as follows.

$$Y = Y_0 \left( \frac{BP^n}{1 + BP^n} \right) \dots\dots\dots(5)$$

Furthermore, the molar fraction of A in the adsorbed phase can be obtained from the following equation:

$$Y_{o,a} \ln \left( 1 + \frac{B_a P_t^{n1} y}{x} \right) - Y_{o,b} \ln \left( 1 + \frac{B_b P_t^{n2} (1 - y)}{(1 - x)} \right) = 0 \dots\dots\dots(6)$$

where  $Y_{0,a}$ ,  $B_a$  and  $n_1$  are the Langmuir–Freundlich fitting parameters of adsorption equilibrium of pure A,  $Y_{0,b}$ ,  $B_b$  and  $n_2$  are Langmuir–Freundlich parameters of adsorption equilibrium of pure B. The unknown  $x$  in Eq. (6) has been solved by Matlab (Version 7.8 (R2009a), The MathWorks, Inc.) for fixed  $P_i$  and  $y$  values.

Then calculated the predicted adsorption selectivity, which is defined as

$$S = \left( \frac{x_1}{y_1} \right) \left( \frac{x_2}{y_2} \right) \dots\dots\dots(7)$$

where  $x_i$  and  $y_i$  are the mole fractions of component  $i$  ( $i = 1, 2; A, B$ ) in the adsorbed and bulk phases, respectively. The IAST calculations were carried out for equimolar gas–phase mixtures of  $\text{CO}_2$  and  $\text{CH}_4$ , and binary mixture containing 15%  $\text{CO}_2$  ( $y_1$ ) and 85%  $\text{N}_2$  ( $y_2$ ), which is typical of flue gases.

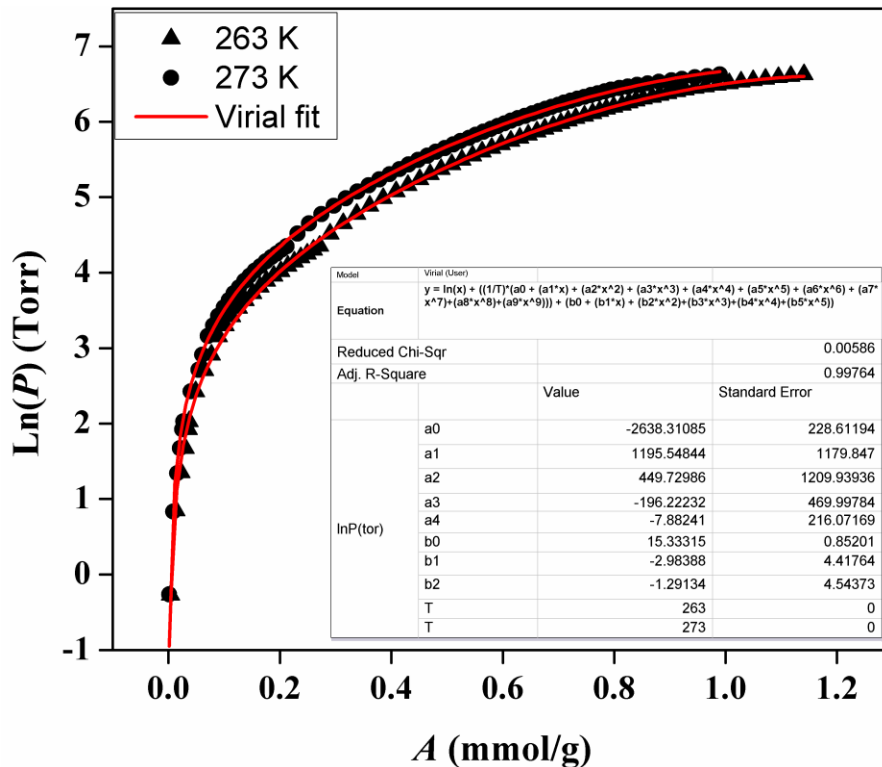


**Figure 22:**  $\text{CO}_2$  adsorption isotherms of MOF1IRa measured at 273 K (circle) and 263 K (triangle). Fitted curves (red solid lines), obtained from the virial-type expansion, were used for the  $Q_{st}$  estimation.



## 6.4: Conclusion

In conclusion, two photoactive porous MOFs of Cd<sup>II</sup>, [ $\{\text{Cd}(\text{pzdc})(\text{bpee})\}_2 \cdot 3\text{H}_2\text{O}\}_n$  (**MOF1**) and [ $\{\text{Cd}(\text{pzdc})(\text{bpee})\}_2 \cdot (\text{bpee})_{0.5} \cdot \text{H}_2\text{O}\}_n$  (**MOF2**) based on mixed linkers have been synthesized and structurally characterized. The parallel arrangement of the bpee pillars in the structure supported by  $[\text{Cd}_2(\mu\text{-O})_2]$  unit brings two ethylenic double bonds closer, thus postsynthetic modification in a single-crystal-to-single-crystal manner based on photo-induced [2+2] cycloaddition reaction is comprehended. **MOF1** shows structural contraction after dehydration regulated by weak C-H...O interactions. However, by modulating such a weak interaction through postsynthetic modification induced by light, framework expansion is realized after dehydrating **MOF1IR**. **MOF1R** exhibits a higher uptake of CO<sub>2</sub> at 195 K and 273 K compared to **MOF1**. Such a dramatic tuning in adsorption properties corresponds to the decrease in diffusion barrier after photo-modification. This conjecture has been supported by the kinetic measurements based on the methanol vapor adsorption study. Finally, the results of this chapter unravel the role of C-H...O interactions in controlling the physical properties of metal-organic frameworks, though it has been considered as a weaker interaction than other conventional strong hydrogen bonding.

## 6.5: References

- (a) S. Achmann, G. Hagen, J. Kita, I. Malkowsky, C. Kiener and R. Moos, *Sensors*, 2009, **9**, 1574; (b) J. J. Gassensmith, J. Y. Kim, J. M. Holcroft, O. K. Farha, J. F. Stoddart, J. T. Hupp and N. C. Jeong, *J. Am. Chem. Soc.*, 2014, **136**, 8277; (c) Z. R. Herm, E. D. Bloch and J. R. Long, *Chem. Mater.*, 2013, **26**, 323; (d) P. Horcajada, C. Serre, G. Maurin, N. A. Ramsahye, F. Balas, M. a. Vallet-Regí, M. Sebban, F. Taulelle and G. r. Férey, *J. Am. Chem. Soc.*, 2008, **130**, 6774; (e) J. Lee, O. K. Farha, J. Roberts, K. A. Scheidt, S. T. Nguyen and J. T. Hupp, *Chem. Soc. Rev.*, 2009, **38**, 1450; (f) L. J. Murray, M. Dinca and J. R. Long, *Chem. Soc. Rev.*, 2009, **38**, 1294; (g) R. Haldar, R. Matsuda, S. Kitagawa, S. J. George and T. K. Maji, *Angew. Chem. Int. Ed.*, 2014, **53**, 11772; (h) S. Bhattacharyya, A. Chakraborty, K. Jayaramulu, A. Hazra and T. K. Maji, *Chem. Commun.*, 2014, **50**, 13567; (i) O. K. Farha, I. Eryazici, N. C. Jeong, B. G. Hauser, C. E. Wilmer, A. A. Sarjeant, R. Q. Snurr, S. T. Nguyen, A. Ö. Yazaydin and J. T. Hupp, *J. Am. Chem. Soc.*, 2012, **134**, 15016; (j) Z. Hu, B. J. Deibert and J. Li, *Chem. Soc. Rev.*, 2014, **43**, 5815.

2. (a) K. L. Mulfort, O. K. Farha, C. L. Stern, A. A. Sarjeant and J. T. Hupp, *J. Am. Chem. Soc.*, 2009, **131**, 3866; (b) B. Li, Y. Zhang, R. Krishna, K. Yao, Y. Han, Z. Wu, D. Ma, Z. Shi, T. Pham, B. Space, J. Liu, P. K. Thallapally, J. Liu, M. Chrzanowski and S. Ma, *J. Am. Chem. Soc.*, 2014, **136**, 8654; (c) R. Haldar, N. Sikdar and T. K. Maji, *Mater. Today*, 2015, **18**, 97; (d) R. Haldar, S. Bonakala, P. Kanoo, S. Balasubramanian and T. K. Maji, *CrystEngComm*, 2014, **16**, 4877; (e) N. Sikdar, A. Hazra and T. K. Maji, *Inorg. Chem.*, 2014, **53**, 5993; (f) H. Li, M. Eddaoudi, M. O'Keeffe and O. M. Yaghi, *Nature*, 1999, **402**, 276; (g) S. S.-Y. Chui, S. M.-F. Lo, J. P. H. Charmant, A. G. Orpen and I. D. Williams, *Science*, 1999, **283**, 1148; (h) W. Lu, Z. Wei, Z.-Y. Gu, T.-F. Liu, J. Park, J. Park, J. Tian, M. Zhang, Q. Zhang, T. Gentle Iii, M. Bosch and H.-C. Zhou, *Chem. Soc. Rev.*, 2014, **43**, 5561; (i) R. Haldar and T. K. Maji, *CrystEngComm*, 2013, **15**, 9276; (j) R. Vaidhyanathan, S. S. Iremonger, G. K. H. Shimizu, P. G. Boyd, S. Alavi and T. K. Woo, *Angew. Chem. Int. Ed.*, 2012, **51**, 1826.
3. (a) O. K. Farha, C. D. Malliakas, M. G. Kanatzidis and J. T. Hupp, *J. Am. Chem. Soc.*, 2010, **132**, 950; (b) J.-R. Li, R. J. Kuppler and H.-C. Zhou, *Chem. Soc. Rev.*, 2009, **38**, 1477; (c) J.-R. Li, J. Sculley and H.-C. Zhou, *Chem. Rev.*, 2012, **112**, 869; (d) M. C. Das, H. Xu, S. Xiang, Z. Zhang, H. D. Arman, G. Qian and B. Chen, *Chem. Eur. J.*, 2011, **17**, 7817; (e) J. G. Nguyen and S. M. Cohen, *J. Am. Chem. Soc.*, 2010, **132**, 4560.
4. Y. Sakata, S. Furukawa, M. Kondo, K. Hirai, N. Horike, Y. Takashima, H. Uehara, N. Louvain, M. Meilikhov, T. Tsuruoka, S. Isoda, W. Kosaka, O. Sakata and S. Kitagawa, *Science*, 2013, **339**, 193.
5. (a) Z. Wang and S. M. Cohen, *Chem. Soc. Rev.*, 2009, **38**, 1315; (b) K. K. Tanabe and S. M. Cohen, *Chem. Soc. Rev.*, 2011, **40**, 498.
6. (a) H. Fei, S. Pullen, A. Wagner, S. Ott and S. M. Cohen, *Chem. Commun.*, 2015, **51**, 66; (b) M. Kim, J. F. Cahill, K. A. Prather and S. M. Cohen, *Chem. Commun.*, 2011, **47**, 7629; (c) Z. Wang and S. M. Cohen, *J. Am. Chem. Soc.*, 2007, **129**, 12368; (d) K. K. Tanabe, Z. Wang and S. M. Cohen, *J. Am. Chem. Soc.*, 2008, **130**, 8508; (e) H.-L. Jiang, D. Feng, T.-F. Liu, J.-R. Li and H.-C. Zhou, *J. Am. Chem. Soc.*, 2012, **134**, 14690; (f) W. Morris, C. J. Doonan, H. Furukawa, R. Banerjee and O. M. Yaghi, *J. Am. Chem. Soc.*, 2008, **130**, 12626.
7. (a) S. J. Reitmeier, O. C. Gobin, A. Jentys and J. A. Lercher, *Angew. Chem. Int. Ed.*, 2009, **48**, 533; (b) Z. Zhang, S. Xian, Q. Xia, H. Wang, Z. Li and J. Li, *AIChE J.*, 2013, **59**, 2195; (c) J. An and N. L. Rosi, *J. Am. Chem. Soc.*, 2010, **132**, 5578.
8. (a) N. Yanai, T. Uemura, M. Inoue, R. Matsuda, T. Fukushima, M. Tsujimoto, S. Isoda and S. Kitagawa, *J. Am. Chem. Soc.*, 2012, **134**, 4501; (b) D. N. Dybtsev, H. Chun and K. Kim, *Angew. Chem. Int. Ed.*, 2004, **43**, 5033; (c) L.-H. Xie and M. P. Suh, *Chem. Eur. J.*, 2011, **17**, 13653; (d) S. Henke, A. Schneemann and R. A. Fischer, *Adv. Funct. Mater.*, 2013, **23**, 5990.

9. (a) H. Sato, W. Kosaka, R. Matsuda, A. Hori, Y. Hijikata, R. V. Belosludov, S. Sakaki, M. Takata and S. Kitagawa, *Science*, 2014, **343**, 167; (b) T. K. Maji, G. Mostafa, R. Matsuda and S. Kitagawa, *J. Am. Chem. Soc.*, 2005, **127**, 17152.
10. (a) S. Sarkhel and G. R. Desiraju, *Proteins: Structure, Function, and Bioinformatics*, 2004, **54**, 247; (b) K. Uemura, K. Saito, S. Kitagawa and H. Kita, *J. Am. Chem. Soc.*, 2006, **128**, 16122; (c) K. Uemura, S. Kitagawa, K. Fukui and K. Saito, *J. Am. Chem. Soc.*, 2004, **126**, 3817; (d) S. Kitagawa, R. Kitaura and S.-i. Noro, *Angew. Chem. Int. Ed.*, 2004, **43**, 2334.
11. (a) G. R. Desiraju, *Acc. Chem. Res.*, 1996, **29**, 441; (b) S. S. Kuduva, D. C. Craig, A. Nangia and G. R. Desiraju, *J. Am. Chem. Soc.*, 1999, **121**, 1936; (c) G. R. Desiraju, *Cryst. Growth Des.*, 2011, **11**, 896; (d) *Acc. Chem. Res.*, 2002, **35**, 565; (e) *Chem. Commun.*, 2005, 2995.
12. (a) S. Kitagawa and K. Uemura, *Chem. Soc. Rev.*, 2005, **34**, 109; (b) S. K. Sommer, L. N. Zakharov and M. D. Pluth, *Inorg. Chem.*, 2015, **54**, 1912; (c) K. Nagayoshi, M. K. Kabir, H. Tobita, K. Honda, M. Kawahara, M. Katada, K. Adachi, H. Nishikawa, I. Ikemoto, H. Kumagai, Y. Hosokoshi, K. Inoue, S. Kitagawa and S. Kawata, *J. Am. Chem. Soc.*, 2003, **125**, 221.
13. G. J. Halder, C. J. Kepert, B. Moubaraki, K. S. Murray and J. D. Cashion, *Science*, 2002, **298**, 1762.
14. T. K. Maji, K. Uemura, H.-C. Chang, R. Matsuda and S. Kitagawa, *Angew. Chem. Int. Ed.*, 2004, **43**, 3269.
15. M. D. Cohen, G. M. J. Schmidt and F. I. Sonntag, *J. Chem. Soc.*, 1964, 2000.
16. S. V. a. SMART (V 5.628), XPREP, SHELXTL; Bruker AXS Inc. Madison, Wisconsin, USA, 2004.
17. G. M. Sheldrick, *SADABS, Empirical Absorption Correction Program, University of Göttingen, Göttingen*, 1997.
18. A. Altomare, G. Cascarano, C. Giacovazzo and A. Guagliardi, *J. Appl. Crystallogr.*, 1993, **26**, 343.
19. G. M. Sheldrick, *SHELXL 97, Program for the Solution of Crystal Structure, University of Göttingen, Germany*, 1997.
20. A. Spek, *J. Appl. Crystallogr.*, 2003, **36**, 7.
21. L. Farrugia, *J. Appl. Crystallogr.*, 1999, **32**, 837.
22. (a) X. Zou, F. Zhang, S. Thomas, G. Zhu, V. Valtchev and S. Mintova, *Chem. Eur. J.*, 2011, **17**, 12076; (b) H. R. Abid, H. Tian, H.-M. Ang, M. O. Tade, C. E. Buckley and S. Wang, *Chem. Eng. J.*, 2012, **187**, 415.



# Chapter 7

**Fluoro-functionalized Superhydrophobic Metal-organic  
Frameworks: Enhanced CO<sub>2</sub> uptake by Postsynthetic Modification  
using Light**



## Summary

This chapter describes the synthesis of two fluorinated metal-organic frameworks  $[\{\text{Cd}(\text{bpee})(\text{hfbba})\} \cdot \text{EtOH}]$  (**1**) and  $[\{\text{Co}(\text{bpee})(\text{hfbba})\} \cdot \text{EtOH}]$  (**2**) constructed by using 4,4'-(hexafluoroisopropylidene)bis(benzoic acid) (hfbba), Cd/Co(NO<sub>3</sub>)<sub>2</sub> and 1,2-bis(4-pyridyl)ethene (bpee) as precursors. Due to the presence of -CF<sub>3</sub> functionality, these compounds exhibit superhydrophobicity which is established from both water adsorption isotherms and contact angle measurements. The parallel arrangement of the bpee linkers makes compound **1** a light responsive material which transforms to  $[\{\text{Cd}_2(\text{rctt-tpcb})(\text{hfbba})_2\} \cdot 2\text{EtOH}]$  (**1IR**) by [2+2] cycloaddition reaction. After the photo-induced postsynthetic modification (PSM) of the framework through [2+2] cycloaddition reaction, **1IR** exhibits increased uptake of CO<sub>2</sub> at ambient condition. The increased CO<sub>2</sub> uptake in **1IR** compared to as-synthesized framework **1** is realized due to the expansion of pore window after photo-modification. Furthermore, DFT based calculations also correlates the decrease of the diffusion barrier after the photo-reaction.

A. Hazra, S. Bonakala, S. Balasubramanian, T. K. Maji; *Manuscript to be submitted for publication*





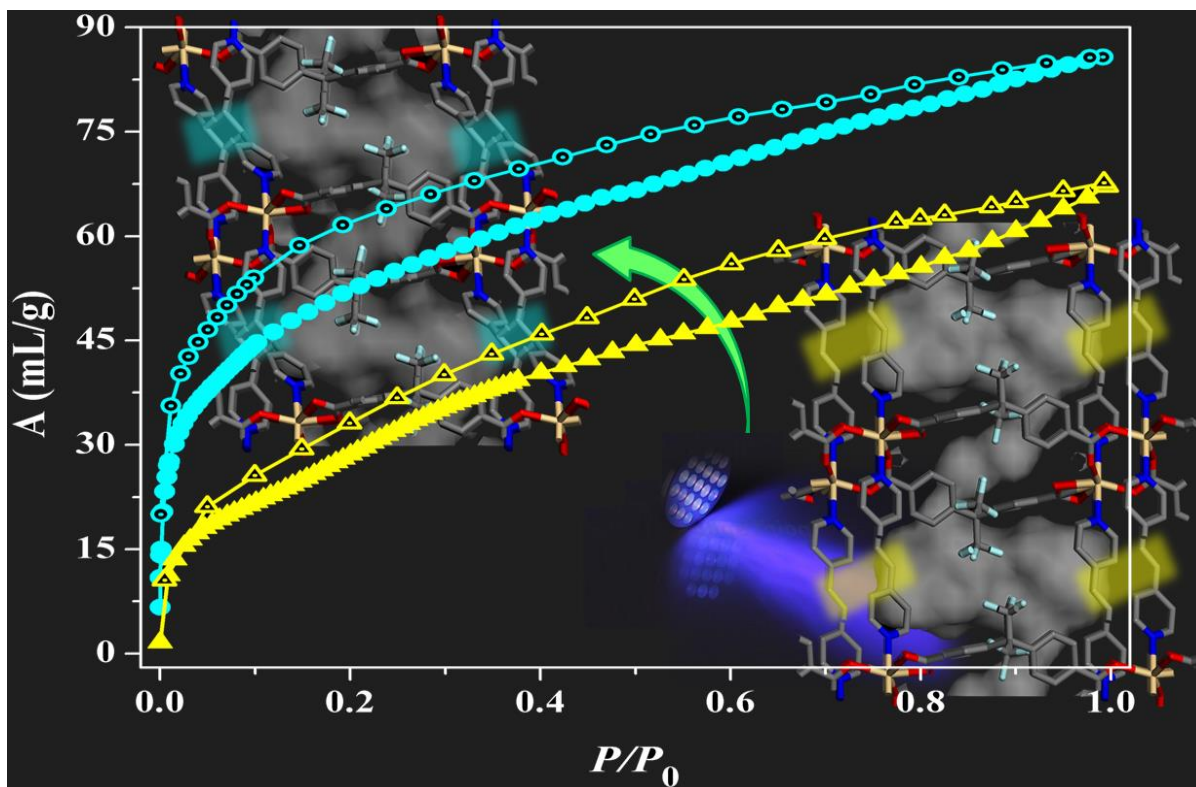
## 7.1: Introduction

In the modern era of civilization, light is undoubtedly a major source of energy and the implementation of light as an effective low cost energy modulator has widely been attempted by the physicist, chemist and material scientists.<sup>1</sup> In this regard, fabrications of new photo-responsive materials are of highest priority. Tuning of the physical properties of materials by an external stimulus like light will offer a new class of photo-responsive compounds, which can open up a new horizon in material science.<sup>2</sup> Furthermore, such solids would be attractive candidates for molecular switches, data storage and photomechanical actuators.<sup>1c, 3</sup> In this context design and synthesis of photo-responsive porous coordination polymers (PCPs) or metal-organic frameworks (MOFs) are of paramount interest where the modulation of physical properties like surface area, molecular recognition, magnetism, optical and mechanical strength can be achieved post-synthetically by light.<sup>4</sup> Furthermore tuning of pore size and polarity of the pore surface will allow selective uptake of the specific adsorbate molecules.<sup>5</sup> Modification of surface area, feasibility of tuning the pore size and polarity are among many which can be easily be achieved by post-synthetic approaches induced by physical forces like pressure, light, heat and pH *etc.*<sup>6</sup> Realizing this fact, in MOFs, several groups have employed light induced conformational switching of the azo group containing organic linker (*trans* to *cis* and *vice versa*) which results in significant changes in the pore surfaces as well as physical properties.<sup>4c, 7</sup> In this context, photochemical [2+2] cycloaddition reaction is another popular choice for introducing photo-switchable structure-property relationship in MOFs.<sup>8</sup> There are several reports of low dimensional coordination polymer where photo-chemical cycloaddition reaction has been implemented to tune the photo-physical property.<sup>9</sup> However, very few attempts have been adopted which shows the tuning of adsorption property of MOFs by postsynthetic structural modification by [2+2] cycloaddition reaction.<sup>10</sup> Therefore, change of properties like adsorption, magnetism, luminescence *etc.* in MOFs induced by photochemical cycloaddition reaction are of immense interest and yet to be widely explored.

To demonstrate the practical efficiency of such material for CO<sub>2</sub> capture and separation, performance should be retained in the presence of liquid vapour or moist air as the flue gas contains certain amount water vapour along with other gases. Nevertheless, the

adsorbent material should show fast kinetics of CO<sub>2</sub> adsorption and long-time stability under working condition. So far reported MOFs with high CO<sub>2</sub> capture capacity contains unsaturated metal sites (UMSs) in the pore surface which show high affinity toward water molecules. Thus CO<sub>2</sub> capture capacities of these highly porous materials are diminished in presence of moisture. Therefore, new generations of hydrophobic MOFs with high CO<sub>2</sub> capture capacity should be designed.<sup>11</sup> For this purpose, fluorinated metal-organic frameworks (FMOFs) would be of potential interest as the hydrophobic nature of the fluorine-lined pore surface would offer the opportunity to enhance the CO<sub>2</sub> capture capacity based on increase CO<sub>2</sub>···F interaction in presence of moisture.<sup>12,13</sup>

In this chapter, two porous fluorinated metal-organic frameworks (FMOFs) [ $\{\text{Cd}(\text{bpee})(\text{hfbba})\} \cdot \text{EtOH}$ ] (**1**) and [ $\{\text{Co}(\text{bpee})(\text{hfbba})\} \cdot \text{EtOH}$ ] (**2**) have been synthesised where the interconnected discrete pores embedded with the  $-\text{CF}_3$  functionality depict good CO<sub>2</sub>-MOF interaction. The fluorinated surface also induces superhydrophobicity in the system which makes the material ideal for showing good CO<sub>2</sub> selectivity over H<sub>2</sub>O molecules. The parallel arrangement of bpee pillar guided by the dimeric  $[\text{Cd}_2(\text{OCO})_2]$  unit in **1** offers the possibility of [2+2] cycloaddition reaction between two ethylenic groups of bpee using UV irradiation. Successfully, compound **1** yields compound **1IR** [ $\{\text{Cd}_2(\text{rctt-tpcb})(\text{hfbba})_2\} \cdot 2\text{EtOH}$ ] keeping the single crystallinity intact with significant change in emission properties. Interestingly, isomorphous compound **2** does not undergo any [2+2] cycloaddition reaction. Finally, this work demonstrates enhanced CO<sub>2</sub> capture in a superhydrophobic MOF by PSM using light as a lost cost external stimulus (Scheme 1).



**Scheme 1:** Schematic representation of photo induced post-synthetic modification of porous framework which results improved gas uptake capacity.

## 7.2: Experimental Section

### 7.2.1: Materials

All the reagents and solvents employed were commercially available and used as supplied without further purification. Cd(NO<sub>3</sub>)<sub>2</sub>·6H<sub>2</sub>O, Co(NO<sub>3</sub>)<sub>2</sub>·6H<sub>2</sub>O, 1,2-bis(4-pyridyl)ethylene (bpee) and 4,4'-(hexafluoroisopropylidene)bis(benzoic acid) (hfbba) were obtained from the Aldrich Chemical Co.

### 7.2.2: Synthesis

**7.2.2.1: Synthesis of [{Cd(bpee)(hfbba)}·EtOH] (1) :** Compound **1** was synthesized according to the following procedure. Cd(NO<sub>3</sub>)<sub>2</sub>·4H<sub>2</sub>O (0.5 mmol; 0.154 g) was dissolved in 50 mL of water. 1,2-bis(4-pyridyl)ethylene (bpee) (0.5 mmol; 0.092 g) and sodium salt of 4,4'-(hexafluoroisopropylidene)bis(benzoic acid) (Na<sub>2</sub>-hfbba) (0.5 mmol; 0.214 g) was dissolved in a water-ethanol mixture (20 mL and 30 mL respectively). In a crystal tube, 2 mL of this ligand mixture was carefully layered on the top of the metal solution (2 mL) using an

ethanol:water buffer solution (2 mL, 1:1). After five days, transparent block shaped crystals of **1** were appeared in the middle of the crystal tube. The crystals were sensitive to open atmosphere and slowly lose single crystallinity. Good quality single crystals were picked up from the mother liquor and immediately covered with paraffin oil and subjected to single crystal X-ray diffraction. Bulk sample was obtained by scaling up the above reaction procedure. Yield: 67%, relative to Cd<sup>II</sup>. Anal. calc. for C<sub>31</sub>H<sub>24</sub>CdF<sub>6</sub>N<sub>2</sub>O<sub>5</sub>: C, 50.94; H, 3.31; N, 3.83. Found: C, 50.58; H, 3.61; N, 3.65. IR (KBr, cm<sup>-1</sup>): ν<sub>Ar</sub>(C-H) 2924, 2852; ν<sub>as</sub>(COO) 1623, ν<sub>s</sub>(COO) 1365, ν<sub>Ar</sub>(C=C) 1618, 1608 (Figure 1). A strong band around 1618 cm<sup>-1</sup> indicates the presence bpee molecule.

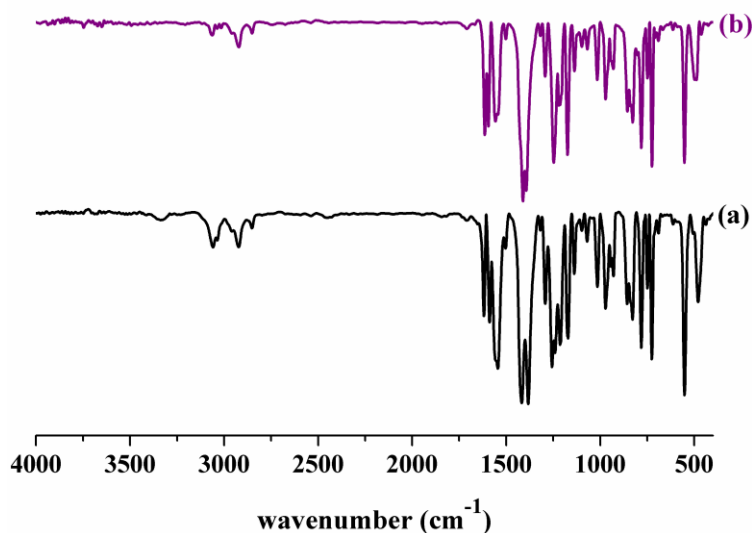


Figure 1: IR spectra of compound **1** (a) and **1IR** (b).

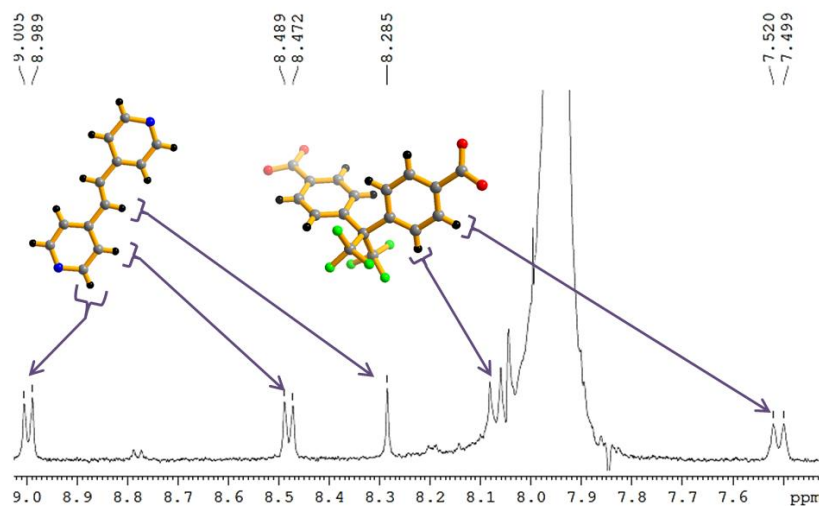
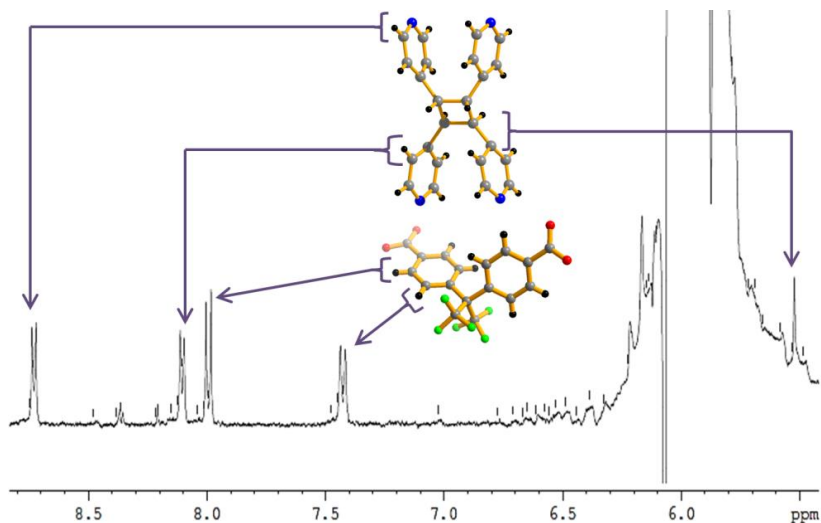


Figure 2: <sup>1</sup>H-NMR spectra of compound **1** digested in DMSO-*d*<sub>6</sub>/HCl at 298 K.

**7.2.2.2: Preparation of  $\{[Cd(bpee)(hfbba)]\}$  (1a) :** Compound **1** was placed in a glass sample cell and heated at 90 °C for 5h under reduced pressure of 0.1 Pa that results **1a**. Removal of ethanol molecules was confirmed from TGA (Figure 7(1)) and CHN analysis. Anal. calc., for C<sub>29</sub>H<sub>18</sub>CdF<sub>6</sub>N<sub>2</sub>O<sub>4</sub>: C, 50.86; H, 2.65; N, 4.09. Found: C, 51.05; H, 2.79; N, 3.95.

**7.2.2.3: Preparation of  $\{[Cd_2(rctt-tpcb)(hfbba)_2]\cdot 2EtOH\}$  (1IR) :** Irradiated compound of **1** was prepared by using a UV photochemical reactor with 365 nm LASER light made by Hamamatsu, Japan. Before photoreaction, compound **1** was continuously ground for 5 min. Then the powder sample was sandwiched between a pair of quartz glass plates and irradiated for 10 h. During the photo reaction, the sample was mixed properly every 30 min to make sure about the homogeneous irradiation. The phase purity was checked with the PXRD (Figure 9B) and elemental analysis Anal. calc. for C<sub>62</sub>H<sub>48</sub>Cd<sub>2</sub>F<sub>12</sub>N<sub>4</sub>O<sub>10</sub>: C, 50.94; H, 3.31; N, 3.83. Found: C, 51.29; H, 3.32; N, 3.85; and <sup>1</sup>H-NMR (400 MHz, *d*<sub>6</sub>-DMSO) spectroscopy (Figure 2 and 3). IR (KBr, cm<sup>-1</sup>): ν<sub>as</sub>(COO) 1624, ν<sub>s</sub>(COO) 13645, ν<sub>Ar</sub>(C-H) 2930, 2873; ν<sub>Ar</sub>(C=C) 1617, 1595.



**Figure 3:** <sup>1</sup>H-NMR spectra of compound **1IR** digested in DMSO-*d*<sub>6</sub>/HCl at 298 K.

**7.2.2.4: Preparation of  $\{[Cd_2(rctt-tpcb)(hfbba)_2]\}$  (1IRa) :** Compound **1IR** was placed in a glass sample cell and heated at 90 °C for 5h under reduced pressure of 0.1 Pa that results **1IRa**. Removal of ethanol molecules was confirmed from TGA (Figure 7(2)) and CHN

analysis. Anal. calc. for C<sub>58</sub>H<sub>36</sub>Cd<sub>2</sub>F<sub>12</sub>N<sub>4</sub>O<sub>8</sub>: C, 50.89; H, 2.65; N, 4.09. Found: C, 51.09; H, 2.75; N, 4.01.

**7.2.2.5: Synthesis of [{Co(bpee)(hfbba)}·EtOH] (2) :** Compound **2** was synthesised by following the similar procedure as of compound **1**. Yield: 66%, relative to Co<sup>II</sup>. Anal. calc. for C<sub>31</sub>H<sub>24</sub>CoF<sub>6</sub>N<sub>2</sub>O<sub>5</sub>: C, 54.96; H, 3.57; N, 4.14. Found: C, 55.10; H, 3.75; N, 4.43. IR (KBr, cm<sup>-1</sup>): ν<sub>as</sub>(COO) 1645, ν<sub>s</sub>(COO) 1330, ν<sub>Ar</sub>(C-H) 2910, 2892; ν<sub>Ar</sub>(C=C) 1554, 1538 (Figure 4). A strong band around 1554 cm<sup>-1</sup> indicates the presence bpee molecule.

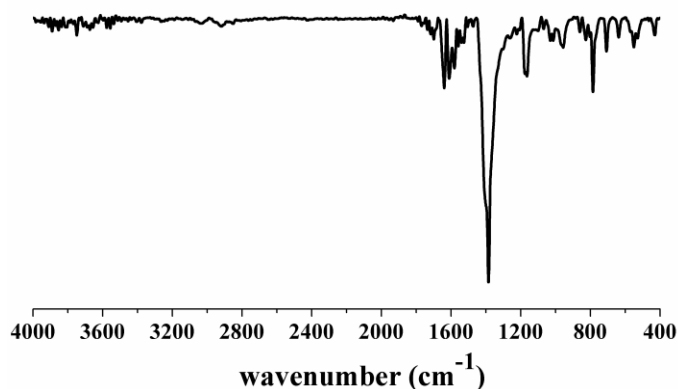


**Figure 4:** IR spectra of compound **2**.

**7.2.2.6: Preparation of [{Co(bpee)(hfbba)}] (2a) :** Compound **2** was placed in a glass sample cell and heated at 90 °C for 5h under reduced pressure of 0.1 Pa that results **2a**. Removal of ethanol molecules was confirmed from TGA (Figure 8) and CHN analysis. Anal. calc. for C<sub>29</sub>H<sub>18</sub>CoF<sub>6</sub>N<sub>2</sub>O<sub>4</sub>: C, 55.17; H, 2.87; N, 4.44. Found: C, 55.68; H, 2.98; N, 4.12.

### **7.2.3: Physical Measurements**

The elemental analyses of the compounds and their different state were carried out on a Thermo Fisher Flash 2000 Elemental Analyser. Infra-red (IR) spectroscopic studies were carried out in the mid-IR region by making samples with KBr pellet (Bruker IFS-66v). Thermogravimetric analysis (TGA) was carried out (Mettler Toledo) in nitrogen atmosphere (flow rate = 50 ml min<sup>-1</sup>) in the temperature range 30 – 700 °C (heating rate = 5°C min<sup>-1</sup>). Powder XRD pattern of the products were recorded by using Cu-K<sub>α</sub> radiation (Bruker D8 Discover; 40 kV, 30 mA). <sup>1</sup>H-NMR spectra were measured on a Bruker AV-400 spectrometer with chemical shifts reported as ppm (in HCl/d<sub>6</sub>-DMSO, TMS as internal

standard). Contact angles were measured mostly using an indigenous set up coupled with a Logitech camera for capturing the images. Contact angles were also measured using dedicated contact angle analyzer, OCA30 from Data Physics instrument (GmbH, Germany). 4  $\mu$ L of the sessile water droplets were employed for measuring the static contact angles. A minimum of ten measurements were made for each surface.

#### 7.2.4: Single Crystal X-ray Diffraction

Suitable single crystals of compound **1**, **1IR** and **2** were mounted on a thin glass fiber with commercially available super glue. X-ray single crystal data were collected on a Bruker Smart-CCD diffractometer equipped with a normal focus, 2.4 kW sealed tube X-ray source with graphite monochromated Mo- $K\alpha$  radiation ( $\lambda = 0.71073 \text{ \AA}$ ) operating at 50 kV and 30 mA. The program SAINT<sup>14</sup> was used for integration of diffraction profiles and absorption correction was made with SADABS<sup>15</sup> program. The structures were solved by SIR 92<sup>16</sup> and refined by full matrix least square method using SHELXL.<sup>17</sup> All the hydrogen atoms were fixed by HFIX and placed in ideal positions. Potential solvent accessible area or void space was calculated using the PLATON<sup>18</sup> multipurpose crystallographic software. All crystallographic and structure refinement data of **1**, **1IR** and **2** are summarized in Table 1. Selected bond distances and angles are shown in Table 2-7. All the calculations were carried out using SHELXL 97,<sup>17</sup> PLATON,<sup>18</sup> SHELXS 97<sup>17</sup> and WinGX system, Ver 1.80.01.<sup>19</sup>

**Table 1:** Crystal data and structure refinement parameters for **1**, **1IR** and **2**.

Parameters	<b>1</b>	<b>1IR</b>	<b>2</b>
Empirical formula	C <sub>31</sub> H <sub>24</sub> CdF <sub>6</sub> N <sub>2</sub> O <sub>5</sub>	C <sub>31</sub> H <sub>24</sub> CdF <sub>6</sub> N <sub>2</sub> O <sub>5</sub>	C <sub>31</sub> H <sub>24</sub> CoF <sub>6</sub> N <sub>2</sub> O <sub>5</sub>
<i>M</i>	730.93	730.93	677.46
Crystal system	Triclinic	Triclinic	Triclinic
Space group	<i>P</i> $\bar{1}$ (No. 2)	<i>P</i> $\bar{1}$ (No. 2)	<i>P</i> $\bar{1}$ (No. 2)
<i>a</i> ( $\text{\AA}$ )	8.4843(5)	8.9415(3)	8.6087(8)
<i>b</i> ( $\text{\AA}$ )	12.8971(7)	11.5059(4)	12.7783(12)
<i>c</i> ( $\text{\AA}$ )	15.1326(8)	15.1023(6)	14.6834(13)
$\alpha$ ( $^\circ$ )	90.331(3)	97.888(2)	89.436(5)
$\beta$ ( $^\circ$ )	98.602(2)	98.005(2)	81.423(6)
$\gamma$ ( $^\circ$ )	100.878(3)	96.326(2)	77.158(5)
<i>V</i> ( $\text{\AA}^3$ )	1606.82(16)	1510.73(10)	1556.8(3)
<i>Z</i>	2	2	2

<i>T</i> (K)	295	295	295
$\lambda$ (Mo-K $\alpha$ )	0.71073	0.71073	0.71073
$D_c$ (g cm <sup>-3</sup> )	1.511	1.607	1.445
$\mu$ (mm <sup>-1</sup> )	0.755	0.803	0.628
$\theta_{\max}$ (°)	27.2	25.0	25.0
Total data	29650	22621	20336
Data [ $I > 2\sigma(I)$ ]	5467	5163	3198
Uniq. Data	7038	5163	5381
$R_{int}$	0.056	0.061	0.097
$R^a$	0.0411	0.0339	0.0715
$R_w^b$	0.1092	0.1026	0.2429
<i>GOF</i>	1.03	1.13	1.00
Min./Max. Resd.	-0.40, 0.53	-0.41, 0.70	-1.05, 0.58
Dens. [e/Å <sup>3</sup> ]			

$$^a R = \sum |F_o| - |F_c| / \sum |F_o|; \quad ^b R_w = [\sum \{w(F_o^2 - F_c^2)^2\} / \sum \{w(F_o^2)^2\}]^{1/2}$$

**Table 2:** Selected bond distances (Å) for compound **1**.

Bonds	Distance (Å)	Bonds	Distance (Å)
Cd1–O1	2.244(3)	Cd1–N1	2.337(3)
Cd1–N2_b	2.339(3)	Cd1–O2_c	2.223(2)
Cd1–O3_d	2.387(3)	Cd1–O4_d	2.385(2)

**Table 3:** Selected bond angles (°) for compound **1**.

Angles	Degree (°)	Angles	Degree (°)
O1–Cd1–N1	88.83(9)	O1–Cd1–N2_b	87.96(10)
O1–Cd1–O2_c	120.06(9)	O1–Cd1–O3_d	142.59(8)
O1–Cd1–O4_d	87.78(9)	N1–Cd1–N2_b	176.79(10)
O2_c–Cd1–N1	96.37(10)	O3_d–Cd1–N1	90.45(9)
O4_d–Cd1–N1	90.38(9)	O2_c–Cd1–N2_b	85.10(10)
O3_d–Cd1–N2_b	92.20(10)	O4_d–Cd1–N2_b	89.67(10)
O2_c–Cd1–O3_d	97.19(9)	O2_c–Cd1–O4_d	151.36(9)
O3_d–Cd1–O4_d	54.82(8)		

**Table 4:** Selected bond distances (Å) for compound **1IR**.

Bonds	Distance (Å)	Bonds	Distance (Å)
Cd1–O1	2.243(3)	Cd1–N1	2.333(3)
Cd1–N2_a	2.359(4)	Cd1–O3_c	2.346(3)
Cd1–O4_c	2.418(3)	Cd1–O2_d	2.230(3)



**Table 5:** Selected bond angles (°) for compound **1IR**.

Angles	Degree (°)	Angles	Degree (°)
O1–Cd1–N1	92.70(10)	O1–Cd1–N2_a	85.72(11)
O1–Cd1–O3_c	94.68(10)	O1–Cd1–O4_c	149.55(10)
O1–Cd1–O2_d	112.60(10)	N1–Cd1–N2_a	175.55(11)
O3_c–Cd1–N1	91.92(11)	O4_c–Cd1–N1	89.80(11)
O2_d–Cd1–N1	92.81(10)	O3_c–Cd1–N2_a	92.36(11)
O4_c–Cd1–N2_a	93.68(11)	O2_d–Cd1–N2_a	83.98(10)
O3_c–Cd1–O4_c	54.89(10)	O2_d–Cd1–O3_c	152.02(10)
O2_d–Cd1–O4_c	97.56(10)		

**Table 6:** Selected bond distances (Å) for compound **2**.

Bonds	Distance (Å)	Bonds	Distance (Å)
Co1–O1	2.208(4)	Co1–O2	2.175(3)
Co1–N1	2.148(5)	Co1–N2	2.163(5)
Co1–O4_c	2.017(3)	Co1–O3_e	2.012(4)

**Table 7:** Selected bond angles (°) for compound **2**.

Angles	Degree (°)	Angles	Degree (°)
O1–Co1–O2	60.01(14)	O1–Co1–N1	91.12(16)
O1–Co1–N2	89.16(16)	O1–Co1–O4_c	95.05(13)
O1–Co1–O3_e	150.83(12)	O2–Co1–N1	90.21(16)
O2–Co1–N2	89.18(16)	O2–Co1–O4_c	154.94(15)
O2–Co1–O3_e	90.82(14)	N1–Co1–N2	179.08(17)
O4_c–Co1–N1	87.65(16)	O3_e–Co1–N1	88.69(16)
O4_c–Co1–N2	93.19(16)	O3_e–Co1–N2	90.64(16)
O3_e–Co1–O4_c	114.08(13)		

a = -1+x,1+y,z; b = x,y,-1+z; c = x,y,1+z; d = 1+x,-1+y,z

### 7.2.5: Adsorption Study

N<sub>2</sub> (77 K), CO<sub>2</sub> (195 K, 273 K and 283 K) adsorption studies were carried out with the dehydrated samples (*i.e.* **1a**, **1IRa** and **2a**; prepared at 438 K under high vacuum (<10<sup>-1</sup> Pa) for 72 hours) by using AUTOSORB IQ2 instrument. The adsorptions of different solvents like water, ethanol and benzene at 298 K were measured in the vapour state by using BELSORP-aqua-3 analyzer. The different solvent molecules used to generate the vapour were degassed fully by repeated evacuation. Dead volume was measured with helium gas. The adsorbates were placed into the sample tubes, then the change of the pressure was

monitored and the degree of adsorption was determined by the decrease in pressure at the equilibrium state. All operations were computer controlled and automatic.

### 7.2.6: Computational details

Periodic density functional theory (DFT) calculations were carried out to find the position of a gas molecule inside **1a** and **1IRa**, using the QUICKSTEP module in CP2K software. All valence electrons were treated in a mixed basis set with an energy cut-off of 280 Ry. The short-range version of the double- $\zeta$  single polarization basis set was used. The effect of core electrons and nuclei was considered by using pseudo-potentials of Goedecker–Teter–Hutter (GTH). The exchange and correlation interaction between electrons was treated with the Perdew–Burke–Ernzerhof (PBE) functional. van der Waals interactions between the gas and the framework are very important, their effects were accounted for by employing empirical corrections developed by Grimme. Two schemes, DFT-D3 were used to calculate the cell volume. Binding energy was calculated using PBE-D3 scheme. A 2x1x1 unit cell was considered as the simulation cell for **1a** and **1IRa**. The optimized cell parameters of **1**, **1a**, **1IR**, and **1IRa** are shown in Table 8 and 9 respectively. The convergence of the maximum force on any atom during geometry optimization has considered as  $1 \times 10^{-4}$  a.u. The binding energy of the gas molecule (CO<sub>2</sub>) is calculated using following formula:

$$\Delta E = E_{(\text{MOF-CO}_2)} - E_{(\text{MOF})} - n \times E_{(\text{CO}_2)}$$

where  $\Delta E$ ,  $E_{(\text{MOF-CO}_2)}$ ,  $E_{(\text{MOF})}$ , and  $E_{(\text{CO}_2)}$  are the binding energy of CO<sub>2</sub>, energy of MOF with CO<sub>2</sub>, energy of MOF, and energy of CO<sub>2</sub> and  $n$  is the number of CO<sub>2</sub> molecules present in the MOF, respectively. Binding energies of CO<sub>2</sub> were corrected for the basis set superposition error using the counterpoise method. All structures were visualized using VMD, Mercury and GaussView.

**Table 8: Optimized cell parameters of 1 and 1a using PBE–D3 method**

Method	$a$ (Å)	$b$ (Å)	$c$ (Å)	$\alpha$ (°)	$\beta$ (°)	$\gamma$ (°)	$V$ (Å <sup>3</sup> )	Diff (%)
Experiment	16.9686	12.8971	15.1326	90.331	98.602	100.878	3213.642	
<b>1</b> , DFT (PBE–D3)	16.269	12.737	15.173	91.031	97.102	98.678	3082.128	-4.092
<b>1a</b> , DFT (PBE–D3)	16.099	12.777	15.233	91.131	97.602	97.778	3074.950	-4.315

**Table 9: Irradiated (solvated)**

Method	<i>a</i> (Å)	<i>b</i> (Å)	<i>c</i> (Å)	$\alpha$ (°)	$\beta$ (°)	$\gamma$ (°)	<i>V</i> (Å <sup>3</sup> )	Diff (%)
Experiment	17.8830	11.5059	15.1023	97.888	98.005	96.326	3021.458	
<b>1IR</b> , DFT (PBE–D3)	17.893	11.106	15.032	97.888	98.005	94.326	2916.416	–3.477
<b>1IRa</b> , DFT (PBE–D3)	17.893	11.076	15.032	97.888	98.005	93.526	2912.259	–3.614

### 7.3: Results and Discussion

**7.3.1: Structural description of  $[\{\text{Cd}(\text{bpee})(\text{hfbba})\}\cdot\text{EtOH}]$  (1):** Single crystal X-ray diffraction study reveals that compound **1** crystallizes in triclinic system with *P1* space group.

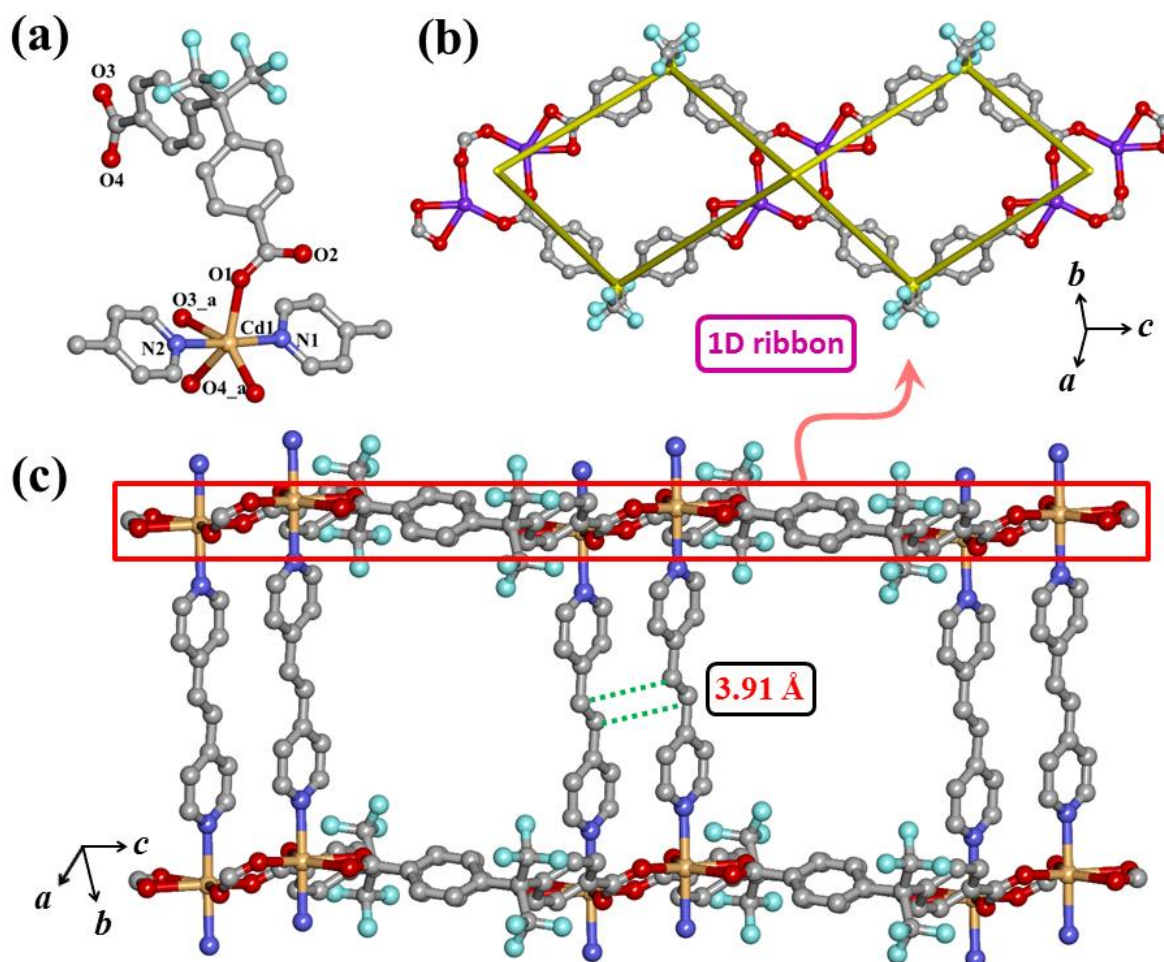


**Figure 5:** (a) Asymmetric unit compound **1**, (b) Formation of 1D chain along the *c* axis by connecting the  $[\text{Cd}_2(\text{OCO})_2]$  unit by hfbba linker, (c) 1D chains are further connected by the pillared bpee ligand to generate 2D sheet like structure.

The structure of compound **1** contains a basic centrosymmetric dimeric unit [Cd<sub>2</sub>(OCO)<sub>2</sub>] with one type of highly distorted octahedral Cd<sup>II</sup> metal center (Figure 5a). In the dimeric unit (Cd...Cd = 4.131 Å), the equatorial positions of Cd<sup>II</sup> centers are occupied by two types of oxygen atoms, one from a chelating carboxylate and other two oxygen atoms from two different bridging carboxylate ligands (Figure 5b). To complete the distorted octahedral coordination sphere, two nitrogen atoms from two different bpee ligands are ligated in the axial positions (Figure 5c). In compound **1**, one carboxylate group of hfbba ligand acts as *syn-syn* bridging to connect two Cd<sup>II</sup> centers whereas another one chelates with Cd<sup>II</sup> center of adjacent dimeric units. Along *c* axis, two such hfbba ligands extend the dimeric [Cd<sub>2</sub>(OCO)<sub>2</sub>] unit as a 1D double chain with the two adjacent di-cadmium cores in a distance of 15.133 Å (Figure 5b).

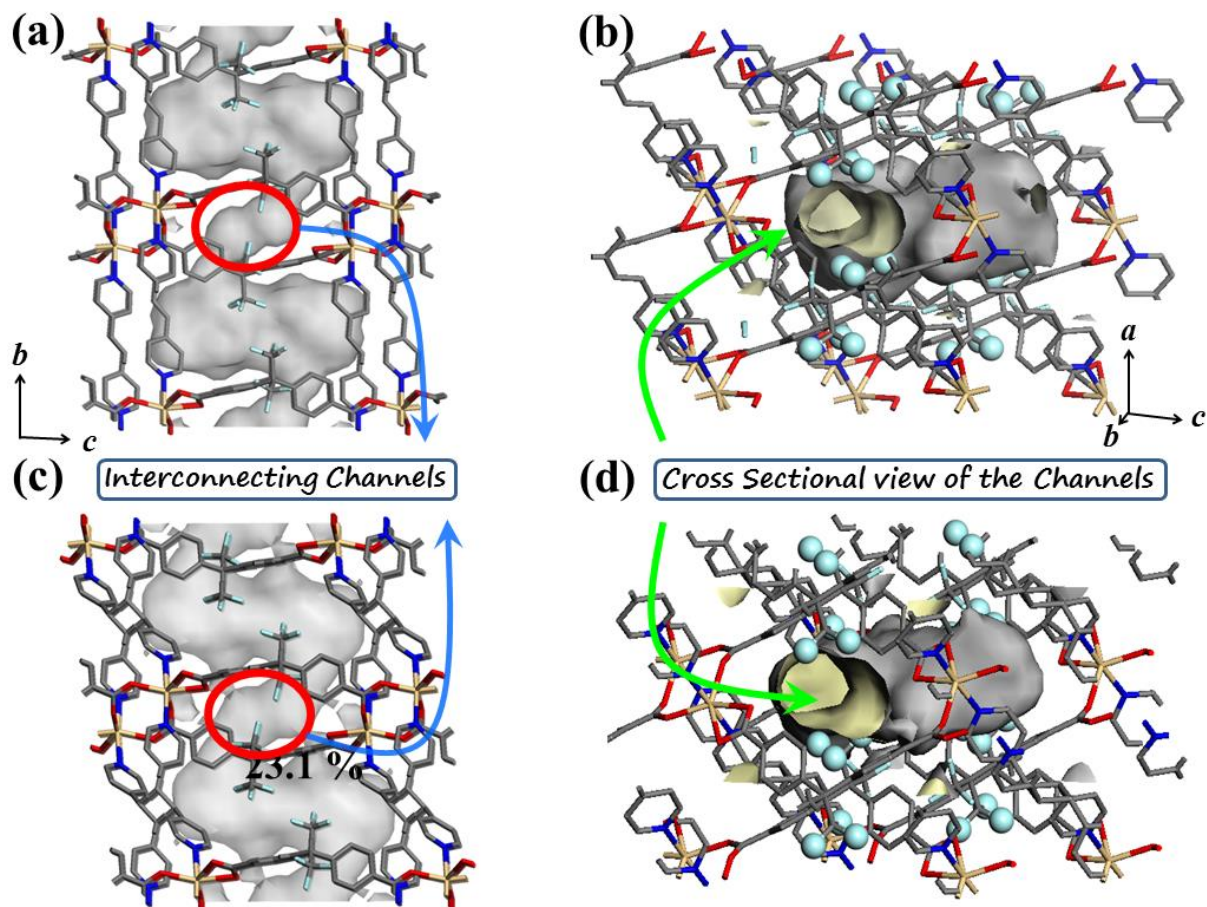


**Figure 6:** Connolly Surface of compound **1** (a) and **1IR** (c), after removing the guest ethanol molecules; (b) and (d) Figures illustrates the cross sectional view of the interconnected 1D channels. Cyan coloured balls are representing the fluoride atoms heading towards the pore surface. The radius of the channels in case of the photo-modified (**1IR**) framework is much higher than that of the mother compound (**1**). This facilitates the inclusion of CO<sub>2</sub> molecules easier in the **1IRa** than **1a**.

These 1D chains are extended by the bi-pillared bpee linkers to form a square grid type 2D network along the *bc* plane (Figure 5c). However, these 2D layers are interdigitated with one another along the crystallographic *a* axis to form a 3D supramolecular architecture (Figure 5d). The structure of **1** can be simplified into a {4<sub>4</sub>.6<sub>2</sub>} net. This host houses discrete cages which are connected through a 1D channel consisting of two pairs of flexible –CF<sub>3</sub> rotors that provide entry to the hydrophobic cavity (Figure 6b). The –CF<sub>3</sub> lined channels account for 23.1% of the unit cell volume as calculated by PLATON (Figure 6a). It is very interesting to note that the olefinic double bonds of bpee pairs in a 2D square structure are aligned parallel with the support of [Cd<sub>2</sub>(OCO)<sub>2</sub>] unit where the distance between the center of C=C bonds is 3.9 Å (Figure 5c). The pyridyl parts of the bpee ligands are also aligned parallel with strong π···π interaction with a center-to-center distance of 4.0 Å. This geometry is ideal for the photoreactivity in the solid state as postulated by Schmidt.<sup>20</sup> Compound **1** was found to undergo 100% photodimerisation to yield compound **1IR**.

**7.3.2: Structural description of {Cd<sub>2</sub>(*rctt*-*tpcb*)(*hfbba*)<sub>2</sub>·2H<sub>2</sub>O} (**1IR**):** Single crystal structure determination of compound **1IR** shows that the framework structure almost remains

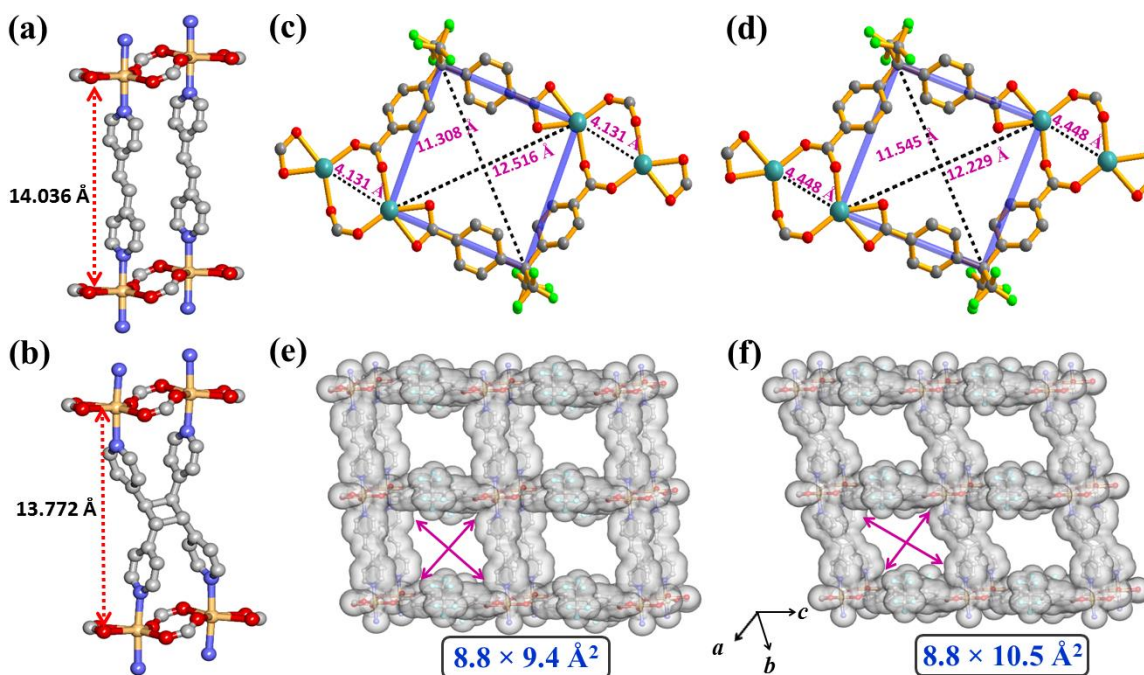


**Figure 7:** (a) Parallel arrangement of two bpee in compound **1** supported by the [Cd<sub>2</sub>(OCO)<sub>2</sub>] unit (b) transformation of the bpee pillars to new linkers *rctt*-*tpcb* by photochemical [2+2] cycloaddition reaction (c) and (d). The figure reflects the change in distance between the adjacent metal dimeric units after photoreaction. (e) and (f) View of the 2D framework (van der Waals surface added) before and after postsynthetic modification.

unchanged except for the formation of new C–C bonds across the ethylene bonds between the parallel *bpee* ligands along the [0–11] direction (Figure 7b). The newly formed C–C single bond distance is 1.595 Å which is comparable to that of normal C–C single bonds. The Cd–Cd# (# =1+x, y, -1+z) separation along the newly formed 4,4'-*rctt* tpcb linker is 13.772(3) Å which is shorter than the distance through the *bpee* pillar in the as-synthesized compound (14.036 (4) Å) (Figures 7a and 7b). The distance between the metal centers in the dimeric unit has increased from 4.131 Å to 4.448 Å. Further subtle changes in the structure are also reflected from figure 7 (c-f) where the alterations of distances have also been shown. After the 100% photo-irradiation, the deviation of the Cd<sup>II</sup> ion has further increased to 0.051 Å from the mean plane formed by the six equatorial oxygen atoms from the dicarboxylate linkers. This structural compression is also reflected from the reduced unit cell volume of the irradiated product (Table 1) where the void volume has been decreased to 20.3% calculated from PLATON. It is worth to mention that, due to the formation of *rctt*-tpcb linker, the diameter of the interconnected channels which is embedded with –CF<sub>3</sub> groups has increased as reflected from Figures 6b and 6d. The enhancement in diameter renders significant effect on the CO<sub>2</sub> uptake application which has been discussed in the adsorption sections.

**7.3.3: Structural description of [Co(*bpee*)(*hfbba*)]·EtOH (2):** Compound **2** is isostructural with compound **1**. Briefly, the Co–O and Co–N distance varies from 2.017(3) to 2.208(4) Å. Like compound **1**, the dimeric units [Co<sub>2</sub>(OCO)<sub>2</sub>] are linked by two *hfbba* ligands to result in a 1D ribbon with the two adjacent di-cobalt cores in a distance of 13.729 Å. The two dimensional bipillared-layer 2D grid like structure of **2** is formed by the *bpee* ligands coordinating to two Co atoms in two adjacent 1D chains. These chains are further interdigitated to one another along the crystallographic *a* axis to form a 3D supramolecular architecture.

#### **7.3.4: Framework stability: Thermogravimetric (TG) and PXRD analysis**

Thermal studies were carried out to analyse the stability and integrity of the frameworks. TG analysis of compound **1**, **1IR** (Figures 8) under nitrogen flow suggests the release of guest ethanol molecules (calc. 5.1%; obs. 4.8% and 4.1% for **1** and **1IR** respectively) in the temperature range 90–110 °C.

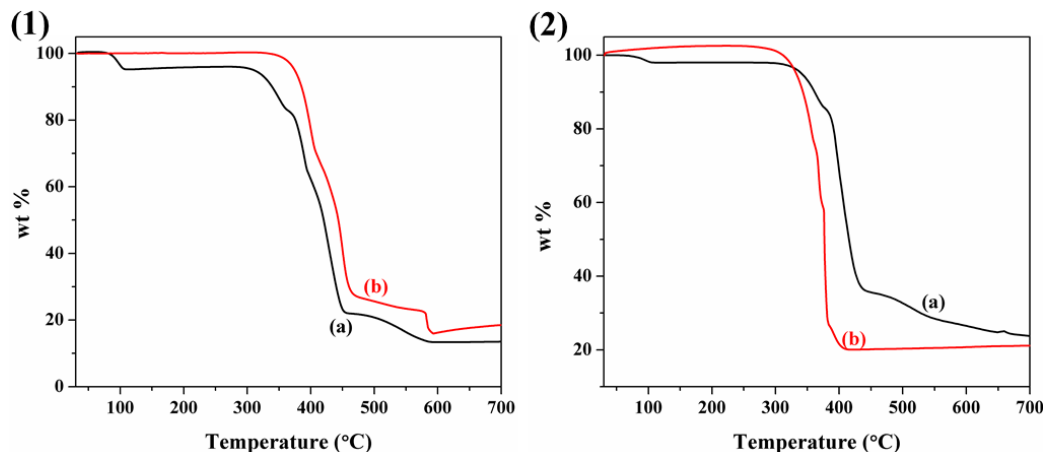


**Figure 8:** (1) TGA profile of **1** (black) and **1a** (red) recorded under N<sub>2</sub> atmosphere in the temperature range 30 – 700 °C. (2) TGA plots of compounds **1IR** (black) and **1IRa** (red) over the temperature range 30 – 700 °C under nitrogen atmosphere.

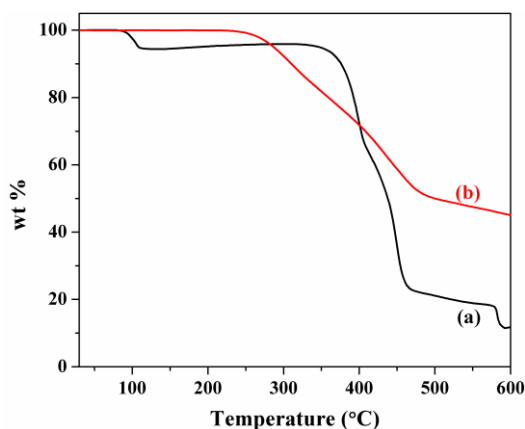


**Figure 9:** TGA plots of compound **2** (black) and **2a** (red) over the temperature range 30 to 600 °C under nitrogen atmosphere.

The discrepancy in weight loss of the bulk irradiated compound may be attributed to the fact that during photo-irradiation, some of the guest ethanol molecules were evaporated from the structure. Compound **2** (Figures 9) also loses all the guest ethanol molecules (calc. 6.2%, obs. 5.8%) at 120 °C. The desolvated frameworks are stable up to 260 – 300 °C.

The PXRD patterns of compounds **1**, **1IR** and **2** are shown in Figures 10 and 11. Good correspondence of the different peak positions in the simulated and as-synthesized patterns suggests the phase purity of the as-synthesized compounds. Powder X-ray diffraction (PXRD) patterns of **1a**, **1IRa** and **2a** were recorded after heating the sample at 90 °C under vacuum.

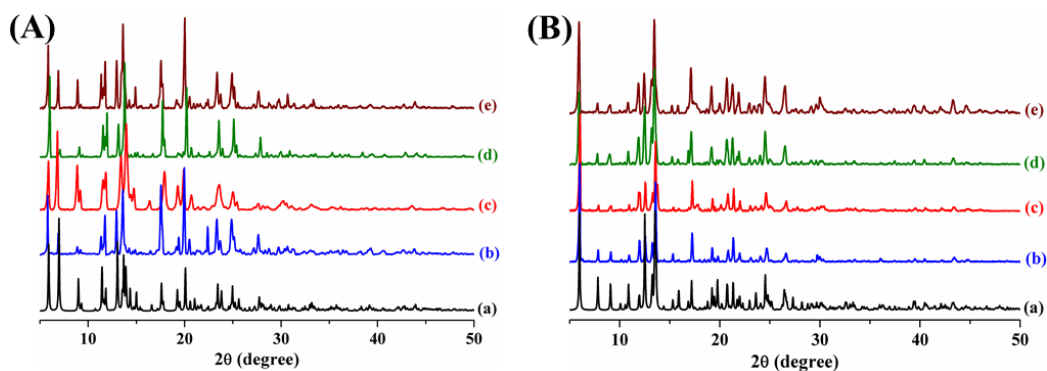


**Figure 10:** PXRD patterns of compounds **1** (A) and **1IR** (B) in different conditions; (a) simulated, (b) As-synthesized (c) activated at 90 °C, (d) exposed to ethanol vapour for 2 days and (e) exposed to water vapour for 2 days.

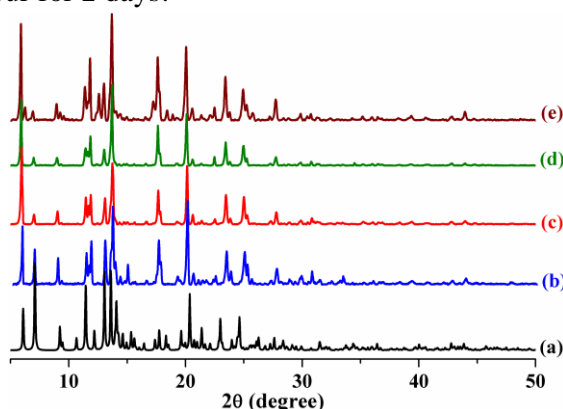


**Figure 11:** PXRD patterns of compound **2** in different conditions; (a) simulated, (b) As-synthesized (c) activated at 90 °C, (d) exposed to ethanol vapour for 2 days and (e) exposed to water vapour for 2 days.

The patterns suggest that the 2D supramolecular structure remain intact even after the removing of guest ethanol molecules. We have also exposed the dehydrated samples to water vapour which also renders structural stability in moist condition.

### 7.3.5 Gas Adsorption Study

Removal of guest ethanol molecules offers a 1D channel which encouraged us to study the permanent porosity and storage capacity of compound **1a**, **1IRa** and **2a**. N<sub>2</sub> adsorption at 77 K results a final uptake of 46 mL/g (**1a**), 47 mL (**1IRa**) and 57 mL/g (**2a**) (Figure 12). The lesser uptake at low pressure region may be attributed to the high diffusion barrier for N<sub>2</sub> molecules (3.6 Å) as the pore structure are connected with smaller tunnel as shown in figure 6a. However, with increasing pressure, gradual filling of pore was observed.



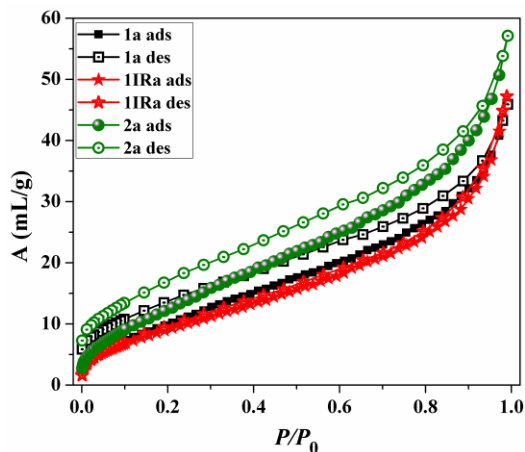


**Figure 12:** N<sub>2</sub> adsorption isotherm of compound **1a** (black square), **1IRa** (red star) and **2a** (green circle) measured at 77K.  $P_0$  is the atmospheric pressure.

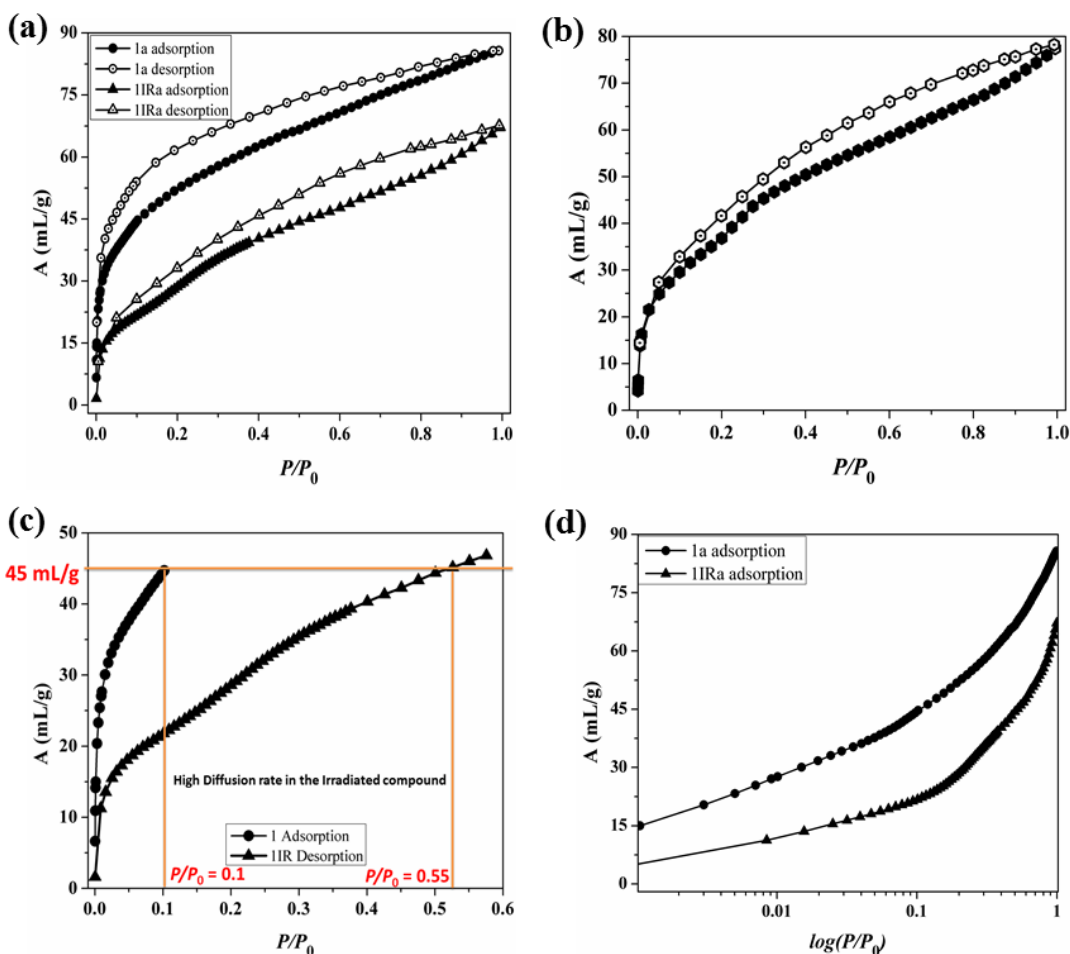


**Figure 13:** CO<sub>2</sub> adsorption-desorption isotherm (at 195 K) of (a) compound **1a** (triangle) and **1IRa** (circle); (b) compound **2a** (hexagon), (c) Comparison between the adsorption isotherms of compound **1** and **1IR** at the low pressure region. (d) Adsorption isotherm plotted in log scale.  $P_0$  is the atmospheric pressure.

On the contrary, CO<sub>2</sub> adsorption measurement at 195 K shows a typical type-I profile with a reasonable amount of uptake at low pressure regions (Figures 13 (a) and (b)). Compound **1a** and **2a** adsorbs 15 and 18 mL/g respectively at  $P/P_0 = 0.1$ . After that, a gradual increase in the uptake profile was observed with increase in pressure which ends to final amount of 68 and 77 mL/g for **1a** and **2a** respectively. Compared to **1a**, the CO<sub>2</sub> adsorption profile of compound **1IRa** shows a steeper uptake up to  $P/P_0 = 0.1$  (45 mL/g; Figure 13c). After that, a gradual increase in the uptake amount was observed which reaches to final amount of 88 mL/g. It is worth mentioning that the adsorption profile of **1IRa** is much smoother than that of **1a** which reflects that CO<sub>2</sub> molecules are experiencing lesser diffusion barrier in the irradiated compound compared to its mother compound (Figure 13d).

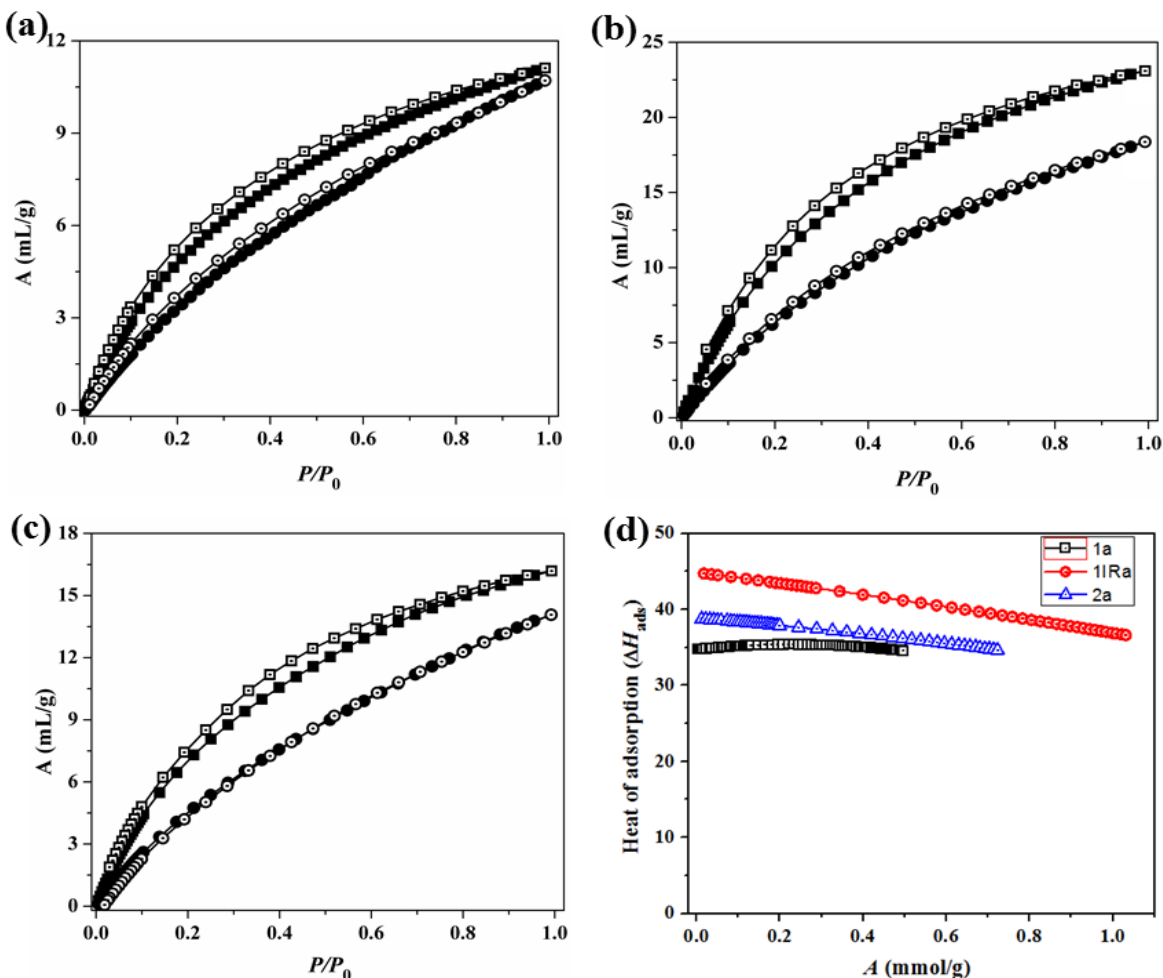


**Figure 14:** (a)-(c) CO<sub>2</sub> adsorption isotherms of compounds **1a** (a), **1IRa** (b) and **1a** (c) measured at 273 K (square) and 283 K (circle). Filled and empty symbols represent adsorption and desorption respectively. (d) Change of enthalpy of adsorption for CO<sub>2</sub> with increase of loading for **1a** (black square), **1IRa** (red circle) and **2a** (blue triangle).  $P_0$  is the atmospheric pressure.

Interesting observation was recorded when we examine the CO<sub>2</sub> capture capacity of **1a** and **1IRa** at 273 and 283 K (Figure 14a-b). At 273 K, the uptake amount of **1a** is found to be ~11 mL/g which is less compared to the amount adsorbed by **1IRa** (23 mL/g) although there is an overall decrease in the void space after photo-irradiation (Figure 6). The difference in the uptake amount at 273 K and fluorinated pore surface encouraged us to determine the CO<sub>2</sub>-MOF interaction for both the compounds. We have used a virial type expression<sup>21</sup> of the following type to fit the combined isotherm data collected at 273 and 283 K for CO<sub>2</sub>.

$$\ln(P) = \ln(A) + \frac{1}{T} \sum_{i=0}^m a_i A^i + \sum_{i=0}^n b_i A^i$$

Employing this equation on CO<sub>2</sub> adsorption isotherms measured at 273 and 283 K, we have determined the heat of adsorption which were turned out to be 35 kJ/mol and 45 kJ/mol respectively for **1a** and **1IRa** (Figure 14d). We have also measured the CO<sub>2</sub> storage capacity of compound **2a** at 273 K and 283 K which depicts an uptake amount of 17 mL/g and 13 mL/g respectively ( $Q_{st} = 38$  kJ/mol at zero coverage uptake region).

The significant increase in the  $Q_{st}$  value in case of **1IRa** can be rationalized based on the structural change after [2+2] cycloaddition reaction. The pore surfaces in **1a** and **1IRa** are embedded with -CF<sub>3</sub> functionality. But the larger pore window facilitates the inclusion of CO<sub>2</sub> molecule in the photo-modified framework. Thus CO<sub>2</sub> can easily access the adsorption sites in **1IRa** which is realized in higher  $Q_{st}$  value in the photo-modified framework. To the best of our knowledge, this is the first example where the photo-induced postsynthetic modification enhanced CO<sub>2</sub> uptake capacity based on changes on the pore structure.

### 7.3.6: Computational Study

**7.3.6.1: CO<sub>2</sub> binding energy:** Periodic DFT calculations were performed to understand and to obtain an insight into the CO<sub>2</sub> adsorption phenomenon in **1a** and **1IRa**. Calculations using the PBE-D3 method well reproduced the experimental cell parameters; hence the further calculations were done using this method. The CO<sub>2</sub> positions were identified in **1a** and **1IRa** based on the positions of the solvent molecules in the as-synthesized MOF. Furthermore, the

electron density difference maps have been calculated to delineate the nature of interaction exhibited by CO<sub>2</sub> with the framework molecular groups. This is calculated using the relation,

$$\Delta\rho = \rho_{(\text{MOF-CO}_2)} - \rho_{(\text{MOF})} - \rho_{(\text{CO}_2)}$$

where  $\Delta\rho$ ,  $\rho_{(\text{MOF-CO}_2)}$ ,  $\rho_{(\text{MOF})}$  and  $\rho_{(\text{CO}_2)}$  are the electron density difference of the system, total electron density of MOF with CO<sub>2</sub>, individual electron density of MOF and isolated CO<sub>2</sub>, respectively. The specific nature of interactions of CO<sub>2</sub> in **1a** and **1IRa** are shown in Figure 15.

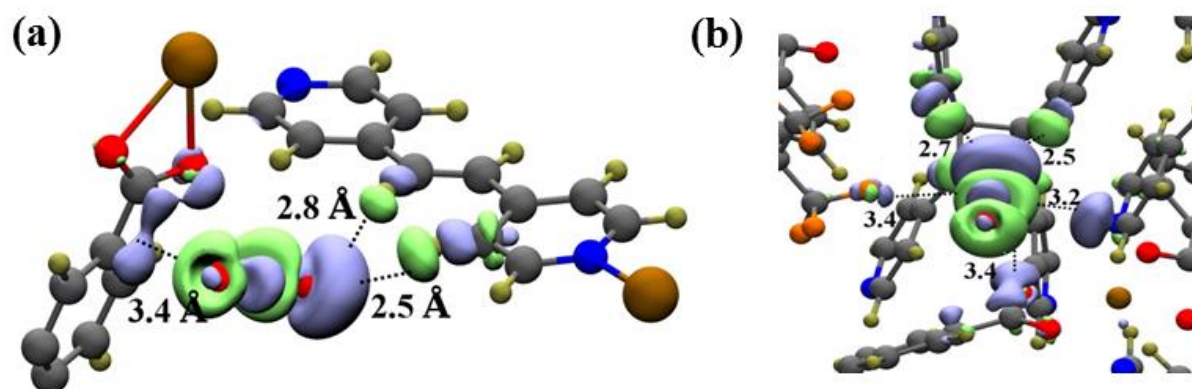


**Figure 15:** a), b) Electron density difference maps of CO<sub>2</sub> in **1a** and **1IRa** respectively. Iso-surface value is 0.0004 a.u. Blue and lime color indicate the increased and decreased electron densities brought about by adsorption of CO<sub>2</sub> in **1a** and **1IRa** respectively. These maps are calculated for the entire MOF but, only the proximal region around the CO<sub>2</sub> is shown for clarity. Color scheme: C- gray, H- tan, O- red, and Cd- Ochre.

In **1a**, there is one type of binding site, where CO<sub>2</sub> interact with  $\pi$  cloud of 4,4'-(hexafluoroisopropylidene)bis(benzoate) and hydrogen of ethylene consecutively via  $\pi\cdots\pi$  and hydrogen bond interactions. In case of **1IRa**, CO<sub>2</sub> exhibits similar type of interaction ( $\pi\cdots\pi$  and hydrogen bonding interactions) same as in **1a** along with the Lewis acid-base interactions with fluorine atom of the  $-\text{CF}_3$ . Given that there are eight and ten possible sites in **1a** and **1IRa** respectively. Thus, a maximum of eight and ten CO<sub>2</sub> molecules can be adsorbed per simulation cell of **1a** and **1IRa**, which matches with the experimental observation of 2 and 2.6 CO<sub>2</sub> molecules per formula unit of **1a** and **1IRa** respectively (a simulation cell of **1a** and **1IRa** contain the four formula units). The calculated binding energies for CO<sub>2</sub> in **1a** and **1IRa** are 35.2 kJ/mol and 44.5 kJ/mol. These values compare very well against the experimentally obtained low coverage isosteric heat of adsorption (35 and 45 kJ/mol in **1a** and **1IRa** respectively). The binding energy values are analogous to the

experimental adsorption isotherms (as shown in the Figure 13a: **1IRa** adsorbs more CO<sub>2</sub> than the **1a**).

According to adsorption isotherm (shown in Figure 13a), the uptake amount of CO<sub>2</sub> is increased upon irradiation. To study this phenomenon, we have employed adoptive biasing force method to calculate free energy of CO<sub>2</sub> on one dimensional surface in **1a** and **1IRa**. These were obtained by considering 3×2×2 super cell at 298 K.

### 7.3.6.2 Free energy calculations

Both MOFs have the one-dimensional pore along the crystallographic *b* axis. The distance was considered between one of the C atoms and the center of mass of the CO<sub>2</sub>. The projection of this distance along *b* axis is defined as the reaction coordinate. Using the colvars module in LAMMPS, ‘distance Z’ style was employed to determine such free energy profiles.

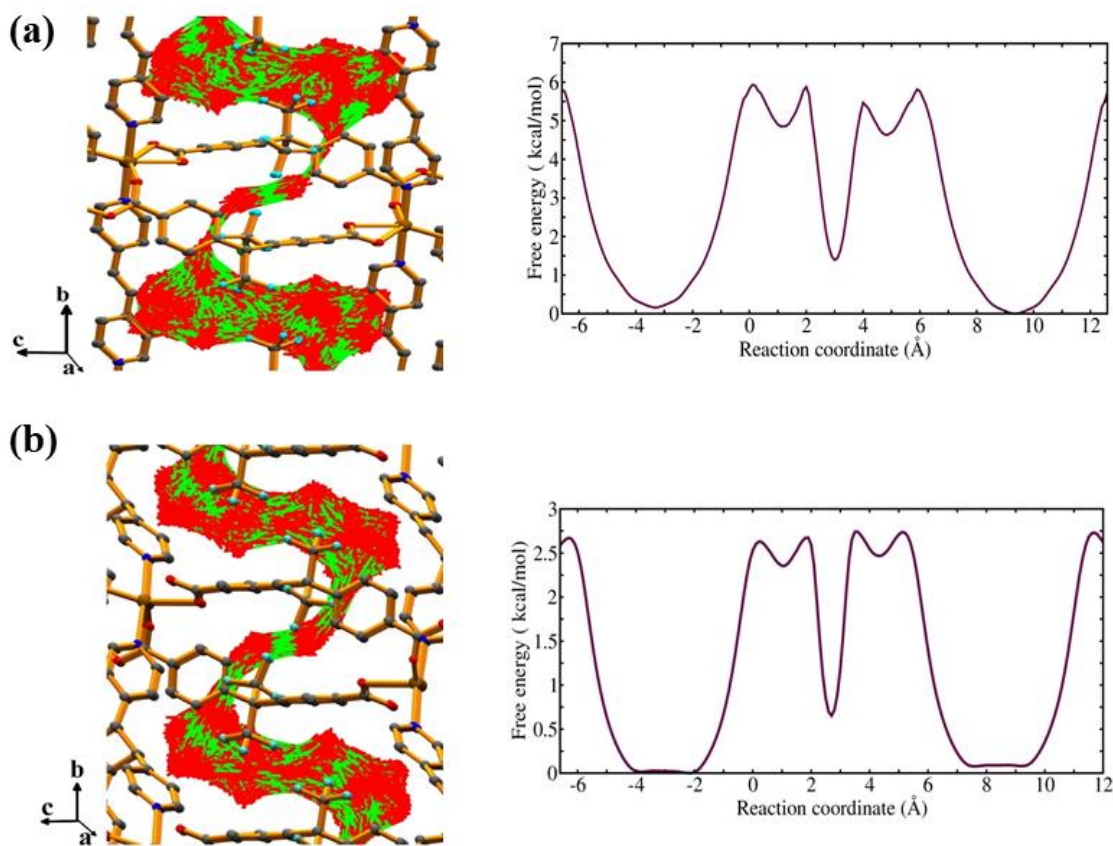


**Figure 16:** Dynamical pathways (left) and computed free energy surfaces (right) for CO<sub>2</sub> molecule in (a) **1a** and (b) **1IRa**. Vertical bars are free energies in kcal/mol at 298 K. The framework and CO<sub>2</sub> are represented as sticks. H atoms of the frameworks are hidden for the sake of clarity.

The dynamical pathway of CO<sub>2</sub> and free energy in **1a** and **1IRa** are shown in Figure 16. The movement of the CO<sub>2</sub> molecule through the pores is accompanied with energy barriers of around 2.5 kcal/mol and 6.0 kcal/mol in **1a** and **1IRa** respectively. It is thus clear that the process of irradiation broadens the pores. The same is captured through enhanced barriers in free energy for CO<sub>2</sub> in **1IRa**, relative to the values in **1a**. Thus, CO<sub>2</sub> can adsorb easily in **1IRa** than in **1a**. These results are well correlated with the experimental adsorption isotherms.

### 7.3.7 Solvent vapor adsorption and superhydrophobicity study of the compounds

To investigate the polarity of the hydrophobic group embedded pore surface, we have probed the solvent vapour adsorption study at room temperature (298 K). As expected, the water adsorption isotherms of all three compounds characteristically showed no uptake at relative higher humid condition (Figure 17). The trifling water adsorption isotherms of all the compounds is due to the weak guest–host interactions between MOF walls and water molecules as a consequence of the presence of a fluorine lining in the channel walls. The ethanol adsorption isotherms show a steep adsorption up to  $P/P_0 \approx 0.1$  which suggests a quick pore filling at low relative pressure. After that, the gradient of uptake profiles decreased with increase in pressure and finally they end up with a final volume uptake of 37 mL/g (1.2 molecule/formula unit), 39 mL/g (1.2 molecule/formula unit) and 57 mL/g (1.6 molecule/formula unit) respectively for compounds **1a**, **1IRa** and **2a** (Figure 17). The narrow channel window also restricts the inclusion of benzene molecules which is reflected from the negligible amount of uptake at saturation (Figure 17).

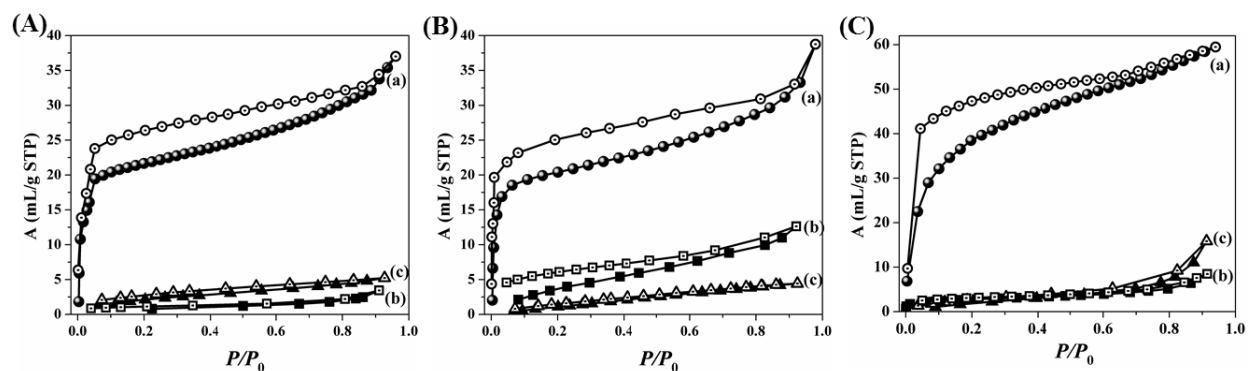


**Figure 17:** Solvent vapour adsorption (EtOH (a), C<sub>6</sub>H<sub>6</sub> (b) and H<sub>2</sub>O (c)) isotherms of compound **1a** (A), **1IRa** (B) and **2a** (C) measured at 298 K.  $P_0$  is the saturated vapour pressure of the respective solvents at measuring temperature.

The selective ethanol uptake by the dehydrated frameworks may be attributed to the presence of the ethyl group, which fits well on the hydrophobic pore surfaces decorated with the  $-\text{CF}_3$  groups.

The solvent vapour adsorption study motivates us to examine the hydrophobicity of the material. To examine its hydrophobic characteristic of the **1**, **1IR**, **2** and their dehydrated frameworks, around 20 mg of solid powders were first dispersed in 4 mL of ethanol and then coated on a glass substrate. In circle fitting mode, the contact angle for water droplet was determined to be  $150.4^\circ(\pm 1)$  (Figures 19 and 20) with a roll-off angle less than  $10^\circ$  which reflects the characteristic of a superhydrophobic solid. For each case, we have measured the contact angle in six different places on the coated plate and after that an average value has been reported. Details of the measured values have been shown in tabulated form below (Table 10-12). The depicted superhydrophobicity is because of the fact that, the surface of the material is decorated with  $-\text{CF}_3$  bond which has a high dipole moment that exhibits a strong binding with dipolar water molecules. This tends the water molecules to form a thin film via strong H-bonding interactions between the water molecules and outside the superhydrophobic surface. Formation of the water thin film leads to the prevention of water molecules from entering into the channels.<sup>12a, 22</sup>

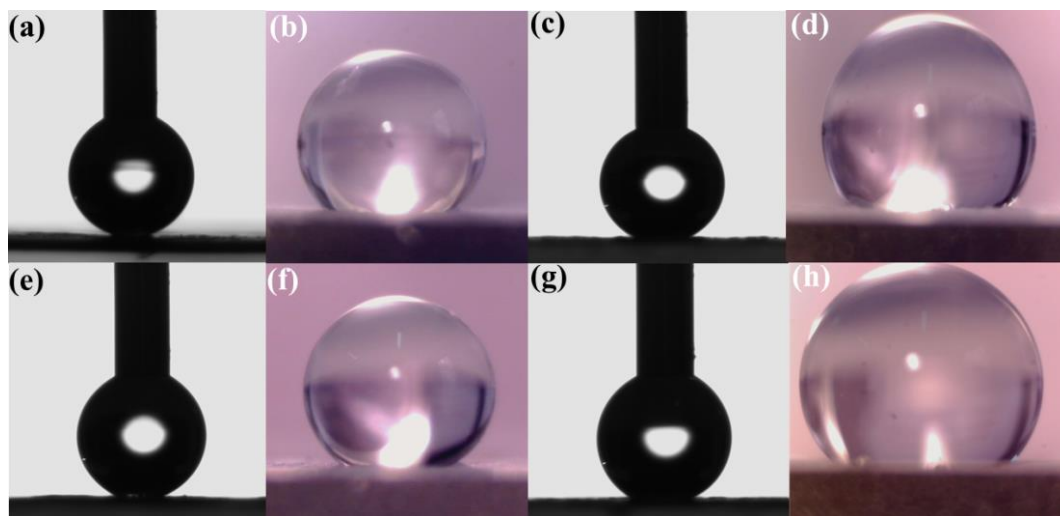


**Figure 19:** (a) (compound **1**), (c) (compound **1a**), (e) (compound **1IR**) and (g) (compound **2**). Advanced contact angle measurement using a OCA30 from Data Physics instrument (GmbH, Germany). (b), (d), (f) and (h) static contact angle measurement performed on the same substrates.

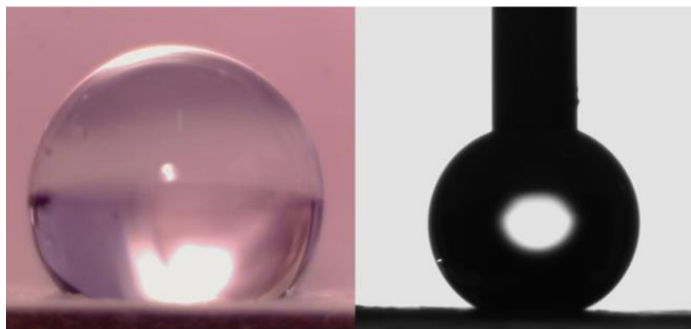


**Figure 20:** Left, static contact angle measurement of compound **2** and right, the same substrate used for advanced contact angle measurement

**Table 10:** Details value of the contact angle measurement of compound **1** and **1a**.

Compounds	Measurements	Contact angle (°)	Average Contact Angle (°)
Compound <b>1</b>	1	149.2	150.3
	2	149.1	
	3	152.1	
	4	148.9	
	5	151.1	
	6	151.8	
Compound <b>1a</b>	1	147.7	149.8
	2	149.4	
	3	150.2	
	4	149.0	
	5	151.6	
	6	151.3	

**Table 11:** Details value of the contact angle measurement of compound **1IR** and **1IRa**.

Compounds	Measurements	Contact angle (°)	Average Contact Angle (°)
Compound <b>1IR</b>	1	148.5	150.9
	2	149.2	
	3	152.8	
	4	149.1	
	5	152.0	
	6	153.9	
Compound <b>1IRa</b>	1	148.7	150.3
	2	151.9	
	3	151.2	
	4	149.3	
	5	149.5	
	6	151.3	

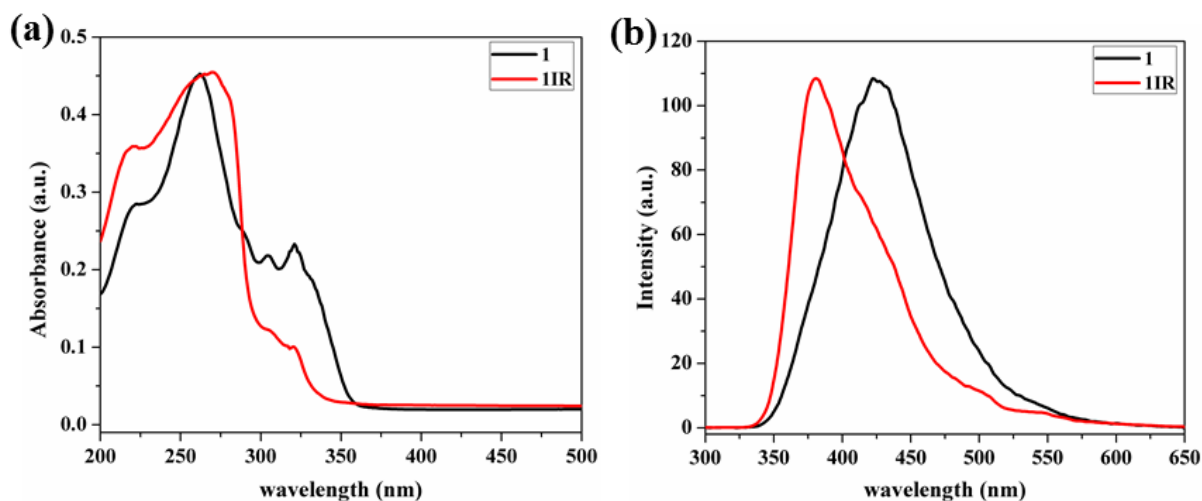


**Table 12:** Details value of the contact angle measurement of compound **2**.

Compounds	Measurements	Contact angle (°)	Average Contact Angle (°)
Compound 2	1	152.4	149.5
	2	148.8	
	3	150.1	
	4	149.3	
	5	146.7	
	6	149.6	

### 7.3.8 Photo-Physical Study

The UV-vis absorption spectrum of **1** shows a strong absorbance in the UV region with maximum at 262 nm and a distinct shoulder at around 325 nm (Figure 18a). These transitions are  $\pi \rightarrow \pi^*$  transition of bpee and hfbba from the framework and commonly observed in such  $\pi$  conjugated aromatic molecules. Upon excitation at 280 nm **1** emits in blue region with emission maximum at 422 nm. After UV irradiation of **1**, the formation of a new ligand through [2+2] cycloaddition is evident from the UV-vis and emission spectra. As the newly formed linker do not possess the similar  $\pi$  conjugated structure as that of bpee, the  $\pi \rightarrow \pi^*$  transition at  $\sim 325$  nm in the absorbance spectrum diminishes. Further, excitation at 280 nm shows a blue shifted emission compared to that of **1** with maximum at  $\sim 378$  nm indicating loss of the  $\pi$  conjugated electronic structure in the bpee linker (Figure 18b).

**Figure 18:** (a) UV-Visible spectra of compound **1** (black) and **1IR** (red line), (b) excitation at 280 nm for compounds **1** (black) and **1IR** (red line).

## 7.4: Conclusion

In conclusion, two new isomorphous superhydrophobic 2D metal-organic frameworks (MOFs) have been synthesized and structurally characterized. The superhydrophobicity was demonstrated based on contact angle measurements, which was attributed to the trifluoro methyl ( $-\text{CF}_3$ ) groups embedded surface. The dehydrated MOF structures can adsorb CO<sub>2</sub> molecules while they completely exclude water vapour. Furthermore, photo-induced post-synthetic modification of compound **1** based on [2+2] cycloaddition reaction between two bpee pillars yields photo-modified compound **1IR**. The change in pore aperture and channel structure in compound **1IR** is comprehended in enhanced CO<sub>2</sub> uptake properties at 195 K and 273 K compared to the parent compound. Furthermore, emission properties of **1** and **1IR** are also tuned by photo-modification. These results provide a roadmap for the design and synthesis of novel photoactive porous materials, where the simple strategy of [2+2] cycloaddition reaction can be utilized to tune the pore surface as well as the surface area of the material. This work demonstrated the synthesis of new generation porous materials with potential selective capture CO<sub>2</sub> in presence of moisture thus may find application in separation of CO<sub>2</sub> from flue gas.

## 7.5: References

- (a) N. Darwish, A. C. Aragonès, T. Darwish, S. Ciampi and I. Díez-Pérez, *Nano Lett.*, 2014, **14**, 7064; (b) R. Gostl, A. Senf and S. Hecht, *Chem. Soc. Rev.*, 2014, **43**, 1982; (c) Z. S. Kean, S. Akbulatov, Y. Tian, R. A. Widenhofer, R. Boulatov and S. L. Craig, *Angew. Chem. Int. Ed.*, 2014, **53**, 14508; (d) J. C. G. Walker, L. Margulis and M. Rambler, *Nature*, 1976, **264**, 620.
- (a) D. G. Patel, I. M. Walton, J. M. Cox, C. J. Gleason, D. R. Butzer and J. B. Benedict, *Chem. Commun.*, 2014, **50**, 2653; (b) J. Yu, Y. Cui, C.-D. Wu, Y. Yang, B. Chen and G. Qian, *J. Am. Chem. Soc.*, 2015; (c) H. Sato, R. Matsuda, K. Sugimoto, M. Takata and S. Kitagawa, *Nature Mater.*, 2010, **9**, 661; (d) S. Diring, D. O. Wang, C. Kim, M. Kondo, Y. Chen, S. Kitagawa, K.-i. Kamei and S. Furukawa, *Nat. Commun.*, 2013, **4**; (e) D. Hermann, H. Emerich, R. Lepski, D. Schaniel and U. Ruschewitz, *Inorg. Chem.*, 2013, **52**, 2744; (f) A. Staykov, J. Areephong, W. R. Browne, B. L. Feringa and K. Yoshizawa, *ACS Nano*, 2011, **5**, 1165; (g) A. Perrier, F. Maurel and D. Jacquemin, *Acc. Chem. Res.*, 2012, **45**, 1173.

3. (a) M. Irie, *Chem. Rev.*, 2000, **100**, 1685; (b) A. Modrow, D. Zargarani, R. Herges and N. Stock, *Dalton Trans.*, 2011, **40**, 4217; (c) S. Bernt, M. Feyand, A. Modrow, J. Wack, J. Senker and N. Stock, *Eur. J. Inorg. Chem.*, 2011, **2011**, 5378; (d) *Eur. J. Inorg. Chem.*, 2011, **2011**, 5378; (e) Y. Yokoyama, *Chem. Rev.*, 2000, **100**, 1717; (f) G. Berkovic, V. Krongauz and V. Weiss, *Chem. Rev.*, 2000, **100**, 1741; (g) D. Sud, T. B. Norsten and N. R. Branda, *Angew. Chem. Int. Ed.*, 2005, **44**, 2019.
4. (a) F. Luo, C. B. Fan, M. B. Luo, X. L. Wu, Y. Zhu, S. Z. Pu, W.-Y. Xu and G.-C. Guo, *Angew. Chem. Int. Ed.*, 2014, **53**, 9298; (b) I. M. Walton, J. M. Cox, J. A. Coppin, C. M. Linderman, D. G. Patel and J. B. Benedict, *Chem. Commun.*, 2013, **49**, 8012; (c) N. Yanai, T. Uemura, M. Inoue, R. Matsuda, T. Fukushima, M. Tsujimoto, S. Isoda and S. Kitagawa, *J. Am. Chem. Soc.*, 2012, **134**, 4501.
5. N. Yanai, K. Kitayama, Y. Hijikata, H. Sato, R. Matsuda, Y. Kubota, M. Takata, M. Mizuno, T. Uemura and S. Kitagawa, *Nature Mater.*, 2011, **10**, 787.
6. (a) M. Ohba, W. Kaneko, S. Kitagawa, T. Maeda and M. Mito, *J. Am. Chem. Soc.*, 2008, **130**, 4475; (b) S. Horike, S. Shimomura and S. Kitagawa, *Nature Chem.*, 2009, **1**, 695; (c) X. Lin, I. Telepeni, A. J. Blake, A. Dailly, C. M. Brown, J. M. Simmons, M. Zoppi, G. S. Walker, K. M. Thomas, T. J. Mays, P. Hubberstey, N. R. Champness and M. Schröder, *J. Am. Chem. Soc.*, 2009, **131**, 2159.
7. (a) J. Park, L.-B. Sun, Y.-P. Chen, Z. Perry and H.-C. Zhou, *Angew. Chem. Int. Ed.*, 2014, **53**, 5842; (b) J. W. Brown, B. L. Henderson, M. D. Kiesz, A. C. Whalley, W. Morris, S. Grunder, H. Deng, H. Furukawa, J. I. Zink, J. F. Stoddart and O. M. Yaghi, *Chem. Sci.*, 2013, **4**, 2858; (c) J. Park, D. Yuan, K. T. Pham, J.-R. Li, A. Yakovenko and H.-C. Zhou, *J. Am. Chem. Soc.*, 2011, **134**, 99; (d) S. Thies, H. Sell, C. Schütt, C. Bornholdt, C. Näther, F. Tucek and R. Herges, *J. Am. Chem. Soc.*, 2011, **133**, 16243; (e) R. Lyndon, K. Konstas, B. P. Ladewig, P. D. Southon, P. C. J. Keperter and M. R. Hill, *Angew. Chem. Int. Ed.*, 2013, **52**, 3695.
8. (a) D. Liu, Z.-G. Ren, H.-X. Li, J.-P. Lang, N.-Y. Li and B. F. Abrahams, *Angew. Chem. Int. Ed.*, 2010, **49**, 4767; (b) K. M. Hutchins, T. P. Rupasinghe, L. R. Ditzler, D. C. Swenson, J. R. G. Sander, J. Baltrusaitis, A. V. Tivanski and L. R. MacGillivray, *J. Am. Chem. Soc.*, 2014, **136**, 6778; (c) S. Dutta, D.-K. Bucar, E. Elacqua and L. R. MacGillivray, *Chem. Commun.*, 2013, **49**, 1064; (d) R. Medishetty, A. Husain, Z. Bai, T. Runčevski, R. E. Dinnebier, P. Naumov and J. J. Vittal, *Angew. Chem. Int. Ed.*, 2014, **53**, 5907; (e) R. Medishetty, L. L. Koh, G. K. Kole and J. J. Vittal, *Angew. Chem. Int. Ed.*, 2011, **50**, 10949; (f) D. Liu, H.-F. Wang, B. F. Abrahams and J.-P. Lang, *Chem. Commun.*, 2014, **50**, 3173.
9. (a) J.-K. Sun, W. Li, C. Chen, C.-X. Ren, D.-M. Pan and J. Zhang, *Angew. Chem. Int. Ed.*, 2013, **52**, 6653; (b) Y.-C. Ou, W.-T. Liu, J.-Y. Li, G.-G. Zhang, J. Wang and M.-L. Tong, *Chem. Commun.*,

- 2011, **47**, 9384; (c) G. S. Papaefstathiou, Z. Zhong, L. Geng and L. R. MacGillivray, *J. Am. Chem. Soc.*, 2004, **126**, 9158; (d) R. Medishetty, R. Tandiana, L. L. Koh and J. J. Vittal, *Chem. Eur. J.*, 2014, **20**, 1231; (e) I. Iwakura, S. Kato, R. Hino, A. Fukumoto, K. Komori-Orisaku and Y. Koide, *RSC Adv.*, 2013, **3**, 5354.
10. H. Sato, R. Matsuda, M. H. Mir and S. Kitagawa, *Chem. Commun.*, 2012, **48**, 7919.
11. (a) S. S. Kaye, A. Dailly, O. M. Yaghi and J. R. Long, *J. Am. Chem. Soc.*, 2007, **129**, 14176; (b) S. Hausdorf, J. Wagler, R. Moßig and F. O. R. L. Mertens, *J. Phys. Chem. A*, 2008, **112**, 7567; (c) H. K. Chae, D. Y. Siberio-Perez, J. Kim, Y. Go, M. Eddaoudi, A. J. Matzger, M. O'Keeffe and O. M. Yaghi, *Nature*, 2004, **427**, 523.
12. (a) C. Yang, U. Kaipa, Q. Z. Mather, X. Wang, V. Nesterov, A. F. Venero and M. A. Omary, *J. Am. Chem. Soc.*, 2011, **133**, 18094; (b) B. Xia, Z. Chen, Q. Zheng, H. Zheng, M. Deng, Y. Ling, L. Weng and Y. Zhou, *CrystEngComm*, 2013, **15**, 3484; (c) A. Santra, M. S. Lah and P. K. Bharadwaj, *Z. Anorg. Allg. Chem.*, 2014, **640**, 1134.
13. (a) N. Yanai, T. Uemura, N. Uchida, S. Bracco, A. Comotti, P. Sozzani, T. Kodani, M. Koh, T. Kanemura and S. Kitagawa, *J. Mater. Chem.*, 2011, **21**, 8021; (b) S.-i. Noro, Y. Hijikata, M. Inukai, T. Fukushima, S. Horike, M. Higuchi, S. Kitagawa, T. Akutagawa and T. Nakamura, *Inorg. Chem.*, 2013, **52**, 280; (c) P. Kanoo, S. K. Reddy, G. Kumari, R. Haldar, C. Narayana, S. Balasubramanian and T. K. Maji, *Chem. Commun.*, 2012, **48**, 8487; (d) P. S. Nugent, V. L. Rhodus, T. Pham, K. Forrest, L. Wojtas, B. Space and M. J. Zaworotko, *J. Am. Chem. Soc.*, 2013, **135**, 10950; (e) P. Deria, J. E. Mondloch, E. Tylianakis, P. Ghosh, W. Bury, R. Q. Snurr, J. T. Hupp and O. K. Farha, *J. Am. Chem. Soc.*, 2013, **135**, 16801.
14. S. V. a. SMART (V 5.628), XPREP, SHELXTL; Bruker AXS Inc. Madison, Wisconsin, USA, 2004.
15. G. M. Sheldrick, *SADABS, Empirical Absorption Correction Program, University of Göttingen, Göttingen*, 1997.
16. A. Altomare, G. Cascarano, C. Giacovazzo and A. Guagliardi, *J. Appl. Crystallogr.*, 1993, **26**, 343.
17. G. M. Sheldrick, *SHELXL 97, Program for the Solution of Crystal Structure, University of Göttingen, Germany*, 1997.
18. A. Spek, *J. Appl. Crystallogr.*, 2003, **36**, 7.
19. L. Farrugia, *J. Appl. Crystallogr.*, 1999, **32**, 837.
20. M. D. Cohen, G. M. J. Schmidt and F. I. Sonntag, *J. Chem. Soc.*, 1964, 2000.
21. (a) M. Dinca and J. R. Long, *J. Am. Chem. Soc.*, 2005, **127**, 9376; (b) J. L. C. Rowsell and O. M. Yaghi, *Angew. Chem. Int. Ed.*, 2005, **44**, 4670.

22. (a) J. C. Biffinger, H. W. Kim and S. G. DiMagno, *ChemBioChem*, 2004, **5**, 622; (b) V. H. Dalvi and P. J. Rossky, *Proc. Natl. Acad. Sci. U.S.A.*, 2010, **107**, 13603; (c) I. A. Larmour, S. E. J. Bell and G. C. Saunders, *Angew. Chem. Int. Ed.*, 2007, **46**, 1710.



## List of Publications

1. **A. Hazra**, P. Kanoo, S. Mohapatra, G. Mostafa, T. K Maji, *CrystEngComm*, 2010, 12 (10), 2775-2780
2. **A. Hazra**, P. Kanoo, TK Maji, *Chem. Commun.*, 2011, 47(1), 538-540
3. **A. Hazra**, K. L. Gurunatha, T. K. Maji, *CrystGrowthDesign*, 2013, 13 (11), 4824-4836
4. **A. Hazra**, S. Bonakala, S. K. Reddy, S. Balasubramanian, T. K. Maji, *Inorg. Chem.*, 2013, 52 (19), 11385-11397
5. N. Sikdar, **A. Hazra**, T. K. Maji, *Inorg. Chem.*, 2014, 53 (12), 5993-6002
6. K. Jayaramulu, S. K. Reddy, **A. Hazra**, S. Balasubramanian, T. K. Maji, *Inorg. Chem.* 2012, 51, 7103-7111
7. K. Jayaramulu, N. Kumar, **A. Hazra**, T. K. Maji, C. N. R Rao, *Chem. Eur. J.*, 2013, 19 (22), 6966-6970
8. S. Bhattacharyya, A. Chakraborty, K. Jayaramulu, **A. Hazra**, T. K. Maji, *Chem. Commun.*, 2014, 50 (88), 13567-13570
9. S. Choubey, K. Bhar, S. Chattopadhyay, **A. Hazra**, T. K. Maji, J. Ribas, B. K. Ghosh, *Dalton Transactions*, 2012, 41(38), 11551-11554
10. **A. Hazra** and T. K. Maji; *Manuscript Communicated*
11. **A. Hazra** and T. K. Maji; *Manuscript under preparation*
12. **A. Hazra**, S. Bonakala, K. Bejagam, S. Balasubramanian, T. K. Maji. *Manuscript Communicated*
13. **A. Hazra** and T. K. Maji. *Manuscript Under Preparation*
14. **A. Hazra**, S. Bonakala, S. Balasubramanian, T. K. Maji. *Manuscript under Preparation*
15. **A. Hazra**, A. Jain, T. K. Maji, *Manuscript under Preparation*